www.jresm.org

Research on Engineering Structures and Materials

Volume 11
Issue 3
June 2025

P-ISSN: 2148-9807 E-ISSN: 2149-4088

The International Journal of **Research on Engineering Structures and Materials (RESM**) is a peer-reviewed open access journal (p-ISSN: 2148-9807; o-ISSN: 2149-4088) published by MIM Research Group. It is published in February, April, June, August, October, and December.

The main objective of RESM is to provide an International academic platform for researchers to share scientific results related to all aspects of mechanical, civil, and material engineering areas.

RESM aims the publication of original research articles, reviews, short communications technical reports, and letters to the editor on the latest developments in the related fields.

All expenditures for the publication of the manuscripts are most kindly reimbursed by *MIM Research Group*. Thus, authors do not need to pay for publishing their studies in the journal.

The scope of the journal covers (but not limited to) behavior of structures, machines and mechanical systems, vibration, impact loadings and structural dynamics, mechanics of materials (elasticity, plasticity, fracture mechanics), material science (structure and properties of concrete, metals, ceramics, composites, plastics, wood, etc.,), nano-materials performances of new and existing buildings and other structural systems, design of buildings and other structural systems, seismic behavior of buildings and other structural systems, repair and strengthening of structural systems, case studies and failure of structural systems, safety and reliability in structural and material engineering, use of new and innovative materials and techniques in energy systems and mechanical aspects of biological systems (biomechanics and biomimetics).

The topics covered in JRESM include:

- Structural Engineering
- Mechanical Engineering
- Material Engineering
- Earthquake Engineering
- Nano-technology
- Energy Systems (Focus on Renewable)
- Biomechanics and Biomimetics
- Environment (Material and Engineering System Related Issues)
- Computer Engineering and Data Science (Material and Engineering System-Related Issues)

Abstracting and Indexing
Please visit http://www.jresm.org for more information.

Graphics and Design

Mehmet Yılmaz myilmaz@jresm.net

RESEARCH on ENGINEERING STRUCTURES & MATERIALS

Research Group

RESEARCH on ENGINEERING STRUCTURES & MATERIALS

Editorial Board

Editorial Office

Publishing Manager		
Mehmet Yılmaz	MIM Research Group	Türkiye
Language Editors		
Gaye Kuru	Uşak University	Türkiye
Mete Çal	MIM Research Group	Türkiye

Advisory Board Members

A. Abdelbary	Alexandria University	Egypt
A. Karthik	SRM Institute of Science and Technology	India
Abbasali Sadeghi	Islamic Azad University	Iran
Abdelhalim Bensaada	University of Yahia Fares of Medea	Algeria
Abdellah Douadi	Ferhat Abbas University of Setif 1	Algeria
Abdel-Nasser Sharkawy	Faculty of Engineering, South Valley University	Egypt
Abdul Haseeb Wani	Presidency University, Bengaluru	India
Abid Ustaoglu	Bartın University	Türkiye
Abrham Gebre	Addis Ababa University	Ethiopia
Ahmed Maamoun	McMaster University	Canada
Aicha Rouabeh	University of Bouira	Algeria
Alaa M. Rashad	Housing & Building National Research Center (HBRC)	Egypt
Aleksandar Ašonja	University Business Academy	Serbia
Ameer Baiee	University of Babylon	Iraq
Amirreza Sadeghi	University of Birjand	Iran
Andi Yusra	Universitas Teuku Umar	Indonesian
Andriy Huts	Rzeszow University of Technology	Poland
Anthony N. Papathanassiou	National and Kapodistrian University of Athens	Greece
Arash Rahimi	University of Perugia	Italy
Arun KK	Kumaraguru College of Technology Coimbatore	India
ARUNKUMAR K	Mangalam College of Engineering	India
Ary A. Hoyos-Montilla	Construction School at Universidad Nacional de Colombia	Colombia
Ashhad Imam	National Institute of Technology Jamshedpur	India
Ayoub Souileh	University Mohammed V	Morocco
Azad A. Mohammed	University of Sulaimani	Iraq
Azzura Ismail	Universiti Tun Hussein Onn Malaysia	Malaysia
B.P.R.V.S. Priyatham	GMR Institute of Technology	India
Badrinarayan Rath	Wollega University	Ethiopia
Bengi Gözmen Şanlı	Mersin University	Türkiye
Berrin ikizler	Ege University	Türkiye
Bilge Demir	Karabuk University	Türkiye
Cagri Yardimci	Usak University	Türkiye
Canan Kandilli	Usak University	Türkiye
Caroline S. Sobhy	Fayoum University	Egypt
Catur Harsito	Universitas Sebelas Maret	Indonesia
Chau-Khun Ma	Universiti Teknologi	Malaysia
Christopher Fapohunda	Federal University Oye-Ekiti	Nigeria
Damilola Oyejobi	University of Botswana	Botswana
Daniel Cruze	Mohamed Sathak A J College of Engineering	India
Deep Tripathi	University of Sherbrooke	Canada
Dr Abhilash P P	Indian Institute of Technology (BHU)	India
E.R. Teixeira	University of Minho	Portugal
Ebrahim Sharifi Teshnizi	Ferdowsi University of Mashhad,	Iran
Edwin Klu	Virginia Tech	USA
Elavenil S	Vellore Institute of Technology	India
Emin Erdem	Pamukkale University	Türkiye
Ercan Isik	Bitlis Eren University	Türkiye
Eric M. Lui	Syracuse University	USA
Erion Bukaci	Polytechnic University of Tirana	Albania
Erion Bukaci	Polytechnic University of Tirana	Albania
Essam H. Mohamed	South Valley University	Egypt
Fatih Ahmet Senel	Süleyman Demirel University	Türkiye
Fokruddin Ahmad	Washington State University	USA

Advisory Board Members

Gaurav Dhadse	G. H. Raisoni Institute of Engineering and Business Management Jalgaon Maharashtra	India
Ghasan Fahim Huseien	Universiti Teknologi Malaysia	Malaysia
Gökhan Gece	Bursa Teknik University	Türkiye
Gururaj Hatti	KLS VDIT	India
Gustavo Bosel Wally	Federal University of Rio Grande do Sul	Brazil
Güneş Harman	Yalova University	Türkiye
Gür Emre Güraksın	Afyon Kocatepe University	Türkiye
Haithem Boumediri	Université Constantine 1	Algeria
Hakan Sarikaya	Uşak University	Türkiye
Halit Cetiner	Isparta University	Türkiye
Hamid Saberi	University of Eyvanekey	Iran
Hamoon Fathi	Islamic Azad University	Iran
Hasan ULUS	Selcuk University	Türkiye
Hasibullah Azizi	Andhra University	India
Hayri B. Ozmen	Usak University	Türkiye
HILTON AHMAD	Universiti Tun Hussein Onn Malaysia	Malaysia
Hossein Jarrahi	University of Birjand	Iran
Hossein Kabir	University of Illinois	USA
Hüsnügül YILMAZ ATAY	Izmir Katip Celebi University	Türkiye
Irina Volokitina	Karaganda Industrial University	Kazakhstan
J. Eswari	National Institute of Technology	India
J. Paulo Davim	University of Aveiro	Portugal
J. Paulo Davim	University of Aveiro	Portugal
Javad Vaziri	University of Semnan	Iran
Jayalalitha Subbaiah	SASTRA Deemed University	India
Jesús Castro	Universitat Politecnica de Catalunya	Spain
Kabiru Mustapha	Kwara State University	Nigeria
Kamel Chaoui	Badji Mokhtar University	Algeria
Kaplan Kaplan	Kocaeli University	Türkiye
Kourosh Mehdizadeh	Islamic Azad University	Iran
Lavanya Prabha	SRM Easwari Engineering College	India
Lawrence Zahemen Tuleun	University of Ilorin	Nigeria
Leonid Dvorkin	National University of Water and Environmental Engineering	Ukraine
Lomesh Mahajan	Dr. Babasaheb Ambedkar Technological University	India
Luiz Rocha	Federal University of Rio Grande do Sul	Brazil
Lyamine Briki	University of Batna2	Algeria
M. Jafaryar	Babol Noshirvani University of Technology	Iran
Madhulika Sinha	National Institute of Technology	India
Maheswaran Muthiah	Kalasalingam Academy of Research and Education	India
Majid M.A. Kadhim	University of Babylon	Iraq
Majid Pouraminian	Islamic Azad University	Iran
Matthew Martianus Henry	Bina Nusantara University	Indonesia
Md. Golam Kibria	Rajshahi University of Engineering & Technology	Bangladesh
Md. Zia ul haq	Panjab University	India
Mehdi Khorasani	Isfahan University of Technology	Iran
Mehdi Panji	Islamic Azad University	Iran
Mehmet Kaya	Bozok University	Türkiye
Melika Mahmoodabadi	Islamic Azad University	Iran
Mevlüt Gürbüz	Ondokuz Mayıs University	Türkiye
Mihir Mishra	Texas A&M University	USA
Mohammad Lesani	University of Tehran	Iran
Mohammad. I Al Biajawi	Universiti Malaysia Pahang Al-Sultan Abdullah	Malaysia

Advisory Board Members

Mohammad Afrazi	Tarbiat Modares University	Iran
Mohammad Hossein Razmkhah	Semnan University	Iran
Mohammad Naeim Moradi	Amirkabir University of Technology	Iran
Mohammadreza Baghoolizadeh	Shahrekord University	Iran
Mohammed Jalal Al-Ezzi	University of Bilad Al-Rafidain	Iraq
Mohd Nasim	IPS Academy, Indore	India
Mohd Syahrul Hisyam Mohd Sani	Universiti Teknologi MARA (UiTM)	Malaysia
Mohsen Hajizamani	Graduate University of Advanced Technology	Iran
Moslem Paidar	Islamic Azad University	Iran
Motahhareh Nezafat Tabalvandani	Islamic Azad University	Iran
Mounika Ganta	Vignana Bharathi Institute of Technology	India
Mukaila Anifowose	Federal Polytechnic Offa	Nigeria
Murtala Namakka	Universiti Malaysia Sarawak	India
Mutluhan Akin	Nevşehir Hacı Bektaş Veli University	Türkiye
N. Arunachelam	Mepco Schlenk Engineering College	India
N.L.N. Kiran Kumar	Sri Venkateswara University	India
N.Venkata Sairam Kumar Namepalli	R.V.R & J.C College of Engineering	India
Nabil Bella	Tahri Mohamed University of Bechar	Algeria
Nahida Nazim Musayeva	Azerbaijan National Academy of Sciences	Azerbaijan
Naveen S	National Institute of Technology, Raipur	India
Nazime Seda Şaşmaz Karacan	Usak University	Türkiye
Neeraj SN	Visvesvaraya Technological University	India
Nermin Demirkol	Kocaeli University	Türkiye
Nhlanhla Nyembe	University of the Witwatersrand	South Africa
Nilesh Masne	GESCOEMSR	India
Ninu Praseetha N S		India
Ola Mazen Makki	University of Al-Qadisiyah	Iraq
Oladimeji Olatunji Ojo	Federal University of Technology Akure	Nigeria
Oleg V. Devitsky	Federal Research Centre Southern Scientific Centre of the Russian Academy of Sciences	Russia
Oleksii Hrechanyi	Zaporizhzhia National University,	Ukraine
Orhan Gülcan	General Electric Aerospace	Türkiye
Oritonda Muribwathoho	Cape Peninsula University of Technology	South Africa
P. Manoj Kumar	KPR Institute of Engineering and Technology	India
P. Marimuthu	SASTRA Deemed to be University	India
Parmo Parmo	UIN Sunan Ampel Surabaya	Indonesia
Partheeban Pachaivannan	Chennai Institute of Technology	India
Qasim M. Shakir	University of Kufa	Iraq
Qiang Ou	Chongqing University, Chongqing	China
Ramnarayan Sahu	Rajeev Gandhi Technical University	India
Rayeh Nasr Al-Dala'ien	Universiti Tenaga Nasional	Malaysia
Revathi Srinivasan	Mepco Schlenk Engineering College	India
Roberto Nascimbene	School of Advanced Studies IUSS Pavia	Italy
ROYAL MADAN	Chandigarh University	India
S. Ali Faghidian	Islamic Azad University	Iran
S. Ali Faghidian	Islamic Azad University	Iran
S. Gholizadeh	Urmia University	Iran
Saeid Foroughi	Selçuk University	Türkiye

Advisory Board Members

Sai Krishna Pinnamaneni	University of Texas at Arlington	USA
Saifulnizan Jamian	Universiti Tun Hussein Onn Malaysia	Malaysia
Saman Saadatfar	Islamic Azad University	Iran
Saman Mansouri	UNISTRAPG	Italy
Samuel Awe	Automotive Components Floby AB	India
Sangeetha Palanivelu	SSN College of Engineering	India
Sarmila Sahoo	Heritage Institute of Technology Kolkata	India
Sasikumar Palanisamy	Kumaraguru College of Technology	India
Sastri M V S S	Vasavi College of Engineering	India
Saumen Mandal	National Institute of Technology Karnataka	India
Selcuk Selimli	University of Karabük	Turkey
Serdar Gungor	Bilecik Şeyh Edebali University	Türkiye
Serkan Elcin	Pamukkale University	Türkiye
Seymur Bashirzade	Azerbaijan University	Azerbaijan
Shahazadi Begum	Baba Institute of Technology and Sciences	India
Shahrul Niza Mokhatar	Universiti Tun Hussein Onn Malaysia	Malaysia
Shaise K. John	College of Engineering Trivandrum	India
Shashi Prakash Dwivedi	G. L. Bajaj Institute of Technology & Management	India
Shoulong Zhang	Harbour Engineering Research Institute Co. Ltd.	China
Siti Aisyah Nurjannah	Universitas Sriwijaya	Indonesia
Somayyeh Pourbakhshian	Islamic Azad University	Iran
Srinivasan Anandhan	National Institute of Technology Karnataka	India
Sumanth Ratna Kandavalli	New York University	USA
Sunday Chukwuemeka	Ceramics Research and Production Dept. (CRPD)	Nigeria
Suriyaprakash Rajadesingu	SRM Institute of Science and Technology	India
Talha Taskanat	Erciyes University	Türkiye
Tasnia Ahmed	Military Institute of Science and Technology (MIST)	Bangladesh
Toufik Sebbagh	University of Skikda	Algeria
Upendra K. Mallela	Aerospace Vertical, Largy Services Limited	India
Utsav Koshti	Nirma University	India
Venkatesh Chava	CVR College of Engineering, India	India
Victor Rizov	University of Architecture	Bulgaria
Vijayasarathy Rathanasalam	ATRIA Institute of Technology	India
Vinicius Pepe	University Ritter dos Reis	Brazil
Waleed A Abbas	University of Technology	Iraq
Xiaojian Wang	Xinjiang University	China
Yamini Sreevalli I	Vellore Institute of Technology	India
Yuliang Chen	Guangxi University of Science and Technology	China
Yuvaperiyasamy M	Saveetha School of Engineering	India
Yuvaraj K	K.S.Rangasamy College of Technology	India
Zafer Kaya	Dumlupınar University	Türkiye
ZAINORIZUAN MOHD JAINI	Universiti Tun Hussein Onn Malaysia	Malaysia
Zainab Tolu Giwa	Kwara State University	India
Zeynep Ekincioğlu Küzeci	Kırşehir Ahi Evran University	Türkiye
Ziyauddin Seikh	Aliah University	India

In This Issue

Research on Engineering Structures & Materials
MIM Research Group Publications
P-ISSN: 2148-9807
E-ISSN: 2149-4088
http://www.jresm.org

ABSTRACTING / INDEXING

The international journal of Research on Engineering Structures and Materials (RESM) is currently Abstracted/Indexed by Asos Indeks, CiteFactor, Cosmos, CrossRef, Directory of Research Journal Indexing, Engineering Journals (ProQuest), EZB Electronic Journal Library, Global Impact Factor, Google Scholar, International Institute of Organized Research (I2OR), International Scientific Indexing (ISI), Materials Science & Engineering Database (ProQuest), Open Academic Journals Index, Publication Forum, Research BibleScientific Indexing Service, Root Indexing, Scopus, Ulakbim TR Index (Tubitak), Universal Impact Factor and under evaluation by many other respected indexes.

Check web site for current indexing info, www.jresm.org

Research on Engineering Structures & Materials
www.jresm.org
Research Group

Research Article

Thermal conductivity of functional fibrous inhomogeneous materials

Kriven Galina [*,a], Ryzhova Elizaveta [b]

Moscow Aviation Institute (National Research University), Russia

Article Info

Article history:

Received 27 Feb 2024
Accepted 12 May 2024

Keywords:

Modified fibrous composites;
Nanofibers;
Whiskers;
Effective thermal conductivity coefficient;
Polydisperse model;
CNT

Abstract

The study focuses on developing new methods for assessing the effective properties and modeling the thermal conductivity of fibrous composites with functional fibers for lightning protection systems on aircraft. The aim is to create more efficient and lightweight composites to enhance flight safety and reduce maintenance costs. The research methodology involves analyzing two types of whiskerized interphase layers in composites and modeling their thermal conductivity using a two-step homogenization procedure. The results indicate that composites with functional fibers can significantly outperform classical composites in terms of thermal conductivity. For composites where the whiskerized layer is formed by randomly grown and interwoven carbon nanotubes, the effective thermal conductivity in the plane perpendicular to the fiber axis and in the direction along the fiber can exceed those of classical composites by more than 2 and 1.2 times, respectively. For composites where the whiskerized layer consists of carbon nanotubes grown perpendicular to the fiber surface, these values can exceed those of classical composites by more than 3 and 1.1 times, respectively. Such findings suggest the potential use of functional composites as an effective replacement for metallic meshes in lightning protection systems on aircraft.

1. Introduction

Polymer composite materials (PCM) are widely used in aviation. Such materials are light in weight and have higher strength and stiffness values compared to materials such as aluminum, titanium and steel. For example, in the structures of Boeing 787 and Airbus A380 aircraft, the volume of PCM used in the structure reaches 50% by weight. However, polymer matrix composites are poor heat conductors, so non-conductive aircraft structures can be damaged by lightning strikes.

Lightning strikes can directly affect aircraft and sometimes cause sparks that pose a risk of igniting materials inside aircraft skins. A lightning bolt takes the path of least resistance. Therefore, if an aircraft is encountered on the way, it passes through its metal skin without penetrating inside and without touching important devices. To do this, the skin sheets must be tightly fitted to each other. In the case of using composite materials, it is necessary to apply additional technologies to protect against lightning, for example, the aircraft skin is covered with a layer of conductive copper foil mesh.

Efforts to enhance the thermal conductivity of carbon fiber and epoxy resin composites have been made in studies [1-3]. In study [4], zinc oxide particles hexagonally shaped and coated with boron nitride were introduced into the composite to increase conductivity. The thermal conductivity of such composite laminates increased by 78% and 90% at

*Corresponding author: kriven_galina@inbox.ru
[a] orcid.org/0000-0003-2340-2320; [b] orcid.org/0000-0002-3104-2743
DOI: http://dx.doi.org/10.17515/resm2024.196cs0227rs

temperatures of 25°C and 100°C, respectively. In study [5] was shown that CNT/Al composite with a layered configuration exhibits the highest thermal conductivity. When the volume fraction of CNTs is approximately 3.7%, the CNT/Al composite demonstrates an outstanding effective thermal conductivity of 400 W/m·K, representing an increase of approximately 84% compared to that of the Al alloy.

In a number of works ([1-3]), it was shown that the addition of a small amount of carbon nanotubes (CNTs) leads to a disproportionate increase in the thermal conductivity of the composite. Thus, polymer composites can be converted into conductive materials, which increases their versatility. For example, in [1] it was found that adding 1% of single-walled carbon nanotubes (SWCNTs) of the total weight to epoxy resin leads to an increase in the thermal conductivity of the material by 125% at room temperature. In [2], an increase in thermal conductivity by 55% was measured for a composite containing 7% SWCNTs of the total weight of the polymer matrix. Authors of [3] reported a 57% increase in thermal conductivity with the addition of 7% multiwalled CNTs based on the total weight of the phenolic resin. The study [6] explores carbon nanotube (CNT) reinforced composites for honeycomb sandwich structures. Results show that adding CNTs up to 0.075 wt.% increases thermal stability and energy absorption.

Technologies for obtaining modern fibrous composites with special nanostructures (whiskers) grown on the surface are being actively developed at the present time. Such whiskers can be, for example, CNTs (fuzzy fibers) [7]. Since the improvement in the properties of composites depends on the characteristics of the whiskers grown on the fiber surface, the whiskerized fiber system is functional [8-11]. It has already been shown that it is possible to obtain a composite with simultaneously improved stiffness, strength, and damping proper-ties by modifying the CNT fiber surface [12-14]. Tests in [8] showed that the whiskerization of a fiber by CNTs leads to an increase in the interfacial strength of the composite material under longitudinal shear by 206% compared to the classical fibrous composite. Similar tests carried out in [9-10], showed an increase in the interfacial strength of whiskerized composites com-pared to classical composites by 175% and 150%, respectively. And authors of [11] conducted tests to determine the longitudinal and transverse compressive strengths, and showed that the longitudinal strength of the whiskerized composite increases by 43% compared to the classical composite, and the transverse strength, in turn, increases by 94%.

The dynamic properties of modified fibrous composites containing fibers with a whiskerized layer were first studied in works [15-17]. It was assumed that the fibers and the microstructure of the whiskerized layer are elastic, and the damping properties of the composite as a whole are related to the viscoelastic properties of the matrix. It was shown that the effective loss properties of the modified composite exceeded the loss modulus of the matrix by more than 20 times. Improved aircraft performance and reduced airframe weight can be achieved with new conductive modified composite materials with whiskerized fibers, since such materials combine high mechanical, thermal, electrical and physical proper-ties.

Two types of modified composites that differ in the orientation of whiskers in the interfacial layer are considered in the proposed work: 1) a modified compo-site, in which the whiskerized interfacial layer consists of randomly located and intertwined whiskers, 2) a modified composite in which the whiskers are grown perpendicular to the fiber surface. The purpose of the study is to simulate the effective thermal conductivity of modified composites with whiskerized fibers using a method based on a polydisperse model of a medium with spherical inclusions. The problems of determining the influence of the volume content of whiskers, the thickness of the interfacial layer and the volume content of the modified fiber on the effective thermal conductivity of the studied modified

composites with whiskerized fibers are solved within the framework of the study. For the case when the interfacial layer is formed by whiskers grown perpendicular to the fiber surface, the effect of the whiskers radius and packing density (number of whiskers) on the effective thermal conductivity of the modified composite is estimated.

2. Study Description

Figure 1 shows the structure of the studied modified composite material with whiskerized fibers. The whiskerized interfacial layer is a nanocomposite that consists of whiskers and a matrix.

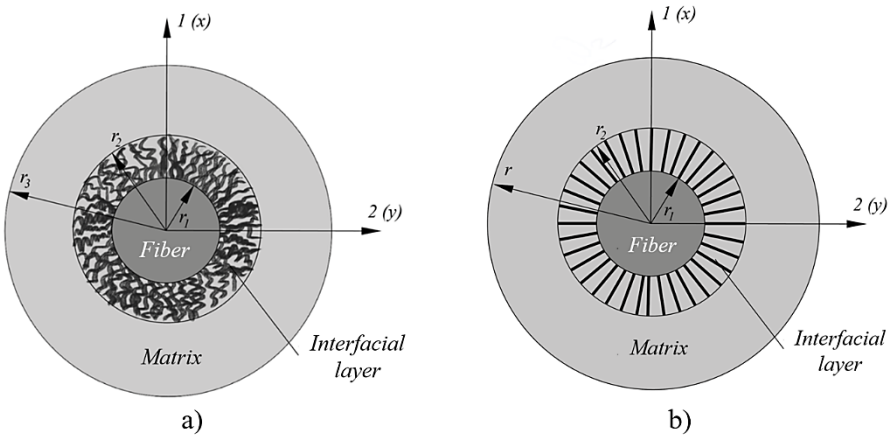

Fig. 1. Structure of modified composite material with whiskerized fibers: a) whiskers are arranged randomly and intertwined (case 1), b) whiskers are grown perpendicular to the fiber surface (case 2)

When modeling the effective thermal conductivity of such composites, we assume that the composite has a transversally isotropic structure with an isotropy plane across the fiber. Fiber and matrix are isotropic materials. In the case when the whiskers are randomly located in the interfacial layer and intertwined with each other (Fig. 1a), the whiskerized interfacial layer is also considered an isotropic material. And in the case when the whiskers are grown perpendicular to the surface of the base fiber (Fig. 1b), we consider that the whiskerized interfacial layer corresponds to a transversely isotropic material with an isotropy plane across the whiskers (case 2). Kriven, Shavelkin [18] study a fiber with a whiskered layer of CNTs grown randomly and intertwined. Carbon fiber with CNT whiskers grown perpendicular to the fiber surface was demonstrated in study [19].

The two-stage homogenization procedure is used to determine the effective thermal conductivity of the modified composite. At the first stage, the effective coefficient of thermal conductivity of the whiskerized layer is determined. The effective thermal conductivity coefficient of the whiskerized layer is determined using the polydisperse model of the medium in the case when it is assumed that the whiskerized layer is a macroscopically isotropic heterogeneous medium. And the effective thermal conductivity coefficient of the whiskerized layer is determined using a polydisperse model of a medium with cylindrical inclusions in the case when the whiskered layer is considered as a transversely isotropic material with an isotropy plane across the whiskers. When determining the effective thermal conductivity coefficient of such a composite, the volumetric content of whiskers in the interfacial layer is found taking into account all the geometric and physical parameters of the whiskers layer - the length of whiskers, their

density, diameter, and thermal conductivity coefficient. After determining the effective thermal conductivity of the whiskerized interfacial layer, the effective thermal conductivity of the whiskered fibrous composite is found. For this, a polydisperse model of a medium with cylindrical inclusions, extended to a multiphase medium, is used.

A comparative evaluation of the effective thermal conductivity coefficients of modified composites with whiskerized fibers with the effective thermal conductivity coefficients of similar classical composites is carried out. The studied composites are formed by T-650 [20] carbon fiber and an epoxy matrix with thermal conductivity coefficients indicated in Table 1. In the modified composite, CNTs are grown on the surface of the carbon fiber. The influence of the volumetric content of inclusions (whiskers) on the effective thermal conductivity coefficient of the interfacial layer, as well as the influence of the thickness of the whiskerized layer, the volumetric content of whiskers and the volumetric content of modified fiber on the effective thermal conductivity of the entire composite is assessed. The volumetric content of whiskers in the interfacial layer and the volumetric content of modified fiber in the composite vary from 0 to 78%.

3. Effective Thermal Conductivity Coefficient Of The Studied Composite

The effective thermal conductivity of the modified whisker fiber composite is determined using a two-stage homogenization procedure. At the first stage, the effective coefficient of thermal conductivity of the whiskerized layer is determined.

In the case when the whiskerized layer is considered as an isotropic material, the effective thermal conductivity coefficient s determined by the well-known equation [21] for a three-phase model of a medium with spherical inclusions:

$$k_2^{(1)} = k_M \left(1 + \frac{C_0}{(1 - C_0)/3 + k_M / k_1 - k_M)}\right) \tag{1}$$

where, $c_0 = a^3/b^3$: volume content of whiskers in the whiskerized interfacial layer, a: radius of the whiskers, b: radius of the shell from the matrix, k_1: thermal conductivity of the whiskers, k_m: thermal conductivity of the matrix.

In the case when the whiskerized layer is considered as a transversally isotropic material with the symmetry axis directed along the 1 axis, the Fourier heat conduction law can be written:

$$\begin{aligned} q_i{}^{(2)} &= -k_{ij}{}^{(2)} T_{,j}{}^{(2)} \\ q_i{}^{(2)} &= -k_{ij}{}^{(2)} \theta_{,j}{}^{(2)} \end{aligned} \tag{2}$$

where, q_i: heat flux vector in the whiskerized interfacial layer, $k_{ij}{}^{(2)}$: tensor of thermal conductivity coefficients in the whiskerized interfacial layer, $\theta_{,j}{}^{(2)}$: temperature in the whiskerized interfacial layer. In the last equation, only two components $k_{ij}{}^{(2)}$ are independent:

$$\begin{bmatrix} q_1^{(2)} \\ q_2^{(2)} \\ q_3^{(2)} \end{bmatrix} = \begin{bmatrix} -k_{11}{}^{(2)} & 0 & 0 \\ 0 & -k_{22}{}^{(2)} & 0 \\ 0 & 0 & -k_{33}{}^{(2)} \end{bmatrix} \begin{bmatrix} \theta_{,1}{}^{(2)} \\ \theta_{,2}{}^{(2)} \\ \theta_{,3}{}^{(2)} \end{bmatrix} \tag{3}$$

Then the effective thermal conductivity in the axial direction $k_{11}{}^{(2)}$ is determined by the mixture rule [4]:

$$k_{11}^{(1)} = \sum_{n=1}^{N} c_n k_n \tag{4}$$

where, N: number of phases with volume fractions c_n and thermal conductivity coefficients k_n. The effective thermal conductivity coefficient in the plane perpendicular to the whiskers axis $k_{33}^{(2)}$ is determined by the equation:

$$k_{33}^{(2)} = k_M\left(1+\frac{c_0^{(2)}}{(1-c_0^{(2)})/2+k_M/(k_I-k_M)}\right) \tag{5}$$

The volumetric content of whiskers in the whiskerized layer is determined by the equation:

$$c_0^{(2)} = \frac{M_b^2 d_b^2}{4\pi\left(l_b+D\right)D} \tag{6}$$

where, $c_0^{(2)}$: volume content of whiskers in the whiskerized interfacial layer in the case when the whiskers are grown perpendicular to the fiber surface, M_b: number of whiskers grown on the fiber surface, d_b: whiskers diameter, l_b: whiskers length, D: base fiber diameter. Taking into account the geometric features of the whisker layer, in which the whiskers are grown perpendicular to the fiber surface, it must be taken into account that the number of whiskers is limited:

$$M_b \le \pi D / d_b \tag{7}$$

At the second stage, the effective thermal conductivity of the entire composite is determined. In view of the transversal isotropy of the modified composite with the symmetry axis directed along the 3 axis, the Fourier heat conduction law can be written as:

$$\begin{aligned} q_i &= -k_{ij}T_{,j} \\ q_i &= -k_{ij}\theta_{,j} \end{aligned} \tag{8}$$

where, q_i: heat flux vector, k_{ij}: tensor of thermal conductivity coefficients, θ: temperature. Only two components k_{ij} are independent in the last equation:

$$\begin{bmatrix} q_1 \\ q_2 \\ q_3 \end{bmatrix} = \begin{bmatrix} -k_{11} & 0 & 0 \\ 0 & -k_{11} & 0 \\ 0 & 0 & -k_{33} \end{bmatrix} \begin{bmatrix} \theta_{,1} \\ \theta_{,2} \\ \theta_{,3} \end{bmatrix} \tag{9}$$

The effective thermal conductivity in the axial direction k_{33}^{eff} is determined by the mixture rule:

$$k_{33}^{eff(i)} = \sum_{n=1}^{N} c_n k_n \tag{10}$$

where the index (i) corresponds to the considered case of the symmetry of the whiskerized interfacial layer. The following condition must be satisfied at infinity:

$$\theta\big|_{r\to\infty} \to \beta x_1 \tag{11}$$

where β is the temperature gradient. The stationary equations of heat conduction in the components of the composite have the form:

$$\begin{aligned}
&\nabla^2\theta^1 = 0, \quad && 0 \le r \le r_1,\\
&\nabla^2\theta^2 = 0, \quad && r_1 \le r \le r_2,\\
&\nabla^2\theta^3 = 0, \quad && r_2 \le r \le r_3,\\
&\nabla^2\theta^{eff} = 0, \quad && r_3 \le r \le \infty,
\end{aligned} \tag{12}$$

where θ^1, $\theta^2, \theta^3, \theta^{eff}$ are the temperatures in the fiber, the whiskerized interfacial layer, the matrix, and the effective medium, and ∇ is the Laplace operator. In a cylindrical coordinate system with axial symmetry with respect to x_3 we have:

$$\nabla = \frac{\partial^2 u}{\partial r^2} + \frac{1}{r}\frac{\partial u}{\partial r} + \frac{1}{r^2}\frac{\partial^2 u}{\partial \varphi^2} + \frac{\partial^2 u}{\partial z^2} \tag{13}$$

Then solution (12) with $r \to \infty, \theta_2(r,\theta) \to \beta r\cos\theta$ has the form:

$$\begin{aligned}
&\theta^1 = A_1 r\cos\theta, && 0 \le r \le r_1,\\
&\theta^2 = (A_2 r + \frac{B_2}{r})\cos\theta, && r_1 \le r \le r_2,\\
&\theta^3 = (A_3 r + \frac{B_3}{r})\cos\theta, && r_2 \le r \le r_3,\\
&\theta^{eff} = (A_{eff} r + \frac{B_{eff}}{r})\cos\theta, && r_3 \le r \le \infty,
\end{aligned} \tag{14}$$

It is assumed that a uniform field is realized at infinity, which corresponds to $B_{eff} = 0$ with a unit heat flux $A_{eff} = 1$ [21-22]. To write the boundary conditions, we assume that the heat fluxes are also continuous at the phase boundary. Six unknowns, including the effective thermal conductivity k_{eff}, are determined from a system of six equations:

$$\begin{aligned}
&1)\ \theta^I - \theta^2 = 0, && r = r_1,\\
&2)\ \theta^2 - \theta^3 = 0, && r = r_2,\\
&3)\ \theta^3 - \theta^{eff} = 0, && r = r_3,\\
&4)\ -k_1\frac{\partial\theta^1}{\partial r} + k_2^{(i)}\frac{\partial\theta^2}{\partial r} = 0, && r = r_1,\\
&5)\ -k_2^{(i)}\frac{\partial\theta^2}{\partial r} + k_3\frac{\partial\theta^3}{\partial r} = 0, && r = r_2,\\
&6)\ -k_3\frac{\partial\theta^3}{\partial r} + k_{11}^{eff\,(i)}\frac{\partial\theta^{eff}}{\partial r} = 0, && r = r_3,
\end{aligned} \tag{15}$$

Thus, in the case of a whiskerized interfacial layer with isotropic properties $k_2^{(i)} = k_2^{(1)}$ (1), and in the case of a whiskerized interfacial layer with transversally isotropic properties $k_2^{(i)} = k_{33}^{(2)}$ (4).

The solution of the system of equations (15) taking into account (14) with respect to $k_{11}^{eff\,(i)}$ has the form:

$$k_{11}^{eff(i)} = -k_3\left(2 - \frac{3}{1 + D/(k_1k_3m - k_1k_2^{(i)}n + (k_2^{(i)})^2 m - k_2^{(i)}k_3n)}\right) \quad (16)$$

where $m = (-2+l)l$, $n = 2+(-2+l)l$, $l = r_2 - r_1$ is the thickness of the interfacial layer, $D = k_1k_3c_{vol}a + k_1k_2^{(i)}c_{vol}b - (k_2^{(i)})^2 c_{vol}a - c_{vol}k_2^{(i)}k_3b$. Thus, the effective thermal conductivity coefficients of the whiskered layer ($k_2^{(1)}, k_{11}^{(2)}, k_{33}^{(2)}$) and the modified composite with whiskered fibers in the direction along the fiber $k_{33}^{eff(i)}$ and in the plane perpendicular to the fiber axis $k_{11}^{eff(i)}$ are determined.

4. Results and Discussion

The effective thermal conductivity of the modified composite with whiskerized fibers was determined using a two-stage homogenization procedure. In the first stage, the effective properties of the whiskerized interfacial layer were determined.

This study investigated the influence of the volume content of inclusions (whiskers) on the effective thermal conductivity of the interfacial layer formed by grown CNTs in two versions. The first variant of the interfacial layer is formed by randomly grown, intertwined CNTs, considered as an isotropic material. The second variant of the interfacial layer is formed by CNTs grown perpendicular to the fiber surface, considered as a transversely isotropic material. The properties of the structural elements of the interfacial layer are shown in Table 1.

Table 1. Physical properties of structural elements of a modified composite with whiskerized fibers [20, 23.24]

	Carbon fiber T-650	CNT	Epoxy Matrix
Thermal conductivity coefficient (W/(m·K))	14	3000	0.195-0.255

The effective thermal conductivity of the interfacial layer, considered as an isotropic material, was determined by equation (1). The effective thermal conductivity coefficients of the interfacial layer, considered as a transversally isotropic material, were determined by equations (4) and (5).

The effective thermal conductivity coefficient of the interfacial whiskerized layer in the plane perpendicular to the fiber surface (case 2), as the volume content of the inclusion increases, grows commensurately with the increase in the effective thermal conductivity coefficient of the interfacial whiskerized layer, considered as an isotropic material (case 1) (Figure 3). And the effective thermal conductivity of the interfacial whiskerized layer in the direction along the whiskers (case 2) rapidly increases with the increase in the volume content of CNTs (Figure 4) - more than 12,000 times compared to the thermal conductivity of the matrix. However, in the direction across the whiskers, the whiskerized layer formed by interwoven whiskers allows achieving an effective thermal conductivity exceeding that in the whiskerized layer formed by whiskers grown perpendicular to the fiber by more than 1.5 times. But in the direction along the whiskers, in the case where whiskers intertwine, the effective properties of the whiskerized layer (case 1) remain the same as in the direction across the whiskers, while the properties of the whiskerized layer formed by whiskers grown perpendicular to the fiber (case 2) increase by more than 1000 times compared to the effective properties of the whiskerized layer formed by interwoven

whiskers (case 1). The effective thermal conductivity of the whiskerized layer with a low volume fraction (up to 2.5%) of randomly oriented and interwoven whiskers (case 1) is approximately 0.2-0.3 W/(m·K), which corresponds to the experimental results obtained in [4].

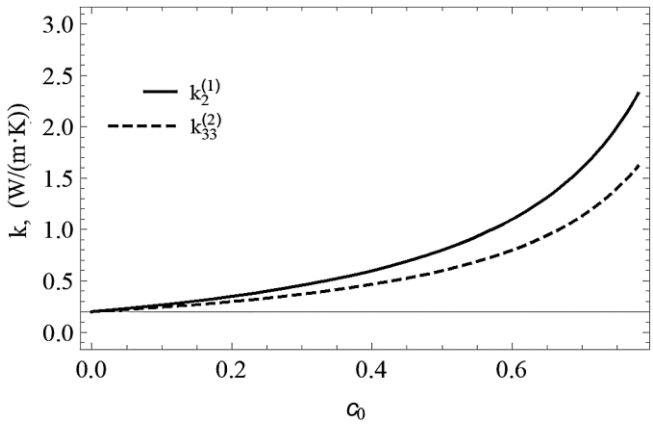

Fig. 2. Dependence of the effective thermal conductivity coefficient (in the direction along the fiber axis) on the volume content of CNTs in the interfacial layer

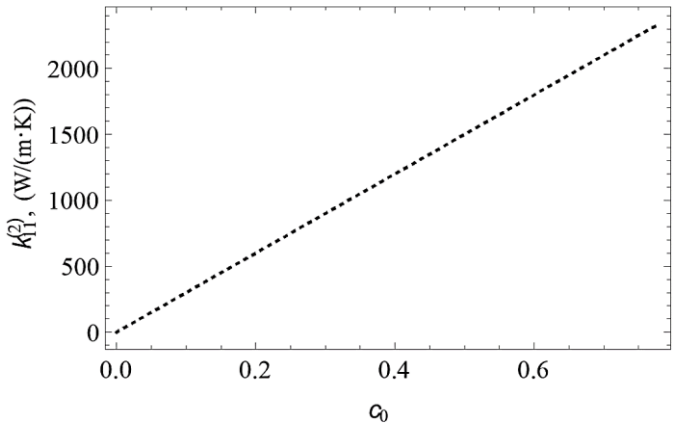

Fig. 3. Dependence of the effective coefficient of thermal conductivity in the direction along the CNT of a transversally isotropic layer on the volume content of CNTs in the interfacial layer

The effective thermal conductivity coefficient for a modified composite with whiskerized fibers, consisting of T-650 carbon fiber, CNTs, and an epoxy matrix, has been studied. The properties of the structural elements of such a composite are shown in Table 1. For the cases where the whiskerized layer is a macroscopically isotropic heterogeneous medium and when the whiskered layer is a transversely isotropic medium, the effective thermal conductivity coefficient in the plane perpendicular to the fiber axis was obtained using equation (16), and the effective thermal conductivity coefficient in the direction along the fiber axis was obtained from equation (10).

It is necessary to evaluate the effect of the thickness of the whiskerized layer on the effective thermal conductivity of the composites under consideration. For this, we consider

a composite with a constant modified fiber radius $r_2 = 1$, the thickness of the whiskerized interfacial layer Δ / r_2, and the matrix radius r_3 depending on the volume content of the modified fiber $r_3 = r_2 / \sqrt{c_{vol}}$ at $c_{vol} = 78\%$ and $c_0 = 78\%$ characteristic of the most dense packing of inclusions in a square periodic structure. Figure 5 shows the plots of effective thermal conductivity coefficients in the plane perpendicular to the fiber axis $k_{11}^{eff(i)}$ and in the direction along the fiber axis $k_{33}^{eff(i)}$ on the thickness of the whiskerized layer Δ / r_2.

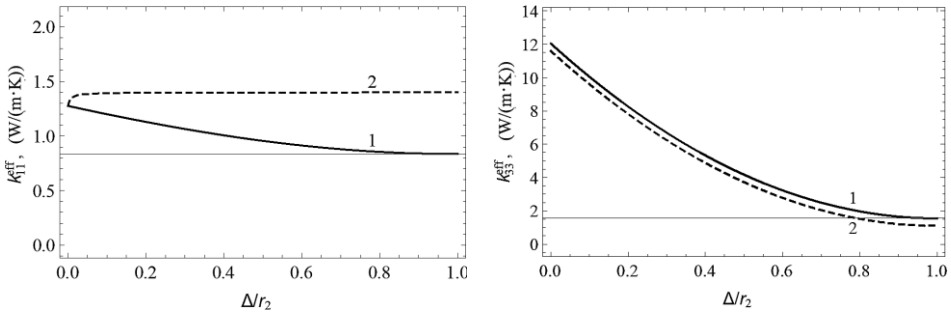

(a) (b)

Fig. 4. Graphs of dependences of effective thermal conductivity coefficients on the thickness of the whiskered layer: a) $k_{11}^{eff(i)}$ - in the plane perpendicular to the fiber axis, b) $k_{33}^{eff(i)}$ - in the direction along the fiber axis

In Figure 5 and all subsequent figures, the graph corresponding to the case when the whiskerized interfacial layer is an isotropic medium is indicated by the number 1, and the graph corresponding to the case when the whiskerized interfacial layer is a transversely isotropic medium is indicated by the number 2.

Figure 5a illustrates that the effective thermal conductivity in the plane perpendicular to the fiber surface remains practically unchanged for the case when the whisker layer is a transversely isotropic medium, regardless of the thickness of the whisker layer. However, for the case when the whisker layer is an isotropic medium, there is a slight decrease in the thermal conductivity coefficient as the thickness of the whisker layer increases. In Figure 5b, the decrease in the effective thermal conductivity in the direction along the fiber is shown as the thickness of the whisker layer increases for both considered cases.

Since the study involved a fixed radius of modified fibers, the decrease in the effective thermal conductivity is associated with the replacement of fibers by a whiskerized layer with a low thermal conductivity matrix. The effect of reducing the effective thermal conductivity is observed only in case 2 in the plane perpendicular to the fiber axis because in such a composite, the effective properties of the whiskerized layer in the direction across the fiber axis (along the whisker axis) significantly exceed the properties of the carbon fiber (Figures 2 and 3), and there is no substitution of a high thermal conductivity layer with a low thermal conductivity layer. From the perspective of achieving stable high values of the effective thermal conductivity in both considered directions, case 2 is preferred, where short fibers are grown perpendicular to the fiber surface.

The influence of the volume content of whiskers on the effective thermal conductivity of the modified composite is shown in Figure 6. When plotting graphs (Figure 6), the fixed values were the thickness of the whiskerized layer ($0{,}2\Delta / r_2$) and the volume content of the modified fiber c_{vol}= 75%.

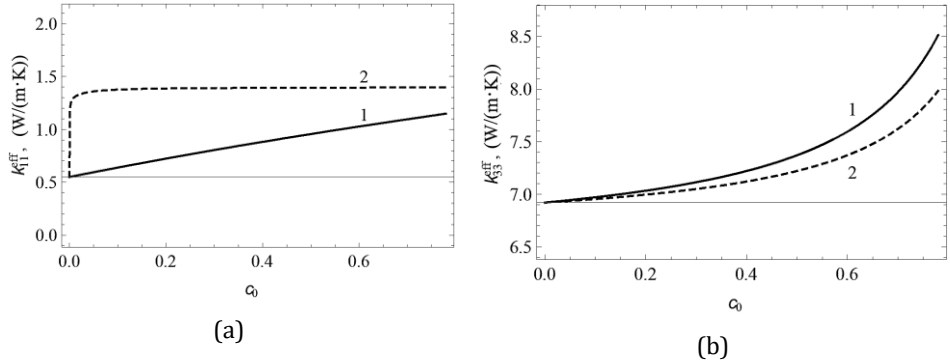

(a) (b)

Fig. 5. Graphs of dependences of effective thermal conductivity coefficients on the volume content of CNTs in the whiskerized interfacial layer: a) $k_{11}^{eff(i)}$ - in the plane perpendicular to the fiber axis, b) $k_{33}^{eff(i)}$ - in the direction along the fiber axis

Figure 6a shows that even with a slight increase in the volume content of whiskers in the interfacial layer of the composite with CNTs grown perpendicular to the fiber surface, the effective thermal conductivity coefficient in the plane perpendicular to the fiber axis is more than 2 times higher than the thermal conductivity coefficient of the classical composite (the value on the graph at $c_0 = 78\%$) with the same volumetric fiber content ($c_{vol} = 78\%$). At the same time, these properties remain stable with a further increase in the volume content of CNTs in the interfacial layer. In the direction along the fiber, the composite with CNTs grown randomly and intertwined with each other demonstrates slightly higher effective thermal conductivity than the composite with CNTs grown perpendicular to the fiber surface (Figure 6b). The effective thermal conductivity simultaneously takes the highest values in both considered directions with the maximum volume fraction of whiskers in the whiskerized interphase layer. However, in the plane perpendicular to the fiber axis, the effective thermal conductivity for case 2 exceeds that for case 1 by more than 1.2 times, while in the direction along the fiber axis, the effective thermal conductivity for case 1 exceeds that for case 2 by more than 1.06 times. This is because in the direction along the fiber axis, which corresponds to the direction across the whisker axis, the properties of the whiskerized layer formed by both whiskers grown perpendicular to the fiber and randomly grown whiskers differ, but not as significantly as in the direction perpendicular to the fiber axis, which corresponds to the direction along the whisker axis (Figures 2 and 3). Therefore, the optimal structure of the modified composite with whiskerized fibers can be considered as the composite with the maximum possible volume fraction of whiskers grown perpendicular to the fiber (case 2).

When constructing graphs (Figure 7), the volume content of CNTs in the interfacial layer was a fixed value equal to $c_0 = 70\%$ and the length of the whiskers was also a fixed value equal to $0{,}2\Delta / r_2$. Figure 7 also plots the dependence of the effective coefficient on the volumetric fiber content in the classical composite.

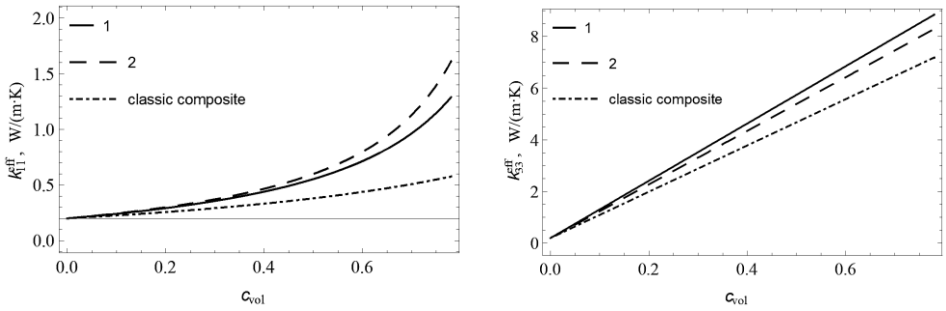

(a) (b)

Fig. 6. Graphs of dependences of effective thermal conductivity coefficients on the volume content of the modified fiber: a) $k_{11}^{eff(i)}$ - in the plane perpendicular to the fiber axis, b) $k_{33}^{eff(i)}$ - in the direction along the fiber axis

It can be seen (Figure 7) that at the maximum volume content of the modified fiber $c_{vol} = 78\%$ it is possible to achieve a significant increase in the effective thermal conductivity coefficients in the plane perpendicular to the fiber axis compared to the effective thermal conductivity coefficients of similar classical composites (more than 2 times for case 1 and more than 3 times for case 2). In such composites, the matrix layer with a low thermal conductivity is practically absent, and the role of the binder is performed by the whiskerized layer, the effective thermal conductivity properties of which depend on how this whiskerized layer is formed. In the plane perpendicular to the fiber axis, the effective thermal conductivity for case 2 exceeds that for case 1 by more than 1.2 times, while in the direction along the fiber axis, the effective thermal conductivity for case 1 exceeds that for case 2 by more than 1.01 times. Therefore, the optimal structure of the modified composite with whiskerized fibers can be considered as a composite with the maximum volume fraction of modified fibers, in which the modification is carried out by growing whiskers perpendicular to the fiber surface (case 2).

Let us consider a specific example of a modified composite consisting of a 5 μm diameter carbon fiber and carbon nanotubes grown perpendicular to the fiber surface. The geometric parameters include whisker lengths ranging from 1 to 2 μm and whisker diameters ranging from 0.00051 to 0.00085 μm [19], [23]. The physical properties of the composite under study are provided in Table 1. According to equation (7), with a whiskers diameter of 0.00051 μm, the maximum number of whiskers grown perpendicular to the fiber surface is 30 799, and with a whiskers diameter of 0.00085 μm, the maximum number of whiskers is 18,480. With a whiskers length of 1 μm, this is corresponding to the volumetric content of whiskers in the interfacial layer 65%, and with a whiskers length of 2 μm - 56% (eq. 6). It has already been shown (Figure 4) that an increase in the length of the whiskers (thickness of the whisker layer) negatively affects the effective thermal conductivity in the direction along the fiber. It has also been shown that an increase in the volume content of the modified fiber is accompanied by an increase in the effective thermal conductivity in all directions (Figure 7). Therefore, having fixed the minimum possible CNT length equal to 1 μm and the maximum possible volume content of the modified fiber $c_{vol} = 78\%$, we estimate the effect of the number of whiskers on the effective thermal conductivity of the composite under study.

Figure 8 shows the dependences of the effective thermal conductivity coefficients on the number of whiskers associated with the whiskers diameters. It can be seen (Figure 8 a) that the effective thermal conductivity in the plane perpendicular to the fiber axis grows rapidly as the number of whiskers increases, but when the number of whiskers reaches a certain value (in this case, 5000 whiskers), the effective thermal conductivity in the plane perpendicular to the fiber axis remains practically unchanged at further increase in the number of whiskers. Also, the effective thermal conductivity in the plane perpendicular to the fiber axis is not significantly affected by the whiskers diameter. And in the direction along the fiber axis (Figure 7b), the following trend is observed: an increase in the thermal conductivity coefficient is achieved only with simultaneous increases in the number and diameter of the whiskers, as only in this case can a dense packing of whiskers with a high thermal conductivity coefficient be obtained. Otherwise, the space between the whiskers in the whiskerized layer is occupied by a matrix with a low thermal conductivity coefficient, which leads to a decrease in the effective thermal conductivity of the whiskerized interphase layer in the direction perpendicular to the whiskers, and consequently, to a decrease in the effective thermal conductivity of the entire composite in the direction along the fiber axis. Therefore, if it is important to maintain high values of the effective thermal conductivity coefficient in the direction along the fiber axis, it is necessary to select the number of whiskers taking into account their diameter so that the volume fraction of whiskers in the whiskerized layer is maximum (Equation 7).

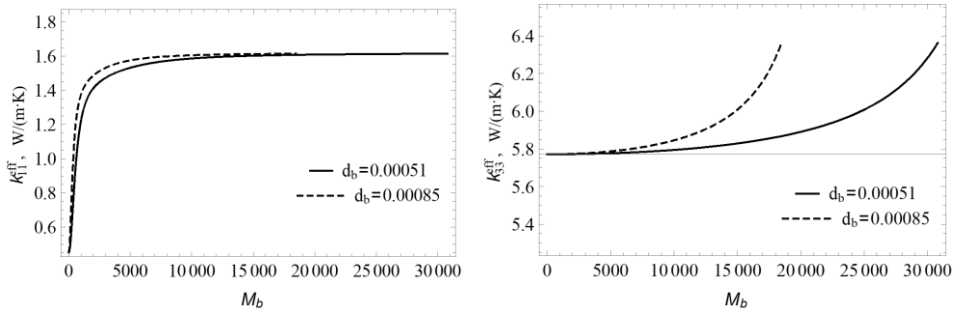

(a) (b)

Fig. 7. Graphs of dependences of effective thermal conductivity coefficients on the number of CNTs in a whiskerized interfacial layer, in the case when whiskers are grown perpendicular to the fiber surface: a) $k_{11}^{eff(i)}$ - in the plane perpendicular to the fiber axis, b) $k_{33}^{eff(i)}$ - in the direction along the fiber axis

Thus, modified composites with whiskers grown perpendicular to the fiber surface are preferable to modified composites with whiskers grown randomly and intertwined with each other from the perspective of increasing the effective thermal conductivity in the plane perpendicular to the fiber axis. The effective coefficient of thermal conductivity in the direction along the fiber axis is insignificant but higher for modified composites with whiskers grown randomly and intertwined with each other. Despite this, it is difficult to control the volume content of whiskers that are randomly located and intertwined with each other, and in fact, the interfacial layer consisting of such whiskers and a matrix has anisotropic properties. Therefore, to ensure the planned thermal conductivity coefficients, it is preferable to use modified composites with whiskers grown perpendicular to the fiber surface. Growing CNTs perpendicular to the fiber surface makes it possible to control the effective thermal conductivity in various directions and in a wide range by changing the thickness of the whisker layer, the volume content of the modified fiber, and the volume

content of whiskers, which depends on the length of the interfacial layer, the diameter of the whiskers, and the number of whiskers.

5. Conclusion

In this research study, an analysis of the effective thermal conductivity of modified composites with whiskerized fibers was conducted. The impact of various parameters such as the thickness of the whiskerized interphase layer, volume fraction of whiskers, number, and diameter of whiskers on the thermal conductivity of the composite in different directions was investigated. To achieve this, a polydisperse medium model with spherical inclusions, as proposed by Hashin and Shtrikman, was used to determine the effective thermal conductivity coefficient of the composite with whiskerized fibers. The obtained results were analyzed to identify the optimal structure of the composite with the maximum effective thermal conductivity coefficient.

The study revealed that the effective thermal conductivity coefficient of modified composites with whiskerized fibers can be significantly increased by increasing the thickness of the whiskerized interphase layer. For instance, when the thickness of the whiskerized layer increases from 1 μm to 2 μm, the effective thermal conductivity coefficient in the direction along the fiber can increase by more than 1.2 times. It was found that the optimal structure of modified composites with whiskerized fibers is those with the maximum possible volume fraction of whiskers, grown perpendicular to the fiber surface. Such composites provide a high effective thermal conductivity coefficient both in the plane perpendicular to the fiber axis and in the direction along the fiber axis. The effective thermal conductivity coefficient of modified composites with whiskerized fibers increases depending on the increase in the volume fraction of whiskers in the interphase layer. For example, when the volume fraction of whiskers increases from 30% to 65% in the plane perpendicular to the fiber axis (case 2), the effective thermal conductivity coefficient can increase by more than 2 times.

Analysis showed that increasing the volume fraction of modified fibers also contributes to the increase in the effective thermal conductivity coefficient. For instance, with the maximum volume fraction of modified fibers (volume fraction of whiskers in the interphase layer being 65%), the effective thermal conductivity coefficient in the plane perpendicular to the fiber axis can increase by more than 3 times compared to classical composites. A numerical analysis was conducted to investigate the influence of the number of whiskers on the effective thermal conductivity coefficient. The dependency graphs of effective thermal conductivity coefficients on the number of whiskers show that in the plane perpendicular to the fiber axis, the effective thermal conductivity coefficient rapidly increases with the increase in the number of whiskers and reaches an almost constant value after a certain value (for example, around 5000 whiskers).

As a result of analyzing the influence of whisker diameter and their number on the effective thermal conductivity coefficient, it was revealed that the optimal value of the effective thermal conductivity coefficient is achieved with a certain combination of whisker number and diameter. This highlights the necessity of careful control over these parameters when designing modified composites with whiskerized fibers.

Our studies also confirmed that modified composites with whiskerized fibers, grown perpendicular to the fiber surface, are preferable compared to composites where whiskers are grown randomly and intertwined. This preference is due to higher values of the effective thermal conductivity coefficient in the plane perpendicular to the fiber axis.

Funding

This work was supported by Russian Science Foundation grant no. 23-19-00680.

References

[1] Biercuk MJ, Llaguno MC, Radosavljevic M, Hyun JK, Johnson AT. Carbon nanotube composites for thermal management. Appl Phys Lett. 2002;80(15):2767–9. https://doi.org/10.1063/1.1469696
[2] Bonnet P, Sireude D, Garnier B, Chauvet O. Thermal properties and percolation in carbon nanotube-polymer composites. Appl Phys Lett. 2007;91:201910. https://doi.org/10.1063/1.2813625
[3] Kim YA, Kamio S, Tajiri T, Hayashi T, Song SM, Endo M. Enhanced thermal conductivity of carbon fiber/phenolic resin composites by the introduction of carbon nanotubes. Appl Phys Lett. 2007;90:093125. https://doi.org/10.1063/1.2710778
[4] Kim HS, Jang J, Yu J, Kim SY. Thermal conductivity of polymer composites based on the length of multi-walled carbon nanotubes. Compos Part B Eng. 2015;79:505–12. https://doi.org/10.1016/j.compositesb.2015.05.012
[5] Zhou L, Yuan TB, Yang XS, et al. Micro-scale prediction of effective thermal conductivity of CNT/Al composites by finite element method. Int J Therm Sci. 2022. https://doi.org/10.1016/j.ijthermalsci.2021.107206
[6] Lida N, Zhong H. Effects of Carbon Nanotubes on Thermal Behavior of Epoxy Resin Composites. J Compos Sci. 2023;7(8):313. https://doi.org/10.3390/jcs7080313
[7] Chatzigeorgiou G, Siedel GD, Lagoudas D. Effective mechanical of "fuzzy fiber" composites. Compos Part B Eng. 2021;43:2577–93. https://doi.org/10.1016/j.compositesb.2012.03.001
[8] Song Q, Li K, Li HL, Li HJ, Ren C. Grafting straight carbon nanotubes radially onto carbon fibers and their effect on the mechanical properties of carbon/carbon composites. Carbon. 2012;50:3943–60. https://doi.org/10.1016/j.carbon.2012.03.023
[9] Zhang FH, Wang RG, He XD, Wang C, Ren LN. Interfacial shearing strength and reinforcing mechanisms of an epoxy composite reinforced using a carbon nano-tube/carbon fiber hybrid. J Mater Sci. 2009;44(13):3574–7. https://doi.org/10.1007/s10853-009-3484-x
[10] Peng L, Feng Y, Zhang P, Chen HM, Zhao N, Feng W. Increasing the interfacial strength in carbon fiber/epoxy composites by controlling the orientation and length of carbon nanotubes grown on the fibers. Carbon. 2011;49:4665–73. https://doi.org/10.1016/j.carbon.2011.06.064
[11] Sharma SP, Lakkad SC. Compressive strength of carbon nanotubes grown on carbon fiber reinforced epoxy matrix multi-scale hybrid composites. Surf Coat Technol. 2010;205:350–5. https://doi.org/10.1016/j.surfcoat.2010.06.055
[12] Lurie SA, Kriven GI, Rabinsky LN. О прочности модифицированного композита с вискеризованными волокнами. Композиты и наноструктуры. 2019;11(1):1–15.
[13] Kriven GI, Lurie SA, Thang TQ, Orekhov AA. Strength, stiffness, and damping properties of whiskerized fiber composites with longitudinal shear. Compos Mech Comput Appl Int J. 2021;12(4):1–22. https://doi.org/10.1615/CompMechComputApplIntJ.2021039237
[14] Kriven GI. Оценка демпфирующих свойств композитов. Труды МАИ. 2022;(127).
[15] Lurie S, Minhat M, Tuchkova N, Soliaev J. On remarkable loss amplification mechanism in fiber reinforced laminated composite materials. Appl Compos Mater. 2014;21(1). https://doi.org/10.1007/s10443-013-9371-2
[16] Lurie SA, Minhat M, Tuchkova N. Estimation of effective dynamic properties of bristled fiber composite materials based on self-consistent Eshelby method. J Eng Math. 2015;95(1):7–29. https://doi.org/10.1007/s10665-014-9719-0

[17] Volkov-Bogorodsky DB, Lurie SA, Kriven GI. Modeling the effective dynamic properties of fiber composites modified across length scales. Nanosci Technol Int J. 2018;9(2):117–38. https://doi.org/10.1615/NanoSciTechnolIntJ.2018026537
[18] Kriven GI, Shavelkin DS. Моделирование тепловых свойств модифицирован-ных композитных материалов с вискеризованными волокнами. Механика композиционных материалов и конструкций. 2023;29(1):81–97. https://doi.org/10.33113/mkmk.ras.2023.29.01.06
[19] Sager RJ, Klein PJ, Lagoudas DC, Zhang Q, Liu J, Dai L. Effect of carbon nanotubes on the interfacial shear strength of T650 carbon fiber in an epoxy matrix. Compos Sci Technol. 2009;69:898–904. https://doi.org/10.1016/j.compscitech.2008.12.021
[20] Thornel T650/35 fiber PAN-Based Fiber [Internet]. Fibermax Composites. Available from: https://www.fibermaxcomposites.com/shop/datasheets/T650.pdf. Accessed 25 Jan 2023.
[21] Christensen RM. Introduction to the mechanics of composites. New York: Wiley; 1982. p. 334.
[22] Hashin Z, Shtrikman S. A variational approach to the theory of the effective magnetic permeability of multiphase materials. J Appl Phys. 1962;33:3125. https://doi.org/10.1063/1.1728579
[23] Wan X, Demir B, An M, Walsh TR, Yang N. Thermal conductivities and mechanical properties of epoxy resin as a function of the degree of cross-linking. Int J Heat Mass Transf. 2021;180:121821. https://doi.org/10.1016/j.ijheatmasstransfer.2021.121821
[24] Lee DK, Yoo J, Kim H, Kang BH, Park SH. Electrical and thermal properties of carbon nanotube polymer composites with various aspect ratios. Materials (Basel). 2022;15(4):1356. https://doi.org/10.3390/ma15041356

Research on Engineering Structures & Materials
www.jresm.org
Research Group

Research Article

Experimental research of a structural health monitoring system concept based on fiber Bragg grating sensors on composite panels of an aircraft

Maksim Soldatkin [*,a], Ekaterina Prilipko [b], Kirill Ibrishev [c], Konstantin Illarionov [d]

Moscow Aviation Institute (National Research University), Moscow, Russia

Article Info

Article history:

Received 14 May 2024
Accepted 15 Aug 2024

Keywords:

Fiber Bragg grating; Health monitoring system; Composite materials; Static and dynamic tests

Abstract

In the dynamic realm of aviation, ensuring the structural integrity of aircraft stands as an imperative pillar of safety and operational efficiency. Amidst this landscape, the advent of Fiber Bragg Grating (FBG) sensing technology has propelled structural health monitoring (SHM) into a new era of precision and reliability. This paper embarks on an exploration of SHM in aviation, using the transformative capabilities of FBG sensing. The primary objective was to evaluate the sensitivity of FBG-based sensors to static and dynamic loads as well as the response to defects formed upon fracture. The study involves fifteen experiments with FBG setups on a composite panel. Using interrogators, the distortions in optical signals were obtained and recalculated to provide data on deformations. Based on the results, FBG sensing technology proved to be sensitive to the mentioned load types, outputting consistent data.

1. Introduction

The aviation industry is actively trying to reduce expenses by adopting composite materials for weight reduction and cost benefits. However, the novelty of these materials and their potential risks make designers cautious. Regular evaluations of these materials can help optimise aircraft structural design. Maintenance, Repair, and Overhaul (MRO) account for a significant portion of operational costs due to the discarding of parts, despite them being structurally sound [1]. A system for continuous structural health monitoring can help address these issues and reduce costs [2]. Various sensors are used in Structural Health Monitoring (SHM), including strain gauges and piezoelectric sensors, each with their limitations such as sensitivity to electromagnetic interference [3]-[6]. Fiber Bragg Grating (FBG) sensors, immune to such interference and capable of multiplexing, offer a significant advancement. They are lightweight, compact, and can cater to various sensing needs, making them ideal for aviation applications. [7]. FBG-based SHM systems offer high sensitivity, electromagnetic interference immunity, and real-time monitoring, making them ideal for aerospace applications. They can monitor fatigue, stress, temperature, and vibrations in aircraft components, aiding in maintenance and safety. Future research should focus on advanced sensor integration, data analysis techniques, and cost reduction to enhance their capabilities and applications. FBG sensors are widely used by European Space Agency for strain and temperature measurement of structural composites [8]. The extensive use of FBG in aviation is also acknowledged in [9], where experimental tests

*Corresponding author: soldatkinmy@mai.ru
[a]orcid.org/0009-0006-6141-5906; [b]orcid.org/0000-0001-7063-5261; [c]orcid.org/0009-0006-4345-3335; [d]orcid.org/0009-0005-4534-0089
DOI: http://dx.doi.org/10.17515/resm2024.287cs0514rs

were carried out comparing the surface attached FBG sensors with resistance strain gauges. Results clearly demonstrate the superiority of FBG sensors due to higher sensitivity and accuracy of deformations read. Using embedded FBG sensors allowed for the detection of delamination in [10] as well as vibration loads in [7]. Uniaxial tension tests were conducted in [11], the difference in FBG and Vic3D system did not exceed 6%.

This study used surface attached FBG sensors (using cyanoacrylate adhesive [12]) to explore the possibilities of detecting applied loads and compare them to Rayleigh sensors. The experiments carried out involved static, dynamic, and failure loads, comparing the results of each subsequent test [13] - [17]. The outcome is evidential of FBG sensing technology demonstrating high sensitivity, consistently producing reliable data, which is proven by a series of comparative tests with various loading conditions, including destruction of a panel, results of which clearly demonstrate the smallest changes in deformations (and specifically, residual deformations). The equipment in use (interrogator x30-700) is capable of reading wavelength signals up to 1000 Hz, which is sufficient for real-time monitoring of a structure; as well as having a tolerance of 1% (in terms of wavelengths measured in the range 1510 – 1590).

2. Methods and Materials

The research utilised optical fibers from Micron Optics with an applied Fiber Bragg Grating (FBG), which serves as the sensitive element of the sensor, as well as the SM-125 measuring device. The supplied FBGs are compatible with Micron Optics' measurement equipment and can be used in measurement tasks that require deformation measurement of small parts, embed into polymer and composite materials, including carbon fiber-reinforced plastic.

This system quickly and consistently performs peak centre wavelength measurements on a 0.25 nm FBG over a wide range of input conditions and sensor signal attenuation, without the need to manipulate gain settings or peak detection parameters. In most typical cases, the main part of the data transmitted by the receiving and recording devices consists of primary readings of measured wavelengths. An FBG-based sensor is a segment of optical fiber with a periodic refractive index gradient (Bragg grating) [18]. As a result, a portion of the radiation passing through the fiber is reflected, with the wavelength at the peak of the reflection coefficient corresponding to the grating period. Any changes to this period due to physical processes (such as deformation or temperature changes) also alter the reflection wavelength of the Bragg grating [19] – [21]. In this manner, authors of [20] have conducted numerous experiments with similarly attached FBGs (using cyanoacrylate adhesive), and an analogues interrogator (with the range of 1480-1580 nm), resulting deformations of which are in the same order of magnitude as those, presented in results and discussion section of this paper. Aforementioned researchers have come across similar difficulties related to the FBG installation process.

To obtain specific values of deformations from FBG sensors, experimental results (acquired wavelengths) must be divided by 0.78 to yield deformation in μm/m, which is considered in further work. Without this division, initial raw data from the device is the relative change in wavelength; after the division, the result is micro strain over time (με) [22].

$$\lambda_{BG} = 2\Lambda n_{eff} \tag{1}$$

$$\Lambda = \Lambda_0(1 + \varepsilon) \tag{2}$$

$$\frac{dn}{d\varepsilon} = -\frac{(n)^2}{2}\left(p_{12} - \nu(p_{11} + p_{12})\right) \tag{3}$$

$$\lambda_{BG} = \lambda_{BG}(\varepsilon) \quad (4)$$

$$\frac{1}{\lambda_{BG}}\frac{d\lambda_{BG}}{d\varepsilon} \approx 0.78 \cdot 10^{-6}\mu\varepsilon^{-1} \quad (5)$$

Where

λ_{BG} – the Bragg resonance wavelength;

Λ – Bragg grating period;

n_{eff} – the effective RI (refractive index) of the fiber core for the central wavelength;

ε – deformations;

n – index of refraction;

ν – Poisson's ratio;

p_{11}, p_{12} – elastooptic tensor components

Table 1 – Metrological and technical characteristics

No	Characteristic	Value
	Interrogator	
1	Measuring device	x30-700
2	Range of wavelength measurement, nm	1510 – 1590 Tolerance ± 20
3	Range of changes in temperature, ºC	From - 40 to + 120 ± 2,0
4	Range of deformation measurement, %	0,01 – 0,25 ± 1
5	Scanning frequency, Hz	1000
6	Number of optical channels	4
	Sensors	
7	Sensing element	FBG
8	Sensitivity, pm/μm -1	~1.2
9	Coating material	Acrylate, Polyimide
10	Coating diameter, μm	145-165
11	Length, mm	10
12	Optical fiber type	Single-mode, compliant with SMF-28
13	Number of optical endings	2
14	Cable bending diameter, mm	≥17

The research procedure using (FBG) consists of:

- Preparation of samples, tools, fixtures, and sensors;
- Assembly of the data analysis system for the deformation of the object under study;
- Selection of sensor adhesion technology, load calculations;
- Direct adhesion of sensors to the sample;
- Calibration of the monitoring system;
- Conducting experiments by applying various types of loads.

Values of metrological and technical characteristic of the measuring apparatus and optical fibers used in the research are presented in table 1.

2.1. The Research Objective and Testing Procedure

The study investigates the sensitivity of FBG-based sensors to static loads and impacts of varying energy applied to a composite panel with both honeycomb-filled and solid parts. A schematic view of the panel is presented in Fig. 1, with the thickness values (h) averaged.

The health monitoring system consists of the recording equipment - NTM130 optical interrogator; the strain sensors - a single-mode fiber with a thickness of 145 micrometres (10 micrometres for the core, 125 micrometres for the cladding, and 145 micrometres for the protective coating). The operational wavelength for this type of sensors ranges from 1.5 to 1.6 micrometres. Software – Micron Optics. Sensors are attached to the surface of the panel with dimensions of 1 m^2 using a cyanoacrylate adhesive, both on the solid part and on the area filled with honeycomb.

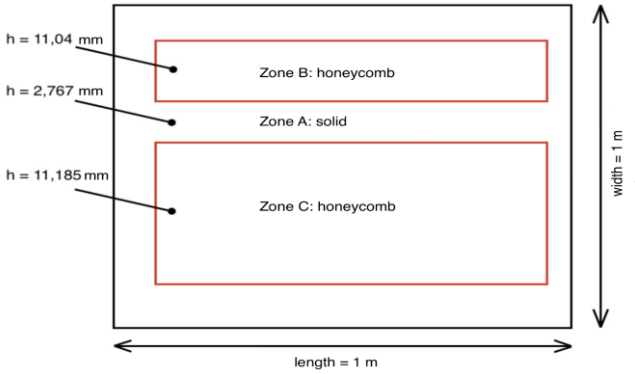

Fig. 1. Schematic view of the panel, zones of interest and geometrical parameters

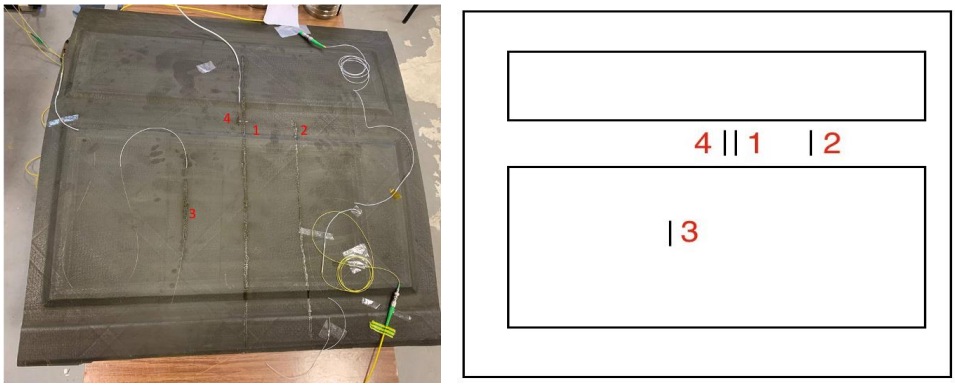

(a) (b)

Fig. 2. Composite panel with FBG installed a) General layout; b) Schematic representation of FBG-based sensors disposition

The positioning of the sensors and the general layout of the panel is presented in Fig. 2 a). The numeration corresponds to the order in which sensor were attached as well as the approximate location of FBG. The terms "acrylate" and "polyimide" sensors refer to the type of protective coating applied to the fiber optic sensor. The types of sensors attached to the plate, which measures 1 m^2, are illustrated in Fig. 2 b) as follows:

- Acrylate sensor on the monolithic part of the plate;

- Acrylate sensor on the monolithic part of the plate (damaged grating);
- Acrylate sensor on the honeycomb part of the plate;
- Polyimide sensor on the monolithic part of the plate.

The sampling frequency in all tests (both static and dynamic loads) was 1 kHz. Static tests were conducted by loading the panels with weights of 1, 5 and 10 kg.

2.2 Description of the Conducted Tests

Experiments 1 through 4 served a purpose of calibrating the equipment and setting up the workspace. In the static tests the loading step was 1 kg at a time on each side of the sensor. Next, a reduction of 5 weights of 1 kg each took place, followed by the application of a 5 kg weight. This process was repeated with a 10 kg weight. As a result, the panel was subjected to a total load of 25 kilograms. In the subsequent static experiments, the positioning of the loads, the methodology of application, and the mass were analogous to those previously outlined. The loaded zones of the panel are represented in Fig. 3.

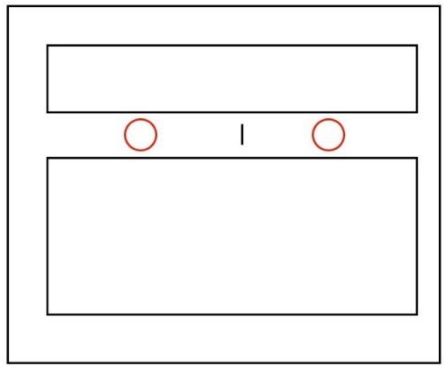

Fig. 3. The zones loading was applied

The dynamic tests consisted of applying individual impacts along different zones of the panel from various heights using a handmade drop test rig (appearance presented in Fig. 4 a). The order of impacts in experiment 2 is schematically represented in the Fig. 4 b).

In subsequent experiments, four sensors were used. Acrylic sensor No. 3 was attached to the honeycomb part of the plate (Zone C) to compare the resulting data depending on the plate structure. The difference between acrylic (1) and polyimide (4) sensors was examined to compare different types of optical fiber coating, where no significant differences were found. Acrylic sensors are more prone to damage during adhesion, whereas polyimide sensors exhibit less stiffness. The plate was subjected to static loads, dynamic loads of varying energy, drilling, and hammering loads, list of experiments is presented in table 2. After each event that damaged the plate (12, 14), static tests were carried out. Data processing takes the changes of deformations into account.

The decoding of the graphs, loads, and sensors in the experiment results are as follows:

- Acrylic sensor on the monolithic part of the plate (red graph, labelled "central");
- Acrylic sensor on the monolithic part of the plate (pink graph, damaged sensor, labelled "side");
- Acrylic sensor on the honeycomb part of the plate (black graph, labelled "on honeycombs");
- Polyimide sensor on the monolithic part of the plate (blue graph, labelled "polyimide").

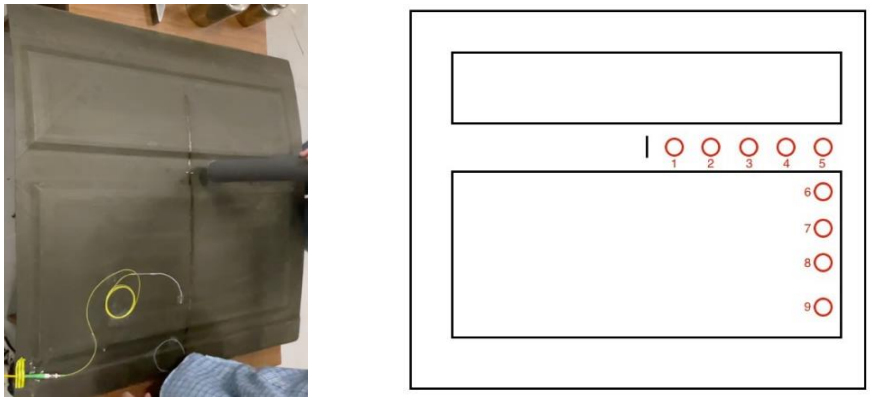

(a) (b)

Fig. 4. (a) Device for applying impact loads and (b) diagram and order of single impact with a drop test rig in experiment 2

Table 2. List of experiments carried out

No exp.	Number of sensors	Sensor type	Loading type
1	1	Acrylate	Static
2	1	Acrylate	Dynamic
3	2	Acrylate	Static
4	2	Acrylate	Dynamic
5	4	3 acrylate ones, 1 polyimide one	Static
6	4	3 acrylate ones, 1 polyimide one	Static
7	4	3 acrylate ones, 1 polyimide one	Dynamic
8	4	3 acrylate ones, 1 polyimide one	Dynamic
9	4	3 acrylate ones, 1 polyimide one	Dynamic
10	4	3 acrylate ones, 1 polyimide one	Dynamic
11	4	3 acrylate ones, 1 polyimide one	Dynamic
12	4	3 acrylate ones, 1 polyimide one	Drilling
13	4	3 acrylate ones, 1 polyimide one	Static
14	4	3 acrylate ones, 1 polyimide one	Fracture using a hammer
15	4	3 acrylate ones, 1 polyimide one	Static

The investigation of static deformation during the operation of an aircraft using fiber-optic sensors is necessitated by the need for continuous real-time monitoring of the aircraft's structural integrity. Fiber-optic sensors, due to their high sensitivity and measurement accuracy, afford the opportunity for detailed analysis of deformations and stresses that occur in the aircraft's structure under various operating conditions. Conducting such investigative measurements allows for the timely detection of potential defects, cracks, or fatigue damage that may lead to emergency situations during flight. Thus, the use of fiber-optic sensors for monitoring static deformation during aircraft operation is a necessary step to ensure flight safety and extend the aircraft's service life.

The use of fiber-optic sensors to measure impact energy during an aircraft's operation is critical for analysing dynamic loads that result from external influences on the aircraft's structure. Fiber-optic sensors are valued for their high sensitivity and ability to measure a wide range of parameters, which enables a precise calculation of impact energy and evaluation of its effect on the aircraft's structural integrity. These measurements facilitate the identification of potential weak points in the structure that are vulnerable to damage from significant impacts, thereby enhancing flight safety and the overall reliability of air transportation.

3. Results and Discussions

The resulting deformations of the first static experiment (gradual loading of the panel) are shown in Fig. 5. Here, the small loading steps can be clearly seen in the graph 5 a), represent each consecutive installation of a 1 kg weight, while bigger steps demonstrate their removal (5 to 10 kg at a time).

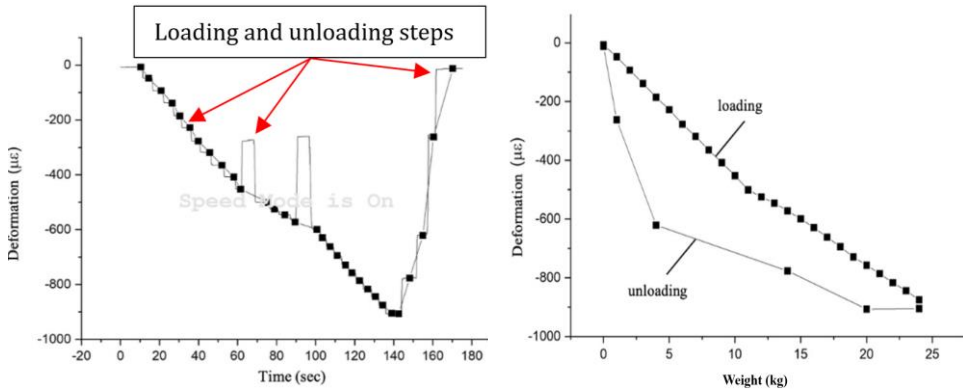

(a) (b)

Fig. 5. A deformation-time graph (a) and deformation-load graph (b) resulting from the first static test measured by an acrylic sensor

Fig. 6 presents the deformation-time graph based on the conducted dynamic test 2 in which the loads were applied using a handmade drop test rig (appearance presented in Fig. 4 a). On this graph, the moment of each impact is clearly visible, demonstrating the sharp sensitivity of the FBG-based sensors to dynamic loads. After each subsequent strike there is a noticeable amount of noise, representing the removal of the rig. The initial deformation in this and subsequent experiments is non-zero because of the residual deformations from the static experiments.

Experiment 7 involved impacts from a consistent height of 1 meter across the entire length, at various distances from the sensors, of the monolithic part of the composite plate. The place and order of impacts using the drop rig is schematically represented in the Fig. Fig. 7 (a), and the deformation-time graphs are presented in the Fig. Fig. 7 (b) and Fig. Fig. 8. All the sensors had a clear and similar response. A clear tendency to the increased magnitude of deformations is seen upon impacts 2 and 3 as those are positioned the closest to the FBG sensors which is evident of higher sensitivity within the short range of a sensor. This dependency would be useful in an FBG-array for determining an exact position of an impact.

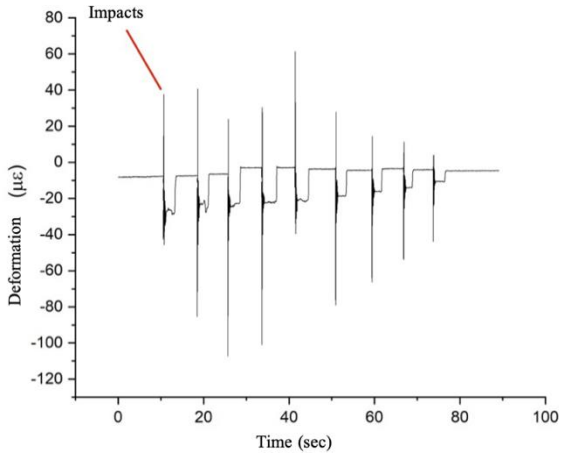

Fig. 6. Deformation-time graph resulting from dynamic tests measured by an acrylic sensor

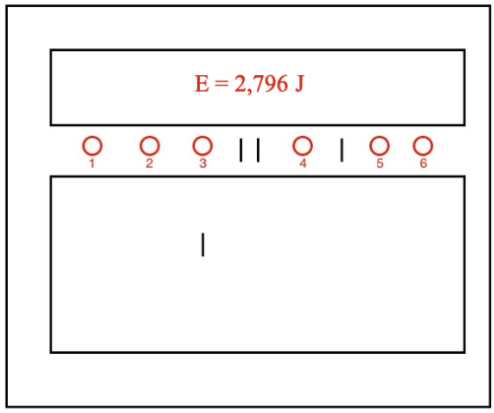

(a)

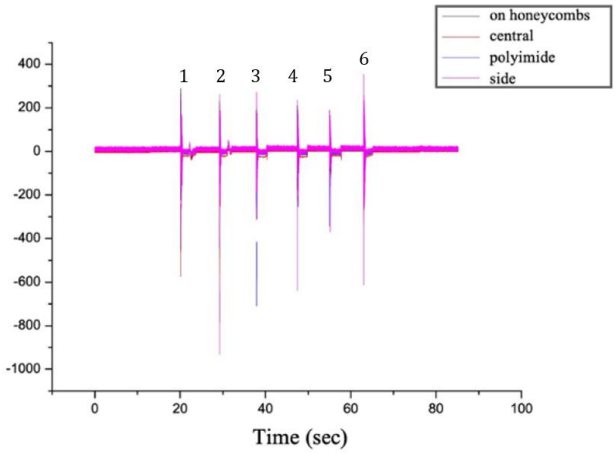

(b)

Fig. 7. (a) Order and disposition of dynamic impacts and (b) the deformation-time graph resulting from dynamic tests measured by three acrylic sensors and one polyimide sensor

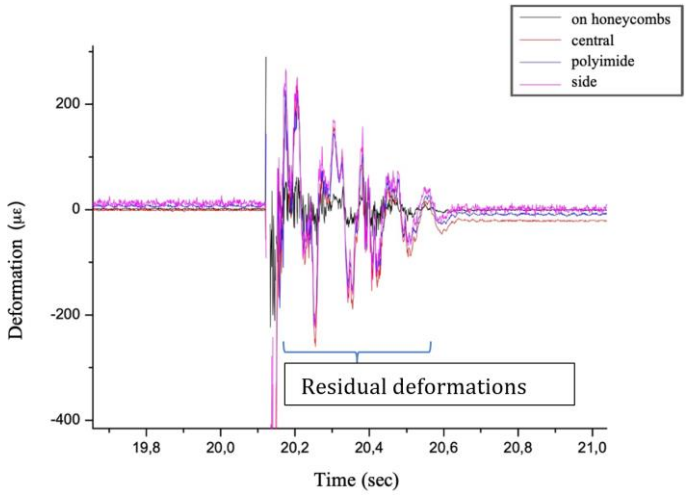

Fig. 8. The deformation-time graph of the first impact close up

The residual deformations resulting from the impact should be taken upon consideration while analyzing the results as to not be confused with the impact itself. Experiment 14 involved the fracture of the panel at two locations (both monolithic and honeycomb-filled parts of the composite panel) using hammer impact as to see how FBG sensors would react to the destruction of a said composite material. The locations of impacts and subsequent defects are shown in Fig. 9. The external appearance of the destroyed panel is shown in Fig. 10. These strikes were carried out for further comparison of the static experiments before and after destruction of the composite of the panel with respect to the remaining stresses and deformations introduced to the structure.

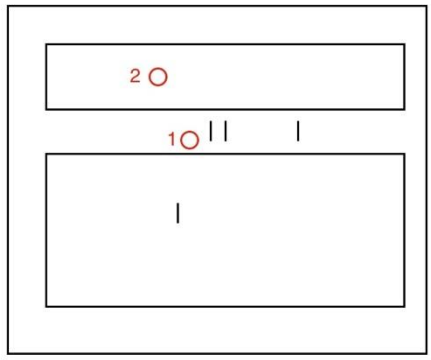

Fig. 9. Locations of the hammer impacts

Fig. 11 – 12 present the results of static tests of all sensors post-impact, post-drilling, and after fracture with a hammer. It can be observed that the sensor located on the honeycomb part experiences the least deformation in each experiment, while the side-located acrylic sensor (2) (pink line on the graph) exhibits "jumps" on the deformation-time dependency graph, which is a consequence of damaging the fiber during the unsatisfactory adhesive process. The following description was obtained based on the comparison of static tests of each sensor before and after dynamic tests:

- acrylate sensor in the centre – Fig. 13;

- acrylate sensor on the side – Fig. 14;
- acrylate sensor on the honeycomb part – Fig. 15;
- polyimide sensor on the monolithic part – Fig. 16.

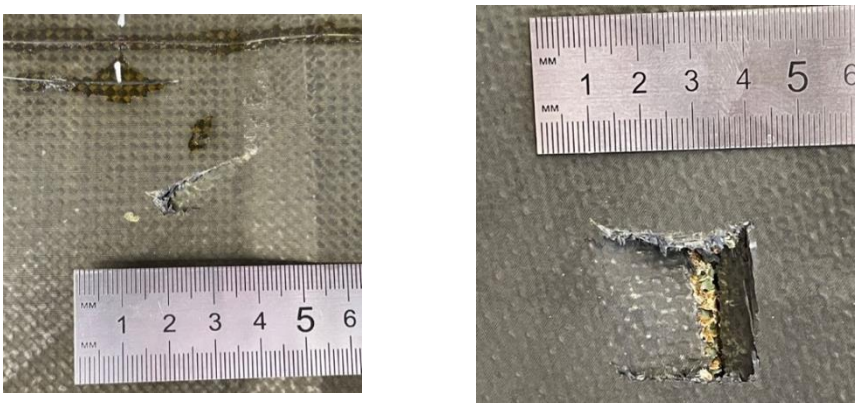

(a) (b)

Fig. 10. Appearance of the subsequent defects on the monolithic part of the panel (a) strike 1 on the monolithic part, (b) strike 2 on the honeycomb part

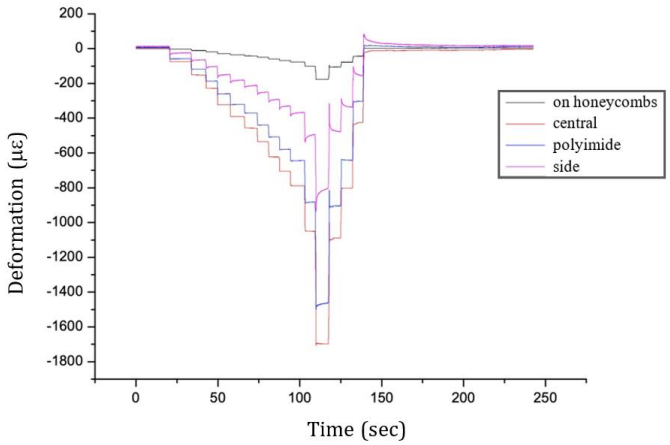

Fig. 11. The deformation-time graph resulting from static tests post-impact and post-drilling measured by three acrylic sensors and one polyimide sensor

This sensor experiences the most deformations after the dynamic impacts thus proving the presence of residual stresses in the monolithic part of the panel. The resulting data from acrylate sensor on the side (2) demonstrates uneven response (in comparison with the other sensors 1, 3 and 4) which is a consequence of a defect emerging because of a poor adhesion of the optical fiber to the panel.

The sensors used on the honeycomb part demonstrates a non-typical behaviour (in comparison with sensors 1 and 4) in the sense of the minimal deformations appearing after the destruction, rather than before any of the impacts took place. The reason for such an anomaly is not obvious and should be researched further.

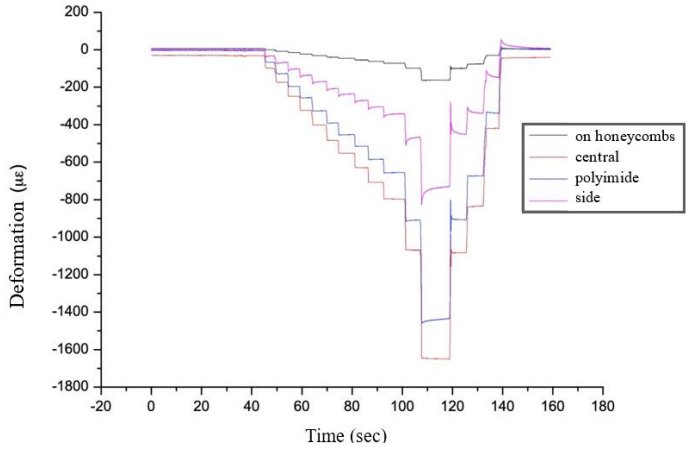

Fig. 12. The deformation-time graph resulting from static tests after fracture by hammer measured by three acrylic sensors and one polyimide sensor

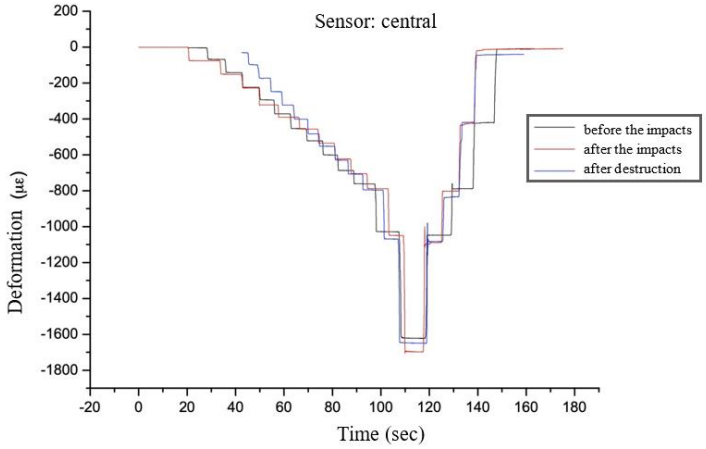

Fig. 13. The deformation-time graph resulting from three static tests measure by a single acrylate sensor (1)

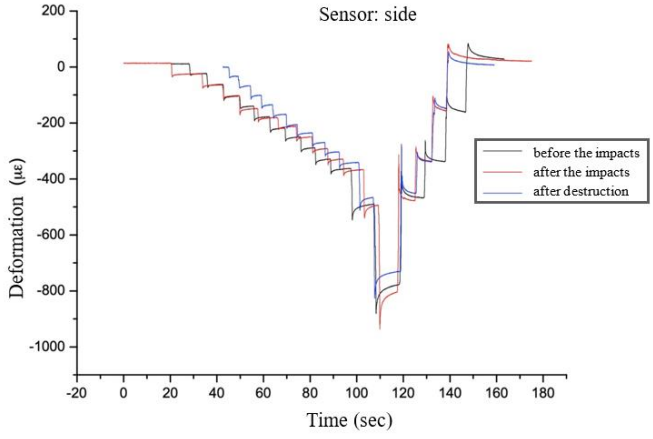

Fig. 14. The deformation-time graph resulting from three static tests measure by a single acrylate sensor (2)

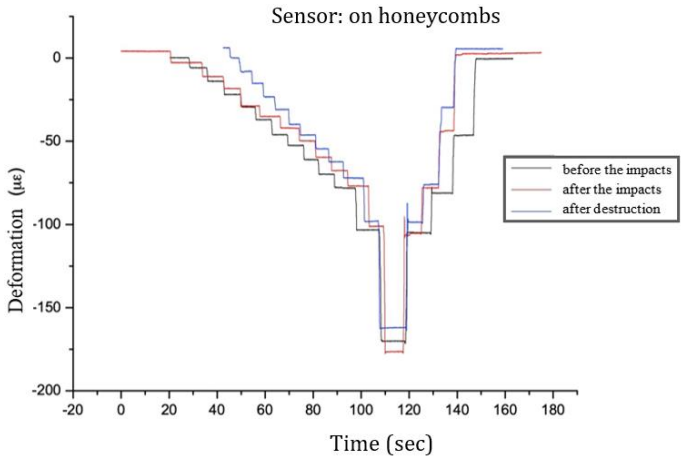

Fig. 15. The deformation-time graph resulting from three static tests measure by a single acrylate sensor (3)

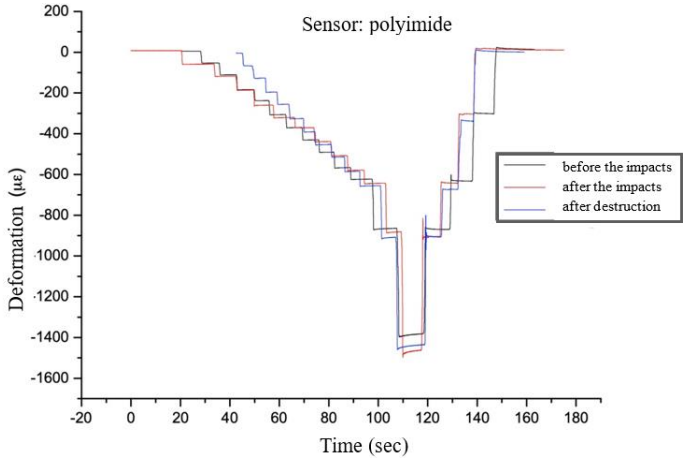

Fig. 16 – The deformation-time graph resulting from three static tests measure by a single polyimide sensor (4)

It should be denoted that after each successive dynamic test the deformations of the panel increase during the static tests upon application of the similar mass. This phenomenon is relevant to detecting delamination [23]. Summing up the interim results of the studies, the following theses can be formulated:

- Fiber Bragg Grating (FBG) sensors reliably detect deformations resulting from static loads. They also have the capability to sense impact loads with clear increases in deformations, which suggests their versatility and adaptability to different types of load conditions.
- The testing results reveal an increase in deformations of the composite panel due to the stress-strain state post impacts and fracture. This indicates the sensors' ability to monitor and reveal damage progression and structural integrity loss over time, addressing the durability of a structure.

- FBG sensors can be attached to any composite structure using cyanoacrylate adhesive but embedding the sensors is more desirable due to reduced risks of spontaneous damage.

4. Conclusions

Based on the conducted study, we can conclude the following:

- Analysing the literature reveals that Fiber Bragg Grating sensors possess several distinct advantages over Rayleigh-based sensors. FBG sensors demonstrate insensitivity to variations in the quality of optical fibers, which provides a considerable degree of reliability under diverse operating conditions. This characteristic ensures their performance remains consistent even in less-than-ideal environments, thereby enhancing the robustness of the structural health monitoring systems in which they are employed.
- The stability of FBG sensor readings during the detection of deformations in static tests further corroborates their reliability. This stability is crucial for SHM applications, as it ensures that the sensors provide accurate and consistent data over extended periods, thus facilitating long-term monitoring and assessment of structural integrity.
- The equipment and software required for researching with FBG-based sensors are notably simpler and more intuitive compared to those needed for other sensor types. This simplicity allows for real-time observation and analysis of results, which significantly enhances the efficiency of data management and decision-making processes. The ease of use associated with FBG technology also reduces the training burden on personnel and minimises the likelihood of operational errors.

In summary, FBG sensing technology has demonstrated significant potential in the realm of structural health monitoring. The inherent advantages of FBG sensors, including their high sensitivity, reliability, and operational simplicity, make them a promising candidate for further study and implementation. Future research should concentrate on enhancing the reliability of FBG sensors, developing more effective data interpretation algorithms, and exploring the potential for integration with other sensor technologies. Additionally, investigating the economic feasibility of large-scale implementation of FBG-based SHM systems in aviation is imperative. This evaluation should not only consider the direct costs associated with sensor installation and maintenance but also account for potential savings from improved maintenance efficiency, reduced downtime, and enhanced safety. By addressing these areas, future studies can pave the way for more widespread adoption of FBG technology in SHM applications, ultimately contributing to the advancement of safety and efficiency in the aviation industry.

As per detecting the exact position of an in-flight impact, a net-like structure of sensors should be installed (as one usually used in SHM systems with Rayleigh-based sensors). Further work should focus on optimising the sensor network configuration for maximum coverage and accuracy, as well as developing advanced algorithms for real-time impact detection and analysis.

Acknowledgement

The authors acknowledge that Laboratory № 3 "Modelling of composite structures" of the Center for Aerospace Materials and Technologies of the Institute № 14 "Advanced Engineering School" and Center of Composite Structures support this study in the Moscow Aviation Institute (MAI).

References

[1] Pogosyan M, Nazarov E, Bolshikh A, et al. Aircraft composite structures integrated approach: a review. J Phys Conf Ser. 2021;1925(1):21-34. https://doi.org/10.1088/1742-6596/1925/1/012005

[2] Gupta N, Augustin MJ, Sathya S, et al. Structural Health Monitoring of Composite Aircraft Structures Using Fiber Bragg Grating Sensors. J Indian Inst Sci. 2013;93(4).

[3] Sundaram R, Kamath GM, Gupta N. Structural Health Monitoring of Composite Structures-Issues and Challenges. Int J Veh Struct Syst. 2012;4(3):74-85. https://doi.org/10.4273/ijvss.4.3.01

[4] Roach D. Real time crack detection using mountable comparative vacuum monitoring sensors. Smart Struct Syst. 2009;5(4):317-328. https://doi.org/10.12989/sss.2009.5.4.317

[5] Galea SC, Velden S, Powlesland I, et al. Flight demonstrator of a self-powered SHM system on a composite bonded patch attached to an F/A-18 aileron hinge. Asia-Pacific Workshop on Structural Health Monitoring; 2006; Yokohama, Japan. p. 146-154.

[6] Arms SW, Townsend CP, Galbreath JH, et al. Flight Testing of Wireless sensing Networks for Rotorcraft Structural Health and Usage Management Systems. In: Proceedings of the Fourteenth Australian International Aerospace Congress, 7th DSTO International Conference on Health & Usage Monitoring (HUMS 2011); 2011. Corpus ID: 51946739.

[7] Friebele EJ, Askins CG, Bosse AB, et al. Optical fiber sensors for spacecraft applications. Proc SPIE. 1999;5554:120-131. https://doi.org/10.1117/12.562393

[8] McKenzie N, Karafolas N. Fiber Optic Sensing in Space Structures: The Experience of the European Space Agency. Proc SPIE. 2005;5855:262-269. https://doi.org/10.1117/12.623988

[9] Seryeznov AN, Kuznetsov AB, Lukyanov AV, et al. Application of fiber optic technologies in the creation of embedded self-diagnostic systems for aviation structures. Aviatsiya, Raketnaya i Kosmicheskaya Tekhnologiya, Nauchnyi Vestnik NSTU. 2016;64(3):95-105. doi: 10.17212/1814-1196-2016-3-95-105. https://doi.org/10.17212/1814-1196-2016-3-95-105

[10] Güemes A, Fernández-López A, Díaz-Maroto PF, et al. Structural Health Monitoring in Composite Structures by Fiber-Optic Sensors. Sensors (Basel). 2018;18(4):1094. https://doi.org/10.3390/s18041094

[11] Kosheleva NA, Shipunov GS, Voronkov AA, et al. Determination of the stress-strain state fields of samples from a polymeric composite material using fiber optic sensors. PNRPU Bull. Aerosp Technol. 2017;12(50):295-305.

[12] Shramko K, Kononov N, Ibrishev K, et al. Simulation of Adhesive Bonding of a Fiber-Optic Rayleigh Sensor with Composite Material as Part of the Design of a Monitoring System. E3S Web Conf. 2023;446:302-314. https://doi.org/10.1051/e3sconf/202344603002

[13] Качура СМ, Постнов ВИ. Перспективные оптоволоконные датчики и их применение (обзор) (Perspective optical fiber sensors and their application (review)). Trudy VIAM. 2019;5(77):52-61. https://doi.org/10.18577/2307-6046-2019-0-5-52-61

[14] Syzrantsev VN, Syzrantseva KV. Определение напряжений и остаточного ресурса по показаниям датчика деформаций интегрального типа переменной чувствительности (Determination of stresses and residual life in accordance with indications of variable sensitivity integral strain gauge). Bull Tomsk Polytech Univ Geo Assets Eng. 2017;328(9):82-93.

[15] Шершак ПВ, Яковлев НО, Орешко ЕИ. Application of optical deformation sensors for estimating the deformativity of CFRP samples near the stress concentrators. Trudy VIAM. 2022;107:111-122. https://doi.org/10.18577/2307-6046-2022-0-1-111-122

[16] Леонович ГИ, Олешкевич СВ. Гибридные датчики на волоконно-оптических брэгговских решетках (Hybrid sensors on fiber-optic bragg gratings). Izv Samar Nauch Cent Ross Akad Nauk. 2016;18(7):1340-1345.
[17] Ramlya R, Kuntjoro W, Rahman MK. Using Embedded Fiber Bragg Grating (FBG) Sensors in Smart Aircraft Structure Materials. Procedia Eng. 2012;41:600-606. https://doi.org/10.1016/j.proeng.2012.07.218
[18] Kister G, Winter D, Badcock RA, et al. Structural health monitoring of a composite bridge using Bragg grating sensors. Part 1: Evaluation of adhesives and protection systems for the optical sensors. Compos Struct. 2007;29(3):440-448. https://doi.org/10.1016/j.engstruct.2006.05.012
[19] Ye Q, Quan-bao W, Hai-tao Z, et al. Review on Composite Structural Health Monitoring Based on Fiber Bragg Grating Sensing Principle. J Shanghai Jiaotong Univ (Sci). 2013;18(2):129-139. https://doi.org/10.1007/s12204-013-1375-4
[20] Trutzel MN, Wauer K, Betz D, et al. Smart sensing of aviation structures with fiber optic Bragg grating sensors. In: Proceedings of the Smart Structures and Materials 2000: Sensory Phenomena and Measurement Instrumentation for Smart Structures and Materials; 2000. p. 134-143. https://doi.org/10.1117/12.388099
[21] Zhou Y, Zhao Y, Liu D, et al. Review on Structural Health Monitoring in Metal Aviation Based on Fiber Bragg Grating Sensing Technology. In: Proceedings of the 2020 Prognostics and Health Management Conference (PHM-Besancon); 2020. p. 97-102. https://doi.org/10.1109/PHM-Besancon49106.2020.00022
[22] Dong T, Kim NH. Cost-Effectiveness of Structural Health Monitoring in Fuselage Maintenance of the Civil Aviation Industry. Aerospace. 2018;5(4):87. https://doi.org/10.3390/aerospace5030087
[23] Tinchurina D, Kononov N, Permyakov A, et al. Registration of the Growth of Manufacturing Defects by the Monitoring System During the Operation of the Structure. E3S Web Conf. 2023;446:34-43. https://doi.org/10.1051/e3sconf/202344603003

Research on Engineering Structures & Materials
www.jresm.org
Research Group

Research Article

Investigation of the features of destruction of fillers of structures made of reinforced polymer composite materials

Sergey Grazion [1,a], Valery Spiryagin [*,2,b], Mikhail Erofeev [3,c], Ilnur Khuramshin [4,d], Vyacheslav Nikolenko [4,d]

[1]*JSC Corporation, Moscow Institute of Thermal Engineering, Russia*
[2]*Moscow Aviation Institute, National Research University, Russia*
[3]*Institute of Mechanical Eng. of the Russian Academy of Sciences named after A.A. Blagonravov, Russia*
[4]*26 Central Design Institute, 31 State Design Institute for Special Construction, Gagarin, Russia*

Article Info

Article history:

Received 28 June 2024
Accepted 13 Aug 2024

Keywords:

Mechanical testing;
Polymer composite materials;
Acoustic emission

Abstract

The paper presents the results of experimental studies of the destruction of fillers of polymer composite materials (PCM) with the control of acoustic emission (AE) signal parameters. As object of research were considered silica filaments K11C6-180, carbon filaments UKN-M-12K-1-7-380 and aramid technical fiber Rusar-C600 type A. Based on the experimental data obtained, acoustic emission portraits of the destruction processes of various types of PCM fillers were obtained. This allows, when loading a structure made of PCM with AE control, to fix the destruction of the filler, and, consequently, to increase the reliability and safety of operation of products made of PCM.

1. Introduction

Currently, structures made from reinforced polymer composite materials (PCM) are becoming more widely used in aviation, aerospace, and fire extinguishing systems for gas, compressed natural gas vehicles, respiratory protective equipment, and various other technological fields [1-5]. PCM comprises two main components: a filler and a binding agent. Fiberglass, carbon fibers, and organic fibers are often used as fillers in modern PCM structures. One method of nondestructive testing that allows for assessing the technical condition of a PCM structure is the acoustic emission (AE) technique [6-9].

The AE technique is based on the production of elastic waves generated during structural changes within the material, such as the formation and development of flaws in the filler or binding agent. The primary source of information is an acoustic signal, which is captured using a receiving device connected to a data acquisition and processing system. During the analysis of standard parameters (such as amplitude, duration, and rise or fall time of the acoustic emission pulse), certain criteria are calculated, based on which the level of danger posed by the acoustic signal source can be assessed.

The key advantages of this method include its high sensitivity, wide range of application possibilities, and ability to not only determine the hazard class but also locate the defect. However, a potential drawback of this approach is the registration of numerous noise signals, which can complicate the analysis process.

[*]Corresponding author: v.v.spiryagin@yandex.ru
[a] orcid.org/0000-0002-7040-8744; [b] orcid.org/0000-0001-6114-8138; [c] orcid.org/0000-0002-1048-3574; [d] orcid.org/0009-0007-5965-6652; [e] orcid.org/ 0009-0009-9686-018X
DOI: http://dx.doi.org/10.17515/resm2024.288cs0628rs

Currently, the AE method is used to solve a wide range of scientific and engineering problems, from corrosion control [10], fatigue and corrosion cracking of metals [11, 12] and studying the structural behavior of reinforced concrete elements [13] and critical passenger transport infrastructure facilities [14-15] to studying the patterns of formation and change of acoustic emission signals in composite materials [16-17].

The method has become widespread due to its advantages, described in detail in the works of Ivanov V.I. and Vlasov I.E. [18], Popov A.V. and co-authors [19] and a number of other researchers [20-22]. With regard to PCM, the use of traditional methods of technical diagnosis is difficult or even impossible. So, for example, the ultrasonic method has a number of disadvantages, the main of which is low sensitivity, mainly because when monitoring through an air gap, only a small part of the ultrasonic probing signal enters the product due to the large difference in acoustic resistances at the boundaries of the electroacoustic transducer — air medium and air medium — the object of control [23]. It should also be noted that the ultrasonic method is an active control method that allows you to determine only the presence of a defect, but does not provide information about its danger, including its tendency to develop and brittle destruction.

In the study [24], the authors chose radio frequency identification methods for detecting defects based on antenna deformation. However, this method does not provide information about the actual nature of the destruction of the PCM. It is rightly noted in [25] that the detection of structural damage to PCM at an early stage is impossible, since interruptions, which are damage states detected using the proposed method, occur at very high deformations - more than 20%. The main disadvantages of the proposed method include the following:

- the need to load the object, since in this state it is possible to start the process of defect development and generation of acoustic signals;
- high sensitivity to electromagnetic and acoustic interference.

Additional difficulties in the propagation of AE waves in PCM arise due to the anisotropy of the material. As a result, the signals received by the processing program can give only a limited idea of the real sources of damage. Nevertheless, these signals can still be considered sufficient for further analytical processing [26]. In [27], the authors propose a new approach to regional positioning, which allows for more accurate localization of defects. The purpose of this study is to study the characteristics of AE signals in case of failure of the PCM winding in order to develop a reliable method for monitoring the failure processes of both the entire PCM structure and individual components, in particular, the filler.

Table 1. Physico-mechanical properties of silica threads К11С6-180

Material	Linear density (tex)	Twist amount (tw/m)	Breaking load (N(kgf), not less)
К11С6-180	1014.22	1099.71	23.1

The aim of this study is to investigate the characteristics of AE signals during the failure of PCM winding, in order to develop a reliable method for monitoring the failure processes of both the overall PCM structure and individual components, specifically the filler. The silica К11С6-180 fibers, carbon UKN-M-12K-1-7-380fibers, and technical fiber Rusar-C600 of the A brand are the objects of this investigation. In the following, we will refer to these materials using their Russian labels. With respect to their physical and mechanical properties, these materials meet the specifications outlined in Tables 1-3.

Table 2. Physico-mechanical properties of carbon threads UKN-M-12K-1-7-380ЭД

Material	Thread density, (g/cm3)	Specific breaking load of thread when breaking loops, (cN/tex, not less)	Elastic modulus, (GPa)	Breaking stress of an elementary thread (filaments) under tension, (GPa, not less)
UKN-M-12K-1-7-380	1.75±0.04	10	225±20	3.5

Table 3. Physico-mechanical properties of aramid technical fiber Rusar-C600

Material	Linear density (tex)	Number of threads in the fiber, pcs	Breaking load (N(kgf), not less)	Dynamic modulus of elasticity of complex thread, GPa, (kgf/mm2), not less	Twist of filament thread, tw/m
Rusar-C600A	1.75±0.04	10	225±20	3.5	

2. Materials and Methods

To investigate the process of filament destruction while monitoring AE signal parameters, a testing setup was developed, the appearance of which is depicted in Fig. 1. The main components of the experimental set-up are: 1 a loading device; 2 an acoustic emission system, UNISCOPE; 3 the object of study; 4 acoustic emission converters (AEC) of the GT200 and GT205 types; 5 waveguide grips. The main challenge in setting up the experiment was ensuring the acoustic contact between the object under study, in this case the filaments, and the AEC. To achieve this, we designed and tested the waveguide grips shown in Fig. 1b. The waveguide grip is composed of two plates and four screws. The working plate is made of steel. The main parameters of the waveguide were selected based on the following criteria: 1) the frequency range of operation is 30-300 kHz; 2) the controllers used are DR15I, DR6I from the MALACHITE system or GT200 and GT205 from UNISCOPE; 3) an average wave speed of approximately 3000 m/s as recorded by AEC devices. Based on these criteria, the wavelength lies in the range of 1.5-6 cm.

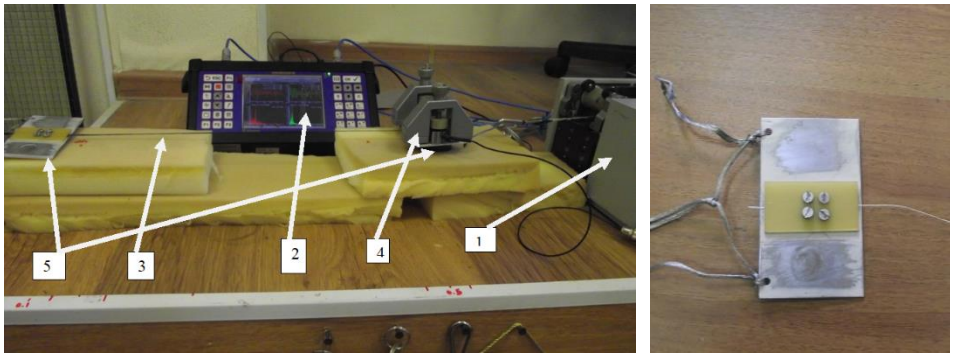

Fig. 1. Experimental setup: left general view; right waveguide grip

Based on this information, the dimensions of the work plate are 115 x 65 x 3 mm. These dimensions allow for the installation of AEC DR15I, DR6I, or GT200, GT205 using magnetic clamps, as shown in Figure 2. The thickness of the waveguide should be commensurate with the wavelength, in order to ensure optimal performance. The characteristics of the AEC used in this study are presented in Table 4.

Fig. 2. AEC is used in conjunction with a waveguide grip

The second plate is manufactured from a material with a high level of attenuation and is designed to apply pressure to the thread. The high attenuation of acoustic signals within the pressure plate results in a significant reduction of the reverberant component when the signal travels through the pressure plate. For the study, 70 mm-long threads were utilized. The ends of the threads were bonded at each end, approximately 10 cm apart, using butyral phenolic glue (BF adhesive), in accordance with Russian standards for determining breaking strength and elongation upon rupture of textile fiber materials (GOST 6943-79).

Table 4. Characteristics of AEC

#	Characteristics	Type of acoustic emission converter			
		DR6I AT	DR15I AT	GT200	GT205
1	Nominal resonant. frequency, kHz	60	150	165	50
2	Operating frequency range, kHz	30–120	75-300	100-200	40-100
3	Gain, dB	34	34	20	20
4	Supply voltage, V	15	15	6	6
5	Dimensions without cable (diameter/height, mm	28 □ 38	28x32	16x15	
6	Weight, g	100	90	14	22x25,5
7	Tread material	Ceramics			
8	Execution	hermetically			

The ends of the glued threads were positioned between the plates, with the protruding end being approximately 2-3 centimeters in length, and secured with screws. An AEC was mounted on the receiving waveguide using an acoustically transparent lubricant. One end of the waveguide was fixed to a stationary support, while the other end was connected to a loading device. The thread was pulled with a force of approximately 2-2.5 kilograms. AE signals were generated for testing. The Su-Nielsen simulator was utilized as a substitute. The signals were produced on a waveguide equipped with an AEC, as well as on a filament located at distances of 10, 20, 30, 40, and 50 centimeters from the receiving waveguide. Prior to simulating the signal on the filament, a rigid support was positioned beneath it near the point of simulation in order to eliminate any vibrations in the filament as a string. Consequently, an attenuation curve for acoustic signals was derived, as shown in Figure 3. The "0" distance corresponds to the amplitude of signals when simulated on the receiving waveguide with an AEC.

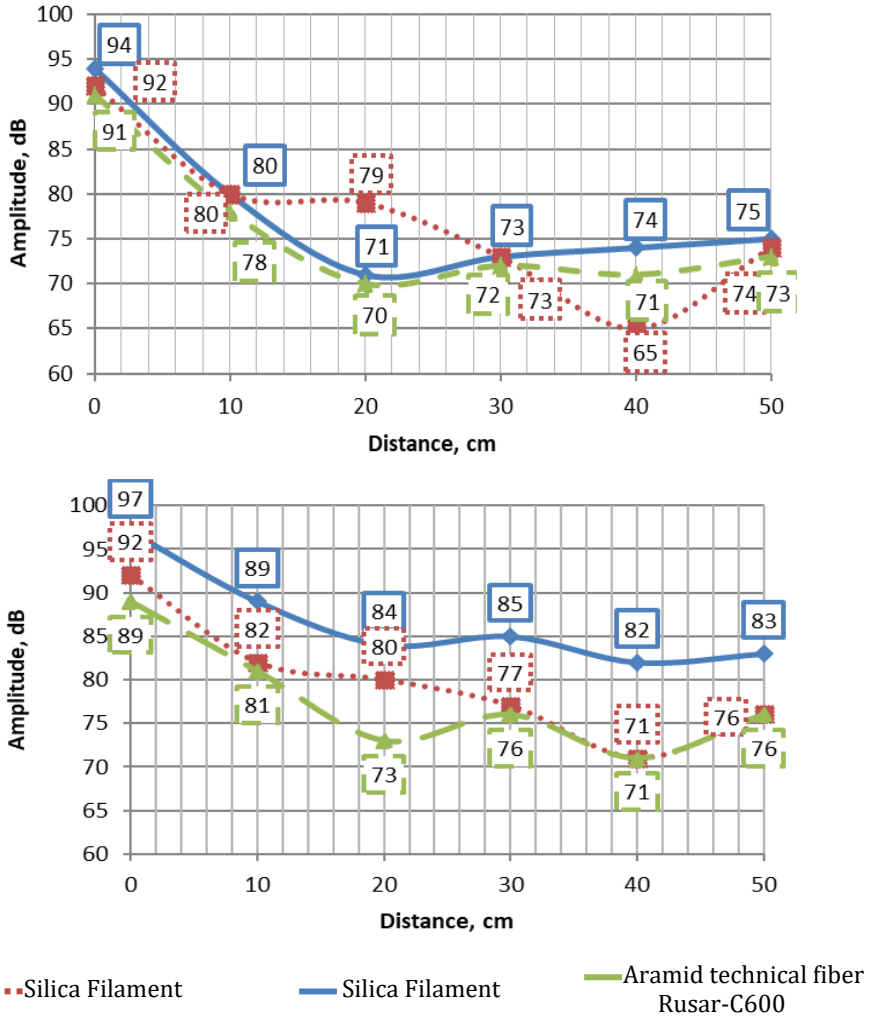

Fig. 3. Decay curves when recording signals: top – AEC GT200; below – AEC GT205

It can be observed from the attenuation curves that:

- the attenuation of signals during the transition from filaments to waveguide is approximately 12-14 dB for AEC GT200 and 8-10 dB for GT 205;
- signal attenuation during propagation in filaments:
- in silica filaments, the order of attenuation is 10 dB/m for GT200 and 12 dB/m for GT205; In carbon filaments, it is approximately 12 dB/m for GT200 and 10 dB/m for GT205;
- the technical fiber attenuation of the Rusar-C600A is approximately 8 dB/m for GT200 and 10 dB/m for GT205.

Amplitude-frequency characteristics (frequency response) of AEC GT205 and GT200, when simulating signals on waveguide capture and filament, at a distance of 10 and 40 cm from waveguide capture, are shown in Figures 4-6.

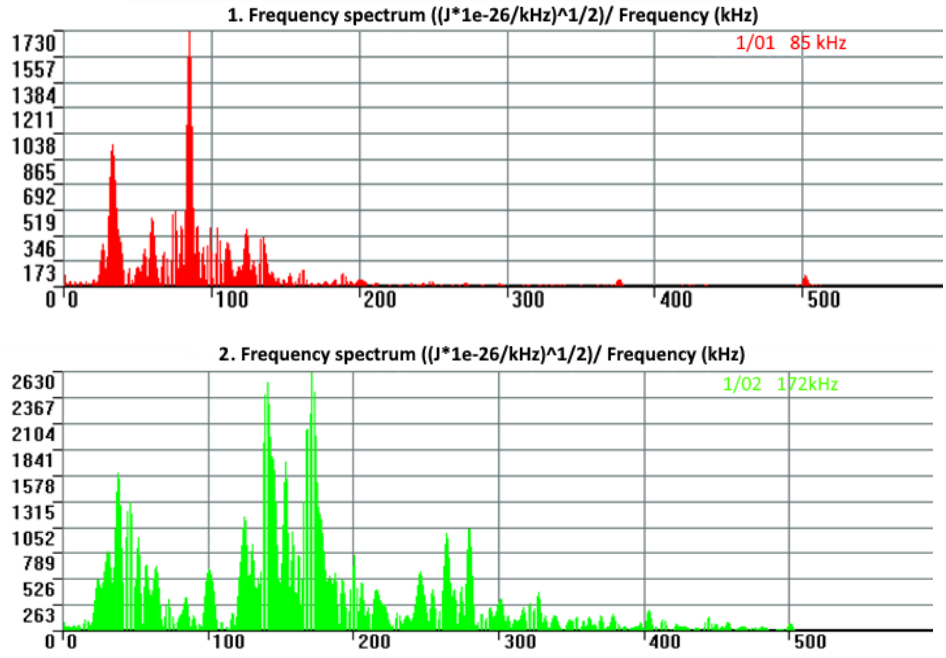

Fig.4. Amplitude-frequency characteristics when recording GT205 (top) and GT200 (bottom) signals when simulating signals on a waveguide grip

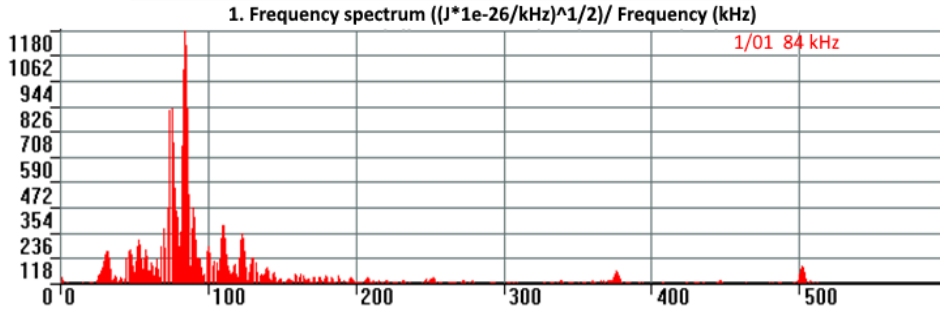

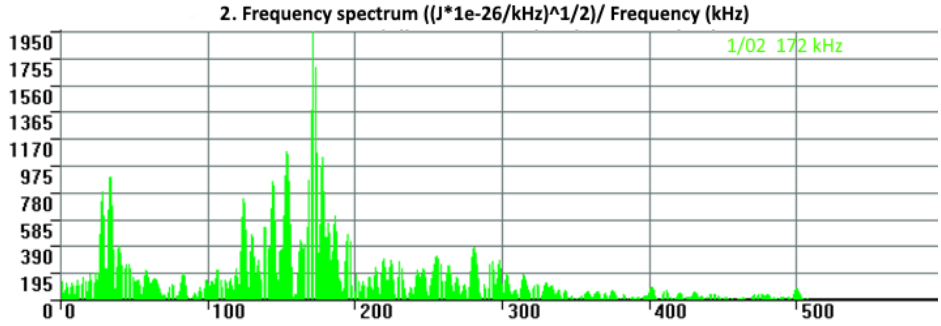

Fig. 5. Amplitude-frequency characteristics when recording GT205 (top) and GT200 (bottom) signals when simulating signals on a filament at a distance of 10 cm from the waveguide grip

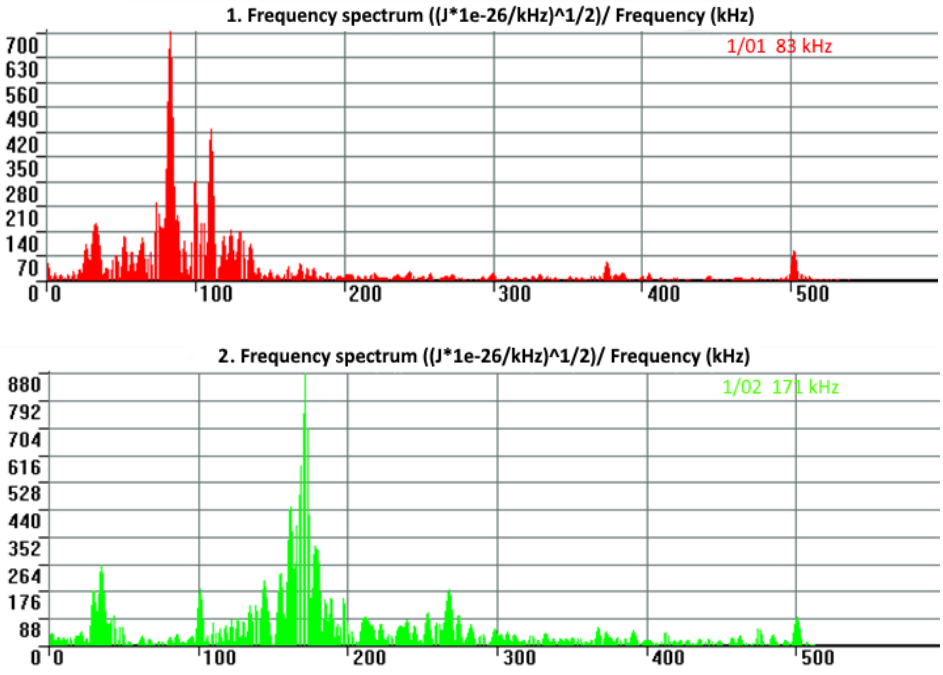

Fig. 6. Amplitude-frequency characteristics when recording GT205 (top) and GT200 (bottom) signals when simulating signals on a filament at a distance of 40 cm from the waveguide grip

A comparison of the frequency response when simulating signals on the capture waveguide and on the filament shows the absence of distortion of the recorded signals during the transition from the filament to the waveguide for AEC GT205 and GT200. For example, Fig. 4-6 shows the frequency response for Rusar-C600A technical fiber. The frequency response for silica and carbon filaments is similar. The same installation was used to determine the propagation velocity of ultrasonic vibrations in the threads and technical fiber. At the same time, the distance between the AEC is 1000 mm and three grippers were used. Two grippers were used, among other things, as waveguides on which the AEC was installed, the third gripper (pads. 1 in Fig. 7) was used to tighten the section

of threads on which the AE signals were simulated (Su-Nilsson source). It has been established that the acoustic wave propagation velocity is on the order of 1422 m/s for silica filament, 2099 m/s for carbon filament and 1805 m/s for a technical fiber.

Using the above setup, the parameters of AE signals arising from the destruction of filaments were studied. Threads and a 500 mm long tourniquet were used for the study. The threads and the technical fiber were loaded to destruction with simultaneous registration of AE signals using AES GT205 and GT200. Changes in the average amplitude and AE activity were selected as acoustic emission parameters, which serve as an acoustic emission portrait of a specific material. The amplitude parameter of acoustic signals directly depends on the properties of the material and allows you to reliably determine its type against the background of external noise and/or concomitant destruction of materials (for example, simultaneous destruction of the liner material and the power shell of a metal-composite high-pressure cylinder) [9]. Apply AE activity to PCM, that is, the number of registered pulses of acoustic emission per unit of time, gives an idea of the structure of the material. Thus, when fibrous materials are destroyed, the activity will be higher due to the generation of acoustic signals from the destruction of single fibers.

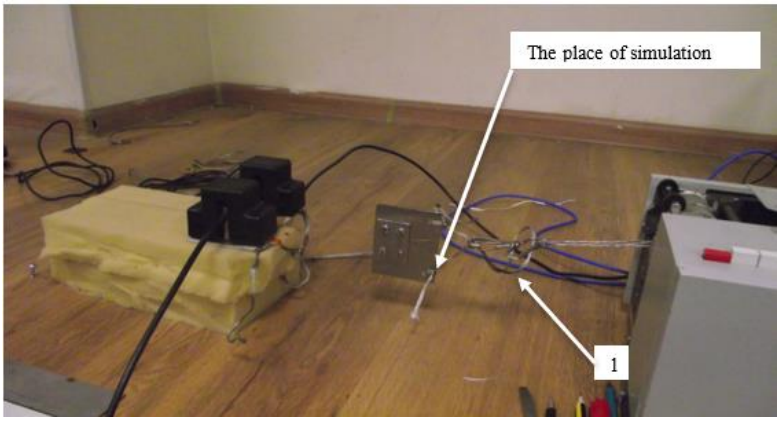

Fig. 7. Experimental setup for determining the speed of propagation of ultrasonic vibrations

3. Results and Discussion

Analyzing the dynamics of changes in the parameters of AE signals during destruction, it can be noted that such parameters as the average amplitude and activity allow us to conclude about the type of collapsing filaments. Figure 8 shows generalized graphs of changes in the average amplitude during the destruction of the filaments and technical fiber, and Figure 9 shows graphs of changes in AE activity. A sign of the failure of the Rusar -C600 technical fiber, in the context of the failure of silica and carbon fibers, is the detection of pulses with amplitudes exceeding 70 decibels. A sign of failure of carbon fibers, in the presence of failed silica fibers and the technical fiber, is the recording of acoustic emission (AE) activity exceeding 50 events per second.

The nature of the variation in the temporal characteristics of AE pulses (mean duration and mean rise time) is consistent across all samples. Graphs depicting the relationship between the mean rise time and the duration of the pulses are presented in Figure 10.

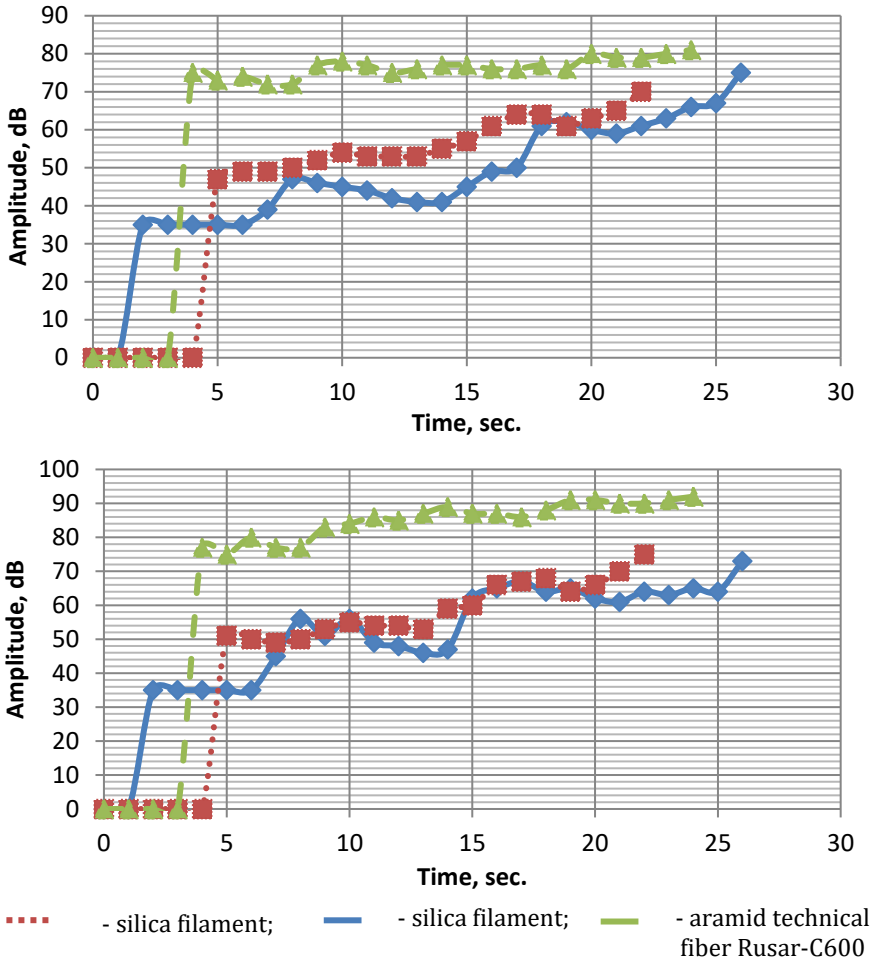

Fig. 8. Graphs of changes in the average amplitude during the destruction of filaments and technical fibers: top - AEC GT200; below is the AEC GT205

Silica filaments are characterized by a high ratio at the initial and final moment of destruction. Carbon filaments are characterized by a small ratio range, lying in the range of 0.28-0.38. Aramid technical fiber is characterized by a spread from 0.1 to 0.3. I.e., the harness is characterized by a short pulse rise time. The destruction occurred by sequential destruction of individual groups of elementary strands during the order of 23-26 seconds. The appearance of the destroyed fibers and the aramid technical fiber are shown in Fig. 10.

The destruction of the threads was fragile, which is confirmed by the enlarged images in Figure 10. The analysis of the frequency response at the rupture of filaments for EACH GT205 and GT200 (Fig. 12-14) showed that the highest energy is recorded when the technical fiber is destroyed, and the lowest when the silica filament is destroyed. The energy released in the low-frequency spectrum is concentrated in the frequency range of 50-120 kHz, in the high-frequency spectrum it is concentrated in the range of 140-300 kHz, while in the range of 50-120 kHz the amount of energy released is almost 3-5 times higher.

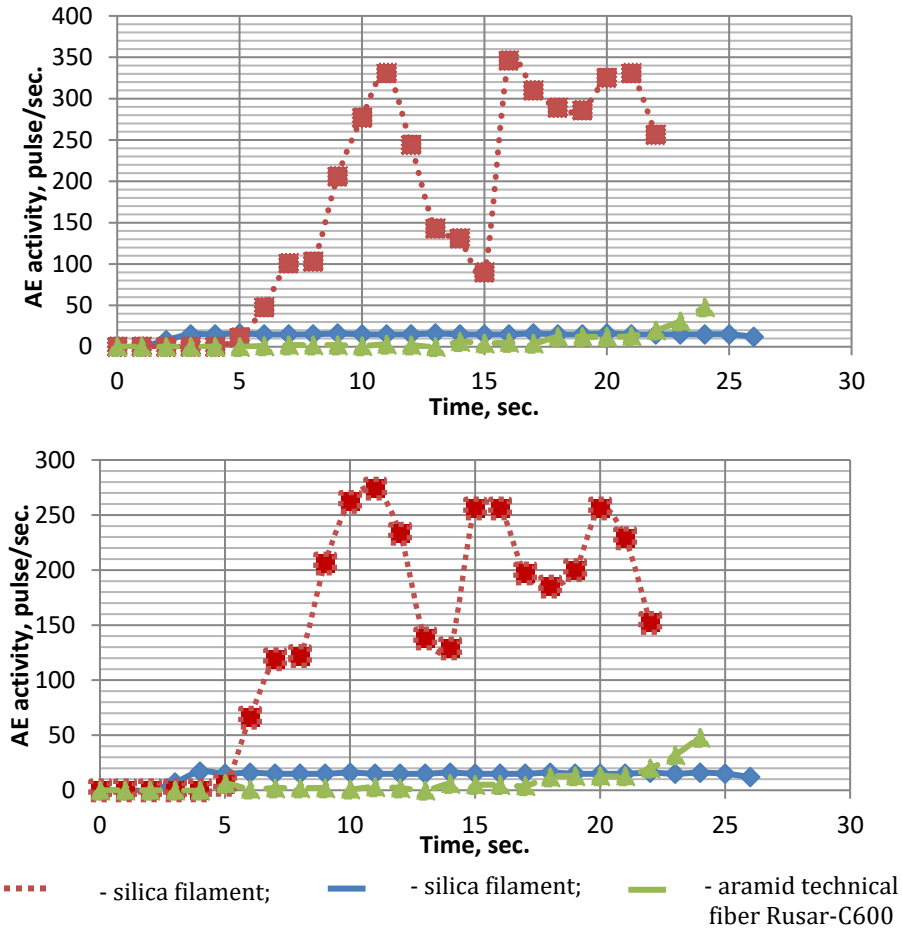

Fig. 9. Graphs of changes in AE activity during the destruction of filaments and technical fibers: top – AEC GT200; below is the AEC GT205.

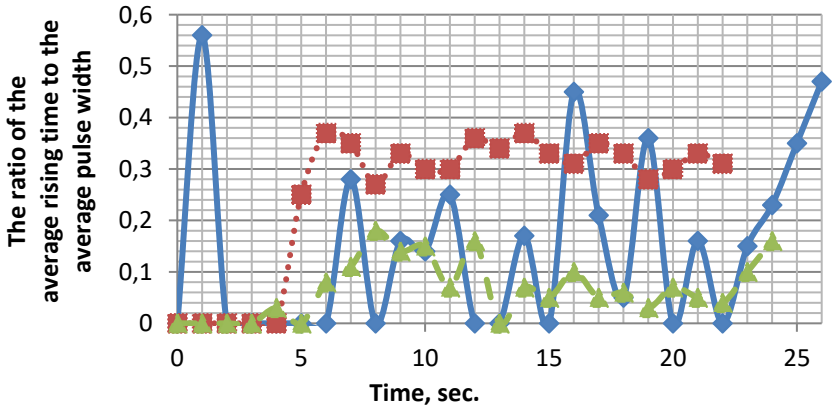

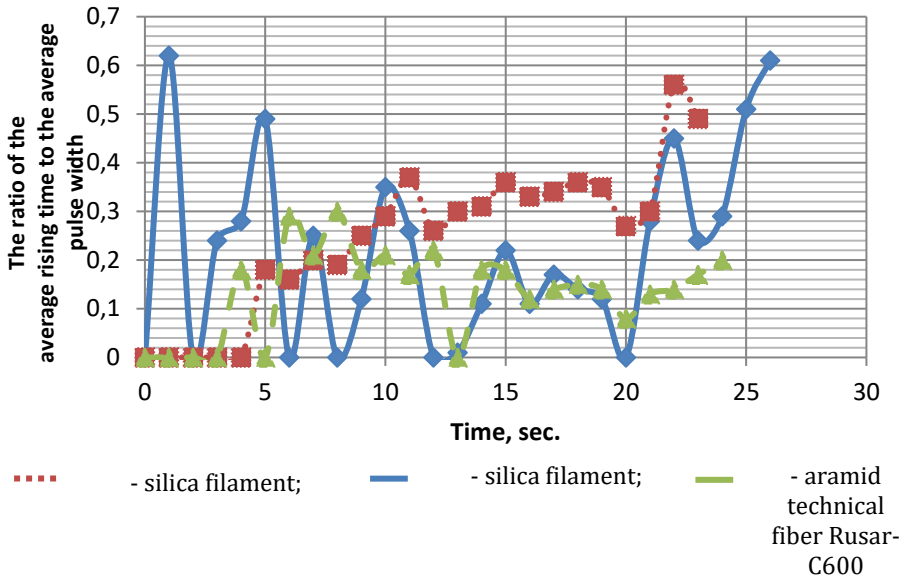

Fig. 10. Ratios of the average rise time of pulses to their average duration: top – AEC GT200; below is the AEC GT205

Fig. 11. Appearance of destroyed filaments and technical fiber, 1) silica filament; zoom in x182 on the right; 2) carbon filament; zoom in x102 on the right; 3) aramid technical fiber Rusar-C600; zoom in x139 on the right

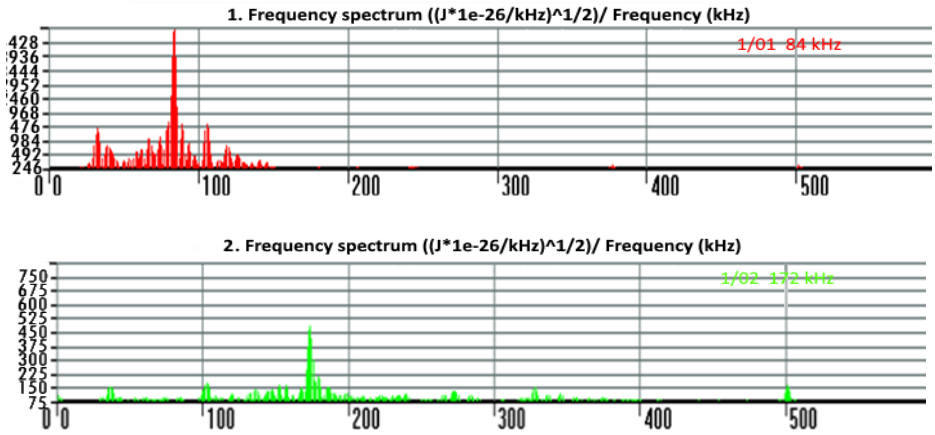

Fig. 12. Amplitude-frequency characteristics when silica filament breaks: top - GT205; below GT200

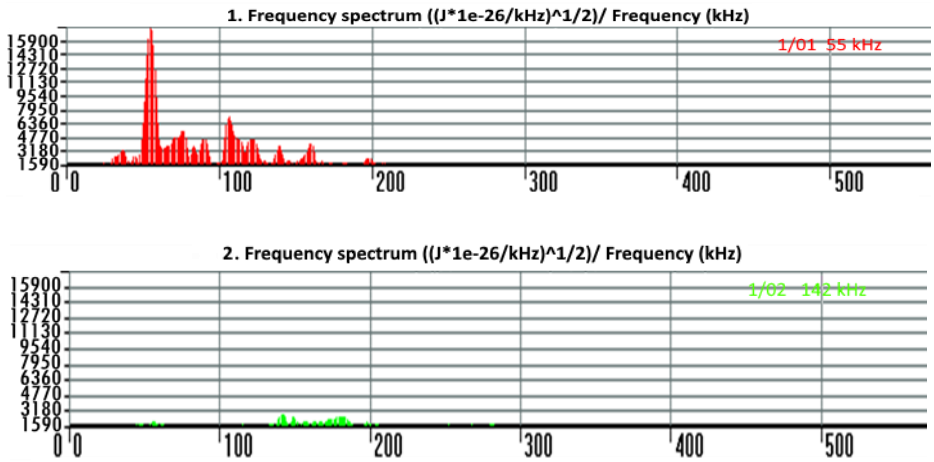

Fig. 13. Amplitude-frequency characteristics when carbon filament breaks: top - GT205; below GT200

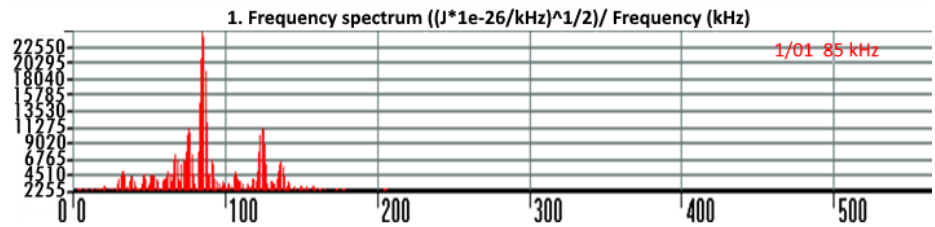

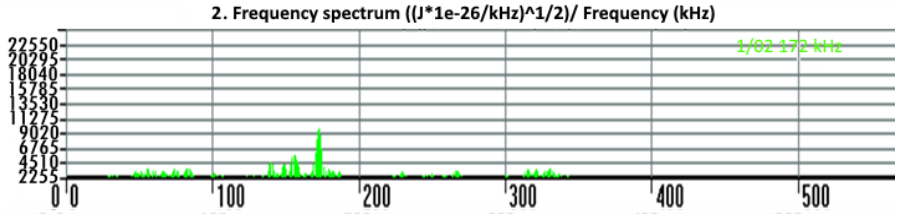

Fig. 14. Amplitude-frequency characteristics when aramid technical fiber Rusar-C600 breaks: top - GT205; below GT200

5. Conclusions

The study confirmed the possibility of detecting cases of destruction of the filler when loading of the of structures made of reinforced polymer composite materials and determining the type of destroyed filler of reinforced structures made of PCM. The obtained data on the features of the destruction of fillers allowed us to obtain an acoustic emission portrait of the destruction of reinforced PCM materials, which allows us to conclude about the type of collapsing filaments according to the following distinctive features:

- A sign of the destruction of technical fiber Rusar – C600A against the background of the destruction of silica and carbon filaments is the registration of pulses with an amplitude of more than 70 dB.
- A sign of the destruction of carbon filaments against the background of the destruction of silica and technical fiber filaments is the registration of AE activity above 50 imp/sec.
- An additional feature in case of destruction is the energy parameter: the highest energy is recorded when the technical fiber is destroyed, and the lowest when the silica filament is destroyed.

It was also found that the most informative frequency range for recording AE signals in PCM is the 40-120 kHz range. In order to register AE signals arising from the destruction of carbon or silica filaments, it is advisable to use PAE type GT205 or DR6I.Thus, the use of the acoustic emission control method makes it possible not only to assess the technical condition of PCM products, but also to predict their performance due to the possibility of early detection of hidden developing defects, such as the destruction of single fibers of silica or carbon filaments. In the complex with the research of the parameters of acoustic emission signals during the destruction of the liner material and the power shell of a metal-composite high-pressure cylinder [9], acoustic emission parameters of AE signals arising from the destruction of filaments of PCM fillers, binder, micro composite and liner metal were obtained. The obtained acoustic emission portrait is an integral part of the development of a program for technical diagnostics of products made of PCM and will be used in the further development of criteria for evaluating AE sources in accordance with their degree of danger.

References

[1] Markin V, Myagkova N. High-pressure cylinders of gas-fuel system made of composite materials. IOP Conf Ser Mater Sci Eng. 2021;1100:012011. https://doi.org/10.1088/1757-899X/1100/1/012011

[2] Chauhan G, Awasthi A. Design and analysis of high-pressure composite vessels. Int J Latest Eng Manag Res. 2018;03(06):96-102.

[3] Stepanova L, Ramazanov I, Chernova V. Acoustic and emission analysis of the defect nucleation process in carbon fiber reinforced plastic samples. Transp Res Procedia. 2021;54:320-327. https://doi.org/10.1016/j.trpro.2021.02.078
[4] Берлин АА, редактор. Полимерные композиционные материалы: структура, ствойства, технология: учеб пособие. 3-е испр. изд. СПб.: ЦОП «Профессия»; 2011. 560 с.
[5] Lebedev IK, Lebedev KN, Moroz NG. Experimental studies of life characteristics of metal-composite cylinders. Civil Aviat High Technol. 2015;(212):137-142. (In Russ.).
[6] Bo K, Liu S, Cheng L, Yuan Y, Luo H. Experiment research on acoustic emission of impact-damaged fully-wrapped composite gas cylinder with non-metallic liner. In: Proceedings of the 14th International Conference on Non-destructive Testing in Aerospace; 2021; Berlin, Germany. https://doi.org/10.1007/978-981-15-9837-1_33
[7] Jiang P, Liu X, Li W, et al. Damage characterization of carbon fiber composite pressure vessels based on modal acoustic emission. Materials. 2022;15:4783. https://doi.org/10.3390/ma15144783
[8] Ono K, Gallego A. Research and applications of ae on advanced composites. J Acoust Emiss. 2012;30:180-220.
[9] Erofeev M, et al. The effects of ultrasonic treatment on the structure and properties of alloys. J Phys Conf Ser. 2021;2131:022062. https://doi.org/10.1088/1742-6596/2131/2/022062
[10] Hua W, Chen Y, Zhao X, et al. Research on corrosion detection method of oil tank bottom based on acoustic emission technology. Preprints. 2024; 24: 3053. https://doi.org/10.20944/preprints202404.0165.v1
[11] Bhuiyan MY, Lin B, Giurgiutiu V. Acoustic emission sensor effect and waveform evolution during fatigue crack growth in thin metallic plate. J Intell Mater Syst Struct. 2018;29(7):1275-1284. https://doi.org/10.1177/1045389X17730930
[12] Bi HS, Li HY, Zhang W, et al. Evaluation of the acoustic emission monitoring method for stress corrosion cracking on aboveground storage tank floor steel. Int J Press Vessels Pip. 2020;179:7. https://doi.org/10.1016/j.ijpvp.2019.104035
[13] Manthei G, Koob M, Walther M, Minnert J. Analysis of the structural behavior of reinforced concrete components with acoustic emission analysis. e-J Nondestruct Test. 2024;29. https://doi.org/10.58286/29893
[14] Zhang J, Shen G, Chen D, et al. Application of acoustic emission technology for bearing condition monitoring on passenger ropeway. e-J Nondestruct Test. 2024;29.
[15] Liu R, Liang YJ, Liu S, et al. Applicability of a new composite amusement ride safety device based on acoustic emission monitoring technology. Mater Res Express. 2024;11. https://doi.org/10.1088/2053-1591/ad43c0
[16] Filonenko S, Stakhova A, Bekö A, Grmanova A. Acoustic emission during non-uniform progression of processes in composite failure according to the Von Mises Criterion. J Compos Sci. 2024;8:235. https://doi.org/10.3390/jcs8070235
[17] Wei D, Yang Y, Si J, Wen X. Study on acoustic emission detection technology of fiber reinforced plastic pressure vessel. In: ASME Pressure Vessels and Piping Conference. 2020. https://doi.org/10.1115/PVP2020-21088
[18] Ivanov VI, Vlasov IE. Acoustic emission method. In: Klyuev VV, editor. Non-destructive testing: Handbook. Vol. 7. Book 1. Moscow: Mechanical Engineering; 2005; page 340.
[19] Popov AV, Voloshina VYu, Zhuravsky KA, Labina MA. Acoustic emission method of diagnostics of structures made of composite materials based on invariants. Adv Eng Res. 2022;22(4):331-337. https://doi.org/10.23947/2687-1653-2022-22-4-331-337
[20] Lyu NT, Nguyen KD, Demchenko SK, Chernoverskaya VV. Application of the acoustic emission method in problems of control and monitoring of the technical condition of diagnosed objects. In: Proceedings of the International Symposium "Reliability and Quality"; 2021; 2:77-82.

[21] Zaki A, Chai HK, Behnia A, et al. Monitoring fracture of steel corroded reinforced concrete members under flexure by acoustic emission technique. Constr Build Mater. 2016. https://doi.org/10.1016/j.conbuildmat.2016.11.079
[22] Ono K. Application of acoustic emission for structure diagnosis. Konferencja Naukowa. 2010; pp.317-341.
[23] Kachanov VK, Sokolov IV, Karavaev MA, Kontsov RV. Selecting optimum parameters of ultrasonic noncontact shadow method for testing products made of polymer composite materials. Russ J Nondestruct Test. 2020;56(10):831-842. https://doi.org/10.1134/S1061830920100046
[24] Korzec I, Samborski S, Łusiak T. A study on mechanical strength and failure of fabric reinforced polymer composites. Adv Sci Technol Res. 2022;16:120-130. https://doi.org/10.12913/22998624/146686
[25] Pecho P, Hrúz M, Novák A, Trško L. Internal damage detection of composite structures using passive RFID tag antenna deformation method: basic research. Sensors. 2021;21(24):8236. https://doi.org/10.3390/s21248236
[26] Fowler TJ, Gray E. Development of an acoustic emission test for FRP equipment. In: Preprint 3583, American Society of Civil Engineers; 1979.
[27] Wei D, Yang Y, Si J, Wen X. Study on acoustic emission detection technology of fiber reinforced plastic pressure vessel. 2020. https://doi.org/10.1115/PVP2020-21088

Research on Engineering Structures & Materials
www.jresm.org
MIM Research Group

Research Article

Experimental research of quality of the adhesive repairs of composite structures using non-destructive testing

Kirill Ibrishev *[,a], Ekaterina Prilipko [b], Maksim Soldatkin [c], Nikolay Kononov [d]

Moscow Aviation Institute (National Research University), Moscow, Russia

Article Info

Article History:

Received 12 July 2024

Accepted 18 Dec 2024

Keywords:

Adhesive repair;
Composite materials;
Non-destructive testing;
Honeycomb panels;
Shearography

Abstract

The increasing use of polymer composite materials in aviation necessitates adhesive repairs of aircraft structures in situ, minimizing disassembly and manufacturer return to reduce costs and repair time. This paper discusses the required repair technologies and equipment, as well as the quality analysis and the defect assessment of these repairs through various non-destructive testing (NDT) methods. An experimental investigation was conducted on adhesive repairs of a three-layer carbon fiber panel, evaluating defects qualitatively assessing the applied technologies, and providing recommendations for NDT applicability for this type of sample. The study's analysis produced several key conclusions regarding repair zones. In Zone 1, using the vacuum method, non-adhesions and voids from resin curing were identified, detectable by all NDT methods, with staff qualifications significantly impacting repair quality. In Zone 2, also applying the vacuum method with excess pressure, minor non-adhesions, and voids (2-3 mm) were observed, which were left undetected by rapid NDT (shearography), while detailed NDT (tomography) revealed fewer defects, rating the repair as satisfactory. In Zone 3, utilizing the vacuum method at elevated temperatures, multiple local non-adhesions, and significant delamination (up to 40x40 mm) were discovered, classifying this repair as defective, confirmed by all NDT methods. Smaller defects were only detected by tomography, underscoring the importance of detailed NDT for accurately assessing repair integrity across various technologies.

1. Introduction

During The competitiveness of composite materials significantly depends on the dispersion of physical and mechanical properties, as well as the availability of effective NDT methods for finished products and the complexity of repairing damages during the operation of aircraft [1]. During the operation of aircraft, products made from polymer composite materials (PCMs) are subjected to random impact influences caused by the environment (both under normal conditions and abnormal natural phenomena); crew errors during take-off and landing; the destruction of units with the formation of non-localized debris; technical staff errors when working on the aircraft; technical staff errors when moving airport equipment; displacement of poorly secured cargo. With the increase in the volume of application of PCM products, the development of new repair technologies and the improvement of existing ones is required.

In the creation of repair techniques, the original design specifications serve as a foundation. These specifications include restoring the rigidity of the original structure, restoring static strength under expected operating conditions up to the limit load, ensuring durability during the remaining service

*Corresponding author: ibrishevKK@mai.ru
[a]orcid.org/0009-0006-4345-3335; [b]orcid.org/0000-0001-7063-5261; [c]orcid.org/0009-0006-6141-5906; [d]orcid.org/0009-0002-2665-4785
DOI: http://dx.doi.org/10.17515/resm2024.351ma0712rs

life of the component, compliance with the requirements for the admissibility of damage to the original part [2].

There are many types of PCM product repairs, however, most used ones are mechanical (bolted) and adhesive, as they allow to achieve the mechanical characteristics of the original structure to the greatest extent. These methods are most used in the aviation industry by aircraft operators, but at the same time, they are not universal, as they depend on the type and structure of the repaired object, parameters of the defect, as well as the qualifications of the specialist. While the study primarily focuses on adhesive repair and NDT of three-layer honeycomb PCM, the methodologies discussed are not exclusive to PCM. Various composite structures, such as laminated composites, fiber-reinforced composites, sandwich composites, and carbon fiber reinforced polymers (CFRP), can also benefit from these adhesive repair techniques and NDT procedures. Each composite type may present unique characteristics and defect types that necessitate tailored approaches; however, the fundamental principles of adhesive bonding and NDT remain applicable across different composite materials. Therefore, highlighting these other composite structures is advisable to emphasize the broader relevance of the study's findings.

Repairs using mechanical connections can only be used for thick-walled monolithic structures [3]. Bolted repairs in aviation structures have several drawbacks, including reduced fatigue durability due to stress concentration in the bolt holes, limited applicability to thick-walled structures (not suitable for thin-walled or composite materials), increased weight from added hardware, complexity in installation requiring specialized skills, and restricted flexibility in design. These repairs are generally not advisable for thin-walled composite, curved, or highly loaded components, making their use context-specific and necessitating careful consideration of the repair conditions. The presence of additional holes negatively affects fatigue durability and is a potential place for the initiation of cracks, however, this type of repair allows restoring the strength and rigidity of the structure [4].

At present time, there are several types of adhesive repairs, as they are more suitable for the repair of both monolithic thin-walled and thick-walled claddings of PCM products, as well as for three-layer carbon fiber honeycomb panel. Currently, there are several types of adhesive repairs, as they are more suitable for the repair of both monolithic thin-walled and thick-walled structures of composite materials, as well as for three-layer sandwich panels. Adhesive bonding offers advantages such as even stress distribution, reduced weight compared to mechanical fasteners, and the ability to bond dissimilar materials. Additionally, adhesive repairs can enhance the fatigue resistance of the structures and allow for greater design flexibility.

There are two traditional methods of conducting adhesive repair:

- Vacuum forming using dry fabrics and cold-curing binders. This method has its drawbacks. The lifetime of repaired areas in this way is limited due to the low mechanical characteristics of the adhesive connection. Additionally, we do not use prepreg materials because they are more expensive and require specific storage conditions, which can complicate the repair process. This makes the overall approach less practical for certain applications where cost and ease of handling are crucial.
- Autoclave forming using prepregs in factory conditions. While this method is known for producing high-quality repairs, it has significant disadvantages. The process involves lengthy dismantling, transportation, and repair times at the factory, which can lead to increased downtime and operational inefficiencies. Additionally, using an autoclave is considerably more expensive, adding to the repair cost.

Based on the above-mentioned disadvantages of repair methods, this work will consider a non-autoclave repair method based on impregnated dry fabric.

Currently, several scientific studies explore constructive and technological solutions for performing adhesive repairs under operational conditions [5]. In [6], the repair process of PCM products with a honeycomb filler is described: the necessary technical equipment for mechanical processing and thermo-vacuum forming.

Adhesive repairs in [7], were carried out using prepregs made for repair tasks with non-autoclave curing. These prepregs offer significant benefits, such as reduced processing time and lower equipment costs, making them suitable for in-situ repairs [8]. However, challenges remain, including the need for precise temperature control during the curing process and potential limitations in achieving optimal mechanical properties compared to traditional autoclave-cured composites, the advantages and disadvantages of using which are depicted in [9]. Furthermore, the long-term durability and performance of these repairs under varying environmental conditions require thorough investigation to ensure reliability in aviation applications.

To assess the condition of the repaired products, NDT methods are used, including ultrasound, acoustic, optical, and radiation techniques [10]. These methods allow for the detection of internal defects, such as delaminations, voids, and cracks, without damaging the material. Ultrasound testing is particularly effective for identifying flaws in composite materials, while acoustic emission can monitor structural integrity during loading [11]. Optical methods provide high-resolution imaging, enabling detailed surface inspections. Radiation techniques, such as X-ray or gamma-ray inspection, offer insights into the internal structure of components. By employing a combination of these NDT methods, a comprehensive evaluation of the repair quality can be achieved, ensuring that the repaired products meet safety and performance standards [13].

In several articles experimental work was carried out to determine the applicability of various NDT methods to samples of honeycomb structure with repairs carried out using different technologies [14]. Samples were considered, manufactured according to various technologies; additional samples were prepared with a deliberately violated technological process. The study aimed to evaluate the effectiveness of each NDT method in detecting flaws and assessing the integrity of the repaired structures [15]. Various parameters, such as the size and type of defects, as well as the specific characteristics of the repair techniques used, were analysed. The results indicated that certain NDT methods, such as ultrasonic testing, were more effective in identifying internal defects in repaired samples, while others, namely optical inspection, excelled in detecting surface irregularities. This comprehensive analysis did not only highlight the strengths and limitations of each technique but also provided valuable insights into optimising repair processes and ensuring the reliability of honeycomb structures in practical applications [16]. Further research is suggested to refine these methods and explore their integration for enhanced assessment capabilities [17].

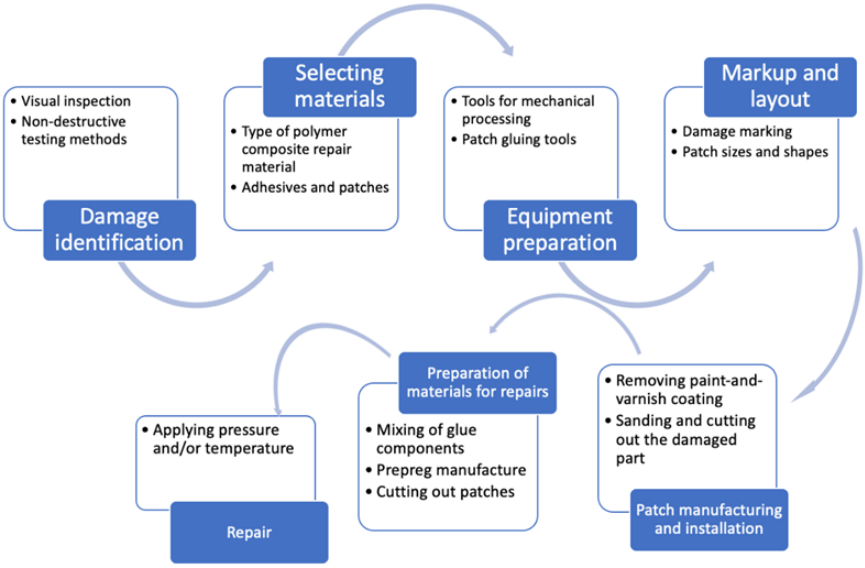

Fig. 1. Overall repair procedure flowchart

Analysing the aforementioned studies, the relevance of this work can be formulated: in light of the difficulties arising from the use of prepreg technology, it is advisable to use adhesive repair technology as the most practical and accessible method, particularly with the rapid assessment using NDT methods. The analysis provides an opportunity to evaluate the presence of defects in the structure and provides a quality check of the methods used.

The essence of the work is to carry out repairs, quality analysis, and evaluate adhesive repair defects using various NDT methods. The scientific investigation of the repair of a three-layer honeycomb panel made of polymer composite material includes the identification and evaluation of damaged zones by assessing areas with defects for further repair. It involves the selection of materials for repair work, choosing suitable adhesive compositions and materials for restoration. Additionally, it requires the preparation of equipment, gear, and tools for repairing the structures by gathering necessary tools and equipment for the repair process. Marking and laying out damaged areas is crucial, as it involves clearly defining the zones that require repair. The removal of paint from the repair area is necessary for cleaning the surface to ensure high quality adhesion. Mechanical processing of damaged areas prepares the repair zone by removing damaged materials. Furthermore, preparation of adhesive compositions entails mixing adhesive materials according to repair specifications. Cutting out patches layer by layer involves creating patches from material that matches the original structure. Laying out the repair composition includes applying adhesive to the prepared surface. Finally, making the repair patch using the chosen technology completes the repair process by installing the patch according to the selected method. The overall process is presented with a flowchart in figure 1.

2. Methods and Materials

2.1 Description of the Control Object

The subject of this research is a three-layer honeycomb panel, consisting of a middle layer of honeycomb filler and external top and bottom skins. The panel is made of composite material, used in the aviation industry. This research focuses on the repair process of the panel, represented in figure 2, to study its structural properties after damage upon impact. Defects are inflicted by singular impacts along the monolithic part of the panel and across the part of the panel with a honeycomb filler from a height of 0.5 meters using a drop test rig with an impact energy of E = 1.398 J.

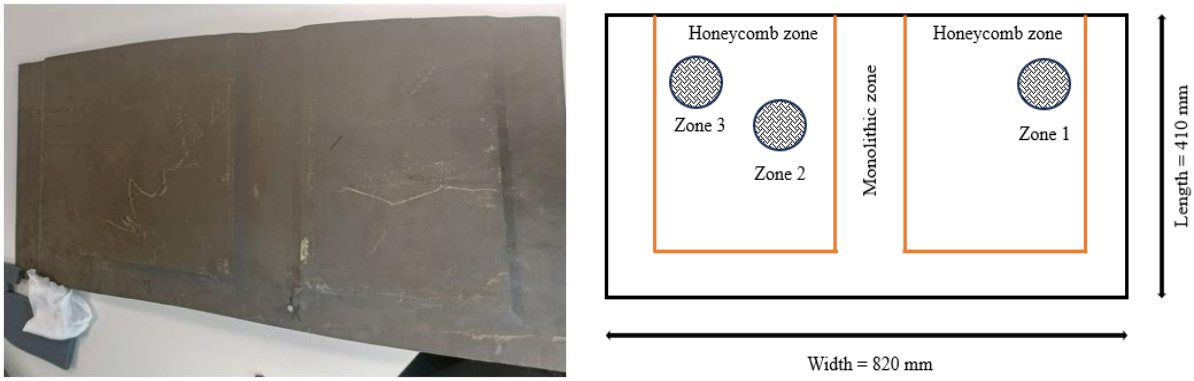

(a) (b)

Fig. 2. Repair three-layer carbon fiber honeycomb panel (a) External appearance of the panel (top view); (b) Schematic view of the repair panel with marked repair zones and overall dimensions

3. Description of Repair Technology

3.1. Description of The Repair Device

The existing repair device consists of two blocks: a control unit and a unit for ensuring the necessary technological parameters of the repair process for glued honeycomb and monolithic structures of an aircraft, made of polymer composite materials. The installation provides necessary pressure (vacuum within the range from negative 0.09 MPa to negative 0.073 MPa and excess up to 1.0 MPa) when gluing (forming) the repair patches.

The difference between the device being developed and those in operation in Russia [18] and abroad lies in additional options, among which:

- The possibility of using the control unit at a significant distance from the repair unit;
- The possibility of using excess pressure during repairs, in addition to vacuum pressure, in various combinations: vacuum pressure, combined pressure (vacuum + excess pressure), and only excess pressure. Excess pressure is extremely relevant, practically indispensable for the repair of non-sealed units, on which vacuum pressure is inapplicable;
- The possibility of using not only factory-made heaters but also ones made by the operating organisation, for the thermal regulation of repair zones which significantly reduces the time spent on repair work, and in some cases can be crucial for its implementation.

Four Russian patents [19-22] have been issued on the topic related to the development of the proposed device. The patent [19] describes a portable device designed specifically for the repair of polymer items. It emphasises ease of use and mobility, allowing repairs to be conducted in situ. Another patent [20] describes a special approach to repairing the aerodynamic surfaces of aircraft using glue. It focuses on methods that ensure strong adhesion and structural integrity, which are crucial to maintaining aerodynamic performance. The patent [21] presents a method tailored for situations where access to the repair area is limited to one side. It details techniques that optimise the repair process while ensuring effective bonding and restoration of the material's properties. The patent [22] addresses the challenges associated with repairing thin-walled structures, which are often found in aerospace applications. It proposes methods that minimise the risk of further damage during the repair process and enhance the overall durability of the repaired structure.

3.2 Repair Material

Polymer repair adhesive is a two-component composition used in repairs as a filler and an impregnator. The mass of the prepared ACM12K adhesive is obtained after achieving a homogeneous structure by mechanical mixing of the components A and B, the weight ratio of which is indicated on the package and is about 100:30 by weight. The curing time of the adhesive is 2 hours at a temperature greater than 20 ºC.

Layers of the repair patch are cut out of a roll of carbon unidirectional tape, considering the size of the separating film on which all layers of the patch are applied. The scientific research of the repair of a three-layer honeycomb panel made of polymer composite material includes the calculation of the schematic arrangement of the patch. The scientific investigation of the repair of a three-layer honeycomb panel made of polymer composite material includes:

- Identification and evaluation of damaged zones;
- Selection of materials for repair work;
- Preparation of equipment, gear, and tools for repairing the structures;
- Marking and laying out damaged areas;
- Removal of paint from the repair area;
- Mechanical processing of damaged areas;
- Preparation of adhesive compositions;
- Cutting out patches layer by layer;
- Laying out the repair composition;
- Making the repair patch using the chosen technology.

According to the scheme presented in figure 3 for the calculation of all patches, placement is performed in the centre of the three-layer honeycomb panel. The patch has a specific geometric shape and sizes, corresponding to the requirements of the calculation of the structure repair. The process of calculating the patch size for the repair of composite structures involves several critical steps. Initially, it is essential to determine the size and shape of the damage by accurately measuring the affected area. Following this, the selection of the type and size of the patch becomes imperative, as the optimal dimensions are contingent upon both the nature and extent of the damage, as well as the specific materials employed in the composite structure. Subsequently, the design of the patch must be tailored to conform to the contours of the damaged area, thereby ensuring a secure and effective connection. Additionally, it is crucial to consider the overlap; the dimensions of the patch

should extend beyond the damaged area by several centimetres (typically 2-5 cm) to guarantee adequate overlap and structural integrity.

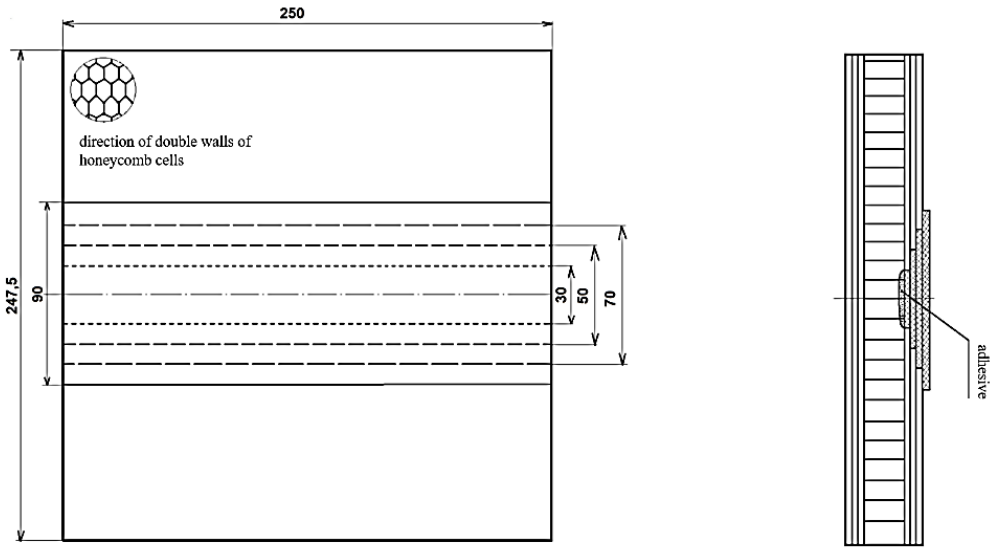

Fig. 3. Scheme of the arrangement of layers of the repair patch

3.3 Repair Types and Technological Modes

3.3.1 Vacuum

The vacuum bag is designed to provide vacuum (suction) and is installed on the repair zone, as shown in Figure 4. Repair under vacuum pressure is performed without heating for 2.0 hours, then the vacuum bag and technological materials are removed from the repair zone.

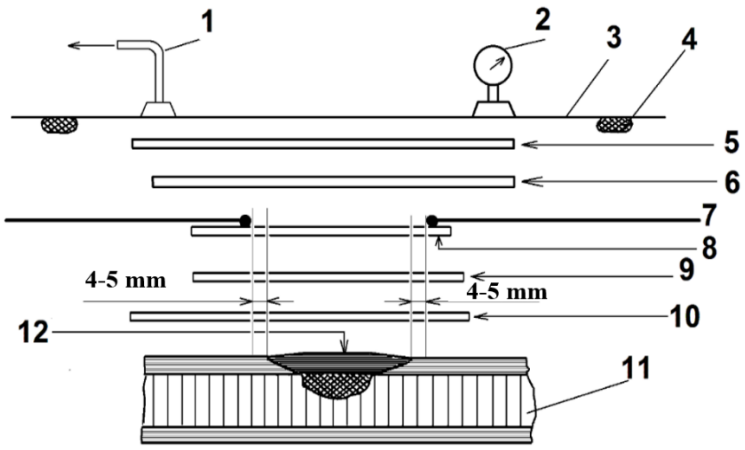

Fig. 4. Assembly scheme of the vacuum bag: 1- air suction; 2- device for controlling the suction in the vacuum bag; 3- vacuum bag shell; 4- sealing gasket; 5- vacuum bag's drainage layer (padding polyester, fiberglass); 6- heater (thermal blanket); 7- thermocouple; 8- non-perforated separating film; 9- layers of fabric absorbing excess resin (glue) – nylon or polyethylene terephthalate; 10-perforated separating film; 11-repaired structure; 12-repair patch layers in the repair zone

3.3.2 Excess Pressure

Excess pressure is the main type of technological pressure when it is impossible to ensure the airtightness of the repair zone (when it is impossible to install a vacuum bag). Providing heating in the repair zone is carried out through a heater (thermal blanket), laid on a non-perforated separating film. The curing temperature of the adhesive is set at 150 degrees Celsius, while the

maximum temperature of the thermal blanket can reach up to 200 degrees Celsius. This ensures that the adhesive cures effectively while maintaining the integrity of the surrounding materials.

Air bags in boxes can also be utilised as a source of excess pressure in the repair zones as presented in figure 5, alongside with power elements, clamps, and bags with sand as counterpressure, by which excess pressure can be provided.

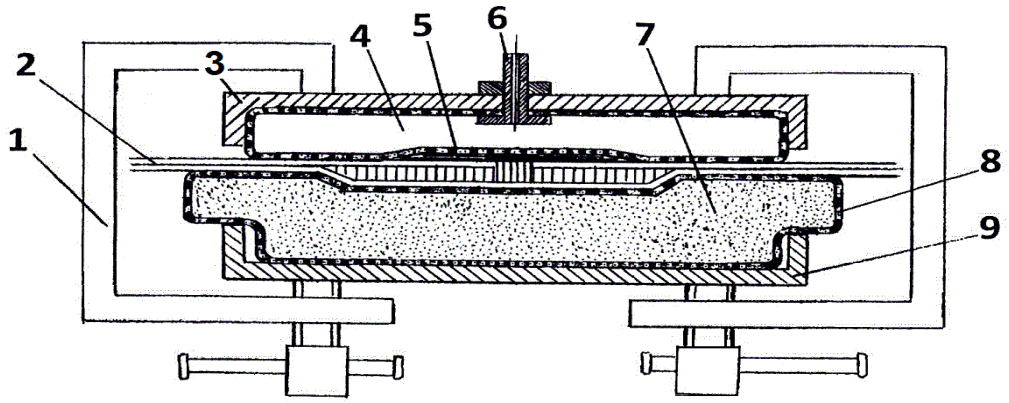

Fig. 5. Scheme of providing excess pressure during repair: 1 - clamp; 2- repaired structure; 3- air bag box; 4- air bag; 5- repair zone; 6- fitting for compressed air supply; 7- sand; 8- shell of the sand-filled bag; 9- the sand-filled bag supports

Two sample zones were repaired using different technologies: the first – vacuum, the second – vacuum with excess pressure, the third – vacuum with exceeding the curing temperature. The repair of the third sample zone was performed with a deliberately violated technology for the guaranteed presence of defects of various nature, which is necessary for the analysis of the detection of these defects by various NDT methods.

4. Description of Non-Destructive Testing Methods

4.1. Tomography

To detect potential defects in repair areas, a non-destructive testing method, X-ray computed tomography (CT), is used. CT provides a detailed analysis of the heterogeneities of the inspected object's structure. A planar radiography system, utilising a laminographic scanning algorithm, is used for this purpose. The research object (in this case, 3 samples with completed repairs) is placed inside the X-ray system, then the operator selects the optimal voltage and current values. To reduce data collection time, the number of projections for each sample is chosen in the range from 700 to 4000.

The process of material tomography involves several key stages: scanning, reconstruction, and post-processing. In the initial phase, scanning, the material is subjected to X-rays or other imaging techniques to capture a series of projections from different angles. This data provides a comprehensive view of the internal structure of the sample. Following the scanning, data reconstruction is performed using third-party software. This software processes the collected projections to create a 3D representation of the object, employing advanced algorithms to accurately reconstruct the internal features based on the scanned data. In the final stage, post-processing is conducted to refine the 3D model. This includes determining the centre of rotation for the sample, selecting a local area of interest, and adjusting the tone curve to enhance visibility and detail. As a result of this post-processing, a detailed 3D model of the research object is produced, allowing for cross-sectional views and further analysis of the material's properties. This comprehensive approach enables researchers to gain valuable insights into the internal structure and characteristics of materials without destructive testing.

4.2. Shearography

Shearography is an optical express non-destructive testing (NDT) method, which detects material defects through the measurement and analysis of surface deformations. These deformations are formed as a response to the internal structure's external influence. By combining the image of the object in its initial state with the image taken in the excited state, the change in any given point of the image can be determined [23]. During shearography, the test object's surface is illuminated with laser radiation [24]. The radiation reflected from the object's surface is received by a CCD-camera equipped with "shifting optics", which projects the object's image onto the camera matrix twice. Each point of the object is displayed twice on the CCD matrix [25].

Shearography is a flexible method in terms of the applied impacts for exciting the reaction of internal heterogeneity (thermal, vacuum, vibration). The optimal type of impact applied is depended on the structure and material of the control object, as well as the size, position (depth of bedding), and type of the defect [26]. Upon impact on the research object, the laser radiation reflected by each part of the surface also changes. These changes are detected by the system. This gives an idea of the defect's nature through its reaction on the surface. The method is implemented using a shearograph, consisting of an optical block combined with a thermal heating block, and an electronic block controlled by a PC, as shown in figure 6 [26]. The optical block is placed on a tripod in close proximity to the object's surface.

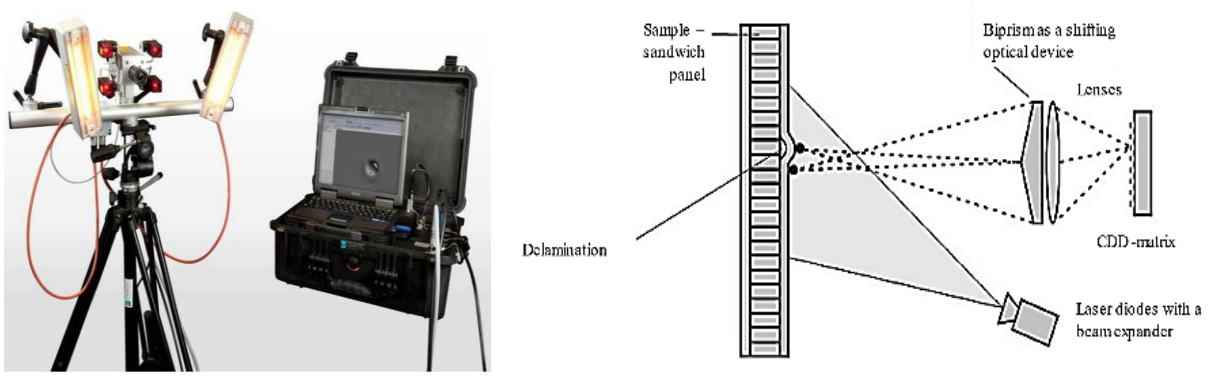

(a) (b)

Fig. 6. Apparatus of shearography system(a) - System with automatic loading by heating; (b) - The principle of the shearograph's operation

The view area is varied depending on the type and depth of bedding of the defect (ranges from 150x150 mm to 500x500 mm). This range differs according to the reflectivity of an object and the laser system power, as well as optic's focusing range.

5. Analysis of Experimental Results

5.1 Tomography

The general view of repair zone 1, done by vacuuming and the isometry view of the 3D model are presented in figure 7. The results of the study of repair samples by means of X-ray computed tomography are given in figure 8.

The general view of zone 2, executed by a vacuum method with excess pressure, and a 3D isometric view of the model, are presented in figure 9. When examining the projections of the repair patch, areas of non-adhesion, measuring 25 mm x 35 mm, and metallic inclusions were found, as shown in figure 10.

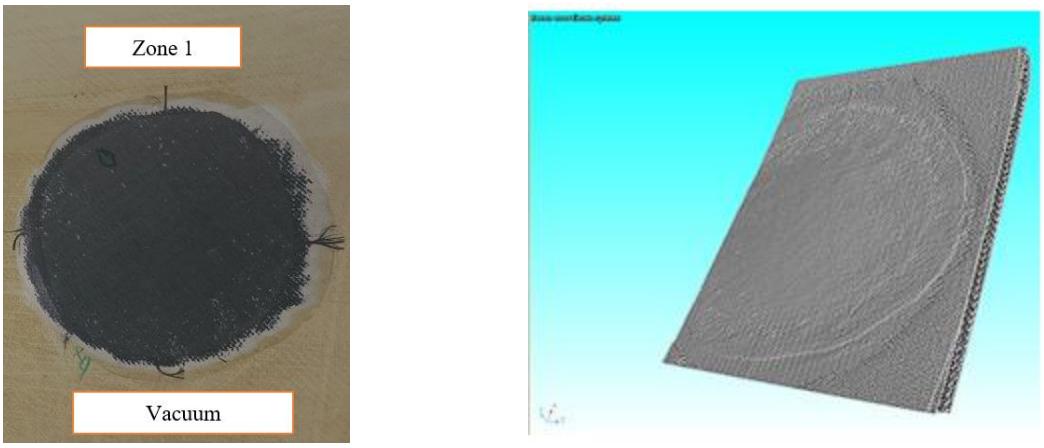

Fig. 7 – Repair patch in zone 1

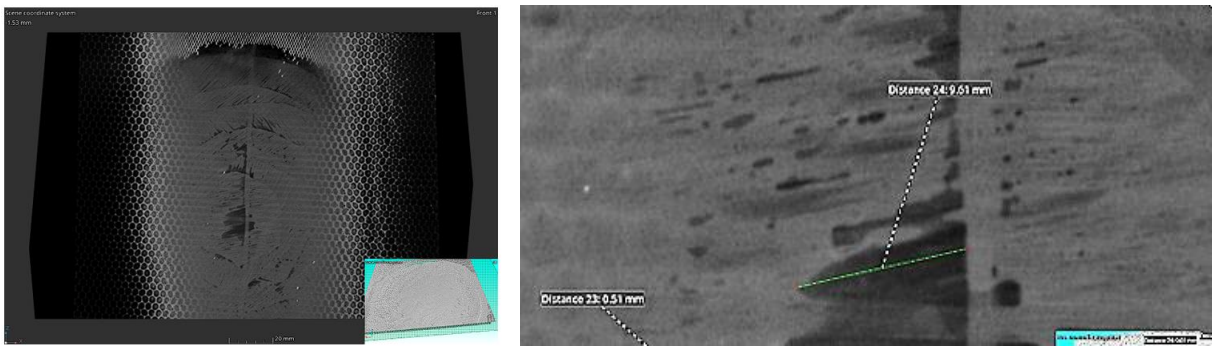

(a) (b)

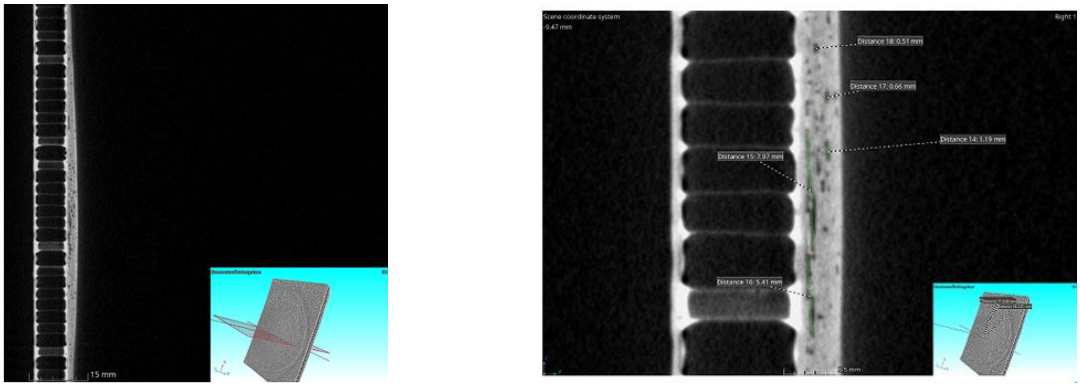

(c) (d)

Fig. 8. Results of tomography of repair zone 1, performed by vacuum method(a) General view of the repair patch section; (b) Local repair patch section zone; (c) Side section of the repair patch; (d) Local zone of the side section of the repair patch

From the results of tomography, we can conclude that there are image defects in the form of a ring on 3D models of repair patches, associated with the capture of the axis of rotation of samples when collecting projections. These defects do not affect the research results and are merely superficial display problems. When analysing the results of tomography on the side section of the repair patch, voids related to non-adhesions up to 2.9 mm in size were found. On the sections of the repair patch, numerous defects in the form of metallic inclusions and non-adhesions were also found.

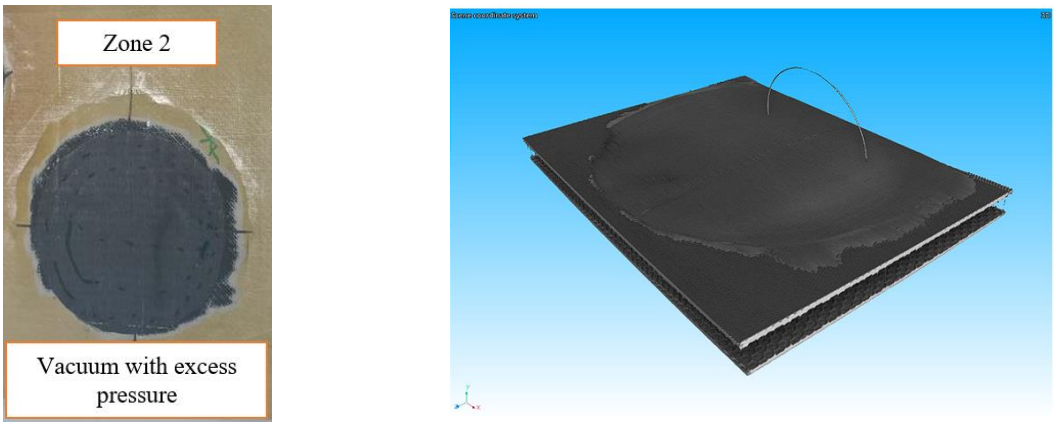

Fig. 9. Repair patch in zone 2, performed by vacuum method with excess pressure

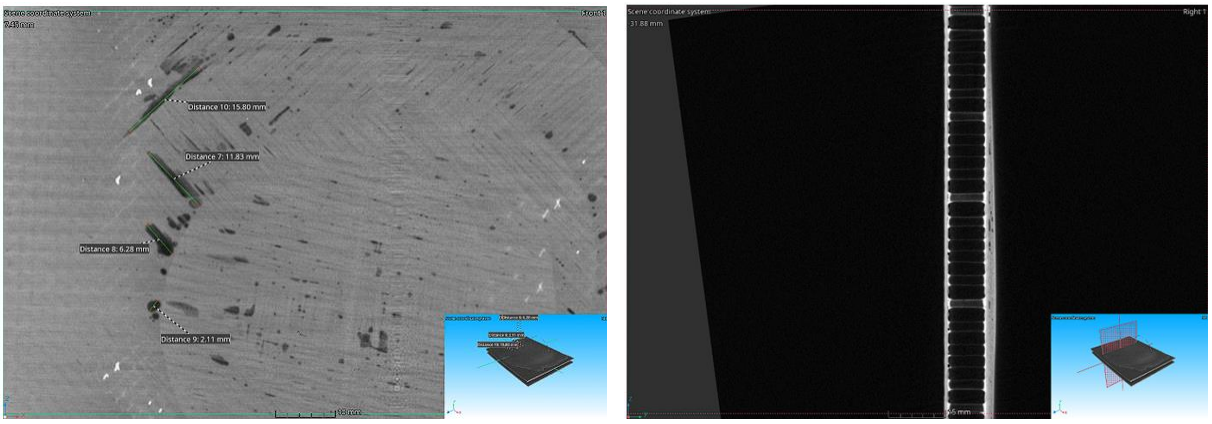

(a) (b)

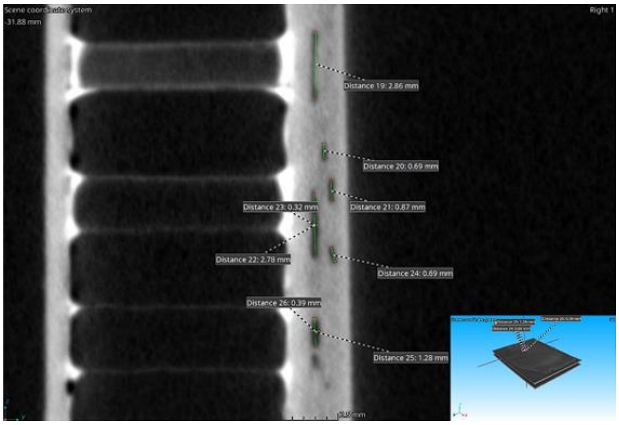

(c)

Fig. 10. Results of tomography of the patch of zone 2, performed by vacuum method with excess pressure (a) - Cross-section of the repair patch of zone 2; (b) - General view of the side section of the repair patch of zone 2; (c) - General view of the side section of the repair patch of zone 2

The general view of zone 3 with a repair performed by a vacuum method with an exceeding curing temperature and a 3D isometric view of the model are presented in figure 11. When studying the sections of the repair patch, numerous voids of sizes from 2 to 10 mm were also found, as shown in figure 12.

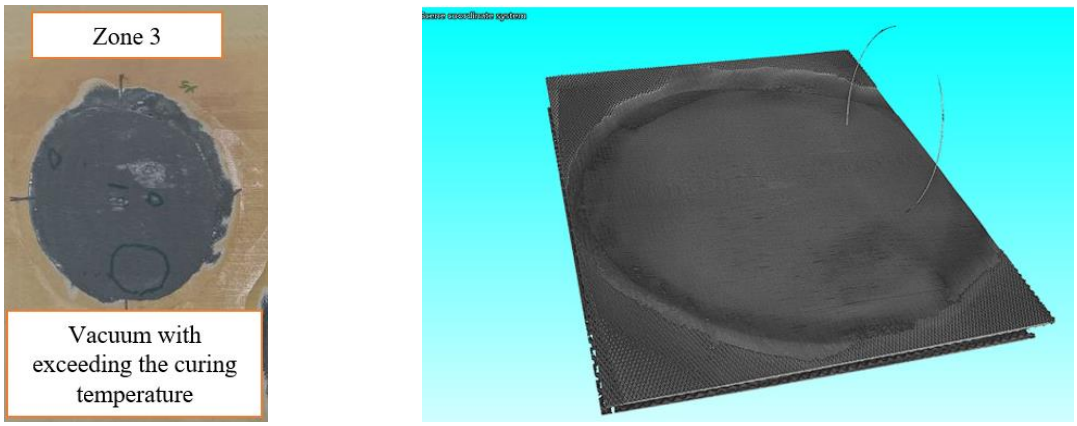

Fig. 11. Repair patch in zone 3

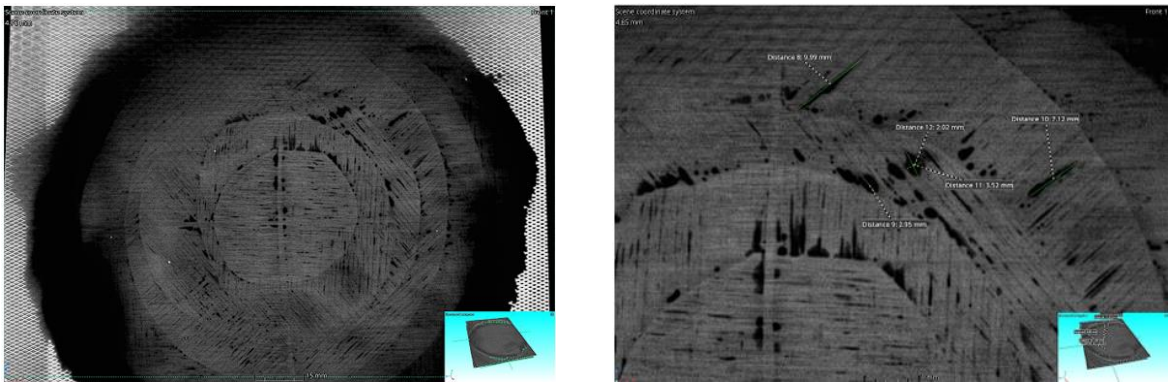

(a) (b)

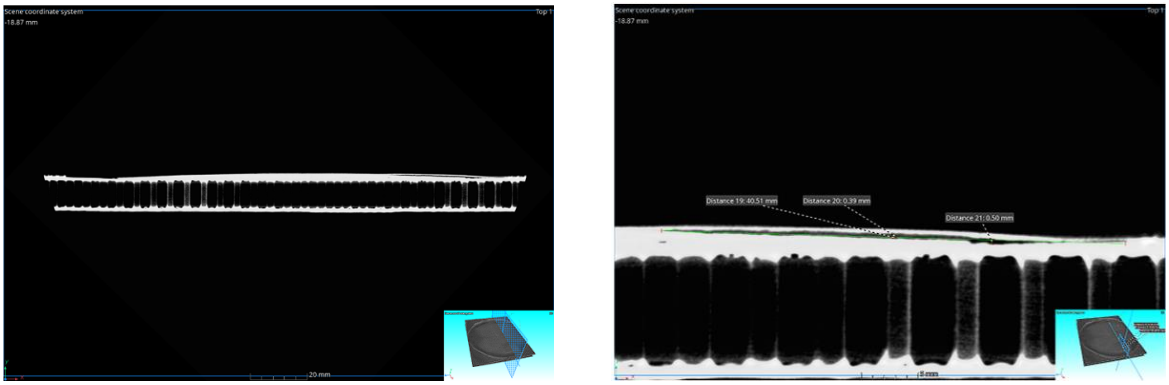

(c) (d)

Fig. 12. Results of tomography of the patch of zone 3, performed by vacuum method with exceeding curing temperature(a) - Cross-section of the repair patch of zone 3; (b) - Local area of the cross-section of the repair patch; (c) - General view of the side section of the repair patch of zone 3; (d) - Local area of the side section of the repair patch with extensive delamination

The side section of the patch was also studied for defects. In the XY plane, in the transition area of repair patch - honeycomb filler, extensive delamination was found with a linear size of 40 mm. Based on the results of tomography, the following conclusions can be made:

- This method of NDT can identify most types of defects (down to micro-defects), which can be obtained during production and operation, with the ability to determine linear dimensions, area and depth.
- Despite all the advantages of this method, there is a significant limitation in its use – the dimensions of the samples to be studied, which are limited by the dimensions of the

tomograph. It should also be noted that this method of non-destructive testing cannot be used for on-site inspection (which shearography allows).

- Sample examination on a tomograph provides a full volume of information for assessing the quality of repair and allows you to adjust technological processes for further, higher-quality repair.
- For a detailed study of the sample, about 5-6 hours are required (including setting up the sample, setting up scan parameters, the scanning process, processing the results).

5.2 Shearography

Analysis of shearography results of a patch obtained using a vacuum method revealed characteristic features of the material structure. On the images obtained, shown in figure 13, there is pronounced layering and inhomogeneity, presumably due to the specifics of the technological process of composite material production. Defects found on shearograms indicate possible defects or uneven distribution of components within the material.

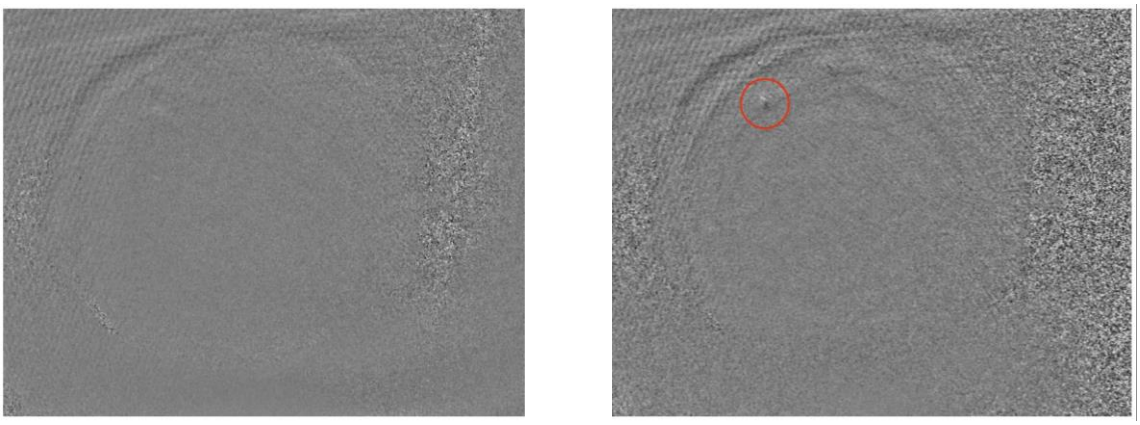

Fig. 13. Shearograms of the patch performed by vacuum method

The research of layering and inhomogeneity of the patch by shearography allows a deeper understanding of the processes of forming composite material and identifying potential problems that occurred during its production. Further analysis of the shearography results may contribute to the optimisation of technological processes and improvement of the quality of the final product.

The results of the analysis of the patch obtained by vacuum method with excess pressure demonstrated that the structure can be clearly seen on the shearograms without identified inhomogeneities and defects, as shown in figure 14. This observation testifies to the high level of quality of the patch manufacture and its homogeneity. The absence of inhomogeneities indicates that the vacuum process with excess pressure was performed in accordance with the technological requirements, which contributes to obtaining a material with a homogeneous structure.

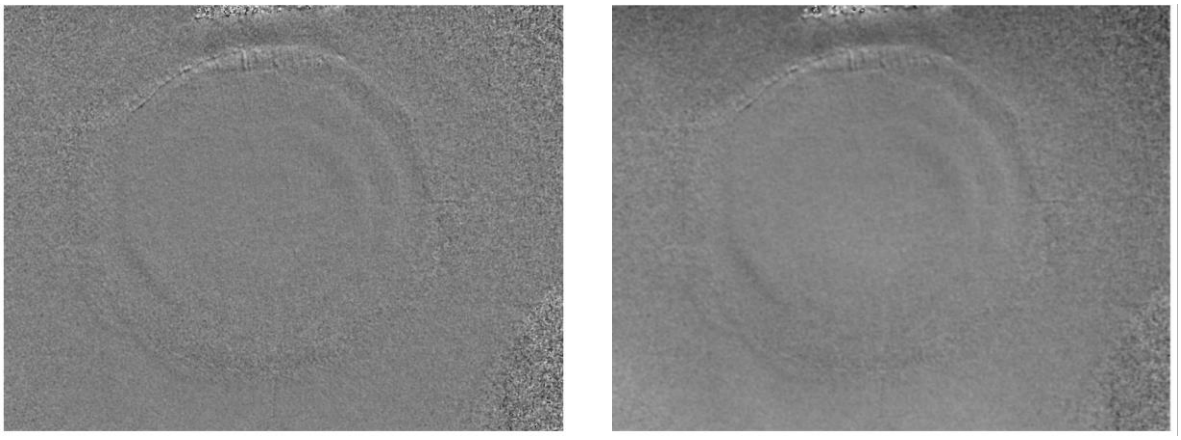

Fig. 14. Shearograms of the patch performed by excess pressure

Thus, the results of shearographic analysis confirm the high quality of the patch, distinguished by the absence of identified defects and inhomogeneities. This study is important for quality control and optimisation of production processes in the field of composite materials. The patch performed by vacuum method with exceeding the curing temperature was also studied by shearography, the results of which clearly indicate the presence of inhomogeneity in the form of delamination in the structure, indicating a violation of the technological regime of the repair process, as shown in figure 15.

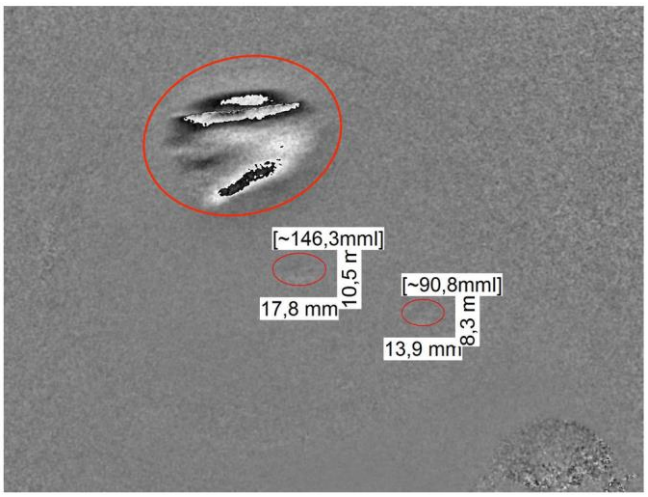

Fig. 15 – Shearograms of the patch obtained using vacuum and exceeding curing temperature

The detected inhomogeneity in the material structure, confirmed by shearographic analysis, may have a negative impact on the mechanical properties and durability of the patch.

Based on the results of shearography, the following conclusions can be made:

- With this method of non-destructive testing, it is possible to see transitions between structures (transitions from honeycomb filler to monolithic material).
- The shearography method, like the other non-destructive testing methods used, recorded extensive delamination of the repair zone 3, obtained by vacuuming with an excess curing temperature.
- With a shearograph, you can see the transition between the layers of the patch.
- Shearography requires less time for equipment calibration, the calibration mechanism is less labour-intensive.
- Shearography is a more visual method of defect detection compared to, for example, ultrasonic testing, but it does not allow classifying damage.

Based on the results of the conducted studies, the following conclusions can be made:

- Comparison of defectoscopy indications

6. Discussions

When analysing the results of the conducted studies, we can conclude:

- Zone 1: In the repair zone 1, performed by vacuum method, non-adhesions between the layers of the patch and voids formed during the curing of the resin were found. These types of defects were detected by all NDT methods used in the research. One of the factors for the formation of non-adhesions is the experience and qualification of the staff performing the repair activities, which directly affects the quality of the technological process.

- Zone 2: In repair zone 2, performed by vacuum method with excess pressure, minor non-adhesions and voids were found in the repair patch area. The linear dimensions of the non-adhesions are 2-3 mm, so it was not possible to assess defects with such geometric dimensions using the express method of NDT (shearography). The quality of the repair

performed in zone 2 can be assessed as satisfactory, with the smallest number of defects detected by the detailed method of NDT (Tomography).

- Zone 3: In repair zone 3, performed by vacuum method exceeding the curing temperature, numerous local non-adhesions in the patch area were found, including extensive delamination between the repair layers with linear dimensions of 40x40 mm. The largest defect, due to the detection of which this repair patch can be classified as defective, was determined by all NDT methods used. Smaller linear defects - only by tomography, confirming the need to use the most detailed and lengthy method of analysing the structure of repaired samples at the stage of working out repairs according to various technologies.

7. Conclusions

The following conclusions can be made from the tomography results:

- Using this NDT method, most types of defects (down to micro-defects) that can occur during production and operation can be identified. It also allows for the determination of location, linear dimensions, area, and depth of the defect.
- Shearography method is not informative in tasks of detecting small defects but can be used in tasks of surface analysis of the structure for the presence of obvious defects of relatively large sizes. The advantages of this method over tomography should be considered, the main one of which is the possibility of studying large structures on site.
- A comparative analysis is needed to evaluate the applicability and effectiveness of these NDT's on other types of samples (monolithic panels, three-layer panels of different thickness, samples with varying curvature). At the stage of refining technological processes and choosing the optimal repair strategy, tomography is necessary for a comprehensive assessment of the repair quality.
- In future, during technical maintenance of the aircraft, it is recommended to use shearography and ultrasonic testing methods.

This article makes a unique contribution to the repair of polymer composite materials in aviation, emphasising the use of adhesive technologies to repair aircraft structures on site. This minimises disassembly, reducing costs and reducing repair time. The article offers a comprehensive approach to the analysis of repair technologies and non-destructive testing (NDT) methods. An experimental study of adhesive repair of a three-layer carbon fiber panel examines in detail the various repair areas and identified defects, demonstrating the relationship between control methods and repair quality. In addition, the emphasis on staff qualifications highlights the importance of the human factor. The work offers recommendations to improve the quality and reliability of repair operations. The results of the study also emphasise the need for detailed non-destructive testing to assess the integrity of repairs, which is critical for flight safety. The practical focus of the article includes specific recommendations that enhance the reliability of processes.

Acknowledgement

The authors acknowledge that Laboratory № 3 "Modelling of composite structures" of the Centre for Aerospace Materials and Technologies of the Institute № 14 "Advanced Engineering School" and Centre of Composite Structures support this study in the Moscow Aviation Institute (MAI).

References

[1] Pogosyan M, Nazarov E, Bolshikh A, et al. Aircraft composite structures integrated approach: a review. J Phys Conf Ser. 2021;1925(1):21-34. https://doi.org/10.1088/1742-6596/1925/1/012005
[2] Amsc N, CMPS A. Composite materials handbook: polymer matrix composites materials usage, design, and analysis. 2002;3.
[3] Zhao C, Guan ZD, Guo X. Compression performance of repaired composite stiffened panels: bolted repair and scarfed bonded repair. Mater Sci Forum. 2015;813:152-160. https://doi.org/10.4028/www.scientific.net/MSF.813.152
[4] Xu J, et al. Numerical and experimental study on stiffened composite panel repaired by bolted joints under compressive load. J Appl Math Phys. 2018;6(8):1763-1771. https://doi.org/10.4236/jamp.2018.68151

[5] Lupkin BV, Nitka VP. Method of repairing of assemblies made of composite materials with tubular (honeycomb) filler under field conditions. Otkrytye Informatsionnye i Kompyuternye Integrirovannye Tekhnologii. 2014;63:33-41.
[6] Reznichenko VI. Особенности ремонта сотовых конструкций из композиционных материалов методом термокомпрессионного формования (Features of repair of cellular structures made of composite materials by thermocompression molding). Инновации и Инвестиции. 2020;11:236-240.
[7] Préau M, Hubert P. Bonded repairs of honeycomb sandwich structures: process monitoring and quality assessment. Proceedings of the 20th International Conference on Composite Materials (ICCM-20). 2015.
[8] Ghazali E, et al. Mechanical performance of repaired sandwich panels: experimental characterization and finite-element modelling. J Sandwich Struct Mater. 2019;21(4):1357-1378. https://doi.org/10.1177/1099636217716059
[9] Centea T, Grunenfelder LK, Nutt SR. A review of out-of-autoclave prepregs-Material properties, process phenomena, and manufacturing considerations. Compos Part A Appl Sci Manuf. 2015;70:132-154. https://doi.org/10.1016/j.compositesa.2014.09.029
[10] Mitchell KR, et al. Nondestructive evaluation of composite repairs. ASNT Annu Conf. 2013;170-176.
[11] Grunenfelder LK, et al. Effect of room-temperature out-time on tow impregnation in an out-of-autoclave prepreg. Compos Part A Appl Sci Manuf. 2013;45:119-126. https://doi.org/10.1016/j.compositesa.2012.10.001
[12] Heslehurst RB. Defects and damage in composite materials and structures. Boca Raton, FL, USA: CRC Press; 2014. https://doi.org/10.1201/b16765
[13] Tomblin JS, Salah L, Welch JM, Borgman MD. Bonded repair of aircraft composite sandwich structures. Federal Aviation Administration, Office of Aviation Research; 2004. Accessed April 16, 2013. Available from: http://www.tc.faa.gov/its/worldpac/techrpt/ar03-74.pdf
[14] Pieczonka L, et al. Nondestructive testing of composite patch repairs. 11th European Conference on Non-Destructive Testing (ECNDT 2014). 2014.
[15] Blain P, et al. Artificial defects in CFRP composite structure for thermography and shearography nondestructive inspection. Fifth Int Conf Opt Photon Eng. 2017;10449:562-571. https://doi.org/10.1117/12.2271701
[16] Dattoma V, et al. Ultrasonic and thermographic studies for CFRP inspections with real and simulated defects. Mater Today Proc. 2021;34:224-234. https://doi.org/10.1016/j.matpr.2020.02.915
[17] Cheng L, et al. Comparison of nondestructive testing methods on detection of delaminations in composites. J Sensors. 2012;2012(1):408-437. https://doi.org/10.1155/2012/408437
[18] Titov PA, et al. Способ ремонта конструкций из полимерных композиционных материалов (Method of repairing structures made of polymer composite materials). Patent 2740214 USA. Req. 19.03.2020. Published 12.01.2021.
[19] Vilents VP. Портативное устройство для ремонта изделий из полимеров (Portable device for repairing polymer items). Patent RU2089393C1. Req. 25.04.1995. Published 10.09.1997.
[20] Vilents VP. Способ клеевого ремонта аэродинамических поверхностей летательных аппаратов (Method of adhesive repair of aerodynamic surfaces of aircraft). Patent RU2754706C1. Req. 07.10.2020. Published 06.09.2021.
[21] Vilents VP. Способ ремонта изделий из полимерных композиционных материалов с односторонним доступом в зону ремонта (Method of repairing items made of polymer composite materials with one-sided access to the repair zone). Patent RU2723868C1. Req. 30.07.2019. Published 17.06.2020.
[22] Vilents VP. Способ ремонта тонкостенных конструкций (Method of repairing thin-walled structures). Patent RU2181083C2. Req. 26.06.2020. Published 10.04.2002.
[23] Vollen MW, et al. Application of shearography techniques for vibration characterization and damage detection in sandwich structures. Meeting Proc RTO-MP-AVT. 2005;124:21-1.
[24] Waldner S, Goudemand N. Quantitative strain analysis with image shearing speckle pattern interferometry. Interferometry in Speckle Light: Theory and Applications. Springer Berlin Heidelberg; 2000:319-326. https://doi.org/10.1007/978-3-642-57323-1_40
[25] Polymer composites. Shearography of polymer composite materials, sandwich core materials and filament-wound pressure vessels: (Russian State Standard) ГОСТ Р 56795-2015. 2016. Req. 01.01.2017. M.: Standartinform. P. 23.
[26] Nevatecnology: official website. Moscow; 2022. Available from: https://nevatec.ru/ . Accessed March 19, 2024.

Research on Engineering Structures & Materials
www.jresm.org
Research Group

Research Article

Experimental and computational investigation of stiffened composite panels with compression after impact

Aleksandr Bolshikh [*,a], Marina Klesareva [b], Egor Nazarov [c], Bogdan Ustinov [d]

Moscow Aviation Institute (National Research University), Moscow, 125993, Russia

Article Info

Article history:

Received 31 July 2024
Accepted 23 Nov 2024

Keywords:

Finite element methods;
Low-speed impact;
Load-bearing capacity;
Delamination,
Barely visible impact damage

Abstract

In this paper the load-bearing capacity of a stiffened stringer panel made of polymer composite materials (PCM) reinforced by intermediate modulus carbon fiber under compression after impact was investigated. Computational-experimental investigations were conducted to assess obtained results where stringer panel was loaded to failure. In this paper, a computational and experimental method for modeling the compression after Impact and failure mode for single-span composite panels with barely visible impact damage (BVID) is proposed based on the building block approach. The above-mentioned approach implies step-by-step test series coupled with simulations which are carried out on each stage gradually introducing larger and structurally more sophisticated test samples. That approach serves as the base for design of composite structures by means of increasing the number of smaller test samples and carrying out a lot of simulations in order to reduce the margin of error and to reduce the number of large test structures (wing, fuselage, etc.) required for proof of compliance of the proposed airframe to available design objectives thus cutting the cost of experimental program. Further the model of material behavior was developed considering combined loading caused by growth of cracks and delaminations. For that material model a series of coupon tests were performed to refine elastic and strength parameters of material. Consequently, a ply-by-ply solid finite element model (FEM) of the stiffened two-stringer panel with cohesive interface behavior was developed. Test samples of the stiffened panels made by vacuum resin infusion were subjected to impact damage between the stringers followed by compression in the testing machine with two edges fixed as cantilever beams. Robustness of the proposed simulation method and suggested modelling approach was confirmed by similarity of obtained numerical results and experimental data as well as the similarities of the failure mode and state upon failure.

1. Introduction

Today, it is probably impossible to name the areas of technical systems where composite structures are not used. Aircraft manufacturing is considered to be the leading industry employing load-bearing structures made of polymer composite materials (PCM). A large number of research programs are carried out all over the world to implement new composite technologies in various types of structures and new methods of analysis of strength under different loading modes [1-3]. In recent years, a number of articles containing strength criteria and various modelling techniques using numerical simulation of composite materials have been published [4-5]. Damage tolerance of aircraft stiffened composite panels has recently been a major concern.

*Corresponding author: bolshikhaa@mai.ru
[a]orcid.org/0000-0002-6740-3870; [b]orcid.org/0009-0005-4341-964X; [c]orcid.org/0000-0002-8614-9126; [d]orcid.org/0009-0002-3685-7682
DOI: http://dx.doi.org/10.17515/resm2024.372cs0623rs

Numerical modelling is a powerful tool to better understand the mechanics of complex multilayer composite structures. Previous works related to numerical and experimental studies of behaviour of composite structures with impact damage, delamination failures and damage tolerance were presented in [6-7]. Improving the efficiency of such structures requires a deep understanding of the types and principles of their operation, the use of a comprehensive approach, as well as multidisciplinary research. The experimental and numerical approach presented in [8] is applicable to all industries: helicopter, marine, automotive and many other areas are all employing experimental and numerical building block approach, sometimes referred to as "certify by analysis".

The contribution of the authors of this work to the development of the above-mentioned approach consists, among other things, in introduction of the principles of creating universal numerical models applicable for simulation of static, dynamic and fatigue strength of composite structures at different stages of design. The assessment of the residual strength of the reinforced composite panel during operation, presented in this work, is an integral part of the comprehensive work on the justification of the durability of the structure, considering potential manufacturing defects (delaminations), in-service damage of the four main categories, restoration of strength through local repairs and maintaining the load-bearing capacity of the structure at the ultimate load level until the design service goal [9]. The resistance to impact damage remains an important issue in the design damage tolerant structures found in fuselage compartments, wing boxes, tail planes, etc. Impact damage, which is mainly characterized by matrix cracking, delamination and fiber breakage, usually extends far beyond the point of impact. Such damage [10] is mainly present inside the laminate and is difficult to detect visually from the outside. Even in the case of a low velocity/low energy impact, the residual compressive strength can be significantly reduced.

To study the compressive load-bearing capacity of double-stringer reinforced panels with impact damage in the interstringer zone, a review of modern works on the considered subject [11-15] was conducted and a list of structural-like single-span flat panels, representing a rectangular plate (skin) reinforced in the longitudinal direction by two stringers, was formed. The thickness and width of the skin are variable parameters in the problem under consideration. At the first step, an impact with energy of 140 J, 103 ft-lb was simulated to represent a maintenance toolbox dropped on the skin surface [16]. Absolutely rigid clamps on all edges of the panel were defined by boundary conditions according to ASTM D7136 [17]. Post-impact compression was implemented by creating rigid plates simulating the base and traverse of the testing machine. The motion of the traverse of the testing machine was defined via boundary conditions in the form of displacement along the longitudinal axis, while the remaining degrees of freedom were fixed.

The panel was supposed to fail along the cross section weakened by impact damage accompanied by disbonding between the skin and stringers. The results of simulations based on the presented FE model in accordance with the building block approach [8] should allow to refine the material allowable normally established at the conceptual design stage in order to prove compliance to the requirements of articles CS-25.571 and CS-25.631 during certification [9]. In accordance with the requirements of the Advisory Circular [18] to the article CS-25.571 [9], the design of airframe primary structures made of PCM must ensure an appropriate load-bearing capacity for each of the four categories of in-service damage. According to that article, the design must meet: 1) environmental effects (including specified design parameters and impact damage); 2) static strength (including repetitive loads, tests of environmental effects, manufacturing process, dispersion of properties and impact strength); 3) evaluation of fatigue strength and allowable damage; 4) others - flutter, repairability, maintainability, etc. Compliance with

these requirements and competitive level of weight perfection of modern construction made of PCM is achieved by selection of design parameters for optimal joint operation of shells and stringers as well as by using the highest design characteristics of the material and by allowing for manufacturing defects of certain size and impact damage of certain energy values.

Building block approach followed by this study for the composites analysis is similar to unit cell concepts periodic structures (only one unit cell is used for analysis to get results for whole structure) finite element free vibration and flutter analysis applied to periodic line supported plate and shell as in [19-20] and some review studies that related to static, free vibration and buckling analysis of composite beam, plate and shell panels [21].

This topic has been extensively studied by simulating low-velocity impact with different energy values [22-25], modelling residual strength, combined fracture modes on the example of thin panels [26-31]. Approaches to solving the problems vary. A modern method can be considered "layer-by-layer modelling", which gives a sufficiently high accuracy and allows taking into account the properties of each layer with initialization of the fracture criterion. This allows getting the most complete picture of delamination not only of the entire panel, but also of an individually selected layer.

Most of the publications focus on simulating impact on thin-walled panels. However, when dealing with thicker laminates, additional problems arise. In particular, local compressive stresses significantly affect the initiation and propagation of interlayer damage and the occurrence of cross plane effects (interlayer shear and normal stresses). In addition, impact can cause damage that can locally divide the package into several sub-packages. Such damage may lead to local buckling under compression or shear action, redistributing critically these loads and causing both in-plane and out-of-plane stress concentrations. While undoubtedly most structures are made of thin laminates, in some aerospace and automotive applications the laminate is several centimetres thick. For long-haul aircraft, this can be in excess of 20-30 mm. This paper proposes a methodology for numerical "layer-by-layer modelling" of a large-thickness panel, considering an extended formulation of the model of cohesive interlayer interaction. The results of calculations according to the proposed method are in satisfactory agreement with the test results.

2. Research Methods

2.1 Tests

In accordance with the experimental and numerical building block approach, the proof of airframe primary structures is mainly performed by PCM coupon and structure-like specimen tests with various in-service damages. The purpose of such tests is to determine the residual safety factor, to confirm the design stresses and deformations accepted at the design stage, and to study the failure mechanism. Structural-like specimens are normally a set of structural elements, the tests of which allow estimating the strength characteristics of a full-scale structure without any recalculations and additional analysis.

In this work, experimental studies of the compressive strength of double stringer wing panels after an impact damage with an energy of 140 J in the interstringer zone and further determination of the load-bearing capacity of a typical section of the wing boxes skin under compressive load were carried out. The impact energy of a pile driver with an energy of 140 J was chosen to inflict BVID type impact damage in double stringer wing panel in the interstringer zone.

BVID includes acceptable defects and damage that may remain undetected during routine inspections. Tolerance of damage in this category requires demonstration of static strength under design loads throughout the service life of the aircraft. Such damage

includes defects and damage that occur during both manufacturing and service, such as minor delaminations, porosity, minor scratches, and minor environmental damage. The object of tests is single-span double-stringer flat panels made from carbon tape and epoxy resin by vacuum infusion method. The overall dimensions of the panel are presented in Table 1.

Table 1. Panel dimensions

Length, mm	Width, mm	Skin thickness, mm
350	231	10.8

The panel edges are reinforced with fiberglass overlays to prevent fracture where forces are applied Fig. 1. General view of Double-stringer panel on the test bench before and after fracture illustrated in Fig. 1. and Fig. 2.

Fig. 1. Double-stringer panel on the test bench before fracture

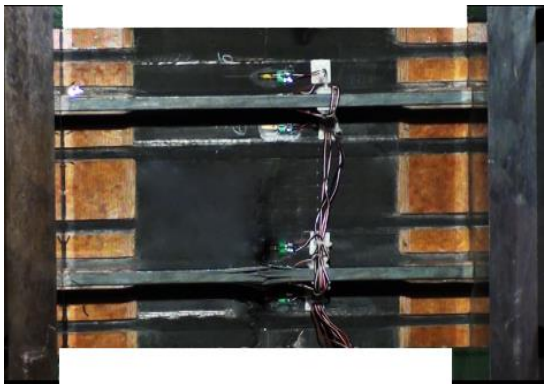

Fig. 2. Double-stringer panel on the test bench after fracture

A carbon bundle was placed between the stringers and the cladding. This test requires that the center of gravity of the panel cross section coincide with the line of action of the compressive forces of the testing machine. The stiffness of the test machine supports must be sufficient to ensure uniform distribution of compressive forces, which were monitored by means of strain gauges mounted on the panels. The panels were loaded until their bearing capacity was exhausted, and the following parameters were recorded: velocity of the impactor, force in the contact zone, compression force, displacement in the middle

section of the panel on the skin and on the stringer walls. The panels with a nominal thickness of 10.8 mm of cladding were destroyed in a section weakened by impact damage, with delamination of the cladding and stringers material. The defect area was 49x52 mm, the critical load was 1630 kN.

2.2 Computational Model

2.2.1. Geometry and boundary conditions

The finite element model consists of several parts: skin, L-shaped part of stringer, filler and impactor. The dimensions of the panel are shown in Table 1. The general view of the panel is shown in Fig. 3.

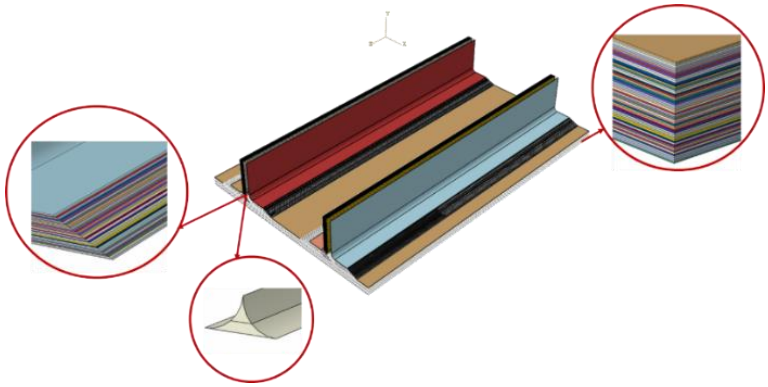

Fig. 3. General view of the panel

The impactor was modeled as a solid body with a mass of 5.5 kg. It has a spherical impact surface with a diameter of 25 mm and a height of 22.5 mm. The velocity of the impactor has only a vertical component equal to 7067 mm/s and is set by means of the initial velocity. At the same time, the initial velocity of the impactor was set using a special function of the Abaqus software - Predefined field, Initial velocity. The impact supports are not modeled in this calculation. We assume that this jig is absolutely rigid and contacts the panel in such a way that it is possible to accept a completely rigid termination (clamped tip) as boundary conditions on all sides of the panel according to ASTM D7136 [20], that is, clamping on all components of displacement and rotation.

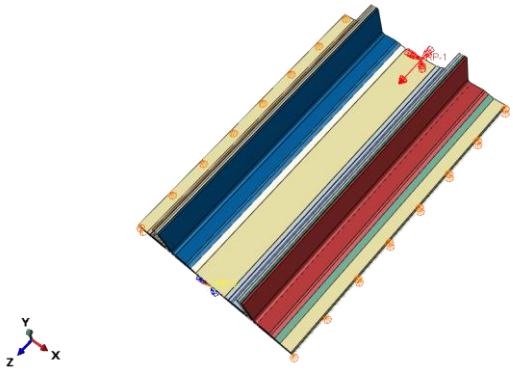

Fig. 4. Boundary conditions for compression after impact

The simulation of compression after impact was implemented as follows: 1) the test machine was simplistically modeled using absolutely rigid plates, that is, one of the plates was responsible for the base of the test machine and absolutely rigid boundary conditions were applied to it, the second plate was responsible for the movable crosshead of the test machine, to which boundary conditions were applied as longitudinal motion; 2) a reinforced double stringer panel was placed between the two plates; 3) inter-surface contacts were specified between the plates and the panel, and an additional gap was specified between the panel and both plates to avoid penetration of the surfaces into each other. In addition, additional boundary conditions were applied at the free edges to avoid loss of stability of the free edges of the cladding (anti-buckling supports), and thus preventing critical stress redistribution from occurring, allowing the weakened section to be incorporated after impact (Fig. 4.).

2.2.2 Description of The Finite Element Model

To investigate the compressive load-carrying capacity of a double stringer flat panel with impact damage in the interstringer zone, a layer-by-layer solid rectangular plate (cladding) supported in the longitudinal direction by two stringers was modeled. The stacking scheme is shown in Table 2.

Table 2. Layout

	Number of layers	Monolayer thickness	Packages Stacking
Skin	60	0.18	+45/0/-45/0/90/0/-45/0/+45
Stringer	29	0.18	+45/0/-45/0/90/0/-45/0/+45

A 0-degree layer is placed between the neighboring packages consisting of 9 layers. The calculation of the finite-element model is performed in two steps in the Abaqus software package - Dynamic Explicit:

- The first step simulates the impact
- The second step simulates the compression after the impact

The impactor is assigned with an initial velocity in the vertical direction. Its value should not be more than 1 percent of the speed of sound propagation in the medium (material):

$$\upsilon \leq 0.01 \cdot a \tag{1}$$

Where υ - initial velocity in the vertical direction, a - speed of sound propagation in the medium (material). This relationship was obtained after a series of computational tests to eliminate unrealistic local element stresses and inertial effects that cause increased initial strain resistance. Observing the condition (1), the value of kinetic energy equal to 140 J is selected. Residual strength is determined by the value of the reaction force occurring in the termination (plate).

All parts were modeled as solid with C3D8 mesh elements Fig. 5 using full integration to avoid additional element distortion (hourglass). Due to the good correlation between the calculation results and the tests, it can be concluded that the choice of the FE mesh size is optimal.

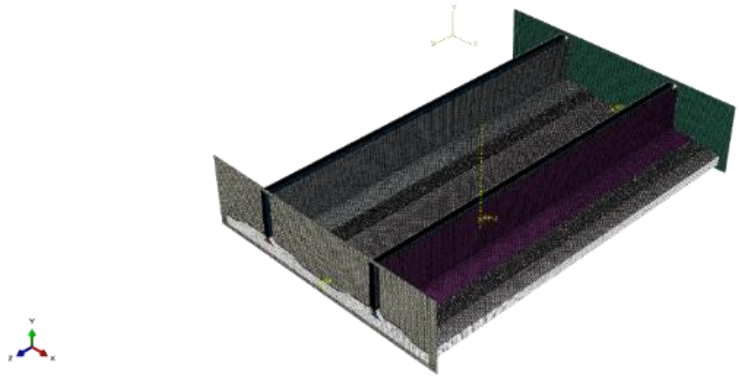

Fig. 5. Finite element model of the panel

2.2.3 Material model

One of the key factors in post-impact compression modeling is the material model, which requires a set of input properties to work correctly. For unidirectional carbon fiber reinforced plastic, this involves testing to obtain the most accurate material properties, a thorough characterization that includes separate fiber, matrix and interface tests. Both standardized and non-standardized test methods can be used to measure the elastic properties of the material, allowing to obtain the following necessary material characteristics: values of layer strength, interface and critical energy release rates in three dimensions of material direction (longitudinal, transverse and shear). Since in this mathematical model the methodology of layer-by-layer modeling was used, the compression properties of the monolayer are set as the elastic properties of the composite material (Table 3).

Table 3- Material properties

Properties	ASTM standard	Value
Elastic properties of the monolayer		
E_{1t}, GPa	ASTM D7291	159
E_{1c}, GPa	ASTM D3410	144
E_{2t}, GPa	ASTM D3039	9.095
E_{2c}, GPa	ASTM D3410	8.85
$G_{12} = G_{13}$,GPa	ASTM D3518	4.17
$\nu_{13} = \nu_{12}$	ASTM D3039	0.34
ν_{23}	ASTM D3410	0.34
Strength properties of the monolayer		
X^{T}, MPa	ASTM D7291	3255
Y^{C}, MPa	ASTM D3410	1325
Y^{T}, MPa	ASTM D3039	77
Y^{C}, MPa	ASTM D3410	232

S^{ι}, MPa	ASTM D2344	103
Destruction Modes		
$g_{1+}, kJ/m^2$	Pinho et al.	150
Cross-layer properties		
τ_3^0	ASTMD7291	53.5
τ_{sh}	ASTM D2344	105
$G_{Ic,\theta=0^\circ}, kJ/m^2$	ASTM D5528	0.177

Moreover, the differentiation of load orientation is of paramount importance, since these materials exhibit different fracture properties and modes depending on whether they are subjected to tension or compression. When making non-flat joints of composite reinforced panels, such as the connection of the sheeting to the T-rib, filler is required to fill the voids between the flanges, walls and sheeting. This model uses a unidirectional carbon fiber bundle to provide local reinforcement and increase bending stiffness. Properties of the filler are presented in Table 4 [32].

Table 4. Properties of the filler

Properties	E_1, MPa	E_2, MPa	E_3, MPa	$\nu_{13}=\nu_{12}$	$G_{12}=G_{13}$,MPa	G_{23}, MPa
Value	72000	8000	8000	0.3	5000	3000

2.2.4 Model for Crack Growth and Delamination

During loading of laminated composites, the key defect is delamination, because it reduces the strength of the structure and it is very difficult to detect it without the use of special equipment. This process can be modeled using a bonded layer, for which contact stresses are set and a failure criterion is initialized. The law is then determined which damage growth occurs. With this in mind, elements are removed, allowing the process of layer separation to be visualized. The quadratic nominal stress traction-separation law" [33] used in this paper considers the interaction between the stress components and is defined as:

$$\left(\frac{\langle t_n \rangle}{t_n^0}\right)^2+\left(\frac{t_s}{t_s^0}\right)^2+\left(\frac{t_t}{t_t^0}\right)^2=1, \quad (2)$$

where t_n^0, t_s^0 and t_t^0 - peak values of nominal stress when the interface deformation occurs exclusively in the normal direction or in the first or second shear direction. The symbol $\langle\ \rangle$, used in the nominal stress designation in the normal direction is interpreted as a pure compressive stress that does not cause damage.

The law of damage evolution describes the rate at which the cohesive stiffness deteriorates after the corresponding criterion is reached. A scalar variable D, varying from 0 (no damage) to 1 (delamination), is introduced. This new variable modifies the stress components predicted by the elastic tensile/separation behavior for an undamaged material $\left(\overline{t}_n, \overline{t}_s, \overline{t}_t\right)$:

$$t_n = \begin{cases} (1-D)\,\overline{t}_n, & \overline{t}_n \geq 0 \\ \overline{t}_n \end{cases}$$
$$t_s = (1-D)\,\overline{t}_s \tag{3}$$
$$t_t = (1-D)\,\overline{t}_t$$

Damage growth with a combination of normal and shear deformation at the interface is described by the effective displacement:

$$\delta_m = \sqrt{\langle \delta_m \rangle^2 + \delta_s^2 + \delta_t^2}$$
$$G_n = \int_0^{\delta_n^f} t_n d\delta_n$$
$$G_s = \int_0^{\delta_s^f} t_s d\delta_s \tag{4}$$
$$G_t = \int_0^{\delta_t^f} t_t d\delta_t$$

Where G_n, G_s, G_t - fracture energies of the normal and two shear modes. In this case, the sum of all energies:

$$G_T = G_n + G_s + G_t \tag{5}$$

Since only two of the three previously defined relations are independent, we introduce a new value:

$$G_S = G_s + G_t \tag{6}$$

The definition of damage development is given by the energy when the criterion is fulfilled:

$$\left(\frac{G_n}{G_n^C}\right)^\alpha + \left(\frac{G_s}{G_s^C}\right)^\alpha + \left(\frac{G_t}{G_t^C}\right)^\alpha = 1, \tag{7}$$

The second component of the damage development definition is the variable D, which describes linear softening:

$$D = \frac{\delta_m^f (\delta_m^{\max} - \delta_m^0)}{\delta_m^{\max} (\delta_m^f - \delta_m^0)}, \tag{8}$$

Where δ_m^f - displacement calculated from the fracture energy G^C; δ_m^0 - displacement at the start of fracture; $\delta_m^{\max}$ - maximum value of effective displacement achieved during the loading history to simulate compression after impact, computational repetition of elementary specimen tests according to ASTM D5528 and ASTM D7905 was performed to obtain additional properties to specify the cohesive contact and to further develop delamination and fracture. The first and second modes of interlayer fracture toughness were determined from the simulation results Fig. 6 [34-35]:

$$G_{Ic} = \frac{3P\delta}{2ba}, \tag{9}$$

Where P - force, N, δ - displacement of the load application point, mm, b - specimen width, mm, a - delamination length, mm

$$G_{IIc} = \frac{3mP_{max}^2 a_0^2}{2B}, \tag{10}$$

Where P_{max} - maximum strength, , a_0 - crack length, mm, B - specimen width, mm, m - calibration factor. Damage variable for cohesive is a dimensionless quantity that determines the presence of delamination. A value of damage variable for cohesive surfaces >1 indicates the presence of delamination.

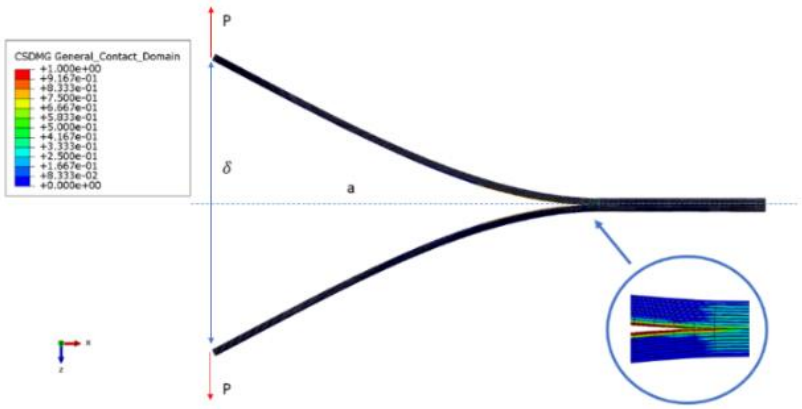

(a)

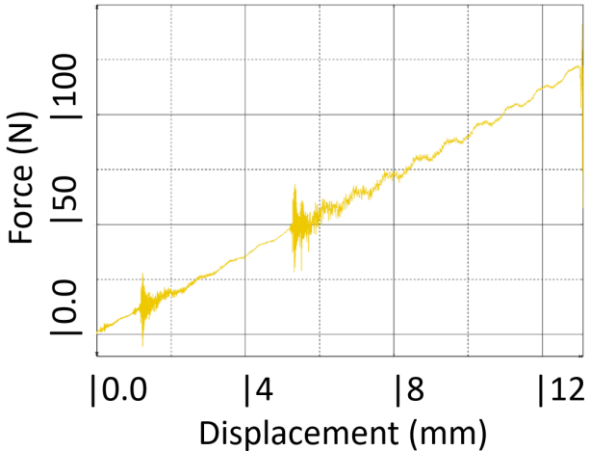

(b)

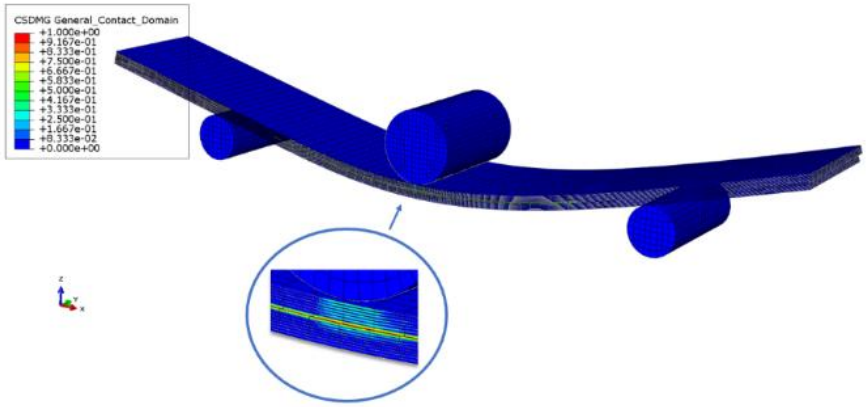

(c)

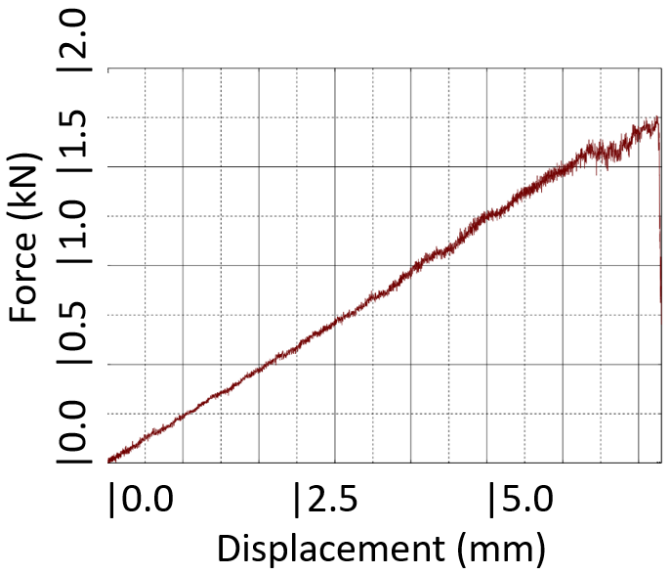

(d)

Fig. 6. (a) Damage variable for cohesive surfaces (delamination)*. General view of ASTM D5528, (b) Force (N) vs. displacement (mm) (ASTM D5528), (c) Damage variable for cohesive surfaces (delamination)*. General view of ASTM D7905 EE, (d) Force (N) vs. displacement (mm) (ASTM D7905)

3. Results and discussion

After bench tests, determination of interlayer fracture properties based on the calculation of elementary specimens, preparation of a finite-element model and additional specification of characteristics to set the material model, the following results were obtained:

- When simulating impact in the panel 10.8 mm, the defect zone was obtained in the size of 46x50 mm, in the conducted tests - 49x52 mm;
- Force in the FEM simulation was obtained as 1700 kN, in tests 1630 kN (Table 5);

- Fracture pattern corresponds to the bench tests - failure occurred along the weakened section in the impact zone.

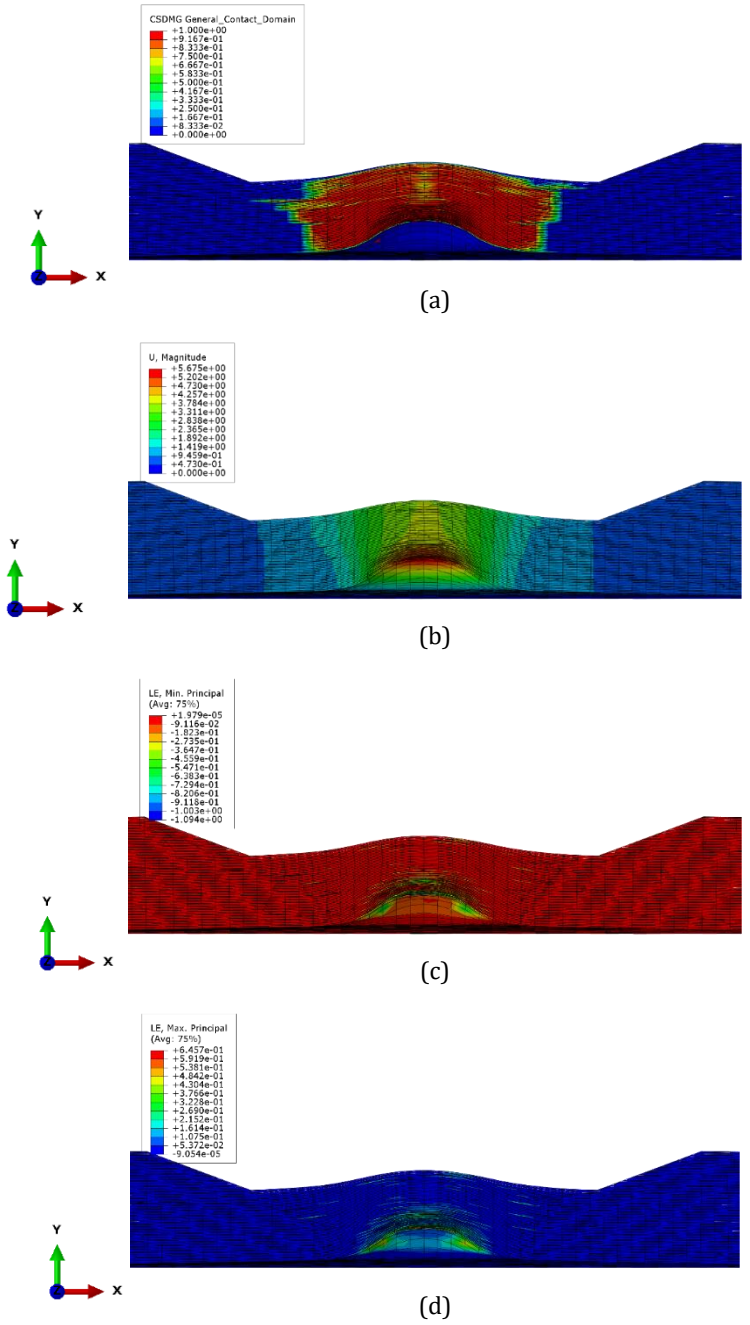

Fig. 7. (a) - Damage variable for cohesive surfaces (delamination) * after impact, (b) Total displacement in all directions (mm) in the panel after impact, (c) Maximum principal deformations (mm/mm) in the panel after impact, (d) Minimum principal deformations (mm/mm) in the panel after impact

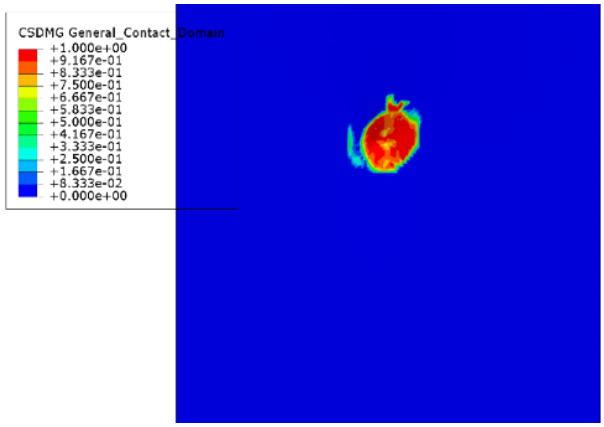

Fig. 8. 90-degree monolayer damage variable for cohesive surfaces (delamination) * (46 x 50 mm)

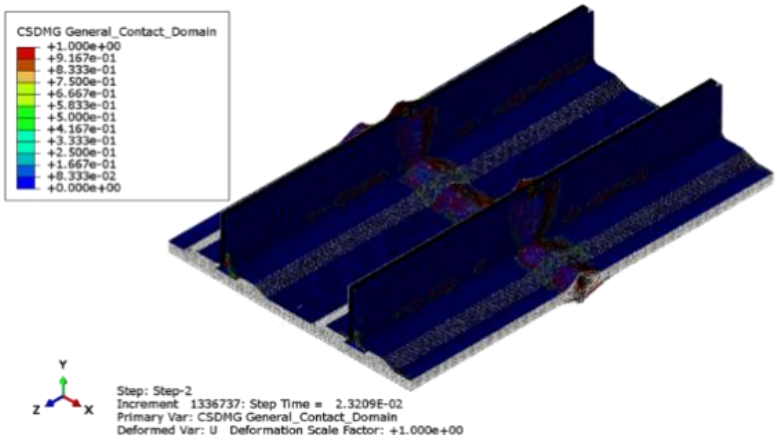

Fig. 9. Condition of the panel after fracture (Damage variable for cohesive surfaces *)

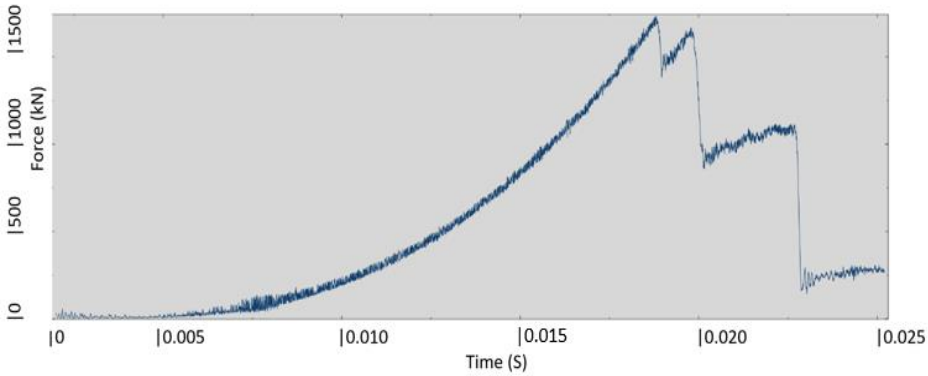

Fig. 10. Graph of the reaction force (kN) of the FEM under compression over time (s)

The discrepancy in the ultimate compression force of the damaged panel was 4.1 %. Fig 7 shows a cross-section of the panel in the XY plane after the first step of the finite-element model. The state of the panel after compression is shown in Fig. 9 and the variation of the reaction force with time obtained from FEM is presented in Fig. 10. An example of delamination in a monolayer for 90-degree direction is presented Fig. 8.

Table 5. Comparative analysis of research results

Criterion	Experiment	FEM analysis
Dimensions of the defect zone after impact damage, mm	49x52	46x50
Reaction force when determining residual compressive strength, kN	1630	1700

4. Conclusion and Future Work

The modeling methodology proposed in this paper allows for a direct comparison of not only the values of forces, stresses and deformations, but also the geometric dimensions, shape and depth of delamination between experimental samples of structures and calculation models.

The modeling technique developed and tested within the framework of the proposed study allows not only to take into account the three-dimensional stress-strain state of the structure at the monolayer level, unlike most approaches, but also allows for delamination due to detailed modeling of the contact between each layer, taking into account the compliance of the binder and the interlayer fracture toughness. Based on the calculated repetition of elementary samples according to ASTM D7905 and ASTM D5528 standards, the nature of delamination and the values of interlayer fracture toughness showed good convergence with the test results. Thus, the developed model makes it possible to obtain a representative picture of delamination for panels of great thickness, the application of which is relevant in the aerospace industry in the design of long-haul aircraft.

An acceptable qualitative similarity of the modeled fracture mechanism and form with that observed in the experiments was noted. The discrepancy in the ultimate compression force of the damaged panel was 4.1 %. The given provisions prove the possibility to use the developed technology for modeling shock damage and subsequent compression to failure of composite aircraft structures with an accuracy acceptable for engineering solutions.

In the future, the authors of this work plan to perform an assessment of the residual strength of reinforced composite panels when impact damage is applied to areas of manufacturing defects i.e. delamination, an assessment of strength recovery after impact damage repair, and an assessment of their residual strength when repeated impact damage is applied to the repair area, using the demonstrated layered modeling method to represent the adhesive repair patch and its connection to the prepared panel surface.

References

[1] Park D, Yu T, Park S, Shin D, Kim Y. Improvement of impregnation quality on out-of-autoclave processed CFRP aircraft wing spar through resin flow simulation. The Functional Composites and Structures. 2021;3:025001. https://doi.org/10.1088/2631-6331/abf480

[2] Mangalgiri P. Design allowable considerations for use of laminated composites in aircraft structures. J Indian I Sci. 2013;93(4):571.

[3] Geng J, Zhang X, Wang C. Predicting dynamic response of stiffened-plate composite structures in a wide-frequency domain based on Composite B-spline Wavelet Elements

Method (CBWEM). Int J Mech Sci. 2018;144. https://doi.org/10.1016/j.ijmecsci.2018.06.031
[4] Fedulov B, Fedorenko A, Kantor M, Lomakin E. Failure analysis of laminated composites based on degradation parameters. On-line J Meccanica. 2017; Springer:14. https://doi.org/10.1007/s11012-017-0735-9
[5] Zhang X, Chen Y, Hu J. Recent advances in the development of aerospace materials. Prog Aerosp Sci. 2018;97:34. https://doi.org/10.1016/j.paerosci.2018.01.001
[6] Barricelli B, Casiraghi E, Fogli D. A Survey on Digital Twin: Definitions, Characteristics, Applications, and Design Implications. IEEE Access. 2019;7:19143996. https://doi.org/10.1109/ACCESS.2019.2953499
[7] Alam M. Crack penetration and deflection behavior at interfaces. PhD dissertation. Oregon State University; 2016. Corvallis, OR, p. 77.
[8] Pogosyan M, Nazarov E, Bolshikh A, Korolskii V, Turbin N, Shramko K. Aircraft composite structures integrated approach: a review. J Phys Conf Ser. 2020;1925. https://doi.org/10.1088/1742-6596/1925/1/012005
[9] Easy Access Rules for Large Aeroplanes (CS-25) (Amendment 26). European Union Aviation Safety Agency; 2021.
[10] Feigenbaum YM, et al. Ensuring the strength of composite aircraft structures considering the random operational shock effects: a monograph. Moscow: TECHNOSPHERA; 2018. 506 p.
[11] Mitrofanov O, Pavelko I, Varickis S, Vagele A. An applied method for predicting the load-carrying capacity in compression of thin-wall composite structures with impact damage. Mech Compos Mater. 2018;54(1):99-110. https://doi.org/10.1007/s11029-018-9722-z
[12] Mitrofanov OV, Pavelko IV, Konstantinov VA, Esaulenko AV. Features of the methodology of designing load-bearing panels of composite materials in compression considering the damage from shock influences. Nat Techn Sci. 2018;1(115):109-112.
[13] Thorsson SI, Sringeri SP, Waas AM, Justusson BP, Rassaian M. Experimental investigation of composite laminates subject to low-velocity edge-on impact and compression after impact. Composite Structures. 2018;186:335-346. https://doi.org/10.1016/j.compstruct.2017.11.084
[14] Sachse R, Pickett AK, Middendorf P. Simulation of impact and residual strength of thick laminate composites. Compos Part B Eng. 2020;195:108070. https://doi.org/10.1016/j.compositesb.2020.108070
[15] Lopes CS, Camanho PP, Gürdal Z, Maimí P, González EV. Low-velocity impact damage on dispersed stacking sequence laminates. Part II: Numerical simulations. Compos Sci Technol. 2009;69:937-947. https://doi.org/10.1016/j.compscitech.2009.02.015
[16] Ratwani MM. Effect of damage on strength and durability. PhD thesis; 2012.
[17] ASTM International. Standard Test Method for Measuring the Damage Resistance of a Fiber-Reinforced Polymer Matrix Composite to a Drop-Weight Impact Event. ASTM D7136-14. 2014.
[18] FAA Advisory Circular AC 20-107.
[19] Pany C. An insight on the estimation of wave propagation constants in an orthogonal grid of a simple line-supported periodic plate using a finite element mathematical model. Front Mech Eng. 2022;8:926559. https://doi.org/10.3389/fmech.2022.926559
[20] Pany C, Li G. Application of periodic structure theory with finite element approach. Front Mech Eng. 2023;9:1192657. https://doi.org/10.3389/fmech.2023.1192657
[21] Sreadha AR, Pany C. Static, free vibration and buckling analysis of composite panels; a review. Adv J Graduate Res. 2021;9(1):21-45. https://doi.org/10.21467/ajgr.9.1.21-45
[22] Shah SZH, Karuppanan S, Megat-Yusoff PSM, Sajid Z. Impact resistance and damage tolerance of fiber reinforced composites: A review. Composite Structures. 2019;217:100-121. https://doi.org/10.1016/j.compstruct.2019.03.021

[23] Jefferson AJ, Srinivasan SM, Dhakal AH. Parameters influencing the impact response of fiber-reinforced polymer matrix composite materials: A critical review. Composite Structures. 2019;224:111007. https://doi.org/10.1016/j.compstruct.2019.111007
[24] Malhotra A, Guild FJ. Impact Damage to Composite Laminates: Effect of Impact Location. Appl Compos Mater. 2014;21(1). https://doi.org/10.1007/s10443-013-9382-z
[25] Kudryavtsev OA, Ignatova AV, Olivenko NA. The influence of thickness on residual flexural strength of composite with low-velocity impact damages: Experimental study. Bull Perm Natl Res Polytech Univ. Mech. 2021;3:6-11. https://doi.org/10.15593/perm.mech/2021.3.01
[26] Sergeichev IV, Anton FK, Safonov AA, Ushakov AE. Estimation of the residual strength of the elements of composite structures after a low-speed impact. J Mach Manufact Reliab. 2013;42(1):29-35. https://doi.org/10.3103/S1052618813010111
[27] Tuo H, Lu Z, Ma X, Xing J, Zhang C. Damage and failure mechanism of thin composite laminates under low-velocity impact and compression-after-impact loading conditions. Compos Part B Eng. 2019;163:642-654. https://doi.org/10.1016/j.compositesb.2019.01.006
[28] Tan W, Falzon BG, Chiu LNS, Price M. Predicting low velocity impact damage and Compression-After-Impact (CAI) behaviour of composite laminates. Compos Part B Eng. 2015;71:212-226. https://doi.org/10.1016/j.compositesa.2015.01.025
[29] Li N, Chen PH. Experimental investigation on edge impact damage and Compression-After-Impact (CAI) behavior of stiffened composite panels. Composite Structures. 2016;138:134-150. https://doi.org/10.1016/j.compstruct.2015.11.060
[30] Soto A, González EV, Maimí P, Martín de la Escalera F, Sainz de Aja JR, Alvarez E. Low velocity impact and compression after impact simulation of thin ply Laminates. Compos Part A Appl Sci Manuf. 2018;109(1):413-427. https://doi.org/10.1016/j.compositesa.2018.03.017
[31] Panettieria E, Fanteriaa D, Montemurrob M, Frousteyc C. Low-velocity impact tests on carbon/epoxy composite laminates: A benchmark study. Compos Part B Eng. 2016;107:9-21. https://doi.org/10.1016/j.compositesb.2016.09.057
[32] Hexcel. 8552 IM7 Unidirectional Prepreg 190 gsm & 35%RC Qualification Material Property Data Report. CAM-RP-2009-015 Rev B.
[33] Olivares-Ferrer JA. Finite elements modeling of Compression-After-Impact test for laminated composite thin plates with initial delaminations. Master's Thesis. Universidad de Politècnica de València, Valencia, Spain; 2018.
[34] ASTM International. Standard Test Method for Mode I Interlaminar Fracture Toughness of Unidirectional Fiber-Reinforced Polymer Matrix Composites. ASTM D5528/D5528M-21. 2021.
[35] ASTM International. Standard Test Method for Determination of the Mode II Interlaminar Fracture Toughness of Unidirectional Fiber-Reinforced Polymer Matrix Composites. ASTM D7905/D7905M-14. 2014. doi:10.1520/D7905_D7905M-14. https://doi.org/10.1520/D7905_D7905M-14

Research on Engineering Structures & Materials
www.jresm.org
MIM Research Group

Research Article

Influence of micro-addition of lanthanum on grain characteristics, mechanical properties, and corrosion behavior of CuAlNiMnLa shape memory alloy

Samuel J. Aliyu [1,a], Timothy Adeniyi Adekanye [*1,b], Adeolu A. Adediran [1,2,c], Oluwasogo L. Ogundipe [1,d]

[1]*Department of Mechanical Engineering, Landmark University, Omu- Aran. Nigeria*
[2]*Department of Mechanical Engineering Science, University of Johannesburg, South Africa*

Article Info

Article history:

Received 10 July 2024
Accepted 22 Aug 2024

Keywords:

Copper-based alloys;
Surface morphology;
Grain characteristics;
Rare earth metal;
Mechanical properties;
Corrosion behavior

Abstract

The study investigated the grain size criteria, mechanical characteristics, and corrosion behavior of Cu-14Al-4.5Ni-0.7Mn shape memory alloy (SMA) with the micro-addition of 0.06 wt% Lanthanum (La). Using standard melting and casting procedures, the alloy compositions were melted at 1300 °C in an arc furnace with an argon atmosphere. The cast compositions without thermal treatment were machined and tested for physical properties including density and percentage porosity, corrosion behavior, and mechanical properties like hardness, ultimate tensile strength, yield strength, fracture strain, percentage elongation, specific strength, and fracture toughness. The average grain size, profile plot, and grain size distribution were all determined using ImageJ software. The microstructural observations revealed the presence of α-phase, β-phase, and intermetallic phases, including the coarse α+γ2 phase, which contributed to the improved characteristics. The inclusion of lanthanum resulted in a drop in the average grain size of the parent alloy from 9.25 µm to 6.08 µm, indicating a clear correlation between property improvement and microstructure refinement. The composition's tensile strength and yield strength increased with the La micro-addition by 22.14% and 20.31% respectively while the hardness value increased by 17.3%. The fracture strain of the modified composition increased by 20% compared to the unmodified composition while the percentage elongation increased by 7.7% and a 22.5% increase in fracture toughness was achieved. The modified CuAlNiMn SMA also showed a significant improvement in corrosion resistance to NaCl solutions which was so evident at 144 hours of the study for 0.5 M of NaCl solution and at 96 hours for 1.0 M of NaCl solution. The results showed that CuAlNiMn SMA with micro-addition of La had better physical, corrosion, and mechanical characteristics than unmodified CuAlNiMn alloys.

1. Introduction

Shape memory alloy (SMA) materials are advanced metallic materials that can revert to their original position after deformation when subjected to relevant thermal treatment. They have two distinct crystal structures: the higher-temperature Austenite structure and the lower-temperature Martensite structure [1]. A reversible austenite to martensite phase transformation is a prerequisite for the memory effect. Thermal (cooling and heating) or mechanical (loading) techniques can be used to achieve such phase transformation [2]. Shape memory alloys have been notably distinguished from other types of materials because of their pseudo-elasticity [3] and shape memory effect (SME) features [4]. In the biomedical and

*Corresponding author: adekanye.adeniyi@lmu.edu.ng
[a] orcid.org/0000-0002-5281-9494; [b] orcid.org/0000-0002-7581-8785; [c] orcid.org/0000-0001-9457-1071; [d]orcid.org/0009-0001-4630-2253
DOI: http://dx.doi.org/10.17515/resm2024.347me0710rs

engineering industries, SMAs have been reported in various research as the main components in products like thermal actuators [5], pumps, linear engines [6], separators, automated arms [7], hydraulic tube couplings [8], lens frames, and electrical system breakers [9].

Shape memory alloys are categorized according to the alloying elements. We can differentiate between alloys based on Nickel (such as; Ni-Ti, Ni-Mn-Ga), Copper (such as; Cu-Zn-Al, Cu-Al-Ni), Iron (such as; Fe-Mn, Fe-Mn-Si), Rare metals (such as; Au-Cd, Au-Ag, Pt-Al), etc. depending on this base material [10]. They are regarded as the SMA systems with the most potential for both functionality and commerce. For technological and industrial applications, Cu-based SMAs are widely recognized as the most affordable and processing-sustainable SMA systems. The primary benefit of Cu-based SMAs over other SMAs is specifically their economic effect (affordable cost) [11]. Specifically, Cu-Al-Ni alloys have applications in a variety of industrial domains, particularly where elevated transformation temperatures (up to 200 °C) are necessary [10]. High transformation temperatures, strong corrosion resistance, high resistance to functional property deterioration during aging processes, and a fair price all influence the choice of this class of alloys for application. They have a significant strain recovery (about 5%), which is second only to the NiTi systems (about 8%) [12], and they may be processed by conventional casting methods [13]. In light of this, Cu-based SMAs are now well-regarded when it comes to applications in electrical and thermo-responsive industrial [14], technological systems and biomedical industries [15].

As a consequence of the high elastic anisotropy of the parent β phase, large grain size, brittle Ɣ2 (Cu_9Al_4) phase, and formation of stress-induced martensites along grain boundaries upon quenching equiaxed polycrystalline CuAlNi alloy is prone to intergranular fracture during plastic deformation [16] and lack of cold-working ability due to high brittleness [17], which has been reported to have limited the alloy's engineering applications [18]. A potential remedy to this challenge is the addition of suitable rare metals (refining elements) such as Ce, La, Co, B, and Ti, which form the precipitates that restrict the size and growth of the grains. Moreover, the rapid-solidification technique or powder metallurgy used in the alloy's production is very effective in achieving a fine-grain microstructure of SMA. Grain modification and texture control are two significant methods used to improve the mechanical properties of the polycrystalline CuAlNi alloy. These two techniques are crucial in relieving the concentration of stress at grain boundaries, which in turn prevents fractures between granular layers and increases the alloy's flexibility [19]. By partially substituting the aluminum component, Manganese is introduced as an alloying element to the CuAlNi alloy to improve its ductility and stability. Additionally, it permits the betatising process to be carried out at lower temperatures and expands the β phase's stable domain [20]. In addition, Manganese is added to improve thermoelastic and pseudoelastic performance [21] and Saud et al. [22] reported that the inclusion of Manganese also lowers the rate of corrosion.

This research aimed to investigate the effect of micro-addition of La as a rare metal on the CuAlNiMn SMA in its as-cast condition through casting techniques. The findings provide information on the porosity, hardness, tensile, specific strength, fracture toughness, and corrosion behavior of the CuAlNiMn SMA system.

2. Materials and Method

2.1. Materials

To produce the Cu-Al-Ni-Mn base composition for shape memory alloys, pure-grade billets of copper, nickel, manganese, and aluminum were used as the base materials. Analytical high-quality lanthanum (La) powder was chosen to be the microalloying additive. The components for Cu, Al, Ni, Mn, and La were purchased from authorized local suppliers.

2.2. Method

2.2.1. Alloy Design and Production

Cu-14%Al-4.5%Ni-0.7%Mn and Cu-14%Al-4.5%Ni-0.7%Mn-0.06La were the two components that piqued curiosity in this study. The study followed Alaneme et al.'s approach in adopting charge computations and alloy production methods to reach these alloy compositions [23]. The alloy compositions were developed in an arc furnace with an argon atmosphere using standard melting and casting procedures. The melts were then poured into cylinder-shaped cast iron metal molds that measured 200 mm in length and 20 mm in diameter using 1300 °C temperature as the heat index. The cast specimens were taken out, fettled, and then machined into different test specimens for microstructural, mechanical, and corrosion examination. Table 1 displays the chemical compositions of the alloys developed and the matching sample designations.

Table 1. Composition of the CuAlNiMn SMA, both unmodified and modified with La

Compositions	Cu	Al	Ni	Mn	La
C 1	80.80	14	4.5	0.7	-
C 2	80.75	14	4.5	0.7	0.06

2.2.2. Microstructural Characterization

The CuAlNiMn alloys that were produced, both modified and unmodified, had their microstructures observed under an optical microscope (Model: L2003A). The sample's surfaces were polished to a mirror-like metallographic finish by a series of grinding operations using abrasive papers with grit sizes of 220, 500, 1000, and 1200. Etching was done with a solution of 2.5 g $FeCl_3$, 10 mL HCl, and 48 mL ethanol. The grain analysis, comprising the estimation of average grain size (using Eq 1), profile plot, and grain size distribution, was accomplished with the support of ImageJ software (using the simple linear intercept approach) adopting the method outlined by Peregrina-Barreto et al [24].

$$Average\ Grain\ Size = \frac{Line\ Length}{Number\ of\ Grains} \tag{1}$$

2.2.3. Measurement of Density and Porosity in Percentage

Density measurements were used to estimate the compositions' levels of porosity. This was accomplished by analyzing the theoretical and experimental densities of every composition. An Ohaus Pioneer digital weighing balance (Model: PA214) with a high-precision tolerance of 0.0001g was used to weigh the test samples to determine the experimental density of the samples. In every instance, the measured weight was divided by the volume of the corresponding samples. The rule of mixture as stated in Eq (2), was used for the computation of the theoretical density.

$$\rho_C = \sum V_E * \rho_E \tag{2}$$

Where ρ_C is the density of the composition; V_E is the volume fraction of the element ;

ρ_E is the density of the element. Using the relations stated in Eq (3), the percent porosity of the composites was determined.

$$\%\ Porosity = \left(\frac{\rho_T - \rho_{EX}}{\rho_T}\right) \times 100 \tag{3}$$

Where, ρ_T *is the Theoretical Density* $\left(\frac{g}{cm^3}\right)$; ρ_{EX} *is the Experimental Density* (g/cm^3)

2.2.4. Mechanical Characterization

- Hardness Testing

The Emcotest Durascan Microhardness Tester was equipped with the cutting-edge application ecos Workflow, was utilized to assess the hardness of the Cu-Al-Ni-Mn-based alloys that were produced. The samples were prepared using a finely finished cylindrical flat surface, and the ASTM E92–23 standard was followed during the testing process [25]. A 100g load was used for the hardness test, with a 10-second dwell period. The hardness indentation was performed at least five times, and the average hardness values were determined.

- Tensile Test

A universal testing device (Instron model 3369) was utilized to perform tensile testing on the as-cast CuAlNiMn SMA. The test samples were machined following the tensile test standards, measuring 30 mm in length of the gauge and 5 mm in diameter. Samples were mounted on the testing platform, the test samples were drawn under tension with a strain rate of 10^{-3}/s until they fractured. The ASTM E8/E8M-22 criteria were followed during the preparation of samples, evaluation, and data analysis [26]. For every composition of CuAlNiMn SMA produced, three repeatable tests were carried out to ensure the test results' dependability and repeatability.

- Fracture Toughness

The fracture toughness values of the CuAlNiMn SMA were evaluated by using the circumferential notch tensile (CNT) testing method as reported by Alaneme [23] and Alaneme & Umar [27]. The CuAlNiMn SMA compositions were shaped to precisely measure the 30 mm gauge length, 6 mm gauge diameter (D), 4.5 mm notch diameter (d), and 60° of the notch angle to conduct the evaluation. A standardized testing device with a strain rate of 10^{-3}/s was used to bend the samples until they broke while they were in the stage of testing. The relation was used to determine the fracture loads (Pf) obtained from the load-extension data of the alloys to evaluate their fracture toughness using Eq (4) as stated by [27].

$$K_{1c} = \frac{p_f}{D^{3/2}} \left[1.72 \left(\frac{D}{d}\right) - 1.27\right] \tag{4}$$

Where the specimen diameter (D) and the notched section diameter (d) are the corresponding values. By using the relationships described in Eq (5) [27], the values for the fracture toughness were obtained for validation under plane strain conditions.

$$D \geq \left(\frac{K_{1c}}{\sigma_y}\right)^2 \tag{5}$$

For every composition of CuAlNiMn SMA, three tests were rerun to make sure the results were dependable and accurate.

2.2.5. Corrosion Test

The following materials, instruments, and reagents were employed in the study following Edoziuno et al [28]: 500-milliliter beakers, 100-milliliter volumetric flasks, emery paper, distilled water, 0.5 M and 1.0 M sodium chloride (NaCl) solutions made with laboratory-quality materials, filter paper, and dry clothes, analytical grade acetone substance including unmodified and modified CuAlNiMn SMA specimens in the form of cylindrical 20 mm diameter by 10 mm length are all included.

Before any further processing, the alloy specimens were cleaned and polished using emery papers of different sizes (such as 400, 800, and 1,200 grit), filter paper, and dry clothes. They were rinsed with distilled water from the faucet and thoroughly cleaned using acetone. Following a thorough air-drying process, the samples were weighed to four decimal places

(0.0001) on an analytical scale. After the samples were weighed, they were immersed in the measured NaCl concentrations. At 48-hour intervals (up to 240 hours), the compositions were removed from the test solutions and immediately given a quick washing with distilled water. Finally, an analytical scale was used to weigh the specimens, and the variations in weight at each period were recorded. Each sample's weight loss (mg) and corrosion rate (mm/yr) were assessed using ASTM G31-21 guidelines [29].

3. Results and Discussion

3.1 Microstructure Analysis, Grain Size Distribution, and Average Grain Size

CuAlNiMn and CuAlNiMn modified with 0.06 weight percent La alloying additions are shown in their as-cast microstructures in Fig. 1(a-b). The distribution of grain sizes in the CuAlNiMn and CuAlNiMn0.06La alloy systems is presented in Fig. 2. Based on the microstructures of the parent alloy shown in Fig. 1a, the structures composed of α-phase, β-phase, and a huge coarse intermetallic compound called α+γ2. The grains are coarse and dendritic, evenly distributed, but with an overabundance of undissolved copper. As illustrated in Fig. 1a, the composition alloy's microstructure revealed more of an undissolved Cu-alloy complex (dendritic grain) with an average grain size of 9.25 µm, which gave rise to the hard and brittle eutectoid α+γ2 phase which is the predominant phase [11,30]. This resulted in the low performance of mechanical properties displayed by the composition (CuAlNiMn). In contrast, Fig. 1b shows a notable increase in the number of rosette-shaped β-phase grains that were uniformly distributed throughout the α-phase, indicating full wettability of the grains and improved mechanical properties displayed by the CuAlNiMn–0.06%La alloy. Additionally, it was noted that the micro-addition of La to the concentration of the parent alloy system (CuAlNiMn) resulted in a reduction of the huge coarse grains (α+γ2 phase), indicating the soluble nature of elements in the copper matrix. The enhanced mechanical features exhibited by the alloy can be attributed to the size and dispersion of its grain [31].

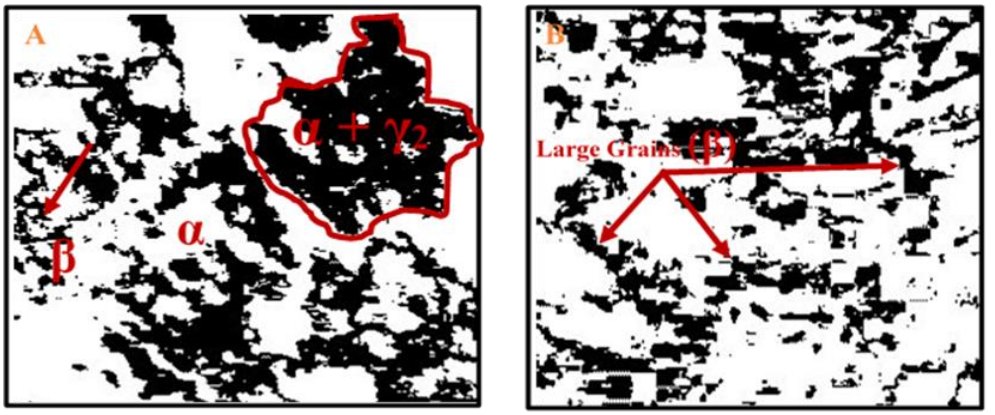

Fig. 1. Representative Optical Micrograph of as-cast structure for (a) CuAlNiMn and (b) CuAlNiMnLa

When 0.06 wt.% La was added to the parent alloy system (CuAlNiMn), a decrease in grain size was observed with a decrease in the solid solution region (Figure 1), which improved the mechanical properties. The average grain size of the parent alloy decreased from 9.25 µm to 6.08 µm after being doped, as shown in Fig. 2(a-b). As evident in Fig. 2, the strength and hardness of the Cu-14Al-4.5Ni-0.7Mn-0.06La alloy system increased by about 28.44 % and 10.77 %, respectively, as compared to the parent alloy. It is noted that the micro-addition of La

caused the average grain size to reduce drastically from 9.25 µm to 6.08 µm. Evidently, Fig. 2b showed a superior grain size distribution than the composition of the parent alloy.

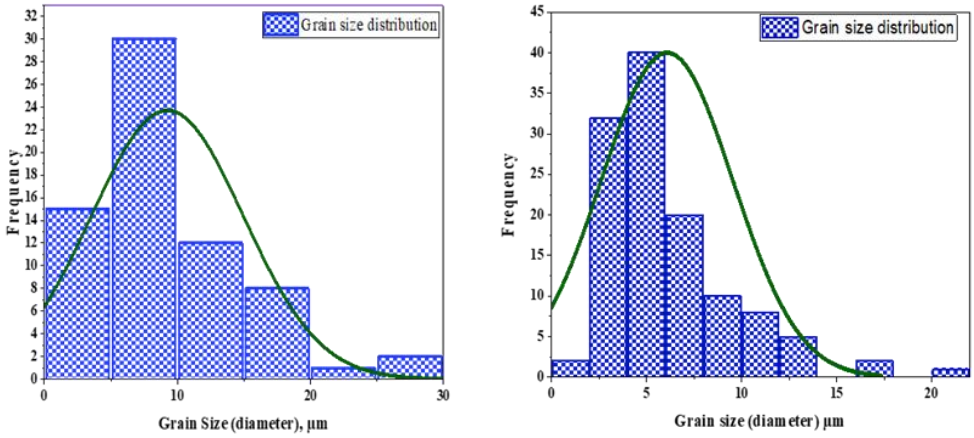

(a) (b)

Fig. 2. Grain size distribution of (a) CuAlNiMn (b) CuAlNiMnLa

3.2 Measurement of Density and Porosity

Table 2 displays the result of the percent porosity and density measurements of the CuAlNiMn SMA system. Comparing the two compositions, it is shown that the modified CuAlNiMn (C2) had lower porosity levels than the unmodified CuAlNiMn (C1) SMA system.

Table 2. The percentage porosity for the produced CuAlNiMn SMA

Composition	Theoretical density, (gcm^{-3})	Experimental density, (gcm^{-3})	Porosity (%)
C1	8.05323	7.963	1.12
C2	8.05162	7.963	1.10

It is observed that the micro-addition of the La causes the composites' percentage porosity to decrease. This shows that rare earth elements contribute to the excellence of the SMA produced by decreasing the percentage porosity. Additionally, the dispersion of La particles in the CuAlNiMn SMA was improved by the procedure, because the maximum permissible porosity value in sand casting composition is less than 4% [32], for porosity has a significant impact on material behavior.

3.3 Mechanical Characteristics

3.3.1 Hardness Properties

Figure 3 shows the variation in the CuAlNiMn SMA hardness with and without the micro-addition of La. The inclusion of La was found to marginally boost the alloys' hardness; in comparison to the unaltered CuAlNiMn, the weight percentage of La increased the composition's hardness value by 17.3%. The inclusion of La as a micro-alloying addition is responsible for the increased hardness found in the modified CuAlNiMn SMA. This change in grain edge morphology and reduction of elongated grain width (i.e., grain thickness) were the outcomes of these additions [33]. A hardening effect caused by the finely dispersed particles

could account for the modified CuAlNiMn SMA's increased hardness value [34]. The Hall-Petch relation is supported by the enhanced resistance to indentation with smaller grain sizes [35].

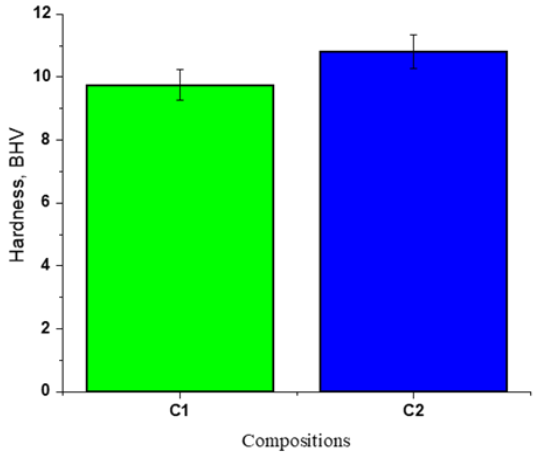

Fig. 3. Variation in hardness value of the produced composition

3.3.2. Tensile Properties

The ultimate tensile and yield strength are shown in Fig. 4. As observed, the tensile strength and yield strength of the composition increase with the micro-addition of La by 22.14% and 20.31% respectively. However, it was observed that the ultimate tensile and yield strengths for unmodified alloys were lower compared with the La-modified CuAlNiMn SMA. Hence, it is noteworthy that the inclusion of rare earth elements significantly improved the strength of the composition. The Rare earth elements help in achieving a refined and homogeneous structure by removing voids and micro-voids and also help in redistributing the particulates and second-phase particles resulting in considerable elimination of particle clusters and segregation. The elimination of a considerable number of voids and porosity in the composition strengthens its ability by lowering the possibility of particle separation under tensile loading [36,37].

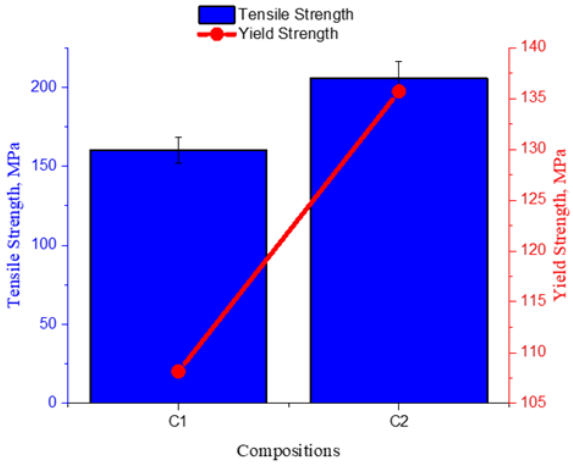

Fig. 4. Ultimate tensile strength and yield strength of the compositions

3.3.3 Fracture Strain Properties

The fracture strain for the compositions is shown in Fig. 5. It is noted that there was an increase in the fracture strain owing to the addition of La compared with the unmodified CuAlNiMn SMA. Sample C2 has the greatest strain improvement with a 20 % increase compared with C1. This shows the possibility of the CuAlNiMn system to withstand plastic deformation and therefore the rare earth metals modification improves their cold workability especially when the alloy is solution heat-treated [38,39].

3.3.4 Percentage Elongation Properties

Figure 5 shows the percentage elongation of the produced compositions. The highest percentage elongation was observed in sample C2 (0.06 wt % of La addition) with a 7.7 % increase when compared with the unmodified CuANiMn alloy. This is due to the ability to achieve better interphase interaction between the CuAlNiMn SMA particles and the rare earth metals.

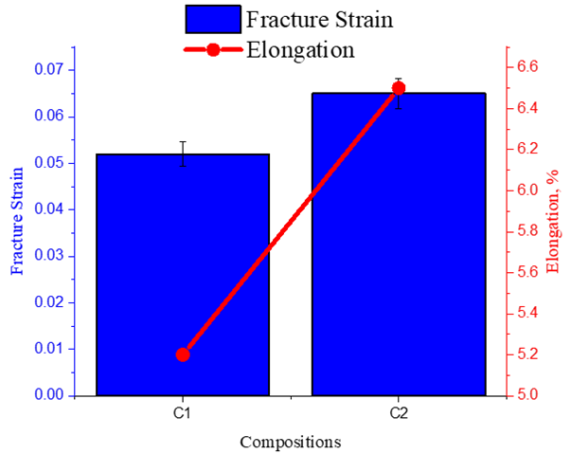

Fig. 5. Variation of fracture strain and percentage elongation of the produced compositions

It is worth noting that rare metals are naturally ductile compared to the brittle CuAlNiMn system [22,40,41]. It implies that the CuAlNiMn SMA enhanced with La will have a greater ability to withstand plastic deformation. The reduction in percentage elongation of unmodified CuAlNiMn alloy can be ascribed to its sharp end grain boundaries, which can limit deformation through plasticity because of the triaxial stress condition that is formed at these locations [23].

3.3.5 Specific Strength Properties

Specific strength, commonly referred to as a material's strengths-to-weight ratio, is an indication of a substance's durability. It is noted from Fig. 6 that the micro-addition of La increases the specific strength of the composition. C2 which has 0.06 wt% of La has the highest specific strength, compared to C1 which is an unmodified alloy, this is a result of the relatively higher density of the composition as shown in Table 2. This implies that grain structures with thinner walls of higher material strength-to-weight ratio can be produced using La as an additive to CuAlNiMn SMA without any adverse effect on strength performance [42,43].

3.3.6 Fracture Toughness Properties

Figure 6 shows the evaluation of the fracture toughness for the CuAlNiMn SMA. The stated values are valid for fracture toughness, as condition, $D \geq (\frac{K_{1c}}{\sigma_y})^2$, given for the requirements for planar strain for the cylindrical round sample geometry were satisfied [27]. The micro-addition of La is noted to increase the fracture toughness of the CuAlNiMn SMA. 22.5% increase in fracture toughness was achieved for C2 with La addition. The inclusion of the rare metal in the alloy composition enhances the ability of the CuAlNiMn SMA to prevent the propagation of cracks. This is because the addition of La to CuAlNiMn SMA causes a stabilizing and refining impact on the grain, enhancing the alloy's toughness and resistance to the propagation of crack [39]. This means that in an application where impact absorption and resistance to fracture are essential service requirements, the CuAlNiMn SMA with La will be more dependable [42].

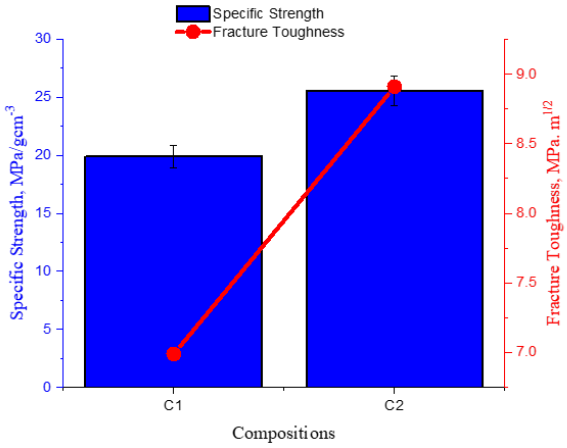

Fig. 6. Variation of specific strength and fracture toughness of the produced compositions

3.4 Corrosion Behavior

The variation of weight loss (mg) and corrosion penetration rate (mm/yr.) of the CuAlNiMn SMA in 0.5 M NaCl and 1.0 M NaCl solutions are presented in Fig. 7 and Fig. 8 respectively. Fig. 7(a), shows that the weight losses of the two alloy systems produced were less than 9 mg in the NaCl solution after 240 hours of experiment. The micro-addition of La has a modest effect on the alloy's resistance to corrosion in the solution, as may be seen by careful observation. Compared to the unmodified composition (C1) the corrosion tendency of the alloy was slightly reduced with the addition of the rare element. Fig 7(b) shows the weight loss variation in 1.0 M NaCl solution. It was noted that the weight losses of the compositions were less than 10.0 mg in the NaCl solution after 240 hours of experiment. The compositions are influenced by the addition of La rare earth metal, which results in a considerable weight decrease compared to the unmodified alloy (C1), which exhibits the greatest weight loss throughout the experiment. Figure 8 shows the corrosion penetration rate of the produced compositions in 0.5 M and 1.0 M of NaCl solutions. It was observed that the corrosion rate of the La-modified composition was reduced compared with the unmodified composition. It was also observed in Fig. 8(a) and 8(b) that C2 showed a resistance to corrosion (lowest corrosion penetrated rate) throughout the study while it was so evident at 114 hours for 0.5 M of NaCl solution and 96 hours for 1.0 M of NaCl solutions. In Fig. 7 and 8, it is observed that the addition of La to the CuAlNiMn SMA resulted in a significant improvement of the corrosion resistance of the CuAlNiMn SMA in NaCl solution.

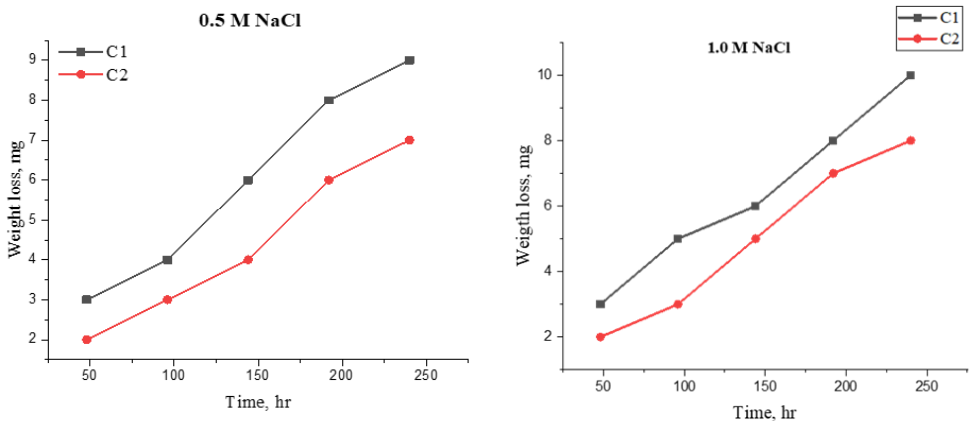

(a) (b)

Fig. 7. (a) Variation of weight loss for the produced CuAlNiMn-based SMA immersed in 0.5M NaCl solution, (b) Variation of weight loss for the produced CuAlNiMn-based SMA immersed in 1.0M NaCl solution

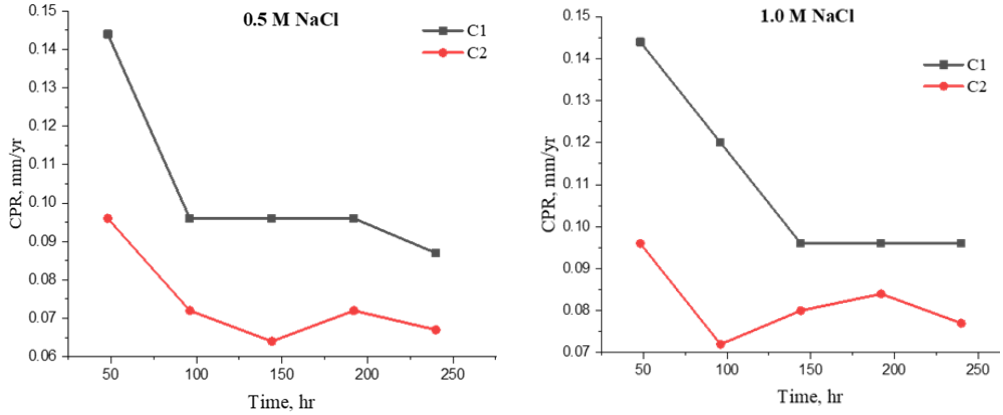

(a) (b)

Fig. 8. (a) Variation of Corrosion Penetration Rate for the produced CuAlNiMn-based SMA immersed in 0.5 M NaCl solution, (b) Variation of Corrosion Penetration Rate for the produced CuAlNiMn-based SMA immersed in 1.0 M NaCl solution

After the corrosion test, the surfaces were subjected to an ultrasonic treatment in deionized water, dried in a desiccator, and then evaluated under an optical microscope at a magnification of 10 to ascertain the surface state, as illustrated in Fig. 9. Pits are evident on the surfaces of C1 and C2 as shown in Fig. 9a and 9b, which show a 0.5 M NaCl solution, but the surface of C2 shows less pitting corrosion. Also, both C1 and C2 of the 1.0 M NaCl solution in Fig. 9c and 9d follow the same pattern as Fig. 9a and 9b but there is more evidence of pitting corrosion compared to Fig. 9a and 9b due to the higher concentration of NaCl in the solution. This is a positive indicator that micro-additions of La into CuAlNiMn alloy can improve the corrosion resistance for applications in environments with moderate NaCl concentrations

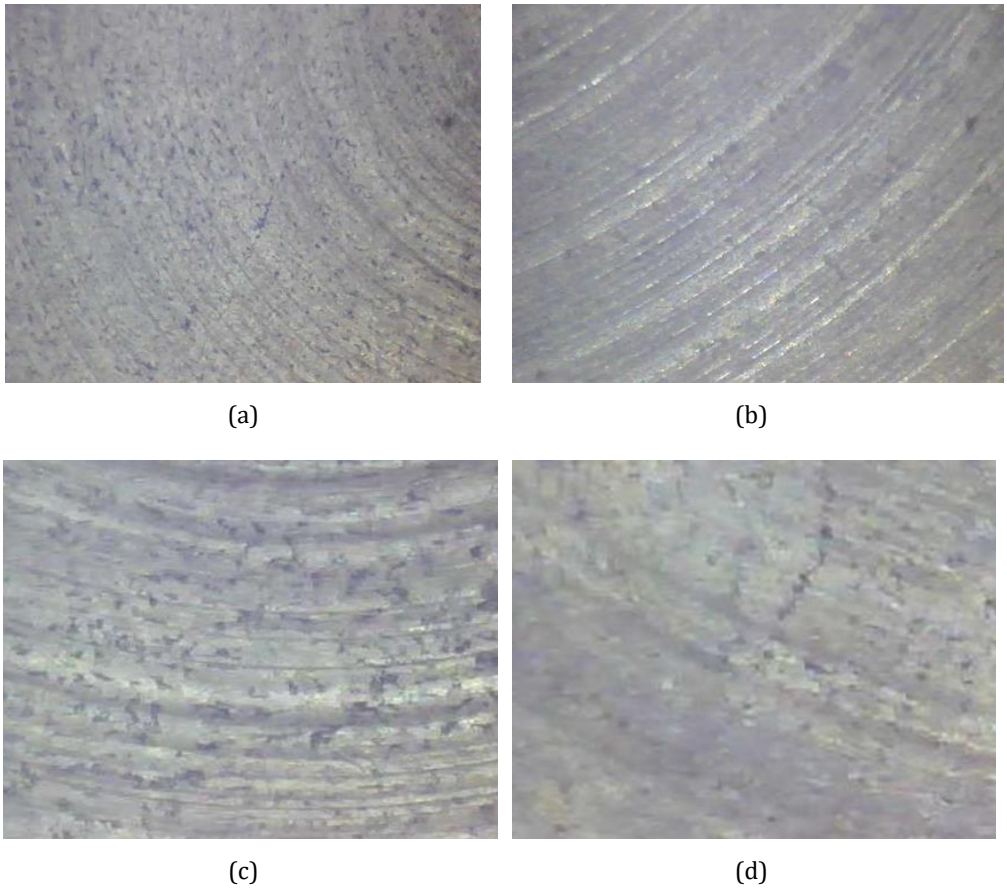

Fig. 9. Optical Microscope images of the samples with corroded surfaces; (a) C1 of 0.5 M of NaCl solution, (b) C2 of 0.5 M of NaCl solution, (c) C1 of 1.0 M of NaCl solution, and (d) C2 of 1.0 M of NaCl solution

4. Research Significance

Rare metals can greatly improve the performance of copper-based shape memory alloys (SMAs), providing several benefits for both basic science and practical applications. La metal addition to CuAlNiMn system is an active field of study with broad implications for applied engineering. It results in improved mechanical properties, increased resistance to corrosion, and the possibility of new, cutting-edge applications. This study attempts in developing a high-performance material suited for harsh environment.

5. Knowledge Gaps

Rare earth metals have been employed by several authors in their SMA research, it has been discovered that these metals are limited in availability in Cu-based SMAs. The influence of Lanthanum as an enhancer for improved grain characteristics, mechanical, and corrosion properties of CuAlNiMn shape memory alloy in its as-cast state have been examined in this study. Although the as-cast condition is the main emphasis, these alloys may be optimized by investigating various benefits and constraints in the solution treatments. Furthermore, alternative metal-forming processes (such as powder metallurgy and rapid solidification) and

their effects on the inclusion and dispersion of rare metals in Cu-based SMAs have not been well explored. This requires a grasp of how processing factors influence the final properties of the alloy's system.

6. Comparison of Previous Studies with The Current Study

It is evident from Table 3, that the inclusion of rare elements in the Cu-based SMA affects its properties. These elements produced a shape memory alloy system with a refined grain structure and could control the amount of austenite to martensite transition [47]. More study is necessary to fully understand the potential of La addition to Cu-based SMA since the effect has not been well studied.

Table 3. Comparative table showing the properties' results of the previous studies on Cu-based SMA and the current study with additions of rare metals

Reference(s)	Shape Memory Alloy (SMA)	Hardness (HV)	Strength (MPa)	Strain (%)	Porosity (%)	Corrosion Rate (mm/yr.)
[45]	CuAlNi	223.6	270	1.65	-	-
	CuAlNi0.97wt%Mn	225.4	450	3	-	-
	CuAlNi0.99wt%Ti	236.4	680	2.8	-	-
	CuAlNi1.14wt% Co	345	650	7	-	-
[46]	Cu11Al5Mn0.7Ti	190	266.5	0.65	-	-
	Cu11Al5Mn0.7Ti1Ta	233.5	386.1	1.05	-	-
	Cu11Al5Mn0.7Ti2Ta	247.2	393.6	1.22	-	-
	Cu11Al5Mn0.7Ti3Ta	211.9	357.4	0.98	-	-
[47]	Cu-14Al-4.5Ni	-	622	12.66	-	-
	Cu-14Al-4.5Ni-0.3Ce	-	659	16.45	-	-
	Cu-14Al-4.5Ni-1Ce	-	637	15.35	-	-
	Cu-14Al-4.5Ni-3Ce	-	340	6.99	-	-
[48]	Cu-11.9Al-2.5Mn	-	380	3.5	-	-
	Cu-11.9Al-2.5Mn-0.4CuZr	-	540	4.3	-	-
	Cu-11.9Al-2.5Mn-0.5CuZr	-	530	7.0	-	-
	Cu-11.9Al-2.5Mn-0.7CuZr	-	545	7.2	-	-
	Cu-11.9Al-2.5Mn-0.9CuZr	-	720	8.5	-	-
	Cu-11.9Al-2.5Mn-1.0CuZr	-	450	3.7	-	-
[49] (Cu83Al12Mn5)$_{1-x}$ Ce$_x$	(Cu83Al12Mn5)$_{100}$ Ce$_0$	-	600	11	-	-
	(Cu83Al12Mn5)$_{99.5}$ Ce$_{0.05}$	-	890	15	-	-
	(Cu83Al12Mn5)$_{99.90}$ Ce$_{0.1}$	-	800	16.7	-	-
	(Cu83Al12Mn5)$_{99.85}$ Ce$_{0.15}$	-	790	20.5	-	-
[50]	Cu-12.5Al-4Ni	-	-	-	12.96	2.68

	Cu-12.5Al-4Ni-1Ta	-	-	-	9.0	1.79
	Cu-12.5Al-4Ni-2Ta	-	-	-	7.5	0.74
	Cu-12.5Al-4Ni-3Ta	-	-	-	11.0	0.29
Current Study	Cu-14Al-4.5Ni-0.7Mn	9.75	160.21	5.2	1.12	0.087
	Cu-14Al-4.5Ni-0.7Mn-0.06La	10.8	205.77	6.5	1.10	0.067

7. Conclusions

CuAlNiMn alloy containing Lanthanum micro-alloying element has its mechanical properties, corrosion behavior, and grain characteristics adequately studied. The detailed outcomes of the present study are as follows:

- The microstructures and grain features directly affect the remarkable increase in mechanical properties that alloyed CuAlNiMn alloy demonstrates. The microstructure was composed of combinations of Cu-rich α-phase, β-phase with a substantial volume portion, and a huge coarse intermetallic compound called α+γ2.
- Adding La to the CuAlNiMn alloy caused a notable increase in the alloy's characteristics through grain refining. Following the micro-addition of the alloying element, the parent alloy's average grain size reduced from 9.25 μm to 6.08 μm, resulting in improved mechanical characteristics.
- The CuAlNiMn alloy without alloying elements performed the least favorably in terms of physical properties, with 1.12% porosity, and mechanical properties, with 9.75 BHV of hardness, 160.21 MPa of UTS, 108.15 MPa of yield strength, 0.052 of fracture strain, 5.2% of elongation, 19.89 MPa/gcm^3 of specific strength, and 6.99 MPa.m$^{1/2}$ of fracture toughness. In contrast, the CuAlNiMnLa alloy system achieved a lower percentage of porosity, higher value of hardness, UTS, yield strength, fracture strain, %elongation, specific strength, and fracture strain, with values of 1.10%, 10.80 BHV, 205.77 MPa, 135.71 MPa, 0.065, 6.5%, 25.57 MPa/gcm^3, and 8.91 MPa.m$^{1/2}$, respectively.
- Within the chosen media (0.5 M and 1.0 M of NaCl solutions), it was noticed from the corrosion rate and weight loss plots that the developed modified CuAlNiMn SMA exhibited a notable increase in corrosion resistance.
- After 240 hours in a 0.5 M NaCl solution, the corrosion rates of CuAlNiMn decreased from 0.144 mm/yr. to 0.087 mm/yr. while CuAlNiMnLa from 0.096 mm/yr. to 0.067 mm/yr. Additionally, after 240 hours of exposure to 1.0 M NaCl solution, the corrosion rates of CuAlNiMn decreased from 0.144 mm/yr. to 0.096 mm/yr., while CuAlNiMnLa decreased from 0.096 mm/yr. to 0.077 mm/yr.
- The micro-addition of lanthanum considerably enhanced the corrosion behavior, mechanical, and physical properties of the CuAlNiMn alloy.

Acknowledgments

The authors express their gratitude to Landmark University for aiding and fostering an environment that allowed them to begin the experimental work.

Nomenclature

SMA – Shape Memory Alloy
SME – Shape Memory Effect
C1 – Composition 1
C2 – Composition 2
Cu - Copper
Al – Aluminum
Ni – Nickel
Mn – Manganese
La – Lanthanum
Ce – Cerium
Ti – Titanium
Ga – Gallium
Zn – Zinc
Fe – Iron
Si – Silicon
Au – Gold
Ag – Silver
Cd – Cadmium
Pt – Platinum
Co – Cobalt
$FeCl_3$ – Iron (III) Chloride
HCl – Hydrochloric Acid
NaCl – Sodium Chloride
CPR – Corrosion Penetration Rate
ρ_C = Density of the composition
ρ_E = Density of the element
V_E = Volume fraction of the element
$\sum$ = Summation
ρ_T = Theoretical density
ρ_{EX} = Experimental density
CNT = Circumferential notch tensile
K_{1c} = Fracture toughness
p_f = Fracture load
D = Guage diameter
d = Notch diameter

References

[1] Kanayo Alaneme K, Adebayo Ogunsanya O, Abiodun Kareem S. On The Mechanical Properties and Damping Behaviour of Thermally Aged Unmodified And Ni Modified Cu-Zn-Al Shape Memory Alloys. Vol. 58, Journal of Chemical Technology and Metallurgy. 2023. https://doi.org/10.59957/jctm.v58i6.158
[2] Anzel I, Lojen G, Ivanić I, Kosec B, Gojic M, Kòuh S, et al. Microstructural and phase analysis of CuAlNi shape-memory alloy after continuous casting. Materials and Technology [Internet]. 2013;47(2):149-52.
[3] Malinin VG, Malinina NA, Malinin G V, Malukhina OA. Development of methods of structural-analytical mesomechanics that take into account the statistical properties of martensitic transformations in materials with shape memory effect. IOP Conf Ser Mater Sci Eng. 2018;441(1). https://doi.org/10.1088/1757-899X/441/1/012030
[4] Najah Saud Al-Humairi S. Cu-Based Shape Memory Alloys: Modified Structures and Their Related Properties. In: Basheer Al-Naib U, Vikraman D, Karuppasamy K, editors. Recent Advancements in the Metallurgical Engineering and Electrodeposition [Internet]. IntechOpen; 2020. https://doi.org/10.5772/intechopen.86193
[5] Muntasir Billah AHM, Rahman J, Zhang Q. Shape memory alloys (SMAs) for resilient bridges: A state-of-the-art review. Structures. 2022 Mar 1;37:514-27. https://doi.org/10.1016/j.istruc.2022.01.034
[6] Mohamed OA, Masood SH, Xu W. Nickel-titanium shape memory alloys made by selective laser melting: a review on process optimisation. Adv Manuf. 2022 Mar 1;10(1):24-58. https://doi.org/10.1007/s40436-021-00376-9
[7] Agrawal A, Dube RK. Methods of fabricating Cu-Al-Ni shape memory alloys. J Alloys Compd. 2018 Jun 25;750:235-47. https://doi.org/10.1016/j.jallcom.2018.03.390
[8] Abolhasani D, Han SW, VanTyne CJ, Kang N, Moon YH. Enhancing the shape memory effect of Cu-Al-Ni alloys via partial reinforcement by alumina through selective laser melting. Journal of Materials Research and Technology. 2021 Nov 1;15:4032-47. https://doi.org/10.1016/j.jmrt.2021.10.040

[9] Mazzer EM, Da Silva MR, Gargarella P. Revisiting Cu-based shape memory alloys: Recent developments and new perspectives. J Mater Res [Internet]. 2022;37(1):162-82. https://doi.org/10.1557/s43578-021-00444-7
[10] Volkov-Husović T, Ivanić I, Kožuh S, Stevanović S, Vlahović M, Martinović S, et al. Microstructural and cavitation erosion behavior of the cualni shape memory alloy. Metals (Basel). 2021 Jul 1;11(7). https://doi.org/10.3390/met11070997
[11] Nwaeju C, Edoziuno F, Adediran A, Nnuka E, Adesina O. Structural and properties evolution of copper-nickel (Cu-Ni) alloys: a review of the effects of alloying materials. Matériaux & Techniques. 2021 Dec 21;109:204. https://doi.org/10.1051/mattech/2021022
[12] Yang S, Zhang J, Chen X, Chi M, Wang C, Liu X. Excellent superelasticity and fatigue resistance of Cu-Al-Mn-W shape memory single crystal obtained only through annealing polycrystalline cast alloy. Materials Science and Engineering: A. 2019 Feb 1;749. https://doi.org/10.1016/j.msea.2019.02.033
[13] Tian J, Zhu W, Wei Q, Wen S, Li S, Song B, et al. Process optimization, microstructures and mechanical properties of a Cu-based shape memory alloy fabricated by selective laser melting. J Alloys Compd. 2019 May 1;785. https://doi.org/10.1016/j.jallcom.2019.01.153
[14] Alaneme KK, Okotete EA, Anaele JU. Structural vibration mitigation - a concise review of the capabilities and applications of Cu and Fe based shape memory alloys in civil structures. Journal of Building Engineering. 2019;22:22-32. https://doi.org/10.1016/j.jobe.2018.11.014
[15] Alaneme K, Okotete E. Reconciling viability and cost-effective shape memory alloy options - A review of copper and iron based shape memory metallic systems. Engineering Science and Technology, an International Journal. 2016;19. https://doi.org/10.1016/j.jestch.2016.05.010
[16] Ivanić I, Gojić M, Kožuh S, Kosec B. Microstructural analysis of CuAlNiMn shape-memory alloy before and after the tensile testing. Materials and technologies [Internet]. 2014;713-8.
[17] Ivanić I, Gojić M, Anzel I, Kožuh S, Rimac M, Beganović O, et al. Microstructure and properties of casted CuAlNi and CuAlNiMn shape memory alloys. Vol. 55, Ljevarstvo: glasilo Hrvatskog udruženja za ljevarstvo. 2013. 79-85 p.
[18] Wang Z, Liu X, Xie J xin. Effects of solidification parameters on microstructure and mechanical properties of continuous columnar-grained Cu-Al-Ni alloy. Progress in Natural Science: Materials International. 2011;21:368-374-368-374. https://doi.org/10.1016/S1002-0071(12)60071-9
[19] Anzel I, Lojen G, Ivanić I, Kosec B, Gojic M, Kòuh S, et al. Microstructural and phase analysis of CuAlNi shape-memory alloy after continuous casting. Materials and Technology [Internet]. 2013;47(2):149-52.
[20] Akash K, Mani Prabu SS, Gustmann T, Jayachandran S, Pauly S, Palani IA. Enhancing the life cycle behaviour of Cu-Al-Ni shape memory alloy bimorph by Mn addition. Mater Lett. 2018 Sep 1;226:55-8. https://doi.org/10.1016/j.matlet.2018.05.008
[21] Guniputi BN, S.M. M. Effect of manganese and homogenization on the phase stability and properties of Cu-Al-Be shape memory alloys. Journal of Materials Research and Technology. 2021 Sep 1;14:1551-8. https://doi.org/10.1016/j.jmrt.2021.07.027
[22] Saud SN, Hamzah E, Abubakar T, Bakhsheshi-Rad HR, Zamri M, Tanemura M. Effects of Mn additions on the structure, mechanical properties, and corrosion behavior of Cu-Al-Ni shape memory alloys. J Mater Eng Perform. 2014 Oct 1;23(10):3620-9. https://doi.org/10.1007/s11665-014-1134-1
[23] Alaneme KK, Umar S. Mechanical behaviour and damping properties of Ni modified Cu-Zn-Al shape memory alloys. Journal of Science: Advanced Materials and Devices. 2018;3(3):371-9. https://doi.org/10.1016/j.jsamd.2018.05.002
[24] Peregrina-Barreto H, Terol-Villalobos IR, Rangel-Magdaleno JJ, Herrera-Navarro AM, Morales-Hernández LA, Manríquez-Guerrero F. Automatic grain size determination in

microstructures using image processing. Measurement. 2013;46(1):249-58. https://doi.org/10.1016/j.measurement.2012.06.012
[25] ASTM E92-23. Standard Test Methods for Vickers Hardness and Knoop Hardness of Metallic Materials. West Conshohocken, PA; 2023.
[26] ASTM E8/E8M-22. Standard Test Methods for Tension Testing of Metallic Materials. West Conshohocken, PA; 2022.
[27] Alaneme KK. Fracture toughness (K1C) evaluation for dual phase medium carbon low alloy steels using circumferential notched tensile (CNT) specimens. Materials Research. 2011;14(2):155-60. https://doi.org/10.1590/S1516-14392011005000028
[28] Edoziuno F, Adediran A, Adetunla A, Nwaeju C, Nnuka E. RSM-based optimization and predictive modelling of the gravimetric corrosion behaviour of solution-treated copper-based shape memory alloy in HCl solution. International Journal on Interactive Design and Manufacturing (IJIDeM). 2022 Dec 20. https://doi.org/10.1007/s12008-022-01163-x
[29] ASTM G31 -21. Standards: Metals Test Methods and Analytical Procedures. Philadelphia; 2021.
[30] Nnakwo KC, Mbah CN, Nnuka EE. Influence of trace additions of titanium on grain characteristics, conductivity and mechanical properties of copper-silicon-titanium alloys. Heliyon. 2019 Oct 1;5(10). https://doi.org/10.1016/j.heliyon.2019.e02471
[31] Nnakwo KC, Osakwe FO, Ugwuanyi BC, Oghenekowho PA, Okeke IU, Maduka EA. Grain characteristics, electrical conductivity, and hardness of Zn-doped Cu-3Si alloys system. SN Appl Sci. 2021 Nov 1;3(11). https://doi.org/10.1007/s42452-021-04784-1
[32] Alaneme K, Aluko A. Production and Age-Hardening Behaviour of Borax Premixed SiC reinforced Al-Mg-Si alloy Composites developed by Double Stir-Casting Technique. The West Indian Journal of Engineering. 2012;34.
[33] Ahmed RS, Abbass MK, AlKubaisy MM. Effect of Ce addition on mechanical properties and shape memory effect of Cu-14%Al-4.5%Ni shape memory alloy. Mater Today Proc [Internet]. 2020;20:452-60. https://doi.org/10.1016/j.matpr.2019.09.164
[34] Dalvand P, Raygan S, López GA, Chernenko VA. Effect of adding Ti and rare earth elements on properties of Cu-14Al-4Ni shape memory alloy. Mater Res Express [Internet]. 2019;6(11):116512. https://doi.org/10.1088/2053-1591/ab43f7
[35] Naik, S.N., Walley, S.M. The Hall-Petch and inverse Hall-Petch relations and the hardness of nanocrystalline metals. J Mater Sci 55, 2661-2681 (2020). https://doi.org/10.1007/s10853-019-04160-w
[36] Lu X, Chen F, Li W, Zheng Y. Effect of Ce addition on the microstructure and damping properties of Cu-Al-Mn shape memory alloys. J Alloys Compd [Internet]. 2009;480(2):608-11. https://doi.org/10.1016/j.jallcom.2009.01.134
[37] Song ZX, Li YD, Liu WJ, Yang HK, Cao YJ, Bi GL. Effect of la and sc co-addition on the mechanical properties and thermal conductivity of as-cast al-4.8% cu alloys. Metals (Basel). 2021 Nov 1;11(11). https://doi.org/10.3390/met11111866
[38] Pakdel A, Farhangi H, Emamy M. Effect of Extrusion Process on Ductility and Fracture Behavior of SiCp/Aluminum-Alloy Composites. In: Proceedings of 8th International Fracture Conference, Istanbul, Türkiye [Internet]. 2007. http://www.endil.yildiz.edu.tr/proceedings/50.pdf
[39] Alaneme KK, Sulaimon AA, Olubambi PA. Mechanical and corrosion behaviour of iron modified Cu-Zn-Al alloys. Acta Metallurgica Slovaca. 2013;19(4):292-301. https://doi.org/10.12776/ams.v19i4.184
[40] Bhattacharya S, Bhuniya A, Banerjee MK. Influence of minor additions on characteristics of Cu–Al–Ni alloy. mats sci tech. 1993 Aug 1;9(8):654-8. https://doi.org/10.1179/026708393790172358
[41] Basak Deepjyoti. Investigation of Cu based shape memory alloy as a reinforcement for metal matrix composite. 2018.

[42] Alaneme KK, Ojomo AM, Bodunrin MO. Structural analysis, mechanical and damping behaviour of Al-Zn based composites reinforced with Cu and SiC particles. Manufacturing Rev. 2022;9:5. https://doi.org/10.1051/mfreview/2022005
[43] Aliyu SJ, Adekanye TA, Adediran AA, Ikubanni PP, Ogundipe OL. A review on the effect of Rare Metals additions on the mechanical and damping properties of CuAlNi shape memory alloys. In: 2024 International Conference on Science, Engineering and Business for Driving Sustainable Development Goals (SEB4SDG). IEEE; 2024. p. 1-6. https://doi.org/10.1109/SEB4SDG60871.2024.10629969
[44] Adekanye TA, Aliyu SJ, Adediran AA, Ujunwa D, Ochimana J, Isadare B, et al. A review of CuAlNiMn shape memory alloy modified with rare earth metals. In: 2024 International Conference on Science, Engineering and Business for Driving Sustainable Development Goals (SEB4SDG). IEEE; 2024. p. 1-5. https://doi.org/10.1109/SEB4SDG60871.2024.10629987
[45] Saud SN, Hamzah E, Abubakar T, Ibrahim MK, Bahador A. Effect of a fourth alloying element on the microstructure and mechanical properties of Cu-Al-Ni shape memory alloys. J Mater Res [Internet]. 2015;30(14):2258-69. https://doi.org/10.1557/jmr.2015.196
[46] Yang L, Jiang X, Sun H, Shao Z, Fang Y, Shu R. Effect of Ta addition on microstructures, mechanical and damping properties of Cu-Al-Mn-Ti alloy. Journal of Materials Research and Technology. 2021 Nov;15:3825-35. https://doi.org/10.1016/j.jmrt.2021.10.031
[47] Ahmed Adnan RS, Abbass MK, AlKubaisy MM. Effect of Ce addition on mechanical properties and shape memory effect of Cu-14%Al-4.5%Ni shape memory alloy. Materials Today: Proceedings. 2020;20:452-60. https://doi.org/10.1016/j.matpr.2019.09.164
[48] Yang J, Wang QZ, Yin FX, Cui CX, Ji PG, Li B. Effects of grain refinement on the structure and properties of a CuAlMn shape memory alloy. Materials Science and Engineering A. 2016 May 1;664:215-20. https://doi.org/10.1016/j.msea.2016.04.009
[49] Lu X, Chen F, Li W, Zheng Y. Effect of Ce addition on the microstructure and damping properties of Cu-Al-Mn shape memory alloys. J Alloys Compd [Internet]. 2009;480(2):608-11. https://doi.org/10.1016/j.jallcom.2009.01.134
[50] Saud SN, Hamzah E, Bakhsheshi-Rad HR, Abubakar T. Effect of Ta additions on the microstructure, damping, and shape memory behaviour of prealloyed Cu-Al-Ni shape memory alloys. Scanning [Internet]. 2017;2017:1-13. https://doi.org/10.1155/2017/1789454

Research on Engineering Structures & Materials
www.jresm.org
MIM Research Group

Research Article

Optimum and efficient design of steel foot over bridges

Sushant Kumar Jha [1,a], Abhay Bambole [*,2,b], Dhanashri Jadhav [2,c], Archanaa Dongre [3,d], Dulal Goldar [1,e]

[1]*Dept. of Civil Engineering, Lingaya's University, Faridabad, India*
[2]*Dept. of Structural Engineering, Veermata Jijabai Technological Institute, Mumbai, India*
[3]*Dept.of Civil Engineering, Vidyavardhini's College of Engineering and Technology, Vasai, India*

Article Info

Article History:

Received 29 Jan 2024
Accepted 20 Aug 2024

Keywords:

Foot over bridge;
Steel design;
Cost efficiency;
Durability

Abstract

This work used the Finite Element Method (FEM) to estimate the shear force for a blind shear ram type blowout preventer. In recent years, significant advancements have been made in the design of Foot Over Bridges (FOBs) through the utilization of advanced analytical methods, innovative materials, and novel bridge concepts. FOBs have gained popularity in urban India due to their ability to facilitate safe pedestrian crossings without disrupting vehicular traffic flow, thereby enhancing pedestrian safety in areas with heavy traffic. This research focuses on the development of an economically optimized steel FOB design specifically tailored for the Mumbai region. The primary objectives are to ensure durability, stability, safety, and cost-effectiveness in the design. The study involves modelling the typical span of a skywalk structure using STAAD Pro, followed by comprehensive analysis and design iterations for various configurations based on real-world spans of existing pedestrian bridges. Static loading conditions are applied to the FOB models, allowing important characteristics like weight, number of joints, number of members, weld lengths, painting surface area, and natural frequency of pedestrian bridges to be evaluated. These factors are carefully contrasted to determine the bridge design that is the most economical. Additionally, vibration tests are conducted on two selected skywalks to assess their compliance with serviceability criteria. The research scrutinizes the utilization ratio of members in the bridge structures and explores variations in section sizes within the design to achieve the optimal configuration. The findings are presented in detail, offering valuable insights into the process of identifying the most economical FOB design from the skywalks in the Mumbai suburban region. This study contributes to the enhancement of pedestrian infrastructure in urban India by delivering a robust and cost-efficient FOB design approach.

1. Introduction

The importance of providing safe and dedicated pathways for walkers in pedestrian infrastructure, distinct from vehicular traffic, cannot be overstated. Sidewalks and skywalks emerge as critical components of urban planning, offering pedestrians the security and convenience they deserve. However, in many regions of India, these pedestrian facilities face dire challenges marred by neglect, encroachments, and inadequate capacity. As a result, pedestrians often need to be more open to utilising them, and there is a pressing need to transform these neglected walkways into appealing, secure, and efficient avenues for foot traffic. This imperative underscores the significance of conducting thorough investigations into the design and functionality of sidewalks and skywalks, particularly in India. While extensive research exists on pedestrian facilities, much

*Corresponding author: anbambole@st.vjti.ac.in
[a]orcid.org/0000-000 7-7874-0286; [b]orcid.org/0000-0002-5337-5530; [c]orcid.org/0009-0009-9497-7173;
[d] orcid.org/0000-0002-5814-7123; [e]orcid.org/0009-0009-9497-7173
DOI: http://dx.doi.org/10.17515/resm2024.167st0129rs

of it stems from studies conducted in developed countries, leaving a noticeable void when it comes to India's unique conditions and requirements.

This research endeavours to fill this void by analysing and designing pedestrian bridges of diverse types and spans using STAAD PRO software. By examining critical parameters such as weight per meter, the number of structural members, the number of joints, deflection characteristics, and cost per meter span, we aim to determine the most economical bridge design. We aim to develop a comprehensive understanding of the factors that influence pedestrian bridge design, thereby contributing to enhancing pedestrian infrastructure in India. Furthermore, it is essential to navigate the labyrinth of codes and standards governing the construction of road bridges in India. The Indian Road Congress (IRC) codes play a pivotal role in shaping the guidelines for road bridge design, encompassing provisions for load considerations, stress analysis, working stress methodologies, limit state methods, steel road bridges, and seismic load considerations. These codes form the backbone of safe and efficient bridge construction, ensuring structural integrity and reliability. Additionally, this research introduces three predominant truss types frequently employed in constructing skywalks, each characterised by distinct structural attributes and applications. The Pratt Truss is recognised for its cost-effectiveness and suitability for vertical load scenarios; the Warren Truss is notable for its configuration of equilateral triangles, rendering it favourable for distributing spanned loads; and the Howe Truss, which presents an intriguing inversion of structural forces, with diagonal members in compression and vertical loads in tension[1]. In addition to classifying trusses based on their structural attributes, this research also delves into their classification predicated on the positioning of the deck slab. This categorisation yields three primary types: the underslung truss bridge, where the deck carries the live load, demonstrating remarkable cost-effectiveness; the through type truss bridge, ideal for accommodating long spans where underslung trusses may not be suitable; and the semi-through truss bridge, serving as an economical choice for shorter spans[1].

In summary, this introduction lays the groundwork for our research by highlighting the critical significance of pedestrian infrastructure in urban settings, shedding light on the unique challenges faced in India, articulating our research goals, referencing the pertinent codes and regulations, and presenting a comprehensive introduction to various truss types and classifications. These elements collectively prepare the context for our detailed investigation into pedestrian bridge design and its economic aspects, outlining our study's objectives. These objectives include:

- Comparative analysis using STAAD Pro software results for several foot-over bridges in Mumbai.
- Testing the vibrations of footbridges to ascertain their inherent frequencies.
- Interpreting the findings to determine the foot over bridge design that is the most cost-effective.

Additionally, we navigate relevant codes and standards and provide a comprehensive overview of various truss types and classifications. These elements collectively set the stage for our in-depth exploration of pedestrian bridge design and economics. In the past, A pedestrian count experiment was conducted in Cincinnati [2], providing insights into pedestrian behaviour on skywalks during lunch and nighttime peak hours. Further insights into peak-hour pedestrian behaviour were extended [3] through pedestrian counts conducted in Hong Kong's Central Business District, focusing on morning and evening peak flows. The structural efficiency of different truss types was explored [4]through vibration analysis, demonstrating the cost-effectiveness of Howe-type truss bridges. Innovative composite bridge construction using corrugated steel webs and trusses was introduced [5] to reduce material usage and construction costs. Research on the capacity analysis of railway Foot Over Bridges (FOBs) [6] was done with a particular emphasis on geometric aspects and their influence on bridge capacity. A performance evaluation of a novel composite pedestrian bridge design utilising hybrid materials for achieving lightweight, cost-effectiveness, and durability in bridge construction was conducted [7]. A parametric research study [8] focuses on optimising pedestrian traffic for arch bridges with radial hanger arrangements, with a specific mass reduction goal. Detailed structural insights into aluminium alloy truss arch bridges were provided [9],

considering pedestrian comfort and load-bearing capacity factors. A comparative study was carried out between pre-engineered steel structures and conventional steel structures, highlighting the sustainability and cost-effectiveness of pre-engineered designs [10]. An economical and functional pedestrian bridge deck was created. It is composed of two layers: carbon-reinforced polymer fiber on the bottom and cement composite on top [11]. The research was conducted on pedestrian crossing speed and behaviour, finding that city features, geography, and pedestrian characteristics contribute to crossing behaviour [12].

While the research has been comprehensive, it presents several notable gaps: Studies have been conducted on pedestrian behaviour during peak weekday hours but need to capture a complete picture by not including traffic counts over an entire month, which could reveal additional essential patterns. Analyses using STAAD PRO have been completed to compare the performance of various trusses under vibration loads, but these studies still need to consider the impact of different span lengths. Work on cost optimisation has been focused primarily on arch-type pedestrian bridges, excluding other common types of truss bridges, thereby limiting the understanding of cost efficiencies across a broader range of bridge designs. Furthermore, there needs to be a more detailed comparative analysis concerning the influence of span variations on pedestrian bridges, and discussions on cost-affecting parameters such as weld length and paint surface area are absent. Equally, research needs to adequately address the construction ease of bridges, which has significant implications for project timelines and labour costs. Bridging these gaps is essential for advancing the field and could lead to more effective bridge construction and design practices.

2. Foot Over Bridges: Analysis and Modelling - Case Studies

This is the case study completed on the skywalks in the Mumbai region; it includes modelling and on-site visual observations for 14 distinct skywalks, as well as comprehensive data on the skywalks' weight, number of members, number of joints, weld length, and surface area. Table 1 shows the bridge's 3D model and structure at various points. Table 2 displays the bridges' specifics. Table 1 shows the actual bridge structure and the related 3D model.

Table 1. Bridge structures considered for study and related 3D Model

Sr. No.	Location	Bridge at location	3D Model
1	Skywalk at Bandra West		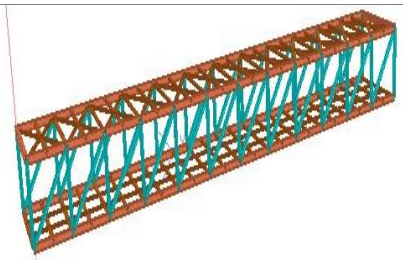
2	Bridge Girder at Andheri		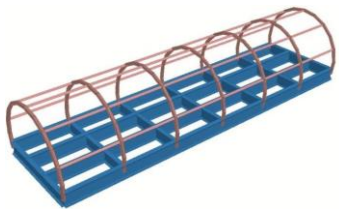

3	Warren truss bridge at Andheri		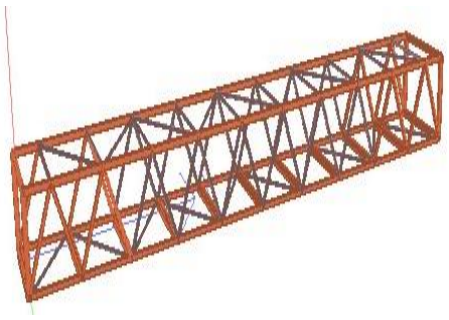
4	Skywalk at Goregaon		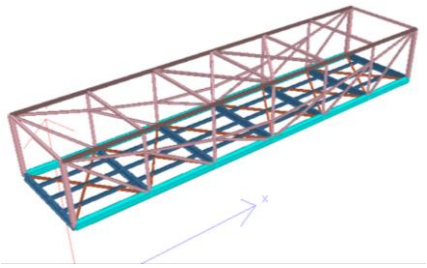
5	Skywalk at Santacruz		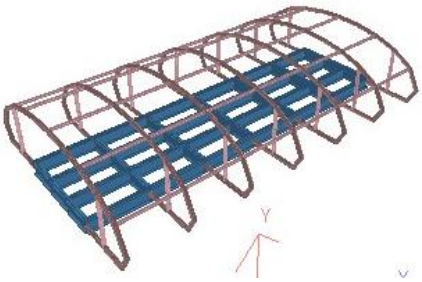
6	Skywalk at Wadala		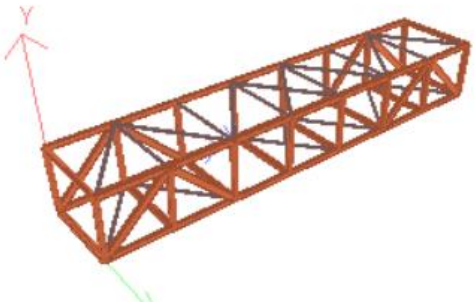
7	Skywalk at Sion East		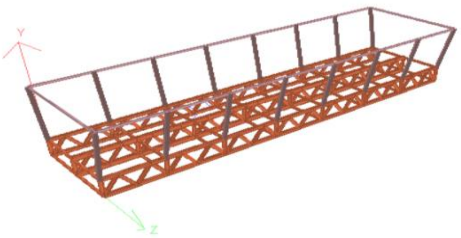
8	Skywalk At Ghatkopar West		

9	Skywalk at Bhandup		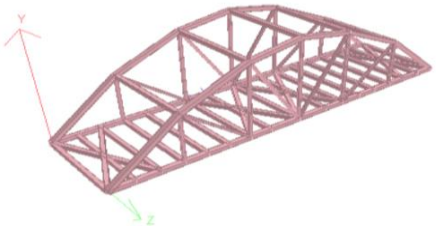
10	Skywalk at Tagore Nagar		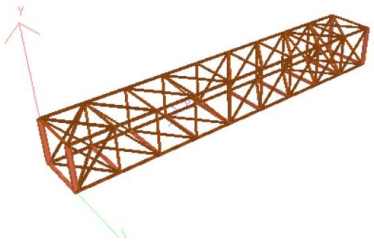
11	Skywalk at Nalanda Nagar		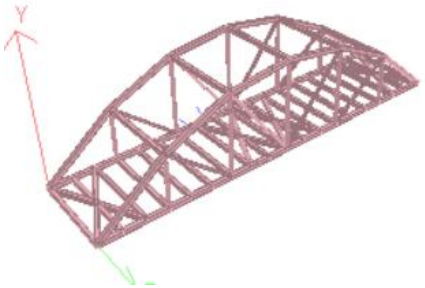
12	Skywalk at Priyadarshini		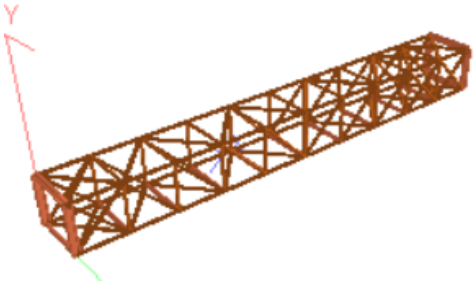
13	Skywalk at Vikhroli		
14	Pravin Hotel Skywalk		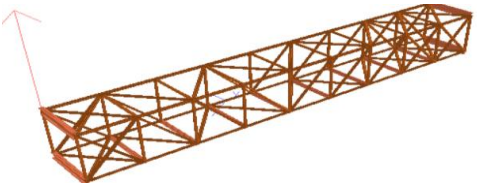

Table 2. Structure of the bridges taken into consideration for the research

Sr. No.	Bridges Considered	Span Length (m)	Width of Bridge	Weight per meter (Kg/m)	No. of Members per meter	No. of Joints per meter	Weld Length per meter	Deflec. (mm)	Max Axial Stress (N/m^2)	Natural freq. Hz
1	Bandra West	28.8	4	862.5	5	2	11.7	24.8	65.77	5.485
2	Andheri Warren Type	30	4	506.5	3	2	19	46.1	141.4	4.05
3	Goregaon	18	4	362.7	5	2	8.98	32.0	91.14	4.37
4	Wadala East	21	4	647.9	3	2	24	36.1	130.1	4.31
5	Sion East	17.5	4	503.6	8	-	12.1	30	108.6	4.06
6	Ghatkopar West	8	4	738.6	20	8	14.3	2.3	14.58	18.22
7	Andheri Bridge Girder	16.4	4.5	1169.7	2	-	12	26.365	135	4.445
8	Santacruz West	16.8	4.5	918.9	3	-	10.12	20.637	85.632	3.46
9	Bhandup	13.6	3.5	416.0	5	2	7.062	15	102.35	13.989
10	Tagore Nagar	22.5	3.15	420.0	6	2	4.302	19.563	106.33	6.784
11	Nalanda Nagar	16.7	3.75	367.1	4	2	5.735	18	117.50	10.424
12	Priyadarsh-ani	27.5	3.15	559.6	5	2	4.16	17	102.94	4.633
13	Vikhroli	18.1	3.75	350.9	4	2	5.322	19	142.55	9.54
14	Pravin Hotel	23.4	3	395.1	6	2	4.427	20	140	6.427

3. Experimental Investigation and Outcome of the Study

To verify the serviceability requirements for the vibration limit, an experimental research was conducted on a variety of bridges. An accelerometer vibration test is used to determine the natural frequency of bridges. The natural frequency of the bridges in these studies was contrasted with the software's output.

3.1 Method of Experimentation

3.1.1 Instrument Calibration

First, the cantilever beam is used to calibrate the device; see Fig. 1.

Fig. 1. Cantilever beam

The following sizes of M. S. steel plate are needed for the cantilever beam. Length (L) = 497 mm, Width = 39.82 mm, and Thickness = 5 mm.

$$\omega_n = C_n \sqrt{\frac{EI}{mL^4}} \quad (1)$$

C_n=In above standard formula C_n depends on vibration mode

- C_1 = 3.516 for 1st mode
- C_2= 22.0345 for 2nd mode
- C_3 = 61.6972 for 3rd mode
- C_4 is 120.0902 for fourth mode.

A beam's mass per unit length (m) is 1.562935 kg/m, its natural frequency is 103.7053 rad/sec, or 16.5 Hz, its moment of inertia (I) is 414.792 mm^4, its Young's modulus (E) is $2x10^5$ MPa, and its natural frequency from the experiment is 14.607 Hz.

3.1.2 Configuration of the Test

Sandpaper is used to clean the surface in order to mount an accelerometer and get precise readings. The test setup completed at the site location is depicted in Figure 2(a). Accelerometer mounting (Fig. 2(b)) Results are obtained in the form of acceleration against time using a data gathering device (see Fig. 2(c)).

(a) (b) (c)

Fig. 2. (a)Test setup (b)accelerometer (c)data acquisition system

3.1.3 Method of Testing

To obtain results, the test setup is followed by the following actions. The testing is carried out at a specific site. Following the test configuration, five or six participants each leaped once at a distance of two meters from the test site in order to produce vibrations and obtain a consistent, undistorted frequency vs time graph. At that same position, three leaps are made in order to collect accurate data. At the other two locations, the test is administered again. The Data Acquisition System is where the data is obtained.

4. Experimental Findings

After conducting a vibration test on two bridges, the Data Acquisition System yielded the following results.

4.1 Skywalk at Priyadarshini Location

The acceleration vs. time curve for the Priyadarshini Skywalk at position 1 is displayed in Figure 3. The acceleration vs. time curve for the Priyadarshini skywalk at position 2 is displayed in Figure 4.

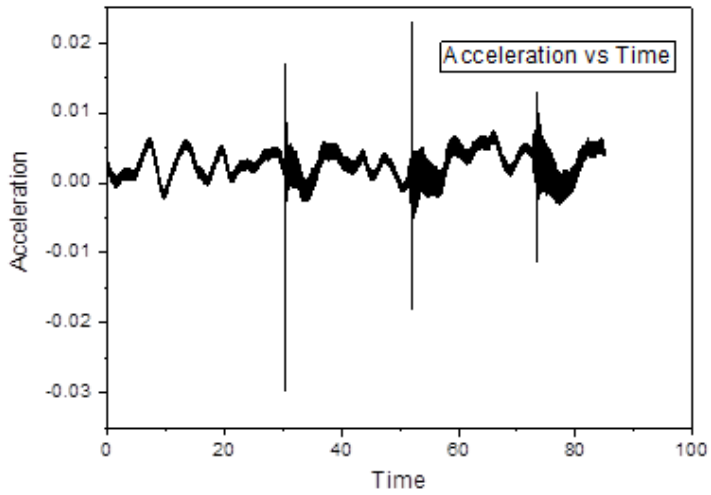

Fig. 3. Priyadarshini Skywalk acceleration against time at Location number 1.

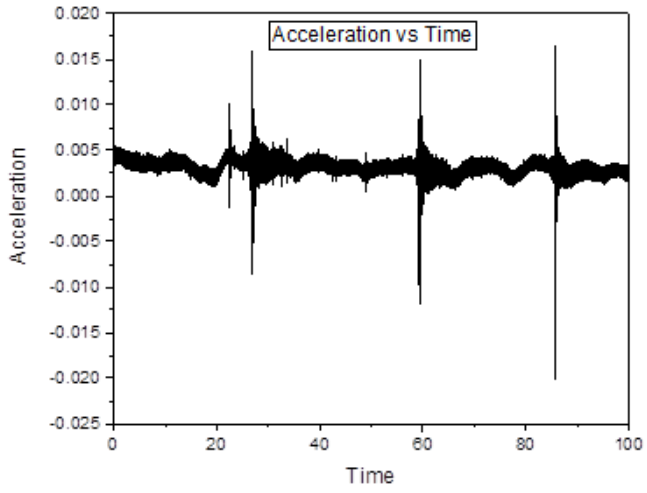

Fig. 4. Priyadarshini Skywalk acceleration against time at Location number 2.

4.2. Skywalk at Wadala Location

The Wadala Skywalk at location 1's acceleration vs. time curve is displayed in Figure 5. The Wadala Skywalk at location 2's acceleration vs. time curve is displayed in Figure 6. The Wadala skywalk at location 3's acceleration vs. time curve is displayed in Figure 7. An accelerometer is used in this experimental setup and process to conduct a vibration test.

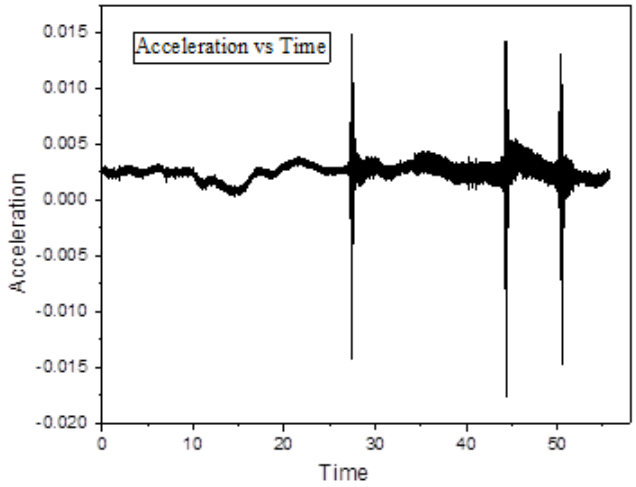

Fig. 5. Wadala Skywalk Acceleration against time for at location1

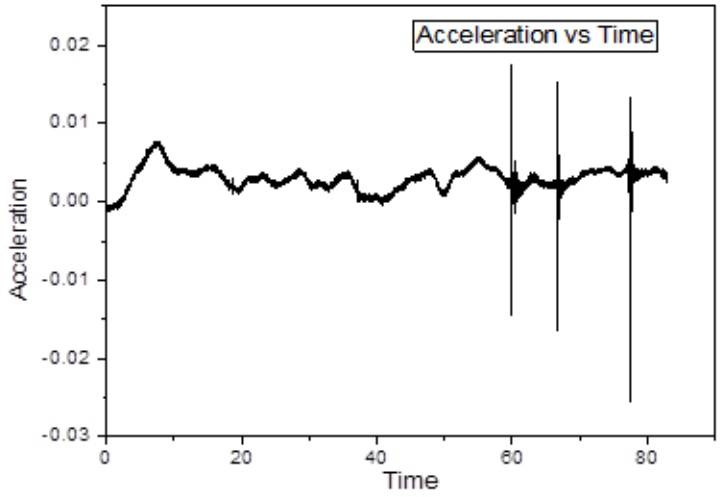

Fig. 6. Wadala Skywalk Acceleration against time for at location2

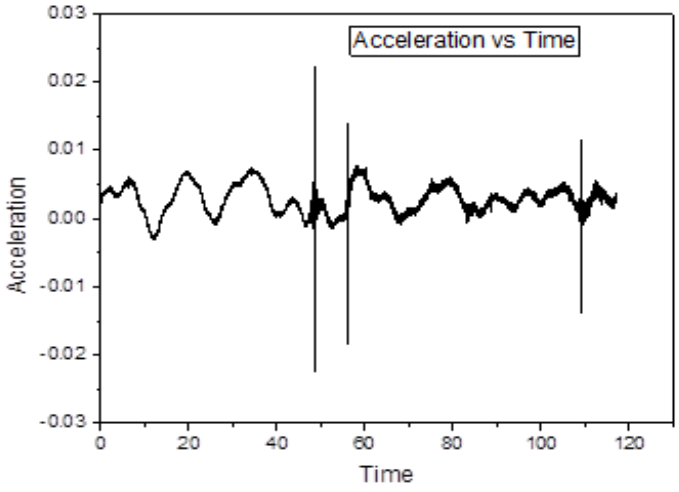

Fig. 7. Wadala Skywalk Acceleration against time at location 3

5. Results and Discussions

The analysis results for the deflection of foot over bridges meet the AASHTHO requirements' permitted serviceability limit.[13]. The foot deflections over bridges are displayed in Table 3. When evaluating the structural performance of foot-over bridges (FOBs), deflection is a crucial factor. Excessive deflection can lead to serviceability issues, discomfort for users, and, in severe cases, structural failure. The deflection values from Table 3, which show the deflection of various bridges under specified loads, are essential for evaluating their safety and performance.

Table 3. Foot over bridges with measured and allowable deflections

Location of Bridge	Measured Deflection	Deflection allowed
Skywalk at Bandra	24.815	57
Bridge Girder at Andheri	26.365	32.8
Andheri warren type	46.154	60
Goregaon	32.091	36
Santacruz	20.637	33.6
Wadala East	36	42
Sion East	31	35
Ghatkopar	2.30	2.2

Bhandup	16	27.3
Tagore	19.60	45
Nalanda	19	33.6
Priyadarshini	18	55
Vikhroli	20	36
Pravin Hotel	21	47

5.1 Analysis of Deflection Values as Given in Table 3

5.1.1 Bandra West Bridge

The deflection value of 24.815 mm is significantly below the permissible limit of 57 mm. This indicates that the Bandra West bridge has a robust design with a substantial safety margin. The low deflection suggests excellent structural integrity and user comfort, with minimal perceptible movement under load

5.1.2 Andheri Girder Bridge

The Andheri Girder bridge deflects 26.365 mm, which is well within the permissible limit of 32.8 mm. While the deflection is close to the upper limit, it still ensures safety and functionality. However, being nearer to the limit means that the bridge should be monitored for any changes over time, especially under increased loads or in case of structural ageing.

5.1.3 Andheri Warren Type Bridge

The deflection of the Andheri Warren Type bridge is 46.154 mm, which is comfortably within the permissible limit of 60 mm. This shows that the bridge is designed efficiently, using materials optimally while maintaining safety standards. The higher deflection compared to other bridges might indicate a design that prioritizes material efficiency and cost-effectiveness without compromising safety.

5.1.4 Ghatkopar West Bridge

With a deflection of 27.09 mm against a permissible limit of 48 mm, the Ghatkopar West bridge demonstrates good structural performance. The deflection value suggests that the bridge has a balanced design, ensuring both safety and comfort for pedestrians.

5.2 Implications for Structural Performance and Safety

- Safety Margins: Bridges like Bandra West and Andheri Warren Type have high safety margins, with deflection values well within permissible limits. This indicates an efficient design that can handle additional loads or unforeseen stress without significant risk.
- Serviceability: Lower deflection values contribute to better serviceability, ensuring that pedestrians experience minimal movement, which enhances comfort and confidence in the bridge's stability.
- Maintenance and Monitoring: Bridges like the Andheri Girder, which have deflection values closer to their permissible limits, require regular monitoring and maintenance. This ensures that any degradation over time is detected early, preventing potential serviceability issues or safety hazards.
- Material Efficiency: The analysis shows that designs like the Andheri Warren Type bridge achieve higher deflection within safe limits, indicating efficient use of materials. This balance between material usage and structural performance is crucial for cost-effective bridge design.

In conclusion, the detailed deflection analysis from Table 3 demonstrates that all the bridges analysed are within their permissible deflection limits, ensuring safety and structural integrity. However, it highlights the importance of regular monitoring, especially for those designs nearing their deflection limits, to maintain long-term performance and safety.

Table 4. Results of comparison between skywalks having width of 4 meters

Sr. No.	Bridge name by location	Length of span (m)	Width	Weight of bridge per meter (Kg/m)	Members per meter	Joints per meter in number	Length of weld per meter	Painting surface area per meter
1	Skywalk at Bandra West	28.8	4	863.00	5	2	11.72	11
2	Warren Type at Andheri	30	4	506.54	3	2	19.00	8.80
3	Skywalk at Goregaon	18	4	363.00	5	2	8.98	19.00
4	Skywalk at Wadala East	21	4	648.00	3	2	24.00	9.00
5	Skywalk at Sion East	17.5	4	503.70	8	-	12.10	13.20
6	Skywalk at Ghatkopar West	8	4	739.00	20	8	14.30	19.27

Most bridges (10 out of 14) have deflections within their allowable limits, indicating they perform within the expected safety margins. The Bandra, Santacruz, Bhandup, Tagore, Nalanda, and Priyadarshini bridges show significantly lower deflections than their allowable limits, suggesting a good safety margin. The Andheri Girder bridge's deflection exceeds its permissible limit, which may indicate potential structural concerns requiring attention. The Goregaon and Sion East bridges are near their maximum allowable deflection, which could warrant close monitoring. The Ghatkopar bridge is notable because its deflection is just slightly above the permissible limit, possibly signalling a critical condition that needs immediate assessment. While within limits, the remaining bridges vary in proximity to their maximum allowable deflection, affecting their respective safety assessments and monitoring needs. The foot-over bridges' comparative outcomes are displayed below. Following the calculation of the parameters, the quantities are transformed into a simplified format and made easier to understand by dividing each by the span itself, as indicated below; refer to Tables 4, 5, 6, and 7.

5.3 Weight and Material Usage

Bandra West has the highest weight per meter (862.52 Kg/m) with a span length of 28.8 meters. This high weight suggests substantial material usage and higher costs. Ghatkopar West also shows a high weight per meter (738.63 Kg/m) but with a much shorter span (8 meters), indicating a dense structure that might be over-designed. Andheri Warren Type and Sion East have moderate weights per meter (506.54 Kg/m and 503.68 Kg/m respectively), making them relatively efficient in terms of material usage for their span lengths (30 meters and 17.5 meters). Goregaon has the lowest weight per meter (362.74 Kg/m) for an 18-meter span, indicating good material efficiency.

5.4 Number of Members and Joints per Meter

Ghatkopar West stands out with the highest number of members (20) and joints (8) per meter, suggesting a complex and potentially costly construction. Sion East also has a high number of members (8) per meter, which could impact the construction time and costs. Bandra West and Goregaon have moderate numbers of members (5 each) per meter, indicating a balanced design. Andheri Warren Type and Wadala East have fewer members (3 each) and joints (2 each) per meter, suggesting simpler and potentially more cost-effective designs.

5.5 Weld Length and Surface Area for Painting

Wadala East has the highest weld length per meter (24.00), which could increase welding costs and maintenance complexity. Andheri Warren Type also has a significant weld length per meter (19.00), impacting initial construction costs. Ghatkopar West and Sion East have moderate weld lengths (14.30 and 12.10 respectively), with potential implications for construction and maintenance costs. Bandra West and Goregaon have lower weld lengths (11.72 and 8.98 respectively), suggesting more efficient welding processes.

5.6 In Terms of Surface Area for Painting

Ghatkopar West (19.27) and Goregaon (18.71) have the highest surface areas per meter, leading to higher long-term maintenance costs. Sion East and Bandra West have moderate surface areas (13.18 and 10.98 respectively), balancing initial and maintenance costs. Andheri Warren Type (8.80) and Wadala East (8.98) have the lowest surface areas, suggesting cost-effective maintenance.

5.6.1 Summary and Recommendations

- Most Material Efficient: Goregaon stands out for its low weight per meter and moderate weld length and surface area for painting.
- Most Cost-Effective: Andheri Warren Type appears to be the most cost-effective in terms of material usage and maintenance costs, despite the higher weld length.
- Complex and Costly: Ghatkopar West is the least efficient due to its high weight, number of members and joints, and extensive weld length and surface area for painting.
- Balanced Designs: Bandra West and Sion East offer balanced designs with moderate weights and material usage, though Sion East's higher number of members might increase complexity.

By optimizing designs to reduce weight, minimize the number of structural members and joints, and control weld lengths and surface areas for painting, bridges can achieve better cost and material efficiency.

Table 5. Results of comparison between skywalks and bridge width of 4 meters

Sr. No.	Location of Bridges	Length of Span (m)	Bridge width	Measured Deflection (mm)	Axial Stress maximum N/mm^2
1	Bandra West	28.8	4	24.81	65.78
2	Andheri Warren Type	30	4	46.15	141.41
3	Goregaon	18	4	32.09	91.14
4	Wadala East	21	4	36.12	130.12
5	Sion East	17.5	4	30.70	108.61
6	Ghatkopar West	8	4	2.31	14.58

The above table outlines characteristics and stress metrics for six different bridges. Bandra West and Andheri, Warren Type bridges have the longest spans at 28.8 and 30 meters, respectively, with the latter experiencing the highest deflection and axial stress, potentially indicating significant load or structural challenges. Goregaon, Wadala East, and Sion East bridges present a mid-range span with moderate deflections and axial stresses. Notably, the Ghatkopar West bridge, with the shortest span of only 8 meters, exhibits the smallest deflection and axial stress, which suggests lighter loads or a sturdier design. The consistency in width across all bridges suggests standardisation in design, but the varying deflection and stress levels point to differences in traffic load, structural materials, or design efficiency.

5.7 Analysis of Comparative Results of Skywalks for Width of Bridge 4m from Table 5

5.7.1 Deflection Analysis

- Permissible Deflection Limits: Typically, the permissible deflection for bridges is span/250 to span/500, depending on the design standards and load conditions. For a 30-meter span, permissible deflection ranges from 60 mm to 120 mm.
- Bandra West: With a deflection of 24.81 mm for a 28.8-meter span, this bridge is well within permissible limits, indicating good structural performance and stiffness.
- Andheri Warren Type: Exhibits the highest deflection at 46.15 mm for a 30-meter span, which is within permissible limits but relatively higher than other bridges, indicating a more flexible structure.
- Goregaon and Wadala East: Deflections of 32.09 mm and 36.12 mm for 18-meter and 21-meter spans respectively, are within limits but higher than Bandra West, suggesting moderate flexibility.
- Sion East: With a deflection of 30.70 mm for a 17.5-meter span, this bridge shows moderate stiffness.
- Ghatkopar West: The lowest deflection at 2.31 mm for an 8-meter span, indicating a very stiff structure.

5.7.2 Maximum Axial Stress Analysis

- Significance: Axial stress impacts the stability and serviceability of the structure. Higher stress values can indicate potential risk of material yielding or failure under load.
- Bandra West: Maximum axial stress of 65.78 N/mm^2, indicating good performance and structural safety.
- Andheri Warren Type: The highest axial stress at 141.41 N/mm^2, which is significantly higher than other bridges, suggesting potential concerns under high load conditions.
- Goregaon and Wadala East: Moderate axial stresses of 91.14 N/mm^2 and 130.12 N/mm^2 respectively, indicating reasonable structural performance.
- Sion East: Exhibits 108.61 N/mm^2 axial stress, suggesting adequate performance but higher stress than Bandra West.
- Ghatkopar West: The lowest axial stress at 14.58 N/mm^2, indicating excellent structural stability and safety under axial loads.

5.7.3 Summary and Recommendations

- Bandra West: Offers the best balance between deflection and axial stress, indicating optimal design for both stiffness and stability.
- Andheri Warren Type: Requires attention due to high deflection and axial stress, potentially necessitating design improvements for enhanced stiffness and reduced stress.
- Goregaon, Wadala East, and Sion East: Moderate performance in terms of deflection and axial stress, suggesting satisfactory design with room for optimization.
- Ghatkopar West: Exhibits the best performance in terms of deflection and axial stress, indicating a very robust design but with potentially higher material costs due to its very low deflection and stress values.
- For optimized design, it is recommended to: Focus on material efficiency: Similar to Bandra West, which provides good performance with moderate deflection and stress values.
- Improve designs with high deflection and stress: Particularly for Andheri Warren Type, by enhancing the structural stiffness and reducing axial stress through material selection or design modifications.
- Balance performance and cost: By aiming for moderate deflection and stress values, ensuring both structural safety and cost-effectiveness.

Table 6. Comparison of skywalk performance at varying bridge widths

Sr. No.	Bridges location and name	Span of bridge (m)	Bridge width	Weight per meter (Kg/m)	Members per meter	Joints per meter	Length of weld per meter	Painting surface area per meter
1	Bridge Girder at Andheri	16.4	4.5	1169.78	2	-	12.00	9.20
2	Santacruz West	16.8	4.5	918.9	3	-	10.12	17.81
3	Bhandup gaon	13.64	3.5	416.70	5	2	7.06	10.57
4	Tagore Nagar	22.5	3.15	420.50	6	2	4.30	9.72
5	Nalanda Nagar	16.79	3.75	367.13	4	2	5.73	8.59
6	Priyadarshani	27.5	3.15	559.66	5	2	4.16	9.48
7	Vikhroli	18.1	3.75	350.91	4	2	5.32	8.30
8	Pravin Hotel	23.4	3	395.09	6	2	4.43	8.84

5.8 Cost Efficiency Analysis

5.8.1 Weight and Material Usage

- Andheri Bridge Girder: Highest weight per meter (1169.78 Kg/m) for a 4.5-meter width. This implies higher material usage and cost.
- Santacruz West: Second highest weight per meter (918.9 Kg/m) for a 4.5-meter width.
- Bhandupgaon and Nalanda Nagar: Lower weights per meter (416.70 Kg/m and 367.13 Kg/m respectively) for 3.5-meter and 3.75-meter widths, indicating material efficiency.
- Vikhroli and Pravin Hotel: Lowest weights per meter (350.91 Kg/m and 395.09 Kg/m respectively) for 3.75-meter and 3-meter widths, showcasing material efficiency.

5.8.2 Number of Structural Members

- Tagore Nagar and Pravin Hotel: Highest number of members per meter (6), indicating potentially higher complexity and assembly costs.
- Andheri Bridge Girder: Lowest number of members per meter (2), suggesting simpler construction but higher weight.

5.8.3 Weld Length and Surface Area for Painting

- Andheri Bridge Girder and Santacruz West: Longer weld lengths (12.00 m and 10.12 m respectively) indicating higher welding costs and potential for increased maintenance.
- Bhandupgaon and Priyadarshani: Shorter weld lengths (7.06 m and 4.16 m respectively), indicating reduced welding costs.
- Santacruz West: Highest surface area for painting per meter (17.81 m^2), indicating higher maintenance costs.
- Nalanda Nagar and Vikhroli: Lowest surface areas for painting (8.59 m^2 and 8.30 m^2 respectively), indicating reduced maintenance costs.

5.8.4 Summary and Recommendations

5.8.4.1. Optimal Designs:

- Vikhroli and Nalanda Nagar: Exhibit the lowest weight per meter and surface area for painting, indicating cost efficiency in both material usage and maintenance.
- Bhandupgaon: Although it has more structural members, its lower weight per meter and moderate surface area for painting make it an efficient choice.

5.8.4.2 Considerations for Improvement

- Andheri Bridge Girder: While having a simpler design with fewer members, its high weight per meter and long weld lengths suggest the need for material optimization.
- Santacruz West: Although lighter than Andheri Bridge Girder, its higher surface area for painting implies increased maintenance costs. Design modifications to reduce painting surface or improve protective coatings could be beneficial.

5.8.4.3 Design Practices for Cost Efficiency:

- Material Optimization: Use lighter materials or optimized designs like those seen in Vikhroli and Nalanda Nagar to reduce overall weight and cost.
- Simplified Construction: Aim for a balance between the number of structural members and material weight, as seen in Bhandupgaon.
- Maintenance Considerations: Designs with lower surface areas for painting, like Nalanda Nagar and Vikhroli, should be preferred to minimize long-term maintenance costs.

These recommendations aim to balance material costs, construction complexity, and long-term maintenance, ensuring cost-effective and efficient bridge designs.

Table 7 presents a comparative analysis of skywalks, examining the effects of varying bridge widths on structural performance. The comparison involves eight bridges, with span lengths ranging from 13.64 to 27.5 meters and widths from 3 to 4.5 meters. Key performance indicators include deflection and maximum axial stress. The Andheri Bridge Girder, with a span of 16.4 meters and a width of 4.5 meters, exhibits a deflection of 26.365 mm and an axial stress of 135 N/mm^2. In contrast, the Santacruz West, slightly longer at 16.8 meters but the same width, has a lower deflection and axial stress. As the spans increase, the Priyadarshini skywalk stands out for its longer span of 27.5 meters and narrower width. It shows lower deflection and moderate stress levels, suggesting it is an efficient design for its length category. Conversely, Vikhroli, with an 18.1-meter span and a 3.75-meter width, has one of the higher stress readings at 142.55 N/mm^2, yet it is considered optimal for bridges with a span of 10-20 meters. These observations indicate that the Vikhroli Skywalk performs best for medium-span bridges, while the Priyadarshini Skywalk is the most economical for longer spans, factoring in variables such as weight, joints, deflection, weld length, and maximum axial stress against the width of the bridges.

Table 7. Comparison of skywalk performance at varying bridge widths

Sr. No.	Bridge locations	Span (m)	Width (m)	Measured Deflection (mm)	Max Axial Stress N/mm^2
1	Andheri Bridge Girder	16.4	4.5	26.365	135
2	Santacruz West	16.8	4.5	20.637	85.63
3	Bhandupgaon	13.64	3.5	15	102.35
4	Tagore Nagar	22.5	3.15	19.563	106.33
5	Nalanda Nagar	16.794	3.75	18	117.50
6	Priyadarshini	27.5	3.15	17	102.94
7	Vikhroli	18.1	3.75	19	142.55
8	Pravin Hotel	23.4	3	20	140

5.9 Analysis of Result from Table 7

5.9.1 Deflection vs. Span Length

The bridge with the highest deflection is the Andheri Bridge Girder, which also has a relatively short span length (16.4 m). This suggests that the design or load conditions of this bridge may cause higher deflection.

5.9.2 Maximum Axial Stress

The highest axial stress is observed in the Vikhroli bridge (142.55 N/mm^2), indicating that it experiences significant stress despite not having the longest span.

5.93. Widest Bridge

The Andheri Bridge Girder and Santacruz West bridges are the widest, both at 4.5 meters. Wider bridges generally can accommodate more traffic but may also face higher stresses and deflections.

5.9.4 Longest Span

The longest span is the Priyadarshini bridge at 27.5 meters, but it has a moderate deflection (17 mm) and stress (102.94 N/mm^2), suggesting efficient design.

5.9.5 Insights

- Design Efficiency: The Priyadarshini bridge, with the longest span but moderate deflection and stress, indicates a potentially more efficient design.
- Potential Issues: The Andheri Bridge Girder, with the highest deflection, and the Vikhroli bridge, with the highest axial stress, may need further inspection or maintenance to ensure safety.
- Comparative Analysis: Comparing the span length, width, deflection, and stress can help identify potential weaknesses in bridge design and prioritize maintenance efforts.

5.9.6. Analysis of result for Acceleration versus frequency

The acceleration vs. frequency plot is displayed in Table 8 following the conversion of the time-domain data into frequency-domain data using MATLAB's Fast Fourier Transform. The basic frequency of vibration is provided by the acceleration vs. frequency graph.

Skywalk Acceleration versus Frequency Data:

- Skywalk at Priyadarshini Location:

Result at Location 1 when at first Jump: Frequency = 3.42035 Hz,

Result at Location 1 when at second Jump: Frequency = 3.80556 Hz

- Skywalk at Wadala:

Jump 1 at Location 1: Frequency = 4.10256 Hz, Jump 2 at Location 1: Frequency = 4.16 Hz

Table 8. Graphical representation in Tabular form

Sr. No.	Skywalk	Acceleration versus Frequency plot	Frequency in Hz
1	Skywalk at Priyadarshini	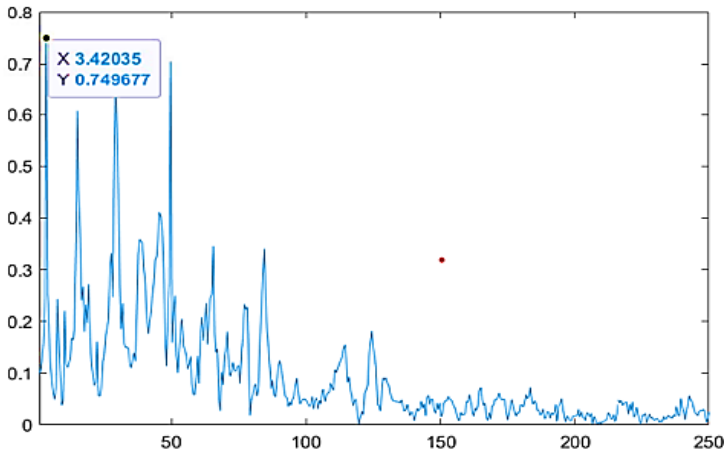 First Jump at Location 1 at Priyadarshini skywalk	3.42035 Hz

2	Skywalk at Priyadarshini	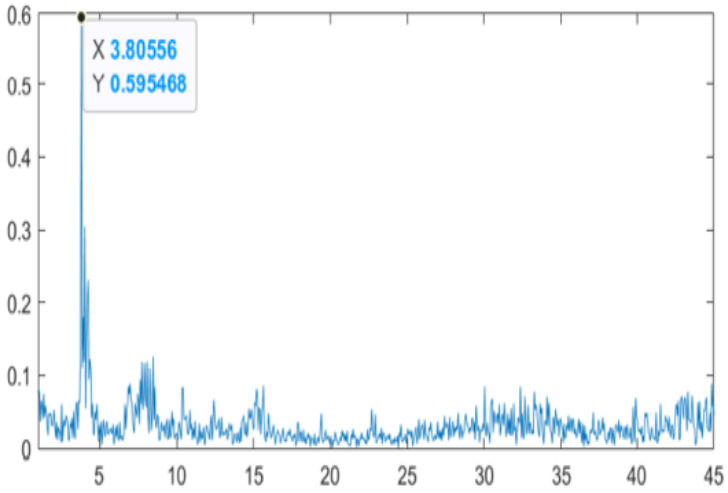 Second jump at location 2 at Priyadarshini skywalk	3.80556 Hz
3	Skywalk at Wadala	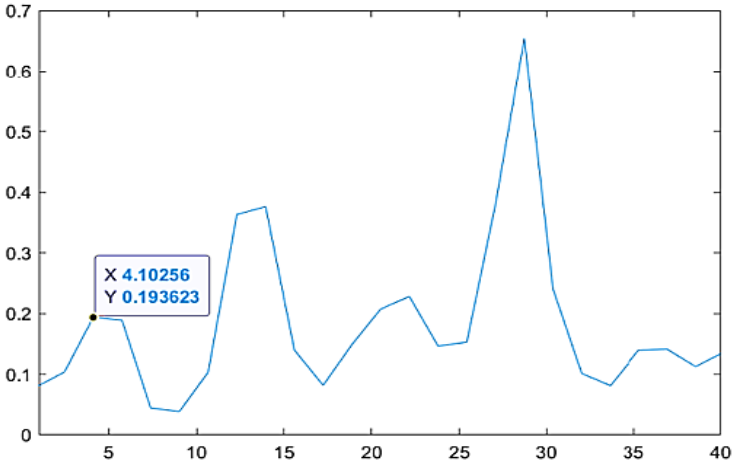 First jump at location 1 for Wadala skywalk	4.10256 Hz
4	Skywalk at Wadala	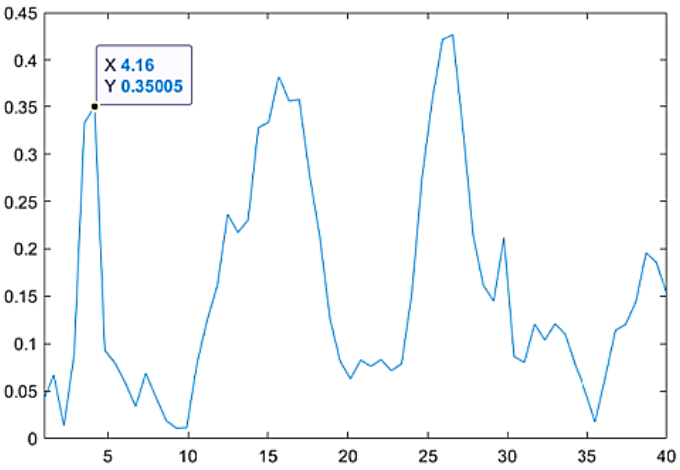 Second jump at location 1 for Wadala skywalk	4.15 Hz

5.10 Analysis of the Data from Table 8

5.10.1 Frequency Variations:

- For the Priyadarshini Skywalk, the frequency values for jumps 1 and 2 are 3.42035 Hz and 3.80556 Hz, respectively.

- For the Wadala Skywalk, the frequency values for jumps 1 and 2 are 4.10256 Hz and 4.16 Hz, respectively.
- The Wadala Skywalk shows slightly higher frequency values compared to the Priyadarshini Skywalk for the same jump locations.

5.10.2 Acceleration Patterns

- The graphs indicate how the acceleration changes with frequency for each skywalk during the jumps.
- Typically, a peak in the graph represents the natural frequency at which the structure tends to resonate.
- Structural Resonance: Both skywalks exhibit specific resonance frequencies. The Wadala Skywalk has higher resonance frequencies than the Priyadarshini Skywalk.
- Potential Impact: Higher frequencies in Wadala Skywalk imply stiffer structural characteristics compared to the Priyadarshini Skywalk.

5.10.3 Recommendations

- Safety Assessments: Regular monitoring and assessment of these frequencies are recommended to ensure the skywalks remain safe under various loading conditions.
- Further Analysis: A detailed modal analysis can be conducted to understand the vibration modes and ensure the design accommodates expected loads and pedestrian traffic.

6. Conclusions

This detailed study thoroughly examined Foot Over Bridges (FOBs) in the Mumbai region to develop an economically optimized steel design suitable for the high-density urban environment. The research highlighted the importance of durability, stability, safety, and cost-effectiveness in these critical structures, which enhance pedestrian safety in busy traffic areas.

The methodology incorporated on-site visual inspections and detailed parameter collection for five distinct skywalks, including weight per meter, the count of structural members and joints, weld lengths, and surface areas for painting. STAAD Pro software was used for 3D modelling, analysis, and design, relying on the actual measurements of existing pedestrian bridges to inform the study.

A series of static loading tests were conducted on the FOB models to evaluate critical parameters. These assessments aimed to determine the most cost-effective design by comparing weight, member count, joint count, weld lengths, paint surface area, and natural frequencies. Vibration testing was also performed on selected skywalks to ensure they met serviceability criteria.

The research delved into the efficiency of using bridge members and the potential for optimizing section sizes to find an ideal balance for an optimized bridge design. Examining these elements revealed insights into the most cost-effective FOB design among the studied skywalks, marking a notable contribution to developing pedestrian infrastructure in urban India. A significant discovery was that the deflections, natural frequencies, and maximum axial stresses of the bridges were within the permissible limits, suggesting that most of the bridges were performing within expected safety margins. The study also identified the Andheri Warren Type Truss Bridge as the most economical option, considering material costs, structural efficiency, and maintenance needs. However, the research also highlighted concerns for certain bridges like the Andheri Girder, where deflections exceeded allowable limits, and for others like Goregaon and Sion East, which were close to their maximum permissible deflection, indicating a need for close monitoring or potential intervention.

The experimental and analytical results revealed variations in the natural frequency of some skywalks, with the Priyadarshini Skywalk showing a 17.395% variation and the Wadala Skywalk a 12.82% variation from expected values. This suggests a discrepancy that warrants further investigation. In conclusion, the study presents a comprehensive approach to improving FOB design, creating economically feasible and structurally sound FOB designs. This approach ensures that the infrastructural needs of pedestrian traffic in Mumbai are met with optimized designs that priorities safety, stability, and cost-effectiveness.

Acknowledgement

The authors acknowledge the lab support from Veermata Jijabai Technological Institute, Matunga, Mumbai, India.

References

[1] Shreyash Watane, Ishant Dahat: Review study on Pratt and Howe truss, International Research Journal of Modernization in Engineering Technology and Science, e-ISSN: 2582-5208
[2] Bhalla V, et al. Pedestrian behaviour on skywalks: A study of pedestrian counts during peak hours in Cincinnati. J Urban Transit. 1985;12(3):267-78.
[3] Wai K, Wan Y. Morning and evening peak pedestrian flows in Hong Kong's Central Business District: A cordon count analysis. J Urban Stud. 2007;34(6):1001-15.
[4] Dewangan A, Majumdar A. Vibration analysis of different truss types in bridge design. Struct Eng. 2018;95(2):42-55.
[5] Chen S, et al. Innovative composite bridge construction with corrugated steel webs and trusses: An experimental study. J Bridge Eng. 2018;23(8):04018070.
[6] Chattaraj P, Behera SK. Capacity analysis of railway Foot Over Bridges (FOBs) with geometric considerations. J Transp Eng. 2020;146(9):04020081.
[7] Ali M, et al. Performance evaluation of a novel composite pedestrian bridge design using hybrid materials. Struct Mater. 2020;6(4):679-91.
[8] Belevicius R, et al. Mass reduction in radial network arch pedestrian bridges: A parametric approach. J Bridge Struct Eng. 2021;6(1):109-21.
[9] Wen H, Ren Q. Structural design of aluminium alloy truss arch bridges focusing on pedestrian comfort. J Struct Des. 2020;3(2):161-75.
[10] Sharma A, et al. Comparative study of pre-engineered and conventional steel structures in bridge construction. J Civ Eng. 2021;8(3):417-29.
[11] Ali S, Thambiratnam D, Liu X, Fawiza S. Performance evaluation of innovative composite pedestrian bridge. Structures. 2020;26:845-58. https://doi.org/10.1016/j.istruc.2020.06.019
[12] Chaudhari A, Shah J, Arkatkar S, Joshi G, Parida M. Investigating effect of surrounding factors on human behaviour at uncontrolled mid-block crosswalks in Indian cities. Saf Sci. 2018;110(Part A):344-52. https://doi.org/10.1016/j.ssci.2018.11.006
[13] American Association of State Highway and Transportation Officials LRFD Bridge Design Specifications (9th Edition), ISBN: 978-1-56051-738-2, 2020.

Research on Engineering Structures & Materials
www.jresm.org
MIM Research Group

Research Article

Mechanical behavior of silty-clayey lateritic soil stabilized with recycled municipal solid waste ash

Lawrence Zahemen Tuleun [*,1,a], John Wasiu [2,b]

[1]*Department of Civil Engineering, University of Ilorin, Tanke, Kwara State, Nigeria*
[2]*Department of Civil Engineering, Edo State University, Iyamho-Uzairue Edo State, Nigeria*

Article Info

Article History:

Received 03 Mar 2024

Accepted 11 Sep 2024

Keywords:

Unconfined compressive strength;
Recycled municipal solid waste ash;
Compaction;
Stress-strain;
Load-deflection;
Soil stabilization

Abstract

Due to the ever growing need to incorporate ecofriendly and sustainable materials in construction projects, this research study was carried out with the purpose of exploring the feasibility of utilizing recycled municipal solid waste ash (RMSWA) as a sustainable material for stabilizing clayey lateritic soils (LS). The research was aimed at investigating the effect of incorporating varying amounts of RMSWA on the engineering properties of weak soils. Laterite specimens were incorporated with the varying ash contents at intervals of 3%, 6%, 9%, 12% and 15% as replacement levels, and tested for Atterberg limits, compaction and unconfined compressive strength (UCS) behavior. The scanning electron microscopic (SEM) test was conducted to determine the morphology changes in the soil when blended with RMSWA contents at curing ages of 1, 7 and 14 days. Based on the results of UCS test, stress - strain behavior, load - deformation relationships curves were also established and analyzed. Results from the Atterberg limit test revealed that the plastic index, plastic limit, liquid limit ranged between 1.6-11.9%, 20.6-24.5% and 26.1-35.0%. The maximum dry density of the samples increased with the ash inclusion, with the maximum dry density value of 2020Kg/m^3 achieved at 6% ash inclusion, thus making it suitable in laterite stabilization.

1. Introduction

Road infrastructure is an important driver of economic growth by way of facilitation of the movement of goods and services [1]. However, the stability of our roads required to enhance its sustainable performance to a large extent depends on the quality of its surface, base, sub-base and subgrade components. Lateritic soils, renowned for their advantageous engineering characteristics such as a low plasticity index and high California Bearing Ratio (CBR), are frequently employed in road construction projects for sub-base and base layers. These layers are critical in distributing traffic loads from the surface to the underlying sub grade, ensuring the durability and longevity of the road structure. The effectiveness of lateritic soils in these applications is due to their ability to provide adequate support and stability, particularly in regions with tropical climates where these soils are abundant. Interestingly, quality laterites are not always readily available within construction sites, hence leading to haulage of laterites from long distances which in-turn leads to an increase in the overall construction cost and carbon footprint of a project [3]. To address this issue, several researchers have proposed various techniques to improve the engineering characteristics of weak lateritic soils. Caro et al. [4] and Teerawattanasuk et al. [5] recommended the use of cement to improve granular soils and this has been embraced by various countries around the world.

*Correspondingauthor: 16-68ge015pg@students.unilorin.edu.ng
[a]orcid.org/0009-0007-1848-0128; [b]orcid.org/0000-0002-3760-3230
DOI: http://dx.doi.org/10.17515/resm2024.204me0303rs

Texas Department of Transport and Thailand Department of Highways recommends a minimum unconfined compressive strength (UCS) of 1.2 MPa and 689 KPa for cement-Lateritic sub-base [6, 7]. Wahab et al. [8] studied the effect of cement inclusion on the unconfined compressive strength (UCS) of laterite. Prior to testing for UCS, they subjected the lateritic specimens to four cement doses (3%, 6%, 9%, and 12%) at a curing period of 7 days. They recorded the maximum value at 6% which was greater than 0.8 MPa, thus meeting the Malaysian standard specification. Mengue et al. [9] varied the cement content in laterite at an interval of 3% and discovered that lateritic soil containing 6 and 9 % of cement met the UCS conditions. Ahmed et al. [10] accessed the efficiency and durability of using cement and shredded pet bottles in soil stabilization. Prior to examination, the sample preparation entailed mixing different proportions of two grades of shredded PET, each displaying diverse shapes, and demonstrated properties resembling fibers. Subsequently, their compacted samples underwent CBR testing to determine the optimum PET content. Based on their findings, it was discovered that both combinations led to better durability when exposed to freeze and thaw, and a reduced brittleness compared to only cement. Soils reinforced with only shredded pets at varying percentage resulted in an improvement in CBR values from 28.5 to 90.7% in comparison to plain soil. Onyekwena et al. [11] recommended that 5% of GGBS or Biochar be added to MgO to reduce carbonation entry rate and improve ductility of the soil. Wang et al. [12] documented an optimal cement to metakaolin mix ratio of 5:1 for optimal strength performance in fine sandy soils provided the specimen is cured for a period of 28 days. They also recorded a linear decrease in strength with an increase in water binder ratio, and a linear rise with curing ages.

However, Kulanthaivel et al. [13] adopted the used of cement mixed with sodium silicate and sodium hydroxide admixtures in accessing the behavior of clayey soils. The experimental variables adopted in their studies included the type of admixtures, the proportion of admixtures, the binder material, and the curing time. And the output of their investigation revealed that an optimum unconfined compressive strength and modulus of elasticity of 215.22KPa and 8.353 MPa was attained when the dosage of 10% OPC + 4% SS + 8 molarity of SH was used. Jose et al. [14] investigated the strength and microstructure of clayey soils stabilized with natural limestone. Before the testing, they substituted the clayey soil specimens with natural lime at intervals of 3%, 6% and 9% replacement levels, with that 0% acting as the reference mix. Based on their findings, an improvement in UCS when6% natural limestone powder waste was used as a stabilizing agent. Wibowo et al. [15] worked on examining the soil bearing capacity of soils when incorporated with the blend of rice husk ash and cement. Results from their investigation displayed better outcome for the blends in comparison with the un-stabilized soils.

However, in spite of research strides being recorded, the major issue of cement usage as soils stabilizer relates to its manufacturing process as high amount of greenhouse gases are emitted into the atmosphere during it production process, thus further thinning the Ozone layer. According to Worrell et al. [16], for every 1 tons of cement produced, 222Kg of CO_2 is emitted into the atmosphere. Other pressing serious problems associated with the use of cement include environmental degradation, natural resource depletion, and air pollution [17, 18].

Secondly, the challenge of the astronomical surge in population globally in relation to the amount of municipal solid waste being disposed cannot be underemphasized. The global waste generated annually was estimated at 2.01 billion tones as of 2018 and was expected to rise to around 3.40 billion by 2050 [19]. Due to the aforementioned, there is an ever-growing need by various countries to continually come up with more sustainable and economical way of managing and recycling waste disposal. Various researchers have keyed into this project by researching and developing mix designs incorporating the waste as additives in construction. Liang et al. [20] investigated the effect of pre-treated municipal waste ash on cement-stabilized soils. The outcome of their investigations revealed an improvement in UCS, cohesion and internal angle of fiction of cement when incorporated with 10% waste as repl. for 5% cement. However, no research was carried out to understand the Stress-strain and load-deformation behaviors of the unstable soils when incorporated with the additives. Amiri et al. [21] investigated the possibility of stabilizing Aeolian sand using municipal solid waste. They investigated the varying MSWA on the unconfined compressive, ph and scanning electron microscopy test of the unstable aeolian sand. Results from their findings revealed a maximum UCS of 5.2 attained after 90 days. The concluded MSWA can

potentially be used in pavement construction works. However, the scope of their research did not include investigating the consistency and setting time (initial and final) performance of weak soils. Similar research was carried out by Yahia et al. [22] on dune stabilization using MSWA. They however conducted compaction, unconfined compression, shear box and hydraulic conductivity performance tests to evaluate the engineering characteristics of the dune sand when replaced with MSWA at a replacement interval of 10% up to 80%. The outcome show that the maximum dry density remained relatively constant up to 30% ash inclusion. Beyond 30%, a drop in maximum density was noticed with ash content. In the case of optimum water content, it increases with the addition of ash content. That of the unconfined compressive strength and the cohesion slightly increased with curing time up to 90 days. However, their investigation excluded studying the effect of this ash inclusion on the consistency, setting time, stress-strain and load-deformation of the soils.

Owing to the fact that most research conducted by researchers focused on the use of cement with various binders, this research will be solely focus on the study of the mechanical performance of lateritic soils incorporated with municipal solid waste ash (MSWA) as additives, with much emphases on addressing the issue of overdependence on the use of non-ecofriendly cement materials in construction works and proffering a smart and sustainable waste recycling approach.

2. Materials and Method

The reddish-brown laterite was obtained from a borrowed pit at Ikpayongu, along Makurdi - Otukpo road, in Nigeria. The collected laterite was dried in an oven at a temperature of 50^0c for 24 hours and afterwards sieved through a 4.75 mm sieve size conforming to ASTM 98 D422-63[23]. The standard entails collecting soil sample and subjecting it to oven drying to remove moisture. The dried soil sample is then sieved through a set of progressively smaller sieves, with the smallest size being 4.75 mm. After sieving, the retained soil on each sieve is weighed to determine the mass of particles retained at each size fraction. Using this data, the percentage of soil retained on each sieve is calculated, and a particle size distribution curve produced as displayed in Figure 1.The results of the preliminary test conducted on the laterite samples are presented in Table 1 while the particle size distribution (PSD) curve for the laterite is shown in Figure 1.The laterite had a dry density of 1930Kg/m^3 and fell within the range of 1500-2000 Kg/m^3 requirement for the construction of stabilized soil bricks. The specific gravity (S.G) of the soil determined as 2.69 fell within the typical range for lateritic soils [24, 25]. The presence of iron oxide concentration in the coarse fraction of soil can be linked to the high S.G of the laterite soil. The PSD of laterite can also be classified as a fine grain soil since more than 50% of the laterite scaled through the 200mm sieve size as required in both the Unified Soil Classification (USCS) and American Association of State Highway and Transport Officials (AASHTO) classification manual. The plastic index of the laterite was 14.4%, thus falling within 20% benchmark for manual compaction. The LL below 50% falls within the low plasticity range [26]. Values of the LL plotted vertically and PI on the horizontal falls below the A line on the plasticity chart, thus falling within the category of Silty clayey soil. Hence, the lateritic material was classified as a low plasticity silt USCE, and as A-5 in accordance to AASHTO. Based on the classification, the materials is rated poorly as a sub-base material. The chemical composition of un-stabilized laterite (LS) and MSWA are presented in Table 2.

Table 1. Physical properties of un-stabilized lateritic soil

Property	Value
Optimum moisture content (%)	12.2
Maximum dry density (Kg/m3)	1930
Atterberg limits	
Liquid limit (%)	35
Plastic limit (%)	20.6
Plastic index (%)	14.4
Plastic shrinkage (%)	14.3
Soil Classification	Silty clayey sandy gravel
Specific gravity	2.69

Particle size distribution (ASTM)	
Gravel (100 -64 mm) (%)	65
Sand (63-17mm) (%)	24
Silt (17-9 mm) (%)	7
Clay (less than 9 mm) (%)	5
Physical properties	
Natural moisture content (%)	7.10
Color	Reddish brown

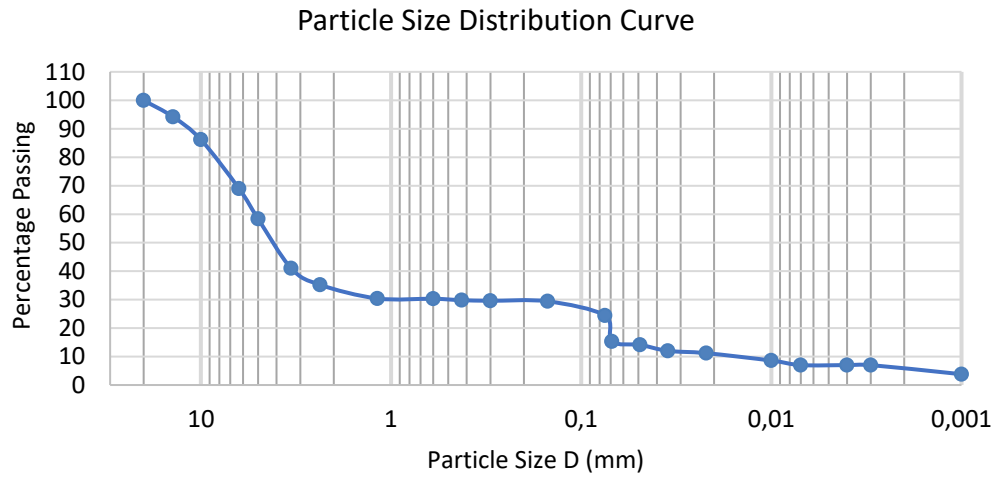

Fig. 1. Particle size distribution of un-stabilized lateritic soil

Table 2. Chemical Composition of LS and MSWA

Chemical composition (%)	LS	MSWA	MSWA [27] China	MSWA [28] France	MSWA [29] Portugal	MSWA [30] Italy
SiO_2	62.5	31.4	55.2	49.3	43.75	37.78
Al_20_3	27.8	9.6	9.6	7.5	6.81	11.88
Fe_2O_3	11.4	9.6	5.7	7.6	2.03	8.01
CaO	3.3	25.0	15.9	16.3	22.77	23.29
SO_3	-	19.3	0.9	0.4	6.34	-
K_2O	-	3.7	1.7	1.1	3.12	1.63
LOI	4.1	3.2	-	-	-	-

The MSWA collected from a government dump site in Makurdi, Nigeria had a specific gravity of 2.69. The result of chemical composition carried out using X-Ray fluorescence spectrometry in the chemical Engineering Department, Ahmadu Bello University Zaria, Nigeria is presented in Table 2. The summation of SO_2, Al_2O_3 and Fe_2O_3 equaled 50.6% and CaO was documented to be 25%, thus falling within pozzolanic class C in accordance to ASTM C618-19 [31].

2.1. Sample Preparation and Testing

Prior to the mixing process, the samples of LS and MSWA were oven dried at a temperature of 50°C for 24 hours and sieved through a 75um sieve size to achieve uniformity in sizes. Before testing, Aspresented in Table 3, LS samples were substituted with MSWA at an interval of 3%, 6%, 9%, 12% and 15%, with 0% used as the control. Afterwards, the dry soils samples were mixed with water at various quantities. The fresh mix was placed in cylindrical molds (50 mm in diameter and 100 mm in height) in five layers and compacted with 25 blows each by a rammer of mass 4.5 kg dropped from a height of 450 mm. Afterwards, measure the height of the compacted soil specimen. Then,

repeat the compaction process using different moisture contents, gradually adding water to achieve the desired moisture content range. Next, determine the wet density of each compacted specimen by weighing it. Subsequently, dry each compacted specimen in an oven and ascertain its dry density. Finally, plot a graph with moisture content on the x-axis and dry density on the y-axis, with the moisture content corresponding to the peak of the dry density curve representing the optimum moisture content (OMC). For the compaction test which conformed to ASTM D1557-02 [32], it was carried out using standard proctor machine to obtain the optimum moisture content and maximum dry density. Compaction test is a process whereby the soil particles are mechanically compressed under controlled temperature conditions into a denser structure with the aim of reducing the voids present. The result of such carefully conducted experiment results in a soil of high strength and deformation resistance.

For the consistency limit test (plastic limit, liquid limit, linear shrinkage and plasticity index test), it was conducted in accordance with (ASTM D4318-00) [33], part 5; this test gave an indication of the expansive behavior of LS when embedded with MSWA. Plastic index is used to classify soils and estimate strength of sub grad soils. Soil displaying high values of plasticity index translates to high expensiveness. For liquid limit, results values exceeding 50% signifies a higher proportion of clay or silt, whereas a low plasticity index indicates a granular soil with little or no cohesion.

Table 3. The details of conducted experiments

S/N	Parameters determined	No. of experiments conducted	Test specification	Reason for determination
1	Specific gravity	2	ASTM D854-02	Preliminary analysis and soil classification
2	Liquid Limit (LL)	6	ASTM D 4318-00	Soil classification and determining the suitability of the soil for road construction
3	Plastic Limit (PL)	6		
4	Plastic Shrinkage (PS)	6		
5	Plastic Index (PI)	6		
6	Particle size distribution (PSD)	1	ASTM 98 D422-63	Preliminary testing, Grading and soil classification
6	Compaction	6	ASTM D1557-02	Suitability of soil as road materials
7	Unconfined compressive strength (UCS)	6	ASTM 2000 D2166	Determine the strength of soil and suitability a construction material
	Total number of experiments		33	

For the Unconfined Compressive Strength (UCS), the test was carried out in accordance to ASTM D2487-17 [34]. The standard proctor was made use of in compacting the samples, and the results of compressive stress at a point when the curve normal stress vs the axial strain reaches a peak value was recorded. The outcome also displayed deformation values at various loadings.

A brief summary of the total number of experiments, standard methods adopted and reasons for conducting the experiment are also presented in Table 3. The results of the UCS that gives the maximum strength value when the soil is blended with ash was analyzed in comparison with un-stabilized laterite soil using scanning electron microscope (SEM). This test was carried out in chemical Engineering Laboratory, Ahmadu Bello University, Zaria with the aim of qualitatively studying the microstructural development in the soil matrix at various curing ages.

Table 3. The details of conducted experiments

S/N	Parameters determined	No. of experiments conducted	Test specification	Reason for determination
1	Specific gravity	2	ASTM D854-02	Preliminary analysis and soil classification
2	Liquid Limit (LL)	6	ASTM D 4318-00	Soil classification and determining the suitability of the soil for road construction
3	Plastic Limit (PL)	6		
4	Plastic Shrinkage (PS)	6		
5	Plastic Index (PI)	6		
6	Particle size distribution (PSD)	1	ASTM 98 D422-63	Preliminary testing, Grading and soil classification
6	Compaction	6	ASTM D1557-02	Suitability of soil as road materials
7	Unconfined compressive strength (UCS)	6	ASTM 2000 D2166	Determine the strength of soil and suitability a construction material
	Total number of experiments		33	

3. Results and Discussion

3.1. Atterberg Limit

Figure 2 shows the plastic limit, liquid limit, Plastic index and linear shrinkage behavior of silty-clayey lateritic soils with the inclusion of MSWA contents at varying percentages. For the liquid limit (LL), Plastic index (PI) and linear shrinkage (PS), a decrease was recorded with increase in the ash content. The least results of LL (26.1%), PI (1.6%) and PS (7.8%) were documented at 15% MSWA addition.

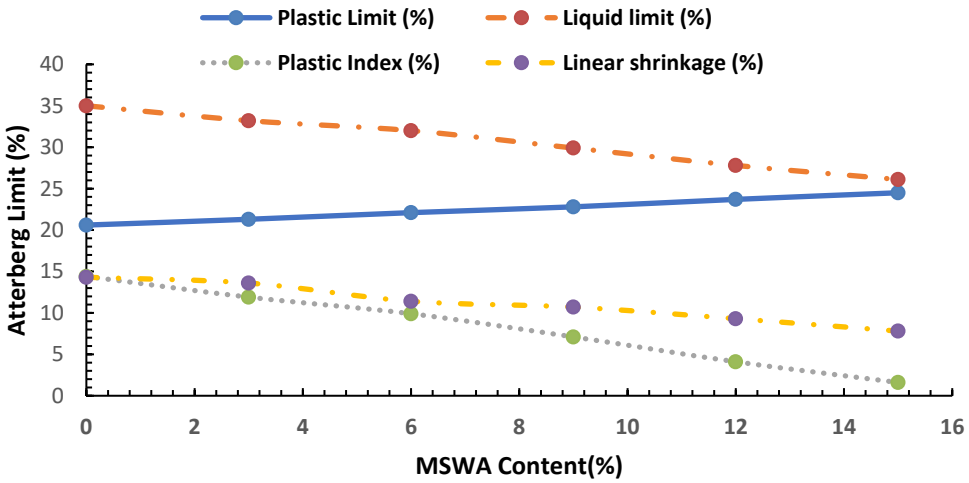

Fig. 2. Atterbergs limits of stabilized soil

The reason for the decline may be attributed to the water absorption and swelling potential of MSWA materials. This outcome suggests that the addition of MSWA at this higher percentage had a significant effect on reducing the plasticity characteristics of the soil. When MSWA was added to soil, it may have altered soil's properties due to the particle size distribution, chemical composition,

and pore structure modification in soil matrix. In this case, at 15% MSWA addition, it's likely that the MSWA particles filled the voids in the soil matrix, reducing the available space for water retention and limiting the soil's ability to exhibit plastic behavior. Additionally, the chemical properties of MSWA, such as its alkalinity, could have contributed to the reduction in plasticity. These chemical reactions may have influenced the soil's mineralogy or its interaction with water, resulting in a decrease in the liquid limit, plasticity index, and plasticity slope. The results of the LL were in agreement with the research carried out by Amadi [35], where a reduction of approximately 70% was documented; However, they worked on stabilization of laterite soils using fly ash. Beetham et al. [36] also attributed the reduction to the reactiveness of the charge-balancing cations in the soil, amid other factor that control the impact of diffused double layers (DDL). The results also conformed to the report made by Kayode and Osemwengie [37]. Contrarily, Report by Ozdemir, [38] revealed an increase in LL of FA- treated soils under temperate conditions but had similar pattern behavior with the results of PL obtained in this research. The LL results for all percentages of MSWA-laterites also fell within the Federal Ministry of Works and housing [39] specification (LL≤35%) for a given soil to be used as a sub-base material in construction.

The pattern of development of the LL results was nonsynonymous with that of the PL, as addition of ash content in the mix led to a continuous increase in the percentage of PL. There was marginal increase of about 1% in the PL when the soil was varied with MSWA at intervals of 3%, with the highest increase of 24.5% recorded at 15%MSWA-L; this was higher than that of the plain sand by 4%. The observed trend tallied with findings recorded by Varaprasad et al [40]; they however attributed their reduction to the cationic exchange that takes place between the Ca, Al, Si in MSWIA and clayey ions in the soil. The observed trends was also in tandem with findings discovered by Okunade [41] and Amade [35]. However, Asunn et al. [42] reported contradicting outcomes in terms of plastic limit behavior when laterite was incorporated with RHA and carbide.

Osman et al. [43] also observed similar patterns when lateritic soils were substituted with groundnut husk ash (0-10%); a drop in Plastic Index from 17.2% to 16.48% was reported in their case. The outcome of the plastic index test was also similar to the outcome reported by Kayode and Osemwengie [37]; they however worked on lateritic soil stabilization using rubber wood ash. As shown in Figure 1, The LL and PI of the stabilized laterite specimens were plotted on the plasticity chart. It was observed that the plasticity of soils continuously dropped below the 50% maximum benchmark indicating lower silt content. According to Das [44], the changes in plasticity behavior with ash inclusion arises from the changes in the thickness of the diffuse double layer of fine content of the laterite. Other reports by Ayodele and Agbede [45], Gidigasu [46] linked soil performance to the reaction that takes place between the Iron and Aluminum oxides in the laterite, clay components and Silica in the ash contents producing cementitious products, thus reducing LL and plasticity of the soil. The result of PI for Soils stabilized with 3-15% MSWA had results ranging from 1.6 – 11.9%, thus falling within the specification (P1≤12) set by Federal Ministry of Work and Housing [39] for a sub- base material. Before incorporating the blends, The PI of the un-stabilized was above the benchmark requirement by 2.4%, clearly showing that the material was not suitable as a sub–base material for construction. With the incorporation of ash, a decline in P1 was noted, with values of 2.49, 4.65, 8.70, 11.52, 13.21, and 14.98 observed at replacement levels of 3%, 6%, 9%, 12%, and 15%. Hence, the inclusion of Municipal Solid Waste Ash (MSWA) significantly reduces the Plastic Index (PI) of soil. This decrease is attributed to MSWA's ability to fill voids between soil particles, its finer particle size, and its chemical interactions with soil, forming cementitious products that reduce plasticity. As MSWA content increases, the soil becomes less plastic and more stable, enhancing its suitability for construction as a sub-base material. While this reduction improves stability, it may also decrease workability. The observed reduction in PI with MSWA aligns with trends seen in other stabilizers, indicating its effectiveness in modifying soil properties.

3.2. Compaction

The results of dry density vs. moisture content for the various percentages of MSWA are shown in Figure 3. For all the samples, the dry density of MSWA increased steadily with water inclusion until it attained peak values, beyond which a decline was observed. However, the addition of 6% MSWA

produced the highest MDD value of 2020Kg/m³ and beyond 12.2% moisture content, a drop in MDD value was noticed; the result of MDD was higher than that plain laterite by 4.7%. The peak values recorded for 3%, 9%, 12% and 15% MSWA were 1990Kg/m³, 1920Kg/m³, 1870Kg/m³ and 1720Kg/m³ at moisture contents of 11.8%, 15.3%, 18.1% and 18.3% respectively. The MDD also ranged between 1720 Kg/m³ and 2020Kg/m³ within the varying MSWA content of 0% and 15%. The pattern of DD development coincided with findings made by Alizera et al. [47].

Figure 4 shows that the Maximum Dry Density (MDD) of stabilized laterite increases with the addition of Municipal Solid Waste Ash (MSWA) up to a certain point. The peak MDD of 2020 kg/m^3 was achieved at 6% MSWA. This initial increase is due to the fine filler effect of MSWA, which effectively fills voids in the soil matrix, allowing for better compaction and increased density. The presence of MSWA particles likely improves the soil's compaction characteristics by enhancing the soil's ability to pack closely. However, beyond 6% MSWA, the MDD begins to decline. This decrease is attributed to the increased water absorption capacity of MSWA. As MSWA content increases, it absorbs more water, which raises the optimum moisture content (OMC) required for compaction. The additional water results in a less efficient compaction process and a subsequent reduction in MDD. This trend is evident in Figure 5, where the polynomial correlation coefficient of 0.5746 indicates a strong negative correlation between MDD and MSWA content.

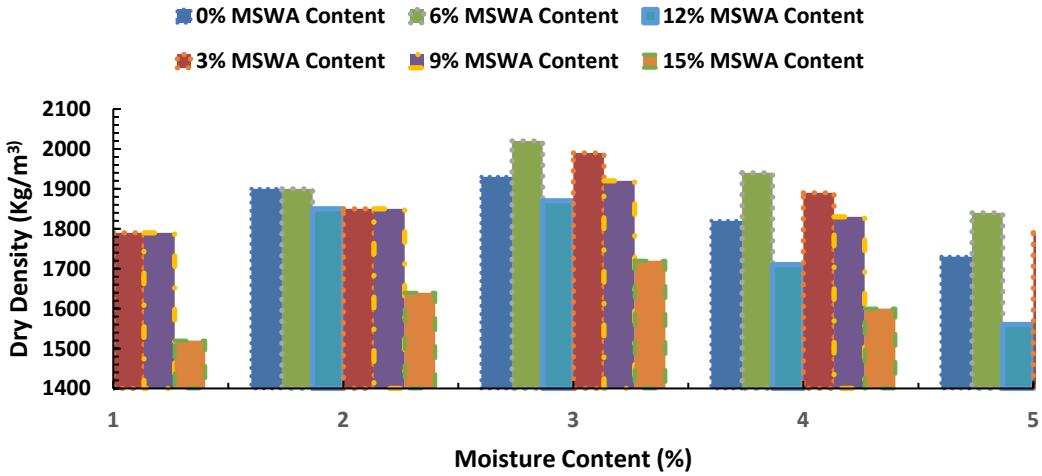

Fig. 3. Dry density vs moisture content at varying MSWA content

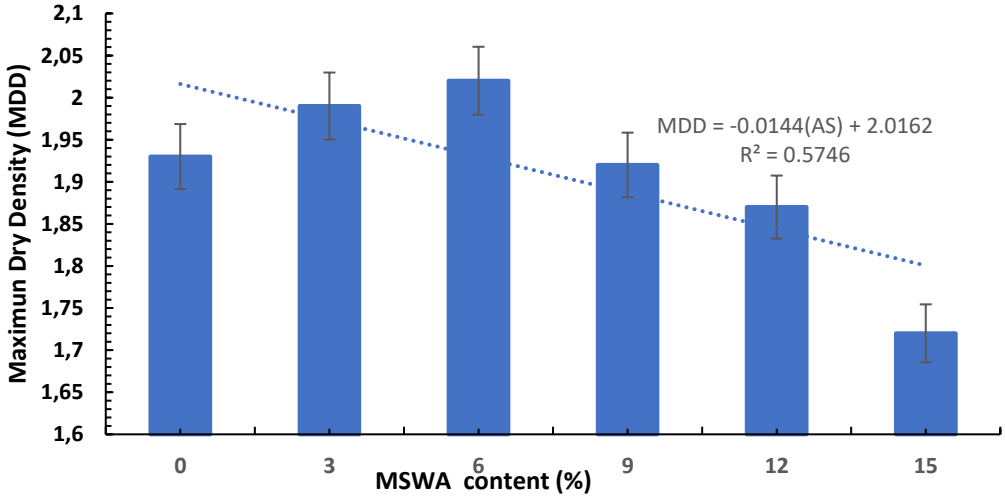

Fig. 4. MDD vs varying percentages of MSWA

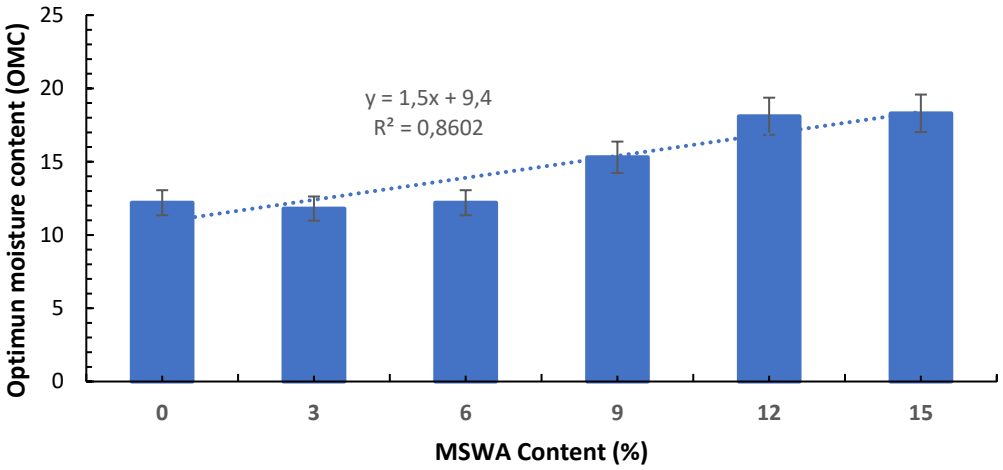

Fig. 5. OMC vs varying percentages of MSWA

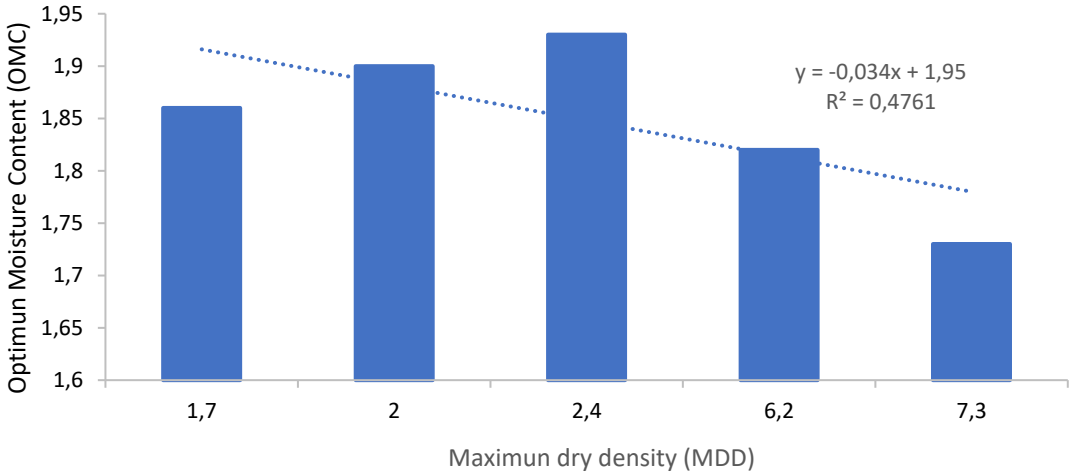

Fig. 6. Relation between the OMC and MDD

The decrease in MDD from 9% to 15% MSWA reflects a point where the soil's capacity to achieve high density is compromised by the higher water content needed for effective compaction. This result aligns with findings from similar studies (e.g., Trivedi et al. [48], Okunade [41]), which observed that beyond a certain threshold, the benefits of MSWA on MDD are outweighed by the drawbacks of increased moisture absorption. Thus, while a moderate addition of MSWA improves MDD, excessive amounts lead to higher moisture content and a decrease in density.

Figure 5 displays the OMC versus the different proportions of MSWA content. It imperative to note that the maximum dry density is dependent on the MSWA. The higher the MSWA ash in laterite, the higher will be the moisture content required achieving maximum density. This is due to the specific surface area of MSWA. The pattern of development showed a slight decline in OMC by 0.4% at 3% and rose steadily up to 15%, with a resultant OMC value of 18.3% attained; this constituted about 50% increase from the initial value. The increase was contrary to results recorded by others [45, 49]. The increase in water content can be related to the role it plays in enhancing cementitious reaction as well releasing the capillary tension from the exposed surface of fine particles [50].The Polynomial correlation coefficient of 0.8606 also gives an indication of s strong relation that exist between optimum moisture content and MSWA.

Figure 6 displays the optimum moisture content verses the maximum dry density of MSWA lateritic soils. From the bar chart, it can be deduced that the optimum moisture content increased steadily with change in the maximum dry density, with the peak maximum value of 1930Kg/m^3 attained at

an optimum moisture content of 2.4%. It then declined with the least MDD and OMC value of 1700 Kg/m^3 and 7.3% recorded. The r^2 value extrapolated was 0.4761.

3.3. Unconfined Compressive Strength

Figure 7 shows the behavior of UCS of laterite soils incorporated with MSWA at varying percentages and cured at various ages. The laterite samples cured at both 7 and 14th day displayed similar behavioral patterns, as both samples experienced a dip at 3% with correponding UCS values of 207.29 KN/m^2 and 216.11KN/m^2.

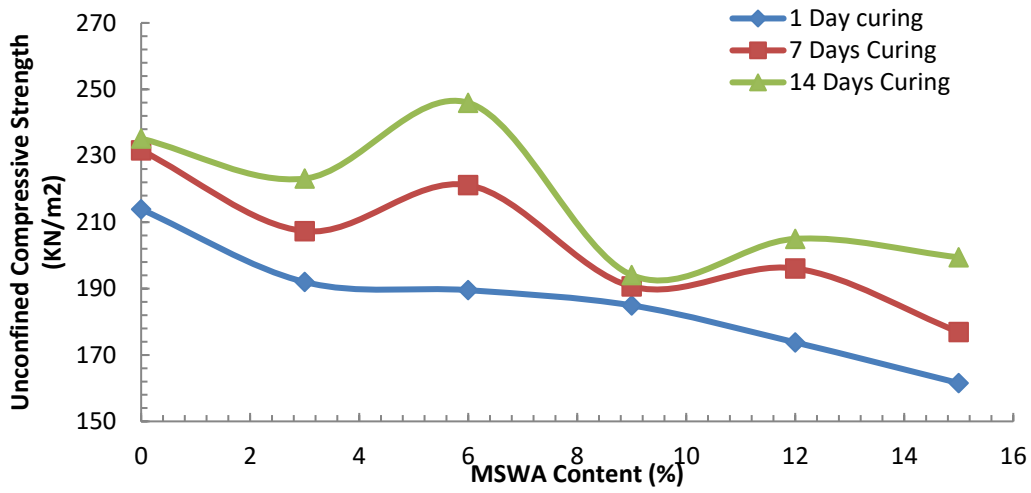

Fig. 7. UCS of Lateritc soils varied with MSWA

At 6% addition, a maximun UCS of 231.62 and 235.16 was documented for both samples cured at 7 and 14 days. Beyound 6%, a gradual drop in UCS was reported with the lowest point reached at 15%. From Figure 1, it is evident that the inclusion of MSWA in the soil improved the UCS strength by 40% and 80% at the 7th and 14th day curing. This is due to the pozolanic reaction that takes place between the MSWA and clayey component of the soil, as cations interacts between the negatively charge clay and silica ions contained in ash resulting in an improvement in strength. This observation is similar to the results obtained by Dulaimi et al. [51]. According to Indraratna and Nutalaya [12], they also echoed that Iron oxide plays a significant role in the agglomeration process of soils particle resulting in a stronger soil matrix. In addition to the pozzolanic reaction, the improvement in density can also be due to the MSWA filling the voids in the soil [52].

3.4. Load- Deformation Behavior

Figure 8-10 shows the load deformation of (0-15%) MSWA-L specimens when subjected to a curing period of 1 day.An increase in the load led to an increase in the deformation rate for boththe ustabilized and 6%MSWA laterite. For the control, a peak load of 192KN corresponded to a deformation of 240mm. While at 6%, the maximun load of 171KN resulted in a deformation of 280mm. The maximun load required to cause deformation was less than the plain Lateritic sample by 10.94%. As for 3% MSWA-L specimens, the load-deformation steadiliy rose to its peak load value of 175KN and deformation of 360mm, slightly above the the load of 171KN recorded for the 6%MSWA-L specimens; however, the difference in deformation between the 3%MSWA-L and 6%MSWA-L specimens was presicely 80mm. That of 9%MSWA-L specimen linearly rose with its maximun load of 166KN attained at a deformation level of 240mm respectively.

The load deformation behavioral pattern of 0%MSWA-L was similar to that at the 7th day curing. However, higher maximun loads and deformation results of 209KN and 280mm were recorded, which gave an indication that curing tends to improve the strength properties of the soils specimen. Preceding the 0%MSWA-L, that of 6% had a peak load and deformation of 202KN and 360mm respectively, with 15%MSWA-L specimens performing the least with a peak load of 145KN and deformation of 240mm.

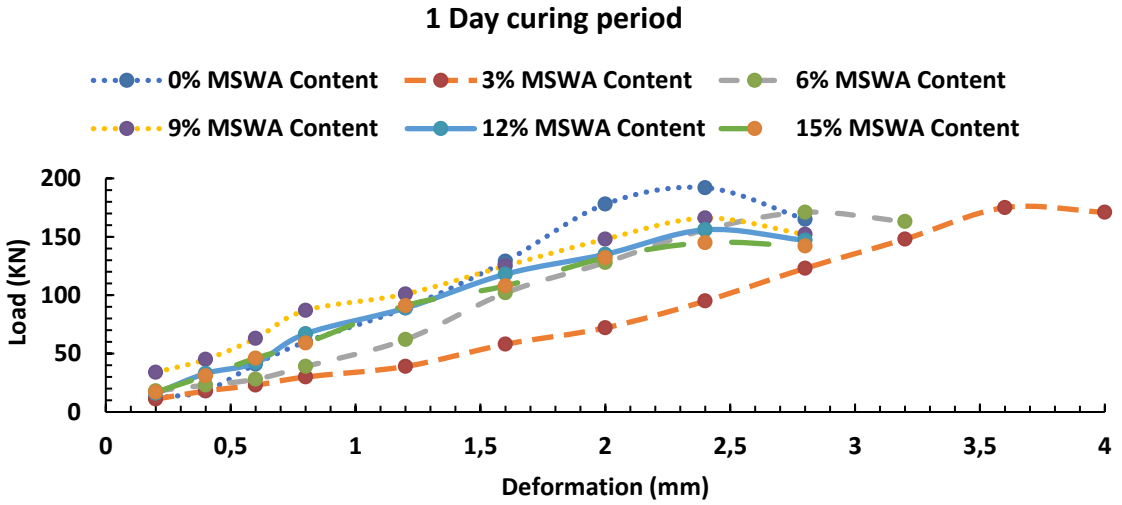

Fig. 8. Load – deformation of stabilizd soils at 1 day curing

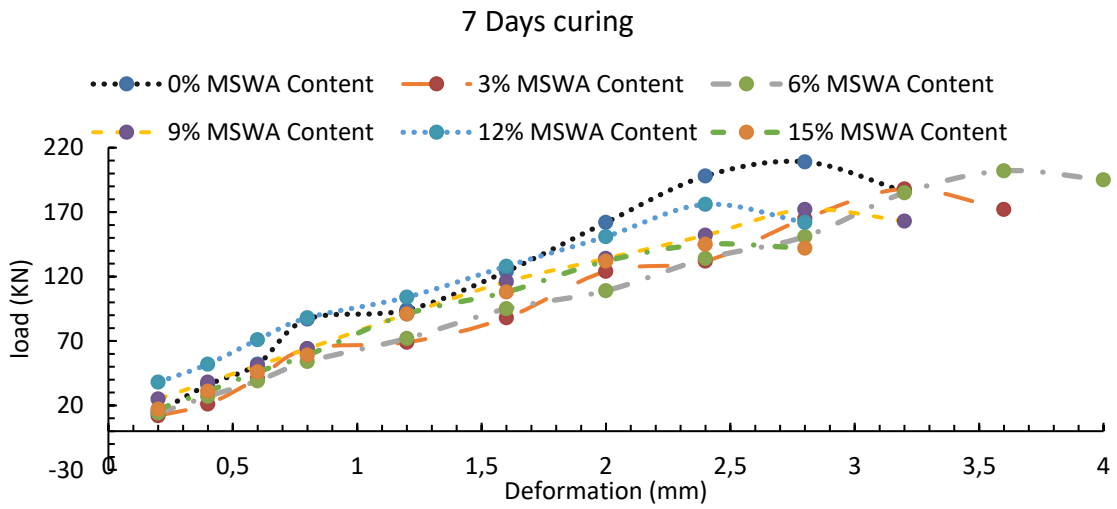

Fig. 9. Load – deformation of stabilizd soils at 7 days curing

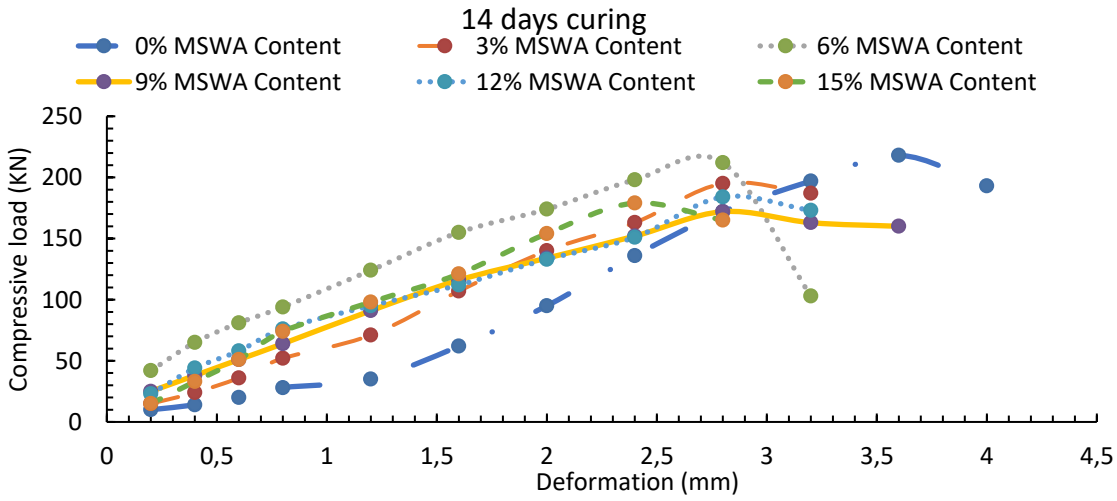

Fig. 10. Load – deformation of stabilizd soils at 14 days curing

At the 14th day curing, as shown Figure 10, That of 9% and 12%MSWA-L experienced similar rise in the load-formation; however, at their peak, 9% and 12% MSWA-L specimens had slighlty peak loads values of 176kN and deformation of 320mm, and 156kN and 240 mm respectively. The maximun load and deformation of 212kN and 280mm was documented when laterite was substituted for 6% MSWA with the least values observed at 15%MSWA-L.

3.5. Stress - Strain Behavior

Figure 11-16 shows the stress and strain curve obtained from the outcome of UCS test. This test depicts the behavior of the different mix proportions of the lateritic soils with additives under varying curing time intervals. In tandem with a typical stress strain response behavior, the stress was found to have risen proportionally with the increasing strain until a peak value was reached. Beyond that, a drop in stress was noticed with further increase in strain for all the samples. The zero un-soaked MSWA- L when cured at 1, 7 and 14days age had a resultant maximum stiffness of 213.88, 231.62 and 235.16 KPa, indicating a percentage rise of 8.29% and 1.53%; this rising patterns with curing age was consistent across board. As shown in Figure 6, at 6% inclusion, the MSWA-L samples exhibited the highest stress-strain value of 238.67 kPa for all the samples cured at the 14th day, which was greater than the control by 3.51%. The maximum stiffness recorded for Laterite included with 3% MSWA was 191.98kPa at the 1st day, 207.29kPa at the 7th day and 216kPa at 14 days. The result at the 14th day fell short of the un-stabilized laterite by 8.15%. This perhaps can be linked to the low pozzolanic activity potential of the ash at this stage. The same kind of patterns was also evidenced by Liuet al. [53] as well as Singh and Kumar [54] in their studies. However, Singh and Kumar adopted a binary mix of cement and MSWA as a soil stabilization agent; they concluded that cement inclusion was the key ingredient responsible for rise in stress, cohesion and internal friction between the soil's particles. For Laterite specimens containing 6% additive at the 14th day curing and 9% additive at the 1st day, they attained a sharp peak in the stress-strain curve and immediate after reaching the maximum deviatoric stress, there was a sharp decline in stress with increase in strain. Gosh and Subbarao [55], attributes this mode of failure to the distinct failure plains that is produced which is usually dependent on ash content inclusion, as an increase in the content led to a decrease in the inclination of failure planes along the vertical lines of the specimen. On the other hand, for the control specimens, and specimens embedded with 3, 12 and 15% MSWA, beyond their peak values on all fronts, there was a slow drop in stress with increase in strain; in this case, the bulging of the specimen without the presence of distinct failure plans was observed [55]; this can be due to the insignificant amount of pozzolanic reaction between CaO present in the ash and lime contained in soil, thus slowing down the microstructural formation of binding crystals in the soil matrix [55, 56].

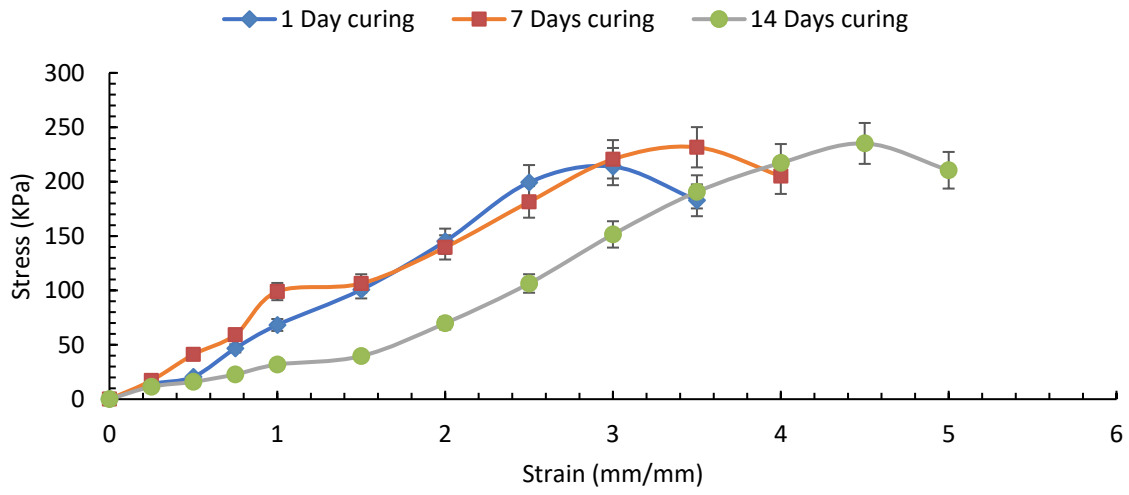

Fig. 11. Stress-strain curve of un-stabilized soil

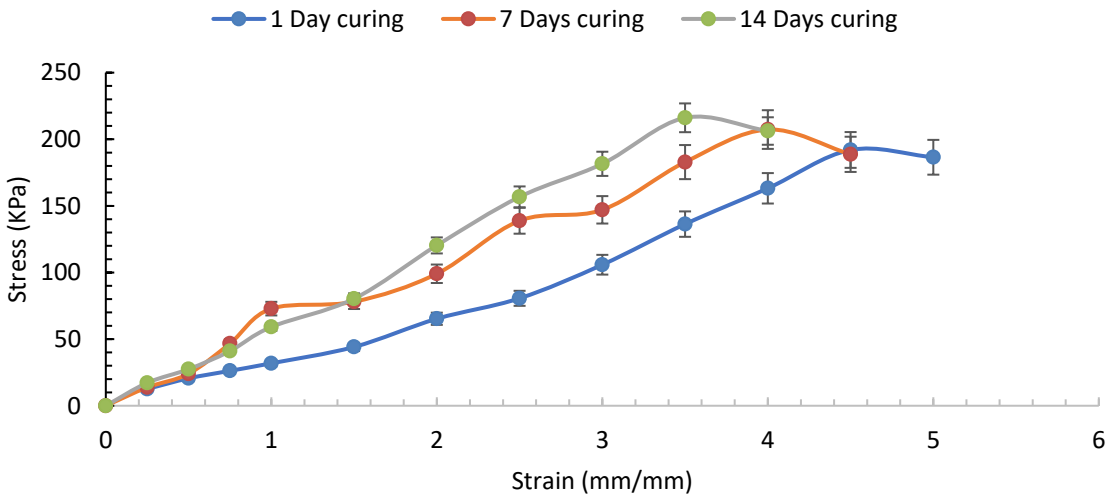

Fig. 12. Stress-strain curve of 3%MSWA-stabilized soil

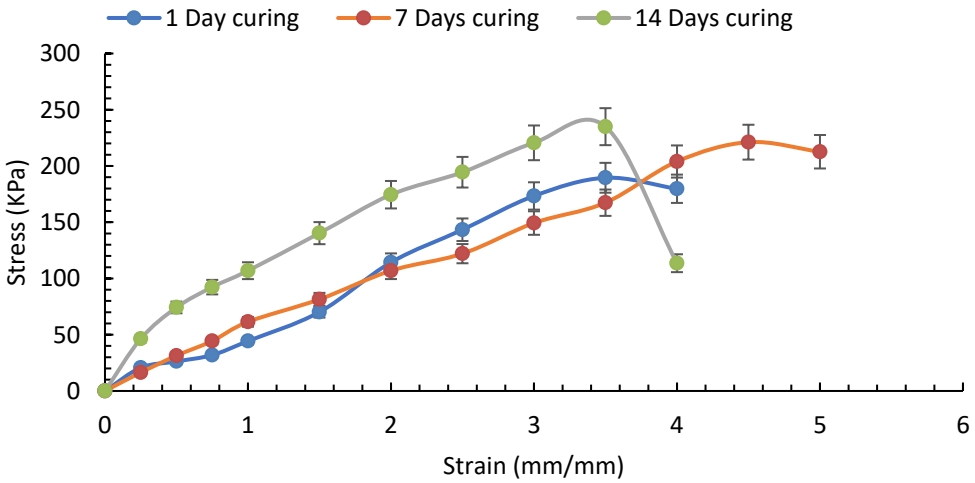

Fig. 13. Stress-strain curve of 6%MSWA-stabilized soil

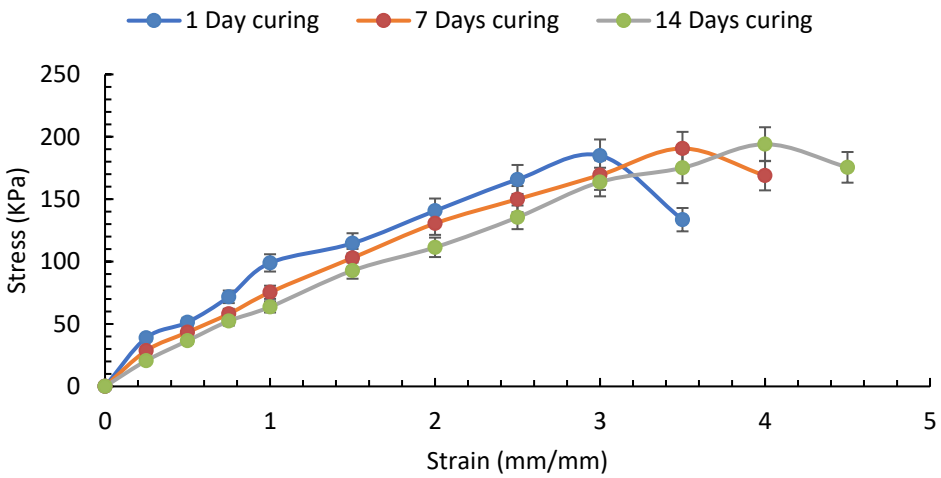

Fig. 14. Stress-strain curve of 9%MSWA-stabilized soil

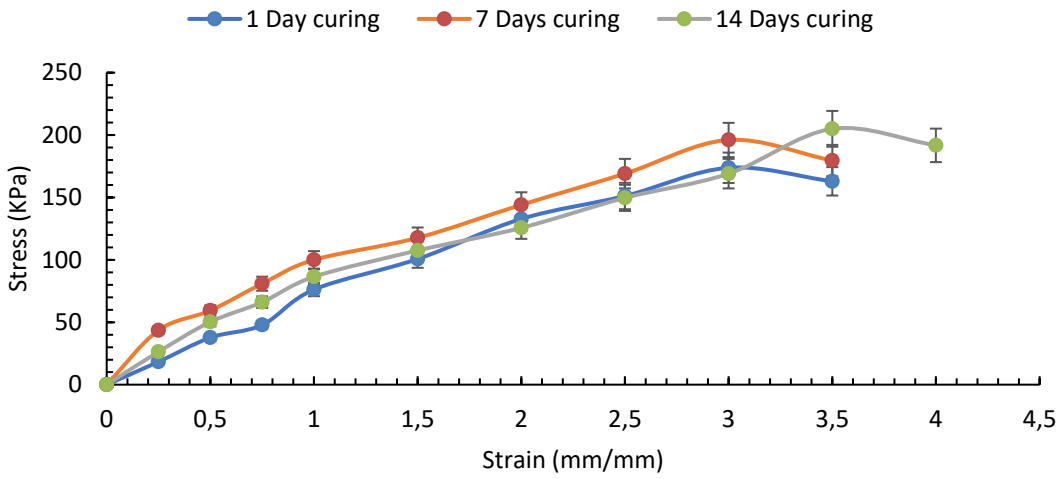

Fig. 15. Stress-strain curve of 12%MSWA-stabilized soil

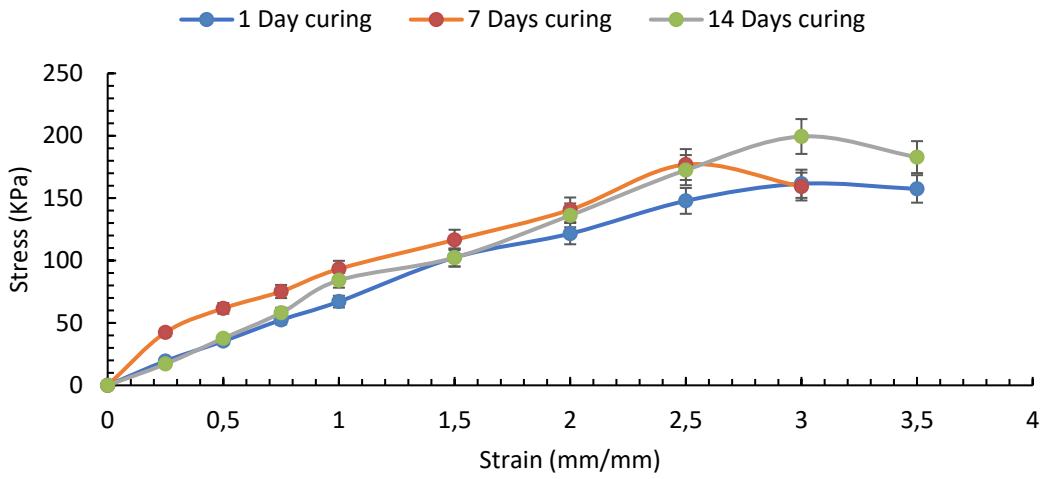

Fig. 16. Stress-strain curve of 15%MSWA-stabilized soil

3.6. Scanning Electron Microscope (SEM)

The results of SEM analysis of the soil blended with 6% RMSWA cured at 1, 7 and 14 days are displayed in Figure 17-19. The reason for the selection of the 6%MSWA as the reference point for the intrinsic analysis was because the maximum UCS was attained using this blend, thus the need to further understand its behavior.

At the 1st day of curing, voids were noticeably observed with whitish substances suspected to be lime. However, as the samples was cured up to the 7th day, a reduction in void spaces was observed; and this may have been due to the initial phase of reaction between the lime and the silica in the ash resulting in the formation of calcium silicatehydrate in the soil mix. At the 14th day curing period, the densification of matrix further increased with the formation of new thin coatings noticed on the surface, which was not present at the 7th. Based on analysis, an increase in microstructural morphology of mix led to increase in the UCS, as also validated by Jafer et al. [57]; Vichan et al. [58]; Katz et al. [59].

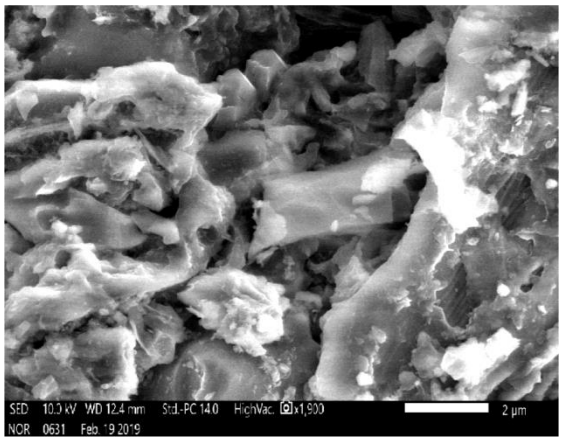

Fig. 17. SEM analysis of 6%RMSWA-L soils at the 1st day curing

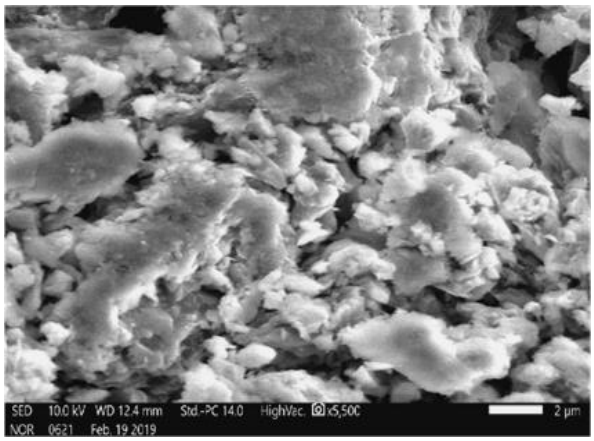

Fig. 18. SEM analysis of 6%RMSWA-L soils at the 7st day curing

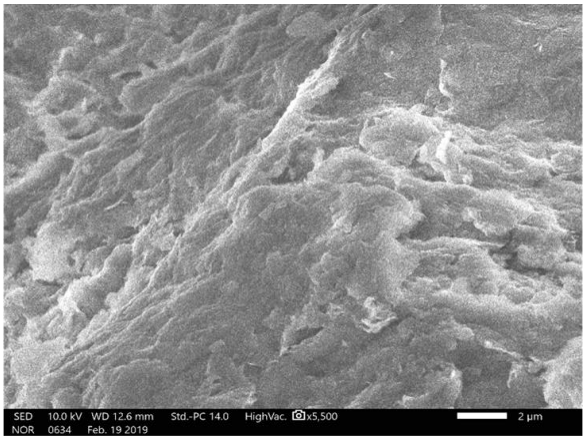

Fig . 19. SEM analysis of 6%RMSWA-L soils at the 14th day curing

4. Conclusion

The main information deduced from the investigation are highlighted below.

- The test results showed that the LS is a poorly graded silt-clayey-sandy gravel and when mixed with MSA as a stabilizing agent, a progressive enhancement in the maximum dry density with a peak value of 234.95KN/m^2 was achieved at 6% MSWA inclusion, provided the soil is kept under un-soaked curing conditions for 14 days.
- An increase in the MSWA content led to an increase in the plastic limit, with greatest result of 16.1% achieved at 15%, and the result being higher than the un-stabilized laterite by 4%. In the case of Plastic index, liquid limit and linear shrinkage, an increase in the ash content led to their decrease with the least results of LL (26.1%), PI (1.6%) and PS (7.8%) recorded at 15% MSWA, the highest percent addition.
- A peak value UCS of 235KN/m^2 was documented at 14 day curing period for Lateritic soils incorporated with 6% MSWA content, which was greater than that of the plain laterite by 12.3%, thus signifying an improvement in strength for laterite with the inclusion of the ash content. Beyond 6%, a drop in strength was documented.
- The stress-strain response behavior of samples was found to have increased proportional to the increasing strain until peak values was reached. The highest maximum stress of 238.67 KPa with a corresponding strain of 3.5mm was deduced for 6%MSWA-L contents when cured for 14 days.

5. Recommendation

- Further experimental testing (California Bearing Ratio test) need be carried out to understand the behavior of the MSWA-L soils when exposed to moderate and freeze-thaw environment.
- Model the mechanical and durability behavior of 6% MSWA-L as a base and sub material under traffic conditions.

List of Abbreviations

RMSWA – Recycled Municipal Solid Waste Ash
SEM- Scanning Electron Microscopic
PET- Polyethylene Terephthalate
OMC- Optimum Moisture Content
MSWA-L, Municipal Solid Waste Ash and Laterite
UCS- Unconfined Compressive Strength
LS- Lateritic Soils
MDD- Maximum Dried Density
DD- Dried Density

References

[1] Prus P, Sikora M. The impact of transport infrastructure on the sustainable development of the region - case study. Agriculture. 2021;11(4).https://doi.org/10.3390/agriculture11040279
[2] Phummiphan I, Horpibulsuk S, Sukmak P, Chinkulkijniwat A, Arulrajah A, Shen SL. Stabilization of marginal lateritic soil using high calcium fly ash based geopolymer. Road Mater Pavement Des. 2016;17(4):877-91. https://doi.org/10.1080/14680629.2015.1132632
[3] Wen P, Wang C, Song L, Niu L, Chen H. Durability and sustainability of cement-stabilized materials based on utilization of waste materials: a literature review. Sustainability. 2021;13. https://doi.org/10.3390/su132111610
[4] Caro S, Agudelo JP, Caicedo B, Orozco LF, Patiño F, Rodado N. Advanced characterisation of cement-stabilised lateritic soils to be used as road materials. Int J Pavement Eng. 2018. https://doi.org/10.1080/10298436.2018.1430893
[5] Teerawattanasuk C, Voottipruex P. Comparison between cement and fly ash geopolymer for stabilized marginal lateritic soil as road material. Int J Pavement Eng. 2018. https://doi.org/10.1080/10298436.2017.1402593
[6] Department of Highways (DOH). Standard for Soil Cement Subbase. DHS206/2532. Thailand: Department of Highways; 1989. (In Thai).
[7] Texas Department of Transportation. Cement Treatment (Plant-Mixed). Austin, TX; 2010. Item 276.
[8] Wahab NA, Roshan MJ, Rashid ASA, Hezmi MS, Jusoh NS, Nik Norsyahariati ND, Tamassoki S. Strength and durability of cement-treated lateritic soil. Sustainability. 2021;13(11). https://doi.org/10.3390/su13116430
[9] Mengue E, Mroueh H, Lancelot L, Eko RM. Physicochemical and consolidation properties of compacted lateritic soil treated with cement. Soils Found. 2017;57:60-79. https://doi.org/10.1016/j.sandf.2017.01.005
[10] Haider AB, Iravanian A, Selman MH, Ekinci A. Using waste PET shreds for soil stabilization: efficiency and durability assessment. Int J Geosynth Ground Eng. 2023;9(48):1-13. https://doi.org/10.1007/s40891-023-00473-8
[11] Onyekwena CC, Li Q, Wang Y, Alvi IH, Li W, Hou Y, et al. Dredged marine soil stabilization using magnesia cement augmented with biochar/slag. J Rock Mech Geotech Eng. 2023. https://doi.org/10.1016/j.jrmge.2023.05.005
[12] Wang S, Zhang X, Zhang P, Chen Z. Strength performance and stabilization mechanism of fine sandy soils stabilized with cement and metakaolin. Sustainability. 2023;15(4):3431. https://doi.org/10.3390/su15043431
[13] Kulanthaivel P, Selvakumar S, Balu S, Krishnaraja AR. Strength enhancement of clay soil stabilized with ordinary Portland cement, silicate and sodium hydroxide. Int J Pavement Res Technol. 2022;16(5). https://doi.org/10.1007/s42947-022-00197-4
[14] Pastor JL, Chai J, Sanchez I. Strength and microstructure of a clayey soil stabilized with natural stone industry waste and lime or cement. Appl Sci. 2023;13:2583. https://doi.org/10.3390/app13042583
[15] Wibowo DE, Ramadhan DA, Endaryanta, Prayuda H. Soil stabilization using rice husk ash and cement for pavement subgrade materials. 2023;22(1):192-202. https://doi.org/10.7764/RDLC.22.1.192
[16] Worrell E, Price L, Martin N, Hendriks C, Meida LO. Carbon dioxide emissions from the global cement industry. Annu Rev Energy Environ. 2001;22(1):303-29. https://doi.org/10.1146/annurev.energy.26.1.303

[17] Prachasaree W, Limkatanyu S, Hawa A, Sukontasukkul P, Chindaprasirt P. Development of strength prediction models for fly ash based geopolymer concrete. J Build Eng. 2020;32. https://doi.org/10.1016/j.jobe.2020.101704
[18] Yoosuk P, Suksiripattanapong C, Sukontasukkul P, Chindaprasirt P. Properties of polypropylene fiber reinforced cellular lightweight high calcium fly ash geopolymer mortar. Case Stud Constr Mater. 2021;15. https://doi.org/10.1016/j.cscm.2021.e00730
[19] Kaza S, Yao CL, Tata PB, Woerden FV. What a Waste 2.0: A Global Snapshot of Solid Waste Management to 2050. Urban Development. Washington, DC: World Bank; 2018. https://doi.org/10.1596/978-1-4648-1329-0
[20] Liang S, Chen J, Guo M, Feng D, Liu L. Utilization of pre-treated municipal solid waste incineration fly ash for cement-stabilized soils. Waste Manage. 2020;105:425-32. https://doi.org/10.1016/j.wasman.2020.02.017
[21] Amiri A, Toufigh MM, Toufigh V. Recycling and Utilization Assessment of Municipal Solid Waste Materials to Stabilize Aeolan Sand. KSCE J. Civ. Eng. 2023;27(1):1042-1053.
[22] Yahia E-A Mohamed Zein, Mohammed Y. Stabilization of Dune Sand using Recycled Municipal Solid Waste Ash. Geotech and Geological Eng. 2012:1335-1344.
[23] ASTM D422-63. Standard test method for particle size distribution of soils. 2018.
[24] Indraratna B, Nutalaya P. Some engineering characteristics of a compacted lateritic residual soil. Geotech Geol Eng. 1991;9(2):125-37. https://doi.org/10.1007/BF00881254
[25] Fall M, Tisot JP, Cisse IK. Untrained behaviour of compacted gravel lateritic soils from western Senegal under monotonic and cyclic triaxial loading. Eng Geol. 1997;47(1-2):71-87. https://doi.org/10.1016/S0013-7952(96)00124-X
[26] Howard AK. The revised ASTM standard on the unified classification system. Geotech Test J. 1984;7(4):216-22. https://doi.org/10.1520/GTJ10505J
[27] Song GJ, Kim KH, Seo YC, Kim S.C. Characteristics of Ash from different Locations at the MSW Incinerator equipped with various Air Pollution Control Devices, Waste Manage. 2004;249(1):99-106
[28] Remond S, Pimienta P, Bentz DP. Effect of the Incorporation of Municipal Solid Waste Incineration Fly Ash in Cement Paste and Mortars. Cement and Concrete Research. 2002;32(1):303-311.
[29] Polettini A, Pomi R, Sirini P. Physical and Mechanical Properties of Cement Based Products Containing Incineration Bottom Ash. Waste Mange. 2003;23(1):145-156.
[30] Carlo C, Sabrina S. Reuse of Municipal Solid Waste Incineration Fly Ashes in Concrete Mix. Waste Mange. 2002;22(1):909-912.
[31] ASTM C618-19. Standard specification for coal fly ash and raw or calcined natural pozzolan for use in concrete. 2018.
[32] ASTM D1557-02. Standard test methods for laboratory compaction characteristics of soil using modified effort (56,000 ft-lbf/ft3 (2,700 kN-m/m3)).
[33] ASTM D4318-00. Standard test methods for liquid limit, plastic limit, and plasticity index of soils. 2018.
[34] ASTM D2487-17. Standard practice for classification of soils for engineering purposes (Unified Soil Classification System).
[35] Amadi A. Evaluation of changes in index properties of lateritic soil stabilized with fly ash. Leonardo Electron J Pract Technol. 2010;9(17):9-78.
[36] Beetham P, Dijkstra T, Dixon N, Fleming P, Hutchison R, Bateman J. Lime Stabilization for Earthworks: A UK Perpestive. Proceeding of the Institute of Civil Eng.- Ground Improvement. 2015;168(2):81-95
[37] Kayode ON, Osemwengie F. Stabilization of Lateritic soil with rubber wood ash and lime for construction. J Appl Sci Environ Manage. 2023;27(7):1551-6.
[38] Ozdemir MA. Improvement in soil bearing capacity of a soft soil by addition of fly ash. Procedia Eng. 2016;143:498-505. https://doi.org/10.1016/j.proeng.2016.06.063
[39] Federal Ministry of Works and Housing. Federal Republic of Nigeria Highway Manual, General Specifications Requirement for Roads and Bridges. 1997.
[40] Varaprasad BJS, Jayaprakash RJ, Suryaprakash RJ. Reuse of municipal solid waste from incinerated ash as stabilization of clayey soil. Slovak J Civil Eng. 2020;28(4):1-7. https://doi.org/10.2478/sjce-2020-0024
[41] Okunade EA. Geotechnical properties of some coal fly ash stabilized Southwestern Nigeria lateritic soils. Mod Appl Sci. 2010;4(12):66. https://doi.org/10.5539/mas.v4n12p66
[42] Azunna SU, Nwafor EO, Ojobo SO. Stabilization of Ikpayongu laterite using cement, RHA and calcium carbide waste mixture for road subbase and base material. Comp Eng Phys Modeling. 2020;3(4):77-96.
[43] Osman NFM, Tajudin SAA, Pakir F. The effect of groundnut shell ash on soil stabilization. J Sus UndergExplo. 2022;2(1):34-40. https://doi.org/10.30880/jsue.2022.02.01.005
[44] Das BM. Principles of geotechnical engineering. India: Thomson; 2006. 480 p.
[45] Ayodele AL, Agbede OA. Influence of electrochemical treatment on a typical laterite. Proc Inst Civ Eng-Ground Improv. 2018;171(2):103-111. https://doi.org/10.1680/jgrim.16.00030

[46] Gidigasu M. Laterite soil engineering: pedogenesis and engineering principles. Amsterdam, Netherlands: Elsevier Scientific Publishing; 2012.
[47] Alireza SGS, Mohammad MS, Hasan BM. Application of nano materials to stabilize a weak soil.
[48] Trivedi JS, Nair S, Iyyunni C. Optimum utilization of fly ash for stabilization of sub-grade soil using genetic algorithm. Procedia Eng. 2013;51(1):250-258. https://doi.org/10.1016/j.proeng.2013.01.034
[49] Parsons RL, Kneebone E. Field performance of fly ash stabilised subgrades. Proc Inst Civ Eng-Ground Improv. 2005;9(1):33-38. https://doi.org/10.1680/grim.9.1.33.58543
[50] Santos F, Li L, Li Y, Amini F. Geotechnical properties of fly ash and soil mixtures for use in highway embankments. In: Proceedings of the World of Coal Ash (WOCA) Conference; 2011 May 9-12; Denver, USA. 2011. p. 125-136.
[51] Dulaimi A, Al Nageim H, Ruddock F, Seton L. High performance cold asphalt concrete mixture for binder course using alkali-activated binary blended cementitious filler. Constr Build Mater. 2017;141:160-170. https://doi.org/10.1016/j.conbuildmat.2017.02.155
[52] Sezer A, İnan G, Yılmaz HR, Ramyar K. Utilization of a very high lime fly ash for improvement of Izmir clay. Build Environ. 2006;41(2):150-156. https://doi.org/10.1016/j.buildenv.2004.12.009
[53] Liu Y, Shedhu KS, Chen Z, Yang EH. Alkali-treated incineration bottom ash as supplementary cementitious materials. Constr Build Mater. 2018;179:371-378. https://doi.org/10.1016/j.conbuildmat.2018.05.231
[54] Singh D, Kumar A. Geo environmental application of solid waste incinerator ash stabilized with cement. J Rock Mech Geotech Eng. 2017;9(2):370-375. https://doi.org/10.1016/j.jrmge.2016.11.008
[55] Ghosh A, Subbarao C. Strength characteristics of class F fly ash modified with lime and gypsum.
[56] Ghosh A, Subbarao C. Microstructural development in fly ash modified with lime and gypsum. J Mater Civil Eng. 2001;13(1):65-70. https://doi.org/10.1061/(ASCE)0899-1561(2001)13:1(65)
[57] Jafer H, Majeed ZH, Dulaimi A. Incorporating two waste materials for the use in fine grain soil stabilization. Civil Eng J. 2020;6(6):1114-1121. https://doi.org/10.28991/cej-2020-03091533
[58] Vichan S, Rachan R, Horpibulsuk S. Strength and microstructure development in Bangkok clay stabilized with calcium carbide residue and biomass ash. Sci Asia. 2013;39(2):186. https://doi.org/10.2306/scienceasia1513-1874.2013.39.186
[59] Katz L. Mechanism of soil stabilization with liquid ionic stabilizer. Transp Res Rec J. 2001;1757(1):50-57. https://doi.org/10.3141/1757-06

Research on Engineering Structures & Materials
www.jresm.org
MIM Research Group

Research Article

Performance of structurally deficient blended RC beam

Aliker Elizah [*,a], Utkrista Pokharel [b], P Poluraju [c]

Dept. Of Civil Engineering, Koneru Lakshmaiah Education Foundation, Vaddeswaram, Guntur, India

Article Info

Article History:

Received 7 June 2024

Accepted 11 Sep 2024

Keywords:

Fly ash;
Blended concrete;
Reinforced concrete beams;
Sustainability;
flexural performance;
Supplementary cementitious materials

Abstract

In this study, the flexural behavior of structurally deficient reinforced concrete (RC) beams incorporating fly ash partially replacing cement was investigated. Structural deficiencies in RC beams typically arise from causes like old age, poor design, and material deterioration. To understand the performance of these deficient beams, a series of flexure tests were conducted. Nine categories of RC beam specimens, each measuring 150mm x 150mm x 700mm, were cast and divided based on steel reinforcement percentages into three sets: 100%, 70%, and 50% of required steel. Within each set, one specimen contained 0% fly ash (100% cement), another contained 20% fly ash (80% cement), and the last one contained 30% fly ash (70% cement). The study focused on analyzing crack propagation, applied load versus mid-deflection relationships, stress-strain relationships, and normalization curve relationships. The results demonstrated that incorporating fly ash improved the flexural performance of RC beams. Beams with fly ash exhibited enhanced crack resistance and higher load-bearing capacities, particularly with 20% fly ash. Lower steel reinforcement percentages increased flexural deficiencies, but the presence of fly ash mitigated some effects. This research provides a significant understanding of optimizing RC beam design for improved durability and performance, showcasing the potential benefits of using sustainable materials such as fly ash in construction.

1. Introduction

The construction industry makes considerable use of concrete because of its many favorable qualities, such as its exceptional strength in compression and other desirable durability features [1]. Plain concrete is frequently inappropriate for a variety of building applications due to poor resistance to vibrations, wind, and tensile stress. Thus, reinforced materials like steel are embedded within concrete such that concrete's compressive strength and steel's tensile strength form a powerful bond to resist these stresses [2]. When transverse loads are applied to structural members like beams and slabs, flexure or bending usually occurs. Errors in design calculations and inadequate reinforcement detailing, subpar construction, poor construction practices, function changes in the structure that result in increased service loads, wind and seismic forces, and corrosion that diminishes or obliterates the reinforcement steel area in severe service environments are all potential causes of flexural deficiencies [3, 4]. Flexural, web shear, flexure-shear, torsion, and bond fractures are some of the ways that can cause concrete cracking. Crack development patterns and beam failure mechanisms are strongly related [5].

The total amount of CO_2 emissions (measured in kg CO_2/tonnes or kg CO_2/m^3) produced throughout the extraction, transportation, and raw materials production into the final product is called embodied CO_2 (ECO_2) [6]. To improve and lessen the environmental effect of CO_2 emissions created during the basic production processes of concrete components, numerous researchers are investigating partial or alternative replacements for concrete elements [7]. Supplementary

*Corresponding author: alikerelizah@gmail.com
[a]orcid.org/0009-0004-7994-5433; [b]orcid.org/0009-0006-7970-7456; [c]orcid.org/0000-0003-1520-624X
DOI: http://dx.doi.org/10.17515/resm2024.312st0607rs

Cementitious Materials (SCMs) namely, Ground Granulated Blast Furnace Slag (GGBS), Pulverized Fly Ash (PFA), Rice Husk Ash (RHA), and Silica Fumes (SF) can be used as partial replacements to reduce ECO_2 of concrete [6]. Fly ash, a fine powder generated during combustion and produced in large quantities annually harms the environment but serves as a pozzolanic cement replacement in concrete, where it reacts with calcium hydroxide and water to form finer hydration products, thereby reducing waste [7]. ECO_2 of Type 1 Portland cement is 228 times that of pulverized fly ash [6]. In order to compare high-volume fly ash concrete—which replaces 70% of cement with fly ash—with conventional concrete (CC), Arezoumandi M, et al [8] investigated experimentally full-scale RC beams to evaluate their mechanical characteristics and bending strength. It was observed that fracture shape and advancement, the behavior of beams of conventional concrete (CC) and high-volume fly ash concrete (HVFAC) are comparable. In addition, flexural strength of HVFAC beams is typically estimated conservatively in design standards. The flexural strength of both beams may be precisely predicted using the Modified Compression Field Theory (MCFT) technique. However, it was noted that MCFT overestimates the deflection of the HVFAC beam by around 14% and underestimates the deflection of the CC beam by about 9%. Also, test findings for HVFAC and the CC mixes agree with the nonlinear regression model fit of CC flexure test database within a 95% confidence interval. Raj et. al. [9] investigated the variation of fly ash proportions between 0% and 60%, binder content between 400 and 450 kg/m^3, and the water-binder ratio between 0.2 and 0.4 to do flexural studies on beams of dimension 0.1x0.2x1.2 meters. The highest load-carrying capability was shown by concrete beams reinforced with 30% fly ash; adding fly ash increased the load-bearing capacity by up to 40%.

The properties of concrete containing fly ash which partially replaces cement and the inherent structural flaws in RC have been the subject of independent investigations by several researchers. But neither of these characteristics had been investigated simultaneously up to now. This study aims to examine the behavior of blended RC beams that show flexural insufficiency by integrating research on the incorporation of fly ash as a partial cement substitute with the evaluation of intrinsic flexural deficiency in reinforced concrete. By integrating investigations on the incorporation of fly ash as a partial cement substitute with evaluation of intrinsic flexural deficiencies in reinforced concrete, this study provides a comprehensive analysis of the synergistic effects of these two factors. Fly ash (FA), by-product of coal combustion, is highly utilized in concrete to attain sustainability and improve certain properties, such as workability and long-term strength. Concurrently, the structural integrity of reinforced concrete is often compromised by intrinsic flaws, particularly in flexural performance, due to factors like inadequate reinforcement, poor material quality, and design flaws. This study addresses the critical need to understand how these flexural deficiencies interact with the modified concrete mix containing fly ash. Through experimental investigations and structural analysis, this research assesses how the integration of FA influences flexural behavior of reinforced concrete beams, particularly those with pre-existing structural weaknesses. The findings aim to reveal whether the incorporation of fly ash mitigates or exacerbates flexural deficiencies, providing valuable insights for structural engineers and construction professionals. Ultimately, the study seeks to enhance the understanding of how to optimize reinforced concrete formulations to achieve better performance and durability, considering both the benefits of fly ash and the challenges posed by intrinsic structural flaws. This dual-focused investigation promises to contribute significantly to the fields of sustainable construction and structural engineering, promoting the development of more resilient and environmentally friendly concrete structures.

The flexural behavior of beams incorporated with fly ash partially replacing cement has been an area of interest due to significant benefits in both performance and sustainability. When FA is used in concrete beams, it can positively influence their flexural performance up to a certain degree by contributing to the formation of a denser and more cohesive microstructure. This densification can lead to improved load-bearing capacity and higher resistance against cracking under flexural stresses [9]. Studies have shown that beams with FA exhibit higher ultimate flexural strength and increased ductility in comparison to beams made with only ordinary Portland cement alone. The pozzolanic reactions of FA also contribute to the gradual strength gain over time, enhancing the durability and lifespan of concrete beams. Moreover, the decreased heat of hydration in fly ash-

modified concrete minimizes thermal cracking, further supporting structural integrity under flexural loads. These findings underscore the viability of incorporating fly ash in reinforced concrete beams not only as a sustainable practice but also to enhance flexural behavior and overall structural performance.

2. Theoretical Analysis

The theoretical capacity was computed by analyzing theoretical calculations on specimens that measured 150mm x 150mm x 700mm and had different balanced steel reinforcement ratios of 100%, 70%, and 50%. As per IS 456:2000[10] prescriptions, these specimens were specifically made not to fail under shearing but rather for study in flexural collapse.

2.1. Calculation of Steel Reinforcement

As per Indian Standard IS 456: 2000[10], Ultimate Moment without applying the factor of safety (M_u) as calculated.

$$M_u = f_y A_{st}(d - 0.42x_{umax}) \quad (1)$$

Where f_y, A_{st}, d, and x_{umax} are the characteristic strength of the reinforcement, area of tension reinforcement, effective depth, and depth of the neutral axis. A balanced section is achieved as the beam reinforcement is designed using three 12 mm diameter reinforcing bars made of Fe500 grade steel.

Table 1. Total reinforcement quantity

Specimen	Diameter	Number of bars	Number of specimens	Length of bar (mm)
100% steel (ρ = 1.5)	12 mm	3	3	660
	10 mm	2	3	660
70% steel (ρ = 1.05)	10 mm	5	3	660
50% steel (ρ = 0.79)	8 mm	2	3	660
	10 mm	3	3	660

Table 1 shows the total quantity of reinforcement for all nine specimens. Each tensile reinforcement and hangar bar is 660 mm long. For 70% of the calculated reinforcement area beam, 3 members of 10mm diameter were used. This gives 69.44% of the original reinforcement. For 50% of the calculated reinforcement area beam, 1 member of 10mm diameter, and 2 members of 8mm diameter were used. This gives 52.7 % of original reinforcement. 8 mm diameter stirrups at 100 mm c/c spacing were used in each beam.

2.2. Mix Design Calculation

Using concrete with characteristics compressive strength of 25 N/mm^2 and a water-cement ratio of 0.42, the design mix for the quantity of concrete materials required for a 150mm x 150mm x 700mm specimen with 100% OPC, the one with 20% and 30% replacement of cement with fly ash were calculated as per IS 10262:2019 [11]. The design values are summarized in Table 2.

Table 2. Mix design constituent quantities

Material	Quantity (kg)		
	For 100% OPC	For 20% Fly Ash Replacement	For 30% fly ash replacement
Cement	400	320	280
Fine aggregate	728	713.6	705.17
Coarse aggregate	1213	1188.5	1174.48
Water	168	168	168
Fly ash		80	120

3. Experimental Investigations

Tests were performed to determine the specific gravity of fine aggregate, coarse aggregate, cement, and fly ash. Fly ash's specific gravity was experimentally checked to verify the value provided by the source factory. And sieve analysis was performed for the fine aggregate to classify the grading zone of sand. Validating calculated values involved the performance of compressive-strength tests on concrete cubes.

This study used cement, fly ash, fine and coarse aggregates, water, and steel rods, with a focus on how the fly ash amount along with the variation of reinforcement affects the strength of the beam. OPC 53 grade cement as specified in IS 12269:2013[12] was used. The aggregates were obtained locally, and the FA is of type F sourced from Vijayawada Thermal Power Station (VTPS). Fig 1 shows the constituent materials of concrete after batching.

Fig. 1. Batching of material

Fig. 2. Sieve analysis

The specific gravity of cement and the aggregates were tested according to Indian standard code[13, 14]. The sieve analysis was also done to determine the zone of fine aggregate as presented in Fig. 2[15]. The specific gravity of FA was obtained from the factory and tested using the density bottle method to check for any variation.

3.1. Mix Design Calculation

Three categories of cubes were cast each using M25 mix design calculation values. The first category was without fly ash (FA), the second with 20% FA, and the last category with 30% fly ash to partially replace cement. In each of the three categories, three cube specimens were cast making a total of nine cubes. The cubes were placed in a water curing tank and tested after 28 days to find their compressive strength. The test was performed as per IS 516 (1959) [16]. Fig 3 shows the concrete cubes immediately after casting them into cubes.

Fig. 3. Wet concrete cubes after casting

3.2. Mix Design Calculation

The arrangement of rebars in the cage was done per the design calculations while taking care of all the necessary cautions. The stirrups bent of 135^0 was maintained. The beam molds were then tightened, and lubricated (greased), and the reinforcement cage was set in the molds using cover blocks of 20mm. Proper compaction was done using a needle vibration, the cast beams were covered using gunny bags after about an hour and allowed to harden for 24 hours. Demolding was then done, and the specimens were marked and then placed in the curing water tank for 56 days to ensure that blended specimens acquired enough strength. Fig 4 shows the reinforcement detail after arranging the rebar in the cage. The beam specimen ready for testing is shown in Fig 5. Table 3 depicts the nomenclature of the specimens.

Fig. 4. Rebar arrangement in the cage

Fig. 5. Beam specimen in use

Table 3. Labelling and identification of the specimens

Identification mark	Description
A1	100% steel with 100% cement (0% fly ash)
A2	100% steel with 80% cement (20% fly ash)
A3	100% steel with 70% cement (30% fly ash)
B1	70% steel with 100% cement (0% fly ash)
B2	70% steel with 80% cement (20% fly ash)

B3	70% steel with 70% cement (30% fly ash)
C1	50% steel with 100% cement (0% fly ash)
C2	50% steel with 80% cement (20% fly ash)
C3	50% steel with 70% cement (30% fly ash)

3.3. Mechanical Testing

The heart of this research involved mechanical testing of the cast beam specimens. The beams were subjected to flexure tests to evaluate load-carrying capacity, deflection characteristics, and crack propagation. For this, state-of-the-art equipment and testing methodologies were employed while high precision recording the data using UTM (Universal Testing Machine). A four-point load method was used. The beams were taken out from the curing tank, dried and the surfaces whitewashed to allow clear visualization of crack patterns and then marked before placing it in the UTM.

The middle third of the beam will experience pure bending as the monotonic flexure loading increases. If the load is within the elastic limit, then any one section will develop a moment that does not exceed the cracking moment and this, in turn, results in tensile stress which is less than the flexural strength of concrete. After the cracking moment has been passed, the maximum tensile stress in concrete surpasses the flexural strength of concrete. Non-linear behavior can be observed after passing the cracking moment. As the load continues to rise, concrete has less ability to carry more load and so reinforcement begins to take part of it [9]. Fig 6 shows the specimen subjected to loading in the UTM in use.

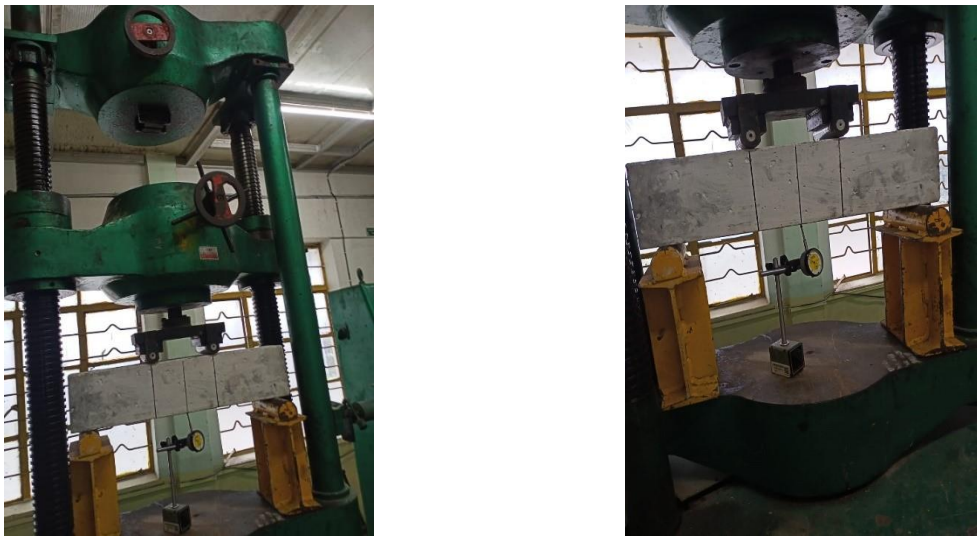

Fig. 6. Flexure test setup of specimen in use

4. Results

The specific gravity of cement used was found to be 3.05 which is approximate to the limit specific gravity of cement which is 3.15. The specific gravity of fly ash was experimentally found to be 1.95, which conforms to the value provided by the manufacturer. The specific gravity of fine aggregate and coarse aggregate was found to be 2.61 and 2.95 respectively. After the sieve analysis, the fine aggregate was found to belong to zone III as per the IS 383-2016[15] method as shown in Table 4 below and its gradation curve is shown in Fig 7 below.

Results obtained from the flexure test are tabulated in Table 6. The flexural strength was calculated as per IS 516 [16]. The flexural strength for balanced RC specimens was highest, followed by that of 70% and then 50% reinforcement area. In each set of three specimens, the flexural strength varied in the way that 20% blended fly ash cement specimens had the highest values followed by

the ones without fly ash content then lastly the ones with 30% fly ash as cement replacement. The design mix test result for nine concrete cube specimens in which three of the specimens were of 100% OPC, three were of 20% fly ash and 80% cement, and the last three were of 30% fly ash and 70% cement was also computed and tabulated in Table 5.

Table 4. Result obtained from sieve analysis

Size of sieve (mm)	Weight retained		Cumulative retained (%)	% Finer	% Passing as per IS 383-2016		
	(g)	(%)			Zone I	Zone II	Zone III
10	0	0	0	100	100	100	100
4.75	0	0	0	100	90-100	90-100	90-100
2.36	4	0.4	0.4	99.6	60-95	75-100	85-100
1.18	44	4.4	4.8	95.2	30-70	55-90	75-100
0.6	124	12.4	17.2	82.8	15-34	35-59	60-79
0.3	656	65.6	82.8	17.2	5-20	8-30	12-40
0.15	130	13	95.8	4.2	0-10	0-10	0-10
pan	42	4.2	100	0	Zone III		
Total	1000						

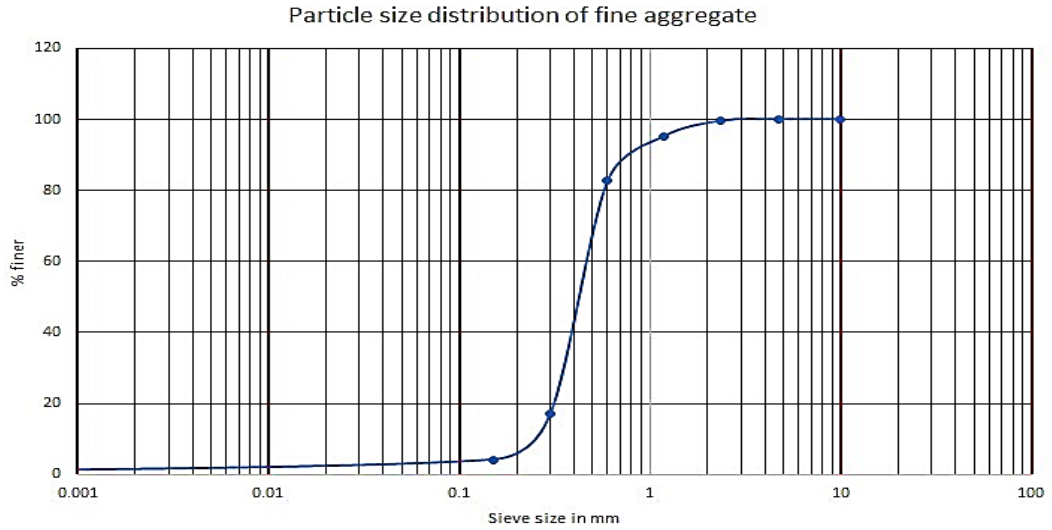

Fig. 7. Particle size distribution of fine aggregate

Table 5. Mix designs results

S. No	Mix	Load (KN)	Compressive strength (MPa)	Average strength (MPa)
1	100% OPC	960	42.67	41.93
2		930	41.33	
3		940	41.78	
4	20% fly ash replacement	890	39.56	38.37
5		860	38.22	
6		840	37.33	
7	30% fly ash replacement	780	34.67	34.52
8		800	35.56	
9		750	33.33	

Table 6. Flexure test results

Identification mark	Position of fracture in cm	Load in KN	Strength in N/mm^2
	For 100% steel specimen		
A1	20.1	200.124	4.23
A2	19.8	190.314	4.25
A3	20.2	190.314	4.02
	For 70% steel specimen		
B1	17.5	200.124	3.17
B2	20	156.96	3.32
B3	22.7	147.15	3.11
	For 50% steel specimen		
C1	27.5	141.264	2.99
C2	27.5	149.112	3.15
C3	17	137.34	2.08

4.1 Cracking Pattern and Failure Mode

For the specimens A1, A2, and A3, at failure, the cracks propagated up to between 60mm to 75mm depth from the bottom while for specimens B1, B2, and B3, it was up to 90mm to 105mm depth, and for C1, C2 and C3 specimen, the cracks propagated to the nearly full depth of the beams (above 130mm). In the test section, only flexural cracking occurred; typical bending failure leading to crushing of the compression-side concrete after the yielding of the tension reinforcement was noted, however, when the applied load exceeded the theoretical value, shear cracks were seen for specimen C towards the supports. There were more than 3-4 cracks in the test section in the C3 specimens. The shear force-generating zone between the loading points and the support points outside the test section did not show any significant shear cracks, and failure in shear did not occur until the test was finished. Fig 8 shows the crack pattern of the specimens with 100% reinforcement. Fig 9 and Fig 10 show the crack pattern for the 70% and 50% specimens respectively.

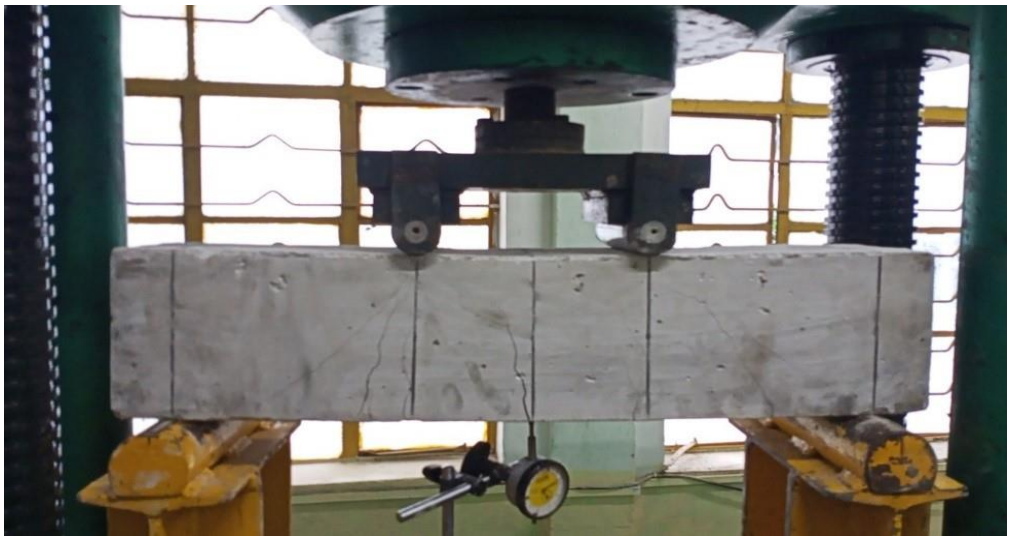

Fig. 8. Specimen crack for 100% reinforcement

Fig. 9. Specimen crack for 70% reinforcement

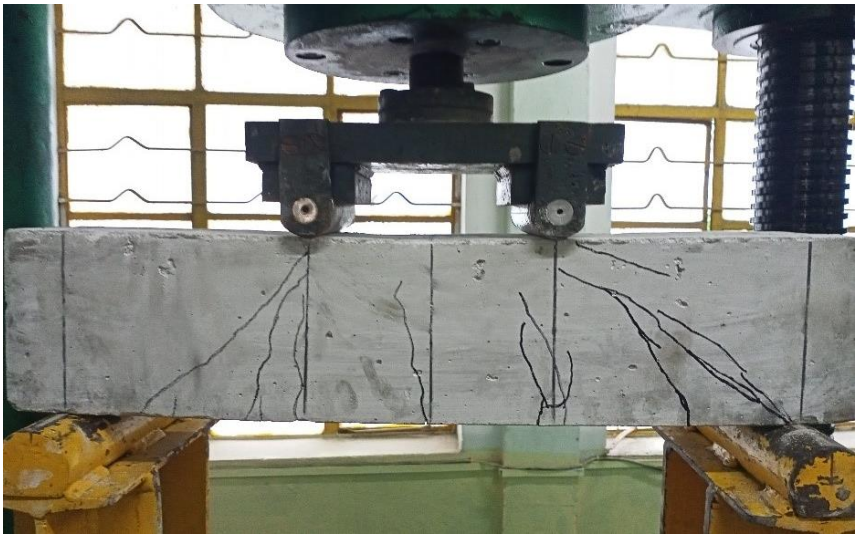

Fig. 10. Specimen crack for 50% reinforcement

4.2 Applied Load vs Mid-Deflection Relations

For specimens with 100% steel reinforcement (balanced section), the mid deflection at ultimate load for pure cement RC specimen was 3mm while that of 20% and 30% fly ash was 4mm and 3.6mm respectively. For 70% reinforcement specimens, the maximum deflections were 2.4mm, 2.9mm, and 5mm for 0%, 20%, and 30% fly ash volume respectively and for 50% reinforcement specimens, the maximum deflections were 3.7mm, 4.6mm, and 5.5mm for 0%, 20% and 30% fly ash volume respectively as shown in Fig 11, 12 and 13.

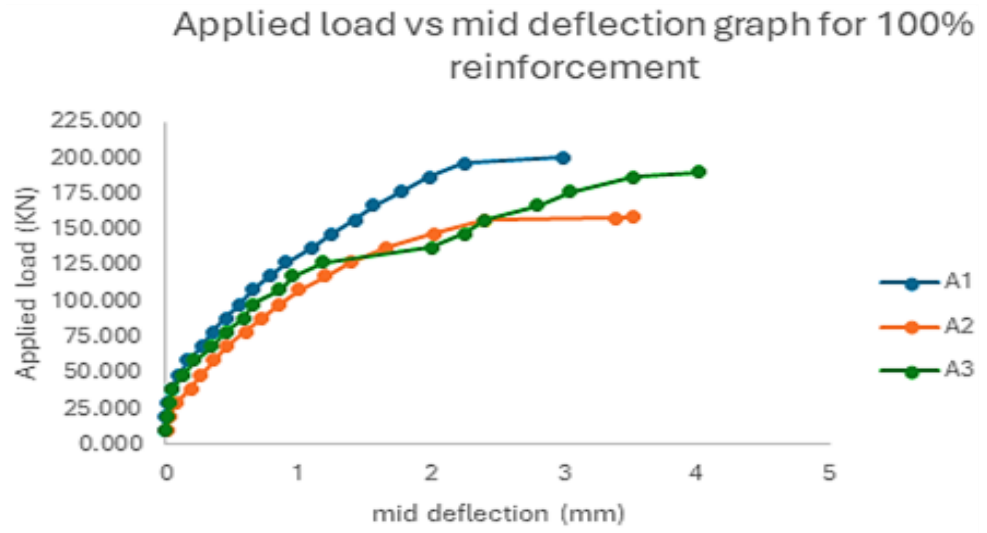

Fig. 11. Applied load vs mid-deflection for 100% reinforcement

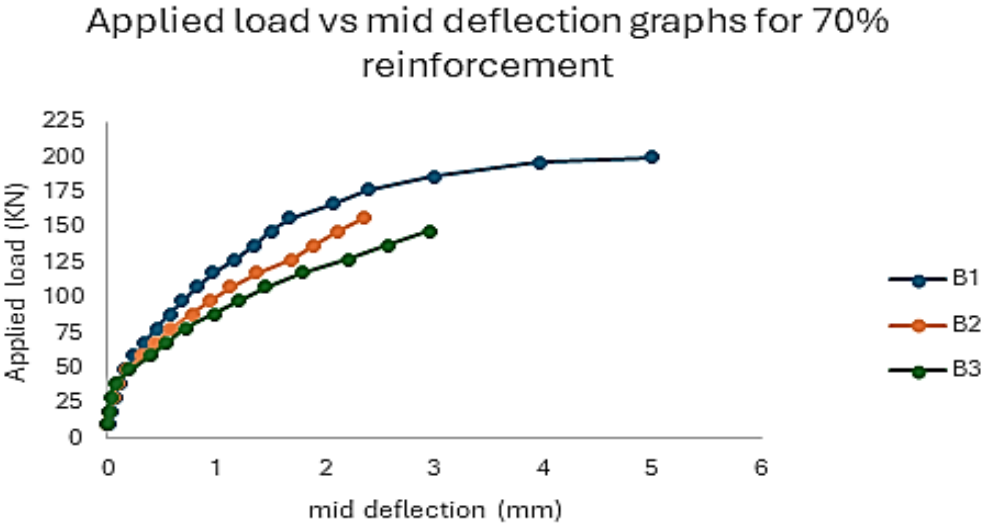

Fig. 12. Applied load vs mid-deflection for 70% reinforcement

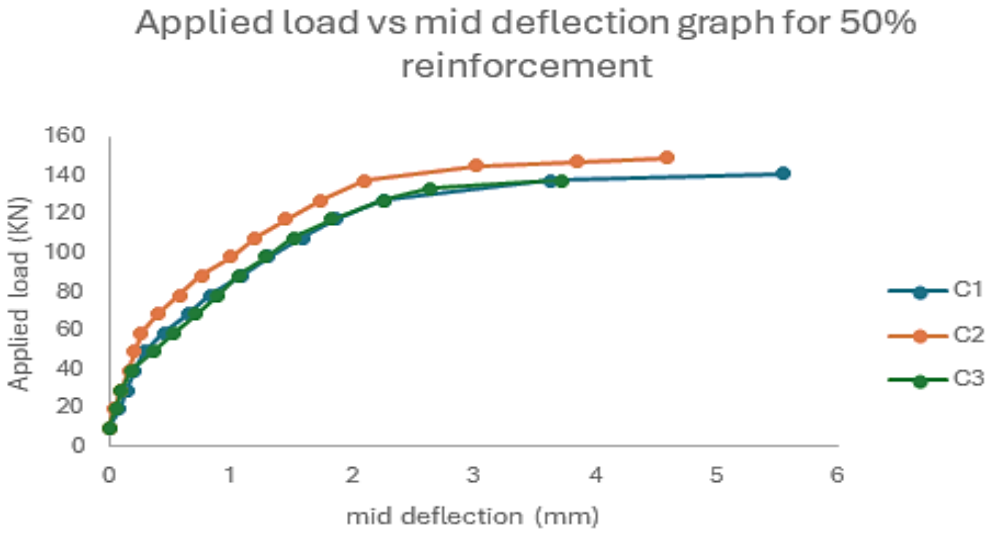

Fig. 13. Applied load vs mid-deflection for 50% reinforcement

4.3 Stress-Strain Relations

As the area of reinforcement steel is reduced to 70% (ρ = 1.05) and then 50% (ρ = 0.79), the maximum stress corresponding to maximum strain is reduced from 9 N/mm² to 8.8 N/mm², to 6.6 N/mm². For 100%, 70%, and 50% steel reinforcement specimens, the stress-strain relation for each fly ash constituent is shown respectively in Fig 14, 15, 16 below.

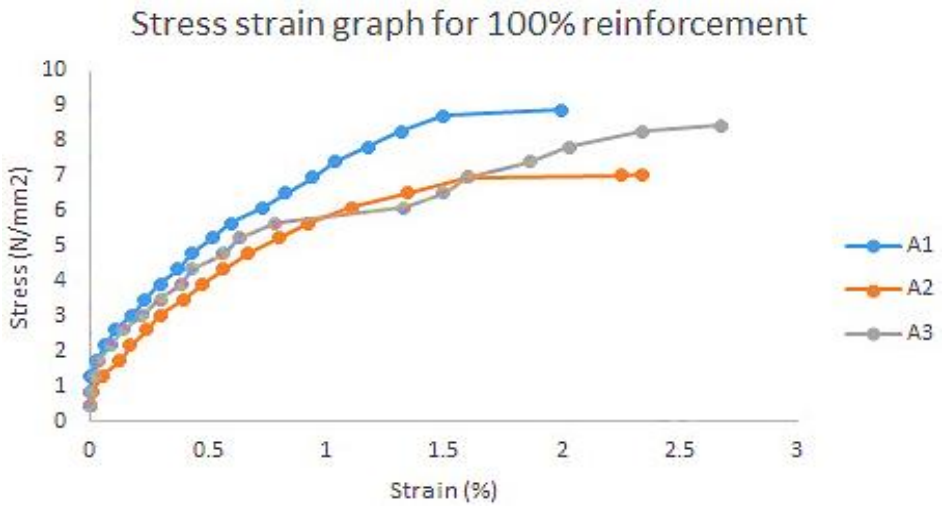

Fig. 14. Stress vs strain for 100% reinforcement

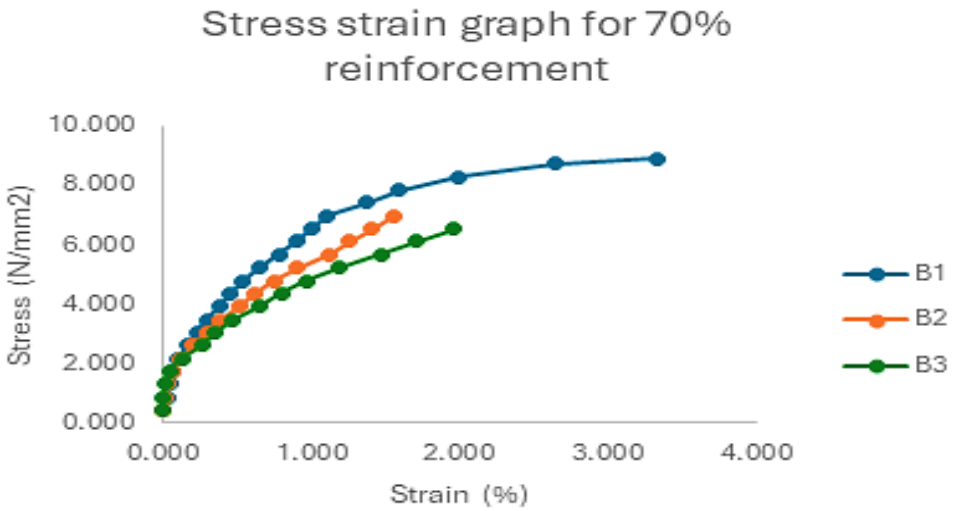

Fig. 15. Stress vs strain for 70% reinforcement

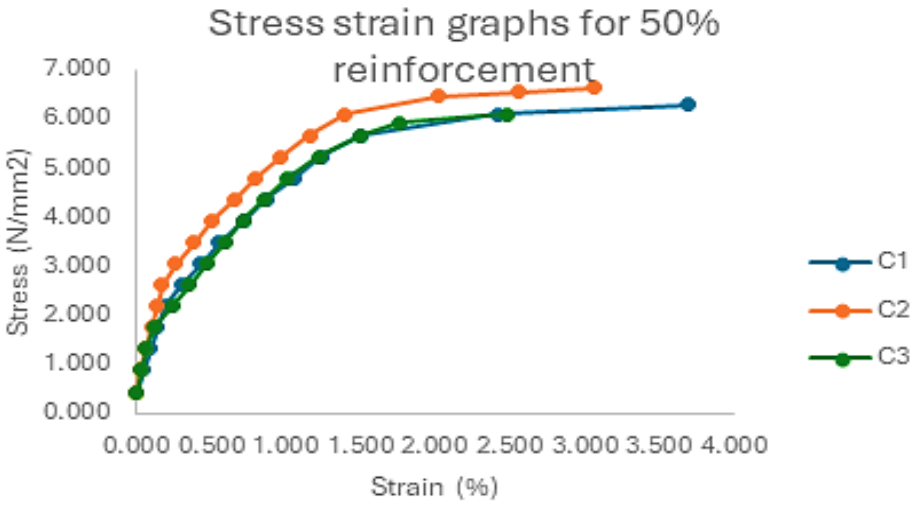

Fig. 16. Stress vs strain for 50% reinforcement

4.4 Normalization Curve

The $\frac{p_u}{f_{ck}bD}$ for the beams decreased with a decrease in the percentage of the area of reinforcement. This was indicated by the downward shift in the $\frac{p_u}{f_{ck}bD}$ against strain curve as from the 100% reinforcement specimens to 70% and 50% respectively.

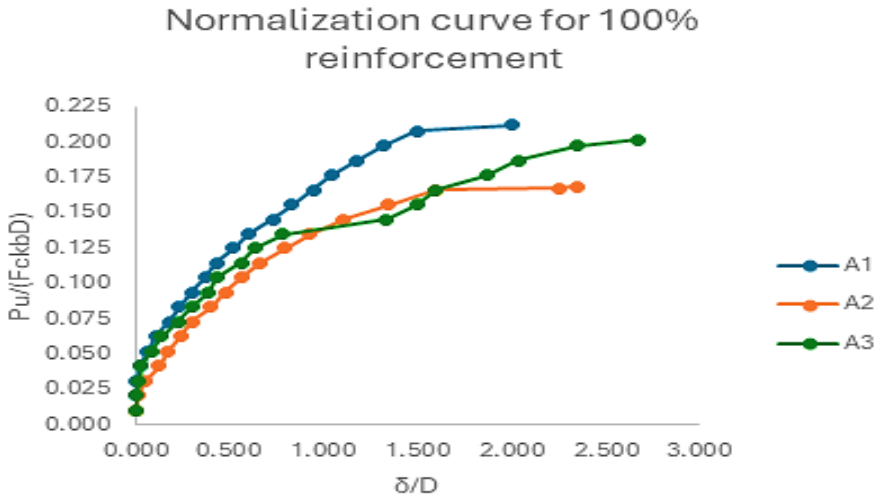

Fig. 17. Normalization curve for 100% reinforcement

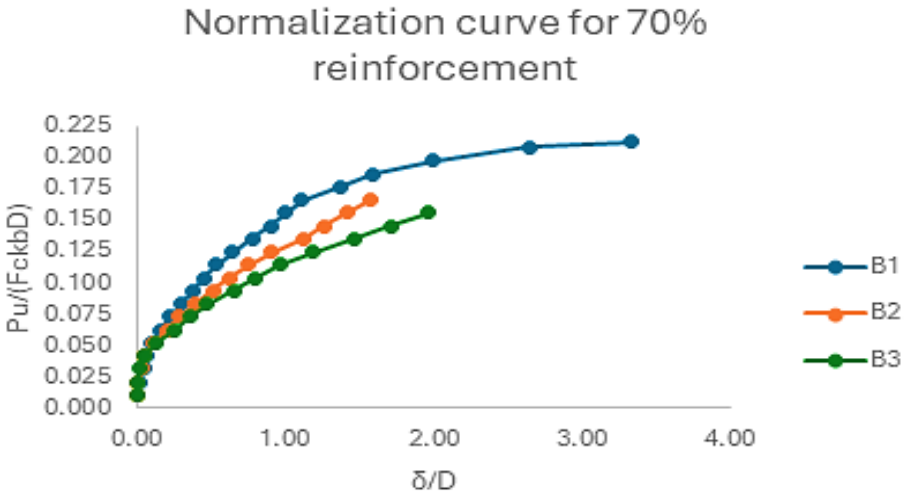

Fig. 18. Normalization curve for 70% reinforcement

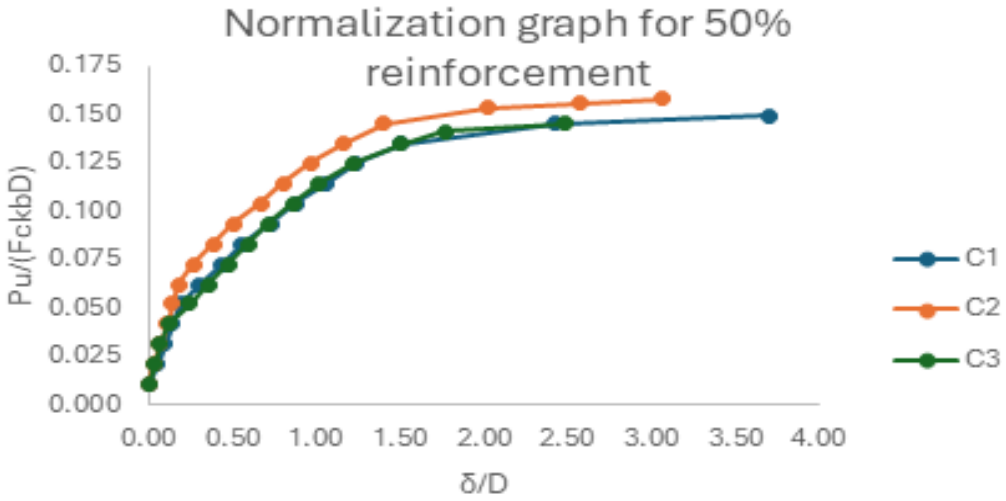

Fig. 19. Normalization curve for 50% reinforcement

Normalization curve relation for 0%, 20%, and 30% FA as replacement of cement for each specimen with varying reinforcement area is as shown below in Fig 17, 18 and 19 respectively.

5. Conclusion

The mix design produced an average strength of 41.93 MPa, 38.37 MPa, and 34.52 MPa for the concrete containing 0%, 20%, and 30% fly ash respectively. This means that all the specimens passed the required value and so the mix designs were used to cast the beams. The cubes in which cement is partially replaced with fly ash showed less compressive strength compared to those with 100% OPC after a 28-day curing period. Fly ash was found not to significantly affect flexural strength of RC beam, however, there was a slight reduction in flexural capacity with an increment in the amount of fly ash to 30%. But for all reinforcement categories, beams with 20% fly ash displayed the highest strength. As the area of reinforcement steel is reduced to 70% ($\rho = 1.05$) and then 50% ($\rho = 0.79$), the overall tensile strength decreased this was because the stress at a given strain level was lowest for 50% ($\rho = 0.79$), and lower for 70% ($\rho = 1.05$) compared to 100% ($\rho = 1.5$) reinforcement specimens.

The beams first deformed elastically, showing that the deformations were directly proportional to the applied load. With an increase in the load, the materials attained their yield point, entering plastic deformation. For some of the materials, this was followed by a strengthening phase of strain hardening, whereby further resistance is built up due to internal structural changes. The stress-strain relationships developed conformed to the usual trend for material behavior: a linear elastic region progressing into a plastic region and finally ending at the material's ultimate strength. The failure modes included flexural failure, whereby beams experienced a crack under tensile stress, particularly in the tension zone. For beams with 50% tensile reinforcement and 8 mm diameter bars at 100 mm Centre to Centre, theoretically maximum load that the beam can take before it fails in shear is 76.6 KN. But in our test, the beams were tested beyond this loading which led to shear cracks.

The normalized ultimate flexure capacity vs δ/D curve shifts downward and the peak shifts to the right as the percentage of the steel is reduced to 70% and 50% of the designed reinforcement area. Hence the ductility and the ultimate strength reduced along with the trend. However, the C specimens can be best used in non-critical structure design and lightly loaded members. For the normalization curves, A specimens with a high reinforcement ratio are ideal for seismic-resistant constructions or strongly loaded members because they have a high ultimate strength and significant ductility. B specimens fit well for normal building construction or moderately loaded structural elements because they have a medium reinforcement ratio and good ultimate strength and ductility. C specimens are a cost-effective option for lightly loaded members or non-critical constructions because of their low reinforcement ratio, moderate ultimate strength, and moderate ductility.

List of Abbreviations

Abbreviation	Full form
FA	Fly Ash
RC	Reinforced Concrete
SCMs	Supplementary Cementitious Materials
CO2	Carbon dioxide
ρ	Tensile reinforcement ratio
ECO2	Embodied Carbon dioxide
CC	Conventional Concrete
HVFAC	High Volume Fly Ash Concrete
IS	Indian Standard
OPC	Ordinary Portland cement
UTM	Universal Testing Machine

Acknowledgement

The authors acknowledge the support of the Structural Engineering and Concrete Laboratory of the Department of Civil Engineering at KL University in this study.

References

[1] Ghanem H, Chahal S, Khatib J, Elkordi A. Flexural Behavior of Concrete Beams Reinforced with Recycled Plastic Mesh. Buildings. 2022 Dec 1;12(12). https://doi.org/10.3390/buildings12122085
[2] Chouhan A, Pitale N. Review on Effect of Corrosion on Flexure, Shear and Torsional Strength of Reinforced Concrete Beam. Int J Sci Res Sci Technol. 2020 May 15;87-91. https://doi.org/10.32628/IJSRST207317
[3] Chaitanya N, Krishna V. An Experimental Study of Flexural Strength of Reinforced Concrete Beam Due To Corrosion [Internet]. Vol. 11, IOSR Journal of Mechanical and Civil Engineering (IOSR-JMCE. https://doi.org/10.9790/1684-114298109
[4] Kadhim MMA, Jawdhari A, Nadir W, Cunningham LS. Behaviour of RC beams strengthened in flexure with hybrid CFRP-reinforced UHPC overlays. Eng Struct. 2022 Jul 1;262:114356. https://doi.org/10.1016/j.engstruct.2022.114356
[5] Layang S. CRACKS IN REINFORCED CONCRETE BEAM. BALANGA: Jurnal Pendidikan Teknologi dan Kejuruan. 2022 Jun 30;10(1):6-12. https://doi.org/10.37304/balanga.v10i1.3277
[6] Samad S, Shah A. Role of binary cement including Supplementary Cementitious Material (SCM), in production of environmentally sustainable concrete: A critical review. Vol. 6, International Journal of Sustainable Built Environment. Elsevier B.V.; 2017. p. 663-74. https://doi.org/10.1016/j.ijsbe.2017.07.003
[7] Soomro RA, Oad M, Aamur SH, Channa IA, Shabbir S, Ali T. Assessment of the Flexural Strength of Binary Blended Concrete with Recycled Coarse Aggregates and Fly Ash. Engineering, Technology & Applied Science Research. 2023;13(3):11020-5. https://doi.org/10.48084/etasr.5924
[8] Arezoumandi M, Ortega CA, Volz JS. Flexural behavior of high-volume fly ash concrete beams: Experimental study. Transp Res Rec. 2015;2508:22-30. https://doi.org/10.3141/2508-03
[9] Raj BS, Rao MK. Flexural Performance of Sustainable Fly Ash Based Concrete Beams. In: IOP Conference Series: Earth and Environmental Science. Institute of Physics; 2023.
[10] IS 456:2000 Code of practice for plain and reinforced concrete. Bureau of Indian Standards, New Delhi
[11] IS 10262: 2019 Concrete Mix Proportioning - Guidelines. Bureau of Indian Standards, New Delhi
[12] IS 12269:2013 Ordinary Portland Cement, 53 grade - Specification. Bureau of Indian Standards, New Delhi
[13] IS 2720 (Part 3):1980 Method of test for soils - Determination of specific gravity. Bureau of Indian Standards, New Delhi
[14] IS 1727:1967 Methods of test for pozzolanic materials. Bureau of Indian Standards, New Delhi
[15] IS 383:1970 Specification for coarse and fine aggregates from natural sources for concrete. Bureau of Indian Standards, New Delhi
[16] IS 516:1959 Methods of tests for strength of concrete. Bureau of Indian Standards, New Delhi

Research on Engineering Structures & Materials
www.jresm.org
Research Group

Research Article

Predictive modeling of glass powder and activator effects on slag-based geopolymers via central composite design

Amirouche Berkouche [1,a], Ahmed Abderraouf Belkadi [*,1,b], Salima Aggoun [2,c], Redha Hammouche [3,d], Samir Benaniba [4,e]

[1]*Dept. of Civil Eng., Mohamed El-Bachir El-Ibrahimi University of Bordj Bou Arreridj, El-Anasser, Algeria*
[2]*CY Cergy Paris Université, L2MGC, F-95000 Cergy, France*
[3]*Materials and Durability of Construction Laboratory, Dept. of Civil Eng., Faculty of Science and Technology, Frère Mentouri University of Constantine 1, Constantine 25000, Algeria*
[4]*Mechanical Eng. Dept., Faculty of Sciences and Technology, University Mohamed El Bachir El Ibrahimi of Bordj Bou Arreridj, El-Anasser, Algeria*

Article Info

Article history:

Received 03 July 2024
Accepted 13 Sep 2024

Keywords:

Geopolymer;
Modeling;
Glass powder;
Optimization;
Central composite design

Abstract

This study investigates the effects of glass powder (GP) content and activator-to-precursor (Ac/Pr) ratio on the properties of slag-based geopolymer mortars using a central composite design approach. GP content ranging from 0% to 30% and Ac/Pr ratios between 0.65 and 0.75 were examined. Response surface methodology was utilized to construct predictive models for slump, 28-day compressive strength, and porosity. Scanning electron microscopy and energy dispersive X-ray spectroscopy were utilized to analyze the microstructure and chemical composition of the geopolymer matrices. Results indicate that both GP content and Ac/Pr ratio significantly influence mortar properties. Increasing GP content and Ac/Pr ratio generally improved workability, while optimal mechanical performance was achieved at moderate levels of both factors. The optimal formulation, determined through desirability analysis, consisted of 18.2% GP content and 0.72 Ac/Pr ratio, yielding predicted outcomes of 16.53 cm slump, 46.64 MPa compressive strength, and 15.85% porosity. This study demonstrates the potential of incorporating waste glass in slag-based geopolymers and provides a framework for optimizing mix designs to achieve desired performance characteristics.

1. Introduction

The global construction industry faces an unprecedented challenge in the 21st century: meeting the growing demand for infrastructure while simultaneously reducing its environmental impact. At the heart of this challenge lies the production of cement, a process responsible for approximately 8% of worldwide CO_2 emissions [1]. This staggering figure underscores the urgent need for sustainable alternatives that can mitigate the environmental footprint of construction activities without compromising on performance or durability. In recent decades, geopolymers have emerged as a promising solution to this pressing issue, offering comparable or superior performance to conventional cement while significantly reducing associated carbon emissions [2, 3].

Geopolymers, a term coined by Joseph Davidovits in the 1970s [4], represent a class of inorganic polymers synthesized through the alkaline activation of aluminosilicate materials, including metakaolin, fly ash, and ground granulated blast furnace slag (GGBFS).

*Corresponding author: ahmedabderraouf.belkadi@univ-bba.dz
[a] orcid.org/0009-0004-1540-139X; [b] orcid.org/0009-0002-5978-9774; [c] orcid.org/0000-0002-2757-1263; [d] orcid.org/0009-0004-4458-8309
DOI: http://dx.doi.org/10.17515/resm2024.337st0703rs

These materials are rich in silicon (Si) and aluminum (Al), which are essential for the geopolymerization process [5, 6]. The geopolymerization process begins with the dissolution of these precursor materials in a highly alkaline environment, typically provided by a combination of sodium or potassium hydroxide and silicate solutions [7]. Once dissolved, the aluminate and silicate species undergo condensation reactions, forming a gel-like network of aluminosilicate hydrates [8]. This network further polymerizes into a three-dimensional matrix, primarily consisting of sodium-aluminosilicate-hydrate (N-A-S-H) gels in low calcium systems or calcium-aluminosilicate-hydrate (C-A-S-H) gels in high calcium systems like those containing GGBFS [9, 10]. This process is responsible for the development of mechanical strength and durability in geopolymer materials [11], making them suitable for various construction applications.

These innovative binding agents offer numerous advantages over traditional Portland cement, including drastically reduced CO_2 emissions—up to 80% less compared to conventional cement production [3]. To regulate sustainability, one must control the kind and quantity of binder used in concrete mixtures, since they account for over 90% of the CO_2 in the mixture [12]. While regular Portland cement emits 306 kg CO_2/m^3 for the same mechanical qualities, geopolymer releases just 169 kg CO_2/m^3, a 45% reduction in emissions, as stated by Biernacki et al. [12]. Additionally, according to Davidovits [13], fly ash-based geopolymers can achieve CO_2 emissions in the range of 0.09 to 0.25 kg CO_2 per kilogram, which translates to a 75 to 90% reduction compared to conventional cement.

Moreover, geopolymers enable the utilization of various industrial by-products, contributing to circular economy principles and waste reduction. Many geopolymer formulations exhibit enhanced durability, demonstrating superior resistance to chemical attack, fire, and extreme temperatures [14], [15], [16]. Perhaps most importantly, geopolymers can achieve strength and performance characteristics that match or exceed those of traditional cement-based materials, making them a viable alternative for a wide range of construction applications.

Despite these compelling advantages, the widespread adoption of geopolymers faces several challenges related to raw material availability, mix design optimization, and long-term performance under various environmental conditions. Ongoing research efforts are focused on addressing these challenges and expanding the application of geopolymers in construction. A critical aspect of this research involves the careful selection and optimization of precursor materials, which play a crucial role in determining the properties and performance of geopolymer systems. Among the various precursors used in geopolymer production, GGBFS has gained significant attention due to its widespread availability and favorable chemical composition. GGBFS, a by-product of the iron and steel industry, is formed when molten iron blast furnace slag is rapidly cooled by water. Its chemical composition typically consists of CaO, SiO_2, and Al_2O_3 [17]. The high calcium content in GGBFS contributes to the formation of calcium silicate hydrate (C-S-H) gels in addition to the geopolymeric network [18], [19], [20], resulting in enhanced mechanical properties and reduced setting times compared to low-calcium precursors.

The Ca/Si and Si/Al ratios in geopolymer systems are critical factors that influence the reaction mechanisms, microstructure development, and ultimately, the properties of the hardened material. A higher Ca/Si ratio promotes the formation of C-S-H gels, which can coexist with the geopolymeric network [21], leading to improved mechanical properties. However, excessive calcium content can hinder the geopolymerization process by competing for available silica, potentially reducing long-term strength development [22], [23]. Similarly, the Si/Al ratio affects the degree of polymerization and the structure of the aluminosilicate network [24]. Higher Si/Al ratios generally result in increased compressive strength and improved durability due to the formation of more stable Si-O-Si

bonds [25], [26]. However, very high Si/Al ratios can lead to unreacted silica and reduced strength [27]. Optimizing these ratios is crucial for achieving the desired balance between early strength development, long-term performance, and durability of geopolymer materials.

In the quest for further enhancing the sustainability and performance of geopolymer systems, researchers have begun exploring the potential of glass powder (GP) as a supplementary precursor. Derived from recycled waste glass, GP offers a promising avenue for incorporating high-silica content materials into geopolymer mixtures. The chemical composition of GP typically includes SiO_2 [28]. This high silica content, combined with the amorphous nature of glass, makes GP an attractive material for geopolymer production, offering several potential benefits. The incorporation of GP in geopolymer systems can enhance silicon availability due to the easier dissolution of amorphous glass in alkaline media, providing readily available silica for geopolymerization reactions. The spherical shape of glass particles can contribute to better flowability of fresh geopolymer mixtures, potentially improving workability [29], [30]. Furthermore, the utilization of waste glass in geopolymers addresses the challenge of glass disposal while reducing the demand for virgin raw materials, further enhancing the environmental credentials of these alternative binding materials.

Several studies have explored the incorporation of GP in alkali-activated systems, demonstrating its potential as a supplementary precursor. Researchers have reported improved compressive strength and reduced porosity with GP addition up to 30% replacement in alkali-activated slag mortars [28], [29], [31], [32], [33]. Synergistic effects have been observed when combining GP with fly ash in geopolymer systems, leading to enhanced mechanical properties and microstructure development [34], [35]. The influence of GP fineness on the properties of alkali-activated slag concrete has also been examined, with finer GP particles leading to improved strength and durability characteristics [36], [37]. Moreover, the use of GP in combination with calcined clay for geopolymer production has shown promise, with studies reporting increased compressive strength and reduced water absorption upon GP incorporation. The introduction of GP as a silica-rich source in geopolymer systems offers several advantages for optimizing the critical Ca/Si and Si/Al ratios. The high silica content of GP allows for fine-tuning of the Si/Al ratio, potentially leading to improved mechanical properties and durability. In slag-based systems, GP can help moderate the high calcium content, promoting a more balanced formation of C-S-H gels and geopolymeric networks. The amorphous nature of GP can contribute to increased dissolution rates and overall system reactivity, potentially accelerating strength development. Furthermore, the incorporation of GP may lead to a more compact and refined microstructure [38], [39], reducing porosity and enhancing long-term performance.

Despite the promising results reported in literature, there remains a need for a comprehensive understanding of the effects of GP incorporation on the properties of slag-based geopolymer systems. Moreover, the development of predictive models for optimizing mix designs is crucial for the practical implementation of GP in geopolymer production. This research aims to address these knowledge gaps by investigating the influence of GP as a partial replacement for GGBFS on the mechanical and physical properties of eco-geopolymer mortars. The primary objective of this study is to elucidate the effects of GP replacement levels (0-30%) and activator-to-precursor ratio (Ac/Pr) on the fresh and hardened properties of slag-based geopolymer mortars. To achieve this, the response surface methodology will be utilized to develop predictive models for slump, compressive strength, and porosity as a function of GP content and Ac/Pr ratio. This approach will enable the optimization of mix designs based on desired performance criteria. Furthermore, microstructural analysis using Scanning Electron Microscopy (SEM)

coupled with Energy Dispersive X-ray (EDX) spectroscopy will be employed to examine the morphological characteristics and chemical composition of the geopolymer matrices, providing insights into the formation of C-A-S-H gels and their distribution within the microstructure. This comprehensive analysis will elucidate the relationship between mix composition, microstructural development, and macroscopic properties of the geopolymer mortars

By addressing these research goals, this study aims to contribute to the development of more sustainable and high-performance geopolymer materials, paving the way for their increased adoption in construction applications. The findings of this research will provide valuable insights into the optimal utilization of GP in slag-based geopolymer systems, offering a pathway for the valorization of waste glass while enhancing the environmental credentials of alternative cementitious materials. Ultimately, this work seeks to advance the state-of-the-art in eco-friendly construction materials, contributing to the global effort to reduce the environmental impact of the built environment while meeting the growing demands for infrastructure development.

2. Materials and Methods

2.1. Materials

This study utilized several key materials to produce the slag-based geopolymer mortars, such as GBFS, GP, sand, and alkaline activators. GGBFS and GP served as the primary precursors for the geopolymer binder. The GGBFS was sourced from a regional steel manufacturer (El-Hadjar complex, Annaba, Algeria) as spherical grains with a particle size of 0/5 mm, which were then crushed to achieve a fineness of 237.1 m^2/kg. The glass waste (sourced from local recycling facilities in Setif, Algeria) was subjected to grinding processes, resulting in a fineness of 280.8 m^2/kg. The appearance of both GGBFS and GP is displayed in Fig. 1.

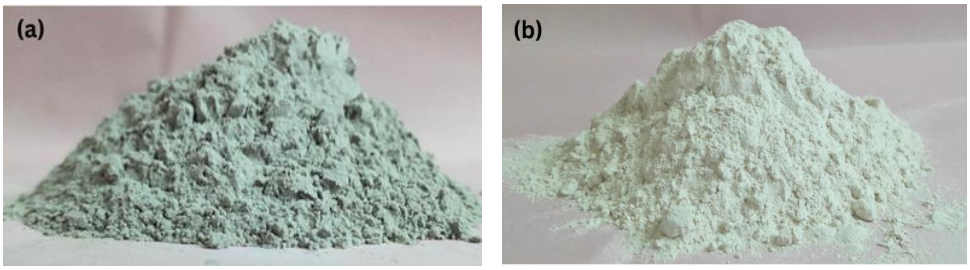

Fig. 1. Visual appearance of precursors (a) GGBFS (b) GP

The chemical compositions of GGBFS and GP are presented in Table 1, which shows their major oxide constituents. Table 2 provides the physical properties of GGBFS and GP, including their densities and Blaine surface areas, which are crucial parameters affecting their reactivity and water demand in the mixtures.

Table 1. Chemical composition of precursors

%	CaO	SiO_2	Al_2O_3	Fe_2O_3	K_2O	Na_2O	MgO	SO_3	LOI
GGBFS	43.1	41.2	6.99	2.9	0.33	0.5	4.9	0.25	0.03
GP	8.31	70.97	1.36	0.47	0.56	14.72	2.41	0.34	0.79

Table 2. Physical properties of precursors

	GGBFS	GP
Bulk density (kg/m^3)	2951	2533
Specific surface area (m^2/kg)	237.1	280.8

The particle size distribution of GGBFS and GP was determined using a laser diffraction analyzer (Cilas 1090), which provides detailed information on particle size by measuring the angle and intensity of light scattered by particles in suspension. This method allows for precise determination of particle size distribution across a wide range of sizes, ensuring the reliability of the data presented. Fig. 2 illustrates the particle size distributions of GGBFS and GP, offering insights into their fineness and potential packing behavior within the geopolymer matrix The particle size distribution of GGBFS ranges from 1.65 µm (d10) to 56.16 µm (d90), meaning that 10% of GGBFS particles are finer than 1.65 µm, and 90% are finer than 56.16 µm. This indicates a broader range of particle sizes, which can contribute to a denser microstructure due to improved packing efficiency. In contrast, the GP's particle size distribution is more uniform, ranging from 4.18 µm (d10) to 68.37 µm (d90), with a median particle size of 18.55 µm. This distribution suggests different mechanical performance characteristics, as the uniformity of GP may influence the reactivity and strength development differently from GGBFS.

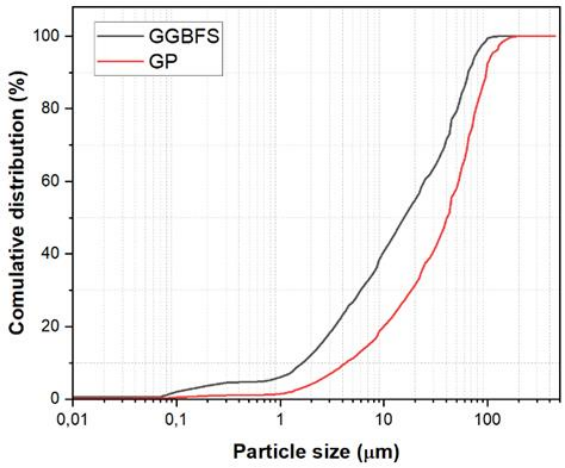

Fig. 2. Particle size distribution of precursors

The broader particle size distribution observed in GGBFS offers the potential for a denser microstructure due to better packing efficiency. When particles of varying sizes are present, smaller particles can fill the voids between larger particles, leading to a more compact arrangement and reducing the overall porosity of the material [40], [41]. This reduction in porosity is directly correlated with increased compressive strength, as the denser structure can better resist the applied loads without fracturing [42]. Additionally, a well-packed microstructure may also contribute to improved durability by reducing the permeability of the geopolymer [43]. On the other hand, the more uniform particle size distribution of GP might lead to different mechanical performance characteristics. While the uniformity in size can promote more consistent reactivity throughout the matrix, it may also result in a less dense microstructure compared to GGBFS if the packing is not optimized. This could lead to higher porosity and potentially lower compressive strength

[44]. However, the use of a uniform particle size distribution can also be advantageous in controlling the workability of the geopolymer mixture, as it may prevent excessive segregation or bleeding, ensuring a more homogenous mixture that can be easily placed and compacted.

The alkaline activation of the precursors was achieved using a combination of sodium hydroxide (NaOH) and sodium silicate (Na_2SiO_3) solutions. NaOH was provided by the SPECILAB laboratory, distributed by the company PROCHIMA SIGMA located in Tlemcen, Algeria, with a density 2130 kg/m^3 and a purity of 99%. NaOH solution was prepared at a concentration of 10M, while Na_2SiO_3 solution contained 26% SiO_2 and 8% Na_2O by mass. The chemical properties of sodium silicates are presented in Table 3.

Table 3. Characteristics of sodium silicates used

Parameter	Composition
SiO_2 (%)	26
Na_2O (%)	8
pH	13.01
Density at 20° C	1,53
Concentration (%)	45
SiO_2/Na_2O	3.25

These activators were combined in a ratio of Na_2SiO_3 to NaOH of 3:1 to provide the optimal alkalinity and silica content for geopolymerization. The sand used in this study was sourced from the Oued Souf dunes in Algeria. This sand is characterized by its high silica content and rounded, smooth-surfaced grains, making it ideal for mortar applications. Its physical properties include an apparent density of 2623 kg/m^3, a fineness modulus of 1.99, and a sand equivalent of 86.49%. The particle size distribution of the sand is well-graded, with a maximum grain size not exceeding 4.0 mm, ensuring good workability and compact packing in the mortar matrix.

2.2. Methodology

One common statistical method for designing and optimizing experiments is the central composite design, or CCD. This research used a two-pronged approach to examine the impact of GP content (0%-30%) and Ac/Pr ratio (0.65, 0.7, and 0.75) on geopolymer mortar characteristics. With its capacity to fit quadratic models and capture higher-order interactions between the components, the CCD efficiently minimizes the number of experimental runs, making it an attractive choice. As shown in Table 4, the CCD for this investigation comprised nine distinct formulations.

Slump, compressive strength, and water-accessible porosity were the intended outcomes of the nine strategic formulations' data collection efforts. The purpose of analyzing these reactions was to shed light on how the input parameters, individually and in combination, affected the physical and mechanical characteristics of the manufactured mortars.

The optimal mix design derived from the desirability analysis, prediction expressions, response surface profiler, and analysis of variance (ANOVA) results are the products of this statistical methodology. To optimize the geopolymer mortar formulation for the intended mechanical and physical properties, these outputs offer useful insights into the effects of the input parameters and how they interact with the responses.

Table 4. Experimental runs and mix composition using CCD

Mix ID	GP (%)	Ac/Pr	GGBFS (kg/m³)	GP (Kg/m³)	Sodium silicate (kg/m³)	NaOH (kg/m³)	Sand (kg/m³)
M1	0	0.65	587,65	0,00	286,48	95,49	
M2	15	0.65	499,50	88,15	286,48	95,49	
M3	30	0.65	411,36	176,30	286,48	95,49	
M4	0	0.7	587,65	0,00	308,52	102,84	
M5	15	0.7	499,50	88,15	308,52	102,84	1250
M6	30	0.7	411,36	176,30	308,52	102,84	
M7	15	0.75	499,50	88,15	330,55	110,18	
M8	30	0.75	411,36	176,30	330,55	110,18	
M9	0	0.75	587,65	0,00	330,55	110,18	

2.3. Sample Preparation

GGBFS, GP, and sand have been carefully weighed according to the proportions specified in the previous formulations. These dry components have been thoroughly mixed to ensure their homogeneity. At the same time, an alkaline activator solution was prepared by mixing NaOH and Na_2SiO_3 solutions in a ratio of 1 to 3 to ensure uniformity and consistency in the geopolymerization reaction [45], [46]. Then the dry mixture was combined with the activator solution using a mechanical mixer for 90 seconds, thus giving rise to a homogeneous geopolymer paste. This preparation was then poured into a spreading cone to evaluate its maneuverability before being carefully poured into molds of dimensions 4x4x4 cm³ (Fig. 3). To facilitate geopolymerization reactions, the specimens were demolded after one day and transferred to a controlled environment, kept at a temperature of 20 ± 2 °C and a relative humidity of ≥ 95%, where they remained until they reached the desired test age.

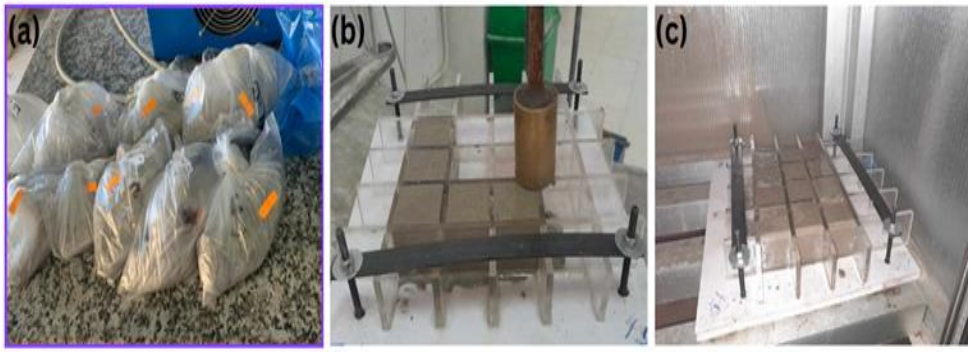

Fig. 3. Preparation of geopolymer mortars (a) preparation of raw materials (b) molding (c) curing

2.4. Experimental Tests

This study conducted three key tests to evaluate the performance of the slag-based geopolymer mortars: slump test, compressive strength test, and water accessible porosity

test. Each test was performed three times according to standard procedures to ensure reliability and reproducibility of results.

The slump test was carried out to assess the workability of the fresh geopolymer mortar mixtures (Fig. 4). The test was performed in accordance with ASTM standard [47] using a mini-slump cone. The cone, with dimensions of 70 mm top diameter, 100 mm base diameter, and 50 mm height, was filled with the fresh mortar and lifted vertically. The resulting spread of the mortar was measured in two perpendicular directions, and the average value was recorded as the slump flow.

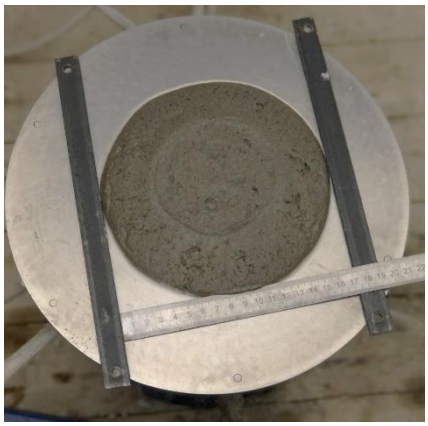

Fig. 4. Slump test of geopolymer mortar

The compressive strength of the hardened geopolymer mortars was determined following the procedures outlined in EN 196-1 standard [48] after 28 days of curing (Fig. 5). The specimens were subjected to uniaxial compression using a hydraulic testing machine. The load was applied at 5 mm/min displacement rate on a 400 kN compression capacity testing machine until failure occurred. The maximum load sustained by each specimen was recorded, and the compressive strength was calculated by dividing this load by the cross-sectional area of the specimen.

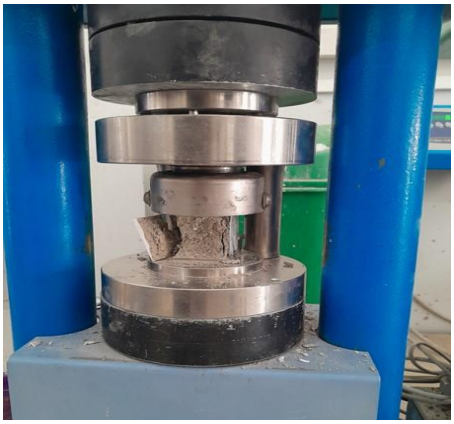

Fig. 5. Compressive strength test of geopolymer mortar

The water accessible porosity of the hardened geopolymer mortars was determined using the vacuum saturation method, following the principles outlined in NBR 9778 [49]. The specimens were first oven-dried to constant mass, then placed in a vacuum chamber and

saturated with water under vacuum conditions. The saturated surface-dry mass and the submerged mass of the specimens were then measured. The water accessible porosity was calculated as the ratio of the volume of water absorbed to the total volume of the specimen, expressed as a percentage. This test provides insights into the porosity and the ability of geopolymer mortars to absorb water, which influences their durability and transport properties. The results from these standardized tests form the basis for optimizing the geopolymer mortar formulations and understanding the effects of GP content and Ac/Pr ratio on the material's performance.

3. Results and Discussion

3.1. Analysis of Variance

The analysis of variance (ANOVA) elucidates the effects of GP content and Ac/Pr on the properties of geopolymer mortars (Table 5). For compressive strength, the ANOVA reveals that the model is statistically significant, with the intercept, Ac/Pr, GP^2, and Ac/Pr^2 all being significant factors ($p<0.05$). The linear effect of GP and the interaction term GP*Ac/Pr are not statistically significant. This suggests that the activator-to-precursor ratio has a strong influence on compressive strength, both in its linear and quadratic terms. The slump model shows significance for both GP and Ac/Pr linear effects, as well as the intercept, while the quadratic terms and interaction term are not statistically significant. For porosity, the model indicates significance for the intercept, GP^2, and Ac/Pr^2, while the linear terms and interaction are not statistically significant.

Table 5. ANOVA metrics

	Intercept	GP	Ac/Pr	GP*Ac/Pr	GP^2	Ac/Pr^2
Compressive Strength	46.7022	-0.74	2.60333	1.095	-5.04333	-4.65333
p-values	0,03	0.3376	0.0279	0.2627	0.0207	0.0257
Slump	15.5	0.916667	1.83333	-0.125	0.25	-1.57E-16
p-values	0,01	0.0154	0.0021	0.6163	0.4883	1.0000
Porosity	15.1967	-0.56	0.178333	-0.4275	1.65	3.195
p-values	0,028	0.1238	0.5473	0.2774	0.0364	0.0060

The perturbation plots (Fig. 6) offer a visual representation of these effects. For slump, both GP and Ac/Pr demonstrate positive effects, with Ac/Pr showing a stronger linear influence as indicated by its steeper slope. GP exhibits a slight curvature, suggesting a minor quadratic effect, though this is not statistically significant according to the ANOVA. The compressive strength plot reveals quadratic effects for both GP and Ac/Pr, with optimal points near the center of the design space. The Ac/Pr curve shows a more pronounced quadratic effect, consistent with its significant linear and quadratic terms in the ANOVA. The GP curve also displays a quadratic trend, but with a lower optimal point, indicating that increasing GP beyond a certain point may decrease strength. The porosity plot demonstrates strong quadratic effects for both factors, forming U-shaped curves. The Ac/Pr curve shows a more pronounced effect, especially at the extremes of the range, while the GP curve has a shallower U-shape, indicating a less severe impact on porosity at the extremes. Both factors appear to have an optimal point (minimum porosity) near the center of the design space.

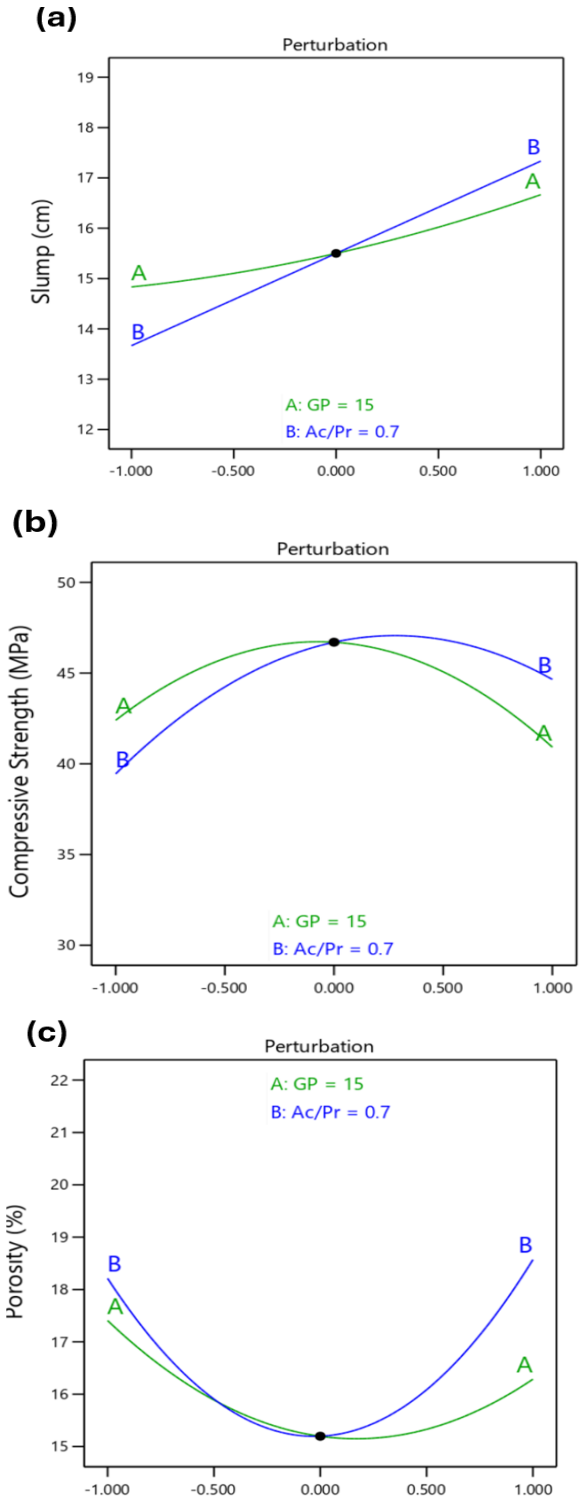

Fig. 6 Perturbation plots of (a) slump (b) compressive strength (c) porosity

These results collectively suggest that slump is positively influenced by both GP content and Ac/Pr ratio, with Ac/Pr having a stronger linear effect. Compressive strength is optimized at moderate levels of both GP and Ac/Pr, with significant quadratic effects. Porosity is minimized at moderate levels of both factors, with strong quadratic effects, particularly for Ac/Pr. These findings highlight the complex interplay between GP content and Ac/Pr ratio in determining the properties of the geopolymer mortar

3.2. Response Surface Plots

3.2.1 Slump

The contour and iso-response surface plots for the slump response (Fig. 7) provide valuable insights into the effects of GP and Ac/Pr contents on the workability of the geopolymer mortar. The contour plot, represented by the 2D color-coded image, shows a clear gradient from blue to red, indicating an increase in slump values from approximately 13 cm to 18.5 cm across the experimental range. This gradient demonstrates that both GP content and Ac/Pr ratio have significant influences on the slump of the geopolymer mortar. The iso-response curves, represented by the contour lines, further illustrate this relationship. The upward sloping nature of these curves from left to right indicates that increasing both GP content and Ac/Pr ratio generally leads to higher slump values, suggesting improved workability of the mixture. The 3D surface plot corroborates these observations, showing a rising plane from the lower left corner to the upper right corner of the plot.

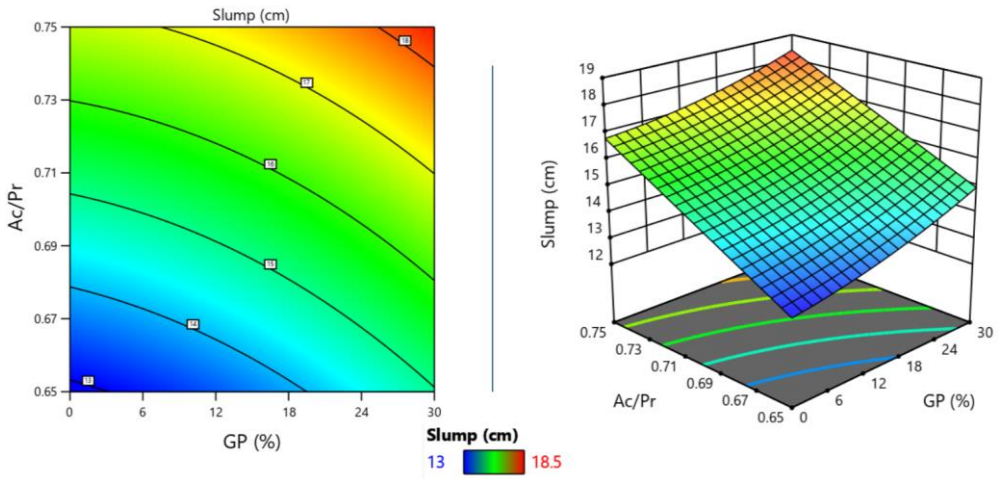

Fig. 7. Contour plot and iso-response curve of slump response

This three-dimensional representation clearly visualizes the combined effects of GP and Ac/Pr on slump. The steeper gradient along the Ac/Pr axis compared to the GP axis suggests that the Ac/Pr ratio has a more pronounced effect on slump than the GP content. This is evident from the more rapid color change and steeper slope in the Ac/Pr direction. The highest slump values, represented by the red region in the contour plot and the peak of the 3D surface, are achieved at high levels of both GP content and Ac/Pr ratio. This indicates that increasing both factors simultaneously lead to the most significant improvement in workability. Conversely, the lowest slump values, shown in blue, occur at low levels of both factors. The relatively linear nature of the iso-response curves suggests that there is limited interaction between GP and Ac/Pr in their effects on slump. Instead, they appear to have additive effects, with each factor independently contributing to increased workability. This linear trend aligns with the earlier ANOVA results, which

showed significant linear effects for both factors on slump. The continuous increase in slump with increasing GP content can be attributed to the spherical nature of GP particles, which may enhance the flowability of the mixture [30]. The positive effect of increasing Ac/Pr ratio on slump is likely due to the higher liquid content in the mixture, which naturally improves workability.

3.2.2 Compressive Strength

The contour and iso-response surface plots for compressive strength (Fig. 8) reveal a complex relationship between GP and Ac/Pr, and the mechanical performance of the geopolymer mortar. The plots exhibit a distinct dome-shaped surface, indicating the presence of an optimal region for compressive strength. This optimal zone is centered around 14.2% GP content and 0.71 Ac/Pr ratio, where the highest compressive strength values are achieved. The contour plot shows concentric elliptical patterns, with the peak strength region colored in red at the center. As we move away from this optimal point, the colors transition through yellow and green to blue, representing a gradual decrease in compressive strength. This pattern suggests that both excess and insufficient amounts of GP or Ac/Pr can lead to reduced strength performance.

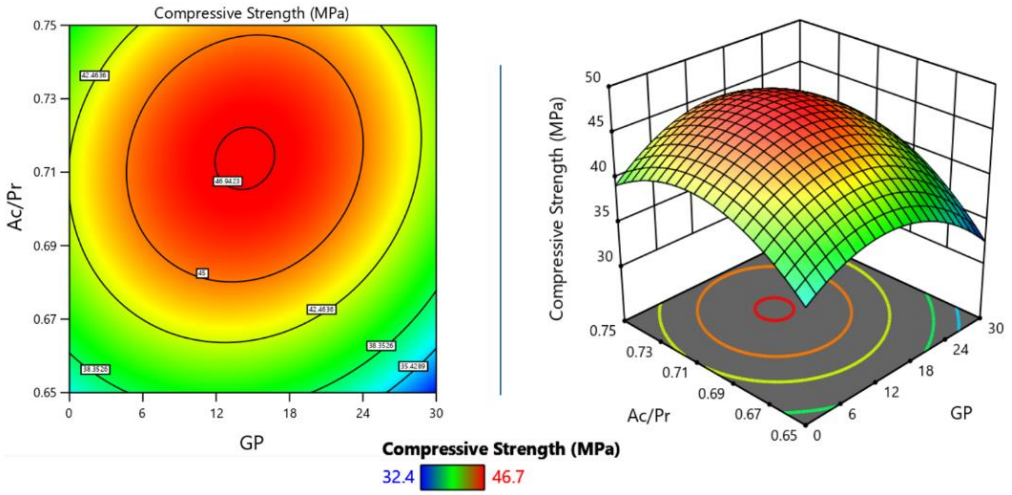

Fig. 8. Contour plot and iso-response curve of compressive strength response

The 3D surface plot further emphasizes this quadratic relationship, displaying a clear peak in the central region. The curvature of the surface is more pronounced along the Ac/Pr axis compared to the GP axis, indicating that the Ac/Pr ratio has a more significant impact on compressive strength than GP content. This observation aligns with the ANOVA results, which showed that both linear and quadratic terms for Ac/Pr were statistically significant.

The existence of an optimal region can be explained by considering the effects of GP and Ac/Pr on the geopolymerization process and the resulting microstructure. The incorporation of GP introduces additional silica into the system, which can modify the Ca/Si and Si/Al ratios of the binder phase. At the optimal GP content (around 14%), there is likely an ideal balance between these ratios that promotes the formation of a strong and stable calcium aluminosilicate hydrate (C-A-S-H) gel structure.

The C-A-S-H gel, which is the primary binding phase in slag-based geopolymers, is sensitive to the Ca/Si ratio. As GP content increases, it initially enhances the Si/Al ratio, potentially leading to a more polymerized and stronger gel structure [24]. However, beyond the optimal point, excessive silica may disrupt the balance, possibly leading to unreacted

particles or a weaker gel structure, thus explaining the decrease in strength at higher GP levels.

The Ac/Pr ratio plays a crucial role in providing the alkaline environment necessary for the dissolution of slag and GP particles and subsequent geopolymerization. The optimal Ac/Pr ratio of 0.71 likely represents the point where there is sufficient alkaline activator to promote adequate dissolution and reaction of the precursors, without excess liquid that could lead to increased porosity and reduced strength.

The significant quadratic effects observed in the ANOVA for both GP^2 and Ac/Pr^2 support the curvilinear relationship seen in the response surface plots. These quadratic effects indicate that both factors have an optimal range, beyond which their benefits diminish or become detrimental to strength development. The interaction between GP content and Ac/Pr ratio, while not statistically significant according to the ANOVA, may still play a subtle role in determining the exact shape and position of the optimal region. This interaction could be related to how the alkaline activator interacts with the different proportions of slag and GP, affecting the dissolution rates and the formation of reaction products.

3.2.3 Porosity

The contour plot and iso-response surface plot for porosity (Fig. 9) reveal a complex relationship between GP content, Ac/Pr ratio, and the resulting porosity of slag-based geopolymer mortars. The optimal region for minimizing porosity is observed corresponding to 17% GP and 0.7 Ac/Pr ratio, where porosity values reach their minimum of around 15%. As we move away from this optimal region, porosity increases, reaching a maximum of about 21.5% at high GP content and high Ac/Pr ratio.

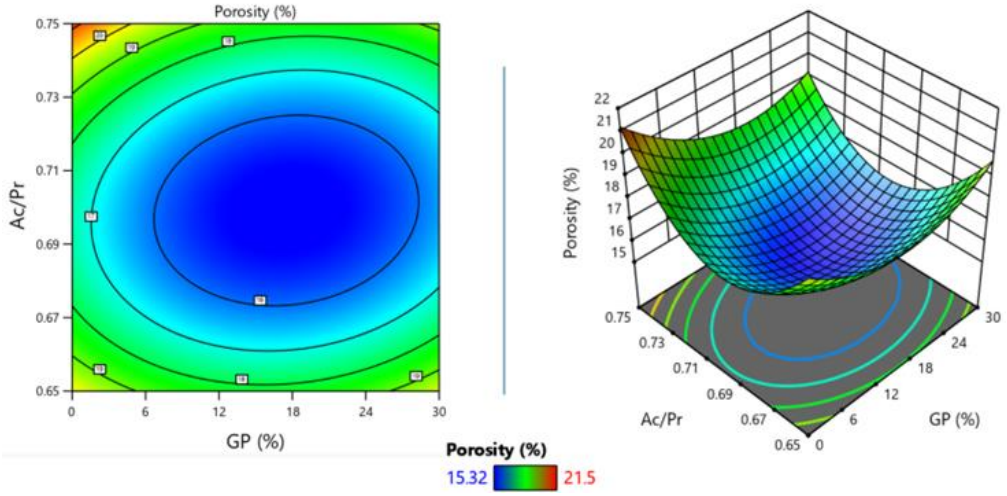

Fig. 9. Contour plot and iso-response curve of porosity response

The interaction between GP content and Ac/Pr ratio is evident from the non-linear contour lines and curved surface in the 3D plot. This interaction suggests that the impact of GP on porosity is influenced by the Ac/Pr ratio, and vice versa. At lower Ac/Pr ratios, the effect of increasing GP content on porosity is less pronounced, possibly because there is insufficient activator to fully react with the glass powder, leading to a more compact structure with unreacted GP particles filling voids. Conversely, at higher Ac/Pr ratios, increasing GP content has a more significant effect on porosity, as there is more liquid available to react with the GP, potentially creating a more open pore structure.

The optimal region of low GP content and low Ac/Pr ratio likely represents a balance where there is sufficient activator to react with the slag precursor without excess liquid, resulting in a denser C-A-S-H gel network with lower porosity. In this region, the formation of C-A-S-H gel is maximized, and the development of voids is minimized. As we move away from this optimal region, either by increasing GP content or Ac/Pr ratio, the balance is disrupted, leading to increased porosity through different mechanisms. Higher GP content may result in more unreacted particles and a less interconnected C-A-S-H gel network, while higher Ac/Pr ratios may lead to excess liquid that creates additional voids upon evaporation, thus increasing the absorption capacity of mortars. This phenomenon can be attributed to the formation of capillary pores as the liquid phase evaporates, leaving behind voids that contribute to a more porous microstructure. The study by Das et al. [50]emphasizes that elevated water absorption values are typically correlated with increased surface porosity. This surface porosity not only influences the immediate physical and mechanical properties of the mortar but also has long-term implications on its durability.

At higher Ac/Pr ratios, the increase in porosity is accompanied by a decrease in compressive strength. This inverse relationship can be explained by the fact that the presence of more voids within the mortar matrix reduces the density and integrity of the structure, leading to weaker mechanical performance. As the porosity increases, the material's ability to bear loads diminishes, which directly affects its compressive strength. Moreover, the interconnected pore network created by the excess liquid not only weakens the material but also makes it more susceptible to the ingress of harmful agents, further compromising its structural capacity over time.

3.3. Model Diagnostics

To create thorough regression models for a range of response variables, the central composite design was used. Strong predictive performance is shown in the fit summary for these models (Table 6), where high R-squared values, ranging from 0.96 to 0.98, indicate excellent model fit. The models are assessed using the mean response values as baseline standards. Furthermore, for all replies, the appropriate precision values—which evaluate the signal-to-noise ratio—are significantly higher than the suggested cutoff point of 4. This suggests that the models have a strong capacity to consistently navigate the design space, indicating that they are appropriate for forecasting how GP and Ac/Pr would affect the properties of mortar.

Table 6. Fit summary

Response	Mean	R^2	Adjusted R^2	Adeq. Precision
Slump (cm)	15.67	0.98	0.93	15.01
Compressive strength (MPa)	40.24	0.95	0.86	10.87
Porosity (%)	18.43	0.96	0.89	11.4

The model's accurate predictions across the range of each response variable are shown in the actual vs predicted plots (Fig. 10). The model's predictions and the actual data are well aligned in these graphs, demonstrating the validity and dependability of the regression models created with the central composite design. This alignment is further supported by the strong R-squared values, which demonstrate the models' capacity to represent the underlying relationships between the response variables and the input factors.

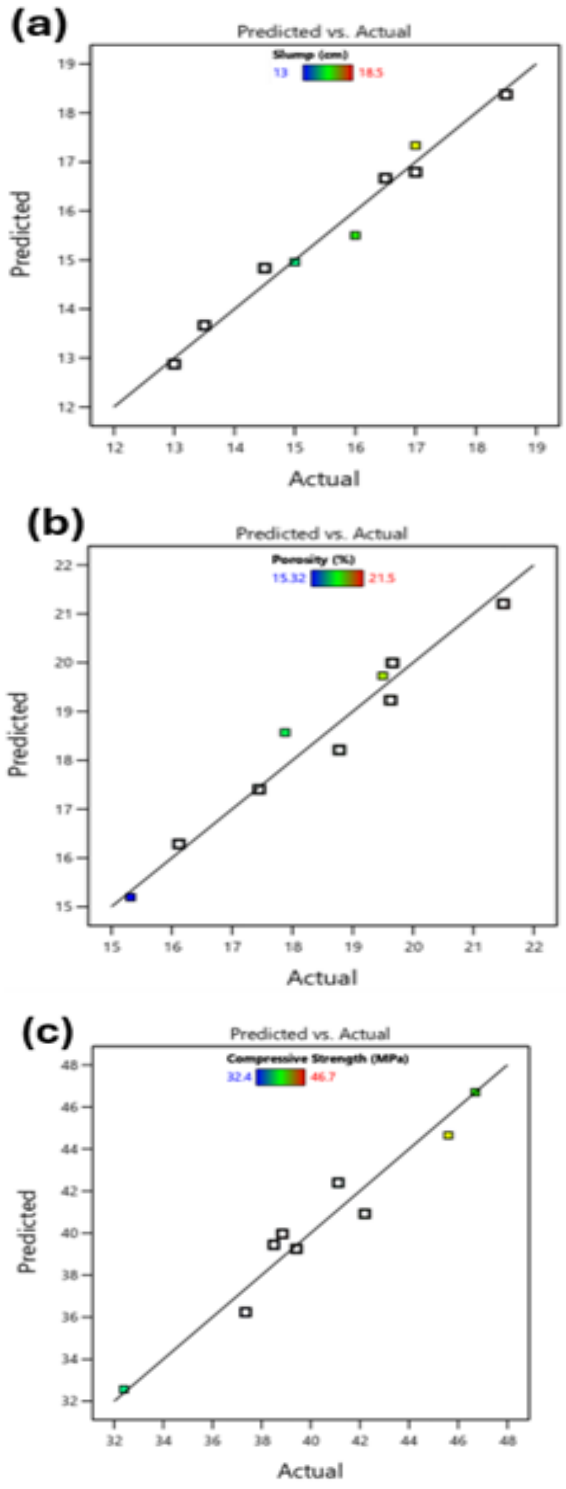

Fig. 10. Actual by predicted plots of (a) slump (b) compressive strength (c) porosity

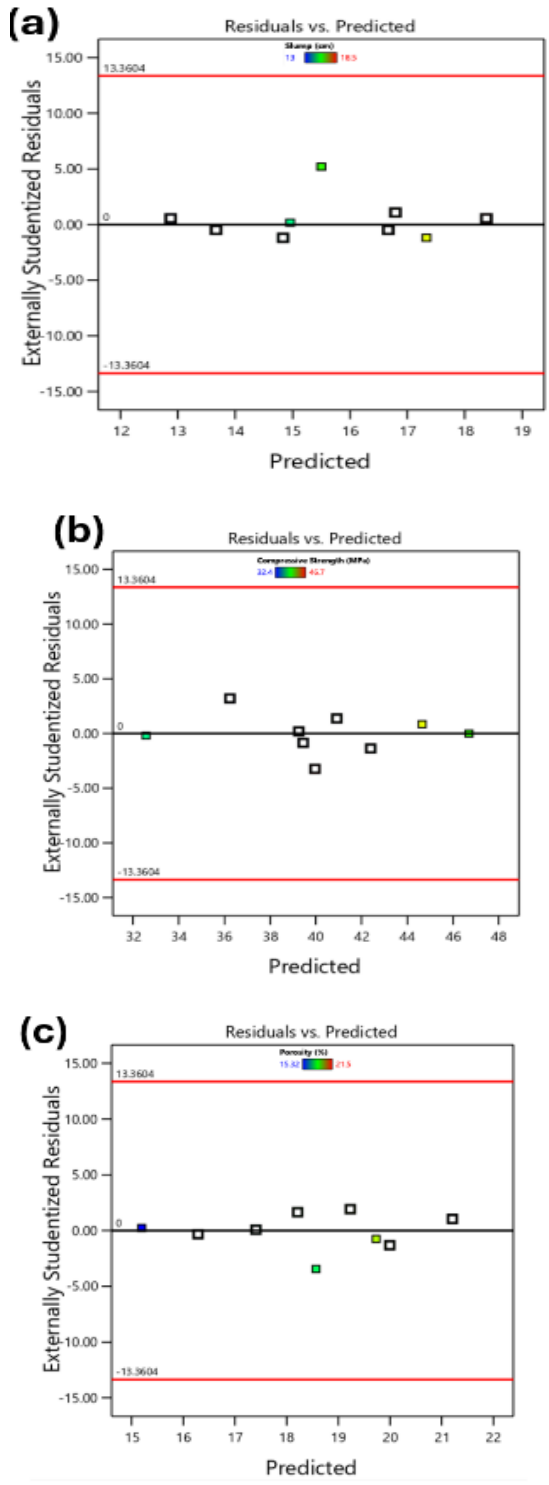

Fig. 11. Residual vs predicted plots of (a) slump (b) compressive strength (c) porosity

Furthermore, the residual plots (Fig. 11) show a random residual dispersion around zero, suggesting that the models have successfully and fairly accounted for the data's variability. This randomness shows that all systematic patterns have been described by the regression models and that the models are well-specified. This demonstrates how well the models capture the important correlations between the response and input variables. The central composite design was used to create all-encompassing regression equations for porosity, compressive strength, and slump. The complex relationship between GP content and Ac/Pr ratio is described by the slump equation Eq. (1), a model of second-order polynomials. The link between Ac/Pr and GP, which includes their interaction, is revealed by the compressive strength model (Eq. (2)). The impact of Ac/Pr and GP on porosity is illustrated by the porosity equation, Eq. (3).

$$Slump\ (cm) = 15.5 + 0.92 * GP + 1.83 * Ac/Pr - 0.125 * GP * Ac/Pr + 0.25 * GP^2 - 1.57e\text{^}(-16) * Ac/Pr^2 \quad (1)$$

$$Compressive\ strength\ (MPa) = 46.7 - 0.74 * GP + 2.6 * Ac/Pr + 1.09 * GP * Ac/Pr - 5.04 * GP^2 - 4.65 * Ac/Pr^2 \quad (2)$$

$$Porosity\ (\%) = 15.1967 - 0.56 * GP + 0.178333 * Ac/Pr - 0.4275 * GP * Ac/Pr + 1.65 * GP^2 + 3.195 * Ac/Pr^2 \quad (3)$$

3.4. SEM/EDX Analysis

Microstructural analysis was conducted using SEM to investigate the morphological characteristics and compositional nature of the geopolymer matrices. Fig. 12 presents SEM micrographs of two key specimens: M1 (0% GP and 0.65 Ac/Pr) and M5 (15% GP and 0.7 Ac/Pr). The SEM image of specimen M1 reveals a heterogeneous microstructure characterized by the presence of C-A-S-H gels, which appear as the predominant binding phase. These C-A-S-H formations are evident as dense, amorphous regions within the matrix. The microstructure also exhibits notable features such as pores and microcracks. The presence of pores, varying in size and distribution, indicates the complex nature of the geopolymerization process and its impact on the material's porosity. In contrast, the SEM micrograph of specimen M5 demonstrates a more refined and homogeneous microstructure. The incorporation of 15% GP and the slightly higher Ac/Pr ratio (0.7) appear to have resulted in a denser matrix with fewer visible pores and cracks. The C-A-S-H gel formation in M5 seems more uniform and interconnected, suggesting a more complete geopolymerization reaction. This observation is consistent with the work of Zhang et al. [51] who found that the incorporation of GP in slag based-geopolymers leads to a more compact microstructure.

To confirm the chemical composition of the binding phases, EDX spectroscopy was performed on three distinct points within the samples, as indicated in Fig. 13. The EDX spectra reveal the elemental composition of the C-A-S-H gels, which are primarily composed of O, Si, Al, Na, and Ca, with minor amounts of Mg. Spectrum (1) shows a high content of Si (21.05%) and O (38.98%), indicative of the silica-rich nature of the geopolymer gel. The presence of Al (5.81%) and Na (11.53%) confirms the formation of sodium aluminosilicate hydrate (N-A-S-H) gels, which are typical in geopolymer systems. The notable Ca content (9.99%) suggests the coexistence of C-A-S-H gels, likely due to the calcium-rich nature of the slag precursor. These findings are in line with recent research by Wang et al. [52], who observed similar elemental distributions in slag-based geopolymers and highlighted the importance of Ca in forming robust C-A-S-H networks. Spectra (2) and (3) show similar elemental compositions but with varying proportions. The increase in Ca content from spectrum (1) to (2) (14.23%) and (3) (21.23%) indicates a higher degree of C-A-S-H gel formation in these regions. This variation in Ca content

across different points suggests a heterogeneous distribution of reaction products within the geopolymer matrix.

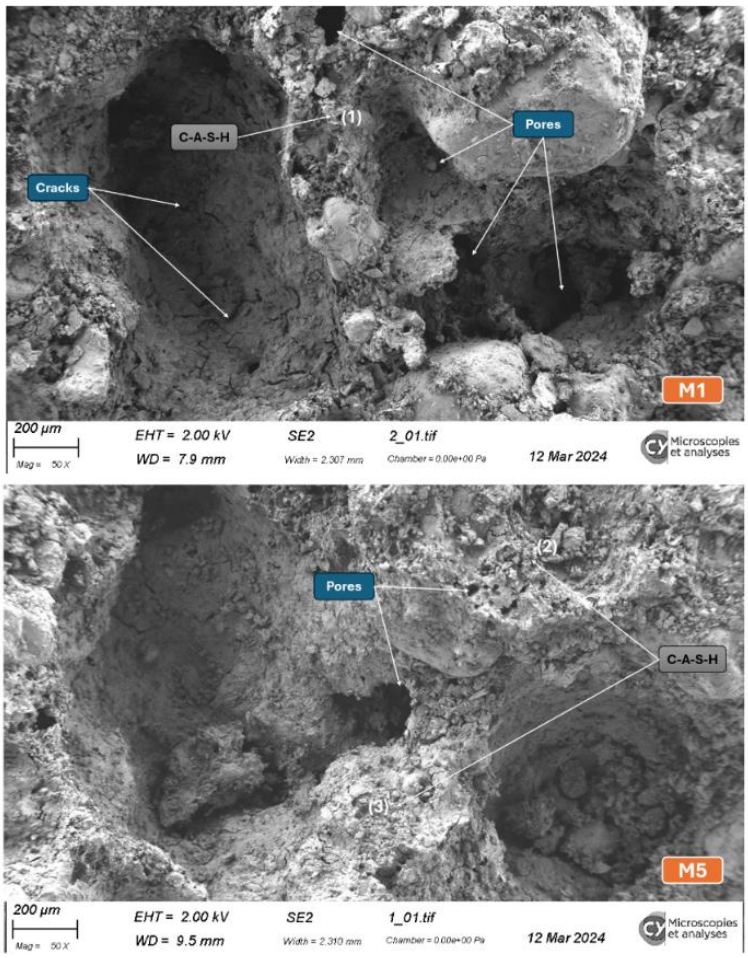

Fig. 12. Scanning electron microscopy micrographs of key mixtures M1 and M5

The presence of Mg in all spectra (1.63%, 0.77%, and 3.06% respectively) can be attributed to the MgO content in the original slag, which has been incorporated into the gel structure during geopolymerization, a phenomenon also reported by Chitsaz et al. [53] and Jin et al. [54] in their study of alkali-activated slag systems. The EDX results corroborate the visual observations from the SEM images, confirming the formation of C-A-S-H gels as the primary binding phase in these slag-based geopolymers. The incorporation of GP in specimen M5 appears to have promoted a more uniform distribution of these gels, resulting in a denser and potentially more durable microstructure. This is consistent with findings by Varma et al. [55] , who demonstrated that the addition of GP in geopolymers leads to a more homogeneous gel formation due to the pore-filling effect of fine glass particles and enhanced dissolution of silica.

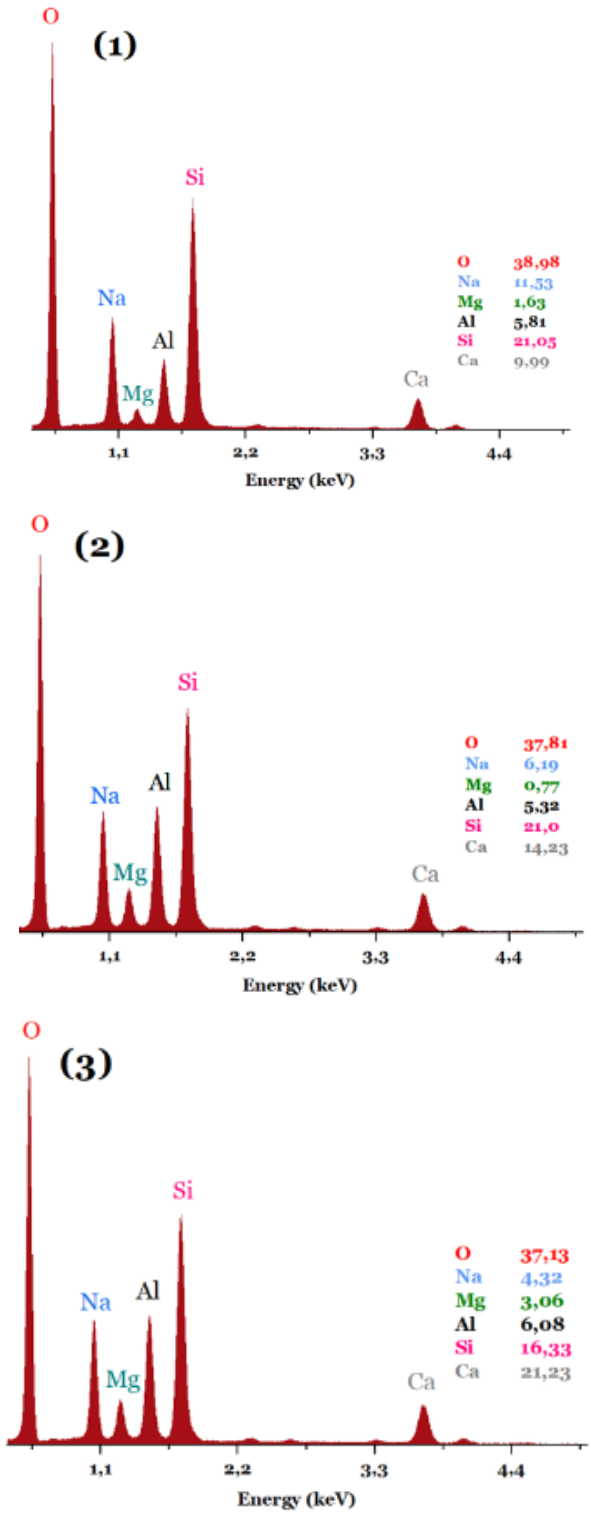

Fig. 13. EDX spectra of identified points in key mixtures M1 and M5

3.5. Optimization

Using a desirable approach, the formulation of the geopolymer mortar was fine-tuned to achieve maximum slump and compressive strength with minimum porosity. Considering their weights and relative importance, the desirability method enables the optimization of numerous responses at once (Table 7). Level 5 weight 0.5 was given to compressive strength because of its crucial significance in determining the geopolymer system's long-term structural performance. Since the slump is so important for making sure the mortar is workable, it was given a weight of 0.3 and an importance level of 5. As a measure of durability that does not have an immediate effect, porosity was given the lowest weight of 0.2 and the fifth most important level.

Table 7. Criteria of desirability analysis

Name	Goal	Lower Limit	Upper Limit	Lower Weight	Upper Weight	Importance
Compressive Strength (MPa)	maximize	32.4	46.7	0.5	1	5
Slump (cm)	maximize	13	18.5	0.3	1	5
Porosity (%)	minimize	15.32	21.5	1	0.2	5

The optimal formulation that comes from the desirability analysis may be easily seen in Fig. 14's contour and iso-response plots. A GP content of 18.2% and an Act/Pr ratio of 0.72 are recommended by the ideal solution.

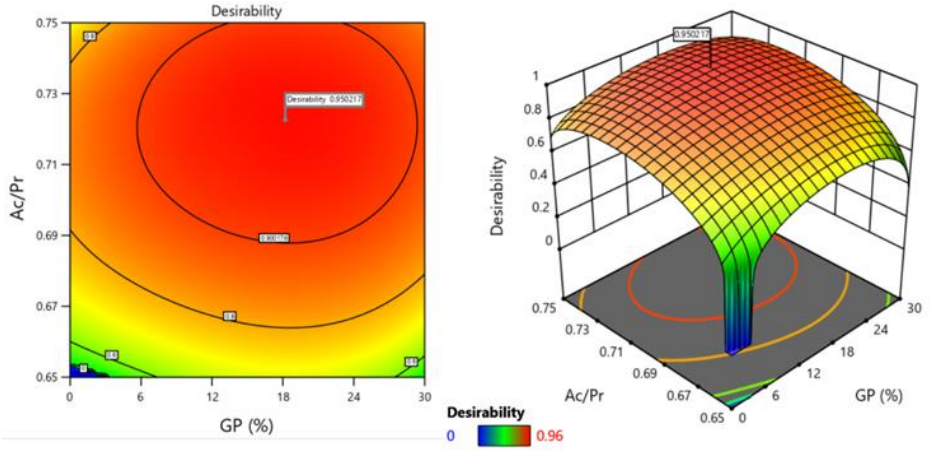

Fig. 14. Contour plot and iso-response curve of optimized formulation

For this optimized mixture, the predicted outcomes are shown in Fig. 15: a slump of 16.53 cm, a compressive strength of 46.64 MPa, and a porosity of 15.85%. A high level of satisfaction with the goals and importance levels assigned to each answer variable is shown by the total desirability value obtained of 0.95.

The point prediction (Table 8) provides valuable statistical information about the predicted responses for the optimized formulation of the slag-based geopolymer mortar. The predicted mean compressive strength of 46.64 MPa, slump of 16.52 cm, and porosity of 15.85% all demonstrate favorable performance characteristics. The relatively small standard deviations for each property (1.59204 MPa, 0.448764 cm, and 0.645938% respectively) indicate good consistency in the mix. The narrow 95% confidence intervals for all three properties suggest high precision in the predictions. The wider 95% tolerance intervals for 99% of the population account for natural variability between samples, with

compressive strength ranging from 32.14 to 61.14 MPa, slump from 12.44 to 20.61 cm, and porosity from 9.96% to 21.73%.

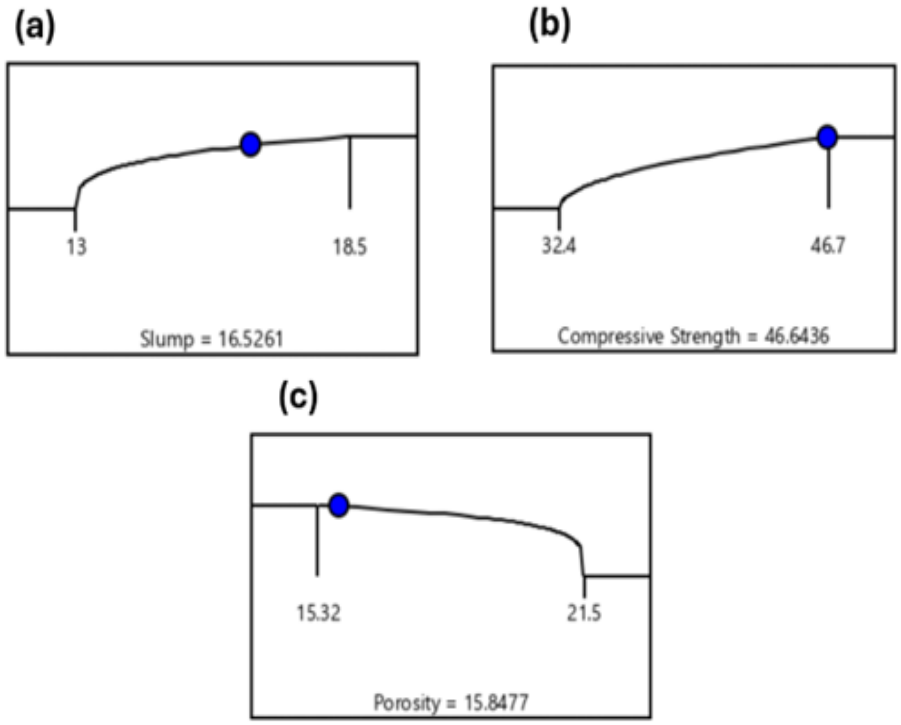

Fig. 15. Predicted responses of (a) slump (b) compressive strength (c) porosity

The relatively narrow confidence intervals for all responses indicate good precision in the predictions, suggesting the model is well-fitted to the experimental data. The small standard deviations, particularly for slump and porosity, suggest that the optimized formulation should produce consistent results in terms of workability and microstructure. The predicted compressive strength is robust, with even the lower bound of the tolerance interval (32.14 MPa) being acceptable for many applications. This indicates that the optimized mix is likely to meet strength requirements consistently.

Table 8. Point prediction

Response	Compressive Strength (MPa)	Slump (cm)	Porosity (%)
Predicted Mean	46.6436	16.5261	15.8477
Predicted Median	46.6436	16.5261	15.8477
Std Dev	1.59204	0.448764	0.645938
SE Mean	1.07329	0.302541	0.435469
95% CI low for Mean	43.2279	15.5633	14.4619
95% CI high for Mean	50.0593	17.4889	17.2336
95% TI low for 99% Pop	32.1433	12.4387	9.96452
95% TI high for 99% Pop	61.1439	20.6134	21.7309

The predicted slump range suggests good workability, with even the extremes of the tolerance interval (12.44 to 20.61 cm) being manageable for most construction applications. While the mean porosity prediction is good, the wider tolerance interval reflects the inherent variability in this property. This variability should be considered when designing for applications where porosity is critical. The fact that all responses have reasonably narrow prediction ranges suggests that the optimized formulation is robust and should perform consistently across batches.

4. Conclusions

This comprehensive investigation into the impact of GP incorporation and Ac/Pr ratio on slag-based geopolymer mortars has produced several key insights:

- The use of central composite design and response surface methodology proved effective in modeling and optimizing the complex interactions between input factors (GP content and Ac/Pr ratio) and response variables (slump, compressive strength, and porosity). These approaches provided reliable predictive models for each response variable, evidenced by high R-squared values (ranging from 0.95 to 0.98) and narrow confidence intervals, laying a strong foundation for future geopolymer optimization studies.
- GP content and Ac/Pr ratio were found to significantly influence the properties of slag-based geopolymer mortars, with their effects varying across different performance metrics. This emphasizes the necessity of precisely controlling these variables to achieve targeted performance outcomes.
- Workability, as measured by slump, generally improved with increased GP content and Ac/Pr ratio, likely due to the spherical nature of glass particles and the higher content of activators. This has practical implications for improving the placement and compaction of geopolymer mortars in construction settings.
- Compressive strength displayed a quadratic relationship with both factors, reaching its peak at moderate GP content and Ac/Pr ratios, indicating an optimal formation of C-A-S-H gel structures. The highest compressive strength was achieved with 14.2% GP and a 0.71 Ac/Pr ratio, demonstrating that these optimized mixes can meet or exceed the strength requirements of many construction applications.
- Porosity was minimized at moderate levels of both factors, with notable quadratic effects, especially for the Ac/Pr ratio. This underlines the need for a carefully balanced mix design to achieve a dense microstructure while preserving sufficient workability.
- Microstructural analysis using SEM and EDX revealed that incorporating GP at optimal levels (e.g., specimen M5 with 15% GP) led to a more refined and homogenous microstructure with a denser C-A-S-H gel network. The EDX spectra confirmed that C-A-S-H gels were the primary binding phase, with elemental composition varying across different matrix regions. This microstructural improvement supports the observed gains in mechanical properties and reduced porosity at optimal GP content and Ac/Pr ratios.
- Desirability analysis identified an optimal formulation with 18.2% GP content and a 0.72 Ac/Pr ratio, balancing workability, strength, and porosity. The optimized mixture is predicted to yield a slump of 16.53 cm, a compressive strength of 46.64 MPa, and a porosity of 15.85%, making it well-suited for practical applications.
- The predictive models developed in this study demonstrated high accuracy and robustness, as reflected in the strong R-squared values and narrow confidence intervals.

These findings highlight the potential for using GP in slag-based geopolymer systems, contributing to more sustainable construction materials without compromising performance. The optimization approach presented offers a valuable methodology for customizing geopolymer mix designs to meet specific performance goals.

Future research should focus on long-term durability assessments of these optimized mixtures, as well as evaluating their performance under varying curing conditions and environmental exposures. Additionally, life cycle assessments could further quantify the environmental advantages of incorporating waste glass in geopolymer formulations.

Acknowledgement

The authors would like to extend their gratitude to the Civil Engineering Laboratory at the University of Bordj Bou Arreridj for their assistance in facilitating the experimental work for this study.

References

[1] Benhelal E, Zahedi G, Shamsaei Ezzatollah A, Bahadori B. Global strategies and potentials to curb CO2 emissions in cement industry. J Clean Prod. 2013 Jul;51:142-61. https://doi.org/10.1016/j.jclepro.2012.10.049
[2] Sandanayake M, Gunasekara C, Law D, Zhang G, Setunge S. Greenhouse gas emissions of different fly ash based geopolymer concretes in building construction. J Clean Prod. 2018;204:399-408. https://doi.org/10.1016/j.jclepro.2018.08.311
[3] McLellan BC, Williams RP, Lay J, Van Riessen A, Corder GD. Costs and carbon emissions for geopolymer pastes in comparison to ordinary portland cement. J Clean Prod. 2011 Jun;19(9-10):1080-90. https://doi.org/10.1016/j.jclepro.2011.02.010
[4] Davidovits J. Geopolymers and geopolymeric materials. J Therm Anal. 1989;35(2):429-41. https://doi.org/10.1007/BF01904446
[5] Krishna RS, et al. A review on developments of environmentally friendly geopolymer technology. Materialia (Oxf). 2021;20:101212. https://doi.org/10.1016/j.mtla.2021.101212
[6] Ren B, Zhao Y, Bai H, Kang S, Zhang T, Song S. Eco-friendly geopolymer prepared from solid wastes: A critical review. Chemosphere. 2021;267:128900. https://doi.org/10.1016/j.chemosphere.2020.128900
[7] Odeh A, et al. Recent progress in geopolymer concrete technology: A review. Iranian J Sci Technol Trans Civ Eng. 2024. https://doi.org/10.1007/s40996-024-01391-z
[8] Xu H, Van Deventer JSJ. The geopolymerisation of alumino-silicate minerals. Int J Miner Process. 2000;59(3):247-66. https://doi.org/10.1016/S0301-7516(99)00074-5
[9] Van Jaarsveld JGS, Van Deventer JSJ, Lorenzen L. Factors affecting the immobilization of metals in geopolymerized flyash. Metall Mater Trans B. 1998;29(1):283-91. https://doi.org/10.1007/s11663-998-0032-z
[10] Das D, Rout PK. A review of coal fly ash utilization to save the environment. Water Air Soil Pollut. 2023;234(2):128. https://doi.org/10.1007/s11270-023-06143-9
[11] Matsimbe J, Dinka M, Olukanni D, Musonda I. Geopolymer: A systematic review of methodologies. Materials. 2022;15(19. https://doi.org/10.3390/ma15196852
[12] Biernacki JJ, et al. Cements in the 21st century: challenges, perspectives, and opportunities. J Am Ceram Soc. 2017;100(7):2746-73. https://doi.org/10.1111/jace.14948
[13] Davidovits J. Geopolymer cement. A review. Geopolymer Institute, Technical papers. 2013;21:1-11. https://doi.org/10.1520/STP156620120106
[14] Kozhukhova N, Kozhukhova M, Teslya A, Nikulin I. The effect of different modifying methods on physical, mechanical and thermal performance of cellular geopolymers as

thermal insulation materials for building structures. Buildings. 2022 Feb;12(2). https://doi.org/10.3390/buildings12020241
[15] Dabbebi R, Barroso de Aguiar JL, Camões A, Samet B, Baklouti S. Effect of the calcinations temperatures of phosphate washing waste on the structural and mechanical properties of geopolymeric mortar. Constr Build Mater. 2018;185:489-98. https://doi.org/10.1016/j.conbuildmat.2018.07.045
[16] Gadkar A, Subramaniam KVL. Tailoring porosity and pore structure of cellular geopolymers for strength and thermal conductivity. Constr Build Mater. 2023;393:132150. https://doi.org/10.1016/j.conbuildmat.2023.132150
[17] Huseien GF, Mirza J, Ismail M, Hussin MW. Influence of different curing temperatures and alkali activators on properties of GBFS geopolymer mortars containing fly ash and palm-oil fuel ash. Constr Build Mater. 2016;125:1229-40. https://doi.org/10.1016/j.conbuildmat.2016.08.153
[18] Puligilla S, Mondal P. Role of slag in microstructural development and hardening of fly ash-slag geopolymer. Cem Concr Res. 2013;43:70-80. https://doi.org/10.1016/j.cemconres.2012.10.004
[19] Fu C, Ye H, Zhu K, Fang D, Zhou J. Alkali cation effects on chloride binding of alkali-activated fly ash and metakaolin geopolymers. Cem Concr Compos. 2020;114:103721. https://doi.org/10.1016/j.cemconcomp.2020.103721
[20] Berkouche A, et al. Enhancing sustainable construction practices: Utilizing heat-treated recycled concrete fines for improving slag-based geopolymer materials. Arab J Sci Eng. 2024. https://doi.org/10.1007/s13369-024-09477-6
[21] Swathi B, Vidjeapriya R. Influence of precursor materials and molar ratios on normal, high, and ultra-high performance geopolymer concrete-A state of art review. Constr Build Mater. 2023;392:132006. https://doi.org/10.1016/j.conbuildmat.2023.132006
[22] Komnitsas K, Zaharaki D. Utilisation of low-calcium slags to improve the strength and durability of geopolymers. 2009; 343-375. https://doi.org/10.1533/9781845696382.2.343
[23] Wu X, Shen Y, Hu L. Performance of geopolymer concrete activated by sodium silicate and silica fume activator. Case Studies in Construction Materials. 2022 Dec;17:e01513. https://doi.org/10.1016/j.cscm.2022.e01513
[24] Kim G, et al. Evaluation of the thermal stability of metakaolin-based geopolymers according to Si/Al ratio and sodium activator. Cem Concr Compos. 2024;150:105562. https://doi.org/10.1016/j.cemconcomp.2024.105562
[25] Duxson P, Provis JL. Designing precursors for geopolymer cements. J Am Ceram Soc. 2008;91(12):3864-9. https://doi.org/10.1111/j.1551-2916.2008.02787.x
[26] Bernal SA, et al. Gel nanostructure in alkali-activated binders based on slag and fly ash, and effects of accelerated carbonation. Cem Concr Res. 2013;53:127-44. https://doi.org/10.1016/j.cemconres.2013.06.007
[27] Wang R, Zhou X, Zhang W, Ye J, Wang J. Transport mechanism of uranyl nitrate in nanopore of geopolymer with different Si/Al ratios: Molecular dynamics simulation. J Solid State Chem. 2024;331:124542. https://doi.org/10.1016/j.jssc.2023.124542
[28] Varma DN, Singh SP. A review on waste glass-based geopolymer composites as a sustainable binder. Silicon. 2023;15(18):7685-703. https://doi.org/10.1007/s12633-023-02629-7
[29] Mendes BC, et al. Evaluation of eco-efficient geopolymer using chamotte and waste glass-based alkaline solutions. Case Stud Constr Mater. 2022;16. https://doi.org/10.1016/j.cscm.2021.e00847
[30] Belkadi AA, et al. Experimental investigation into the potential of recycled concrete and waste glass powders for improving the sustainability and performance of cement mortars properties. Sustain Energy Technol Assess. 2024;64:103710. https://doi.org/10.1016/j.seta.2024.103710

[31] Xiao R, et al. Strength, microstructure, efflorescence behavior and environmental impacts of waste glass geopolymers cured at ambient temperature. J Clean Prod. 2020;252:119610. https://doi.org/10.1016/j.jclepro.2019.119610
[32] Varma DN, Singh SP. Recycled waste glass as precursor for synthesis of slag-based geopolymer. Mater Today Proc. 2023.
[33] Singh RJ, Raut A, Murmu AL, Jameel M. Influence of glass powder incorporated foamed geopolymer blocks on thermal and energy analysis of building envelope. J Build Eng. 2021;43:102520. https://doi.org/10.1016/j.jobe.2021.102520
[34] Khan MNN, Kuri JC, Sarker PK. Effect of waste glass powder as a partial precursor in ambient cured alkali activated fly ash and fly ash-GGBFS mortars. J Build Eng. 2021;34:101934. https://doi.org/10.1016/j.jobe.2020.101934
[35] Hosseini S, Brake NA, Nikookar M, Günaydın-Şen Ö, Snyder HA. Mechanochemically activated bottom ash-fly ash geopolymer. Cem Concr Compos. 2021;118:103976. https://doi.org/10.1016/j.cemconcomp.2021.103976
[36] Zheng K. Pozzolanic reaction of glass powder and its role in controlling alkali-silica reaction. Cem Concr Compos. 2016;67:30-8. https://doi.org/10.1016/j.cemconcomp.2015.12.008
[37] Zhang B, He P, Poon CS. Optimizing the use of recycled glass materials in alkali activated cement (AAC) based mortars. J Clean Prod. 2020;255:120228. https://doi.org/10.1016/j.jclepro.2020.120228
[38] Dey A, et al. Towards net-zero emission: A case study investigating geopolymer concrete's sustainability potential using recycled glass powder and gold mine tailings. J Build Eng. 2024;108683. https://doi.org/10.1016/j.jobe.2024.108683
[39] Siddika A, Hajimohammadi A, Ferdous W, Sahajwalla V. Roles of waste glass and the effect of process parameters on the properties of sustainable cement and geopolymer concrete-A state-of-the-art review. Polymers (Basel). 2021;13(22). https://doi.org/10.3390/polym13223935
[40] Nath SK, Kumar S. Role of particle fineness on engineering properties and microstructure of fly ash derived geopolymer. Constr Build Mater. 2020 Feb;233:117294. https://doi.org/10.1016/j.conbuildmat.2019.117294
[41] Das D, Rout PK. Synthesis and characterization of fly ash and gbfs based geopolymer material. Biointerface Res Appl Chem. 2021;11(6):14506-19. https://doi.org/10.33263/BRIAC116.1450614519
[42] Das D, Rout PK. Synthesis, characterization and properties of fly ash based geopolymer materials. J Mater Eng Perform. 2021;30(5):3213-31. https://doi.org/10.1007/s11665-021-05647-x
[43] Kumar S, Mucsi G, Kristály F, Pekker P. Mechanical activation of fly ash and its influence on micro and nano-structural behaviour of resulting geopolymers. Adv Powder Technol. 2017 Mar;28(3):805-13. https://doi.org/10.1016/j.apt.2016.11.027
[44] Debnath K, Das D, Rout PK. Effect of mechanical milling of fly ash powder on compressive strength of geopolymer. Mater Today Proc. 2022 Jan;68:242-9. https://doi.org/10.1016/j.matpr.2022.08.321
[45] Yadav M, et al. Optimizing the fly ash/activator ratio for a fly ash-based geopolymer through a study of microstructure, thermal stability, and electrical properties. Ceramics. 2023;6(4):2352-66. https://doi.org/10.3390/ceramics6040144
[46] Nana A, et al. Mechanical performance, phase evolution and microstructure of natural feldspathic solid solutions consolidated via alkali activation: Effect of NaOH concentration. Silicon. 2022;14(8):4107-20. https://doi.org/10.1007/s12633-021-01193-2
[47] ASTM C. Standard test method for slump of hydraulic-cement concrete. ASTM International West Conshohocken, PA; 2012.
[48] EN-196-1. Methods of testing cement-Part 1: Determination of strength. Quality and Standards Authority of Ethiopia, ES; 2005.

[49] Técnicas ABDN. NBR 9778: Argamassa e concreto endurecidos-Determinação da absorção de água, índices de vazios e massa específica. Rio de Janeiro; 2005.
[50] Das D, Rout PK. Synthesis of inorganic polymeric materials from industrial solid waste. Silicon. 2023;15(4):1771-91. https://doi.org/10.1007/s12633-022-02116-5
[51] Zhang L, Yue Y. Influence of waste glass powder usage on the properties of alkali-activated slag mortars based on response surface methodology. Constr Build Mater. 2018 Aug;181:527-34. https://doi.org/10.1016/j.conbuildmat.2018.06.040
[52] Wang J, Wu D, Chen K, Mao N, Zhang Z. Effect of Ca content on the synthesis and properties of FA-GGBFS geopolymer: Combining experiments and molecular dynamics simulation. J Build Eng. 2024 Oct;94:109908. https://doi.org/10.1016/j.jobe.2024.109908
[53] Chitsaz S, Tarighat A. Estimation of the modulus of elasticity of N-A-S-H and slag-based geopolymer structures containing calcium and magnesium ions as impurities using molecular dynamics simulations. Ceram Int. 2021 Mar;47(5):6424-33. https://doi.org/10.1016/j.ceramint.2020.10.224
[54] Jin F, Gu K, Al-Tabbaa A. Strength and hydration properties of reactive MgO-activated ground granulated blastfurnace slag paste. Cem Concr Compos. 2015 Mar;57:8-16. https://doi.org/10.1016/j.cemconcomp.2014.10.007
[55] Varma DN, Singh SP. Recycled waste glass as precursor for synthesis of slag-based geopolymer. Mater Today Proc. 2023 Mar.

Research on Engineering Structures & Materials
www.jresm.org
Research Group

Research Article

Experimental determination of creep coefficients for sintered flyash lightweight aggregate based concrete and verification with creep models

Brijesh Singh [1,a], Shamsher Bahadur Singh [2,b], Sudhirkumar V. Barai [2,c], Abhishek Singh [3,d], P N Ojha [4,e]

[1]*Birla Institute of Technology & Sciences Pilani, Pilani & Group Manager at National Council for Cement & Building Materials, Ballabgarh, India*
[2]*Department of Civil Engineering, Birla Institute of Technology & Sciences Pilani, Pilani, India*
[3]*Dalmia Cement (Bharat) Limited, India*
[4]*National Council for Cement & Building Materials, Ballabgarh, India*

Article Info

Article history:

Received 5 July 2024
Accepted 6 Sep 2024

Keywords:

Sintered fly ash lightweight aggregate;
Granite aggregate;
Density;
Modulus of elasticity;
Creep coefficient;
Creep model

Abstract

The experimental creep coefficient has been determined for two concrete strengths of about 40 MPa and 60 MPa using sintered flyash lightweight aggregate and granite aggregate in creep rig with capacity of 1500kN as per ASTM C-512. The creep results indicate that despite both density and modulus of elasticity being on lower side for sintered flyash lightweight based concrete, the creep coefficient has been lower than that of normal weight concrete with granite aggregate for same strength level. The comparison of existing creep models has been carried out with experimental results for both normal and lightweight concrete considering parameters in models such as relative humidity level, concrete mix ingredients, aggregate properties, oven dry density, elastic modulus of both concrete types etc. considered in study. The creep coefficients have been obtained experimentally at loading age of 28-day and testing period of 365 days and has been compared with existing creep models such as B-3, B-4, ACI-209, EN:1992/FIB. For the similar compressive strength level, creep coefficient of structural grade lightweight concrete is found to be lower in comparison to creep coefficient of normal weight concrete as the internally stored water in porous aggregates keeps capillary pores almost saturated and leaves minimal chance for seepage to occur.

1. Introduction

Creep is a time related property of concrete and is of importance particularly in the design of prestressed concrete structures, tall building structures, hydraulic structures such as dam etc. Creep is basically defined as phenomena in which there is volume change in concrete due to sustained load and total creep is summation of both basic creep and drying creep. The basic creep is related to the stress state of materials and can be identified in sealed specimens in which all moisture interactions with the external environment are avoided. It is considered as a material constitutive property and independent from size and shape of specimen. Whereas the drying creep is related to the time dependent deformation coupled with the drying effect of cement-based material. The drying creep is experimentally obtained by subtracting shrinkage, elastic and basic creep components from total measured strain. There are various theories which explain different creep

*Corresponding author: brijeshsehwagiitr96@gmail.com
[a]orcid.org/0000-0002-6512-1968; [b]orcid.org/0000-0001-6847-0701; [c]orcid.org/0000-0001-5100-0607; [d]orcid.org/0000-0002-2343-5934; [e]orcid.org/0000-0003-1754-4488
DOI: http://dx.doi.org/10.17515/resm2024.338ma0705rs

mechanisms of concrete system which still has not been understood properly. The theories available on creep of concrete are seepage theory, viscous theory, micro crack theory and micro prestress solidification theory. In seepage theory, creep basically happens because of water getting squeezed from absorbed portion of calcium silicate hydrate particles. Under loading, the compressed water flows to capillary pores and unconnected pressure comes down leading to reduction in C-S-H particles distance by Vander Waals Force [1]. In the viscous shear phenomena of creep, it is the creep which occurs due slide among C-S-H particles because of shear process causing lubrication effect in water. In this adsorbed water moves under the load to create the change of volume in concrete. As per microcrack theory, microcracks are generated by sustained loading over time resulting in creep deformation. The microcrack formation occurs in the interfacial transition zone (ITZ) consisting of cement paste and aggregates which is generally a weakest link in concrete system. In solidification phenomena, it is presumed that increase in age of concrete is connected to increase in volume of hydration products under non-aging category [2-5]. Increase in volume of products formed during hydration enhances the firmness of concrete system resulting in improved creep resistance performance.

The creep is important because stress generated under sustained loading can lead to large deformation and crack generation in some cases [1]. The most of materials in general nearly behave elastically (recoverable) under small stresses upon immediate loading but when high level stresses are put in, increase in strain occurs gradually over time leading to creep. Creep in concrete structures has led to columns / piers getting shortened in the past wherein columns are not equal leading to differential shortening thereby causing movement of slab from its designated position which generates significant stresses not covered in structural design [2-5]. Creep has also reported to induce relaxation or loss of prestress of tendons of concrete members [5]. Creep also leads to excessive deflection in case of both plain and reinforced concrete structures leading to cracks in the concrete and subsequently affecting its safety. The creep in beginning occurs at fairly slow rate and at in between creep becomes steady and at the end rate of creep intensifies leading to failure. The accurate prediction of creep is important to avoid issues of excessive deformation, crack initiation, prestress loss of tendons etc. in structures. The numerous creep studies have been reported on normal weight concrete [1-4] but the study on lightweight concrete is limited. In the area of lightweight concrete also, studies on creep behaviour of sintered flyash lightweight coarse aggregate based concrete are limited to one or two. Sintered flyash lightweight concrete now a day is being used in construction industry because of its reduced dead load, improved durability performance, better thermal and sound insulation along with improved fire resistance [6-7]. Apart from this, lower water permeability, lower chloride ion penetration and better corrosion resistance of lightweight concrete makes it more durable as compared to normal concrete. The density of structural grade lightweight concrete generally varies from 1100 to 1900 kg/m^3 having minimum compressive strength of 17 MPa [8]. Sintered flyash lightweight aggregate is mainly produced from flyash through sintering process [6-8]. These aggregates possess cell type pore structure and generally contains pores in the size ranging from 5 to 300μm. The pore system of lightweight aggregate consists of open or interrelated pores which governs absorption and closed or connected pores are absent in this case. The porous nature and lower stiffness of lightweight aggregates influences both compressive strength and creep of concrete [9]. Studies has shown that irrespective of properties of lightweight aggregate such as expanded shell or clay, polystyrene and apricot shell, both strength and creep of lightweight concrete gets affected [9-12]. Studies have shown a smaller creep at one-year age compared to normal concrete of similar compressive strength, but later on due to higher rate of creep, lightweight concrete has shown high final creep for few lightweight aggregates [11]. The creep of concrete depends upon the mechanical and physical characteristics of aggregate such as pozzolanic action, porosity and roughness of surface

of aggregate [13-18]. The creep test on lightweight concrete from literature is given in Table-1.

Table 1. Literature review of creep study on lightweight concrete

Sl.No.	Lightweight aggregate Type	Density of Concrete (Kg/m^3)	Compressive Strength (MPa)	Reference
1	Expanded clay aggregate	1700	67.40	Iqbal et al. [15]
2	Expanded slate aggregate	1860	60.90	Kahn and Lopez [28]
3	Expanded clay aggregate	1950	60.80	Bogas et al. [30]
4	Bentonite-flyash aggregate	1980	54.60	Kockal and Ozutran [31]
5	Oil palm shell aggregate	1980	53.10	Shafigh et al. [32]
6	Expanded clay aggregate	1620	60.50	Chen and Liu [33]
7	Expanded shell aggregate	1640	46.10	Choi et al. [34]
8	Hollow microspheres	1990	125.80	Jeong et al. [35]
9	Hollow microspheres	1480	65.20	Inomzemtcev et al. [36]
10	Flyash cenospheres	1720	73.80	Zhou et al. [17]
11	Flyash cenospheres	1560	56.20	Zhang et al. [37]
12	Flyash cenospheres	1390	59.00	Huang et al. [38]

The important parameter of any concrete is its elastic modulus and it depends upon the moduli of both aggregate and cement matrix. In lightweight concrete, the elastic modulus of the aggregate is the weakest link, and it leads to overall reduction of elastic modulus of lightweight concrete. In the lightweight concrete, the elastic modulus of aggregate and paste are closer to each other compared to normal weight concrete leading to uniform stress distribution, simultaneously reducing concentration of stress and destruction occurs at the weakest link which is aggregate in case of lightweight aggregate. The supplementary cementitious materials like silica fume or flyash when used in lightweight concrete mix has been reported to reduce the creep of concrete by improving the microstructure of concrete [15-16]. The lightweight aggregate in air-dried form affects mechanical and time dependent properties of concrete by absorbing the water and adversely affecting creep behaviour as compared to lightweight aggregate in saturated form which is reported to improve the creep performance through internally stored water contributing in curing. The internal curing phenomena inside the lightweight aggregate which is porous in nature has crucial role in reducing creep deformation [16]. As reported earlier, the lightweight concrete with lower water to binder ratio and low stiffness porous lightweight aggregate can have increased creep deformation [17]. This is conflicting with the studies done and creep prediction becomes difficult. Therefore, applicability of existing creep models for lightweight concrete needs to be experimentally determined. The internal curing has been reported to improve strength characteristics, raises internal relative humidity and reduces permeability of lightweight concrete which has impact on creep performance. The shape of aggregate may also affect creep coefficient, an ellipse shaped, or polygon shaped aggregate has shown highest and lowest creep, respectively [19]. The supplementary cementitious materials like silica fume or flyash when used in lightweight concrete has been reported to lower the creep of concrete by improving the microstructure of concrete [20-25].

The study has been conducted on creep of lightweight concrete using varieties of lightweight aggregates such as expanded shale from rotary kiln, expanded slag, shale and clay from sintering process at different replacement levels of sand in proportion of 0, 33.30, 66.70, and 100%. The test results indicate that creep decreases with increase in sand content and at 100% replacement creep coefficient obtained, has been 30 percent less compared to other replacement proportions [26]. The creep coefficient of self-compacting lightweight aggregate-based concrete using clay shale produced through

sintering has been reported to be marginally less compared to normal concrete at one-day loading age with high level creep at this particular age for lightweight concrete [27]. When a loading has been done at 28-day for lightweight concrete, a higher coefficient of creep has been seen in the case of normal weight concrete. Study on creep of lightweight concrete with expanded shale aggregate by Lopez et al. [28] highlights the importance of pre-wetting of lightweight aggregate in comparison to air dried lightweight aggregate. Because of porous nature of these aggregates, if proper care is not taken in water absorption correction for compensating additional mass of water required in lightweight concrete, then specific creep of normal weight concrete and lightweight concrete with lightweight aggregate in air dried form has shown increase of about two times in specific creep of lightweight concrete at 120 days after loading [28-29]. Appropriate water correction considering the effect of cement paste penetration in lightweight aggregate-based concrete can create reservoir for internal curing of concrete which may result in low specific creep and better creep performance.

1.1 Research Significance

As discussed above those only limited studies [30-38] has been done on creep of structural grade lightweight concrete as compared to normal weight concrete. Particularly, for lightweight concrete made with sintered flyash lightweight coarse aggregate, there exists little to no studies in literature. The present research on creep study covers both normal and high strength lightweight concrete made from sintered flyash lightweight coarse aggregate and its comparison with creep coefficient of normal weight concrete of similar strength level. Novelty of the present research lies in the fact that present study evaluates creep coefficient of both normal and high strength lightweight concrete prepared with sintered flyash lightweight coarse aggregates for 337 days of loading and thereafter it examines the applicability of existing creep models such as Bazant's B-3, B-4, ACI-209, EN:1992/FIB with experimental results for lightweight concrete.

2. Materials

In this study for production of normal weight concrete, OPC cement (43 Grade), coarse and fine aggregates, silica fume, superplasticizer and water are used. In the study, crushed fine aggregate that conforms with Zone II of IS: 383-2016 [39] has been used as fine aggregate and coarse aggregate having maximum nominal size of 20 mm has been used. Figure 1 (a) displays the fine aggregate, while Figure 1 (b) displays the coarse aggregate. Table 2 displays the physical characteristics of both coarse and fine aggregate. The mechanical properties of sintered flyash lightweight aggregate used as coarse aggregate are given in Table-3.

(a) (b)

Fig. 1. (a) Fine aggregate (crushed) and (b) coarse aggregate (granite)

The sintered flyash lightweight aggregate is brown in color as shown in Figure-2 and has black core. The microstructure of sintered flyash lightweight aggregate is shown in Figure-3. The samples of sintered flyash lightweight aggregate (LWA) (two fractions 8-16 mm and 4-8 mm) have been used as coarse aggregate.

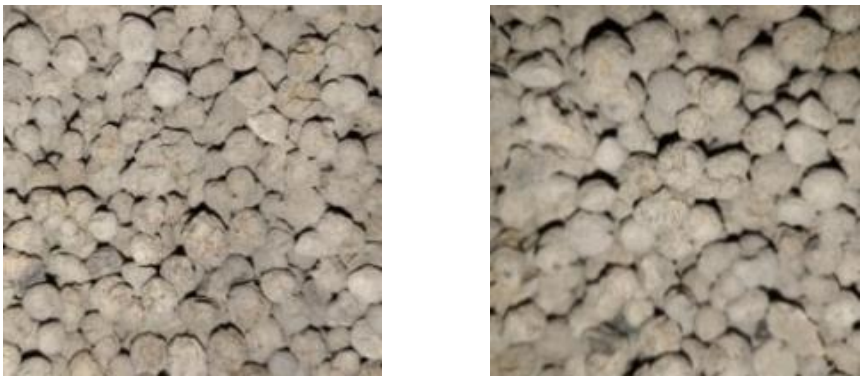

(a) (b)

Fig. 2. (a) Sintered flyash lightweight aggregate, fraction: 4-8 mm and b) sintered flyash lightweight aggregate, fraction: 8-16 mm

Table 2. Aggregates properties

Property		Granite		Sintered Flyash Lightweight Aggregate		Fine Aggregate
		20 mm	10 mm	8-16 mm	4-8 mm	
Specific gravity		2.81	2.82	1.49	1.47	2.65
Water absorption (%)		0.3	0.3	17.93	17.50	0.59
Sieve Analysis Cumulative Percentage Passing (%)	20mm	100	100	100	100	100
	10 mm	1	68	30	100	100
	4.75	0	2	0	13	99
	2.36	0	0	0	2	89
	1.18	0	0	0	0	64
	600 µ	0	0	0	0	43
	300 µ	0	0	0	0	26
	150 µ	0	0	0	0	14
	Pan	0	0	00	0	0

The chemical composition of sintered flyash lightweight aggregate, OPC cement 43 grade (as per IS: 269 [40]) and silica fume is given in Table-3. The fineness of OPC cement is 320 m^2/kg and silica fume is 22000 m^2/kg. For preparation of concrete mixes for lightweight concrete, the fine aggregate (crushed stone) used in study conforms to IS: 383-2016. Also, for lightweight concrete crushed fine aggregate that conforms with Zone II of IS: 383-2016 [39] has been used as fine aggregate The polycarboxylic type chemical admixture conforming to Indian Standard IS:9103[41] has been used for all concrete mixes.

Fig. 3. Microstructure of sintered flyash lightweight aggregate (10 μm and 1.5x)

Table 3. Mechanical properties of sintered flyash lightweight aggregate used in study

Fraction	LWA designation	Specific gravity	Water absorption at 24 hours (%)	Loose bulk density (kg/m^3)	Crushing Strength (N/mm^2)	10 % Fines (Ton)
4-8 mm	LWA-I	1.47	17.50	813	8.80	-
8-16 mm	LWA-II	1.49	17.93	849	7.70	3.60

Table 4. Chemical composition of sintered flyash lightweight aggregate and OPC cement

Component	CaO (%)	SiO_2 (%)	Al_2O_3 (%)	Fe_2O_3 (%)	SO_3 (%)	MgO (%)	$Na_2O_{eq.}$ (%)	Loss of Ignition (%)
Sintered flyash lightweight aggregate	2.45	62.50	25.85	4.19	0.29	0.53	0.77	1.48
Cement OPC 43 grade	59.60	21.22	7.19	4.25	2.50	1.90	1.05	1.94
Silica fume	-	95.02	-	0.80	-	-	-	1.16

3. Mix Design Details

3.1 Normal Concrete Mix Design:

The w/b ratio adopted for concrete mix preparation has been 0.5 and 0.4 for developing normal weight concrete (NWAC) mixes using granite as coarse aggregate. The slump has been kept in the range of 75 -100 mm. The mix design for normal weight concrete has been done in accordance with procedure given in IS: 10262-2019 [42]. The details of concrete mix are given in Table-5.

3.2 Lightweight Concrete Mix Design:

The w/b ratio adopted for concrete mix preparation has been 0.4 and 0.3 for developing lightweight concrete (LWAC) mixes using sintered flyash lightweight coarse aggregate for achieving similar strength level as to normal strength concrete. The sintered flyash lightweight aggregate is porous in nature with very high-water absorption as compared to conventional natural aggregate. When lightweight aggregate is added in dry condition with water correction equal to water absorption of aggregate, it leads to segregation of mix in fresh state as well increase in net free water to cement ratio leading to reduction in

strength in hardened state. Secondly, the direct correction of water absorption does not take into account the effect of cement paste and in actual condition it is the cement paste and not water alone which dictates the water absorption potential of lightweight aggregates. This problem can be tackled by use of lightweight aggregate in dry state condition with appropriate correction in water absorption considering the effect of cement paste for given water cement ratio of concrete mix. The mix design for lightweight concrete with sintered flyash lightweight coarse aggregate has been done in accordance with procedure given in Indian Standard IS: 10262-2019 [42] and curve has been developed for water absorption correction of aggregate. The sintered flyash lightweight aggregate is highly porous and its water absorption is about 18 percent. In the present study, the combined aggregate grading given in IS: 9142-2018 [43] has been adopted. The absorption potential of sintered flyash lightweight aggregate has been determined in the study wherein moisture content of lightweight aggregates has been known. Initially the moisture content and initial weight of the aggregate has been recorded. The mortar paste of w/b 0.7 has been prepared and placed in container. Twenty-five aggregates have been first placed in a cement paste present in the container for the period of 5, 15, 30, 45 and 60 minutes to decide optimum absorption period (soaking period). After the specified period of absorption, the lightweight aggregates have been removed from the cement paste and the excess cement paste attached to the outer surface of aggregates has been separated with help of nylon brush. The removal time of excess paste has been kept not more than one minutes to not absorb the water trapped in the aggregate particles which takes part in further hydration of cement paste. Thereafter, weight of aggregates has been measured. After this the aggregates have been placed inside an oven for period of 48 hours at a temperature of 105°C. Finally, dry weight of aggregate has been determined and aggregate absorption values has been determined.

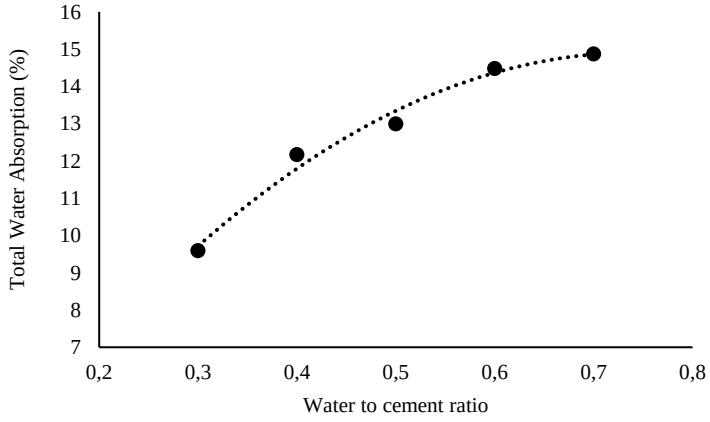

Fig. 4. Relationship between water absorption of sintered flyash lightweight aggregate with water to cement ratio for 45 minutes absorption period

The total absorption by the lightweight coarse aggregate in terms of percentage is calculated as difference of mass of aggregate after 45 minutes of soaking and initial mass of aggregate before soaking divided by initial mass of aggregate before soaking multiplied by 100. The total water absorption by the lightweight coarse aggregate in terms of percentage is calculated as difference of mass of aggregate after 45 minutes of soaking and dry mass of aggregate after oven drying divided by dry mass of aggregate after oven drying multiplied by 100. The difference between the percentage of total absorption by the lightweight coarse aggregate and total water absorption by the lightweight coarse aggregate is termed as total paste absorption potential of lightweight coarse aggregate.

The water absorption values at water to cement ratio of 0.70 for absorption period of 5, 15, 30, 45 and 60 minutes has been 12.84. 13.84, 14.36, 14.86, 14.90, respectively.

Based on study, 45 minutes absorption period for sintered flyash lightweight aggregate has been considered in this study as the absorption capacity of the aggregates beyond this period has been almost negligible. Thereafter, this exercise has been repeated for mortar paste of w/c ratio of 0.3, 0.4, 0.5 and 0.6. Thereafter, correlation has been developed between sintered flyash lightweight aggregate water absorption potential and different w/c ratios. The correlation developed is presented in Figure-4 for absorption period of 45 minutes. The correlation developed is to be used in water absorption correction of sintered flyash lightweight aggregate used as coarse aggregate in concrete mix preparation. The mix design details of both normal and lightweight concrete are given in Table 5.

Table 5. Concrete mix design for normal and lightweight concrete

Mix ID	w/c	Cementitious Content [Cement + Silica Fume] (kg/m^3)	Water Content (kg/m^3)	Chemical Admixture % by weight of cement	Fine Aggregate (kg/m^3)	Coarse Aggregate (kg/m^3)	
						10 mm	20 mm
NWAC-0.5	0.50	340 (316+24)	170	0.60	660	516	775
NWAC-0.4	0.40	425 (382+43)	170	1.00	580	515	775
LWAC-0.4	0.40	425 (382+43)	170 (After Correction 254)	0.70	646	250	385
LWAC-0.3	0.30	566 (481+85)	170 (After Correction 234)	0.80	573	246	371

A 60 kg batch of concrete has been prepared for each concrete mix. Firstly, in the pan mixer both the fractions of lightweight coarse aggregate, fine aggregate and cement has been mixed to obtain homogenous mix and thereafter 80 percent water has been added and mixing has been done for period of 2-3 minutes. After that the remaining 20 percent water along with admixture has been added and mixing has been continued for another 2-3 minutes. It is to be noted that the initial mixing period is critical for sintered flyash lightweight aggregate due to its absorption characteristics. Adjustment has been made in mixing water as a correction for aggregate water absorption. The moulds have been cleaned properly and concrete cube has been compacted on vibration table wherein each of three layers has been properly compacted. The concrete cubes have been demoulded after 24-hours. The environmental conditions of laboratory have been 27±2^{o}C temperature and 65% or more relative humidity. The concrete cube specimen has been tested in surface dried saturated condition. The concrete has been developed to maintain a slump in between 75-100 mm. The 28-day compressive strength, modulus of elasticity and oven dry density of concrete mixes are given in Table-6 which is used as input parameters for determining creep coefficients through existing creep models for comparing it with experimentally determined creep coefficients.

The concrete cubes (150 mm*150 mm*150 mm) and cylinders (150 mm diameter and 300 mm height) for evaluating compressive strength and modulus of elasticity respectively have been tested in a strain-controlled compression testing machine of 3000 KN capacity. The rate of loading maintained has been 14 N/mm^2/Min as per Indian Standard. For each

w/c, total six concrete cubes and six cylinders has been tested and average of six specimens has been reported in Table-6. The standard deviation in compressive strength and modulus of elasticity test results are shown in Table-6. The test results indicates that modulus of elasticity of lightweight concrete with sintered flyash coarse aggregate is around 60-65 percent of normal weight concrete made with granite aggregate. The oven dry density of lightweight concrete varies from 1838 to 1875 kg/m^3 whereas for normal weight concrete it varies from 2291 to 2361 kg/m^3 for same compressive strength level.

Table 6. 28-day compressive strength, modulus of elasticity and oven dry density of concrete

Mix ID	w/c	Average Cube Compressive strength at 28-day (MPa)	Average Modulus of Elasticity at 28-day (MPa)	Oven Dry Density (kg/m^3)
NWAC-0.5	0.50	47.72 (σ=1.95)	35541 (σ=210)	2291 (σ=20)
NWAC-0.4	0.40	58.57 (σ=1.85)	38729 (σ=235)	2361 (σ=25)
LWAC-0.4	0.40	49.80 (σ=1.65)	22575 (σ=175)	1838 (σ=15)
LWAC-0.3	0.30	57.59 (σ=1.75)	24715 (σ=155)	1875 (σ=18)

4. Experimental Procedure for Creep in Compression

The creep test has been performed on 150 mm diameter and 300 mm height cylinder in line with procedure given in ASTM C-512 for both lightweight and normal weight concrete on total four concrete mixes given in Table-5. The compressive strength of each of the four concrete mixes has been considered for determining load /pressure to be placed on creep specimens and load placed has been kept as 40 percent of the average cylindrical compressive strength. The creep testing has been performed in creep test rig of 1500kN capacity (Figure-5). The reaction frame in creep test rig has upper and lower jacks and loading plates including bearing at the end portion of loaded specimen. The hydraulic jack assembly with an air vent inside piston for removing out air and maintaining consistent loading. The hydraulic jack has been designed in such a manner that it holds the load for longer duration. The loading has been checked regularly during the test period of one year. The load gauge accuracy of creep testing rig has been ± 1% from 10% to 90% of full-scale loading. The load indicator has a least count of 10kN. The creep test setup has a provision of slow and fast levers fitted with knob for to and fro movement of lever for load adjustment. The creep specimens have been wrapped in the butyl rubber for the duration of 28-day during curing period. The relative humidity and temperature maintained has been 60% and 27^{0}C, respectively during both 28-day curing and loading period.

The creep test has been performed in line with procedure given in ASTM C-512. As shown in Figure-5 in the shrinkage specimen, the steel plates have been screwed and fixed to the cylindrical specimen. The Linear Variable Displacement Transducer (LVDT) with measuring range of 0-5 mm has been mounted both loaded and shrinkage specimen to measure deformation. Before the placement of LVDT, the distance between the middle of the bolt has been measured and denoted as L. The strain has been calculated by dividing the deformation value obtained from LVDT by L. The readout units have been used for measurement of data from LVDT. For each concrete mix, total four concrete cylinders (a) two loaded in creep rig and (b) two shrinkage specimens kept in same environmental

conditions has been tested. For all four concrete mixes, sixteen concrete cylinders has been evaluated for experimental determination of creep coefficients.

(a) (b) (c)

Fig. 5. Creep Testing Arrangement (a) creep testing rig 1500 kn capacity, (b) loaded specimen, and (c) shrinkage specimen

During the creep examination, cylindrical specimens has been placed for time period of 337 days after 28-day curing period for both shrinkage specimen and loaded specimen where shrinkage specimens kept in same environment as loaded samples and loaded condition for the time period of 365 days (Figure 5). The control specimen and specimen adopted for estimation of compressive strength has been placed in same curing and storage condition as that of the specimen placed in creep rig. Creep is defined as the increase in strain of concrete under constant sustained loading.

Creep depends on various factors such as type of aggregate, mix design, environmental conditions like humidity and temperature, curing regime, member geometry, loading age, loading duration and applied stress. The creep co-efficient ϕ (t, t_o) can be determined per equation below:

$$\phi(t, t_0) = \frac{\varepsilon_{cc}(t)}{\varepsilon_{ci}(t_0)} \quad (1)$$

here, $\varepsilon_{cc}(t)$ = creep strain with time $t > t_0$, (this excludes instantaneous strain at loading time), $\varepsilon_{ci}(t_0)$ = initial level strain at loading, and t_0 = age of concrete at loading

5. Experimental Results of Creep in Compression

The age of the creep specimens at the time of loading has been 28-day and steps for calculating creep for 337 days of loading, for both normal and lightweight concretes have been summarized in Table 7. The test results of average total strain for loaded sample and shrinkage strain at different ages of loading for all the mixes has been tabulated below in Table 8. The shrinkage strain of lightweight concrete is lower than normal weight concrete for similar compressive strength. Similarly, the total stain of loaded samples in case of lightweight concrete is lower than normal weight concrete for similar compressive strength.

The elastic strain developed in cylindrical specimen for all the mixes, at the time of loading (at 28-day age) of specimen in loading frame, has been shown below in Figure 6. The creep induced strain developed in specimen and creep coefficient for all the mixes at different ages has been shown below in Figure 7 and Figure 8. For similar level of compressive strength, light weight concrete shows 1.5 to 1.7 times higher elastic strain, immediately

after application of load, which validates the lower values of Modulus of Elasticity for light weight concrete mixes in comparison to normal weight concrete mixes.

Table 7. Summary of Steps for calculation of creep coefficient at 337 days of loading

Parameters	NWAC w/b=0.5	LWAC w/b=0.4	NWAC w/b=0.4	LWAC w/b=0.3
Average Cylindrical Compressive Strength: f_{cy} (N/mm^2)	35.8	37.4	46.9	45.3
Stress Applied on specimen = 40% of f_{cy} (N/mm^2)	14.3	15	18.7	18.1
Applied Load (kN)	253	265	331	320
Specimen age at loading time (days)	28	28	28	28
Average strain just after load is applied at time t_0 (μ-strain)	407.99	677.85	496.68	752.54
Average strain of shrinkage specimens at time of loading at time t_0 (μ-strain)	21.09	17.83	29.73	23.61
Immediately after loading load induced strain per unit stress (μ-strain/ (N/mm^2))	27.04	44.07	24.91	40.25
365 days period average strain for loaded specimens (μ-strain)	1681.44	1609.32	1553.88	1504.3
365 days period average strain for shrinkage specimens (μ-strain)	422.21	290.8	358.48	226.7
365 days period net load generated strain (μ-strain)	1259.23	1318.52	1195.4	1277.6
365 days period load generated strain per unit stress at 365 days (μ-strain/ (N/mm^2))	87.99	88.04	63.78	70.55
Therefore, the Creep strain per unit stress (μ-strain/ (N/mm^2))	60.96	43.97	38.87	30.3
Creep coefficient at 365 days	2.25	0.99	1.56	0.75

Table 8. Experimental data of strain for loaded sample and shrinkage strain

Duration of loading	Age of concrete	Average Total Strain (μ-strain) For Loaded Samples				Average Shrinkage Strain (μ-strain)			
		NWAC w/b=0.5	LWAC w/b=0.4	NWAC w/b=0.4	LWAC w/b=0.3	NWAC w/b=0.5	LWAC w/b=0.4	NWAC w/b=0.4	LWAC w/b=0.3
0	28	407.99	677.85	496.68	752.54	21.09	17.83	29.73	23.61
28	56	1219.24	1149.55	1060.4	1131.78	318.83	128.17	174.12	119.74
62	90	1401.15	1330.21	1219.37	1257.3	353.23	187.11	195.34	138.43
92	120	1522.03	1411.17	1308.58	1340.57	349.59	207.84	232.54	168.64
122	150	1527.02	1466.77	1388.96	1373.6	360.53	235.68	279.02	183.65
152	180	1585.26	1522.67	1475.22	1435.34	390.48	264.38	322.78	210.85
337	365	1681.44	1609.32	1553.88	1504.3	422.21	290.8	358.48	226.7

The trend and pattern of development of creep induced strain and creep coefficient is similar for light and normal weight concrete mixes, wherein creep increases linearly up to around 50 days of loading and rate of increase in creep strain and creep coefficient gets reduced beyond the duration of 50 days and it tends to reach a constant value after 337 days of loading. The test results of creep strain for both normal and lightweight concrete

decreases as the compressive strength of concrete increases which is anticipated keeping in view that increase in strength increases elastic modulus of concrete which provides more resistance to strain.

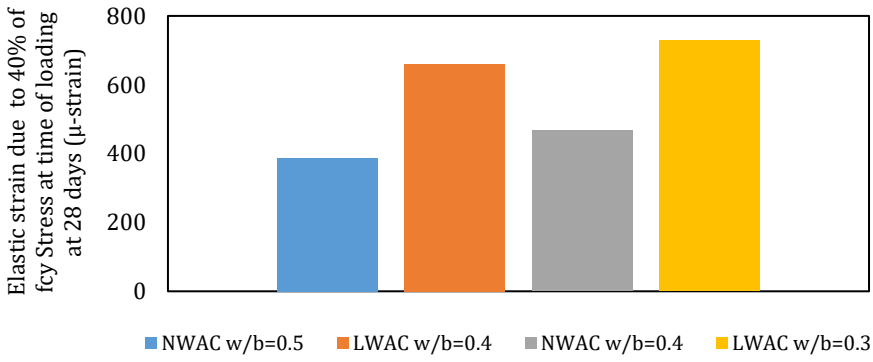

Fig. 6. Elastic strain in specimen of experimental mixes due to application of Stress (40% of f_{cy}) at time of loading at 28 days (μ-strain)

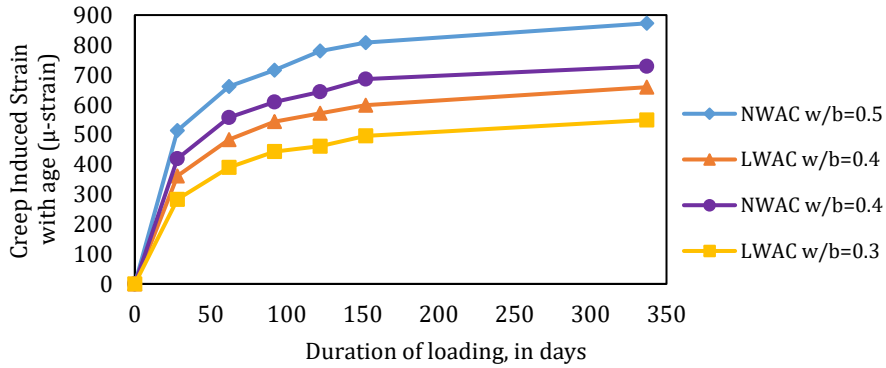

Fig. 7. Creep induced strain (μ-strain) developed with age for experimental mixes

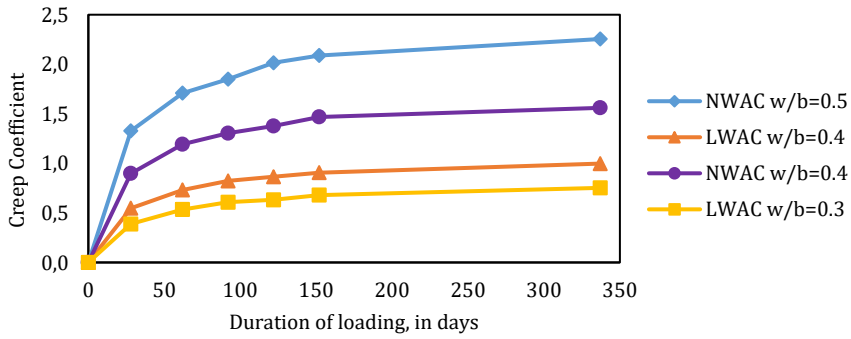

Fig. 8. Plot of Creep coefficient with age for experimental mixes

6. Discussion on Results of Creep in Compression

For the similar compressive strength level, the creep coefficient of lightweight concrete is less compared to creep coefficient of normal weight concrete. The difference in creep coefficient for both normal and lightweight concrete decreases with increase in compressive strength and decrease in w/b ratio. The internally captured water in sintered flyash lightweight aggregate from concrete mix not only improves the strength, interfacial transition zone but also decreases porosity and permeability of concrete system thereby decreasing early age cracking. The stored water also leads to hydration of unhydrated cement particles into C-S-H which helps in strength improvement. The prolonged internal curing causes improvement in hydration leading to denser and stronger microstructure which ultimately helps in better resistance to creep deformation [43-47]. The internally preserved water in porous lightweight aggregate leads to high relative humidity internally and thereby preventing the migration of water from surface of C-S-H gel under sustained loading. The creep mechanism has different theories such as seepage theory, viscous theory, micro crack theory and micro prestress solidification theory. Research fraternity in general is of view that apart from micro cracking in ITZ, creep can be understood from viscoelastic deformation of cement matrix and seepage of water from C-S-H surface to capillary pores under the sustained loading. The basic creep occurs due to viscoelastic deformation whereas drying creep occurs because of water seepage. The internally stored water in porous aggregates keeps capillary pores almost saturated and leaves minimal chance for seepage to occur. Therefore, reason for lower creep in highly porous sintered flyash lightweight coarse aggregate based concrete can be attributed to improved hydration, expansion and water seepage blockage.

7. Comparison of Creep Models with Experimental Results for Both Normal and Lightweight Concrete

The creep coefficients obtained experimentally on cylindrical specimens at 28-day loading age for the loading period of 337 days has been compared with B3 [48], B4 [49], EN 1992/ FIB model [50-51] and ACI 209R-92 [52] and are shown in Figure 9, 10, 11 and 12 for both normal and lightweight concrete. The main parameters and coefficients considered for calculating creep using B3, B4, EN 1992/ FIB model and ACI 209R-92 are type of cement, age of loading, relative humidity, specimen type, specimen size, aggregate content, mineral admixtures, aggregate type, water cement ratio, density of concrete [53-54]. In EN 1992/FIB model, for lightweight aggregate concrete (LWAC), creep coefficient has been calculated as per the equation mentioned below:

$$\varphi\,(LWAC) = \varphi(normal\ density\ concrete) \times \left[\frac{Oven\ Dry\ density\ of\ LWAC}{2200}\right]^2 \qquad (2)$$

The experimentally obtained creep coefficients for normal weight concrete with w/b ratio of 0.5 (Figure-9) is in between and near to creep coefficient determined through B3, B4 model and EN 1992/ FIB model. The creep coefficient predicted by ACI 209R-92 for normal weight concrete with w/b ratio of 0.5 is significantly low as compared to experimental results.

The experimentally obtained creep coefficients for normal weight concrete with w/b ratio of 0.4 (Figure-10) is in between and near to creep coefficient determined through B4 model, ACI 209 and EN 1992/ FIB model. The creep coefficient predicted by B-3 for normal weight concrete with w/b ratio of 0.4 is significantly high as compared to experimental results and one of the main reasons can be mix with low water to binder ratio can lead to reduction in chemical volume and self-desiccation along with decrease in humidity level of pore system.

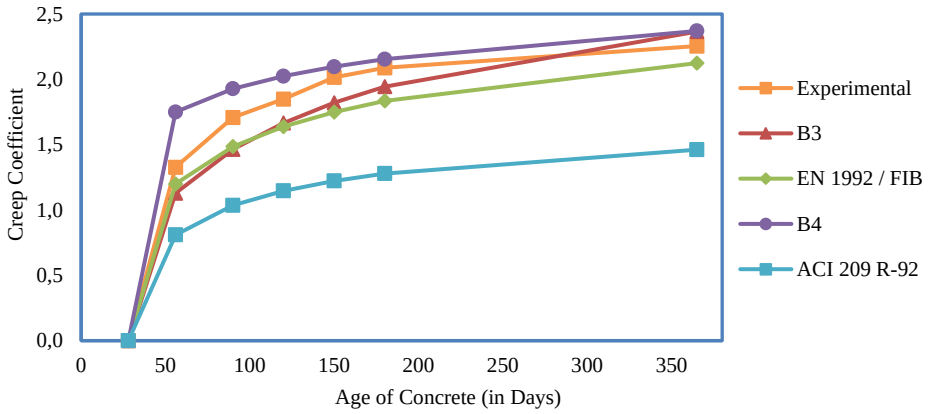

Fig. 9. Comparison of experimentally obtained creep coefficient for Normal Weight Aggregate Concrete (NWAC) with w/b=0.5 and creep coefficient estimated by models

The creep model B-4 and EN-1992/FIB for w/b ratio 0.4 predicts creep coefficients closer to the experimental values and like creep coefficients for normal weight concrete with w/b ratio of 0.5, the ACI 209 gives the lowest value of creep coefficient among all models. In EN-1992/FIB model code, basic creep has been modelled through logarithm function, which is infinite continuous deformation while drying creep reaches to a finite value. The creep predicted by EN-1992/FIB is similar to modelling of shrinkage behaviour and this is main reasons for contributing to accurate estimation of delayed deformations in concrete with low w/b ratio.

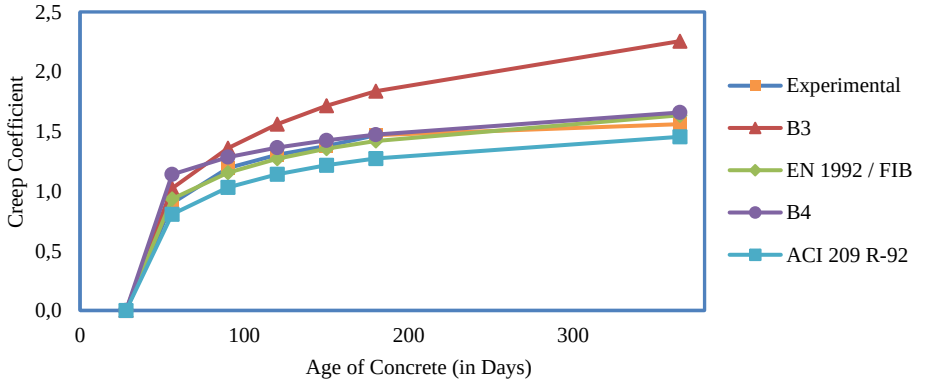

Fig. 10. Comparison of experimentally obtained creep coefficient for Normal Weight Aggregate Concrete (NWAC) with w/b=0.4 and creep coefficient estimated by models

The experimentally obtained creep coefficients for lightweight concrete with w/b ratio of 0.4 (Figure-11) is lower than creep coefficient determined through all five models i.e. B-3, B4, ACI 209 and EN 1992/ FIB model. The creep coefficient predicted by B-3 and ACI-209 for lightweight weight concrete with w/b ratio of 0.4 is significantly high (1.50 times) as compared to experimental results. The creep model B-4 and EN-1992/FIB for w/b ratio 0.4 predicts creep coefficients closer to the experimental values. The creep coefficient of normal weight concrete as compared to lightweight concrete for compressive strength level of about 47 MPa and 58 MPa is 2.3 times and 2 times, respectively.

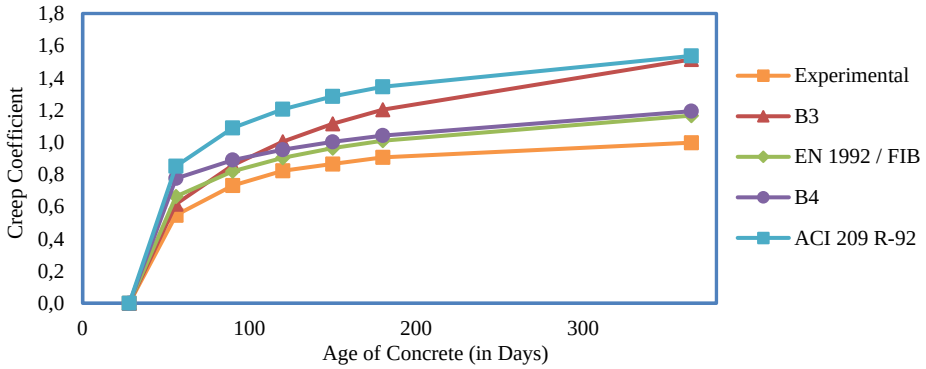

Fig. 11 Comparison of experimentally obtained creep coefficient for Lightweight Aggregate Concrete (LWAC) with w/b=0.4 and creep coefficient estimated by models

The experimentally obtained creep coefficients for lightweight concrete with w/b ratio of 0.3 (Figure-12) is lower than creep coefficient determined through B-3, ACI 209 and EN 1992/ FIB model. The creep coefficient predicted by B-3 and ACI-209 for lightweight weight concrete with w/b ratio of 0.3 is significantly high (about 2 times) as compared to experimental results. The creep model EN-1992/FIB for w/b ratio 0.3 predicts creep coefficients closer and higher to the experimental values. The creep model B-4 on other hand for w/b ratio 0.3 predicts creep coefficients closer and lower to the experimental values.

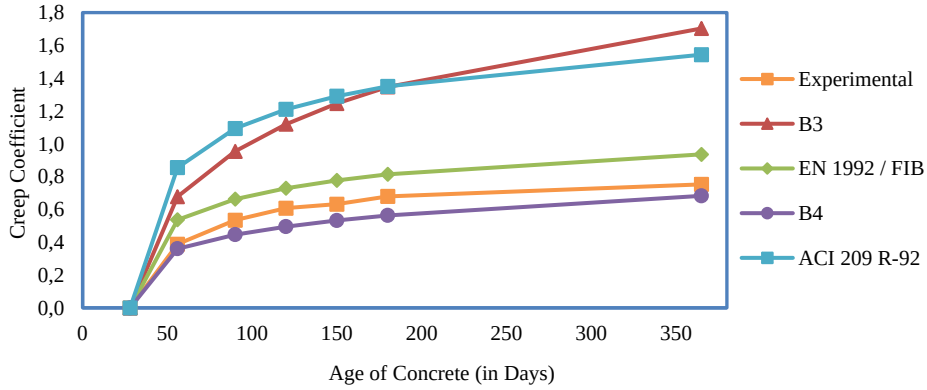

Fig. 12. Comparison of experimentally obtained creep coefficient for Lightweight Aggregate Concrete (LWAC) with w/b=0.3 and creep coefficient estimated by models

The difference in creep coefficient predicted by EN-1992/FIB model code even though it adopts factor for lightweight concrete taking into account the oven dry density can be attributed to fact that it causes reduction in creep coefficient for lightweight concretes for class above LC20/22 considering superior strength of paste matrix but does not takes into consideration the aggregate type and its moisture condition in concrete system resulting because of higher water absorption and porous nature. But for normal weight concrete, the values predicted by EN-1992/FIB creep model agrees with the experimentally determined creep coefficients.

8. Conclusions

The conclusions drawn based on experimental determination of creep coefficient for both normal and lightweight concrete and its comparison with creep models such as B-3, B-4, ACI-209 and EN:1992/FIB are as given below:

- The test results of creep strain per unit stress for both normal and lightweight concrete decreases as the compressive strength of concrete increases which is anticipated keeping in view that increase in strength increases elastic modulus of concrete which provides more resistance to strain. For the similar compressive strength level, the creep coefficient of lightweight concrete is less compared to normal weight concrete.
- The comparison of creep coefficients calculated using various models shows that there is increase in value of creep coefficient in case of all five model upto 330-365 days' age and beyond this period the increase in value of creep is minimal irrespective of the type of model. The creep coefficients determined using B-3 and B-4 model for normal weight concrete for both mixes with w/b ratio 0.5 and w/b ratio 0.4 gives higher value compared to EN-1992 / FIB model and ACI 209 model. The creep coefficients determined using B-3 and B-4 model for lightweight weight concrete for both mixes with w/b ratio 0.4 and w/b ratio 0.3 with similar compressive strength range compared to normal weight concrete gives higher value compared to EN-1992 / FIB model and ACI 209 model. The ACI 209 model gives lowest value among all five models. The creep coefficient enhancement rate beyond 365-day age for Bazant's B3 Model is comparatively on higher side than other four models.
- The experimentally obtained creep coefficients for normal weight concrete with w/b ratio of 0.5 is in between and near to creep coefficient determined through B3, B4 model and EN 1992/ FIB model. The creep coefficient predicted by ACI 209R-92 for normal weight concrete with w/b ratio of 0.5 is significantly low as compared to experimental results. The experimentally obtained creep coefficients for normal weight concrete with w/b ratio of 0.4 is in between and near to creep coefficient determined through B4 model, ACI 209 and EN 1992/ FIB model.
- The experimentally obtained creep coefficients for lightweight concrete with w/b ratio of 0.4 and 0.3 is lower than creep coefficient determined through all five creep models i.e. B-3, B4, ACI 209 and EN 1992/ FIB model. The creep coefficient predicted by B-3 and ACI-209 for lightweight weight concrete with w/b ratio of 0.4 and 0.3 is significantly high (1.50 times and 2.0 times respectively) as compared to experimental results. The creep model B-4 and EN-1992/FIB for w/b ratio 0.4 predicts creep coefficients closer to the experimental values. The creep model EN-1992/FIB for w/b ratio 0.3 predicts creep coefficients closer and higher to the experimental values. The creep model B-4 on other hand for w/b ratio 0.3 predicts creep coefficients closer and lower to the experimental values.
- The difference in creep coefficient predicted by EN-1992/FIB model code even though it adopts factor for lightweight concrete taking into account the oven dry density can be attributed to fact that it causes reduction in the creep coefficient for lightweight concretes for class above LC20/22 considering superior strength of paste matrix but does not takes into consideration the aggregate type and its moisture condition in concrete system resulting because of higher water absorption and porous nature. But for normal weight concrete, the values predicted by EN-1992/FIB creep model agrees with the experimentally determined creep coefficients.

References

[1] Ojha PN, Singh B, Singh A, Patel V, Arora VV. Experimental study on creep and shrinkage behaviour of high strength concrete. Indian Concrete Journal. 2021;95(2):30–42.
[2] Moon HJ, Koo KM, Kim HS, Seok WK, Lee BG, Kim GY. Suggestion of the prediction model for material properties and creep of 60~80MPa grade high strength concrete. Journal of Korea Institute of Building Construction. 2018;18:517-525. https://doi.org/10.5345/JKIBC.2018.18.6.517
[3] Zou D, Liu T, Teng J, Du C, Li B. Influence of creep and drying shrinkage of reinforced concrete shear walls on the axial shortening of high-rise buildings. Construction and Building Materials. 2014;55:46-56. https://doi.org/10.1016/j.conbuildmat.2014.01.034
[4] Ojha P N, Singh B, Singh, Patel V. Comparison of creep models and experimental verification of creep coefficients for normal and high strength concrete. Journal of Asian Concrete Federation. 2020;6(2,): 24-36.
[5] Wendling A, Sadhasivam K, Floyd RW. Creep and shrinkage of lightweight self-consolidating concrete for prestressed members. Construction and Building Materials. 2018;167:205-215. https://doi.org/10.1016/j.conbuildmat.2018.02.017
[6] Singh B, Singh SB, Barai SV. Performance of concrete made using sintered flyash lightweight aggregate- A review. Indian Concrete Journal. 2023;97(7):41-59.
[7] Ojha PN, Singh B, Behera AK. Sintered flyash lightweight aggregate-Its properties and performance in structural concrete. Indian Concrete Journal. 2021;95(6):20-30.
[8] Bate SCC. Guide for structural lightweight aggregate concrete: Report of ACI committee 213. International Journal of Cement Composites Lightweight Concrete. 1979;1(1):5-6. https://doi.org/10.1016/0262-5075(79)90004-6
[9] Kim YH, Trejo D, Hueste MBD, Kim JJ. Experimental study on creep and durability of high-early-strength self-consolidating concrete for precast elements. ACI Materials Journal. 2011;108-128.
[10] Shen D, Jiang J, Shen J, Yao P, Jiang G. Influence of prewetted lightweight aggregates on the behavior and cracking potential of internally cured concrete at an early age. Construction and Building Materials. 2015;99:260-271.
[11] Tang WC, Cui HZ, Wu M. Creep and creep recovery properties of polystyrene aggregate concrete. Construction and Building Materials. 2014;51:338-343. https://doi.org/10.1016/j.conbuildmat.2013.10.093
[12] Wu F, Liu C, Sun W, Zhang L, Ma Y. Mechanical and creep properties of concrete containing apricot shell lightweight aggregate. KSCE Journal of Civil Engineering. 2019;23:2948-2957. https://doi.org/10.1007/s12205-019-0738-2
[13] Chen B, Liu J. Experimental application of mineral admixtures in lightweight concrete with high strength and workability. Construction and Building Materials. 2008;22:1108-1113. https://doi.org/10.1016/j.conbuildmat.2007.03.001
[14] Sajedi F, Shafigh P. High-strength lightweight concrete using leca, silica fume, and limestone. Arabian Journal of Science and Engineering. 2012;37:1885-1893. https://doi.org/10.1007/s13369-012-0285-3
[15] Iqbal S, Ali A, Holschemacher K, Ribakov Y, Bier TA. Effect of fly ash on properties of self-compacting high strength lightweight concrete. Periodica Polytechnica Civil Engineering. 2017;61:81-87. https://doi.org/10.3311/PPci.8171
[16] Iqbal S, Ali A, Holschemacher K, Bier TA. Mechanical properties of steel fiber reinforced high strength lightweight self-compacting concrete (SHLSCC). Construction and Building Materials. 2015;98:325-333. https://doi.org/10.1016/j.conbuildmat.2015.08.112
[17] Zhou Y, Xi B, Sui L, Zheng S, Xing F, Li L. Development of high strain-hardening lightweight engineered cementitious composites: design & performance. Cement

Concrete Composites. 2019;104:103370-103377. https://doi.org/10.1016/j.cemconcomp.2019.103370
[18] Yixue Z, Jianghong M, Weiliang J, Zhang J. Creep model of high-performance concrete at different loading ages. Construction and Building Materials. 2022;357:129379. https://doi.org/10.1016/j.conbuildmat.2022.129379
[19] Li H, Li Y, Jin C, Liu J, Liu Y, Mu J. Meso-scale modelling of the effect of coarse aggregate properties on the creep of concrete. Journal of Building Engineering. 2022;54:104660. https://doi.org/10.1016/j.jobe.2022.104660
[20] Singh B, Patel V, Ojha PN, Arora VV. Analysis of stress block parameters for high strength concrete. Asian Concrete Federation Journal. 2020;6(1):1-9.
[21] Zhang LL, Wu LQ, Yang JX, Zhang K. Effect of fly ash on creep of high performance concrete used in bridge. In Proceedings of Applied Mechanics and Materials. 2018;2192-2195.
[22] Kou SC, Poon CS, Chan D. Influence of fly ash as cement replacement on the properties of recycled aggregate concrete. Journal of Materials in Civil Engineering. 2007;19:709-717. https://doi.org/10.1061/(ASCE)0899-1561
[23] Afroughsabet V, Teng S. Experiments on drying shrinkage and creep of high performance hybrid-fiber-reinforced concrete. Cement Concrete Composites. 2020;106:103481. https://doi.org/10.1016/j.cemconcomp.2019.103481
[24] Shen D, Liu C, Feng Z, Zhu S, Liang C. Influence of ground granulated blast furnace slag on the early-age anti-cracking property of internally cured concrete. Construction and Building Materials. 2019;223:233-243. https://doi.org/10.1016/j.conbuildmat.2019.06.149
[25] Shen D, Jiao Y, Gao Y, Zhu S, Jiang G. Influence of ground granulated blast furnace slag on cracking potential of high performance concrete at early age. Construction and Building Materials. 2020;241:117839. https://doi.org/10.1016/j.conbuildmat.2019.117839
[26] Pfeifer DW. Sand replacement in structural lightweight concrete-creep and shrinkage studies. ACI Journal Proceedings. 1968;65:131-140.
[27] Wendling A, Sadhasivam K, Floyd RW. Creep and shrinkage of lightweight self-consolidating concrete for prestressed members. Construction and Building Materials. 2018;167:205-215.
[28] Lopez M, Kurtis KE, Kahn LF. Pre-wetted lightweight coarse aggregate reduces long-term deformations of high-performance lightweight concrete. Special Publications. 2006;234:661-680. https://doi.org/10.14359/15965
[29] Lopez M, Kahn LF, Kurtis KE. Effect of internally stored water on creep of high-performance concrete. ACI Materials Journal. 2008;105:265. https://doi.org/10.14359/19823
[30] Bogas JA, Gomes A, Pereira MFC. Self-compacting lightweight concrete produced with expanded clay aggregate. Construction and Building Materials. 2012;35:1013-1022. https://doi.org/10.1016/j.conbuildmat.2012.04.111
[31] Rumsys D, Spudulis E, Bacinskas D, Kaklauskas G. Compressive strength and durability properties of structural lightweight concrete with fine expanded glass and/or clay aggregates. Materials. 2018;11:2434. https://doi.org/10.3390/ma11122434
[32] Shafigh P, Jumaat MZ, Mahmud HB, Alengaram UJ. A new method of producing high strength oil palm shell lightweight concrete. Materials & Design. 2011;32:4839-4843. https://doi.org/10.1016/j.matdes.2011.06.015
[33] Chen B, Liu J. Experimental application of mineral admixtures in lightweight concrete with high strength and workability. Construction and Building Materials. 2007;22:1108-1113. https://doi.org/10.1016/j.conbuildmat.2007.03.001

[34] Choi J, Zi G, Hino S, Yamaguchi K, Kim S. Influence of fiber reinforcement on strength and toughness of all-lightweight concrete. Composite Structures. 2014;112:165-178. https://doi.org/10.1016/j.compstruct.2014.02.029
[35] Lu JX, Shen P, Ali HA, Poon CS. Mix design and performance of lightweight ultra-high-performance concrete. Materials Design. 2022;216:110553.
[36] Inozemtcev AS, Korolev EV, Smirnov VA. Nanoscale modifier as an adhesive for hollow microspheres to increase the strength of high-strength lightweight concrete. Structural Concrete. 2017;18:67-74. https://doi.org/10.1002/suco.201500048
[37] Zhang D, Ge Y, Dai Pang S, Liu P. Effect of fly ash content on flexural performance and fiber failure mechanism of lightweight deflection-hardening cementitious composites. Construction and Building Materials. 2021;302:124349. https://doi.org/10.1016/j.conbuildmat.2021.124349
[38] Huang Z, Padmaja K, Li S, Liew JYR. Mechanical properties and microstructure of ultra-lightweight cement composites with fly ash cenospheres after exposure to high temperatures. Construction and Building Materials. 2018;164:760-774. https://doi.org/10.1016/j.conbuildmat.2018.01.009
[39] IS:383. Coarse and fine aggregate for concrete-specification. BIS, Delhi, India; 2016.
[40] IS: 269. Ordinary Portland cement - Specification. BIS, Delhi, India; 2015.
[41] IS: 9103–1999. Concrete admixtures-specification. BIS, Delhi, India; 1999.
[42] IS: 10262. Concrete mix proportioning — Guidelines. BIS, Delhi, India; 2019.
[43] IS: 9142 [Part-2]. Artificial lightweight aggregate for concrete- specification Part 2-Sintered flyash coarse aggregate. BIS, Delhi, India; 2018.
[44] Geiker MR, Bentz DP, Jensen OM. Mitigating autogenous shrinkage by internal curing. in high performance structural lightweight concrete. SP-218. Phoenix, AZ: American Concrete Institute; 2002. p. 143-154.
[45] P. N. Ojha, B. Singh, S. Prakash, P. Singh, M. K. Mandre, and S. Kumar, "Effect of high ratio fly ash on roller compacted concrete for dam construction," Research on Engineering Structures and Materials, 2022, https://doi.org/10.17515/resm2022.374ma1216
[46] Thomas MDA. Chloride diffusion in high-performance lightweight aggregate concrete. in Theodore Bremner symposium on high-performance lightweight concrete. Greece; 2003. p. 77-93.
[47] Jensen OM, Hansen PF. Autogenous deformation and RH-change in perspective. Cement and Concrete Research. 2001;31(12):1859-1865.
[48] Bazant ZP. Prediction of concrete creep and shrinkage: past, present and future. Nuclear Engineering and Design. 2001;203:27-38.
[49] Bazant ZP, Baweja S. Creep and shrinkage Prediction Model for Analysis and Design of Concrete Structures-Model B3. RILEM Recommendation. Materials and Structures. 1995;28:357-365.
[50] FIB Model Code 2010. International Federation for Structural Concrete (fib). ISSN 1562-3610, ISBN 978-2-88394-095-6; 2010.
[51] EN-1992-1-1. Eurocode 2: Design of concrete structures - Part 1-1: General rules and rules for buildings; 2004.
[52] ACI Committee 209. Prediction of Creep, Shrinkage, and Temperature Effects in Concrete Structures (ACI 209R.92). American Concrete Institute (ACI); 1992.
[53] TC-242-MDC. TC-242-MDC multi-decade creep and shrinkage of concrete: material model and structural analysis. RILEM Technical Committee; 2014.
[54] IS 456. Plain and reinforced concrete-code of practice. BIS, New Delhi; 2000.

Research on Engineering Structures & Materials
www.jresm.org
Research Group

Research Article

Influence of graphene oxide on mechanical and microstructural properties of cement composites

Ramamohana Reddy Bellum [1,a], Yaswanth K K [*,1,b], Chereddy Sonali Sri Durga [2,c], Chava Venkatesh [2,d], Sridevi G [3,e]

[1]*Dept. of Civil Engineering, Aditya University, Surampalem, Kakinada, India*
[2]*Dept. of Civil Engineering, CVR College of Engineering, Managalpalli, India*
[3]*Dept. of Electronics and Communication Engineering, Aditya University, Surampalem, Kakinada, India*

Article Info

Article history:

Received 10 July 2024
Accepted 12 Sep 2024

Keywords:

Graphene oxide;
Cement;
Mechanical properties;
Modulus of elasticity;
Microstructure

Abstract

A new nanomaterial known as graphene oxide (GO) has been discovered, and it has the potential to improve the tensile and elongation properties of cement-based composites. In this study, the influence of the content of GO, say 0.01% increment upto 0.05% on fluidity of cement composites was estimated. In addition, the mechanical properties of GO-based cement composites, such as compressive, split tensile, and flexural strengths, are presented with respect to the content of GO to figure out its effect and to identify the right proportion. In this paper, the deformability studies of GO-based cement composites, such as the elastic modulus (E), are also presented. To further investigate the formation of a denser matrix, microstructural studies are also carried out in GO-based cement composites. New avenues for high performance cement composites are opened up by this important and extensive study. The results are revealed that the inclusion GO has shown reduced fluidity values as compared to control mix in all stages of hydration process. Results revealed that the optimum content of 0.04% of GO enhanced the flexural strength by 67.52% which is quite phenomenal. GO with 31.24% of oxygen helps improving the microstructure by enhancing the modulus of elasticity and toughness of the composite.

1. Introduction

Special structures like high rise buildings, marine structures, hydraulic structures, cross sea bridges and under water tunnels desperately require the need of high-performance concrete because of its frequent exposure to the attacks of salts and alkali and would become deteriorated [1]. "Constructing a high-performance structure with high-performance concrete necessitates the use of materials that have several advantages over conventional concrete, such as increased strength and durability as well as improved chloride-ion migration resistance as well as freeze and sulphate resistance" [2]. The excellent compressive and poor tensile or flexural strengths clearly reveals the fractured nature of the concrete. Cement and carbon-based materials are highly improvised by cutting edge technologies like carbon nanotubes, carbon black etc. [3]. Because of the peculiar advantage of smaller size and high specific surface area [4].

Graphene oxide (GO) belongs to the graphite family that has undergone a chemical oxidation process [5,6]. A more compacted core and an increased rate of hydration response are the end results of the high concentration of O_2 functional groups in GO and

*Corresponding author: yaswanthk@adityauniversity.in
[a]orcid.org/0000-0002-0040-5812; [b]orcid.org/0000-0001-5587-6024; [c]orcid.org/0000-0003-0942-9252; [d]orcid.org/0000-0003-0028-7702; [e]orcid.org/0000-0002-7884-3409
DOI: http://dx.doi.org/10.17515/resm2024.344me0710rs

the high specific surface area it provides. Because of the presence of oxygen groups, the GO can be dispersed in water, but this is not enough to scatter carbon nanoparticles in cement mortar. More importantly, GO's high aspect ratio makes it an excellent light absorber. A large volume of water, preventing the cement paste from hydration [7]. Generally, graphene materials show excellent mechanical properties and good matrix adhesion, because of which it is emerged as a promising nano material in concrete-based composites. Graphene was initially isolated from graphite intercalation compounds in 2004 [8], when it was described as a single, planar, 2D honey comb shaped carbon layer.

Some research claim that graphene oxide has no influence on the hydration of cement in any way shape or form and it implies that adding GO does not affect the hydration of the cement process in its composites as demonstrated by Horszczaruk et al [9]. A study using X Ray Diffraction (XRD) demonstrated that the crystal phases of the cement hydration process remained unchanged after the addition of GO. If claims are to be believed, GO's primary function may be to stimulate or compel the twisting and deflection of paste-related fissures. According to certain researchers, GO also inhibited the spread of microcracks in cement-based products. There appears to be a lack of research in this area, hence it is uncertain how graphene oxide strengthens cement-based composites [10,11]. Research has shown that GO can help cement composites increase their strength and ductility, setting the stage for further development of cement composites to make it long-lasting and high-performance. Research into the properties of GO incorporated cement composites is still in its early phases, limited in scope and focused on specifics Few research has examined the impact of key factors. When it comes to concrete Composites of GO and cement, for example, water to cement ratio (w/c) influences the concrete's properties. [12] The high surface area, surface functionalization and significant dispersibility of graphene oxide (GO) in aqueous media make it a possible solution. This study examines the influence of GO w.r.t workability, consistency, microstructural properties (surface morphology) and mechanical properties (compression and flexural tests) of cement pastes. Additionally, the mechanism of the reinforcing and toughening effect is explained [13].

From the literatures it was revealed that, researchers tend to study the content of water in GO based cement mortars upon the fluidity test and also the effect of different particle sizes upon the mechanical properties [12]. Similarly, the hydration of the cement incorporated with GO was studied with the pore structure testing and thermogravimetric analysis. The fracture properties of cement pastes, both with low and high w/c ratios, were evaluated utilizing SEM observation of the GO-cement system's cement hydration products in various spatial situations. GO on cement-based materials was studied for its strengthening mechanism by comparing results from earlier investigations particularly with respect to the influence of its GO content upon the strength characteristics. The impact of polycarboxylate ether superplasticizer use and GO flakes dispersion on material strength are also investigated. Examining the microscopic structures of the cement mortar with and without GO, allows us to detect the graphene dispersion into the cement matrix [14,15].

GO has shown improvement in the strength and hardness of cement concrete, but its penetration into cement paste and concrete can have an adverse effect on their fluidity. The objective of this paper is to experiment the addition of graphene oxide w.r.t various properties of cement composites such as fluidity, mechanical, modulus of elasticity and durability properties. GO dispersion morphology and bonding into cement composites was also studied by conducting microstructural tests. This study is significant as graphene oxide can be incorporated into cement composites to improve toughness and reduce brittleness, which has a wide range of applications in water tight structures, impact resistant buildings, and structural components where ductility is required. GO dispersion in cement pore solution and the strength of GO incorporated cement mortar could be

improved using this study's one-pot method, which has many potential practical applications.

2. Properties of Common Cement Composite and Concrete Nanofillers

Reinforcement materials for fibre reinforced concrete (FRC) have been systematically investigated [30]. Table 1 shows the parameters of different fillers used in cement composites/concrete. When referred to Ordinary Portland Cement (OPC), they have a higher tensile performance. Cement composites' tensile and flexure properties will be enhanced by adding the reinforcing material.

Table 1. Various properties of concrete nanofillers and cement composite

Ref	Material	Thickness/ Diameter (mm)	Density (kg/m^3)	Aspect ratio	Surface area (m^2/g)	Modulus of elasticity (GPa)	Tensile strength (GPa)	Elongati @ break (%)
[16, 17]	Graphene	~0.08	2200	6000–600000	2600	1000	~130	0.8
[18, 19]	GO	~0.67	1800	1500–45000	700–1500	23–42	~0.13	0.6
[20, 21]	CNTs	15–40	1330	1000–10000	70–400	950	11–63	12
[22, 23]	Carbon fiber	6000–20,000	1770	100–1000	0.134	7–400	0.4–5	1.7
[24, 25]	Polymeric fiber (Polypropylene and Nylon)	18,000–30,000	900	160–1000	0.225	3–5	0.3–0.9	18
[26, 27]	Glass fiber	5000–10,000	2540	600–1500	0.3	72	3.45	4.8
[28, 29]	Steel fiber	50,000–900,000	7800	45–80	0.02	200	1.5	3.2

Steel, glass, polymeric, or carbon microfibers have been employed widely in the previous decades to reinforce cement composite/concrete. Table 1 shows the material parameters of these objects, which range from 10 to 1000 aspect ratios, based on existing literature. Steel and concrete structures are routinely retrofitted with carbon fibre [23] due to the material's high modulus of elasticity (above 200 MPa) and tensile strength (3.5 GPa). With the added benefit of limiting the expansion fractures generated by alkali silicate reaction and steel bar corrosion, steel fibres exhibit comparable mechanical properties [28].

It is possible for glass fibres to improve cement's tensile and flexural strength because of their 72.4 GPa elastic modulus [26] and 3.45 MPa tensile strength. strong alkaline medium of OPC can be resisted by the surface treatments and the usage of high zirconia glass and achieve the aforementioned degree of improvement [26]. Mechanical properties can strengthen the fragile cementitious matrix even with polypropylene fibres with weak mechanical characteristics [27]. Cement matrix is strengthened by fibres, which carry a portion of the applied load and are also capable of crack and pore-bridging. Fibers must have a high aspect ratio and high inherent strength in order to provide reinforcement.

Using microfibers as a bridging mechanism has increased the tensile strength and toughness. Microfibers have been shown to form a dense network of microcracks instead of large cracks, but they do not stop the initiation of cracks. Compressive strength is not influenced by the incorporation of microfibers into those material [39]. Furthermore, microfibers in the reinforced cement are a problem because they trap air voids and reduce the workability of the material. Carbon and polymer fibres can be functionalized to form bonds with the cement matrix, but their smaller surface area limits the strength [40]. Compared to traditional fibres, nanomaterials offer a better solution because they can be reinforced or modified at the nanoscale.

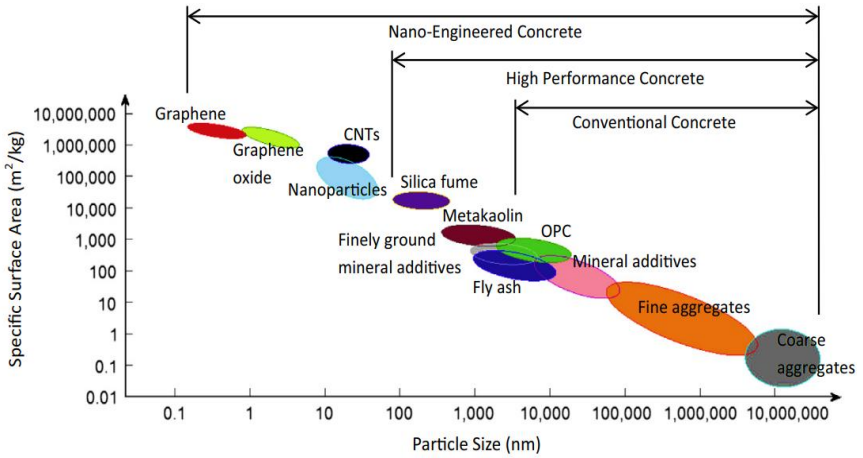

Fig. 1. Nanofillers versus additional cementitious materials in concrete [15]

Nanofillers can enhance the strength and durability of cement composites by using CNTs and GO as well as other nanoparticles. As illustrated in Fig. 1, their dimensions are comparable to the typical components of cement and concrete. Traditional concrete was traditionally held together by cement, which was considered the best ingredient for a strong bond between the aggregates. Supplementary cementitious ingredients like fly ash, slag and metakaolin were introduced after the demand for high performance concrete. Nanomaterials have been incorporated into cement based concrete composites due to advancements in nanotechnology [28,29]. Reinforcing the cement matrix at the nanoscale is expected to improve performance, due to the fact that the size of those particles is similar to the range to that of calcium silicate hydrate (C-S-H) gel.

When it comes to C–S–H nucleation, 2D GO has a higher surface area than even CNTs, which have been extensively studied [22-27]. As a result, GO nanomaterials are extremely reactive because of their vast surface area and numerous functional groups. The functionalization process would affect the mechanical characteristics of graphene as presented in [30]. To put it another way, graphene sheets have much higher mechanical strengths, such as tensile strength and modulus of elasticity, than those made of GO, in spite of the fact that cement has low tensile strength and elastic-modulus compared to GO-based cement composites. While nanoparticles have been shown to enhance hydration rates, nanofibers and 2D nanosheets have also been shown to strengthen the cement matrix due to their huge aspect ratios. As a result, even at extremely low concentrations of nanomaterial, the properties of nanocomposite can be developed. Nanocomposites' improved performance and unique functionality can be attributed to their surface effects rather than their bulk features. Nanomaterials' reactivity is boosted by their larger surface areas. Using these nanomaterials, the average diameter of C-S-H has been determined to

be 5 nm [30]. The strength of cement is derived from its high specific surface area and, as a result, its ability to adhere to surfaces.

3. Experimental Programme

3.1 Materials

OPC 43 cement was used in the study according to ASTM C 150-19a [31] and is obtained from UltraTech Cements Limited, India. The specific gravity and blaine's surface area are 3.13 and 370m^2/ kg respectively. The specific surface area of GO is tested to be 0.122×10^7 m^2/kg. Locally available river sand is used as fine aggregate. Table 2 and 3 represents the chemical analysis test results of cement and GO respectively.

Table 2: Cement- chemical composition

Composition	SiO_2	CaO	Al_2O_3	Na_2O	Fe_2O_3	SO_3	K_2O	MgO	LOI	TiO_2
Cement	21.4	65.1	4.18	0.63	3.10	1.96	1.01	1.97	0.37	-

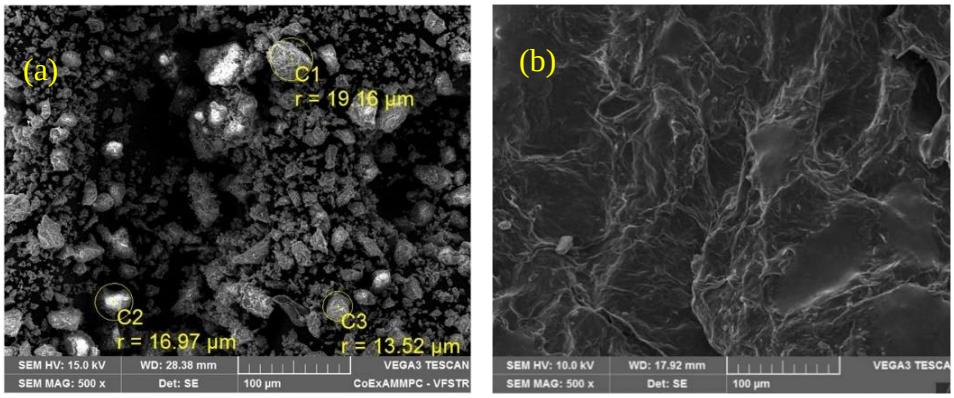

Fig. 2. SEM image, a) cement, b) graphene oxide

Table 3. Composition of GO

Material	C	O	SI	AI	S	MG
GO	66.41	28.95	1.78	0.68	1.67	0.51

Fig. 2 illustrates the SEM images of raw cement and GO where the spherical and irregular shape of particles can be observed (Fig. 2(a)). While the SEM image of GO represents that the particles are closely packed and a denser image was noticed from Fig. 2(b). The closely packed particles can have high specific surface area, that what the GO is called as nanofiller materials to pack the pores present in cement composites.

3.2 Mix calculations

In this work, samples were prepared using GO with the contents of 0%, 0.01%, 0.02%, 0.03%, 0.04% and 0.05%, w.r.t cement's weight. Table 4 presents the mix proportioning of

GO-based cement composites. The parameters of GO-based cement samples are compared using a single control mix (C). A control mix is used to compare samples of GO-based cement composites with those of the cement composite sample.

Table 4. Mix calculations (kg/m^3)

Mix id	Cement	GO (%)	Fine aggregate	Water
C	410	-	820	164
CG1	410	0.01	820	168
CG2	410	0.02	820	171
CG3	410	0.03	820	173
CG4	410	0.04	820	176
CG5	410	0.05	820	177

3.3 Dispersion of GO in Cement Samples

Cement composites can benefit greatly from the incorporation of GO into their formulation, but the process of dispersing graphene into water, which is particularly difficult due to the van der Waals force and the hydrophobic nature of GO, is also a challenge [32]. In case of improper dispersion of GO in cement matrix, it results in defects and the reinforcement terminology is affected [17]. Graphene dispersion in cement matrix has previously been accomplished using three different dispersion techniques viz., dry dispersion (with an electric concrete mixer for mixing), wet dispersion (using a surfactant with mechanical stirs); and another wet dispersion method which uses ultrasonic treatment along with surfactant and mechanical stirrer. Wet dispersion (without ultrasonic treatment) was used in this study due to the fact that this method produces more stronger reinforced composite as per the study [33]. With Graphene oxide to Dispersant ratio of 1:1.25 and ultrasonication time of 40 minutes and ultrasonic power and frequency of 200 W/30 kHz with polycarboxylic ether was used in the dispersion process of GO in cement composites.

3.4 Methods

3.4.1 Fluidity test

According to Indian National Standard IS 1199-1991 [34], the slump-flow of GO-reinforced cement was estimated. First step was to combine 300 g of cement, 100 g of H_2O, and 2 g of GO in a 2-minute mixing period. Then the combination was placed in the cone, which has the dimensions of 60mm, 36mm and 60mm as base diameter, top diameter and height respectively. This newly formed GO-based cement composite will crumble and spread as it is lifted 150 mm above its surface. The horizontal and vertical diameters of the spread were d_1 and d_2. The $(d_1 + d_2)/2$ value is the fluidity of the composite [35].

3.4.2 Water absorption

The cubes of size 70.6mm x 70.6mm were cast using cement composite and utilized to conduct the test in accordance with ASTM C1585-13 [36]. After that, specimens were allowed to cure in water for 28 days. Moisture content, if any, is eliminated by keeping the samples in hot air oven at 90°C for 24 hours. The samples were then weighed to determine their dry weight (W_1). Specimens were immediately preserved in water for 3-4 hours. The specimens were then weighed again, and the wet weight was taken into account (W_2). Average of three specimens were cast and tested for each mix for each curing day. Water absorption is calculated using the Eq (1);

$$Water\ absorption\ (\%) = \left[\frac{(W_2 - W_1)}{W_1}\right] X\ 100 \quad (1)$$

3.4.3 Sorptivity

Sorptivity was measured by using the ASTM C1585-20 [37] standard test procedure. To produce GO-based cement composites for sorptivity test 70.6 mm samples were used, the average three samples sorptivity values were noted. When determining the sorptivity, Eq. 2 was utilised. Average of three specimens were cast and tested for each mix for each curing day.

$$\frac{i}{\sqrt{t}} = S \tag{2}$$

3.4.4 Mechanical Properties

GO-reinforced geopolymer composite compressive strength is measured using ASTM C109/C109M-20b [38] on 70.6 mm cube moulds. Conventional water saturation curing method was followed for all experimentations. Similarly, C1006M-20a [39] and ASTM C293M-16 [40] are used to determine flexural and split tensile strengths on the moulds 50 × 100 mm and 40 × 40 × 160 mm prism (third-point loading), respectively. Average of three specimens were cast and tested for each mix for each curing day.

3.4.5 Modulus of Elasticity

Disc specimens (size 50mmx100mm) made following ASTM C469/C469M -14 were used in this test [41]. Average of 3 specimens were cast and tested for each mix for each curing day. Fig. 3 shows the test setup of all experimentations in this research.

3.4.6 Microstructural Studies

Various microstructural studies including Scanning Electron Microscope (SEM), X-ray diffraction analysis (XRD) and Energy Dispersive X-ray analysis (EDAX) were considered. Broken samples were carefully prepared and subjected to SEM test and similarly the powdered matrix samples were adopted for the XRD analysis such that the influence of GO can be clearly subjected to the test. The chemical elements and the chemical compounds of the hardened matrix materials were analyzed using the EDAX.

(a) (b)

(c)

(d)

(e)

Fig. 3. Experimental setups (a) fluidity test, (b) sorptivity test, (c) compression test, (d) splitting tensile test, and (e) flexural test

4. Result and Discussions

4.1 Fluidity

Fig. 4 presents the fluidity of GO-based cement composite samples. Higher fluidity reduction was observed in the mix CG5 with the inclusion of 0.05 wt% of GO. It was clear that the addition of GO in cement samples has showed in improved hardness and toughness properties, this was one of the major reasons for decrease in the fluidity. Fluidity decreased by 11.16, 10.71, 9.04, 12.78, and 9.38 % for mix CG1 compared to control mixture over various hydration times of 5, 30, 60, 90, and 120 min, respectively. While in the mix CG2 it was decreased by 16.26, 19.39, 15.25, 16.86, and 18.75 % in different hydration periods such as 5, 30, 60, 90, and 120 min, respectively. A huge decrease in the fluidity was observed due to the increase in the GO from 0.01 to 0.05%. The decreased fluidity values were 38.60, 38.87, 39.55, 44.77 and 48.75% for the hydration times of 5, 30, 60, 90 and 120 min, respectively as compared to reference mix. These values are clear that involvement of GO has shown negativity in the improvement of workability of the cement composites. The reason behind the decrement in the fluidity of GO-based cement composites is that the GO is one of the nanomaterials which will help to fill the pore-spaces between the cement particles and enhances the hardening time, so the fluidity of the fresh

composites was decreased with the increase in hydration time as well as increase in the GO content.

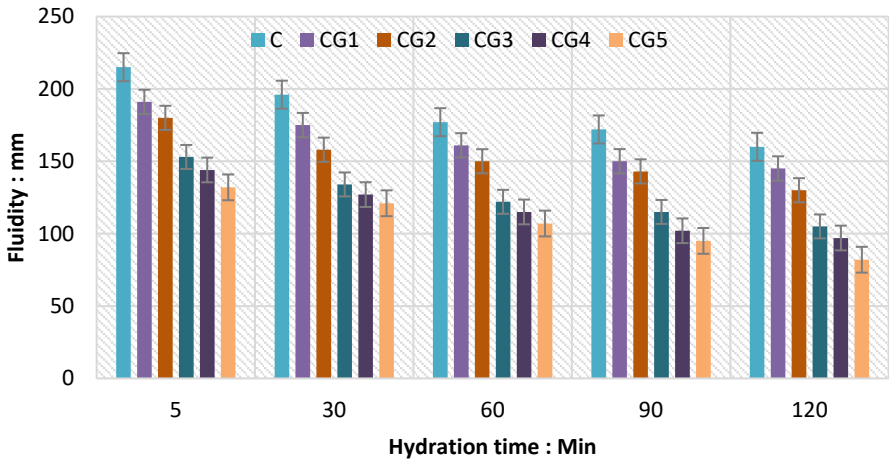

Fig. 4. Fluidity of GO-based cement composites

4.2 Water absorption

Fig. 5 depicts the influence of GO on the water absorption percentage of the composites. According to the findings, the inclusion of small amounts of GO had a vital impact on the water absorption of cement samples.

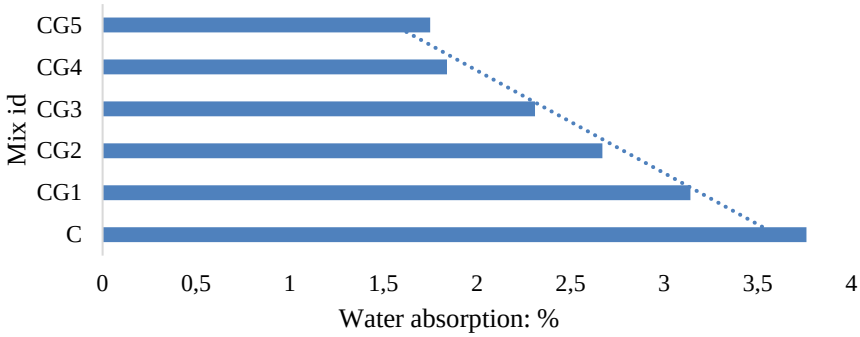

Fig. 5. Water absorption of GO-based cement composites

However, as the amount of GO in cement samples increased, water absorption decreased dramatically. This demonstrates that the inclusion of GO reduces the pore percentage in the composites. The water absorption percentage values for various levels of GO in cement composites mixes CG1, CG2, CG3, CG4 and CG5 are 3.14, 2.67, 2.31, 1.84 and 1.75%, respectively.

4.3 Sorptivity

It can be observed in Fig. 6 that the water sorptivity of GO-based samples is the lowest. Information of this sort indicated that capillary forces of 0.05 w/w % of GO samples shown lowest water permeability into cement samples. There is a reduction in the amount of

water carried by samples of GO-based cement compared to other GO replacement samples. This empirical evidence demonstrates that cement samples fortified with GO have greater resistance to water penetration. The inclusion of GO to cement composites, however, has been shown to improve microstructure parameters in terms of porosity, water absorption, and sorptivity. All five GO-based cement composite mixes (CG1, CG2, CG3, CG4, and CG5) have different sorptivity values: 0.133, 0.097, 0.068, 0.045, and 0.038. These numbers are extremely low in comparison to the control mixture. This is quite similar to research carried by Devi et al [42], as they revealed 0.08% reduces the sorptivity by 46%.

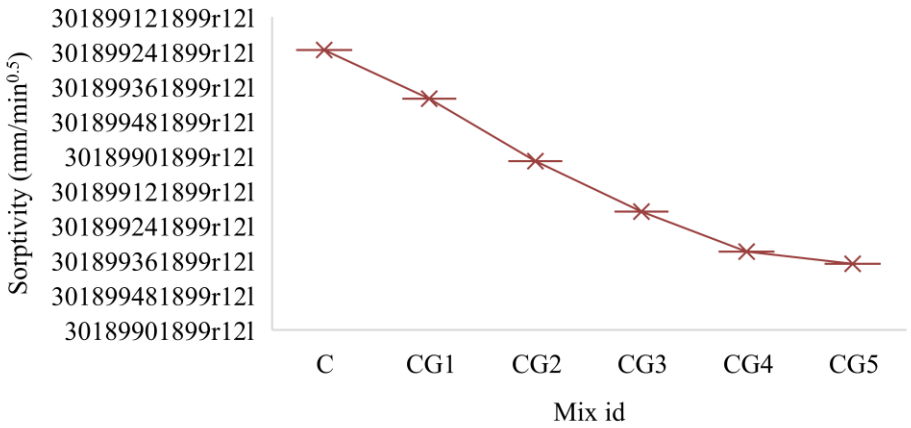

Fig. 6. Sorptivity values of GO-based cement composites

4.4 Compressive Strength

Nanomaterials, such as graphene, nanofibers, nano-silica, or nano-clay, have the potential to increase mechanical qualities because of their huge surface area. Higher efficiency during the early stages w.r.t the mechanical properties are evidence of the usefulness of nanoparticles in promoting the development of tensile and compressive strengths [43]. Cement composites benefit from the GO's particular properties, such as its surface roughness and functional group. As small as 0.05% w/w GO boosts the compressive strength to 51 % [44]. Fig. 7 depicts the test results of GO-based cement composites under different water curing. It was found that adding GO up to 0.04 wt.% increased compressive strength in the experiments. The strength of samples was reduced as the GO level was increased further. The samples with 0.04 w/w % GO doses at 28 days curing had a 27.26 % increment in compressive strength than the samples without GO. As demonstrated in Fig. 7, the compressive strength of cement composite with 0.05 w/w % of GO dose at 28 days of curing increased by 24.63 %. It was clear that the optimum inclusion of GO in the cement samples is limited to 0.04%. However, the microstructural studies are indicated that the inclusion of GO has shown greater impact in the formation of denser structure and leads to good compressive strength compared to reference mix.

GO blended cement samples had an impressive impact on strength properties, as the results of the experiments showed. On the other hand, GO inclusion showed altered microstructure, with the denser structure showing improved mechanical properties being achieved. Similar studies were made by Devi et al [42] and Reddy et al [45], where Devi et al have used the dosage of 0.02% increment up to 0.08% and Reddy et al have used 0.25% increment. In all these literatures, the experimental parameter was to identify the right content of GO oxide towards various properties of concrete. Reddy et al revealed that inclusion of 0.1% of GO was best and it has improved up to 38.46% towards compressive strength. similarly, Sharma et al [46] revealed 1% inclusion of GO improved up to 85% in

compressive strength. this study showed up to 28% improvement when 0.05% GO is used which is highly economical and efficient.

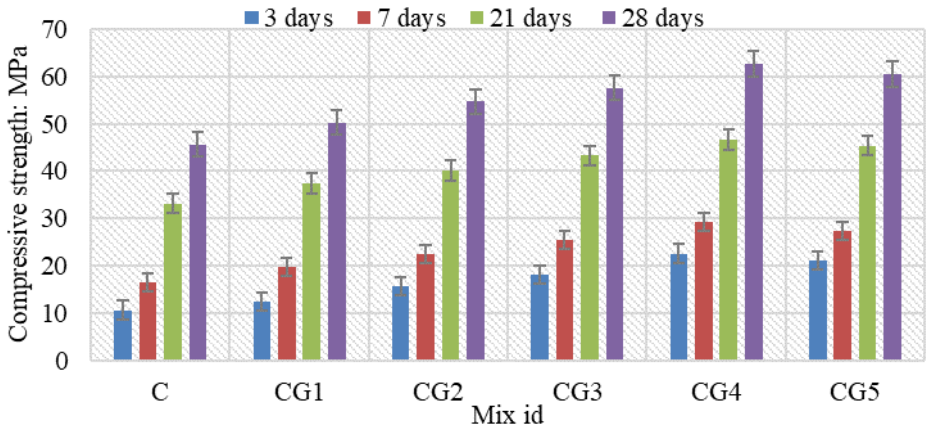

Fig. 7. Compressive strength of GO-based cement composites

4.5 Splitting Tensile Strength

Fig. 8 enumerates the splitting tensile results of GO-based composites. The presence of GO in samples has shown different morphology. However, it was clear that the inclusion GO up to 0.04 wt.% the tensile properties were enhanced gradually while further increase in the GO contents the tensile properties were reduced. The microstructural modifications were also observed in the GO-based cement samples such as identification of better C-S-H gel formation, wrinkle morphology, denser structure and interlocking of particles.

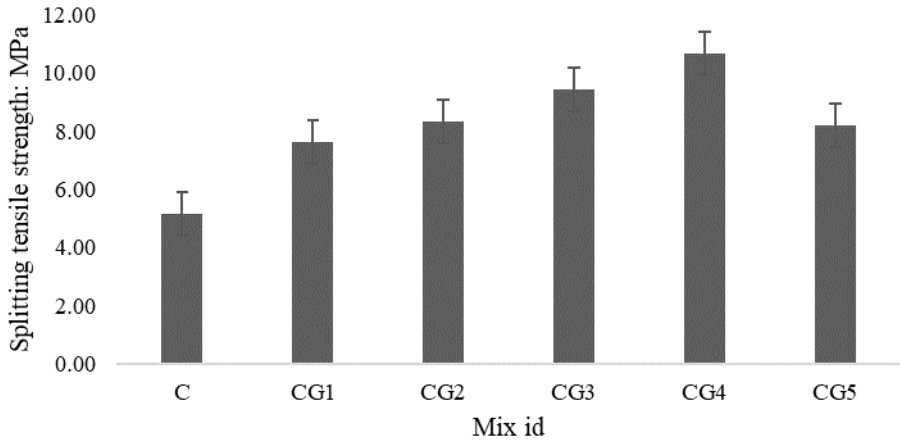

Fig. 8. Splitting tensile strength of GO-based cement composites

The samples with 0.04 w/w % GO doses at the age of 28 days had 51.59 % increase in splitting tensile strength than the reference mix. As demonstrated in Fig. 8, split tensile

strength of samples with 0.05 w/w % of GO dose at 28 days of water curing increased by 36.95%. It was clear that the optimum inclusion of GO in cement samples is limited to 0.04 wt.% in order to improve the tensile properties. It was clear that the inclusion of GO has shown impact in the improvement of splitting tensile strength than the compressive strength. Graphene oxide (GO) of 0.04 wt. % with O_2 content of 28.95 % was found to give cement composites their toughness, according to the results. The micro-structural condition of hydration crystals in those proposed composites has a major impact on mechanical properties.

Similar studies like Devi et al [42] also insisted that higher content of GO does not adhere the tensile properties and they revealed that 0.03% improved the tensile strength by 45%. Similar results were observed in this study as 0.04% was identified to be the most optimum with 51.59% enhancement.

4.6 Flexural Strength

The flexural strength of GO-based cement samples was presented in Fig. 9. Better flexural strength has been achieved with the addition of GO to cement samples of varying microstructural morphology. However, it was evident that the bending properties were gradually improved by the inclusion of GO up to 0.04 wt.%, but were weakened by further increase in the GO content. Better C-S-H gel formation, wrinkle morphology, a denser structure, and particle interlocking were majority of the microstructural changes seen in the GO-based cement samples compared to control mix. This will create more CSH gel and enhances the absorption capacity, and nano-filler effect makes the cement matrix more compact and refined by filling. These are the major reasons for better enhancement in the flexural properties of GO-based composites.

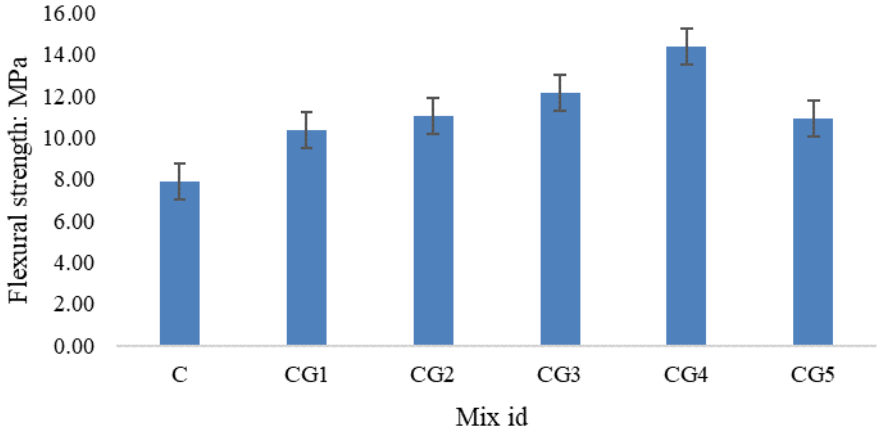

Fig. 9. Flexural strength of mixes

Whereas, increase in the GO content also increases the flexural strength. The inclusion of 0.01, 0.02, 0.03 and 0.04 wt.% of GO in cement composites enhances the strength percentage as 23.88, 28.57, 35.19 and 45.23%, respectively than the reference mix. However, further increment in the GO the reduces the strength. Fig. 9 shows that after 28 days of water curing, the splitting tensile strength of a cement composite with a 0.05 wt.% GO dose is 27.77% higher than it was with no GO addition. This value is lower than that seen with the inclusion of 0.04 w/w% of GO-based samples. This is similar to studies like

Reddy et al [45] where it revealed that 0.1% GO improve the flexural strength by 12.07%. It was observed that the GO nano particle fills the minute pores of the microstructure making it denser thereby showing improvement in tensile and flexural properties, however researchers suggest to figure the optimum content which may depend on other material properties.

4.7 Modulus of Elasticity

The modulus of elasticity results are depicted in Table 5. The addition of GO to cement composites improved the modulus of elasticity. After 28 days, the mixes CG1,CG2,CG3,CG4, and CG5 mixes showed 35.83, 36.57, 38.75, 40.12, and 37.48 GPa, respectively; the control mix was 34.41 GPa. Cement based samples containing 0.04 wt% GO had the highest elastic modulus, whereas samples containing 0.01 or 0.02% GO had the lowest elastic modulus values. As the GO content in the samples increases by 0.04 wt%, the modulus of elasticity decreased. When up to 0.04 wt% GO was added to cement composites under conventional water curing conditions, parameters are improved. The experiments revealed that the inclusion of GO improved the elastic modulus than the control mix. Certain codes and literatures recommended to predict the young's modulus which are as follows,

- As per ACI 318-14 [47], the young's modulus can be calculated using Eq. (3).

$$E_C = 0.043 \times \rho^{1.5} \times \sqrt{f'c} \quad (3)$$

Where, f'c = Characteristic compressive strength (MPa); E_c = Modulus of elasticity (MPa); f_c = Avg 28-day compressive strength in MPa, ρ = Density of concrete (kg/m^3);

- Eq. (4) can be used to calculate the elasticity modulus in accordance with AS 3600 [48].

$$E_C = \rho^{1.5}(0.02430\sqrt{f'c} + 0.12) \quad (4)$$

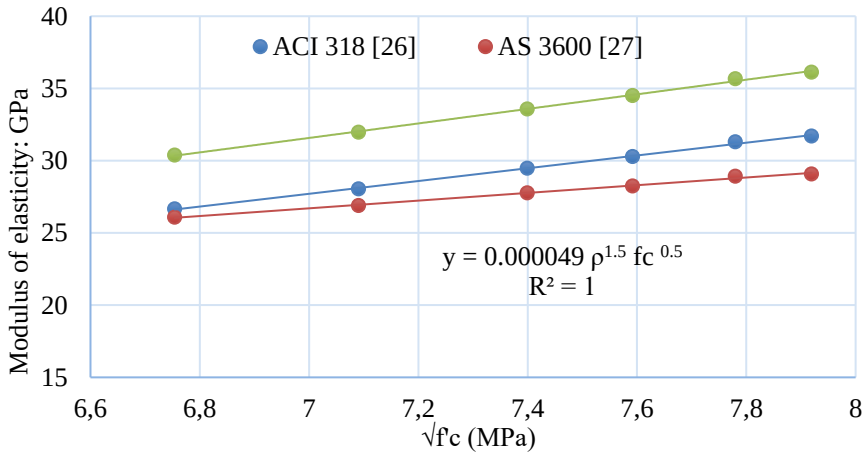

Fig. 10. Predicted modulus of elasticity of GO-based cement composites

Eq. (5) shows the calculation methodology of GO based composites with respect to experimental value of compressive strength. Fig: 10 shows the model of predicting the young's modulus of GO added cement mortar samples which can be anticipated after 28 days of water curing.

$$E_C = 0.000049 \times \rho^{1.5} \times \sqrt{fc} \quad (5)$$

Table 5 shows the elastic modulus of the cement samples as per the codal provisions and this paper. At 0.04 weight percent, the GO-based cement composite samples had a higher modulus of elasticity than the control mix.

Table 5. Experimental and predicted modulus of elasticity values

Mix id	Compressive Strength (MPa)	Density (Kg/m^3)	Modulus of Elasticity (E_c) GPa			
			Experimental (28 days), GPa	ACI 318 [26]	AS 3600 [27]	Present paper
C	45.62	2035	34.41	26.66	26.08	30.38
CG1	50.28	2038	35.83	28.05	26.89	31.97
CG2	54.75	2047	36.57	29.47	27.77	33.58
CG3	57.64	2049	38.75	30.28	28.24	34.50
CG4	62.72	2054	40.12	31.70	29.08	36.12
CG5	60.53	2061	37.48	31.30	28.92	35.67

4.8 X-Ray Diffraction

The XRD peaks indicate that the hydration crystals contained hydration products like AFt, AFm, C-H and C-S--H, and that count on those could be enhanced by increasing the hydration duration, as per Fig. 11. The peaks of CH in each sample were nearly identical; this could be because GO mostly promoted hydration in the early stages. The development of hydration crystals with respect to GO doses revealed that GO may affect the hydration process, marked impact on the mechanical parameters of the cement mortar was framed by the acquired data. The addition of 0.04 wt% of GO has shown better formation of C-S-H gel. This proves that the inclusion of GO in cement composites produces enriched hydration products and steady matrix. These are the additional characters in the improvement of mechanical properties for GO-based cement samples.

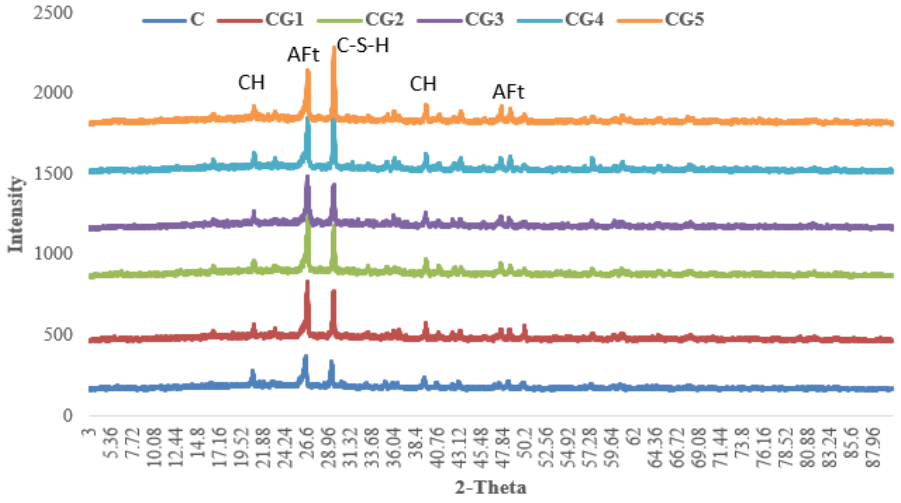

Fig. 11. XRD analysis of GO reinforced cement mixtures

4.9 Scanning Electron Microscope

When it comes to cement composites, the microstructural condition of the hydration crystals is most important for improving mechanical and durability properties [49,50]. It was found through the SEM images that the oxygen functional groups on GO's nanoparticle surfaces react with one another to form C-S-H and CH nano-hydration crystals as well as AFt and AFm hydration crystals. To make dense compacted structures, the hydration crystals can eventually grow and fill in the gaps, which enhances the toughness of cement composites magnificently in the presence of GO. A GO-based cement composite is likely to have better mechanical and durability properties as a result of its incorporation [51].

When GO is incorporated into cement composites, interlinked dense structure is appeared as hydration crystals, as shown in Fig. 12. As a result, at a GO content of 0.01 %, only a weaker C-S-H gel is formed. However, at 0.02 % and 0.03 % of GO content, a medium range of hydration crystal formations were observed, and at 0.04 %, increased gel forms and good dispersion were achieved, allowing the GO to be distributed in a similar pattern in the voids of cement composites.

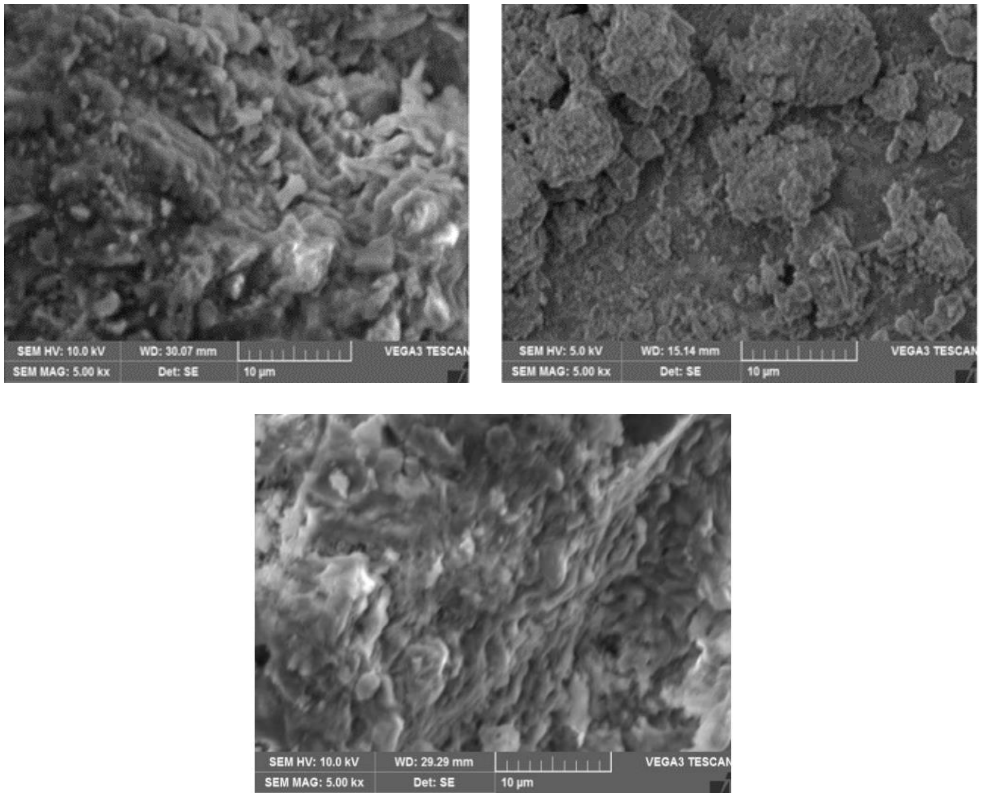

Fig. 12. SEM images of GO-based cement composites, (a) mix-C, (b) mix-CG1 and (c) mix-CG5

With an increase in the GO content, SEM pictures show that the cumulative volume of pores reduced. The cement mortar's pore volume has reduced significantly since the GO was added. furthermore, GO plays an important role in the increasing of hardening time.

4.10 Cost analysis

The cost analysis of the graphene oxide has been compared with other nano materials to check the efficiency and the benefit of the utilization of GO in cementitious materials and presented in Fig. 13. It was observed from the figure that, compared to popular nano materials like nano silica, nano iron oxide etc., GO is considered to be very much cost efficient. The cost of GO is almost similar to Nano alumina and it is 50% less than that of Nano iron oxide. Further, GO is 5 times cost effective than nano silica. Apart from other nano materials, the most expensive one is the carbon nano tubes which is about 200 times to that of other common nano materials. However, it is also to be analyzed that the quantity of GO required for effective utilization is very small compared to other nano materials.

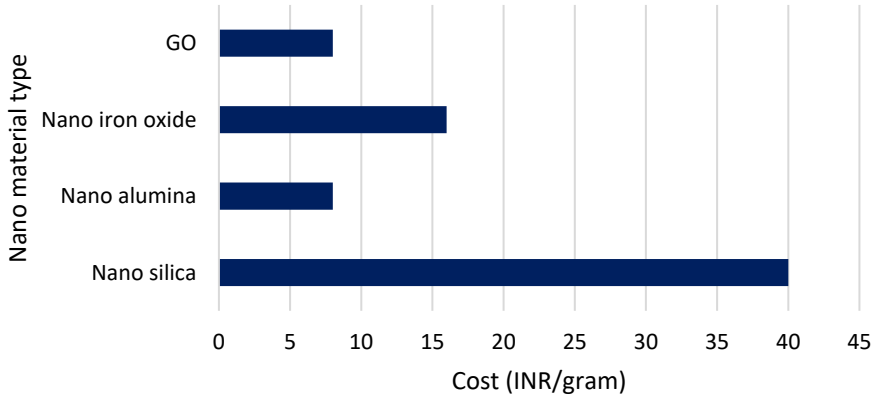

Fig. 13. Cost comparison of different nano materials in concrete

Conclusions

This paper attempted to use GO in cement-based composites with respect to mechanical and microstructural properties. Based on the several experimentations, the following conclusions are made.

- By separating calcium ions adhering to graphene oxide nanosheets, 0.04 wt % of GO was found to improve dispersion of GO, which prevented graphene oxide nanosheet aggregation in cement paste.
- Increase in GO reduces the fluidity of the samples. This clearly indicates the GO helps in improving the hydration process.
- The GO densifies the internal microstructure thereby water absorption and sorptivity is reduced. This relies the addition of GO minimizes the pore structure which also increases the durability.
- At a graphene oxide concentration of 0.04%, flexural strength increased by 67.52%, while at a concentration of 0.05%, cement composites improved by 50.21% after 28 days when compared to the control mix.
- The microstructure of hydration crystals in cement composite was modified by adding GO with a content of 31.24% oxygen, increasing the cement composite's modulus of elasticity and toughness.

- When graphene oxide was added, the hydration crystals were altered and the toughness of the composites increased, resulting in an overall improvement in their toughness.

Acknowledgement

The authors express their grateful thanks to the management of Aditya Engineering College for providing necessary laboratory facilities to complete this research work.

References

[1] Tang J H, Cai J W, Zhou M K. The status of researching and developing in high performance concrete. Science and Technology of Overseas Building Materials, 2006,27 (3): 11-15.
[2] Sun M, Liu Q, Li Z, et al. A study of piezoelectric properties of carbon fiber reinforced concrete and plain cement paste during dynamic loading. Cement and Concrete Research, 2000, 30(10):1593-1595. https://doi.org/10.1016/S0008-8846(00)00338-0
[3] Rawat, G., Gandhi, S. & Murthy, Y.I. Strength and rheological aspects of concrete containing nano-titanium dioxide. Asian J Civ Eng. 2022; 23: 1197-1208 . https://doi.org/10.1007/s42107-022-00476-2
[4] Pathak, S.S., Vesmawala, G.R. Influence of Nano-TiO2 and water to cement ratio on fracture parameters of concrete. Asian J Civ Eng. 2023; 24: 1969-1979. https://doi.org/10.1007/s42107-023-00616-2
[5] Hou Y G, Lv S H, Liu L P, Liu X. High-quality preparation of graphene oxide via the Hummers' method: Understanding the roles of the intercalator, oxidant, and graphite particle size. Ceramics International, 2020, 46(2): 2392-2402. https://doi.org/10.1016/j.ceramint.2019.09.231
[6] Liu, J., Zhao, L., Chang, F. et al. Mechanical properties and microstructure of multilayer graphene oxide cement mortar. Front. Struct. Civ. Eng. 2021; 15: 1058-1070. https://doi.org/10.1007/s11709-021-0747-3
[7] Babak, F, Abolfazl, H, Alimorad, R, et al. Preparation and mechanical properties of graphene oxide: cement nanocomposites. The Scientific World Journal 2014; 276323. https://doi.org/10.1155/2014/276323
[8] Singh, V., Joung, D., Zhai, L., Das, S., Khondaker, S. I. & Seal, S. Graphene based materials: Past, present and future. Progress in Materials Science. 20211; 56: 1178-1271. https://doi.org/10.1016/j.pmatsci.2011.03.003
[9] Horszczaruk, E.; Mijowska, E.; Kalenczuk, R.J.; Aleksandrzak, M.; Mijowska, S. Nanocomposite of cement/graphene oxide-Impact on hydration kinetics and Young's modulus. Constr. Build. Mater. 2015, 78, 234-242. https://doi.org/10.1016/j.conbuildmat.2014.12.009
[10] B. Wang, D. Shuang, Effect of graphene nanoplatelets on the properties, pore structure and microstructure of cement composites, Mater. Exp. 2018; 8(5): 407-416. https://doi.org/10.1166/mex.2018.1447
[11] W.J.Long J.J wei.H. Ma. F. Xing, Dynamic mechanical properties and microstructure of grapheme oxide nanosheets reinforced cement composites, Nano materials. 2017; 7(12): 407. https://doi.org/10.3390/nano7120407
[12] Alla, S., Asadi, S. Investigation on fluidity, microstructure, mechanical and durability properties of snail shell-based graphene oxide cement composite material. Asian J Civ Eng. 2023; 24: 189-204. https://doi.org/10.1007/s42107-022-00497-x
[13] Yang Y G, Chen Ch M, Wen Y F, et al. Oxidized graphene and graphene based polymer composites. New Carbon Materials, 2008, 23(3): 193-200.

[14] Wang, B.; Jiang, R.; Wu, Z. Investigation of the mechanical properties and microstructure of graphene nanoplatelet-cement composite. Nanomaterials 2016; 6: 200. https://doi.org/10.3390/nano6110200
[15] Sobolev K, Gutierrez MF. How nanotechnology can change the concrete world. Am Ceram Soc Bull 2005;84(11):16-9.
[16] Lee C et al. Measurement of the elastic properties and intrinsic strength of monolayer graphene. Science 2008;321(5887):385-8. https://doi.org/10.1126/science.1157996
[17] Stankovich S et al. Graphene-based composite materials. Nature 2006;442(7100):282-286. https://doi.org/10.1038/nature04969
[18] Zhu Y et al. Graphene and graphene oxide: synthesis, properties, and applications. Adv Mater 2010;22(35):3906-24. https://doi.org/10.1002/adma.201001068
[19] Dikin DA et al. Preparation and characterization of graphene oxide paper. Nature 2007; 448:457-60. https://doi.org/10.1038/nature06016
[20] Yu M-F et al. Strength and breaking mechanism of multiwalled carbon nanotubes under tensile load. Science 2000;287(5453):637-40. https://doi.org/10.1126/science.287.5453.637
[21] Peigney A et al. Specific surface area of carbon nanotubes and bundles of carbon nanotubes. Carbon 2001;39(4):507-14. https://doi.org/10.1016/S0008-6223(00)00155-X
[22] Li VC, Obla KH. Effect of fiber length variation on tensile properties of carbonfiber cement composites. Compos Eng 1994;4(9):947-64. https://doi.org/10.1016/0961-9526(94)90037-X
[23] Banthia N, Djeridane S, Pigeon M. Electrical resistivity of carbon and steel micro-fiber reinforced cements. Cem Concr Res 1992;22(5):804-14. https://doi.org/10.1016/0008-8846(92)90104-4
[24] Wang Y, Li VC, Backer S. Tensile properties of synthetic fiber reinforced mortar. Cem Concr Compos 1990;12(1):29-40. https://doi.org/10.1016/0958-9465(90)90033-T
[25] Pelisser F et al. Effect of the addition of synthetic fibers to concrete thin slabs on plastic shrinkage cracking. Constr Build Mater 2010;24(11):2171-6. https://doi.org/10.1016/j.conbuildmat.2010.04.041
[26] Benmokrane B, Chaallal O, Masmoudi R. Glass fibre reinforced plastic (GFRP) rebars for concrete structures. Constr Build Mater 1995;9(6):353-64. https://doi.org/10.1016/0950-0618(95)00048-8
[27] Trens P, Denoyel R, Guilloteau E. Evolution of surface composition, porosity, and surface area of glass fibers in a moist atmosphere. Langmuir 1996;12(5):1245-50. https://doi.org/10.1021/la950531e
[28] Yao W, Li J, Wu K. Mechanical properties of hybrid fiber-reinforced concrete at low fiber volume fraction. Cem Concr Res 2003;33(1):27-30. https://doi.org/10.1016/S0008-8846(02)00913-4
[29] Yazici S, Inan G, Tabak V. Effect of aspect ratio and volume fraction of steel fiber on the mechanical properties of SFRC. Constr Build Mater 2007;21(6):1250-3. https://doi.org/10.1016/j.conbuildmat.2006.05.025
[30] Samuel Chuah, Zhu Pan, Jay G. Sanjayan, Chien Ming Wang, Wen Hui Duan. Nano reinforced cement and concrete composites and new perspective from graphene oxide. Construction and Building Materials. 2014: 73; 113-124. https://doi.org/10.1016/j.conbuildmat.2014.09.040
[31] ASTM C150/C150M-19a, Standard Specification for Portland Cement, www.astm.org.
[32] H. Du, S. Dai Pang, Dispersion and stability of graphene nanoplatelet in water and its influence on cement composites, Constr. Build. Mater. 2018; 167: 403- 413. https://doi.org/10.1016/j.conbuildmat.2018.02.046
[33] H. Sixuan, Multifunctional graphite nanoplatelets (GNP) reinforced cementitious composites, National University of Singapore, Singapore, 2012. Master's Theses.

[34] IS 1199- 1991: Methods of sampling and analysis of concrete, Bureau of Indian Standards manak bhavan, 9 bahadur shah zafar maro, new delhi-110002.
[35] M. Ilg, J. Plank, A novel kind of concrete superplasticizer based on lignite graft copolymers, Cem. Concr. Res. 2016; 79: 123-130. https://doi.org/10.1016/j.cemconres.2015.09.004
[36] ASTM C1585-13, Standard Test Method for Measurement of Rate of Absorption of Water by HydraulicCement Concretes, www.astm.org.
[37] ASTM C1585-20, Standard Test Method for Measurement of Rate of Absorption of Water by Hydraulic-Cement Concretes.
[38] ASTM C109/C109M-20b Standard Test Method for Compressive Strength of Hydraulic Cement Mortars, 2020, www.astm.org.
[39] ASTM C1006 / C1006M-20a, Standard Test Method for Splitting Tensile Strength of Masonry Units, ASTM International, West Conshohocken, PA, 2020, www.astm.org.
[40] ASTM C293 / C293M-16, Standard Test Method for Flexural Strength of Concrete (Using Simple Beam With Center-Point Loading), ASTM International, West Conshohocken, PA, 2016, www.astm.org.
[41] ASTM C469 / C469M-14, Standard Test Method for Static Modulus of Elasticity and Poisson's Ratio of Concrete in Compression, ASTM International, West Conshohocken, PA, 2014.
[42] Devi, S.C., Khan, R.A. Effect of graphene oxide on mechanical and durability performance of concrete. Journal of Building Engineering. 2020; 27: 101007. https://doi.org/10.1016/j.jobe.2019.101007
[43] Vera-Agullo J et al., Mortar and concrete reinforced with nanomaterials, in nanotechnology in construction, vol. 3. Springer; 2009. p. 383-388. https://doi.org/10.1007/978-3-642-00980-8_52
[44] Makar J. The effect of SWCNT and other nanomaterials on cement hydration and reinforcement in nanotechnology in civil infrastructure. Springer; 2011. p. 103-130. https://doi.org/10.1007/978-3-642-16657-0_4
[45] Reddy, P. V. R. K., & Ravi Prasad, D. Graphene oxide reinforced cement concrete-a study on mechanical, durability and microstructure characteristics. Fullerenes, Nanotubes and Carbon Nanostructures. 2023; 31(3): 255-265. https://doi.org/10.1080/1536383X.2022.2141231
[46] Sharma, S., & Kothiyal, N. C. Influence of graphene oxide as dispersed phase in cement mortar matrix in defining the crystal patterns of cement hydrates and its effect on mechanical, microstructural and crystallization properties. Rsc Advances. 2015; 5(65): 52642-52657. https://doi.org/10.1039/C5RA08078A
[47] ACI 318-14, Building Code Requirements for Structural Concrete and Commentary, American Concrete Institute, Farmington Hills, MI 48331, U.S. A., 2014.
[48] AS 3600-2009, Reinforced Concrete Design, Cement Concrete and Aggregates Australia, Australian Standards, GPO Box 476 Sydney NSW 2001.
[49] Yaswanth, K. K., Reddy, K. H. K., Anusha, N., Praveen, B., Chippymol, J., Revathy, J., & Isleem, H. F. Engineered geopolymer composites: a comprehensive state-of-the-art review on materials' perspective. Archives of Civil and Mechanical Engineering. 2024; 24(3): 193. https://doi.org/10.1007/s43452-024-01007-3
[50] Kuppusamy, Y., Jayaseelan, R., Pandulu, G., Sathish Kumar, V., Murali, G., Dixit, S., & Vatin, N. I. Artificial neural network with a cross-validation technique to predict the material design of eco-friendly engineered geopolymer composites. Materials. 2022 15(10); 3443. https://doi.org/10.3390/ma15103443
[51] H. Du, H.J. Gao, S. Dai Pang, Improvement in concrete resistance against water and chloride ingress by adding graphene nanoplatelet, Cem. Concr. Res. 83 (2016) 114-123. https://doi.org/10.1016/j.cemconres.2016.02.005

Research on Engineering Structures & Materials
www.jresm.org
Research Group

Research Article

Analyzing and examining the impact of various fiber types on the mechanical and functional characteristics of UHPC

Mohammad Sadegh Shahid Zadeh [*,a], Amir Hossein Derakhshan Nezhad [b], Mahbobeh Mirzaie Aliabadi [c]

Department of Civil Engineering, Behbahan Khatam Alanbia University of Technology, Behbahan, Iran

Article Info

Article history:

Received 25 July 2024
Accepted 12 Sep 2024

Keywords:

Self-compacting concrete;
Permeability;
Compressive strength;
Tensile strength;
Temperature effect;
Ultrasonic pulse speed

Abstract

In this research, we compared the performance and mechanical properties of (UHPC) produced with varying percentages of waste and recycled fibers, including polypropylene plastic (plastic sack fibers) (PP), polyethylene terephthalate (PET), date palm fibers (DP), Monterey pine tree fibers (MP), human hair (HH), and aluminum (from metal cans) (AF). This was done in relation to a control sample of UHPC (WC). The study investigated the effects of different percentages of these fibers (0, 0.5, 1, 1.5, and 2 percent by weight of cement) with a length of 3 cm in self-compacting concrete. We conducted tests on fresh concrete, including Slump Flow, J-Ring, V-Funnel, L-Box, and U-Box, as well as tests on hardened concrete, such as compressive strength, tensile strength, permeability, crack width control, thermal cracking, Schmidt hammer tests, and ultrasonic pulse velocity. The results indicated that increasing the percentage of fibers (PP, PET, DP, AF, MP, and HH) in UHPC enhances tensile strength, reduces permeability, and increases compressive strength. Additionally, under the influence of temperature, a decrease in both the depth and length of cracks was observed in the concrete slabs. Notably, the inclusion of 2% human hair fibers (HH) in UHPC resulted in superior tensile strength, reduced permeability, and minimized both the length and depth of cracks compared to other fiber types. Conversely, the addition of 2% aluminum fibers (AF) led to a reduction in tensile strength, an increase in permeability, and an increase in both the length and depth of cracks. This research demonstrated that, in terms of mechanical and functional properties, human hair fibers provided better results in UHPC across all tests conducted, significantly enhancing the longevity of the structure.

1. Introduction

Concrete is a composite material that is extensively utilized in the construction industry worldwide [1-3]. It possesses the ability to withstand applied loads without deformation [4-6]. One of the unique features of concrete is its efficiency and fluidity, allowing it to be easily molded into various shapes; thus, it is regarded as the most widely used material in construction [7]. In civil engineering, there has been a growing interest in self-compacting concrete [8]. This type of concrete is still under development and offers a wide range of applications and properties [9]. Self-compacting concrete is characterized by its ability to fill molds easily, even in the presence of reinforcement bars (rebars). Self-compacting concrete can be classified based on four key characteristics: flowability, viscosity, ability to pass through reinforcement, and resistance to segregation. Due to its high viscosity and ability to spread, it fills molds under its own weight and is widely employed [10-13]. The stability of self-compacting concrete encompasses two aspects: 1) Static stability, which

*Corresponding author: shahidzadeh@bkatu.ac.ir
[a] orcid.org/0000-0001-5910-7724; [b] orcid.org/0009-0008-0994-8590; [c] orcid.org/0000-0002-9594-0489
DOI: http://dx.doi.org/10.17515/resm2024.367me0725rs

refers to the ability to resist the separation of paste and aggregate, and 2) Dynamic stability, which pertains to the ability to maintain a uniform distribution of aggregates during the mixing process [14-16]. When combined with rebars, self-compacting concrete enhances the tensile strength and overall tensile properties of the material [17-19]. However, self-compacting concrete (SCC) generally exhibits low flexural strength, low tensile strength, and poor resistance to cracking and shrinkage. Research indicates that the addition of fibers to self-compacting concrete can significantly improve the properties of hardened concrete [20-22]. The incorporation of fibers in concrete offers numerous benefits, including the prevention of sudden failure, enhancement of fracture energy, reduction of crack width, minimization of shrinkage, and increases in flexural strength, tensile strength, and toughness [23-25]. Factors such as fiber type, length, mass, length-to-diameter ratio, shape, surface roughness, and the configuration of fiber ends can directly influence the properties of both fresh and hardened concrete. Fibers have been used to reinforce concrete since ancient times. The inclusion of waste or recycled fibers in concrete can reduce the demand for industrial fibers [26]. This practice contributes to the sustainability of the concrete industry by minimizing environmental pollution and the disposal of industrial waste. Consequently, it presents one of the most viable environmental solutions for the disposal and recycling of industrial waste [27]. Self-compacting concrete reinforced with artificial or natural fibers is effective in enhancing tensile strength, bending behavior, impact resistance, temperature stability, heat transfer, fire resistance, crack control, and overall durability [28]. The addition of fibers to concrete is an efficient method for improving its properties [25]. Fiber-reinforced concrete exhibits enhanced tensile strength, ductility, and resistance to cracking. The fibers act as crack arresters and also reduce the porosity and permeability of concrete, thereby improving its mechanical properties, impact resistance, and reducing brittleness [29]. Compaction of concrete is a crucial factor in maintaining the uniformity and integrity of a structure. Improper compaction can lead to the formation of honeycombs, trapped air, cold seams, and subsidence cracks, all of which contribute to permeability issues, corrosion of steel, and a reduction in the final load-bearing capacity. Research has shown that incorporating fibers into concrete can mitigate these problems [30-31]. Numerous studies have been conducted on the use of fibers to enhance the properties of concrete, and several examples are reviewed below:

Mirabi Moghadam [32] investigated the effect of the shape and quantity of date palm fibers on the tensile strength of concrete. Manjunat et al. [33] conducted an experimental study in 2021 on the use of human hair as fibers to enhance the performance of concrete. Patel et al. [34] reviewed the research on cement concrete reinforced with human hair in 2021. In 2022, Omar et al. [35] examined the impact of human hair fibers on the performance of concrete containing a high dosage of silica fume. Mustafa [36] also in 2022, explored the mechanical properties of high-performance self-compacting concrete reinforced with red pine needle fibers. Jaskowska et al. [39] investigated the properties of self-compacting concrete incorporating plastic waste as aggregate in 2022. Janata et al. [42] evaluated the addition of polypropylene (PP) fibers to self-compacting concrete in 2023 to mitigate cracking and plastic shrinkage. Derakhshan Nezhad et al. [46] in 2024 studied the use of date palm fibers to enhance tensile strength in self-compacting concrete with silica fume. Mirzaie Aliabadi et al. [47] conducted a laboratory investigation in 2024 on the effects of plastic packaging belt fibers and iron oxide on the mechanical properties of self-compacting concrete. Rashidi et al. [48] compared the effects of crushed cement blocks and construction waste on the fresh and hardened properties of self-compacting concrete in 2024. Asghari Pari et al. [49] investigated the influence of rust and iron shavings on the mechanical properties of self-compacting concrete in 2024. Shahidzade et al. [50] examined the effect of palm fibers on the mechanical properties of self-compacting concrete in 2024. Finally, Derakhshan Nezhad et al. [51] studied the impact of recycled

polyethylene terephthalate fibers on the mechanical properties of self-compacting concrete in 2024. Reason: Improved clarity, readability, and technical accuracy by correcting grammatical errors, enhancing vocabulary, and ensuring consistent formatting.

This research is similar to the studies conducted by Mirabi Moghadam [32], Omar [35], Manjunat [33], Janata [42], and Mustafa [36]. However, it differs from these studies in that it incorporates ultrasonic testing, thermal cracking analysis, and the use of nano silica fume in the concrete slab samples. A key aspect of scientific advancement is the emphasis on sustainable development. Sustainable development involves utilizing existing resources and facilities while considering the needs of future generations, ensuring the optimal use of natural resources. Extensive research has been conducted on the potential of using natural or artificial fibers to enhance the tensile and compressive strength of concrete. Fibers serve as an effective solution for improving tensile strength, reducing permeability, enhancing compressive durability, mitigating thermal cracking, and controlling the width of concrete cracks. The innovative aspect of this project lies in the optimal utilization of recycled waste materials, which minimizes waste and environmental pollution. Additionally, nano silica gel was employed to enhance strength, reinforce the transition zone of concrete (the third phase), and utilize Viscosity Modifying Agents (VMA) to control the rheological properties in this mix design. These elements contribute to the innovative nature of this research. In this study, we investigate the mechanical and physical behavior, durability, compressive strength, and tensile strength of (UHPC) with various fibers, including plastic, wood, and metal. The specific fibers examined include polypropylene (PP), polyethylene terephthalate (PT), date palm (DP), Monterey pine (MP), human hair (HH), and aluminum (AF). The objective of this research is to compare the effects of different types of fibers on the properties of both fresh and hardened UHPC, focusing on their impact on tensile strength, concrete durability (as measured by permeability tests), crack width control in concrete slabs, ultrasonic pulse velocity, Schmidt hammer tests, thermal cracking, tensile strength, and compressive strength.

2. consumables

2.1. Materials utilized in the construction of UHPC

2.1.1. Cement

Choosing the appropriate type of cement for Ultra-High-Performance Concrete (UHPC) is crucial. Type II Portland cement was utilized in the mixture design, in accordance with the ASTM C150 standard [52] (as shown in Table 1).

Table 1. Type II Portland Cement

SO_3	MgO	CaO	Fe_2O_3	Al_2O_3	SiO_2	Chemical analysis
0.68	2.08	65.40	3.88	4.82	21.68	Percent
C_3A	C_2S	C_3S	LOI	K_2O	Na_2O	Chemical analysis
6.21	14.46	60.63	0.20	0.88	0.25	Percent

2.1.2. Specifications of Types of Fibers (Plastic, Wood, Metal)

- Polypropylene Fibers (PP) (Plastic Sack Fibers)

Polypropylene fibers are utilized as a reinforcing material in concrete, offering several advantages, including: enhanced durability of fiber-reinforced concrete, reduced surface cracking, increased corrosion resistance, minimized shrinkage, improved flexibility, chemical resistance, and strengthened mechanical properties against hardness and impact. Additionally, they provide resistance to freezing and thawing, decreased corrosion and magnetism, and enhanced performance in wet environments, as well as increased bending

and tensile strength while reducing both cracking and plastic shrinkage cracking. In general, polypropylene fibers are widely employed in various concrete applications to enhance performance and meet specific engineering requirements. Polypropylene is a semi-crystalline polymer composed of propylene monomers, and this semi-crystalline structure imparts flexibility and high mechanical strength to the fibers. The relatively low melting point of polypropylene makes it suitable for many low- to medium-temperature applications. Furthermore, polypropylene exhibits resistance to many acids, bases, organic solvents, and chemicals, a property attributed to its non-polar structure and long hydrocarbon chains. However, polypropylene has limited resistance to ultraviolet (UV) rays, which can cause it to degrade and become brittle when exposed to sunlight. This UV resistance can be improved by incorporating UV stabilizers. Due to its non-polar nature, polypropylene also has minimal water absorption, making it an ideal choice for use in humid environments.

- Polyethylene Terephthalate Fibers (PTF)

Polyethylene terephthalate (PET) is the primary and most common component in various types of plastic bottles that are discarded after use. One innovative application of polyethylene terephthalate is its use as thin fibers in construction, specifically as an additive in concrete. Incorporating polyethylene terephthalate fibers into concrete results in several benefits, including enhanced malleability, increased tensile strength, reduced permeability, and improved durability. Additionally, it offers heightened chemical and thermal resistance, impact resistance, and increased thermal stability at elevated temperatures. The use of PET fibers contributes to greater tensile durability and aesthetic appeal, while also reducing the overall weight of the concrete. It helps minimize surface cracks, enhances corrosion resistance, controls cracking, reduces plastic shrinkage cracking, improves impact resistance, and increases bending strength. PET is a thermoplastic polymer synthesized from terephthalic acid and ethylene glycol. Its crystalline structure endows PET with high mechanical strength and hardness. While PET is resistant to weak and strong acids, oils, and alcohols, it is susceptible to strong bases and concentrated acids. It exhibits very low water absorption, which helps maintain its mechanical properties in humid conditions. Although PET is stable against oxidation, it may decompose at extremely high temperatures, leading to a loss of its desirable properties.

Date Palm Fibers (DP)

The potential benefits of date palm fibers include increased tensile strength and flexibility, reduced weight, enhanced electrical insulation, improved heat resistance, greater corrosion resistance, and superior impact resistance. Additionally, they contribute to crack control, improved efficiency, reduced density, and sustainability, making them environmentally friendly. Generally, palm fiber is utilized in regions where palm trees are abundant, promoting the development of sustainable and eco-friendly construction methods. Date palm fibers possess a tubular structure with thick walls, composed of cellulose, hemicellulose, and lignin. This composition results in relatively high mechanical resistance. Cellulose provides high tensile strength, while lignin contributes to compression resistance and hardness. Due to their high lignin content, date palm fibers exhibit a degree of resistance to biodegradation; however, they may degrade in humid and hot environments. It is important to note that these fibers are not naturally resistant to insect and fungal attacks, necessitating protective treatments. Reason: Improved clarity, vocabulary, and technical accuracy while maintaining the original meaning.

- Monterey Pine Tree Fibers (MP)

The incorporation of pine tree fibers into concrete can enhance its various properties. Some potential benefits of using pine tree fibers in concrete include increased tensile

strength, reduced surface cracking, improved impact resistance, decreased shrinkage, enhanced flexural and tensile strength, crack resistance, reduced permeability, lightweight characteristics, material stability, and increased efficiency. Pine tree fibers are particularly suitable for regions where pine trees are abundant, promoting the use of sustainable and locally sourced materials in construction. Their inclusion can significantly improve the mechanical performance of concrete and its resistance to external factors. While these fibers are resistant to humidity and typical environmental conditions, they are susceptible to strong solvents and concentrated acids. Due to their high lignin and hemicellulose content, pine tree fibers exhibit greater resistance to biodegradation compared to other plant fibers.

- Human Hair Fibers (HH)

Some potential effects of using human hair in various applications include increased tensile strength, improved crack control, environmental sustainability, lightweight properties, thermal insulation, enhanced flexibility, and reduced permeability. While human hair is commonly associated with beauty purposes, it also offers resistance to cracking. Human hair is composed of three main layers: the inner core (medulla), the middle layer (cortex), and the outer covering (cuticle). The cortex contains keratin fibers, which provide high tensile strength and elasticity. Keratin is a protein with a fibrous structure that includes sulfur-containing amino acids, such as cysteine. These amino acids form disulfide bridges that enhance tensile strength and flexibility. Hair is resistant to most acids and weak bases; however, it can be damaged by strong oxidizers and bases. Additionally, hair has the capacity to absorb moisture, allowing it to swell and shrink in response to changes in environmental humidity. Reason: The revised text improves clarity, enhances vocabulary, and corrects grammatical errors while maintaining the original meaning.

- Aluminum Fibers (AF)

Some potential effects include increased heat resistance, reduced weight, enhanced flexibility, corrosion resistance, improved tensile strength, better bending strength, improved conductivity, decreased density, and greater resistance to impact.

Fig. 1. Types of fibers (plastic, wood, metal)

Aluminum fibers are frequently utilized in specialized concrete applications where their unique properties are advantageous, such as in projects that demand conductivity or resilience against harsh environmental conditions.

Table 2. Specifications of types of fibers (plastic, wood, metal)

Diameter (mm)	Thermal bending temperature	Melting point (℃)	Elongation in submission	Elongation at failure	Tensile strength (MPa)	Tensile strength (MPa)	Water absorption (24 hours)	Special Weight (gr/cm³)	Modulus of elasticity (GPa)	Type of fiber	No
0.7	67	207	3.6%	30%	0.08	341	8%	0.90	1.8	(PP)	1
0.6	54	177	1.2%	26%	0.06	725	27%	0.67	4	(PT)	2
0.5	86	277	0.8%	12%	0.07	70	57%	0.80	0.782	(DP)	3
0.9	88	286	0.7%	10%	0.07	61	62%	0.71	0.682	(MP)	4
0.4	80	300	0.9%	17%	0.08	526	52%	0.86	1	(HH)	5
0.8	130	670	5%	53%	0.003	9570	5%	2.7	10	(AF)	6

2.1.3. Aggregates

Almond sand that passed through a 1/2-inch sieve and sand that passed through an 8-inch sieve were used, in accordance with the ASTM C33 standard [53], as indicated in Table 3.

Table 3. detailed specifications of the aggregates

Aggregate type	SSD (gr/m³)	Water absorption percentage	Bulk Density (kg/m³)	Fineness Modulus
Coarse aggregate	2.571	1.3	1526	6.3
Sand	2.544	1.8	1489	2.5

2.1.4. Super Lubricant And Nano Silica Gel

Super Plast PC5000 carboxylate superlubricants are among the most widely utilized chemical additives in high-performance and self-compacting concretes. This research employed these additives, which are based on carboxylate chemistry. By reducing the water-to-cement ratio, the capillary pores within the cement matrix are minimized, enhancing the hydration process of the cement and significantly increasing the compressive strength of the concrete.

Table 4. Mechanical Characteristics of Nano Silica and Super Lubricants

Special Weight (kg/m³)	Color	PH	Specific gravity (kg/liter)	physical condition	Characteristics
			Super lubricant		
1.008	yellow	6	1.1	liquid	Specifications
			Nano silica gel		
325	Black	8	1.6	thick liquid	Specifications

To achieve the mechanical properties characteristic of ultra-high-performance concrete (UHPC), nanosilica—derived from nanopolycarboxylate—was utilized as both a water-reducing agent and a reinforcement for exceptionally strong concrete, in accordance with ASTM C 494 standards [54] (refer to Table 4).

2.1.5. Water

Potable water was utilized in the formulation of the (UHPC) mix for producing and processing the samples, in compliance with the requirements outlined in ASTM C 94 [55] (refer to Table 5).

Table 5. Characteristics of Drinking Water

Chloride ion concentration	PH	Temperature (Celsius)	Characteristics
50	6	20	amount of

2.1.6. Limestone Powder

One essential material for achieving the proper viscosity in (UHPC) is stone powder. As a filler, stone powder possesses a very high specific surface area, which enhances the friction between the particles and consequently increases the viscosity of UHPC.

Table 6. Qom Limestone Powder

LOI	SO_3	Cao	MgO	Fe_2O_3	Al_2O_3	SiO_2	Chemical analysis
43.2	1.24	51.22	0.81	0.5	0.35	2.8	Percent

2.1.7. *Viscosity Modifying Admixtures (VMA)*

VMA powder admixture is designed to produce (UHPC) with enhanced viscosity and controlled rheological properties. VMA is crucial for regulating excess water in concrete, in accordance with the ASTM C 494/C 494M standard [54-56] (as illustrated in Figure 2).

1

2

3

4

5

6



7 8 9

Fig. 2. Materials: UHPC (1. Cement, 2. Stone powder, 3. Viscosity-modifying agent (VMA), 4. Coarse aggregate, 5. Nano silica gel, 6. Pea gravel, 7. Superplasticizer, 8. Sand, 9. Water)

2.2. Mixed Design

25 designs of Ultra-High-Performance Concrete (UHPC) mixes were investigated, focusing on the effects of various fibers on different bases (plastic, wood, metal). The fiber percentages were varied in different ratios: 0%, 0.5%, 1%, 1.5%, and 2% by cement weight. In all 25 mixed designs, the total amount of materials remained constant, while the percentages of the different types of fibers were adjusted (as shown in Table 7). The material units are expressed in kg/m^3, with a concrete grade of 400 and a water-to-cement ratio of 0.31.

Table 7. Mixing Plan for UHPC with and without fibers

Nano silica gel	fibers (plastic, wood, metal)	VMA	Stone powder	super lubricant	Water	sand	Almond sand	pea gravel	Cement
Self-compacting concrete without fibers (control)) 0%									
7	-	0.167	60	12	126	990	250	550	400
Self-compacting concrete with 0.5% fibers									
7	2	0.167	60	12	126	990	250	550	400
Self-compacting concrete with 1% fibers									
7	4	0.167	60	12	126	990	250	550	400
Self-compacting concrete with 1.5% fibers									
7	6	0.167	60	12	126	990	250	550	400
Self-compacting concrete with 2% fibers									
7	8	0.167	60	12	126	990	250	550	400

2.3. Conducting the Test

After mixing the materials in the mixer, it is essential to test the properties of fresh (UHPC) both with and without fibers. In this research, the average percentage of each UHPC variant with the respective fibers is detailed in the results and tests.

Table 8. Symbols for Each Fiber Used in the UHPC Mix Design

No	Fibers	Symbol	Percentage	L/D*	Symbol of total percentages
1	Polypropylene	PP	0.5, 1, 1.5, 2	42.85	PP 0.5 – 2%
2	polyethylene terephthalate	PT	0.5, 1, 1.5, 2	50	PT 0.5 – 2%
3	Date palm	DP	0.5, 1, 1.5, 2	60	DP 0.5 – 2%
4	Monterey pine tree	MP	0.5, 1, 1.5, 2	33.33	MP 0.5 – 2%
5	Human hair	HH	0.5, 1, 1.5, 2	75	HH 0.5 – 2%
6	Aluminum	AF	0.5, 1, 1.5, 2	37.5	AF 0.5 – 2%

*Fiber length to diameter ratio

2.3.1. Slump Flow Test

Slump flow testing is a widely used method for assessing the performance of (UHPC) due to its simplicity. The results of the slump flow test, presented in Figure 3, are based on the average measurements.

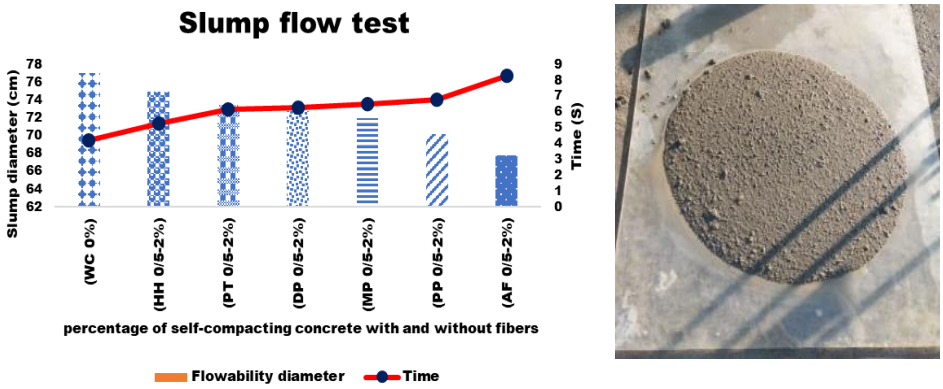

Fig. 3. Slump flow test

The average results of the slump flow test indicated that the water-cement ratio (WC) at 0%, hybrid fibers (HH) at 2-0.5%, polypropylene fibers (PT) at 2-0.5%, and other fibers such as diatomaceous earth (DP) at 2-0.5%, mineral powder (MP) at 2-0.5%, polyethylene fibers (PP) at 2-0.5%, and aramid fibers (AF) at 2-0.5% respectively. By increasing the percentage of fibers in (UHPC), the slump diameter (flowability) decreased by 2.59%, 4.54%, 5.45%, 6.49%, 8.83%, and 11.94% compared to the control UHPC. Additionally, the slump flow time increased by 1.1, 2.0, 2.2, 2.4, 2.8, and 4.1 seconds respectively compared to the control UHPC. This change is attributed to the diameter and water absorption characteristics of the fibers, which influenced the viscosity and flowability of the UHPC. This test adheres to the ASTM C1611 standard [57]. The order of the effect of fibers on the slump flow test is as follows:

- Slump diameter: (WC) > (HH) > (PT) > (DP) > (MP) > (PP) > (AF)
- Time: (WC) < (HH) < (PT) < (DP) < (MP) < (PP) < (AF)

2.3.2. V-Funnel Testing

The V-Funnel test is conducted to assess the ability of (UHPC) to change flow direction and flow characteristics. The results of the V-Funnel test are presented in Figure 4. The average

results of the momentary V-Funnel test and the 5-minute V-Funnel test indicated that as the percentage of various types of fibers increased specifically, (WC 0%), (HH 0.5-2%), (PT 0.5-2%), (DP 2-0.5%), (MP 2-0.5%), (PP 2-0.5%), and (AF 2-0.5%)—the duration of the tests increased to 0.8, 1.7, 2.5, 3.2, 4.1, and 5.3 seconds for the momentary test, and 1.2, 2.1, 3.2, 4.3, 4.9, and 6.6 seconds for the 5-minute test, respectively. This increase in time compared to the UHPC (control) can be attributed to the type, diameter, and texture of the fibers used, in accordance with the ISISIR 3203-9 standard [58]. The order of influence of the fibers on the V-Funnel test is as follows:

- Time: (WC) < (HH) < (PT) < (DP) < (MP) < (PP) < (AF)

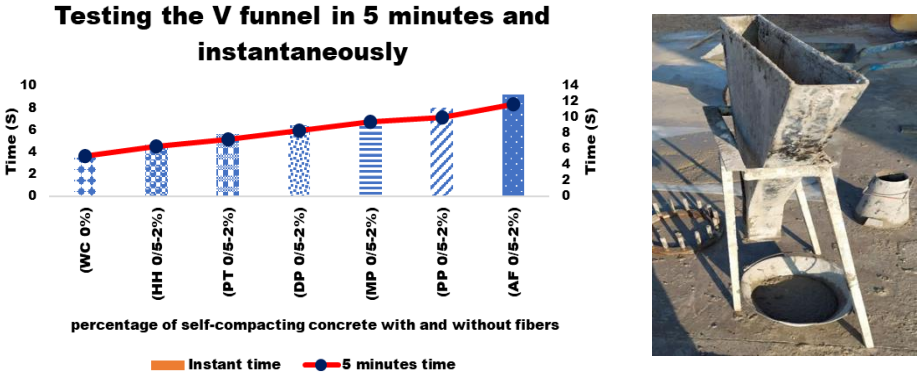

Fig. 4. V-Funnel test

2.3.3. L-Box Test

The L-Box test evaluates the flow of concrete between rebars, its stability against grain separation, and its fillability. The results of the L-Box test are presented in Figure 5.

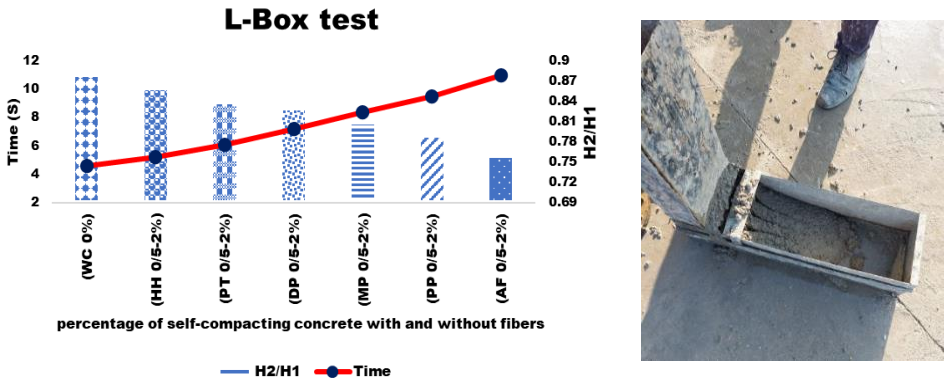

Fig. 5. L-Box test

The average results of the L-Box test indicated that as the percentage of various types of fibers increased—specifically (WC 0%), (HH 2-0.5%), (PT 2-0.5%), (DP 0.5%-2%), (MP 2-0.5%), (PP 2-0.5%), and (AF 2-0.5%)—the test duration also increased, with recorded times of 0.6, 1.5, 2.6, 2.8, 4.9, and 6.4 seconds, respectively. The heights of the concrete at

the end of the horizontal section (H2) and the end of the vertical section (H1) were measured, and the ratio H2/H1, known as the document ratio, was calculated. As the percentage of different types of fibers increased, the document ratio decreased by 2.27%, 4.54%, 5.68%, 7.95%, 10.22%, and 13.63%, in accordance with the INSO 3203-10 standard [59].

- Proportion of documents: (WC) > (HH) > (PT) > (DP) > (MP) > (PP) > (AF)
- Time:(WC) < (HH) < (PT) < (DP) < (MP) < (PP) < (AF)

2.3.4. J-Ring Test

The J-Ring test simulates the flow of concrete through reinforcing bars (rebars) and is used to assess its passability. The results of the J-Ring test are presented in Figure 6.

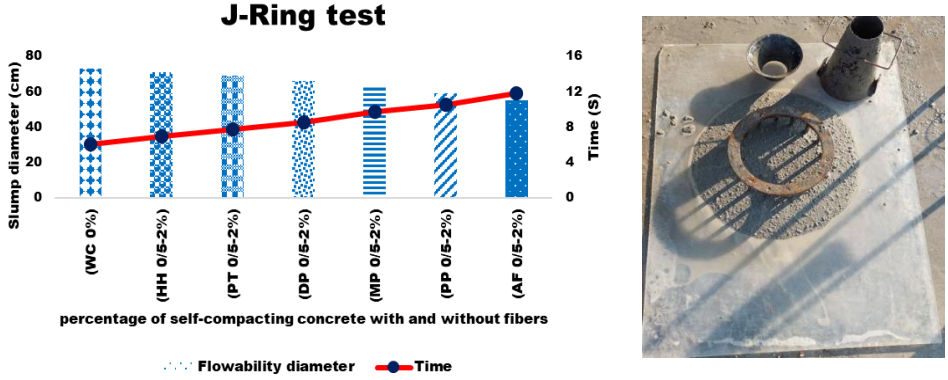

Fig 6. J-Ring test

The results of the J-Ring test indicated that as the percentage of various types of fibers increased—specifically, (WC 0%), (HH 0.5-2%), (PT 2-0.5%), (DP 0.5%-2%), (MP 0.5-2%), (PP 0.5-2%), and (AF 0.5-2%)—the slump diameter (flowability) decreased to 2.73%, 5.47%, 9.58%, 13.69%, 19.17%, and 24.65% compared to the (UHPC) control. Additionally, the time decreased by 0.9, 1.7, 2.5, 3.7, 4.5, and 5.7 seconds compared to the self-compacting concrete control. This effect can be attributed to the diameter of the fibers and their effective texture, as tested according to the INSO 11271 standard [60]. Order of influence of fibers on the J-Ring test:

- Slump diameter:(WC) > (HH) > (PT) > (DP) > (MP) > (PP) > (AF)
- Time:(WC) < (HH) < (PT) < (DP) < (MP) < (PP) < (AF)

2.3.5. U-Box Testing

U-box is utilized to assess the filling ability and flowability of concrete. The results of the U-box test are presented in Figure 7. The results of the U-Box test indicated that as the percentage of various types of fibers increased—specifically, (WC 0%), (HH 0.5-2%), (PT 2-0.5%), (DP 2-5.0%), (MP 0.5-2%), (PP 0.5-2%), and (AF 0.5-2%)—the time taken for the test increased to 1.1, 1.8, 2.5, 3.8, 5, and 6.6 seconds, respectively, compared to self-compacting concrete (control). Additionally, the difference in the height of concrete in the two ducts (H2-H1) increased to 1.5, 3, 4, 5.6, 7, and 11 millimeters, respectively, when compared to ultra-high-performance concrete (UHPC) (control). The difference in concrete height between the two ducts (H2-H1) was less than 30 mm, which was deemed

acceptable. This test adheres to the UNI 11044 standard [61]. The order of influence of the fibers on the U-Box test is as follows:

- H2-H1: (WC) < (HH) < (PT) < (DP) < (MP) < (PP) < (AF)
- Time: (WC) < (HH) < (PT) < (DP) < (MP) < (PP) < (AF)

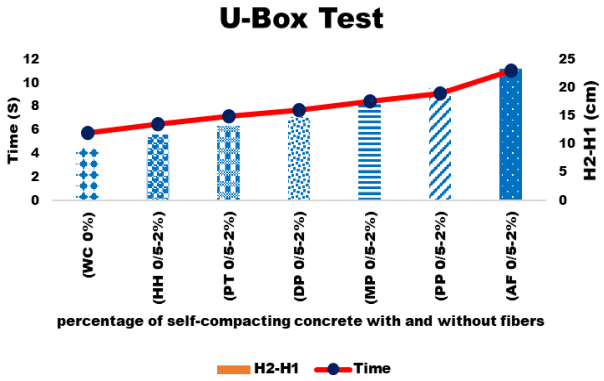

Fig 7. U-Box test

2.4. Sample Processing

Fresh concrete was cast in cubic molds measuring 15 cm x 15 cm x 15 cm and in cylindrical molds measuring 15 cm in diameter and 30 cm in height. After 24 hours, the samples were removed from the molds and submerged in water for curing over periods of 7 and 28 days. A total of 1,500 ultra-high-performance concrete (UHPC) samples were produced, both with and without fibers. Ultimately, the test results were compared to those of high-strength self-compacting concrete without fibers, which served as the control group.

2.5. Schmidt Hammer Test

The Schmidt Hammer (SH) test was employed to assess the compressive strength of both cubic and cylindrical samples. Schmidt's hammer is utilized to evaluate the properties of elastic materials, particularly for measuring the compressive strength of concrete. Today, the SH test is recognized as a non-destructive testing method and has recently become an effective tool for assessing the surface resistance of materials based on their hardness [51]. In this study, reliable readings and index values were recorded using the Schmidt Hammer on the samples, and the average results were documented in accordance with the ISO 1920-7 standard [67] (refer to Figures 8-9). The results of tests on cubic and cylindrical specimens showed that by adding different types of fibers (plastic, wood and metal) to UHPC, the compressive strength decreases with the Schmidt hammer test.

The reason for the decrease in the compressive strength test with the SH for cubic and cylindrical specimens is due to the amount of fibers, their shape and dispersion in concrete. Also, there is a decrease in the compressive strength of the samples with an increase in the percentage of non-adhesion fibers between cement and aggregates in concrete. The effect of different types of fibers in UHPC of cubic and cylindrical specimens with SH test

- Pushing Resistance: (WC)>(AF)> (DP)> (MP)> (HH)> (PT)> (PP)

Fig. 8. Hardness Testing on Cubic and Cylindrical Specimens

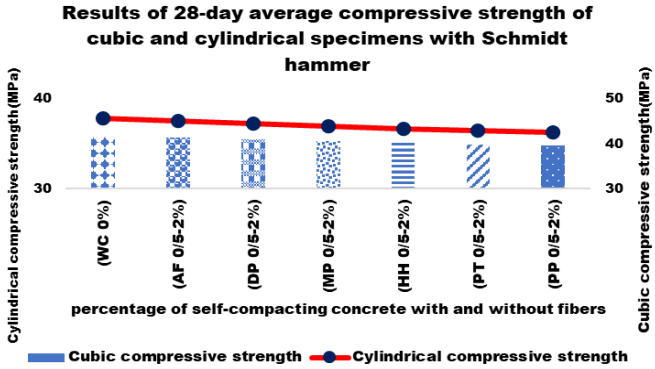

Fig. 9. The average results of the SH test for cubic and cylindrical samples after 28 days of processing

2.6. UPV Test

The UPV (Ultrasonic Pulse Velocity) test is a non-destructive testing method used to assess the homogeneity, uniformity, quality, wear, and the presence of defects, cavities, and internal voids in hardened concrete. The pulse frequency ranges from 20 to 170 kHz. The direct method was employed for this test, with the distance between the two ultrasonic transducers set at 15 cm for cubic samples and 30 cm for cylindrical samples, in accordance with the ISO 1920-7 standard [67] (see Figures 10-11).

Fig. 10. UPV Testing on Cubic and Cylindrical Specimens

The results of the tests conducted on cubic and cylindrical specimens indicated that the addition of various fibers to (UHPC) led to a gradual decrease in the speed of the ultrasonic pulse, which varied based on the type, material, and diameter of each fiber. The reduction in the (UPV) test results for UHPC can be attributed to the quantity, shape, and distribution of the fibers within the concrete. Furthermore, the decrease in pulse speed with an increasing percentage of fibers in the concrete samples is due to the effective water absorption by the fibers, which negatively impacted the results of the pulse speed test.

$$KM/S = \frac{CM}{MS} \times 10 \quad (1)$$

- Ultrasonic Pulse Speed: (WC)>(HH)> (PT)> (DP)> (MP)> (PP)> (AF)

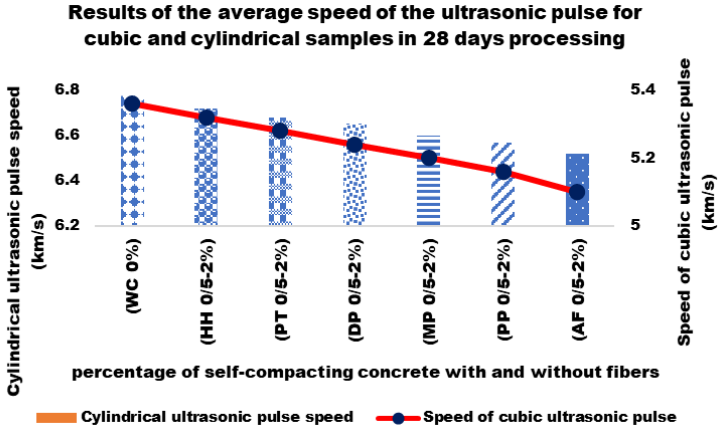

Fig. 11. UPV Test Results for Cubic and Cylindrical Samples After 28 Days of Processing

2.7. Penetration Testing of Cubic Specimens

The permeability test of (UHPC) was conducted on cubic and cylindrical samples, measuring 15 cm × 15 cm × 15 cm and 10 cm × 30 cm, respectively, to assess the durability of the samples. The performance and permeability of concrete are closely linked to its durability, particularly its resistance to gradual deterioration when exposed to extreme weather conditions, as well as compaction and settlement caused by water penetration.

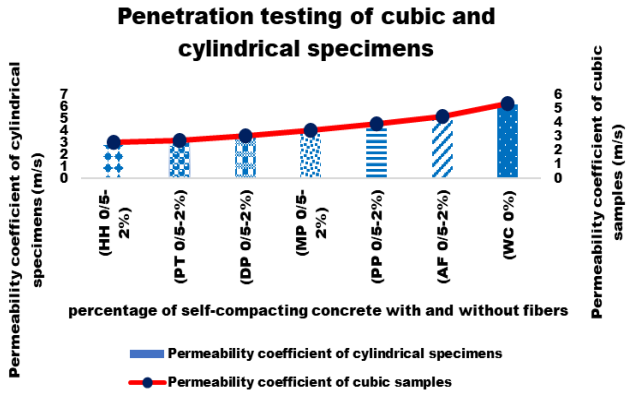

Fig. 12. Concrete Permeability Device and Its Test Results

Using various types of fibers with different textures and diameters in ultra-high-performance concrete (UHPC) can effectively reduce the permeability of the material. Each type of fiber possesses excellent mechanical properties, contributing to the overall strength and bond between the concrete and the fibers. These fibers can help control spalling and cracking while enhancing the concrete's strength as a reinforcing agent. By incorporating fibers into the concrete mix, both the mechanical and physical properties of the concrete are improved, leading to reduced permeability. Additionally, fibers can enhance the internal structure of concrete, including its strength, flexibility, and water resistance. Notably, human hair fibers demonstrated the lowest permeability in concrete tests, thereby increasing the durability of the concrete. This study examines the impact of different fiber types on the permeability of UHPC in both cubic and cylindrical samples.

- Permeability:(HH)<(PT)<(DP)<(MP)<(PP)<(AF)<(WC)

2.8. Thermal Cracking

2.8.1. Thermal Cracking Formula In UHPC

In (UHPC), thermal cracks develop when temperature fluctuations induce compressive stresses that exceed the concrete's compressive strength. Thermal cracking in concrete occurs due to non-uniform contraction or expansion resulting from temperature changes. This type of cracking is particularly prevalent in large concrete structures, such as dams, thick walls, and extensive foundations. In bulk concrete, the high rate of cement hydration can cause the internal temperature to rise significantly, while the outer surface, exposed to air, may remain cooler. This temperature gradient can generate tensile stresses on the outer surface, ultimately leading to cracking.

2.8.2. Factors affecting thermal cracking

- Temperature gradient (T):

When there is a significant temperature difference between the inner and outer sections of the concrete, it can result in tensile stresses in the cooler areas and compressive stresses in the warmer areas.

Modulus of elasticity (E):

Concrete with a high modulus of elasticity (harder) tends to resist deformation, which can lead to increased internal stresses within the material.

- Thermal expansion coefficient (Alpha):

Concrete with a high thermal expansion coefficient undergoes greater longitudinal changes in response to temperature fluctuations, which can lead to the development of thermal stresses.

- Mechanical properties of concrete:

The compressive strength of concrete and the modulus of rupture play a crucial role in its resistance to thermal cracking. Concrete with high compressive strength and a high modulus of rupture can better withstand the compressive stresses that develop.

2.8.3. Thermal Cracking Prediction Models

In this section, response surface methodology (RSM) analysis was employed to investigate the thermal cracking of self-compacting concrete, both with and without fibers. The use of various additives, the selection of different types of cement, the control of processing conditions, and the choice of fiber types can significantly reduce the risk of thermal cracking. For instance, utilizing low-heat cements or incorporating fibers can decrease the

heat of hydration, thereby minimizing the occurrence of thermal cracking. The stress associated with thermal cracking can be calculated using the following Equation (2) [31]:

$$\sigma_{cr} = \frac{E \times \alpha \times T}{f} \quad (2)$$

In this formula, the cracking stress (MPa), the compressive strength of (UHPC) (MPa), Young's modulus of (UHPC) (MPa), the coefficient of linear thermal expansion of (UHPC) (1/°C), and temperature (°C) are all included.

Table 9. Results of Testing the Effect of Temperature on the Resistance of Cubic Samples and Thermal Cracking

No	Type of concrete	The minimum and maximum range of each value in terms of units Cubic compressive strength (MPa)	Young's modulus (MPa)	Thermal expansion coefficient (1/°C)	Temperature (°C)	Cracking stress (MPa)
1	(WC 0%)	2.52 – 11.5	26 – 25.5	4 – 14	10 –160	0.02284 – 0.000097
2	(AF 0/5-2%)	3.31 – 11.94	26.5 – 25.7	3.9 – 13.8		0.017392 – 0.000093
3	(PP 0/5-2%)	3.80 – 12.38	27 – 26	3.8 – 13.6		0.015189 – 0.000090
4	(MP 0/5-2%)	4.15 – 12.81	27.3 – 26.5	3.6 – 13.3		0.013905 – 0.000087
5	(DP 0/5-2%)	4.37 – 13.68	27.7 – 27	3.4 – 13.1		0.013173 – 0.000081
6	(PT 0/5-2%)	4.95 – 14.6	28.2 – 27.9	3.2 – 13		0.011629 – 0.000076
7	(HH 0/5-2%)	5.92 – 15.25	28.6 – 28	3 – 12.9		0.009724 – 0.000073

- Thermal cracking in concrete: (HH)<(PT)<(DP)<(MP)<(PP)<(AF)<(WC)

Fig. 13. Cube testing in the drying oven and failure using the compressive strength device.

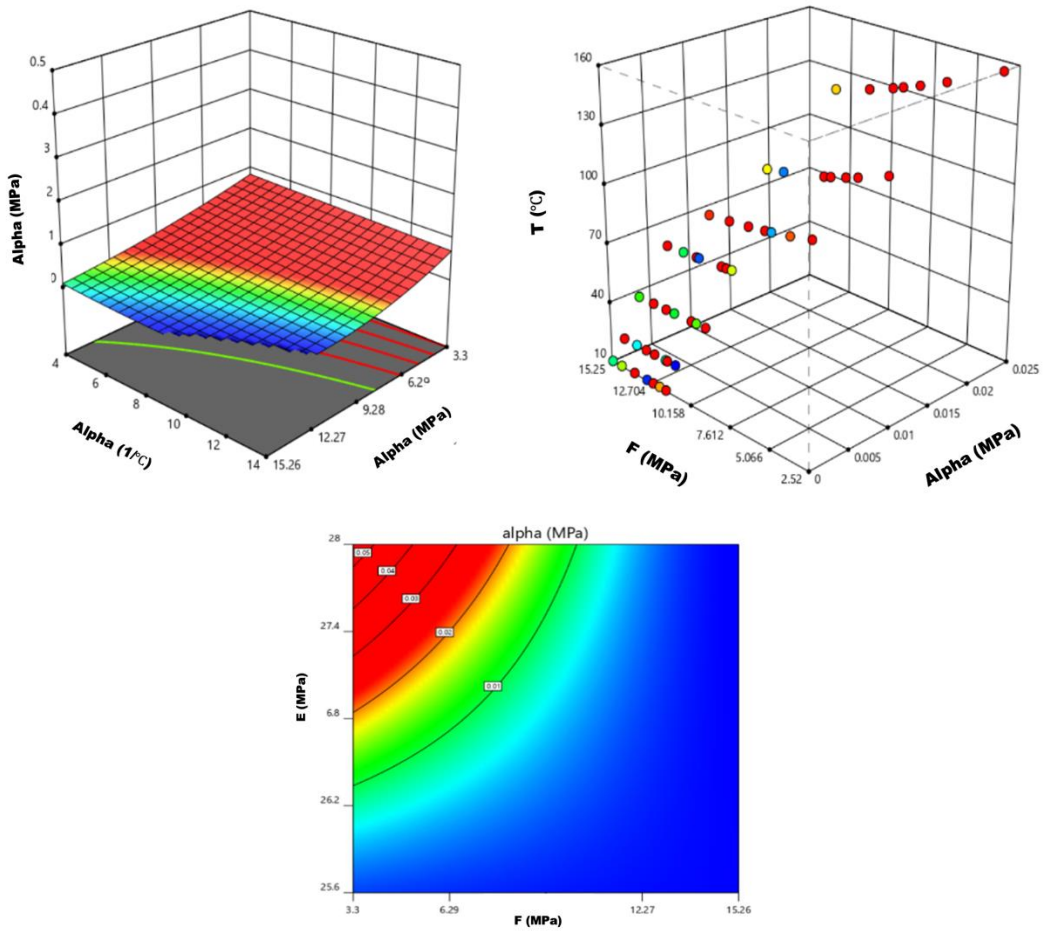

Fig. 14. Testing the Effects of Temperature on the Compressive and Tensile Strength of Cubic and Cylindrical Specimens

2.9. Crack Width Testing in Concrete Slabs with and without Various Types of Fibers

One of the primary factors threatening the durability of concrete is cracking in the concrete slab. Cracks in concrete serve as entry points for water, along with harmful chemical compounds, clay, and corrosive substances, which can lead to the corrosion of reinforcing bars and the deterioration of the concrete itself. Consequently, the durability and serviceability of the concrete decrease. Cracks in self-compacting concrete can facilitate the further growth and expansion of additional cracks, resulting in localized or widespread damage to both the surface and the interior of the concrete. The rate of evaporation from the concrete surface is influenced by various factors, including ambient temperature, relative humidity, and wind speed. When the rate of evaporation equals the rate of water loss from the surface of the concrete slab, the injected water layer is removed, creating negative pore water pressures (capillarity) on the surface. These negative pressures induce contraction in the concrete, and if the concrete is bonded, tensile stresses begin to develop on its surface. Bonding factors in concrete may include coarse aggregates, granular base surfaces or stabilizers, and reinforcing bars or fibers within the concrete slab, all of

which can be affected by various conditions. Due to the low tensile strength of concrete in the early hours after construction, the tensile stress can exceed the material's tensile strength, leading to cracks caused by the shrinkage of the concrete paste. Fibers are one of the reinforcing elements that help resist the tensile stresses induced by various factors. They can enhance the tensile strength of self-compacting concrete and mitigate the expansion and growth of cracks. The high modulus of elasticity of plastic, wood, or metal fibers allows these reinforcing elements to effectively control cracking in concrete. The incorporation of fibers, due to their superior tensile properties in conjunction with reinforcing bars, significantly reduces cracking and strengthens the concrete, making it a critical consideration. In this research, a suitable template has been designed to investigate cracking by simulating practical constraints. Based on the geometric relationships of the mold and the degree of hardness and cracking, molds with dimensions of 60 cm by 90 cm by 5 cm were created. In this configuration, the adverbs are embedded in two perpendicular directions.

Fig 15. Concrete slab reinforced with fibers

During this experiment, environmental conditions such as temperature and humidity were maintained at constant levels. The area of the cracks was determined by multiplying the length by the width of each crack after a period of seven days. The length of the crack was measured using a measuring tape with an accuracy of 1 mm, while the width was assessed with a magnifying glass that had an accuracy of 0.1 mm. The samples were kept in molds for seven days within a controlled environment, which maintained a temperature of 18 ± 2 degrees Celsius, wind speeds of approximately 5 km/h, humidity at 21%, a low UV index, minimal dust, and a moderate Air Quality Index (AQI). From 91 concrete slabs, self-compacting concrete was produced in seven molds, incorporating various fibers in different percentages (0%, 0.5%, 1%, 1.5%, and 2% relative to the weight of the cement) for analysis. The cracking behavior in Ultra-High Performance Concrete (UHPC) mixtures, both with and without different fibers, was evaluated using the ASTM C1579 standard test method [68]. Reason: Improved clarity, vocabulary, and technical accuracy while correcting grammatical and punctuation errors.

- Cracking in concrete slab :(WC)>(AF)>(PP)>(MP)>(DP)> (PT)>(HH)

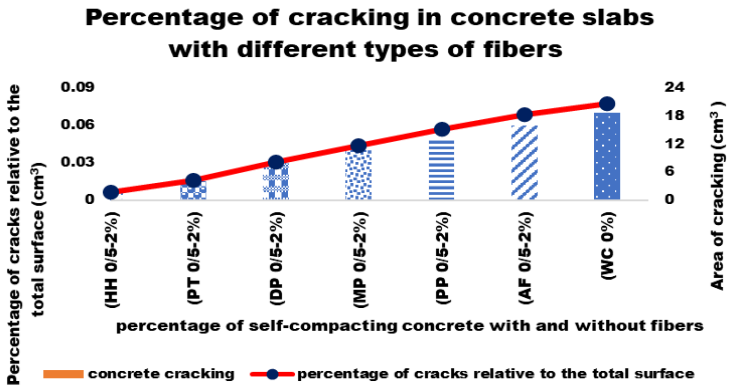

Fig. 16. Percentage of Cracking in Concrete Slabs with Various Types of Fibers

2.10. Testing the Compressive Strength of Cubic Specimens

The results of the compressive strength test on cubic samples measuring 150 mm × 150 mm × 150 mm, conducted in accordance with the ISIRI 3206 standard [65], indicated that the addition of various types of fibers in different percentages to (UHPC) resulted in a decrease in compressive strength (as shown in Figures 17 and 18).

- Pushing Resistance: (WC)>(AF)> (DP)>(MP)> (HH)> (PT)>(PP)

Like previous studies and research, including those by Mirabi Moghadam [32], Omar [35], Manjunat [33], Janata [42], and Mustafa [36], who have worked in the field of fibers, it was concluded that the use of fibers in concrete reduces compressive strength. This finding was also clearly stated in the current research.

Fig. 17. Testing the Failure of a Cubic Specimen Using a Concrete Breaker Jack

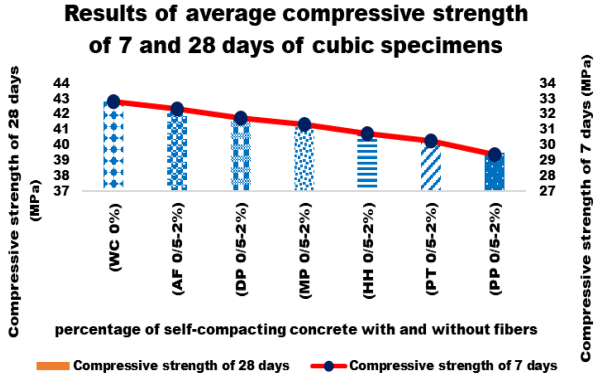

Fig. 18. Compressive Strength Test Results for Cube Specimens Cured for 7 and 28 Days

2.11. Testing the Tensile Strength of Cylindrical Samples (Brazilian Test)

The results of the tensile strength test on cylindrical samples measuring 150 mm by 300 mm, conducted in accordance with the ASTM C496 standard [66], indicated that the tensile

strength increases with the addition of various fibers to (UHPC), as illustrated in Figures 19 and 20.

- Tensile strength : (HH)>(PT)>(DP)>(MP)>(PP)>(AF)>(WC)

Fig. 19. Cylindrical Specimen Failure Test Using a Concrete Breaker Jack

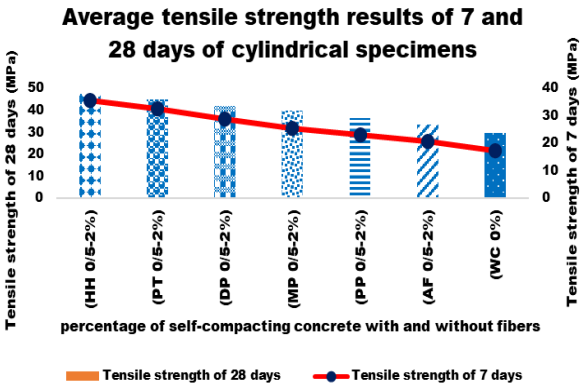

Fig. 20. Tensile Strength Test Results for Cylindrical Specimens at 7 and 28 Days of Curing

3. Conclusion

In this research, the use of various fibers in (UHPC) was examined. This study represents a significant contribution to sustainable development by potentially lowering the costs of structures and materials, mitigating the harmful effects of pollution on the environment, reducing brittleness and cracking in concrete, conserving natural resources, and enhancing both compressive and tensile strength. Based on the primary findings of this article, the following conclusions can be drawn:

- The average data from compressive strength tests of (UHPC) with varying fiber contents (0.5%, 1%, 1.5%, and 2% by weight of cement) revealed the following:
- In cubic specimens after 7 days, the addition of (AF), (DP), (MP), (HH), (PT), and (PP) resulted in reductions of compressive strength of 1.49%, 3.28%, 4.47%, 6.28%, 10.7%, and 14.76%, respectively, compared to the (UHPC) without fibers.
- In cubic specimens tested after 28 days, the addition of (AF), (DP), (MP), (HH), (PT), and (PP) fibers resulted in reductions in compressive strength of 1.60%, 2.51%, 3.89%, 5.03%, 6.17%, and 7.78%, respectively, compared to the (UHPC) without fibers.
-
- The average data from tensile strength tests on (UHPC) with varying fiber contents indicated that
- In cylindrical specimens, after 7 days, the inclusion of (HH), (PT), (DP), (MP), (PP), and (AF) fibers resulted in increases in tensile strength of 106.35%, 88.43%, 65.90%, 47.40%, 33.52%, and 19.65%, respectively, compared to the (UHPC) without fibers.
- In cylindrical specimens after 28 days, the inclusion of fibers (HH), (PT), (DP), (MP), (PP), and (AF) resulted in increases in tensile strength of 59.19%, 50.83%, 41.13%, 32.77%, 22.40%, and 11.70%, respectively, compared to the (UHPC) without fibers.

- The average data from rebound hammer compressive strength tests on (UHPC) with fibers indicated that:
- In cubic specimens after 28 days, the incorporation of (AF), (DP), (MP), (HH), (PT), and (PP) fibers resulted in reductions in compressive strength of 0.9%, 1.87%, 2.81%, 3.75%, 4.46%, and 4.92%, respectively, compared to the (UHPC) without fibers.
- In cylindrical specimens after 28 days, the incorporation of (AF), (DP), (MP), (HH), (PT), and (PP) fibers resulted in reductions in compressive strength of 1.03%, 1.55%, 2.33%, 3.10%, 4.14%, and 4.83%, respectively, compared to the u (UHPC) without fibers.
- The average data from ultrasonic pulse velocity tests on (UHPC) with fibers demonstrated that:
- In cubic specimens after 28 days, the addition of (HH), (PT), (DP), (MP), (PP), and (AF) fibers resulted in a decrease in pulse velocity of 0.7%, 1.49%, 2.23%, 3%, 3.73%, and 4.85%, respectively, compared to the (UHPC) without fibers.
- In cylindrical specimens after 28 days, the addition of (HH), (PT), (DP), (MP), (PP), and (AF) fibers resulted in a decrease in pulse velocity of 0.9%, 1.47%, 1.91%, 2.65%, 3.09%, and 3.83%, respectively, compared to the (UHPC) without fibers.
- The average data from permeability tests on (UHPC) with fibers indicated that:
- In cubic specimens observed over a 72-hour period, the incorporation of (HH), (PT), (DP), (MP), (PP), and (AF) fibers resulted in reductions in permeability of 54.71%, 47.16%, 41.50%, 33.96%, 26.41%, and 16.98%, respectively, compared to the (UHPC) without fibers.
- In cylindrical specimens over a period of 72 hours, the incorporation of (HH), (PT), (DP), (MP), (PP), and (AF) fibers resulted in reductions in permeability of 52.38%, 49.20%, 42.85%, 36.50%, 26.98%, and 17.46%, respectively, compared to the ultra-high-performance concrete (UHPC) without fibers.
- The average data from cracking tests on (UHPC) slabs containing fibers indicated that:
- In concrete slabs after 7 days, the addition of (HH), (PT), (DP), (MP), (PP), and (AF) fibers resulted in a reduction in cracking of 8.57%, 21.42%, 42.85%, 57.14%, 71.42%, and 85.71% relative to the total surface area, compared to slabs without fibers.

Table 9. Total Results of the functional properties of uhpc with and without fibers

Type of concrete	Type of test	Type of functional properties	level of quality compared to the control sample
(WC) > (HH) > (PT) > (DP) > (MP) > (PP) > (AF)	Slump flow test	Fresh properties	Slump diameter reduction
(WC) < (HH) < (PT) < (DP) < (MP) < (PP) < (AF)	V-Funnel test	Fresh properties	Increase flow time
(WC) > (HH) > (PT) > (DP) > (MP) > (PP) > (AF)	L-Box test	Fresh properties	Reducing the blockage ratio (H2/H1)
(WC) > (HH) > (PT) > (DP) > (MP) > (PP) > (AF)	J-Ring test	Fresh properties	Slump diameter reduction
(WC) < (HH) < (PT) < (DP) < (MP) < (PP) < (AF)	U-Box test	Fresh properties	Increasing height difference (H2-H1)

(WC)>(AF)> (DP)> (MP)> (HH)> (PT)> (PP)	Compressive strength with Schmidt hammer	hardened properties	Reducing compressive strength
(WC)>(HH)> (PT)> (DP)> (MP)> (PP)> (AF)	Ultrasonic pulse speed	hardened properties	Reducing the speed of the ultrasonic pulse
(WC)>(AF)>(PP)>(MP)>(DP)> (PT)>(HH)	Permeability	hardened properties	Reduced permeability
(WC)>(AF)>(PP)>(MP)>(DP)> (PT)>(HH)	Thermal cracking	hardened properties	Reduction of thermal cracking
(WC)>(AF)>(PP)>(MP)>(DP)> (PT)>(HH)	Cracking in concrete slab	hardened properties	Reducing cracking in concrete slabs
(WC)>(AF)>(DP)>(MP)>(HH)>(PT)>(PP)	Compressive strength	hardened properties	Reducing compressive strength
(WC)<(AF)<(PP)<(MP)<(DP)<(PT)<(HH)	Tensile strength	hardened properties	Increased tensile strength

References

[1] Fokam CB, Toumi K, Kenmeugne E, Meva'a L, Mansouri K. Cement mortar reinforced with palm nuts naturals fibers: study of the mechanical properties. Revue des Composites et des Matériaux Avancés - Journal of Composite and Advanced Materials. 2020 Feb;30(1):9-13. https://doi.org/10.18280/rcma.300102

[2] Modarres Y, Ghalehnovi M. The effect of recycled steel fibers from waste tires on concrete properties. Civil Engineering Infrastructures Journal. 2023;56(1):1-18. https://doi: 10.22059/ceij.2022.339592.1820

[3] Dounia D, Mourad B, Mohammed B. Effect of date palm and polypropylene fibers on the characteristics of self-compacting concrete: comparative study. Frattura ed Integrità Strutturale. 2023;64:31-50. https://doi.org/10.3221/IGF-ESIS.64.03

[4] Debalina G, Ammar AE, Zhongguo JM, Diana H. Development of high-early-strength fiber-reinforced self-compacting concrete. Construction and Building Materials. 2021;266:121051. https://doi.org/10.1016/j.conbuildmat.2020.121051

[5] Helal HYA, Shen D, Hussein KS. Performance of fiber self-compacting concrete at high temperatures. Civil Engineering Journal. 2021 Dec;7(12):2083-2098. https://doi.org/10.28991/cej-2021-03091779

[6] Jawad AE, Fahid A, Osama Z, Rayed A, Hisham A, Aneel M. Self-fibers compacting concrete properties reinforced with propylene fibers. Science and Engineering of Composite Materials. 2021;28(1):64-72. https://doi.org/10.1515/secm-2021-0006

[7] Jawad A, Osama Z, Ibrahim AS. Mechanical properties and durability assessment of nylon fiber reinforced self-compacting concrete. Journal of Engineered Fibers and Fabrics. 2021;16:1-8. https://doi.org/10.1177/15589250211062833

[8] Tawfeeq AW, Ganesh S. Study on fresh properties, mechanical properties and microstructure behavior of fiber reinforced self-compacting concrete. Materials Today: Proceedings. 2022;62(12):6663-6670. https://doi.org/10.1016/j.matpr.2022.04.666

[9] Daniyar A, Sungat A, Ainur J, Yuri P, Yelena R, Yelbek U, Akbulat A. Effect of low-modulus polypropylene fiber on physical and mechanical properties of self-compacting concrete. Case Studies in Construction Materials. 2022;16 https://doi.org/10.1016/j.cscm.2021.e00814

[10] Wang J, Dai Q, Sun R. Experimental and numerical investigation of fracture behaviors of steel fiber-reinforced rubber self-compacting concrete. Journal of Materials in Civil Engineering. 2022;34(1):1-11. https://doi.org/10.1061/(ASCE)MT.1943-5533.0004010
[11] Adil G, Ahmet B, Mehmet EA, Ahmet HS, Magdalena D, Kambiz A. Fresh properties and fracture energy of basalt and glass fiber-reinforced self-compacting concrete. Journal of Materials in Civil Engineering. 2022;34(1):1-11. https://doi.org/10.1061/(ASCE)MT.1943-5533.0004043
[12] Nadhim HS, Taghreed KMA, Kolimi SV, Hemn UA, Rabar HF, Naraindas B, Amir M. The behavior of sustainable self-compacting concrete reinforced with low-density waste polyethylene fiber. Materials Research Express. 2022;9(3):1-14. https://doi.org/10.1088/2053-1591/ac58e8
[13] Abdullah A, Sivakumar K. Effect of fiber diameter and tensile strength on the mechanical, fracture, and fiber distribution properties of eco-friendly high-strength self-compacting concrete. Construction and Building Materials. 2023;403:133161. https://doi.org/10.1016/j.conbuildmat.2023.133161
[14] Jinping Z, Peijie N, Jianxing C, Minghao W. Study on the impact resistance of steel fiber-reinforced self-compacting concrete after high temperature. Structures. 2023;57:105281. https://doi.org/10.1016/j.istruc.2023.105281
[15] Mirzaei Aliabadi M, Derakhshan Nezhad AH. Monitoring the health of concrete structures using ultrasonics. International Science and Engineering Research Conference and the 4th International Congress on Civil Engineering, Architecture and Urban Planning in Asia. 2023.
[16] Mirzaei Aliabadi M, Derakhshan Nezhad AH. Quality control of concrete structures using the Schmidt hammer method. Proceedings of the 5th International Conference and the 6th National Conference on Civil Engineering, Architecture, Art and Urban Design. 2023.
[17] Mohan MB, Damodhara BR, Panga NR, Kiran K, Aruna SJ, Bode VK, Bharat PK. Experimental investigation on self-compacting concrete reinforced with fibers. Eur Chem Bull. 2023;12(5):5777-5784.
[18] Eskandari A, Omidinasab F, Sahraei AM, Dalvand A. Investigating the effect of different types of fibers in improving the flexural performance of recycled concrete beams in the elastic and plastic zones. Journal of Structural and Construction Engineering. 2021;8(12):344-362. https://doi.org/10.2139/ssrn.4108581
[19] Ujjwal S, Irfan MS. Investigating self-compacting-concrete reinforced with steel and coir fiber. Materials Today: Proceedings. 2021;45(6):4948-4953. https://doi.org/10.1016/j.matpr.2021.01.386
[20] Al-Hadithi AI, Hilal M, Al-Gburi NN, Midher AH. Structural behavior of reinforced lightweight self-compacting concrete beams using expanded polystyrene as coarse aggregate and containing polyethylene terephthalate fibers. Structural Concrete Journal Citation Reports. 2023. https://doi.org/10.1002/suco.202200381
[21] Askar K, Yaman SS, Al-Kamaki S, Hassan A. Utilizing polyethylene terephthalate (PET) in concrete. Polymers. 2023;15(15):1-10. https://doi.org/10.3390/polym15153320
[22] Ayub T, Khan SU, Mahmood W. Mechanical properties of self-compacting rubberised concrete (SCRC) containing polyethylene terephthalate (PET) fibres. Iranian Journal of Science and Technology, Transactions of Civil Engineering. 2021;46:1073-1085. https://doi.org/10.1007/s40996-020-00568-6
[23] Asmaa HS, Khashaa MM. Optimum characteristics of plastic fibers for sustainable self-compacting concrete (SCC). European Journal of Environmental and Civil Engineering. 2022;27(9):2967-2984. https://doi.org/10.1080/19648189.2022.2119605
[24] Widodo S, Alfirahma R, Prawiranegara A, Amir F, Dewi A. Development of eco-friendly self-compacting concrete using fly ash and waste polyethylene terephthalate bottle

fiber. Civil Engineering Journal. 2023;9(2):1-14. https://doi.org/10.28991/CEJ-2023-09-02-014
[25] Ramhormozy A, Kazeminezhad E, Safakhah S. Effect of polyethylene terephthalate (PET) and polypropylene (PP) fibers on the shear behavior of RC deep beams. Revista de la Construcción. 2023;22(1):1-12. https://doi.org/10.7764/RDLC.22.1.223
[26] Bozorgmehr Nia S, Adlparvar MA. The effects of waste polyethylene terephthalate (PET) particles on the properties of fresh and hardened self-consolidating concrete. International Journal of Civil Engineering and Construction. 2022;1(1):6-12. https://doi.org/10.22271/27078329.2022.v1.i1a.3
[27] Nkomo N, Masu L, Nziu P. Effects of polyethylene terephthalate fibre reinforcement on mechanical properties of concrete. Advances in Materials Science and Engineering. 2022;2022:1-10. https://doi.org/10.1155/2022/4899298
[28] Meena A, Surendranath A, Ramana PV. Assessment of mechanical properties and workability for polyethylene terephthalate fiber reinforced concrete. Materials Today: Proceedings. 2022;50(5):2307-2314. https://doi.org/10.1016/j.matpr.2021.10.054
[29] Pachideh GK, Ketabdari H. Investigation of the mechanical properties of self-compacting concrete containing recycled steel springs; experimental and numerical investigation. European Journal of Environmental and Civil Engineering. 2023;27(14):4026-4045. https://doi.org/10.1080/19648189.2023.2169355
[30] Maddikeari M, Kvgd B, Vengala J, Manjunatha L. Experimental study on the use of human hair as fiber to enhance the performance of concrete: a novel use to reduce the disposal challenges. Materials Today: Proceedings. 2021;47:1-12. https://doi.org/10.1016/j.matpr.2021.04.039
[31] Mirzaie Aliabadi, M., derakhshan nezhad, A. H., Mousavi Abdullah nezhad, S. A., Hitavi, A. Investigating the effect of heat transfer from the mold on the mechanical properties of self-compacting concrete with. Journal of Structural and Construction Engineering, 2024; 11(5): -. https://doi: 10.22065/jsce.2023.403066.3155
[32] Mirabi Moghadam MH. The effect of the shape and amount of date palm sis fibers on the compressive and tensile strength of concrete. Struct Constr Eng Sci-Res J. 2021;8(3):169-76.
[33] Maddikeari M, Kvgd B, Vengala J, Manjunatha L. Experimental study on the use of human hair as fiber to enhance the performance of concrete: A novel use to reduce the disposal challenges. Mater Today Proc. 2021;47. https://doi.org/10.1016/j.matpr.2021.04.039
[34] Patel A, Srivastava A. Study of human hair reinforced cement concrete. Int Res J Eng Technol (IRJET). 2021;8(1).
[35] Akbar M, Umar T, Hussain Z, Hole P, Qiang Ou G. Effect of human hair fibers on the performance of concrete incorporating high dosage of silica fume. Appl Sci. 2022;13(1). https://doi.org/10.3390/app13010124
[36] Mustafa TC. Investigation of mechanical properties of red pine needle fiber reinforced self-compacting ultra-high-performance concrete. Case Stud Constr Mater. 2022;16 https://doi.org/10.1016/j.cscm.2022.e00970
[37] Waseem KMF, Abu Bakar BH, Nahla H, Abdulkader IA. Relation between rheological and mechanical properties on the behaviour of self-compacting concrete (SCC) containing recycled plastic fibres. Eur J Environ Civ Eng. 2022;26(10):4761-93. https://doi.org/10.1080/19648189.2020.1868344
[38] Ghasemi AH, Nematzadeh M, Fallahnejad H. Post-fire residual fracture characteristics and brittleness of self-compacting concrete containing waste PET flakes: Experimental and theoretical investigation. Eng Fract Mech. 2022;261:108-263. https://doi.org/10.1016/j.engfracmech.2022.108263
[39] Jaskowska-Lemańska J, Kucharska M, Matuszak J, Nowak P, Łukaszczyk W. Selected properties of self-compacting concrete with recycled PET aggregate. Mater (Basel). 2022;15(7):2566. https://doi.org/10.3390/ma15072566

[40] Safeer A, Malik Asad AI, Syed Minhaj SK, Muhammad JM, Shahid A. Investigating the behavior of waste alumina powder and nylon fibers for eco-friendly production of self-compacting concrete. Mater. 2022;15(13):4515. https://doi.org/10.3390/ma15134515
[41] Hussien AS, Mohammed MK. Optimum characteristics of plastic fibres for sustainable self-compacting concrete SCC. Eur J Environ Civ Eng. 2023;27(9):2967-84. https://doi.org/10.1080/19648189.2022.2119605
[42] Jonatha RP, João Batista LPS, Luísa AG, Antonio CDS, Rosa Cristina CL. Evaluation of the addition of polypropylene (PP) fibers in self-compacting concrete (SCC) to control cracking and plastic shrinkage between different methods. Mater Res. 2023;26(suppl. 1) https://doi.org/10.1590/1980-5373-mr-2022-0567
[43] Derdour D, Behim M, Benzerara M. Effect of date palm and polypropylene fibers on the characteristics of self-compacting concrete: Comparative study. Frattura ed Integrità Strutturale. 2023;64:31-50. https://doi.org/10.3221/IGF-ESIS.64.03
[44] Askar K, Yaman SS, Al-Kamaki S, Hassan A. Utilizing polyethylene terephthalate (PET) in concrete. Polymers. 2023;15(15). https://doi.org/10.3390/polym15153320
[45] Widodo S, Alfirahma R, Prawiranegara A, Amir F, Dewi A. Development of eco-friendly self-compacting concrete using fly ash and waste polyethylene terephthalate bottle fiber. Civ Eng J (CEJ). 2023;9(2). https://doi.org/10.28991/CEJ-2023-09-02-014
[46] Mirzaie Aliabadi M, Derakhshan Nezhad AH, Shahidzadeh MS, Dadpur A. Date palm fibers to improve tensile strength in self-compacting concrete with silica fume. Civ Eng Infrastruct J. 2024. https://10.22059/ceij.2024.368987.1988
[47]Derakhshan Nezhad AH, Mirzaie Aliabadi M, Shahidzadeh MS. Laboratory investigation of the effect of plastic packaging belt fibers and iron oxide on the mechanical properties of self-compacting concrete. Amirkabir J Civ Eng. 2024;56(5). https://10.22060/ceej.2024.23070.8099
[48] Mirzaie Aliabadi M, Shahidzadeh MS, Piran Shahi H, Rashidi Fard H, Derakhshan Nezhad AH. Comparison of the effect of crushed cement block and construction waste on fresh and hardened properties of self-compacting concrete. J Concr Struct Mater. 2024. https://10.30478/jcsm.2024.448781.1365
[49] Asghari Pari SA, Derakhshan Nezhad AH, Mirzaie Aliabadi M. Investigating the effect of rust and iron shavings on the mechanical properties of self-compacting concrete. J Struct Constr Eng. 2024.
[50] Derakhshan Nezhad AH, Mirzaie Aliabadi M, Shahidzadeh MS, Dadpour A. Investigating the effect of date palm fibers on the mechanical properties of self-compacting concrete. J Struct Constr Eng. 2024. https://10.22065/jsce.2024.441194.3351
[51] Mirzaie Aliabadi M, Derakhshan Nezhad AH. Laboratory investigation of the effect of recycled polyethylene terephthalate fibers on the mechanical properties of self-compacting concrete. J Struct Constr Eng. 2024. https://10.22065/JSCE.2024.428815.3293
[52] ASTM C150/C150M. Standard specification for Portland cement. 2012.
[53] ASTM C33. Standard specification for concrete aggregates. Am Soc Test Mater. 2003.
[54] ASTM C494. Standard specification for chemical admixtures for concrete. Annu Book ASTM Stand. 2002.
[55] ASTM C94. Standard specification for ready-mixed concrete. Am Soc Test Mater. 2009.
[56] ASTM C494/C494M. Standard specification for chemical admixtures for concrete. Annu Book ASTM Stand. 2002.
[57] ASTM C1611. Standard test method for slump flow of self-consolidating concrete. 2009.
[58] INSO 3203-9. Testing fresh concrete - Part 9: Self-compacting concrete V-funnel test. 2013.

[59] INSO 3203-10. Testing fresh concrete - Part 9: Self-compacting concrete L-box test. 2013.
[60] INSO 11271. Concrete - Measurement of passing ability of self-consolidating concrete by J-ring - Test method. 2014.
[61] UNI 11044. Standard UTC-0547 U Shape Box Apparatus. RILEM Report No. 23. 2012.
[62] ASTM C805. Standard test method for rebound number of hardened concrete. 2004.
[63] ASTM C597. Standard test method for pulse velocity through concrete. 2003.
[64] DIN 1048. Standard test concrete impermeability test apparatus. 2012.
[65] ISIRI 3206. Standard test determining the compressive strength of concrete samples. 2003
[66] ASTM C496. ASTM C496 tensile concrete test equipment. 2002.
[67] ISO1920-7. Testing of concrete - Part 7: Non-destructive tests on hardened concrete. 2004.
[68] ASTM C1579-06. Standard test method for evaluating plastic shrinkage cracking of restrained fiber reinforced concrete (using a steel form insert). 2005.

Research on Engineering Structures & Materials
www.jresm.org
Research Group

Research Article

Effect of elevated temperature on concrete incorporating zeolite, silica fume and fly ash as replacement for cement

Balaji T [1,a], Jeyashree T M [*,1,b], Kannan Rajkumar P R [1,c], Baskara Sundararaj J [2,d], Jegan M [2,e]

[1]*Department of Civil Engineering, SRM Institute of Science and Technology, Kattankulathur, Chennai, India*
[2]*Centre for Advanced Concrete Research, Department of Civil Engineering, SRM Institute of Science and Technology, Kattankulathur, Chennai, India*

Article Info

Article history:

Received 06 May 2024
Accepted 30 Sep 2024

Keywords:

High strength concrete;
Zeolite;
Silica fume;
Class C fly ash;
Elevated temperature

Abstract

In this study, the effect of utilizing zeolite and industrial by-products, silica fume, and Class C fly ash, as partial replacement for cement is investigated at room and elevated temperatures of 200°C, 400°C, and 600°C. Four different high-strength concrete mixes of M50 concrete grade with varying proportions of zeolite, silica fume, and Class C fly ash are tested and observed for workability, compressive strength, and microstructural characteristics using Scanning Electron Microscope analysis, and the optimum mix has arrived. The results indicate that the addition of zeolite, silica fume, and fly ash resulted in lesser early-age strength development but the strength after 28 days of curing is found satisfactory and the desired target strength is achieved. Temperature rise resulted in degradation of concrete properties for both conventional and optimum mix but the concrete cubes with 10% of zeolite, 7.5% of silica fume, and 10% of fly ash have higher retainment of strength at elevated temperatures compared with conventional mix. The results from the microstructural study are found to correlate with strength test results. Incorporation of 10% zeolite, 7.5% silica fume, and 10% fly ash improved mechanical and microstructural characteristics at room and elevated temperature, however, the replacement is effective for 28 days of curing.

1. Introduction

The building industry has been investigating sustainable alternatives to Portland cement because of its negative environmental impact and large carbon dioxide emissions throughout its manufacturing process. Supplementary Cementitious Materials (SCMs) such as fly ash, zeolite, and silica fume have garnered attention in concrete mixes as a way to improve the material's physical properties and reduce its environmental effect. This introduction examines the use of these SCMs in the specific context of elevated temperatures, which is a crucial consideration for the lifetime and functionality of concrete structures in high-temperature industrial environments or fire scenarios.

Zeolite, a naturally occurring mineral with a high concentration of aluminium oxide (Al_2O_3) and reactive silicon dioxide (SiO_2), is a pozzolanic substance that may strengthen cement pastes by pozzolanic interaction with calcium hydroxide $(Ca(OH))_2$. It reacts more readily with fly ash and silica fume, and it works best in mixes with a lower water to cementitious material ratio [1]. Zeolite mixtures have shown reduced heat of hydration [2], lower drying shrinkage, and increased resistance to sulphate attack and the alkali-silica reaction in

*Corresponding author: jeyashrm@srmist.edu.in
[a] orcid.org/0009-0009-1468-5526; [b] orcid.org/0000-0003-4420-573X; [c] orcid.org/0000-0001-7316-1399; [d] orcid.org/0000-0002-8392-4131; [e] orcid.org/0000-0002-3725-9441
DOI: http://dx.doi.org/10.17515/resm2024.267ma0506rs

comparison to fly ash blends [3]. The incorporation of zeolite into concrete leads to the development of a material that possesses enhanced interfacial microstructure characteristics between the aggregate and the cohesive cement paste [4]. However, they may also need more water due to high surface area [5] and can be less workable [6, 7]. Concrete containing zeolite is observed to have a satisfactory performance at elevated temperatures [8]. Research conducted in the past suggests that the recommended percentage of cement replacement for zeolite is 20%, 15% and 10% [5].

When silicon and ferrosilicon alloys are made, minute amorphous silicon dioxide particles are released into the air, forming silica fume. Because of its potent pozzolanic reactivity and capacity to modify pore structure, it is frequently used to improve the mechanical characteristics and durability of concrete [9]. Furthermore, it has been shown that adding nano silica fume to concrete improves post-fire compressive strength while also greatly reducing temperature shrinkage deformation and mass loss at high temperatures [10]. The optimized percentage for replacing cement with silica fume is 7.5-10% in combination with 10-15% of zeolite and 10% of metakaolin [11]. Another SCM with pozzolanic properties is fly ash, which is produced as a byproduct of burning coal in power plants. It contains both silicon dioxide and calcium oxide, with the latter contributing to its cementitious properties. Fly ash will notably reduce the heat of hydration in concrete and improve its long-term strength development. The concentration of calcium in fly ash may influence its reactivity; fly ash with low calcium content will more obviously slow down the evolution of heat [12]. When exposed to high temperatures, concrete containing various SCMs may function differently. Research has indicated that zeolite and granulated blast furnace slag (GBFS) mortars outperform fly ash and silica fume mortars when it comes to heat resistance [13]. At higher temperatures, the formation of a greater quantity of secondary hydration products leads to improved mechanical properties in concrete that contains zeolite [14]. Moreover, SCMs may affect the mineralogy of cement pastes. Zeolites form during adiabatic curing when combined with a high fly ash content, can immobilize sodium and increase the material's overall stability [15].

In conclusion, adding fly ash, zeolite, and silica fume to concrete mixes in place of some of the cement is a practical way to improve the material's performance and sustainability, especially at high temperatures. The selection and proportioning of these SCMs have a notable impact on the mechanical properties, durability, and thermal behaviour of the finished concrete [16, 17, 18, 19]. Based on the literature review, it is noticed that the studies examining the combined effect of zeolite, silica fume, and fly ash at elevated temperatures are limited and scanty. Hence, the present study focused on studying the performance of concrete incorporating zeolite, silica fume, and fly ash at room and elevated temperatures.

2. Research Significance

The addition of class C fly ash may help the concrete to attain compressive strength in the 28-days curing period. Silica fume and class C fly ash as the cement replacement can enhance the microstructure of the concrete. Examining the properties of the high-strength concrete incorporated with zeolite, silica fume, and class C fly ash can provide advancement in the construction. The endurance of the concrete during the fire accident may improve in the building. The major objectives of the present study are:

- To find the optimum mix for concrete incorporating zeolite, silica fume, and class C fly ash as a replacement for cement
- To study the effect of elevated temperature on mechanical and microstructural properties of concrete incorporating zeolite, silica fume, and class C fly ash.

3. Materials and Mix Design

The preliminary investigation is performed to study the properties of materials utilized in the casting of concrete specimens. Ingredients include coarse aggregate, fine aggregate, cement, zeolite, fly ash, silica fume, and superplasticizer.

3.1. Coarse Aggregate

Within the domain of construction and civil engineering, coarse aggregate denotes a class of granular materials employed in concrete and various other structural applications. These materials commonly encompass sizable particles, including crushed stone, gravel, or recycled concrete, which are combined with cement and fine aggregates to produce concrete mixes. The physical properties of the coarse aggregate are determined as per IS 2386 – part 3 (1963) [20] and IS 383 (2016) [21].

3.2. Fine Aggregate

The process of crushing solid granite stone results in the production of manufactured sand. This crushed sand is characterized by a cubic shape with smoothed edges, having undergone comprehensive washing and sorting procedures, rendering it appropriate for use in construction. The particle size of M-Sand not exceeding 4.75 mm is used in the present study. The shape of the M sand is granular and the determined properties of M-Sand as per IS 2386 – part 3 (1963) [20] and IS 383 (2016) [21] are given in Table 1. Table 1 gives the properties of coarse aggregate and fine aggregate used for the present study.

Table 1. Properties of coarse aggregate and fine aggregate

Material	Properties	Values
Coarse aggregate	Specific gravity	2.74
	Fineness modulus	6.57%
	Water absorption	0.5%
Fine aggregate	Specific gravity	2.35
	Fineness modulus	3.33
	Water absorption	0.5%

3.3. Cement

When combined with water, cement acts as a binding agent for coarse and fine aggregate. The manufacturing process of cement primarily relies on calcium-rich limestone as its fundamental raw material. Upon the reaction between cement and water, water-resistant and chemically durable mineral hydrates are formed. Cement is classified into various grades according to its fineness, with the current study utilizing OPC 53 cement.

3.4. Zeolite

Zeolite is a naturally occurring or synthetic mineral that has been increasingly used in concrete as an alternative supplementary cementitious material. It is a group of hydrated aluminosilicate minerals that possess unique properties, making them suitable for various applications, including concrete production. The combined percentage of SiO_2, Al_2O_3, and Fe_2O_3 is about 83% according to the chemical composition of zeolite which is helpful in the pozzolanic behaviour.

3.5. Silica Fume

The addition of silica fume improves the concrete's compressive strength and aids in void filling. Silica fume helps in reducing the water absorption of the zeolite used in the concrete. Silica fume is also rich in SiO_2 which is helpful in the pozzolanic behaviour.

3.6. Class C Fly Ash

The use of Class C Fly Ash lowers the heat produced during the curing process of concrete, hence reducing the possibility of heat-induced cracking, particularly in big concrete pours. Fly ash addition with zeolite helps in reducing the water absorption by zeolite. Class C fly ash is also high in SiO_2 and Al_2O_3. The chemical composition and properties of cement, zeolite, silica fume, and fly ash are given in Table 2 and Table 3, respectively. Fig. 1 gives the supplementary cementitious materials used for the present study.

Table 2. Chemical composition of cement, zeolite, silica fume and fly ash

Oxides (Percentage)	CaO	SiO_2	Al_2O_3	Fe_2O_3	K_2O	Na_2O	MgO	SO_3	Loss on ignition
Cement	62.34	23.45	4.24	4.32	0.47	0.27	1.12	0.47	3.32
Zeolite	1.68	66.98	14.01	1.52	1.5	2.10	1.3	0.4	10.3
Silica fume	-	94.12	1.21	0.62	-	-	0.9	0.04	1.5
Class C Fly ash	1.5	62	22.5	2.3	-	1.5	3.4	4	2.1

Table 3. Properties of cement, zeolite, fine aggregate and coarse aggregate

Material	Properties	Values
Cement	Specific gravity	3.18
	Initial setting time	47 minutes
	Final setting time	480 minutes
Zeolite	Specific gravity	2.2
Silica fume		2.22
Class C Fly ash		2.3

a) Zeolite b) Silica fume c) Class C Fly ash

Fig. 1. Cementitious materials used for the present study

3.7. Mix Design

The concrete specimens are cast with the designed concrete mix to achieve the required target strength of 50 MPa as per IS 10262 (2019) [22]. The mix design as given in Table 4 is used for casting the conventional concrete without replacement for cement.

The zeolite of 10%, silica fume of 7.5 %, and class C fly ash of 10% are replaced with the cement and other materials are provided as per the conventional concrete. Concrete specimens are cast with three different mixes with varying percentages of zeolite, silica fume, and fly ash. Table 5 represents the various design mixes for the concrete incorporating zeolite, silica fume, and class C fly ash. M50Z10 indicates M50 concrete grade with 10% of cement replaced by zeolite on a weight basis. Similarly, M50SF indicates M50 concrete grade with 7.5% and 10% of silica fume and fly ash replaced for cement.

Table 4. Mix design for the conventional concrete

Description	Composition (kg/m^3)
Cement	450
Fine Aggregate	803
Coarse Aggregate	1101
Water	160
Admixture	2.82

Mix 3 designated as M50ZSF represents the concrete mix with 10% of zeolite, 7.5% of silica fume, and 10% of fly ash for cement replacement. In mix 2 and mix 3, silica fume and fly ash are combined to compare the behaviour of concrete with the existing combination of supplementary cementitious materials without and with concrete containing zeolite.

Table 5. Proportion of concrete ingredients for varying percentage of zeolite, silica fume and fly ash

Composition (kg/m^3)	Mix 1 M50Z10	Mix 2 M50SF	Mix 3 M50ZSF
Cement	405	371.25	326.25
Zeolite	45	0	45
Silica fume	0	33.75	33.75
Class C Fly ash	0	45	45
Fine aggregate	803	803	803
Coarse aggregate	1101	1101	1101
Water	160	160	160
Admixture	2.82	2.82	2.82

4. Methodology

The mechanical specifications of M50 concrete grade are determined by Indian standards. A 100 mm diameter and 200 mm height concrete cylinder and a 100 × 100 × 100 mm concrete cube are cast, cured, and tested to determine the strength properties of concrete. Fig. 2 gives the cast specimens, and the concrete is prepared in the same way as regular concrete but with additional ingredients in addition to cement. The optimal combination for enhanced mechanical features at room temperature is found based on the outcomes of the experimental tests.

Fig. 2. Cast specimens

Optimum mix is determined by the combination of supplementary cementitious materials by modifying the existing combination of cementitious materials in concrete containing zeolite. Further specimens are cast with optimum mix to determine the effect of varying concrete ingredients on the fire endurance of the concrete specimens. Heating of concrete cubes and cylinders is performed in the furnace at the rate of 10°C/minute to reach the desired target temperature of 200°C, 400°C, and 600°C and the specimens are heated for one hour under steady state after reaching maximum temperature. The mechanical properties including compressive strength and split tensile strength are determined after cooling of specimens to room temperature. The results are compared with conventional concrete to determine the effectiveness of utilizing zeolite, silica fume, and class C fly ash in concrete for improved fire resistance.

5. Results and Discussions

5.1. Testing at Room Temperature

The workability of concrete mixes is determined using slump cone test as a preliminary investigation. The slump values obtained for conventional concrete, mix 1, mix 2 and mix 3 are 100 mm, 90 mm, 85 mm and 84 mm respectively.

5.1.1 Compressive strength

Compressive strength is one of the important mechanical characteristics and it gauges how much axial compression that concrete can bear before cracking. Fig. 3 gives the 7-, 14- and 28-day compressive strength for four different mixes determined at room temperature.

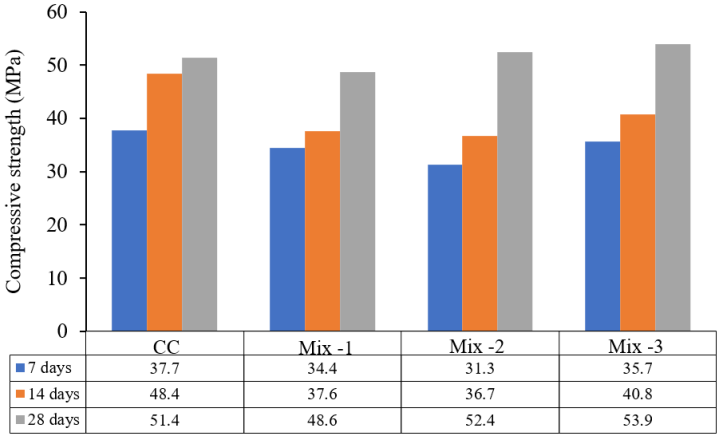

	CC	Mix -1	Mix -2	Mix -3
7 days	37.7	34.4	31.3	35.7
14 days	48.4	37.6	36.7	40.8
28 days	51.4	48.6	52.4	53.9

Fig. 3. Compressive strength for concrete mixes with varying percentage of zeolite, silica fume and fly ash (CC – Conventional concrete)

The target strength of 50 MPa is chosen for this study, and the conventional concrete has a strength of 51.4 MPa whereas mix 1 has 48.6 MPa, mix 2 has 52.4 MPa, and mix 3 has 53.9 MPa after 28 days of curing period. When compared to the conventional concrete, compressive strength for mix 1, mix 2, and mix 3 decreased by 5.4%, and increased by 2% and 4.9%, respectively. The compressive strength of all three concrete mixes with zeolite, silica fume, and fly ash decreased initially (7 and 14 days) and upon curing, the required target strength is reached. The compressive strength of Mix 1 is lower compared to other mixes, and the results are in correlation with studies performed by other researchers [23, 24, 25]. The reactivity of zeolite increases with the increase in the days of curing, and the reactivity depends upon the water-cement ratio [23]. Adding fly ash and silica fume

resulted in the development of target strength comparable to conventional concrete. The compressive strength of concrete mix with silica fume, fly ash, and zeolite increases upon curing age due to secondary hydration induced by the addition of zeolite. The continuous hydration results in the development of higher strength [24] and hence the strength value is higher for Mix 3 under a constant water-cement ratio.

5.1.2 Split Tensile Strength

Split tensile strength testing offers important information on the tensile behaviour of concrete, information that is necessary for the design and assessment of different structural components, such as pavements, slabs, and beams. It also plays a crucial role in the building industry's quality assurance and control procedures. The split tensile result of the conventional concrete is shown in Fig. 4.

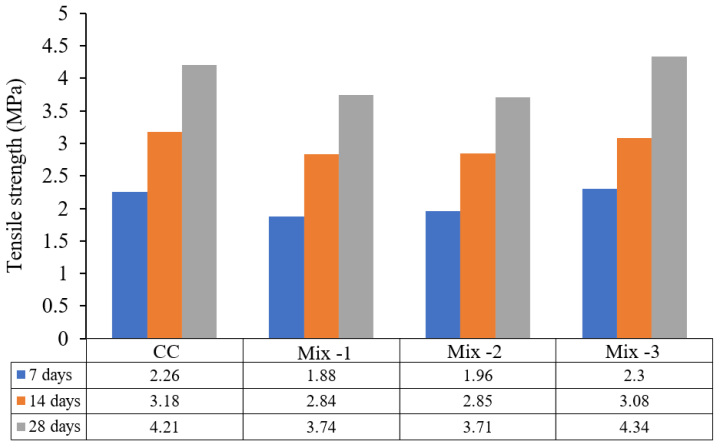

	CC	Mix -1	Mix -2	Mix -3
7 days	2.26	1.88	1.96	2.3
14 days	3.18	2.84	2.85	3.08
28 days	4.21	3.74	3.71	4.34

Fig. 4. Split tensile strength for concrete mixes with varying percentage of zeolite, silica fume and fly ash (CC – Conventional concrete)

The 28-day split tensile strength of the conventional concrete has reached 4.21 MPa, mix 1 has reached 3.74 MPa, mix 2 has attained 3.71 MPa and mix 3 has attained 4.34 MPa. The percentage reduction in split tensile strength for mix 1 and mix 2 is 11% and 11.8% when compared to the conventional concrete and mix 3 has gained the increase in strength value by 3.1%. From the test results, it is noted that the optimum mix is Mix 3 with compressive strength and a split tensile strength greater by 4.9% and 3.1%, compared with conventional concrete. Concrete cubes and cylinders are further cast with the arrived optimum mix and the specimens are tested after exposure to temperatures of 200°C, 400°C, and 600°C. The effect of temperature rise on concrete is examined through percentage of weight loss, compressive strength, split tensile strength, and microstructural characteristics. The effectiveness of utilizing alternative cementitious materials in improving the fire resistance of concrete is studied by comparing the performance of concrete containing zeolite, silica fume, and fly ash with conventional concrete.

5.2. Testing at Elevated Temperature

5.2.1 Weight Loss of Specimens

Fig. 5 gives the percentage of weight loss observed in both conventional concrete mixes and mixes with zeolite, silica fume, and fly ash. The percentage of weight loss for the conventional concrete after exposure to 200°C, 400°C, and 600°C is 0.4%, 4.9%, and 6.3% respectively. The percentage of weight loss observed in the concrete with optimum mix is

0.23%, 4.4%, and 5.35% respectively, after exposure to 200°C, 400°C and 600°C. The percentage of weight reduction is observed lesser in concrete with Zeolite (Z), Silica Fume (S), and Fly Ash (F) compared with conventional concrete at 400°C and 600°C. The comparison in % of weight reduction for specimens with and without ZSF is nominal at 200°C. The reduction in weight of concrete specimens during exposure to elevated temperatures is linked to the degradation that takes place in the concrete during heating.

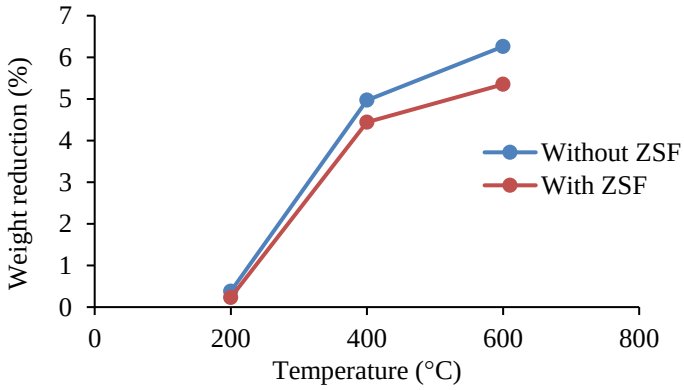

Fig. 5. Percentage of weight reduction after exposure to elevated temperatures

5.2.2 Compressive Strength

Concrete after 28 days of curing are exposed to temperatures of 200°C, 400°C, and 600°C for 1 hour after reaching the target temperature. The specimens are tested after cooling naturally in the furnace and the compressive strength test results are given in Fig. 6. It is inferred that compressive strength values of the mix 3 concrete with ZSF under elevated temperatures are higher at 200°C, 400°C, and 600°C when compared to the conventional concrete. This can be due to the fact of the denser interfacial transition zone with the filling of voids by finer zeolite, silica fumes, and class C fly ash. Mix 3 has 53.1 MPa, 51.3 MPa, and 42.7 MPa after exposure to 200°C, 400°C, and 600°C respectively, whereas conventional has the strength of 51.3 MPa, 48.5 MPa, and 40.2 MPa.

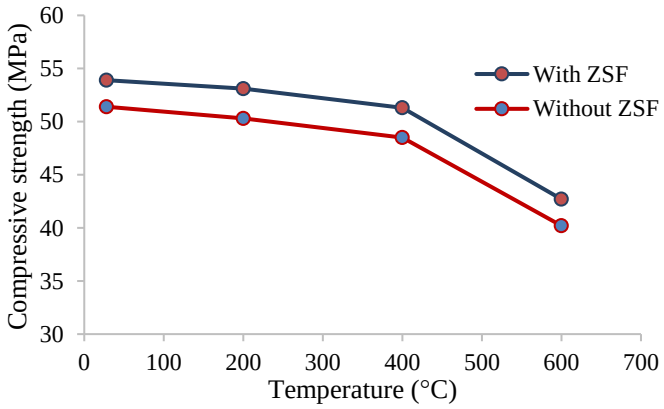

Fig. 6. Compressive strength for concrete mixes with and without ZSF

Table 6 gives the percentage difference in observed values of compressive strength obtained for concrete mixes with and without ZSF. Also, the percentage reduction in

compressive strength upon temperature rise is obtained by comparing the values of strength results obtained for both concrete mixes with and without ZSF. The percentage reduction is observed lesser for concrete mixes with ZSF and this can be due to the formation of highly dense structures in the form of additional strength by CSH formation. The strength retention at a higher rate for concrete mix containing ZSF can be attributed to the fact of greater quantity of additional hydration products developed in concrete containing zeolite upon heating [14].

Table 6. Percentage reduction in compressive strength of concrete mixes with and without ZSF

Concrete mix	Compressive strength (MPa)				% Reduction in compressive strength with respect to room temperature			
	Room temperature	200°C	400°C	600°C	Room temperature	200°C	400°C	600°C
With ZSF	53.9	53.1	51.3	42.7	-	1.5	4.8	20.8
Without ZSF	51.4	50.3	48.5	40.2	-	2.1	5.6	21.8

5.2.3 Split Tensile Strength

Split tensile strength is observed to reduce at a higher rate compared to compressive strength upon temperature rise. Fig. 7 gives the split tensile strength obtained for concrete mixes with and without ZSF. Also, a percentage reduction in split tensile strength is observed higher for mixes without ZSF.

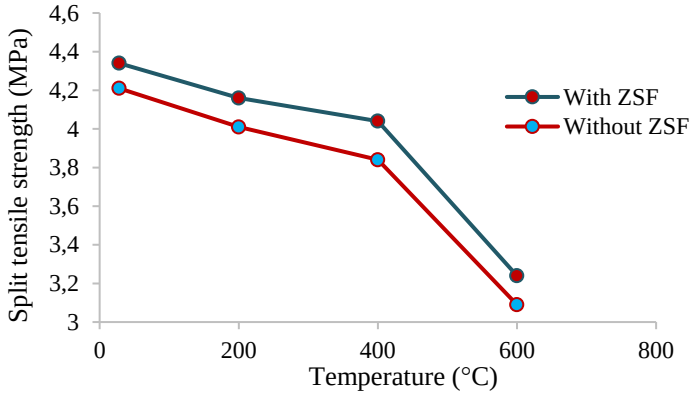

Fig. 7. Variation of split tensile strength for concrete mixes with and without ZSF

The values of split tensile strength for concrete with ZSF retained a higher percentage of tensile strength by 96%, 93.1%, and 75% after exposure to 200°C, 400°C and 600°C whereas conventional concrete without ZSF retained 95.3%, 91.2% and 73% at 200°C, 400°C and 600°C. Table 7 gives the percentage of reduction obtained for split tensile strength after exposure to elevated temperatures for concrete mixes with and without ZSF. The retainment of a higher percentage of tensile strength can be due to the dense transition zone between cement and aggregate particles due to the addition of supplementary cementitious materials.

Table 7. Percentage reduction in tensile strength for concrete mixes with and without ZSF

Concrete mix	Split tensile strength (MPa)				% Reduction in tensile strength with respect to room temperature			
	Room temperature	200°C	400°C	600°C	Room temperature	200°C	400°C	600°C
With ZSF	4.34	4.16	4.04	3.24	-	4	6.9	25
Without ZSF	4.21	4.01	3.84	3.09	-	4.7	8.8	27

5.2.4 Microstructural Characteristics

Fig. 8 gives the images obtained from Scanning Electron Microscope for concrete with ZSF at room temperature and after exposure to 200°C, 400°C and 600°C. From the images, a dense transition zone with the formation of CSH and CH is observed at room temperature. At temperatures higher than 200°C, the microstructure undergoes significant modifications, and at 400°C, the formation of a few voids with the decomposition of a dense matrix is noticed. The increase in temperature results in a decrease in the volume of CH and CSH compared to the room temperature, and temperature rise causes a change in the appearance of CSH crystals. At 200°C, partial decomposition of CH and CSH is observed with the fibrous CSH, and few pores are observed. At 400°C, the breakdown of the dense matrix is observed along with the decomposition of CSH gel. At 600°C, macropores are observed with the formation of cracks. As noticed from the SEM analysis, the EDX analysis performed on the specimens reveals a significant amount of calcium, silicon, and oxygen, in addition to other elements that suggest the formation of hydrated CSH gel.

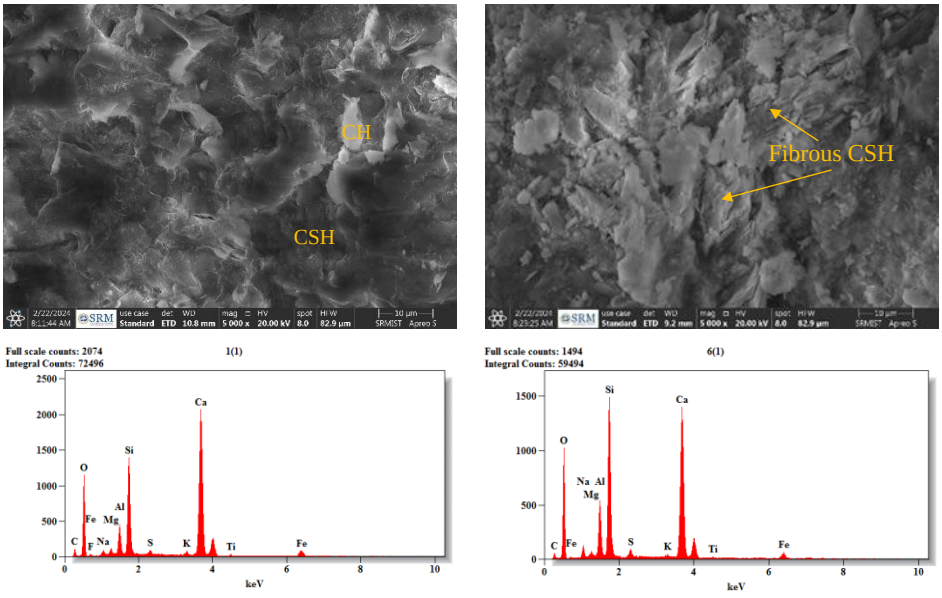

a) Room temperature b) After exposure to 200°C

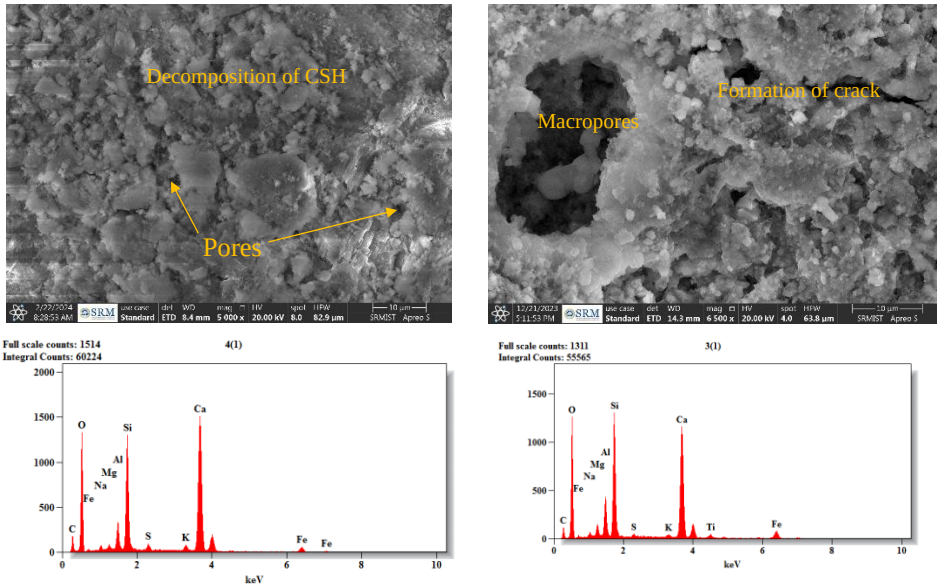

c) After exposure to 400°C d) After exposure to 600°C

Fig. 8. Images of *scanning electron microscope* analysis and EDX analysis obtained for concrete with ZSF

Different peaks of calcium, silicon, and oxygen counts are observed with the temperature rise, and the count decreases with the temperature rise. The results are in correlation with SEM analysis for the observation of the decomposition of CSH and CH crystals at higher temperatures.

5. Conclusions

The objective of the present study is to investigate the concrete behaviour when the cement is replaced with Zeolite, Silica fumes, and class C fly ash, and the performance of concrete mix with ZSF is arrived at by testing the specimens for compressive strength test and split tensile strength. The effect of temperature rise on concrete with and without supplementary cementitious materials is identified and compared. The concluding remarks are as follows:

- In comparison to the standard concrete mix, mix 1 with 10% of zeolite has a reduction in 28 days strength by 5.4%, mix 2 with 7.5% silica fume and 10% fly ash has an increase in strength by 2%, and mix 3 which consists of 10% zeolite, 7.5% silica fume, and 10% class C fly ash has increase in strength by 4.9%. All three types of concrete had originally had lower compressive strengths at the end of 7 and 14 days of curing before eventually reaching the required target strength.
- On comparison of split tensile strength with the conventional mix, mixes 1 and 2 have a reduction in strength by 11% of their value while concrete mix 3 gains 3.1%. The addition of 10% zeolite, 7.5% silica fume and 10% fly ash resulted in the development of concrete mix with the desired compressive and tensile strength comparable with the conventional concrete mix.
- Compressive strength and split tensile strength of concrete mixes with and without ZSF is compared after exposure to elevated temperatures of 200°C, 400°C, and

600°C, and the percentage retention of strength values for concrete mix with ZSF are found higher compared with mixes without ZSF. The percentage retention of compressive strength and split tensile strength for concrete mixes with ZSF is 79.2% and 75%, and for mixes without ZSF is 78.2% and 73% after exposure to 600°C. Additional hydration products developed due to the addition of zeolite, silica fume, and fly ash resulted in the retention of strength values at a higher rate compared with the conventional concrete specimens at elevated temperatures.

- The strength value decreases with the temperature rise, and the percentage reduction in strength values is between the range of 20.8-27% at 600°C in both conventional mix and mix with ZSF. It is possible to ascribe the degradation of the microstructural components to the fact that a considerable loss of mechanical properties occurs at temperatures higher than 400°C. The degradation in mechanical properties is confirmed using EDX-SEM analysis. Microstructural study on concrete specimens presents the decomposition of CSH and CH matrix when the temperature exceeds 400°C.

The present study examined to develop sustainable concrete with the desired characteristics and performance at room and elevated temperatures by incorporating supplementary cementitious materials such as zeolite, silica fume, and class C fly ash.

Acknowledgement

This study acquired no funding from government, commercial, or non-profit organisations. The authors are thankful to the Centre for Advanced Concrete Research Laboratory (CACR), SRM Institute of Science and Technology for completing the experimental studies necessary for this research work. We acknowledge SRM Institute of Science and Technology for high resolution scanning electron microscope (HR-SEM) facility at SRMIST setup with support from The Ministry of New and Renewable Energy (Project No.31/03/2014-15/PVSE-R&D), Government of India.

References

[1] Yazıcı H. The effect of silica fume and high-volume Class C fly ash on mechanical properties, chloride penetration and freeze-thaw resistance of self-compacting concrete. Construction and Building Materials, 2008; 22(4): 456-462. https://doi.org/10.1016/j.conbuildmat.2007.01.002

[2] Poon CS, Lam L, Kou SC, Lin ZS. A study on the hydration rate of natural zeolite blended cement pastes. Construction and building materials, 1999;13(8): 427-432. https://doi.org/10.1016/S0950-0618(99)00048-3

[3] Shon CS, Kim YS. Evaluation of West Texas natural zeolite as an alternative of ASTM Class F fly ash. Construction and Building Materials, 2013; 47: 389-396. https://doi.org/10.1016/j.conbuildmat.2013.04.041

[4] Iswarya G, Beulah M. Use of zeolite and industrial waste materials in high strength concrete-A review. Materials Today: Proceedings, 2021; 46: 116-123. https://doi.org/10.1016/j.matpr.2020.06.329

[5] Shekarchi M, Ahmadi B, Azarhomayun F, Shafei B, Kioumarsi M. Natural zeolite as a supplementary cementitious material-A holistic review of main properties and applications. Construction and Building Materials, 2023; 409, 133766. https://doi.org/10.1016/j.conbuildmat.2023.133766

[6] Mangat PS, Khatib JM. Influence of fly ash, silica fume, and slag on sulfate resistance of concrete. Materials Journal, 1993; 92(5):542-552. https://doi.org/10.14359/9775

[7] Islam MS, Mohr BJ, VandenBerge D. Performance of natural clinoptilolite zeolite in the cementitious materials: A comparative study with metakaolin, fly ash, and blast furnace

slag. Journal of Building Engineering, 2022; 53, 104535. https://doi.org/10.1016/j.jobe.2022.104535
[8] Kushnir AR, Heap MJ, Griffiths L, Wadsworth FB, Langella A, Baud P ... & Utley JE. The fire resistance of high-strength concrete containing natural zeolites. Cement and Concrete Composites, 2021; 116, 103897. https://doi.org/10.1016/j.cemconcomp.2020.103897
[9] Wongkeo W, Thongsanitgarn P, Poon CS, Chaipanich A. Heat of hydration of cement pastes containing high-volume fly ash and silica fume. Journal of Thermal Analysis and Calorimetry, 2019; 138:2065-2075. https://doi.org/10.1007/s10973-019-08641-7
[10] Thomas MD, Shehata MH, Shashiprakash SG, Hopkins DS, Cail K. Use of ternary cementitious systems containing silica fume and fly ash in concrete. Cement and concrete research, 1999; 29(8): 1207-1214. https://doi.org/10.1016/S0008-8846(99)00096-4
[11] Mahdi Valipour, Farhad Pargar, Mohammad Shekarchi, Sara Khani. Comparing a natural pozzolan, zeolite, to metakaolin and silica fume in terms of their effect on the durability characteristics of concrete: A laboratory study. Construction and Building Materials, 2013; 41: 879-888. https://doi.org/10.1016/j.conbuildmat.2012.11.054
[12] Rashad AM, An exploratory study on high-volume fly ash concrete incorporating silica fume subjected to thermal loads. Journal of Cleaner Production, 2015; 87: 735-744. https://doi.org/10.1016/j.jclepro.2014.09.018
[13] Toufigh V, Pachideh G. Cementitious mortars containing pozzolana under elevated temperatures. Structural Concrete, 2022: 23(5): 3294-3312. https://doi.org/10.1002/suco.202100567
[14] Moghadam MA, Izadifard RA. Effects of zeolite and silica fume substitution on the microstructure and mechanical properties of mortar at high temperatures. Construction and Building Materials, 2020; 253, 119206. https://doi.org/10.1016/j.conbuildmat.2020.119206
[15] Brough AR, Katz A, Sun GK, Struble LJ, Kirkpatrick RJ, Young JF. Adiabatically cured, alkali-activated cement-based wasteforms containing high levels of fly ash: Formation of zeolites and Al-substituted CSH. Cement and Concrete Research, 2001; 31(10): 1437-1447. https://doi.org/10.1016/S0008-8846(01)00589-0
[16] Harish C, Kumar TN, Vishnuvardhan V. Strength and Durability Properties by Replacement of Natural Zeolite and Fly ash in Ordinary Portland Cement. International Journal of Innovative Technology and Exploring Engineering, 2020; 2278: 3075. https://doi.org/10.35940/ijitee.C8379.019320
[17] Sabet FA, Libre NA, Shekarchi M. Mechanical and durability properties of self consolidating high performance concrete incorporating natural zeolite, silica fume and fly ash. Construction and Building Materials, 2013; 44: 175-184. https://doi.org/10.1016/j.conbuildmat.2013.02.069
[18] Sanytsky M, Kropyvnytska T, Ivashchyshyn H. Sustainable modified pozzolanic supplementary cementitious materials based on natural zeolite, fly ash and silica fume. In IOP Conference Series: Earth and Environmental Science (Vol. 1254, No. 1, p. 012004). IOP Publishing, October, 2023. https://doi.org/10.1088/1755-1315/1254/1/012004
[19] Kumar BN, Rushikesh M, Kumar AA. An experimental study on high strength self-compacting concrete inclusion of zeolite and silica fume as a potential alternative sustainable cementitious material. Materials Today: Proceedings. 2024. https://doi.org/10.1016/j.matpr.2024.04.063
[20] IS 2386 - Part 3: 1963. Methods of test for aggregates for concrete, PART III: Specific Gravity, Density, Voids, Absorption and Bulking). Bureau of Indian Standards, New Delhi.
[21] IS 383: 2016. Coarse and Fine Aggregate for Concrete - Specification (Third Revision), Bureau of Indian standards, New Delhi, 2016.

[22] IS 10262: 2019. Concrete Mix Proportioning - Guidelines. Bureau of Indian Standards, New Delhi.
[23] He ZH, Han XD, Shi JY, Han C, Yuan Q, Lu J. Volume stability and nano-scale characteristics of concrete composite containing natural zeolite. Journal of Building Engineering; 2022, 59, 105127. https://doi.org/10.1016/j.jobe.2022.105127
[24] Xuan, Z., & Jun, Z. (2021). Influence of zeolite addition on mechanical performance and shrinkage of high strength engineered cementitious composites. Journal of Building Engineering, 36, 102124. https://doi.org/10.1016/j.jobe.2020.102124
[25] Shahmansouri AA, Bengar HA, AzariJafari H. Life cycle assessment of eco-friendly concrete mixtures incorporating natural zeolite in sulfate-aggressive environment. Construction and Building Materials; 2021, 268, 121136. https://doi.org/10.1016/j.conbuildmat.2020.121136

Research on Engineering Structures & Materials
www.jresm.org
Research Group

Research Article

Fabrication and mechanical characterization of composite fiberboard utilizing dry lemon peel powder and epoxy resin

Anil Kumar [1,a], Jayant P. Supale [*,1,b], Dipti Grover [2,c], Bhawna Dahiya [2,d]

[1]*Department of Mechanical Engineering, G. B. Pant DSEU Okhla-I Campus, New Delhi, India*
[2]*Institute of Environmental Studies, Kurukshetra University, Kurukshetra 136119, India*

Article Info

Article history:

Received 12 Aug 2024
Accepted 30 Sep 2024

Keywords:

Composite;
Sustainable materials;
Lemon peel powder;
Scanning electron microscope;
Mechanical properties

Abstract

This research work is related to the manufacturing of a composite fiberboard using dry lemon peel powder and epoxy resin, which can be used as an alternate to the plywood or wood. The objective of this study is to assess the mechanical and microstructural properties of this novel composite fiberboard. To assess its strength and ability to absorb energy, different tests were performed on different specimens. To comprehend the morphology and filler particle distribution within the resin, the microstructure of the fabricated composite was also checked using a scanning electron microscope (SEM). As per the experimental findings, the composite's mechanical properties, such as hardness 22.45 (Vickers), tensile strength 14.7 MPa, flexural strength 27.9 MPa and impact strength 21.76 J/m^2, appeared promising with respect to the plywood. Additionally, perfect bonding was shown by the SEM study between the waste Dry Lemon Peel particles (DLPP) and the epoxy, contributing to improved mechanical properties.

1. Introduction

The agriculture products when used produce the waste in the form of peels or shells and most of the time; these wastes are either dumped in open places or burned to produce energy resulting in generation of dioxins [1]. Five billion tons of food is wasted worldwide each year during the food life cycle including fruits fresh, vegetables, dairy products, baked goods and so forth [2]. The volume of such waste is anticipated to rise over the next ten years as a result of the growing world population [3].

Lemon peels are also such an example of agricultural waste. The global lemon production typically falls within the range of 16 to 18 million metric tons annually, with India emerging as a prominent lemon-producing nation alongside Mexico, Argentina, and Spain. The quantity of waste peel generated from an individual lemon is subject to variation based on factors like lemon size and peel thickness. The lemon peel typically represents around 25% to 30% of the overall weight of the fruit. The remaining 70% to 75% constitutes the edible fruit pulp and juice.

The characteristics of lemon peel powder display variability influenced by factors including preparation methods, drying techniques and the specific attributes of the lemon peels utilized. The drying process is commonly employed to reduce moisture levels and enhance the shelf life of lemon peel powder. The Lemon peel powder emits a distinct citrusy fragrance akin to fresh lemon zest, with the strength of the aroma contingent on

*Corresponding author: jay.researchpaper@gmail.com
[a] orcid.org/0000-0001-8264-0586; [b] orcid.org/0009-0009-8833-2547; [c] orcid.org/0000-0001-6132-8809; [d] orcid.org/0009-0001-0225-8385
DOI: http://dx.doi.org/10.17515/resm2024.394me0812rs

the freshness of the lemon peels and the processing approach. Also, the density of lemon peel powder is subject to change depending on particle size, compaction and moisture content, generally displaying a moderate density relative to other powders. Although not entirely water-soluble, lemon peel powder can disperse and impart its flavor and aroma when incorporated into liquids, exhibiting partial solubility in hot water or other solvents, subsequently releasing its components. Lemon peel powder is comparably soft to various synthetic materials, easily pulverized into a fine powder due to its low hardness. While not inherently brittle, extensive drying may render it fragile, necessitating caution to prevent excessive drying that could lead to brittleness and susceptibility to breakage.

Particleboard made of polymeric composites is created by mixing a polymeric binder with filling materials using suitable conditions and proportions. Urea formaldehyde [4-5], phenol formaldehyde [6] polyethylene [7-8] and polyvinyl acetate [9-10] are the most widely used binders for fabrication of composite fiberboard from different types of agriculture waste powders. The anticipated outcome is that these binders could enhance the mechanical properties, fire and biodegradation resistance of composite materials. To reduce dependency on trees as a source of wood it is essential to assess agricultural residues which usually have a low calorific value for use as filler material in the manufacturing of commercial particleboard. Owing to the distinct cellulose structures in each particleboard manufactured from various agricultural residues have differing physical properties. Assessing agricultural residues to determine their specific characteristics is essential, as these traits may differ based on the geographical location where the plants were cultivated. Various plant fibers and agricultural residues, such as nutshell almond and walnut shell [11-13], peach nut shell [14] bamboo [15] cotton seed hulls [16] wood flour [17] rice husk and starch [18-19], Todo fir and sun flower, have been investigated as filling materials [20-21] and they all offer a diverse range of options. It was found that an increased proportion of coconut fiber adversely impacts both the mechanical strength and the increase in thickness [8]. Various ratios of walnut-almond shell particles [ranging from 0% to 100%] were examined with urea-formaldehyde as the binder. After thorough analysis, the study noted that adding walnut-almond particles notably enhanced the aqua-resistance of the panels. However, increasing the content of walnut-almond shells in the panels led to a decrease in flexural strength [14]. One of the researches outlines a method for producing fiberboard by integrating walnut shell powder particles into epoxy, with the objective of evaluating mechanical properties. After testing a tensile strength of 12.4 MPa, flexural strength of 19.1 MPa, compressive strength of 46.4 MPa and Charpy impact strength of 1.32 KJ/m^2 (notched) have been obtained which is within the acceptable range and comparable with the properties obtained for other fiberboards made from similar types of waste agriculture waste powders [22]. Despite the remarkable physical characteristics of nano and micro-structured materials traditional elasticity theories are unable to adequately explain their behavior. Use of size-dependent elasticity models which take into account the effects of their small scale is necessary to accurately analyze their mechanical responses. These models provide a more accurate understanding of the materials properties and behavior under different conditions by taking into account phenomena like surface effects and size effects that become significant at the nano and micro-scale [23-25]. Incorporating Citrus limetta peel Powder with Epoxy Polymer composites reduce dependency on petroleum-derived Epoxy Polymer products. The possible uses of an epoxy composite strengthened with citrus limetta peel powder include furniture and decorative pieces, as well as doors, tables, and shelves [26-27]. A composite material with remarkable mechanical qualities has been developed by combining pomegranate peel powder with epoxy. This composite exhibits significant potential for use in fields where high strength capacities are essential [28].

Adding lemon peel powder with epoxy resin in a certain ratio in a particular composite fiberboard can enhance the properties of composite fiberboard. Different observations are available which shows that adding graphene oxide [29], carbon nanotubes [30] and surface-modified graphene oxide [31] can enhance the mechanical properties of epoxy-based composite fiberboards. Additionally, the use of different binders in composite fabrication has been found to influence tribological properties and hardness, as observed in studies comparing emulsion and powder binders in epoxy resin composites [32]. Furthermore it's been observed that a composite made of epoxy and powdered lemon peel may exhibit enhanced mechanical strength and tribological performance making it a flexible material with a variety of applications in the automotive and aerospace industries. Polymer composites with natural fibers are a subject of research [33-34]. It has been noted that the strength of SiO_2-epoxy polymer nanocomposite material decreases less than that of unmodified material [35]. It was discovered that incorporating SiO_2 nanoparticles into the epoxy matrix increases the contact forces and energy absorption capabilities [36]. Epoxy composites show better tensile strength [up to 124 MPa], flexural strength (203 MPa) and lower carbon footprints than conventional petroleum-based alternatives. Epoxy has outstanding natural fiber adherence which improves the composites overall mechanical qualities [37].

The leftover lemon peel can be used to make composite fiberboard by drying and powdering it. This strategy fits into the larger idea of using agricultural waste or byproducts for the production of sustainable materials and processes. There are numerous advantages to using leftover lemon peel to make composite fiberboard such as:

- Environmental Sustainability: Recycling leftover lemon peels helps to manage waste in an environmentally friendly way and lowers pollution.
- Resource Efficiency: Their use leads to preservation of precious resources ultimately lowering the demand for virgin materials.
- Renewable and Biodegradable: Lemon peel is an environmentally friendly option since it is a renewable resource that breaks down naturally.
- High dietary fiber content especially insoluble fiber: Incorporating lemon peel powder into composite matrices improves the tensile strength due to its high dietary fiber content especially insoluble fiber makes it suitable for manufacturing the composite fiberboard [38].

So, the objectives of present research work are;

- To manufacture a fiberboard of Dry lemon Peel powder (DLPP) mixed with epoxy.
- To find out the mechanical strength of the fabricated fiberboard.
- To do SEM analysis of the fiberboard to describe its morphology.

2. Material and Methods

2.1. Materials

- Dry Lemon Peel Powder (DLPP): This fine powder is created by mechanically processing dried lemon peels.
- Epoxy Resin: Novolac Epoxy Resin (Araldite LY 556) with Aradur HY 951 as the hardener has been used as matrix for the fabrication of a robust and high-performing composite material.

2.2 Preparation of DLPP

The first step in creating DLPP is obtaining fresh clean lemon peels from nearby sources. Then in order to get rid of any contaminants they must be thoroughly cleaned and rinsed. After cleaning the peels are spread out evenly on trays and dried by either sun-drying for

two to three days while covered with protective netting or roasting them for an entire day at 60°C. After being allowed to dry for a while the peels are manually cut into smaller pieces and then ground in a machine to a fine powder. To avoid thermal damage the grinding process is periodically stopped to allow for cooling. The ground powder is passed through a 200-mesh sieve to guarantee a constant particle size. Once collected the powder is stored in an airtight container that is sealed against moisture in a cool dry location. Because quality control methods are used the DLPP is of the highest quality and suitable for use in the manufacturing of composite fiberboards. Figure 1 shows the image of DLPP obtained from lemon waste.

Fig. 1. Dry Lemon Peel Powder (DLPP)

2.3 XRD Analysis of DLPP

Finding a materials crystallographic structure can be accomplished very successfully with X-ray diffraction (XRD) analysis. In many scientific domains such as geology chemistry physics and materials science it is extensively employed to examine the arrangement of atoms or molecules in a crystalline sample. A crystalline or powdered material is exposed to a monochromatic X-ray beam in an XRD experiment.

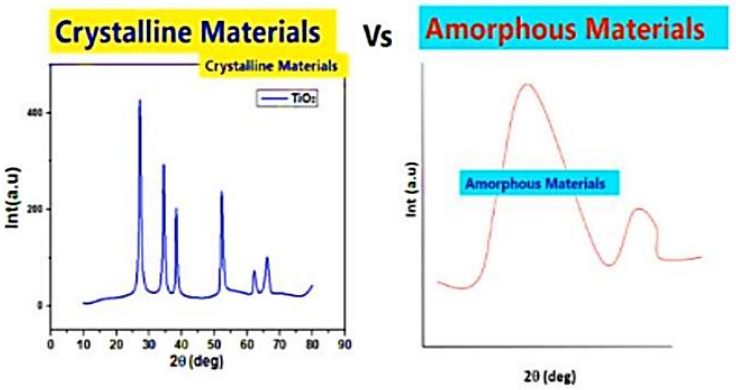

Fig. 2.Crystalline XRD and Amorphous XRD

The sample can be precisely rotated in the X-ray beam since it is mounted on a goniometer. The diffracted X-rays are collected by a detector that is positioned on the other side of the

material. In order to obtain diffraction data, one typically rotates the sample and modifies the angle at which the detector and incident X-ray beam are positioned along a range of scattering angles. Usually, one uses a diffraction data visualization that shows the intensity as a function of the scattering angle (2θ). By analyzing the positions and intensities of the diffraction peaks one can determine the crystalline phases present in the sample along with several structural elements such as crystal orientation lattice parameters grain size and crystallographic defects. Figure 2 shows the graphs obtained after XRD analysis for Crystalline and Amorphous materials.

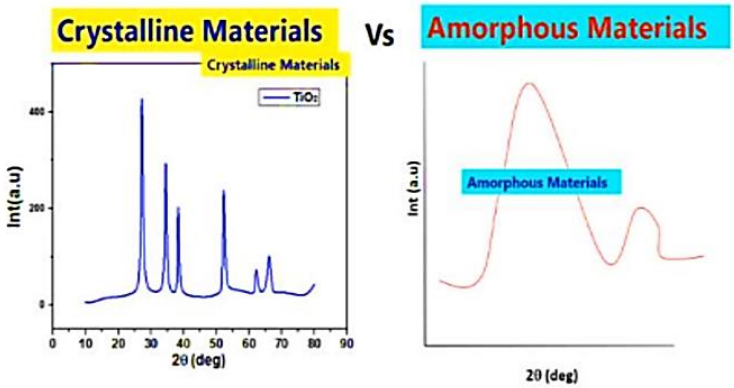

Fig. 2.Crystalline XRD and Amorphous XRD

Figure 3 shows the result of XRD Analysis of the DLPP. After analysis of the XRD Image, it has been observed that the DLPP is amorphous material. There are some impurity peaks in XRD which suggest the presence of unintended or foreign materials in the sample. This may be due to some dust or any other particle during generation of the peel powder. But in all they don't affect the overall nature of the powder particle.

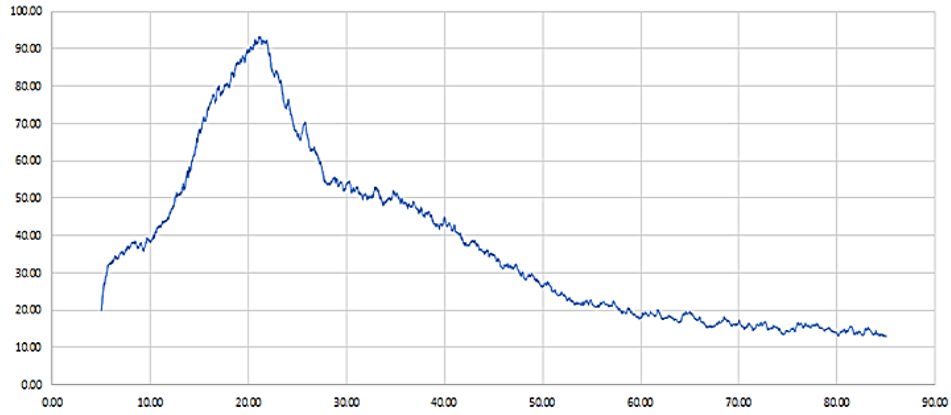

Fig. 3. XRD image of DLPP

2.4 Fabrication of Composite Fiberboard

Weighing the required materials is the first step in the fabrication process. The following number of materials have been selected for fabrication of composite fiberboard;

- 300 grams of DLPP,

- 700 grams of Novolac epoxy (Araldite LY 556),
- 210 grams of Aradur HY 951 hardener.

Mixture having ratio of 30 to 70 of the reinforcement particle and epoxy resin ensures the most appropriate ratio for achieving optimal curing and mechanical properties in the fiberboard [39-40]. Using a mechanical stirrer to ensure even dispersion 300 grams of DLPP are gradually added to 700 grams of epoxy resin (Araldite LY 556) at the start of the fabrication process. The mixture is then progressively stirred with 210 grams of Aradur HY 951 hardener until a homogenous blend is obtained. As shown in Figure 4, a rectangular mold is prepared for molding and curing and it is coated with a release agent to make it easier to remove the cured composite.

Fig. 4. Mold used for making the composite

After thoroughly mixing and degassing, the composite mixture is poured into the mold and leveled out. To guarantee full polymerization and improved mechanical properties, the mold is post-cured at 120°C for two hours after being left to cure at room temperature for 24 hours. Before mechanical testing, post-fabrication processing entails carefully removing the cured composite fiberboard from the mold. Figure 5 shows the finally fabricated Composite fiberboard.

Fig. 5. Fabricated composite fiberboard

2.5 Mechanical Characterization

For the mechanical characterization of the fiberboard, specific tests mentioned below have been performed on specific samples obtained from it:

- Hardness test
- Tensile test
- Flexural test
- Impact test

2.5.1 Hardness Test

The resistance to surface wear indentation and scratches is referred to as hardness. It is a measure of the board's durability and strength, often influenced by the type of fibers, resins and bonding techniques used in its production. Hardness is crucial for applications where the fiberboard will face mechanical stress, such as in furniture, flooring or wall panels. The Vickers hardness test is performed on composites to evaluate their resistance to deformation and wear, which are critical indicators of their mechanical performance. By measuring the hardness, one can assess the effectiveness of the reinforcing materials within the composite matrix. This test also aids in quality control, guaranteeing consistency in production, and allows for the comparison of different composite formulations to identify the most effective combinations. The hardness has been measured using a Leitz Micro-hardness tester. For this test, a diamond indentater has been used which was operating under a load varying from 0.3 N to 3 N and forced throughout the material. Vickers Hardness Index (Hv) is computed by applying the subsequent formulas [41].

$$L = \frac{X + Y}{2} \tag{1}$$

$$H_v = 0.1889 \frac{F}{L^2} \tag{2}$$

Where, X is the horizontal length (mm), Y is the vertical length (mm), F is the applied load (N) and L is the diagonal of square impression (mm).

2.5.2 Tensile Test

Tensile strength refers to the maximum stress that the material can withstand while being stretched before fracture. This property is crucial for assessing the performance and durability of composite materials, particularly those reinforced with natural or synthetic fibers. The standard test procedure according to ASTM D638 has been applied for calculating the tensile strength for this research. Usually, flat specimens are used for the tensile test.

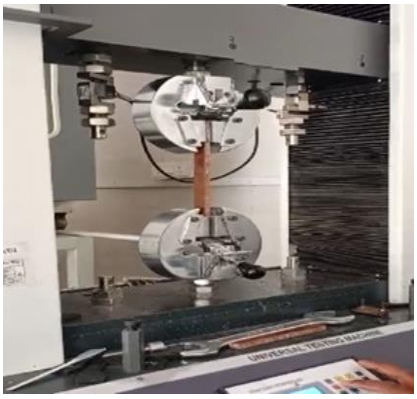

Fig. 6. UTM with Tensile Sample Loaded

The specimen geometries that are most frequently used are the flat specimens. Each Tensile testing sample has a Length of 250 mm, width of 25 mm and height of 10 mm. A Universal Testing Machine (UTM, Saumya Make) is used to conduct the tensile test. Cross head speed during the tests was 2 mm/min. Three composite samples have been tested

and the average value has been obtained for analysis. The testing apparatus and the sample in loading condition are depicted in Figure 6.

2.5.3 Flexural Strength

The flexural strength is also known as the bending strength of a material. Flexural strength represents the higher stress-bearing capacity before fracture. This strength can be evaluated through a 3-point bending test. After fabrication of composite, the specimen has been prepared as per the ASTM D790 standard. To conduct the test, each specimen was placed on machine fixtures of UTM and load was applied constantly as shown in Figure 7. The length of specimen was 150 mm while the breadth 12.5 mm and height has been taken as 10 mm.

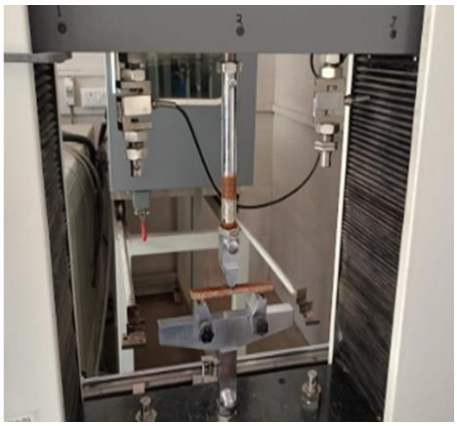

Fig. 7. Flexural test setup

The values of peak load are computed for each specimen from the load vs. deflection curve. The flexural strength for different specimen can be calculated using formula [42];

$$\sigma_{flex} = \frac{3Pl}{2bd^2} \tag{3}$$

Where, P stands for ultimate load (N), l stands for effective length (mm), b stands for breadth (mm) and d stands for height of the specimen(mm).

2.5.4 Impact Strength

The Izod impact strength refers to its ability to absorb energy during impact and is a crucial for applications requiring durability and resistance to sudden forces. The Izod impact strength test as per ASTM 256 is used to evaluate the impact resistance of materials like metals, composites and polymers.

To determine the Impact strength of the composite fiberboard fabricated for this research, three specimens each having length of 50 mm and cross section area of 10x10 mm^2 have been cut from the main fiberboard sheet. Figure 8 shows the test setup for the impact test.

Fig. 8. Izod Impact test setup

2.6 SEM Analysis

Small portions of the composite are cut and coated with gold using sputtering to enhance conductivity. These coated samples are then analyzed using a scanning electron microscope to study how dry lemon peel powder (DLPP) is distributed within the epoxy matrix and to determine the bonding interfaces between the filler and the matrix.

3. Results and Discussion

3.1 Hardness Test

To measure Vickers hardness numbers Leitz Micro-hardness testing machine has been employed. Vickers hardness for the composite material is 22.45. According to this hardness value the mechanical properties of the composite are greatly enhanced when lemon peel powder is added to the epoxy resin matrix as a reinforcing agent. It also shows that the material is reasonably resistant to deformation and indentation under load.

3.2 Tensile Test

The tensile test was conducted in this study on three specimens obtained from composite fiberboard composed of epoxy resin and powdered dry lemon peel in accordance with ASTM D638 standard on a UTM, (Saumya Make). The test findings show that the fiberboard has an average tensile strength of 14.7 MPa.

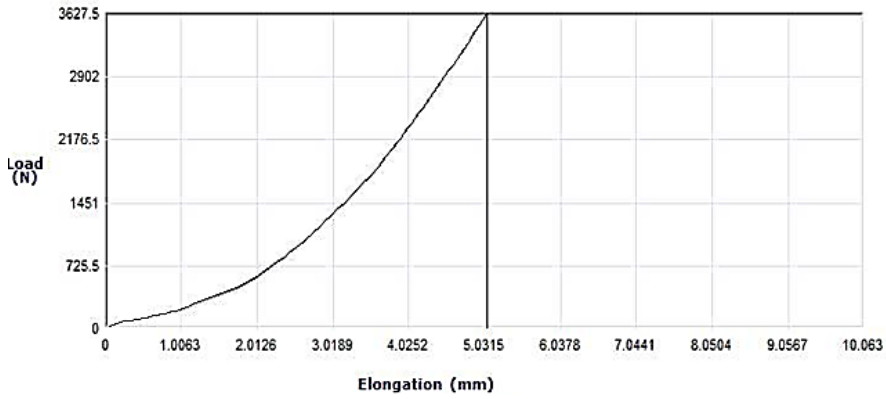

Fig. 9. Load versus deformation curve for tensile test

The Figure 9 shows a curve for Tensile Test of one of the test specimens. The materials elastic behavior wherein the deformation increases at a constant rate as the load is applied is first indicated by the curves non-linear increase. The curve peaks as the load increases at about 5.0315 mm of elongation or roughly 3627.5 N which is the highest load the material can bear before failing. The curve ends at this peak indicating that the specimen has either failed or has reached its breaking point due to significant plastic deformation. Its mechanical characteristics and behavior under tensile stress are highlighted by this curve which shows the materials ability to support increasing loads up to a critical point. DLPP have low tensile strength as compared to synthetic fibers. It has been observed that the composite fiberboard fails due to failure of the filler before the binding agent. As the filler has low strength as compared to that of the epoxy.

3.3 Flexural Test

Dry lemon peel powder and epoxy resin were mixed to create the specimens which were then molded and allowed to cure under carefully monitored circumstances. The three different specimens of the composite fiberboard were subjected to the flexural strength test in accordance with ASTM D790. The UTM (Saumya Make) with a three-point bending configuration was used to conduct the flexural strength tests. Dry lemon peel powder can effectively reinforce epoxy resin as evidenced by the composite fiberboard's average flexural strength of 27.9 MPa.

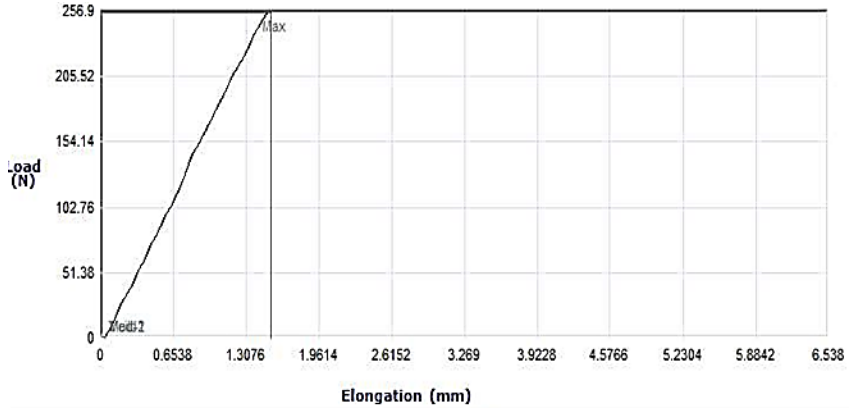

Fig. 10. Load versus deformation curve for flexural test

The graph shown in Figure 10 illustrates the results of a flexural test performed on one of the specimens obtained from a composite fiberboard made from dry lemon peel powder and epoxy resin. The curve begins with a linear region where the load increases proportionally with elongation, indicating the elastic behavior of the material. This means that as the load is applied, the material deforms at a constant rate. The linear portion continues up to a point labeled "Max," where the maximum load of approximately 256.9 N is reached and the corresponding elongation is around 1.9614 mm.

Beyond this maximum load point, the curve sharply declines, indicating the failure of the material. The sharp drop suggests that the composite fiberboard has reached its flexural strength limit and can no longer sustain the applied load, leading to a sudden failure. This graph demonstrates the material's ability to withstand increasing loads up to a certain point, after which it fails. The linear elastic region provides insight into the material's stiffness, while the peak point represents its flexural strength. It has been found that the brittleness of the epoxy which permits little plastic deformation prior to failure is the

reason why the composite fails under flexural loading. Thus it abruptly breaks under flexural stress following a specific load.

3.4 Impact Strength

The method used to evaluate the impact resistance of the composites made of dry lemon peel powder and epoxy resin was the Izod impact strength test which is carried out in accordance with ASTM D256. The notched specimen was subjected to a sudden force during the test using a pendulum and the energy the specimen absorbed up until fracture was measured. After three distinct samples were tested, the average impact strength was found to be 21.7 J/m. The toughness and durability of the material are indicated by this value which shows its resistance to impact forces. It is important for applications where the material may be subjected to sudden or dynamic loads that the results suggest the composite material has a moderate level of impact resistance. From the test it has been observed that the failure of the material is due to the low toughness of DLPP because dry or powdered natural fibers possesses low strength-to-weight ratios compared to synthetic fibers, making the composite less resistant to impact forces.

3.5 SEM Analysis

The composite made up of Dry lemon peel powder and epoxy was subjected to scanning electron microscopy (SEM) using Leo 435 VP equipment. The micro graphs of the composite are shown in Figure 11. Micrographs unequivocally demonstrate that a strong bond between the reinforcement and matrix is achieved in the absence of debonding, fiber chipping out and crack formation.

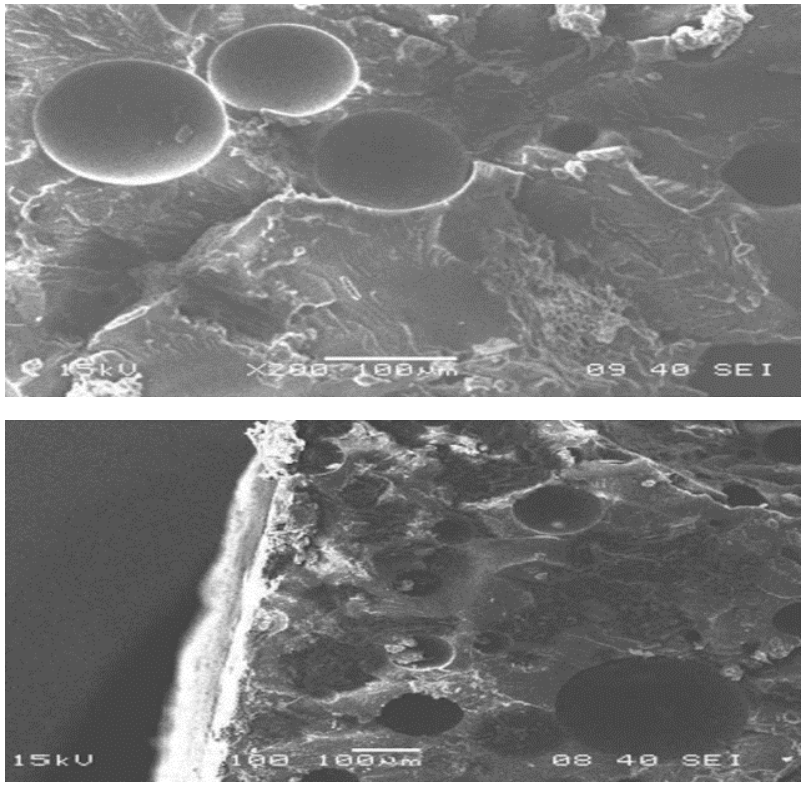

Fig. 11. Micro graphs of the composite

4. Conclusions

The investigation into the mechanical properties of composite materials reinforced with dry lemon peel powder and epoxy resin matrix has yielded significant insights. Based on the various tests and analyses conducted, the following conclusions can be drawn:

- The Vickers hardness number for the composite material was found to be 22.45. As a result, the composites mechanical qualities are greatly improved by the addition of lemon peel powder increasing its resistance to deformation and indentation under load as are comparable to that of plywood or wood.
- The fiberboard has a mean tensile strength of 14.7 MPa according to the results of the tensile test. The tensile strength of present research composite are comparatively higher than that of the properties of plywood or the walnut shell-epoxy composite fiberboard, which has the tensile strength 12.4 MPa Also the tensile performance of this composite could be improved by strengthening the bond adding toughness to the resin or using better filler materials.
- The fiberboard exhibited a mean flexural strength of 27.9 MPa during the flexural strength test. The flexural strength of present research composite are comparatively higher than that of the properties of the walnut shell-epoxy composite fiberboard, whose flexural strength has been previously noted as 19.1 MPa. The flexural strength can be enhanced by fillers like fibers such as carbon or glass fibers. Additionally adding nano-materials to the epoxy matrix like carbon nanotubes (CNTs) or nano-clays can also improve the flexural strength.
- From Impact testing it has been found that the composite fiberboard has mean impact strength of 21.7 J/m2. This value indicates moderate impact resistance, suggesting that the material is suitable for applications involving sudden or dynamic loads. It may be possible to increase the composites resilience to impact loading by strengthening the fiber-matrix bond optimizing the filler treatment or adding additional reinforcing materials.
- An examination using scanning electron microscopy (SEM) demonstrated a robust connection between the epoxy resin matrix and the reinforcement made of dry lemon peel powder. The absence of debonding, fiber chipping out and crack formation in the micrographs underscores the effectiveness of the lemon peel powder as a reinforcing agent.

Therefore, it has been found that the composite material with dry lemon peel powder and epoxy resin has improved mechanical strength such as tensile, flexural strength, hardness and moderate impact resistance. The strong interfacial bonding observed in the SEM analysis further validates the potential of lemon peel powder as a viable reinforcement in composite materials. These findings suggest promising applications for this environmentally friendly composite in various industries where mechanical robustness and sustainability are paramount.

Acknowledgement

We are thankful to Mr. Sonu Singh, PhD Scholar, IIT, Delhi, for his important support in performing the different mechanical tests.

References

[1] Gürü M, Aruntaş Y, Tüzün FN, Bilici I. Processing of urea-formaldehyde-based particleboard from hazelnut shell and improvement of its fire and water resistance. Fire Mater. 2009;33(8):413-419. https://doi.org/10.1002/fam.1011

[2] Que Z, Furuno T, Katoh S, Nishino Y. Effects of urea-formaldehyde resin mole ratio on the properties of particleboard. Build Environ. 2007;42(3):1257-1263. https://doi.org/10.1016/j.buildenv.2005.11.028
[3] Biswas D, Bose SK, Hossain MM. Physical and mechanical properties of urea formaldehyde-bonded particleboard made from bamboo waste. Int J Adhes Adhes. 2011;31(2):84-87. https://doi.org/10.1016/j.ijadhadh.2010.11.006
[4] Tasdemir HM, Sahin A, Karabulut AF, Guru M. Production of useful composite particleboard from waste orange peel. Cell Chem Technol. 2019;53(5-6):517-526. https://doi.org/10.35812/CelluloseChemTechnol.2019.53.52
[5] Zhang L, Hu Y. Novel lignocellulosic hybrid particleboard composites made from rice straws and coir fibers. Mater Des. 2014;55:19-26. doi:10.1016/j.matdes.2013.09.066. https://doi.org/10.1016/j.matdes.2013.09.066
[6] Li B, Zheng Y, Pan Z, Hartsough B. Improved properties of medium-density particleboard manufactured from saline creeping wild rye and HDPE plastic. Ind Crops Prod. 2009;30(1):65-71. https://doi.org/10.1016/j.indcrop.2009.01.006
[7] Kim S, Kim JA, Kim HJ, Kim SD. Determination of formaldehyde and TVOC emission factor from wood-based composites by small chamber method. Polym Test. 2006;25(5):605-614. https://doi.org/10.1016/j.polymertesting.2006.04.008
[8] Kaboorani A, Riedl B. Improving performance of polyvinyl acetate (PVA) as a binder for wood by combination with melamine-based adhesives. Int J Adhes Adhes. 2011;31(7):605-611. https://doi.org/10.1016/j.ijadhadh.2011.06.007
[9] Gürü M, Atar M, Yildirim R. Production of polymer matrix composite particleboard from walnut shell and improvement of its requirements. Mater Des. 2008;29(1):284-287. https://doi.org/10.1016/j.matdes.2006.10.023
[10] Gürü M, Tekeli S, Bilici I. Manufacturing of urea-formaldehyde-based composite particleboard from almond shell. Mater Des. 2006;27(10):1148-1151. https://doi.org/10.1016/j.matdes.2005.03.003
[11] Pirayesh H, Moradpour P, Sepahvand S. Particleboard from wood particles and sycamore leaves: physico-mechanical properties. Engineering in Agriculture, Environment and Food. 2015;8(1):38-43. https://doi.org/10.1016/j.eaef.2014.07.003
[12] Sahin A, Tasdemir HM, Karabulut AF, Guru M. Mechanical and thermal properties of particleboard manufactured from waste peach nut shell with glass powder. Arab J Sci Eng. 2017;42(4):1559-1568. https://doi.org/10.1007/s13369-017-2427-0
[13] Rowell RM. Property enhanced natural fiber composite materials based on chemical modification. In: Science and technology of polymers and advanced materials: emerging technologies and business opportunities. Boston, MA: Springer US; 1998. p. 717-732. https://doi.org/10.1007/978-1-4899-0112-5_63
[14] Gurjar RM. Effect of different binders on properties of particle board from cotton seed hulls with emphasis on water repellency. Bioresour Technol. 1992;43(2):177-178. https://doi.org/10.1016/0960-8524(93)90179-F
[15] Kamdem DP, Jiang H, Cui W, Freed J, Matuana LM. Properties of wood plastic composites made of recycled HDPE and wood flour from CCA-treated wood removed from service. Compos Part A Appl Sci Manuf. 2004; pp. 347-355. https://doi.org/10.1016/j.compositesa.2003.09.013
[16] Tasdemir HM, Sahin A, Karabulut AF, Guru M. Production of useful composite particleboard from waste orange peel. J Cell Chem Technol. 2019;53:517-526. https://doi.org/10.35812/CelluloseChemTechnol.2019.53.52
[17] Sulaiman NS, Hashim R, Hiziroglu S, Hazim M, Amini M, Sulaiman O, Ezwanselamat M. Rubberwood particleboard manufactured using epichlorohydrin-modified rice starch as a binder. Cell Chem Technol. 2016;50(2):329-338.
[18] Ishikura Y. Structural and bending properties of juvenile and mature softwood. Cell Chem Technol. 2017;51:879-887.

[19] Pirayesh H, Khanjanzadeh H, Salari A. Effect of using walnut/almond shells on the physical, mechanical properties and formaldehyde emission of particleboard. Compos B Eng. 2013;45(1):858-863. https://doi.org/10.1016/j.compositesb.2012.05.008
[20] Klímek P, Meinlschmidt P, Wimmer R, Plinke B, Schirp A. Using sunflower (Helianthus annuus L.), topinambour (Helianthus tuberosus L.) and cup-plant (Silphium perfoliatum L.) stalks as alternative raw materials for particleboards. Ind Crops Prod. 2016;92:157-164. https://doi.org/10.1016/j.indcrop.2016.08.004
[21] Benthien JT, Sommerhuber PF, Heldner S, Ohlmeyer M, Seppke B, Krause A. Influence of material origin on the size distribution of wood particles for wood-plastic composite (WPC) manufacture. Eur J Wood Wood Prod. 2017;75(3):477-480. https://doi.org/10.1007/s00107-016-1122-2
[22] Kumar A, Supale JP, Goyal K. Fabrication and material characterization of composite fiberboard made by walnut's waste. Evergreen. 2023;10(4):2153-2160. https://doi.org/10.5109/7160890
[23] Faghidian SA, Elishakoff I. The tale of shear coefficients in Timoshenko-Ehrenfest beam theory: 130 years of progress. Meccanica. 2023;58:97-108. https://doi.org/10.1007/s11012-022-01618-1
[24] Faghidian SA, Darban H. Non-standard interface conditions in flexure of mixture unified gradient nanobeams. Int J Eng Sci. 2024;204:104127. https://doi.org/10.1016/j.ijengsci.2024.104127
[25] Faghidian SA, Elishakoff I. A consistent approach to characterize random vibrations of nanobeams. Eng Anal Bound Elem. 2023;152:14-21. https://doi.org/10.1016/j.enganabound.2023.03.037
[26] Sharma H, Singh I, Misra JP. Mechanical and thermal behaviour of food waste (citrus limetta peel) fillers-based novel epoxy composites. Polymers and Polymer Composites. 2019;27(9):527-535. https://doi.org/10.1177/0967391119851012
[27] Kumar A, Singh S. Fabrication and optimization of wear behaviour of citrus limetta peel particulate composite using hybrid taguchi-gra-pca. Evergreen. 2023;10(3):1323-1329. https://doi.org/10.5109/7151679
[28] Kumar A, Dev K, Dahiya A. Fabrication and mechanical characterization of pomegranate peel powder mixed epoxy composite. Evergreen. 2023;10(4):2173-2179. https://doi.org/10.5109/7160892
[29] Orlov A, Konstantinova A, Korotkov R, Yudaev P, Mezhuev Y, Terekhov I, et al. Epoxy compositions with reduced flammability based on DER-354 resin and a curing agent containing aminophosphazenes synthesized in bulk isophoronediamine. Polymers (Basel). 2022;14(17). https://doi.org/10.3390/polym14173592
[30] Gao J, Wu H, Xiao Y, Ma W, Xu F, Wang R, et al. Synthesis of high-efficiency, eco-friendly, and synergistic flame retardant for epoxy resin. Fire. 2023;6(1). https://doi.org/10.3390/fire6010014
[31] Orduna L, Otaegi I, Aranburu N, Guerrica-Echevarría G. Effect of the simultaneous addition of polycaprolactone and carbon nanotubes on the mechanical, electrical, and adhesive properties of epoxy resins cured with polyetheramine. Polymers (Basel). 2022;14(4). https://doi.org/10.3390/polym14132679
[32] Ma L, Zhu Y, Wu G, Li X, Tian C, Wang Y, Xu L, Song G. Hydroxyl-terminated triazine derivatives grafted graphene oxide for epoxy composites: enhancement of interfacial and mechanical properties. Polymers (Basel). 2019;11(11). https://doi.org/10.3390/polym11111866
[33] Taj S, Munawar MA, Khan S. Natural fiber-reinforced polymer composites. Pakistan Acad Sci. 2007;44(2):129-144.
[34] Kumar R, Kumar K, Bhowmik S. Optimization of mechanical properties of epoxy based wood dust reinforced green composite using Taguchi method. Procedia Mater Sci. 2014;688-696. https://doi.org/10.1016/j.mspro.2014.07.316

[35] Kaybal HB, Ulus H, Tatar AC, Demir O. Influence of seawater on mechanical properties of SiO2-epoxy polymer nanocomposites. Res Eng Struct Mat. 2019;5(2):147-154. https://doi.org/10.17515/resm2018.61is0802
[36] Tatar AC, Kaybal HB, Ulus H, Demir O, Avcı A. Evaluation of low-velocity impact behavior of epoxy nanocomposite laminates modified with SiO2 nanoparticles at cryogenic temperatures. Res Eng Struct Mat. 2019;5(2):115-125. https://doi.org/10.17515/resm2018.55is0704
[37] Kumar B, Adil S, Kim J. Biomass-derived epoxy resin and its application for high-performance natural fiber composites. J Reinf Plast Compos. 2024. https://doi.org/10.1177/07316844241275225
[38] Fakraoui O, Atanase L, Salhi S, Royaud I, Arous M, Ayadi Z. Investigation of lemon peel extract as a natural additive in polyvinyl alcohol/chitosan blend for advanced bioactive food packaging. J Polym Sci. 2024. https://doi.org/10.1002/pol.20240268
[39] Kumar A, Kumar S, Jindal S. Enhancing composite material fabrication through optimization: employing fruit peel or shell powder as reinforcements using Taguchi-GRA-PCA methodology. Evergreen. 2024;11(2):701-712. https://doi.org/10.5109/7183345
[40] Kumar A, Dahiya B, Grover D. Optimizing agricultural waste powder epoxy composite for enhanced strength using a hybrid Taguchi GRA PCA approach. Evergreen. 2024;11(2):713-721. https://doi.org/10.5109/7183347
[41] Tribonet. Hardness calculation Vickers indenter [Internet]. Available from: https://www.tribonet.org/calculators/hardness-calculation-vickers-indenter/.
[42] ASTM Standard. Standard test methods for flexural properties of unreinforced and reinforced plastics and electrical insulating materials. ASTM D790. 1997; Annual Book of ASTM Standards.

Research on Engineering Structures & Materials
www.jresm.org
Research Group

Research Article

Effect of de-icing in conductive concrete by varying carbon powder percent and slab thickness

C B Supriya [1,a], B H Manjunath [1,b], Neeraj S N [*,2,c], Prakash J [3,d], Sagar H [2,e]

[1]*Dept. of Civil Engineering, Sri Siddhartha Institute of Technology, SSAHE University, Karnataka, India*
[2]*Dept. of Civil Engineering, Jawaharlal Nehru New College of Engineering, Karnataka, India*
[3]*Dept. of Civil engineering, Shridevi Institute of Engineering and Technology, Karnataka, India*

Article Info

Article History:

Received 08 Mar 2025

Accepted 09 Apr 2025

Keywords:

M_{40} Conductive concrete;
De-icing concrete;
Electrical conductivity;
Carbon additives;
Thermal properties

Abstract

Deposition of Ice is observed over the road in cold countries and to the greater thickness during winter seasons. This problem is critical at bridge locations. This necessitates the removal of ice frequently. Manual removal is very difficult and time consuming. These need a process of continuous automatic removal. Conductive concrete when provided at bridge portion will continuously de-ice that portion. This is due to the heat generation because of its relatively high conductivity and electrical resistivity in the conductive concrete. In this study, an attempt is made to prepare conductive concrete in the laboratory and tested for its de-icing performance. M_{40} grade conductive concrete mixes were prepared with varying percentages of carbon content and cube strengths are determined for the same. The rate of de-icing is tested by proper electric supply to the casted conductive concrete slabs of 6 inch and 8 inch thick with varying carbon contents (8%, 10% and 12%) by weight of aggregates in the laboratory. Steel fibers are maintained constant at 2% by weight of aggregate. 10mm diameter TMT bars of Fe-415 were used as electrodes. The strength of concrete at 12% carbon content is 41.1MPa and further increase in carbon content shown decrease in strength (i.e. <40MPa) which is not recommended for highway pavements. The temperature of slab increased with increase in an applied voltage. This study confirmed that, the de-icing process is highly effective in conductive concrete and may eliminate ice clearing by manually.

1. Introduction

The need for innovative remedies to reduce the negative impact of ice and snowfall on pavement surfaces has led to the conductive concrete development. It is a material that utilizes the electrical properties to provide de-icing processes. Conventional methods of de-icing like application of salt will harm the infrastructure as well as environment and reminding the researchers to identify alternatives that increase the thermal or heat performance of concrete. Studies have shown that conductive concrete can effectively mitigate these problems with the use of materials like carbon fibres, which will improve the electrical conductivity and causes the heat generation by electrical resistance [1].

Furthermore, studies spotlighted the importance of configuration and composition of conductive materials in conductive concrete for the applications of de-icing in various constructions. Optimization of conductive fillers proportion can increase the conductive concrete overall performance[2]. In addition, many researchers have stated that the thermal efficiency and mechanical properties of conductive concrete are closely related to their characteristics of

*Corresponding author: snneraj@jnnce.ac.in
[a]orcid.org/0009-0007-9676-7925; [b]orcid.org/0009-0005-0450-1640; [c]orcid.org/0009-0002-9349-0901;
[d]orcid.org/0009-0006-0227-7865; [e]orcid.org/0009-0002-0960-4073
DOI: http://dx.doi.org/10.17515/resm2025-732ma0308rs

microstructure [3][1]. This article aims to investigate the production and evaluation of conductive concrete, highlighting its capacity for pavement solutions and chemical treatments and avoiding removal of snow by manually.

The intension of this study is to achieve the following objectives.

- To develop a conductive concrete with varying carbon content (8%, 10%, and 12%).
- To find out the compressive strength of prepared conductive concrete mixes for make sure integrity of structure.
- To evaluate the de-icing performance of conductive concrete under different voltages.

The development of conductive concrete has gathered an attention because of its effective applications in pavements surface de-icing process. Many studies have explained about this material, developed many methodologies and got positive results. This Concrete is the composite material, and it is the ultimate choice for the most structural applications, because of its low cost, easy availability, versatility and essential intended engineering properties. This composite material has an excellent strength properties and durability, but it is a poor conductor of electricity, particularly in dry condition[4]. The mechanical and electrical properties of concrete may have many important applications in different fields like construction industry, military and in other fields[5, 6].

In cold countries during winter seasons ice is deposited all over the road. Clearing the ice from the road becomes inevitable. This problem is much critical at bridge locations, where traffic jam may take place. Manual removal is difficult and time consuming. In such conditions de-icing the Bridge portion is very much essential. This necessitates the need of Conductive concrete, which has relatively high conductivity. In order to produce conductive concrete, certain number of conductive components such as carbon fiber, graphite, steel fibers etc., are added to the conventional concrete, so that its electrical conductivity increases. Here an attempt is made to prepare conductive concrete slabs for pavements and evaluated its efficiency in de-icing [7, 8].

Research on the implementation of conductive concrete for de-icing applications has shown promising results in various studies. A notable example is the application on the Roca Spur Bridge, a 150-foot-long and 36-foot-wide highway bridge over Salt Creek in Lincoln, Nebraska, near U.S. Route 77. This bridge, the first in the world to utilize conductive concrete for de-icing, has demonstrated excellent performance over a five-year period from 2003 to 2008. It has been noted for its energy efficiency and stable electrical conductivity, effectively preventing the accumulation of ice on the bridge deck [9, 10].

Additional studies have explored the composition of conductive concrete, specifically using graphite powder and waste steel fibres to enhance its properties. For example, a mixture containing 5% graphite powder by weight of cement and 15-20% steel fibres by aggregate weight has proven to be effective in de-icing applications[11, 12]. Experimental results indicate that this mixture significantly improves the concrete's conductivity, allowing it to generate sufficient heat for de-icing purposes [7, 13] . Concrete that possesses both electrical and mechanical properties open up various applications in sectors such as the military, electronics, and civil infrastructure [14, 15]. It is particularly effective in electrical heating applications for de-icing highway bridges and airport runways, where maintaining operational surfaces free from ice is critical [16, 17]. Investigations into the effects of different conductive materials, such as steel fibres and graphite powder, have revealed that increasing the graphite content enhances the concrete's conductivity, although it may slightly reduce its structural strength[18, 19]. For example, a mixture with steel fibres at 8.5% by weight and incremental graphite powder additions ranging from 5% to 20% showed that conductivity improved with increased graphite, but this was accompanied by a decrease in strength [20, 21]. Furthermore, the electrical and thermal properties of conductive concrete have been examined with varying graphite percentages, specimen dimensions, and applied voltages[22]. It has been found that increasing the voltage reduces electrical resistivity while increasing the heat generated in the concrete [23]. Smaller specimen sizes tend to produce higher electrical currents and temperatures, indicating that the amount of graphite, the applied voltage, and the size of the specimen significantly impact the thermal and electrical performance of the concrete[24]. Optimal

electrical and thermal properties are achieved with 2% steel and 10% graphite powder in the concrete mixture [25].

The literature review has indicated that, thermal and electrical properties can be improved by making the conventional concrete into conductive concrete and it has many applications, de-icing is one among them. Electrical conductivity leads to the de-icing [26]. Roca Bridge successfully implemented the conductive concrete for de-icing. Here an attempt is made to prepare conductive concrete in the laboratory and tested for its de-icing performance [27, 28]. However, many investigations have shown the application of carbon-based fillers materials such as carbon fibre and graphite in conductive concrete materials, concentrating on improvement of electrical conductivity and mechanical properties, these investigations still leave many gaps. For example, the conductive concrete long-term durability in different environmental conditions remains un-investigated [3]. In addition, almost all studies emphasize the short-term performance rather than long-term performance of conductive concrete, such as self-healing capabilities and crack resistance [2]. Also, there are limited investigations for optimizing the equilibrium between mechanical strength and electrical properties for the field applications in road pavement, airfield pavement, bridges, roofs and structural elements [1]

2. Materials and Methods

The methodology involved in the production and evaluation of Conductive concrete is represented in flowchart as given below.

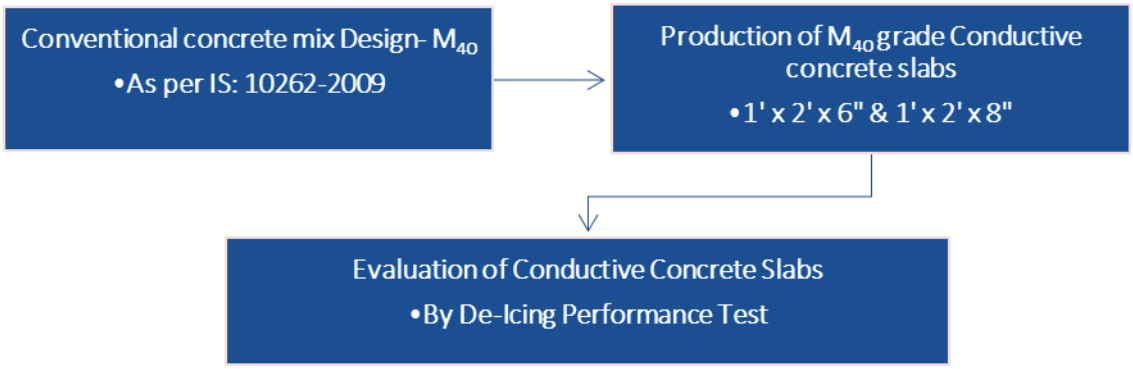

Fig. 1. Flowchart explaining methodology

2.1 Materials

The cement, fine aggregate (M sand) and coarse aggregates were used to prepare the conventional concrete. In addition to that, the carbon powder at varying percentages and constantly maintained 2% steel fiber by weight were added to the conventional concrete mix to make it as conductive concrete. Also, the reinforcement TMT steel as electrodes were inserted to the slab while casting. The materials used in this study is discussed as follows (Fig. 2.).

Fig. 2. Raw materials used

2.1.1 Cement

Cement is the binding material in cement concrete. The Ultratech OPC 43 grade cement was used as primary binder in this study. The physical tests such as Normal Consistency, Setting Time, Soundness, Compressive Strength of mortar (7, 14, 21 days) and Specific Gravity were conducted on the cement in laboratory as per guidelines mentioned in IS 4031: 1988 and results are mentioned as in the table 2.

2.1.2 Aggregates

The aggregates employed in this study were borrowed from a known local quarry in a single batch. Physical tests were conducted to know the suitability of these aggregates (Fine & Coarse aggregates) and the test results were showcased in table 3.

2.1.3 Carbon Powder

The carbon powder or carbon black is the material used as conduction filler in the cement concrete to enhance the electrical conductivity of concrete. Tiny carbon particles will increase the mobility of electrons in concrete by creating continuous electrically conductive pathways by reducing electrical resistivity. The conductive concrete used for applications like De-icing of roads, electromagnetic shielding and self-sensing concrete. It is employed as a cement-based addition in concrete mix with varying percentages by weight of cement. The percentage of carbon powder present in concrete mix will affect the electrical conductivity and mechanical properties of concrete. The carbon powder used in this study was purchased from local scientific materials and equipment dealer.

2.1.4 Steel Fiber

Steel fibers are added in electrically conductive concrete to enhance the electrical conductivity and mechanical strength. 2% steel fibers based on the weight of aggregates were added in the mix in the present study. Steel fibers enhance toughness, ductility and crack resistance of concrete and also create a continuous conductive network. These fibers have a high aspect ratio, which makes them to disperse well in the concrete matrix and providing efficient transfer of electrons. So that, the steel fibers can be used in the concrete which have the de-icing mechanism. The steel fiber material used in this study were brought from online purchase platform.

2.2 Mix Design for Conventional Concrete of M40 Grade and Conductive Concrete

The cement used for the concrete mix is OPC 43 grade, specific gravity of cement is 3.14, the coarse aggregate average specific gravity is 2.65 and of fine aggregate (M-sand) is 2.68, belongs to zone-II as per IS:383-1970(RA 2016). Super plasticizer used is FOSROC SB430 and its specific gravity is 1.145. The mix design for conventional concrete is done as IS: a 10262-2009.The mix proportion by weight in kg per m^3 is as given in table 1 below[29].

Table 1. Mix Design for Conventional Concrete (IS:10262-2009)

Cement		M-Sand		Coarse Aggregate		Water		Admixture
395 kg		724 kg		1168 kg		158.1		3.95
1	:	1.833	:	2.957	:	0.4	:	1%

The conventional concrete is made conductive concrete by adding electrically conductive materials such as steel fibers 2% by weight of aggregate and carbon powder of 8%, 10%, and 12% by weight of cement into the concrete. This makes the concrete to achieve uninterrupted 'electrical percolation' through the specimen. The flow of electrons through the composite constituents in the concrete increases the conductivity. But due to electrical resistivity of concrete, heat is gradually generated and de-icing process starts.

The mix design of electrically conductive concrete was done same as conventional concrete by following the specified IS codes. But the conductive materials like steel fibers, carbon powder and reinforcement steel as electrode were added in extra make the conventional concrete as electrically

conductive. The addition of these materials to the mix has affected the strength properties in very small amount, but achieved the target strength.

2.3 Production of Conventional and Conductive Concrete

The conventional concrete is produced by mixing the dry materials as per the proportions provided in the mix design. Then water and admixture are added, mixed thoroughly, till a homogeneous mix is obtained. Then, cubes are casted and cured for 7days, 14days and 28 days and tested for compressive strength, as per IS: 516-1959 (RA 2008). The Production of Conventional and Conductive Concrete process is shown in fig. 3.

Conductive concrete is produced by adding steel fibers and carbon powder into the conventional M40 grade concrete. The concreting materials are mixed in dry condition thoroughly, then water and super plasticizer is added and mixing is continued in the drum mixer, until a uniform, homogeneous mix is obtained. Carbon powder and steel fibers are added at the end and mixing is continued for another two minutes. Cube specimens for 8%, 10%, and 12% of carbon powder by weight of cement are prepared. Steel fibers are maintained constant at 2% by weight of aggregate. For each percentage of carbon 9 cubes were casted and tested for 7,14 and 28 days.

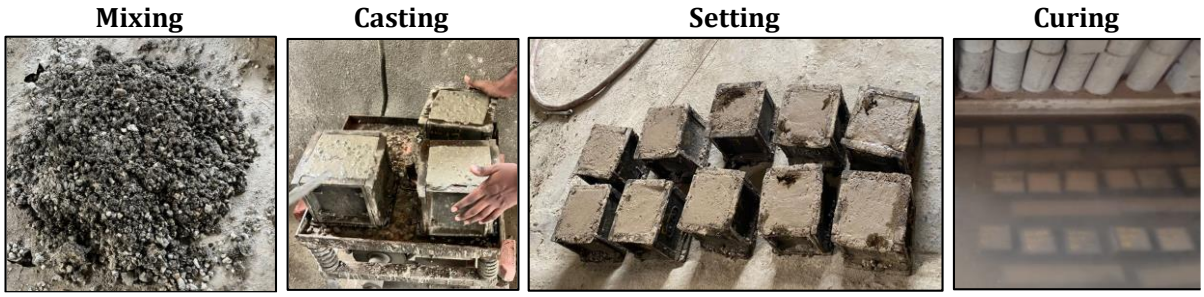

Fig. 3. Production of conventional and conductive concrete

2.4 Casting of Conductive Concrete Slabs

Conductive concrete slabs for 8%, 10% and 12% carbon powder are casted for 6inch and 8inch thickness. The size of the slab is 1feet width and 2feet length. The percentage of steel in the conductive concrete is maintained constant, as 2% by weight of total aggregate mix. The conductive concrete produced is placed in the moulds, assembled for this purpose, in three layers; each layer is vibrated for 2 minutes on the vibration table. From the top 1/3rd height 2 rods of 10mm diameter Fe-415 TMT rods are inserted from the outside of the mould as electrodes at 6inch spacing between them and 3rd layer concrete is poured and vibrated. For each percentage, 2 slabs of 6inch and 8inch thick were prepared. The total numbers of slabs are 6 numbers. These slabs are cured for 28 days by immersing the slabs in water. The process of Casting Conductive Concrete Slabs is sown in Fig. 4.

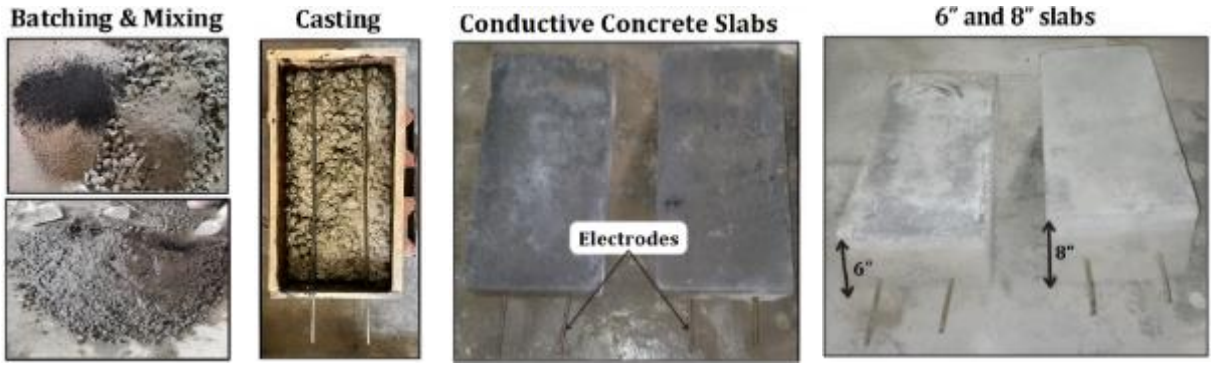

Fig. 4. Casting of conductive concrete slabs

2.5 Testing of Conductive Concrete Slabs for De-Icing Performance

After curing the slabs for 28days, are taken out and kept for surface drying in air. Then the electrodes are connected to 220v AC (Alternative Current), through auto-transformers and isolation transformers. The line diagram of electric setup of various devices is as shown in the Fig. 5.

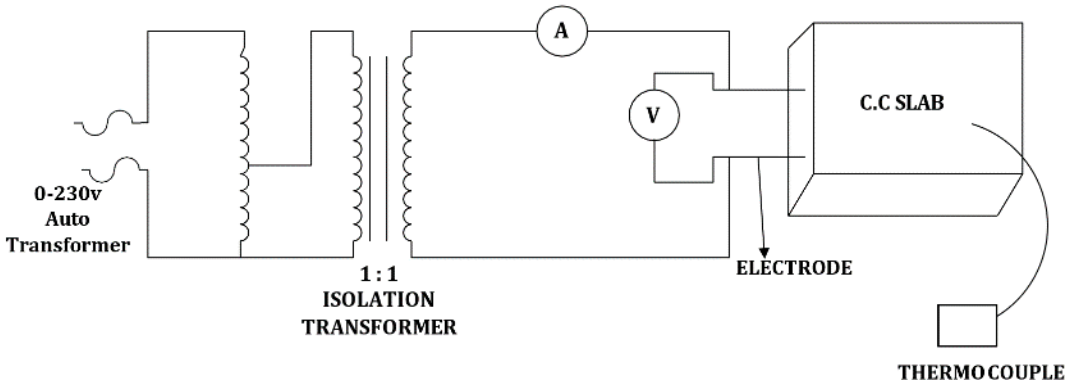

Fig. 5. Line diagram of electrical setup for conductive concrete

2.5.1 Terminology of Electric Setup

- Auto-transformer: It has a single winding on laminated core, here a winding part acts as common to both sides (primary and secondary). In loading condition, a part of current is obtained directly from supply and remaining by transformer action. This works as a voltage regulator.
- Isolation Transformer: A transformer, which will transfer the current from source to some device, by isolating that device from the source of power, for safety purpose to protect against electric shock.
- Ammeter: It is the current measuring instrument in the circuit, in amperes.
- Thermocouple: It is a sensor used to measure temperature.
- For measuring current, voltage and temperature in this study Multimeters are used.

2.6 Experimentation

2.6.1. Slump Test

The slump test was conducted on conventional and electrically conductive concrete to check the workability as per the guidelines of IS 1199 (Part 2): 2021 by slump cone method (Fig. 6). Workability of concrete in terms of Slump value is measured for both the concrete and is shown in the Table 4.

Fig. 6. Slump test

Fig. 7. Compressive strength test

2.6.2. Compressive Strength

The compression test was conducted on conventional and electrically conductive concrete to check the strength as per the guidelines of IS 516 (Part-1) 2021. The cube specimens were subjected to compression loading under compressive testing machine of frame capacity 2000kN (Fig. 7). The compressive strength of cube specimens was calculated by considering the peak load sustained by specimens and surface area of cube specimens. The results of compressive strength test are tabulated in the Table 5.

2.7 Testing for De-icing Performance:

The electrodes of the slab specimen are connected to the power source via auto-transformer & isolation transformer. To measure the current. Voltage and temperature multimeters are connected as shown in the circuit diagram. Current and voltage is measured at every 2°C increases in temperature for all the 6 conductive concrete slabs and the same is tabulated in the Table 6, 7 and 8. The Electrical test setup of conductive concrete and De-Icing process on conductive concrete is shown in Fig. 8.

Fig. 8. Electrical test setup of conductive concrete and De-Icing process on conductive concrete

3. Results and Discussions

3.1 Materials Testing

3.1.1 Tests on Cement

The laboratory test results of cement sample are satisfying the requirements of specifications mentioned in the IS Codes.

Table 2. Physical Test Results of UltraTech OPC 43 Grade Cement

List of Tests	Results	Permissible Limits	IS Code & Part
Normal Consistency (%)	30	-	IS 4031 (Part 4)
Initial Setting Time (minutes)	115	≥ 30	IS 4031 (Part 5)
Final Setting Time (minutes)	295	≤ 600	IS 4031 (Part 5)
Soundness (Le-Chatelier Expansion) (mm)	1.0	≤ 10	IS 4031 (Part 3)
Compressive Strength (MPa) – 3 Days	24.6	≥ 23	IS 4031 (Part 6)
Compressive Strength (MPa) – 7 Days	35.9	≥ 33	IS 4031 (Part 6)
Compressive Strength (MPa) – 28 Days	44.5	≥ 43	IS 4031 (Part 6)
Specific Gravity	3.14	3.10 - 3.15	IS 4031 (Part 11)

3.1.2 Tests on Aggregate

The physical test results of aggregate samples are satisfying the requirements of specifications mentioned in the IS Codes.

Table 3. Physical Test Results of Aggregates

List of Tests	Result	Permissible Limit	IS Code & Part
Fine Aggregates			
Fineness Modulus	2.60	2.2 - 2.9	IS 383:2016
Specific Gravity	2.68	2.5 - 2.9	IS 2386 (Part 3)
Water Absorption (%)	1.50	< 2.0%	IS 2386 (Part 3)
Coarse Aggregates			
Specific Gravity	2.65	2.5 - 2.9	IS 2386 (Part 3)
Aggregate Impact Value (%)	22%	< 30%	IS 2386 (Part 4)
Crushing Value (%)	26%	< 30%	IS 2386 (Part 4)
Water Absorption (%)	1.00	< 2.0%	IS 2386 (Part 3)

3.2 Slump Test on Fresh Concrete

Values of slump test in Table 4 indicate that, the workability decreased progressively with increase in the percentage of carbon powder in M_{40} grade concrete. The plain mix of concrete possessed the maximum value of 72mm slump which indicates good workability. However, on increasing the percentage of carbon powder, the slump values dropped to 68 mm, 62 mm, and 54 mm for 8% carbon powder, 10% carbon powder and 12% carbon powder respectively. This is because, the high surface area and fine particle size of carbon powder will increase the water requirement which was resulted in a reduction in amount of water in the mix.

Table 4. Slump Values of Different Concrete Mixes of M40 Grade

Sl. No.	Type of mix	Slump (mm)
1.	Conventional Concrete	72
2.	Concrete with 8% carbon powder	68
3.	Concrete with 10% carbon powder	62
4.	Concrete with 12% carbon powder	54

3.3 Compression Strength on Hardened Concrete

The strength values in Table 5 indicate a decreasing strength gradually with an increase of the carbon powder content in the concrete mix. The normal concrete mix achieved highest strength of 46.8 MPa at 28-day. Whereas 8%, 10% and 12% carbon powder mixes had slightly lower strengths of 44.1 MPa, 42.8 MPa, and 41.1 MPa respectively.

Table 5. Compressive Strength of Different Concrete Mixes of M40 Grade At Different Curing Periods

Sl. No.	Type of mix	7 Days Strength (MPa)	14 Days Strength (MPa)	28 Days Strength (MPa)
1	Conventional Concrete	29.5	38.6	46.8
2	Concrete with 8% carbon powder	28.2	36.8	44.1
3	Concrete with 10% carbon powder	27.3	34.2	42.8
4	Concrete with 12% carbon powder	25.9	32.7	41.1

The trends are same at 7 and 14 days showing that higher carbon powder content decreases the strength development. This is due to higher voids and lower cement hydration, as carbon powder may interfere with the efficiency of binding. The strength values, however, are within acceptable limits, and carbon powder is a good additive for conductive concrete application.

3.4 De-icing Performance Test

The relationship between the temperature and applied voltage, for different thickness of slabs with varying carbon powder is studied. Voltage is varied by using the regulator in the Autotransformer. As voltage is increased temperature go on increases. Voltage increase is limited to 230V only. For the observed value of temperature, current and voltage is noted. The power consumed can be obtained by taking the product of current and voltage. Current and voltage is measured at every 2°C increases in temperature for all the 6 conductive concrete slabs and the same is tabulated in the Table 6, 7 & 8 and the variation of temperature with respect to carbon powder percentage and voltage were graphically represented in the fig. 9 & 10.

Table 6. Temperature Variation in Conductive Concrete Slabs of 8% Carbon Powder for 6" and 8" Thickness

6 Inch Thickness Slab				8 Inch Thickness Slab			
Sl. No.	Voltage(V)	Current (Amperes)	Temp. (°C)	Sl. No.	Voltage(V)	Current (Amperes)	Temp.(°C)
1.	200	1.70	34	1.	204	1.72	34
2.	208	1.76	36	2.	212	1.79	36
3.	212	2.10	38	3.	216	2.20	39
4.	220	2.20	44	4.	220	2.34	45
5.	228	2.40	52	5.	230	2.46	53

Table 7. Temperature Variation in Conductive Concrete Slabs of 10% Carbon Powder for 6" and 8" Thickness

6 Inch Thickness Slab				8 Inch Thickness Slab			
Sl. No.	Voltage (V)	Current (Amperes)	Temp.(°C)	Sl. No.	Voltage(V)	Current (Amperes)	Temp. (°C)
1.	180	1.58	34	1.	182	1.59	34
2.	190	1.65	36	2.	193	1.63	36
3.	205	2.72	38	3.	208	2.70	38
4.	220	2.21	44	4.	222	2.24	45
5.	225	2.42	52	5.	225	2.44	54
6.	230	2.48	58	6.	230	2.50	58

Table 8. Temperature Variation In Conductive Concrete Slabs of 12% Carbon Powder For 6" and 8" Thickness

6 Inch Thickness Slab				8 Inch Thickness Slab			
Sl. No.	Voltage(V)	Current (Amperes)	Temp.(°C)	Sl. No.	Voltage(V)	Current (Amperes)	Temp.(°C)
1.	162	1.42	36	1.	163	1.41	36
2.	170	1.48	38	2.	172	1.46	38
3.	178	1.60	42	3.	180	1.60	42
4.	200	1.70	52	4.	202	1.72	52
5.	210	2.10	58	5.	210	2.12	58
6.	218	2.24	62	6.	218	2.25	62
7.	225	2.41	68	7.	225	2.42	68
8.	230	2.51	73	8.	230	2.54	76

The result of the de-icing performance test shows a direct correlation between applied voltage and temperature rise in conductive concrete slabs. As more carbon powder is added, the slabs conduct electricity more efficiently, giving a greater rise in temperature at lower voltages. The 6-inch and 8-inch slabs with 12% carbon powder gave the best results, with high temperatures of 73°C and 76°C, respectively, at 230V. To compare, the maximum temperatures of slabs with 10% and 8% carbon powder were lower, meaning more carbon makes them heat better. The thicker slabs use a

greater current, which holds heat better. The results show that carbon powder greatly increases the self-heating ability of concrete, which can be very beneficial for de-icing in cold climates.

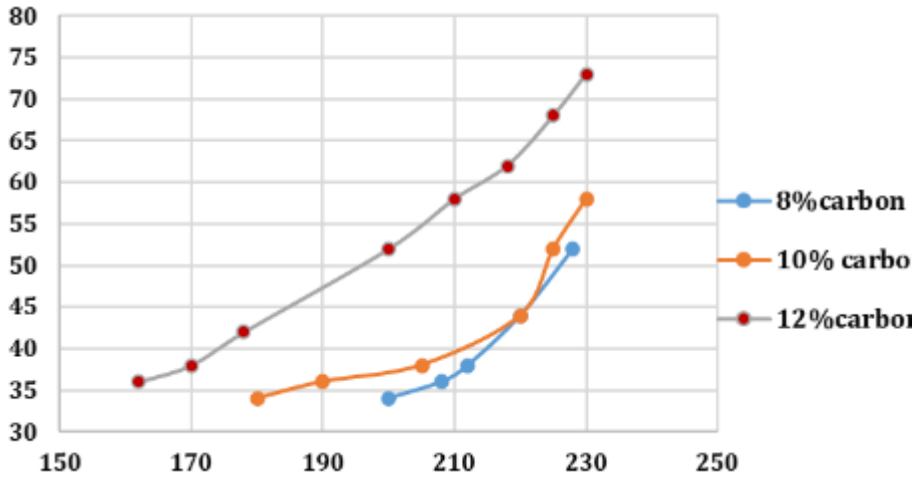

Fig. 9. Voltage v/s Temperature at 6-inch slab

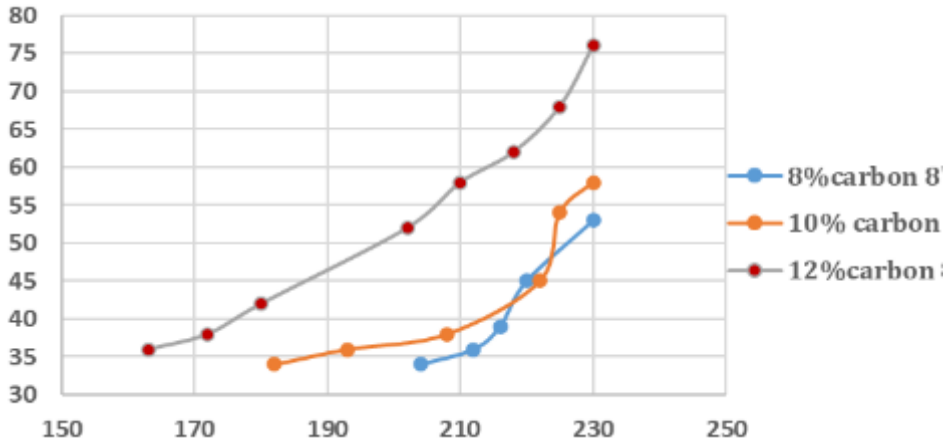

Fig.10. Voltage v/s Temperature at 8-inch slab

4. Conclusions

This study mainly concentrated on the development of electrically conductive concrete by adding carbon powder and steel fibre as conductive materials to the mix and evaluation of the same. Different trial concrete mixes were prepared and subjected to testing for evaluating workability, mechanical performance and thermal response under applied voltage. The aim was to investigate the feasibility of conductive concrete as a pavement concrete for de-icing applications when exposed to extreme cold conditions. The laboratory experimental results illustrated the effect of carbon content on workability, strength and heat generation. Thus, helping in optimizing the proper mix design for functional and structural performance.

Based on the studies, the following conclusions were made.

- A conventional concrete can be utilized as conductive concrete with the addition of commonly easily available conductive materials.
- The average strength of conventional concrete achieved at the end of 28days of curing, is nearest to the mean target strength (mean target strength is 48.5 MPa).
- The workability of concrete mix (slump value) decreases with increase in carbon powder.

- From Table-3, it is evident that compressive strength decreases with increase in carbon powder. The studies limited to 12% carbon content because any further addition reduces the strength below 40 MPa, which is normally does not recommend for highway pavements.
- An ordinary TMT bars can be used as effective electrodes.
- Table-4 to 6 shows that as applied voltage increases, temperature increases. It has been evident from the present study, that thickness of the conductive concrete slabs has little or almost nil effect on thermal property of concrete.
- This study confirms that de-icing processes is very much effective in conductive concrete, which may avoid manual clearing of ice or usage of chemicals.

4.1 Recommendations

Conductive concrete with 12% carbon powder is recommended due to its heat generation efficiency and superior electrical conductivity at lower voltages for effective de-icing applications. Increase in carbon content increases heating performance which will makes it ideal for cold regions where rapid snow and ice removal is required. The optimum slab thickness should be selected based on heating requirements and energy efficiency.

4.2 Scope for Further Work

Conductive concrete may be produced using different conductive materials for other grades of concrete. Effectiveness of electrode may be ascertained with different materials.

Acknowledgement

The authors would like to express their gratitude to all those who contributed to the completion of this research. Special thanks to Dr. L Sanjeev Kumar, HOD, EEE department for their support in setting up of electrical circuit.

References

[1] Sassani A, Arabzadeh A, Ceylan H, Kim S, Sadati S, Gopalakrishnan K, et al. Carbon fiber-based electrically conductive concrete for salt-free deicing of pavements. J Clean Prod. 2018;203:799-809. https://doi.org/10.1016/j.jclepro.2018.08.315

[2] Ernie H, Adam O, Panneer S, Mark K. Developing Anti-Icing Airfield Runways Using Conductive Concrete with Renewable Energy. J Cold Reg Eng. 2014;28(2):04014001. https://doi.org/10.1061/(ASCE)CR.1943-5495.0000064

[3] Ji X, Ge Y, Li M, Wang L, Liu S. Preparation of carbon fiber conductive concrete and study on its mechanical and heating properties. J Mater Res Technol. 2023;27:3029-40. https://doi.org/10.1016/j.jmrt.2023.10.118

[4] Chavan AD, Rattan VK, Patil YS. Improving early strength and durability of eco-friendly mortars: Investigating the influence of limestone filler fineness and blast furnace slag combination. Res Eng Struct Mater. 2024. https://doi.org/10.17515/resm2024.232st0404rs

[5] EL-Afandi M, Yehia S, Landolsi T, Qaddoumi N, Elchalakani M. Self-Consolidated Concrete-to-Conductive Concrete Interface: Assessment of Bond Strength and Mechanical Properties. Fibers. 2023;11(12). https://doi.org/10.3390/fib11120106

[6] Benaddi H, Rebai B, Messas T, Salhi M. Evaluation of self-compacting concrete for concrete repair applications. Res Eng Struct Mater. 2024. https://doi.org/10.17515/resm2024.255st0423rs

[7] Anis M, Abdel-Raheem M. A Review of Electrically Conductive Cement Concrete Pavement for Sustainable Snow-Removal and Deicing: Road Safety in Cold Regions. Transp Res Rec. 2024. https://doi.org/10.1177/03611981231225210

[8] Maleki P, Iranpour B, Shafabakhsh G. Investigation of de-icing of roads with conductive concrete pavement containing carbon fibre-reinforced polymer (CFRP). Int J Pavement Eng. 2019;20:682-90. https://doi.org/10.1080/10298436.2017.1326235

[9] Ren Z, Peng Y, Chen X, Zeng H, Zeng X, Kontoleon K. Research on Electrical Conductivity and Mechanical Properties of Ecological Concrete Prepared from Mine Solid Waste. Adv Civ Eng. 2023;2023. https://doi.org/10.1155/2023/6299237

[10] del Moral B, Ureña A, Sánchez-Rodríguez D, Muñoz M, Nieto JE. Temperature and humidity influence on the strain sensing performance of hybrid carbon nanotubes and graphite cement composites. Constr Build Mater. 2021;284:122786. https://doi.org/10.1016/j.conbuildmat.2021.122786

[11] Li C, Ge H, Sun D, Zhou X. Novel conductive wearing course using a graphite, carbon fiber, and epoxy resin mixture for active de-icing of asphalt concrete pavement. Mater Struct. 2021;54(1):48. https://doi.org/10.1617/s11527-021-01628-7
[12] Bakbolat B, Abduzhanov A, Tuleubekov A, Mukanova A, Kuterbekov K, Ibragimov R, et al. Effectiveness of Bio-Waste-Derived Carbon Doping on De-Icing Performance of an Electrically Resistant Concrete. Coatings. 2022;12(11). https://doi.org/10.3390/coatings12111629
[13] Wang X, Wu Y, Zhu P, Ning T. Snow melting performance of graphene composite conductive concrete in severe cold environment. Materials (Basel). 2021;14(21). https://doi.org/10.3390/ma14216715
[14] Bellatrache Y, Ziyani L, Dony A, Taki M, Haddadi S. Effects of the addition of date palm fibers on the physical, rheological and thermal properties of bitumen. Constr Build Mater. 2020;239:117808. https://doi.org/10.1016/j.conbuildmat.2019.117808
[15] Pereira I, Miranda T, Pereira E. Electrically conductive cementitious composites for marine applications. J Sustain Cem Based Mater. 2024;13(6):899-917. https://doi.org/10.1080/21650373.2024.2338529
[16] Farcas C, Bistrian DA, Dumitru C, Ciuca I, Utu D, Utu I, et al. Heating and de-icing function in conductive concrete and cement paste with the hybrid addition of carbon nanotubes and graphite products. Smart Mater Struct. 2021;30(4):045002. https://doi.org/10.1088/1361-665X/abe032
[17] Wang Y, Zhao W, Tan L, Li Y, Qin L, Li S. Review of Polymer-Based Composites for Electromagnetic Shielding Application. Molecules. 2023;28(15). https://doi.org/10.3390/molecules28155628
[18] Galao O, Bañón L, Baeza FJ, Carmona J, Garcés P. Highly conductive carbon fiber reinforced concrete for icing prevention and curing. Materials (Basel). 2016;9(4). https://doi.org/10.3390/ma9040281
[19] Venkatraman K, Tamizharasan V. Electrically Conductive Concrete. Int J Innov Res Sci Eng Technol. 2007;3297.
[20] Farcas C, Bistrian DA, Dumitru C, Ciuca I, Utu D, Utu I, et al. Heating and de-icing function in conductive concrete and cement paste with the hybrid addition of carbon nanotubes and graphite products. Smart Mater Struct. 2021;30(4):045002. https://doi.org/10.1088/1361-665X/abe032
[21] Lu D, Leng Z, Lu G, Wang D, Huo Y. A critical review of carbon materials engineered electrically conductive cement concrete and its potential applications. Int J Pavement Eng. 2023. https://doi.org/10.1080/19475411.2023.2199703
[22] Li M, Zhong J, Li G, Zhang Q, Cen F, Gao P. Study on the Performance of Polymer-Modified Conductive Cement-Based Materials. Buildings. 2023;13(12). https://doi.org/10.3390/buildings13122961
[23] Wu T, Huang R, Chi M, Weng T. A study on electrical and thermal properties of conductive concrete. Comput Concr. 2013;12(3):337-49. https://doi.org/10.12989/cac.2013.12.3.337
[24] Savytskyi M, Sukhyy K, Savytskyi O, Babenko M, Shevchenko T. Carbon materials for electrically conductive concrete. In: E3S Web Conf. EDP Sciences; 2024. https://doi.org/10.1051/e3sconf/202453401019
[25] Tian X, Hu H. Test and Study on Electrical Property of Conductive Concrete. Procedia Earth Planet Sci. 2012;5:83-7. https://doi.org/10.1016/j.proeps.2012.01.014
[26] Chung DDL. Electrically conductive cement-based materials. Adv Cem Res. 2004;16(4):167-76. https://doi.org/10.1680/adcr.2004.16.4.167
[27] Tuan C. Implementation of Conductive Concrete for Deicing (Roca Bridge). Aug. 2008.
[28] Dehghanpour H, Yılmaz K. Heat Behavior of Electrically Conductive Concretes with and without Rebar Reinforcement. Mater Sci. 2020;26:471-6. https://doi.org/10.5755/j01.ms.26.4.23053
[29] Bureau of Indian Standards. IS 10262 (2009): Guidelines for concrete mix design proportioning.

Research on Engineering Structures & Materials
www.jresm.org
MIM Research Group

Research Article

Thermal and mechanical optimization of polyester-based leveling mortars using crushed dune sand

Boudjemaa Mebarki [*,a], Ahmed Tafraoui [b], Abdelkadir Makani [c]

Department of Civil Engineering and Hydraulic, TAHRI Mohamed University, EMIA ex LFGM (Laboratory of Eco-Materials: Innovations & Applications), P.O. Box 417 Bechar (08000), Algeria

Article Info

Article History:

Received 21 Apr 2025

Accepted 29 May 2025

Keywords:

Crushed dune sand;
Thermal post-curing;
Mechanical testing;
Polymer composites

Abstract

The construction industry in arid regions faces challenges in utilizing locally available dune sand due to its poor gradation and low interparticle friction. This study addresses these limitations by developing a novel leveling mortar composed of thixotropic polyester resin, methyl ethyl ketone peroxide (MEKP) hardener, and crushed dune sand from Taghit, Algeria. The research investigates the synergistic effects of mechanical sand crushing and thermal post-curing (170°C) on the composite's mechanical, thermal, and microstructural properties. Scanning electron microscopy (SEM) and energy-dispersive X-ray spectroscopy (EDS) revealed that crushing transformed rounded dune sand grains into angular particles, enhances surface roughness and interfacial bonding with the resin matrix. Thermal treatment further densified the microstructure, promoting resin cross-linking and reducing organic content, as evidenced by elemental analysis. Mechanical testing demonstrated significant improvements: thermally treated mortars achieved compressive strengths of 116.45–119.9 MPa and flexural strengths of 38.75–45.25 MPa, representing a 10–12% and 89–98% increase over untreated counterparts, respectively. Differential scanning calorimetry (DSC) and thermogravimetric analysis (TGA) confirmed the composite's thermal stability up to 410°C, with decomposition pathways dominated by resin pyrolysis. The findings highlight the valorization of dune sand as a sustainable alternative to conventional aggregates, reducing environmental impact and transportation costs. This work advances the understanding of resin-filler interactions in polymer composites, offering a scalable solution for high-performance, eco-friendly construction materials in resource-constrained arid regions.

1. Introduction

The construction industry continually seeks innovative materials that combine durability, cost-effectiveness, and environmental sustainability [1]. Among these materials, polymer-based composites—including leveling mortars—have garnered significant attention due to their adaptability, mechanical resilience, and potential to incorporate locally sourced aggregates [2,3]. Leveling mortar is a specialized construction material used to create smooth, flat surfaces on floors, walls, or substrates before applying final finishes such as tiles, epoxy coatings, or pavers. Unlike traditional cement-based mortars, polymer-modified leveling mortars offer superior workability, faster curing times, and enhanced bonding strength, making them ideal for both structural and non-structural applications in modern construction.

In arid regions, dune sand represents an abundant yet underutilized resource, often dismissed in traditional construction due to its fine granulometry and rounded particle morphology [4,5]. However, recent advancements in composite technology have demonstrated that such sands can

*Corresponding author: mebarki.boudjemaa@univ-bechar.dz
[a]orcid.org/0009-0006-3973-2526; [b]orcid.org/0000-0002-0278-935X; [c]orcid.org/0000-0002-4027-9929;
DOI: http://dx.doi.org/10.17515/resm2025-834me0421rs

be transformed into viable building materials when combined with polymeric binders, offering a sustainable alternative to conventional aggregates [6-8]. This study explores the development and characterization of a novel thixotropic polyester resin-based leveling mortar composed of methyl ethyl ketone peroxide (MEKP) hardener and crushed dune sand sourced from Taghit, Algeria. By integrating mechanical, thermal, and microstructural analyses, this research elucidates how material processing—particularly crushing and thermal treatment—enhances the performance of dune sand-based composites, paving the way for their broader application in construction.

The utilization of dune sand in construction has historically been limited by its poor gradation and low interparticle friction, which hinder compaction and mechanical stability [9-11]. Unlike river or crushed sands, dune sand grains are shaped by prolonged aeolian transport [12,13], resulting in smooth, spherical particles that reduce interlocking and adhesion in cementitious matrices. However, mechanical crushing has emerged as a promising method to modify sand morphology, creating angular particles with enhanced surface roughness and specific surface area [14,15]. These attributes improve particle-matrix bonding in composites, a critical factor for load-bearing applications. Recent studies have shown that crushed dune sand, when combined with organic binders like polyester resins, can yield mortars with superior mechanical properties compared to untreated counterparts [16]. This approach not only valorizes a readily available natural resource but also reduces reliance on energy-intensive conventional aggregates [17,18].

Thixotropic polyester resins, a class of unsaturated polymers, are particularly suited for composite formulations due to their unique rheological behavior [19]. Under shear stress, their viscosity decreases, enabling easy mixing and application, while stability at rest prevents sagging or segregation [20]. When catalyzed by MEKP hardeners, these resins undergo rapid polymerization, forming a rigid matrix that encapsulates filler materials. The chemical structure of polyester resins—comprising polyhydric alcohols and dibasic acids—facilitates cross-linking, which enhances mechanical strength and thermal resistance [21]. However, the interfacial compatibility between resin and filler remains a critical challenge, as weak bonding can lead to premature failure under stress. To address this, researchers have investigated post-curing treatments, such as thermal exposure, to further densify the matrix and strengthen the resin-filler interface. Such treatments promote additional cross-linking and microstructural refinement, which are pivotal for optimizing composite performance [22-24].

In this study, the synergistic effects of crushed dune sand and thermal post-curing on the properties of polyester-based leveling mortar are systematically investigated. The crushed sand, characterized by its angular morphology and high silica content (>95%), serves as both a filler and reinforcement agent [25]. Its interaction with the resin matrix is analyzed through scanning electron microscopy (SEM) and energy-dispersive X-ray spectroscopy (EDS), which reveal morphological and chemical changes induced by mechanical processing and heat treatment [26]. Differential scanning calorimetry (DSC), differential thermal analysis (DTA), and thermogravimetric analysis (TGA) provide insights into the thermal stability and decomposition pathways of the composite [27,28], while mechanical testing quantifies improvements in compressive and flexural strength [29].

The motivation for this work stems from two key gaps in existing literature. First, while several studies have explored the use of dune sand in concrete, limited attention has been paid to its application in polymer-based mortars, particularly those subjected to thermal modification. Second, the interfacial mechanisms between crushed sand and polyester resins remain poorly understood, especially in the context of post-curing treatments. By addressing these gaps, this research contributes to the development of high-performance, sustainable construction materials tailored for arid environments.

The findings of this study hold significant practical implications. For instance, the enhanced mechanical properties of heat-treated leveling mortars could expand their use in load-bearing structures, flooring systems, or repair applications where traditional materials falter. Additionally, the use of locally sourced dune sand reduces transportation costs and environmental impact, aligning with global trends toward circular economy practices. From a scientific perspective, this

work advances the understanding of resin-filler interactions in composites, offering a framework for optimizing material formulations through controlled processing techniques.

2. Materials and Methods

2.1. Materials

The materials used in this study include thixotropic polyester resin, Butanox M50 resin hardener and dune sand sourced from Taghit (Algeria), which is well classified with indice of classification lower than 2.5 [10]. Thixotropic polyester resin is a type of unsaturated polyester resin with a viscosity that decreases under shear stress, making it easy to mix and apply while maintaining stability at rest [19]. It is commonly formulated from polyhydric alcohols and dibasic organic acids, with the general chemical formula $(C_2H_4O)n(C_8H_6O_4)m$. The Butanox M50 hardener is a methyl ethyl ketone peroxide (MEKP), which serves as a catalyst in the polymerization process of polyester resins [30,31]. Its chemical formula is $C_8H_{18}O_6$, and it ensures proper curing and hardening of the resin matrix. The crushed dune sand primarily consists of silicon dioxide (SiO_2) and is used as a filler material to improve the mechanical properties of the leveling mortar, offering strength and durability.

Particle Size Distribution (PSD) curve of crushed dune sand in The Fig. 1 shows a well-graded material with a mix of fine, medium, and coarse particles, ensuring good compaction and stability. The curve follows a smooth progression from 0% to 100% cumulative passing, indicating a broad range of particle sizes suitable for polymer- leveling mortar s. From a chemical perspective Table 1, it is important to note that this sand has a remarkably high silica content, consisting of fine quartz grains. Its silica concentration exceeds 95%, classifying it as siliceous sand [10,11].

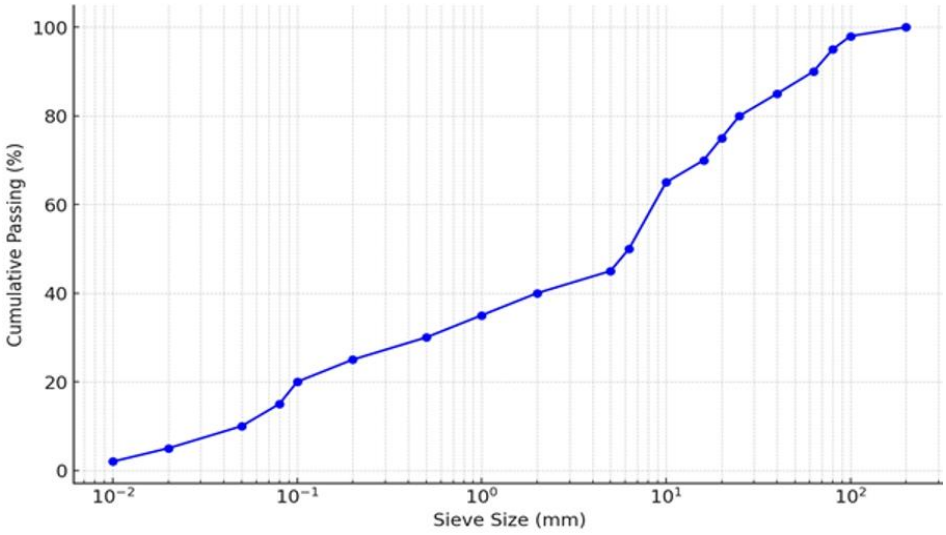

Fig. 1. Particle size distribution curve of Crushed dune sand

Table 1. Crushed dune sand chemical compositions

Composition (%)	SiO2	Al2O3	Fe2O3	CaO	MgO	SO3	Na2O	K2O	Other	LOI
Crushed dune sand	97.15	0.79	0.21	0.11	0.05	0.14	0.18	0.02	< 0.02	0.58

The preparation of the leveling mortar mixture follows a well-defined and systematic procedure. Initially, polyester resin is added to the crushed dune sand and mixed thoroughly to ensure a homogeneous distribution of the resin throughout the granular matrix. Following this, the hardening agent Butanox M50 is carefully introduced into the blend, initiating the polymerization reaction. The curing time of the mixture typically ranges between 40 to 80 seconds, depending on the quantity and proportions of the individual components used in the formulation. Once the

mixture reaches the appropriate consistency, it is poured into predefined molds for shaping. To ensure uniform compaction and to eliminate entrapped air that could compromise the structural integrity, the molds are subjected to a controlled vibration process.

After molding, the samples are left to cure under ambient controlled conditions, allowing for complete polymerization of the resin matrix. In our research, a series of samples also underwent thermal post-treatment to investigate their behavior under elevated temperatures. Specifically, the leveling mortar was gradually heated to 90°C over a period of 20 minutes, then further elevated to 170°C within 50 minutes. This peak temperature was maintained for a specified duration to allow for thermal interaction within the material. Following this, the specimens were cooled in a controlled manner, returning to room temperature over the course of 170 minutes. This thermal treatment protocol enabled us to closely examine the physical and chemical transformations occurring within the mortar, especially with regard to dehydration processes, improvements in thermal stability, and enhancements in mechanical performance following exposure to heat. As shown in Fig. 2, the heat-treated samples demonstrated noticeable changes that provide valuable insights into the mortar's structural behavior under thermal stress.

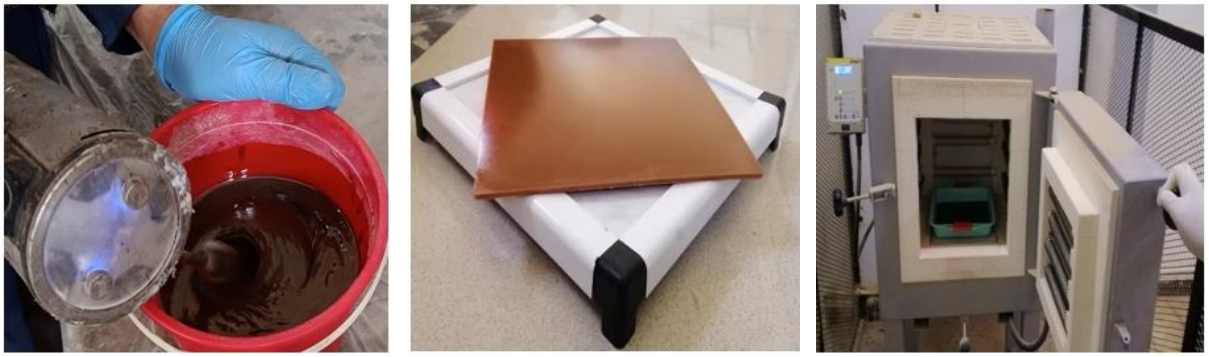

(a) (b) (c)

Fig. 2. Preparation of samples (a) Leveling mortar preparation, (b) leveling mortar, (c) Heat the leveling mortar

Through the Table 2, The mortar mix comprises 55-65% crushed dune sand (primary filler), 30-40% polyester resin (binding agent), and a small 0.15-0.25% hardener (curing agent) by weight. Sand dominates the mix, followed by resin, with hardener used minimally.

Table 2. Composition ranges of mortar constituents by weight

Mortar constituents	Range (% by weight)
Thixotropic polyester resin	30-40
Crushed dune sand	55-65
Hardener	0.15-0.25

2.2. Methods

In our study, we conducted a series of experimental analyses to evaluate the thermal behavior, microstructure, and stability of different composite materials composed of polyester resin and sand derivatives. Our experiments focused on four sample types: dune sand (DS), crushed dune sand (CDS), leveling mortar (M), and heat-treated leveling mortar (TM), as depicted in Fig. 3.

To assess thermal properties, we employed Differential Scanning Calorimetry (DSC), Differential Thermal Analysis (DTA), and Thermogravimetric Analysis (TGA) using a TA Instruments Q600. We carried out the tests under an inert nitrogen (N_2) atmosphere with a controlled heating rate of 20°C/min, spanning a broad temperature range from 40.91°C to 1190.41°C. Prior to testing, all samples were oven-dried at 105°C for 24 hours to remove moisture, and their granulometry was analyzed to ensure a particle size below 100 μm.

Additionally, we used a Scanning Electron Microscope (SEM) to observe the morphological and microstructural changes in the samples before and after crushing and thermal treatment. We also used Energy Dispersive X-ray Spectroscopy (EDS) coupled with SEM to determine the elemental compositions of the samples, tracking how heat exposure influenced the chemical makeup, particularly the degradation of organic resin and the increased visibility of mineral phases. We studied both untreated and thermally treated leveling mortar s to compare mechanical strength and thermal stability, emphasizing the role of heat in polymer cross-linking and microstructural reinforcement.

(a) (b) (c) (d)

Fig. 3. Samples (a) dune sand, (b) crushed dune sand, (c) leveling mortar and (d) treated leveling mortar

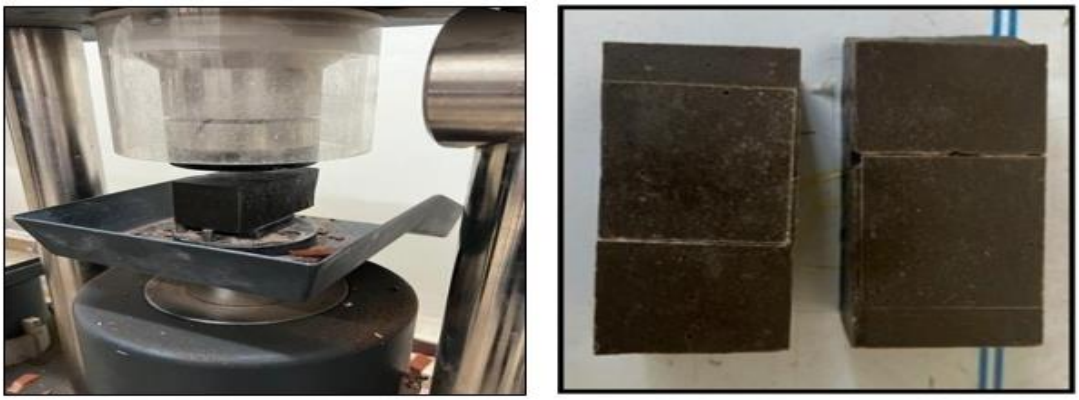

(a)

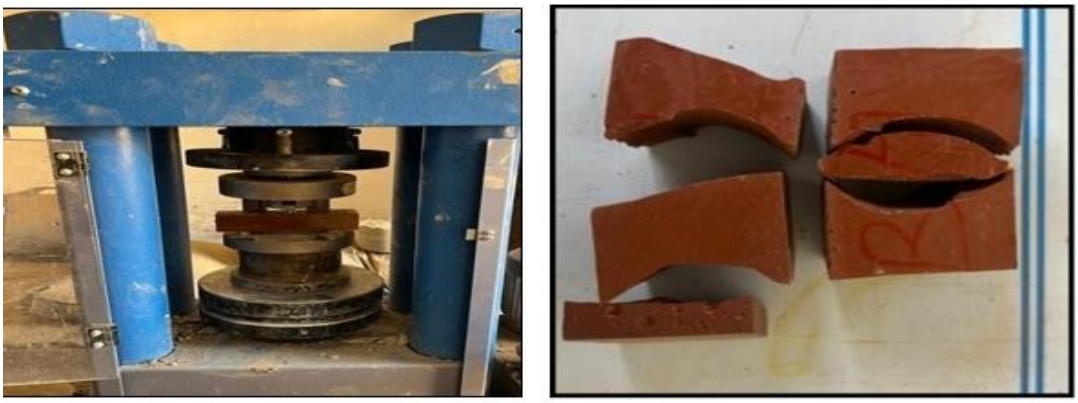

(b)

Fig. 3. Mechanical test (a) compression and (b) flexural of leveling mortars

The compression tests were performed in accordance with the NF EN 772-1 standard. Test specimens had prismatic dimensions of 40 × 40 × 160 mm^3, which is a typical size for mortar

testing. The tests were carried out on a hydraulic press with a maximum load capacity of 300 kN, ensuring a controlled and uniform application of axial load until specimen failure. The loading rate was set to a constant and slow displacement speed of 0.5 N/s applied via the upper platen. Regarding flexural strength, we used the three-point bending test method, according to NF EN 12390-5 standard. The same 40 × 40 × 160 mm^3 specimens were used, with the support span fixed at 100 mm. The loading rate was precisely set to 0.05 kN/s, a relatively slow rate that minimizes vibrations or impact loads that could distort the mechanical response. These tests were conducted using a PILOT COMPACT-Line testing machine.

In this study, we selected the number of samples for each type of analysis to ensure both reliability and reproducibility of the results. For the mechanical testing, I prepared a total of twelve prismatic specimens (40 × 40 × 160 mm^3), divided equally between untreated and heat-treated mortars—three specimens for flexural testing and three for compressive strength per mortar type, respectively. Regarding the thermal analyses, including Differential Scanning Calorimetry (DSC), Differential Thermal Analysis (DTA), and Thermogravimetric Analysis (TGA), I used four distinct sample types: natural dune sand (DS), crushed dune sand (CDS), untreated mortar (M), and heat-treated mortar (TM). For each thermal technique, I tested one sample per material type, amounting to twelve thermal samples in total (4 materials × 3 techniques). Finally, for the microstructural analysis, I performed Scanning Electron Microscopy (SEM) and Energy Dispersive X-ray Spectroscopy (EDS) on four representative samples—DS, CDS, M, and TM—using one specimen per type to capture the morphological and compositional differences introduced by crushing and thermal treatment. Although the sample size (n = 3 per condition) is limited, it aligns with standard preliminary mechanical testing practices for mortar formulations. This study aims to establish foundational insights; future work will include larger sample sets to strengthen statistical power.

3. Results and Discussion

3.1. SEM-EDS Analysis

The dune sand (DS) exhibits a well-rounded and smooth morphology, characteristic of prolonged aeolian transport and weathering processes. These rounded grains provide high fluidity and lower interparticle friction, which influences their behavior in construction applications. However, after the mechanical crushing process, the resulting Crushed Dune Sand (CDS) undergoes significant morphological transformations. The SEM images in Fig. 4 reveal that the grains become angular, fractured, and highly irregular in shape. The smooth surfaces of the natural dune sand are replaced by sharp edges and increased surface roughness, which significantly enhances the specific surface area of the particles.

This change in microstructure directly impacts the physical properties of the sand. The increased angularity leads to better interlocking between particles, which improves the mechanical performance of leveling mortar and concrete formulations. Additionally, the fractured nature of the grains enhances their adhesion capacity when mixed with binding agents such as cement or resin. However, the rough and jagged texture also means that crushed dune sand may require a higher water or binder content in composite materials to maintain workability. This increase in specific surface area can be advantageous in applications requiring enhanced cohesion and compactness in leveling mortar s and concretes. As seen in Fig. 4, the treated leveling mortar surface shows evidence of a reconfigured matrix, where the initially discrete sand-resin interfaces in the uncured leveling mortar (M) evolve into a more complex, interlocking morphology. While some microcracks and fractures are indeed visible, their distribution appears controlled and may reflect a densification process rather than simple structural failure.

The observed microstructural changes can be interpreted as thermal post-curing effects, where elevated temperatures induce further cross-linking within the polymeric resin matrix. This post-curing process leads to increased stiffness and a more rigid bond at the resin–sand interface. Instead of acting purely as a point of mechanical weakness, the interface transitions into a zone of constrained deformation, which may enhance stress transfer between components and improve the composite's load-bearing capabilities. Additionally, the roughened and more textured surfaces of the sand grains in TM, compared to the smoother matrix in M, suggest enhanced mechanical

interlocking. Such morphological features can strengthen particle–matrix adhesion, especially under compressive and shear loads, contributing positively to the overall performance of the leveling mortar. Moreover, the apparent presence of thermally fused resin domains in TM implies a partial redistribution of the binder material, which could fill previously undetected micro voids or reinforce interparticle bridges.

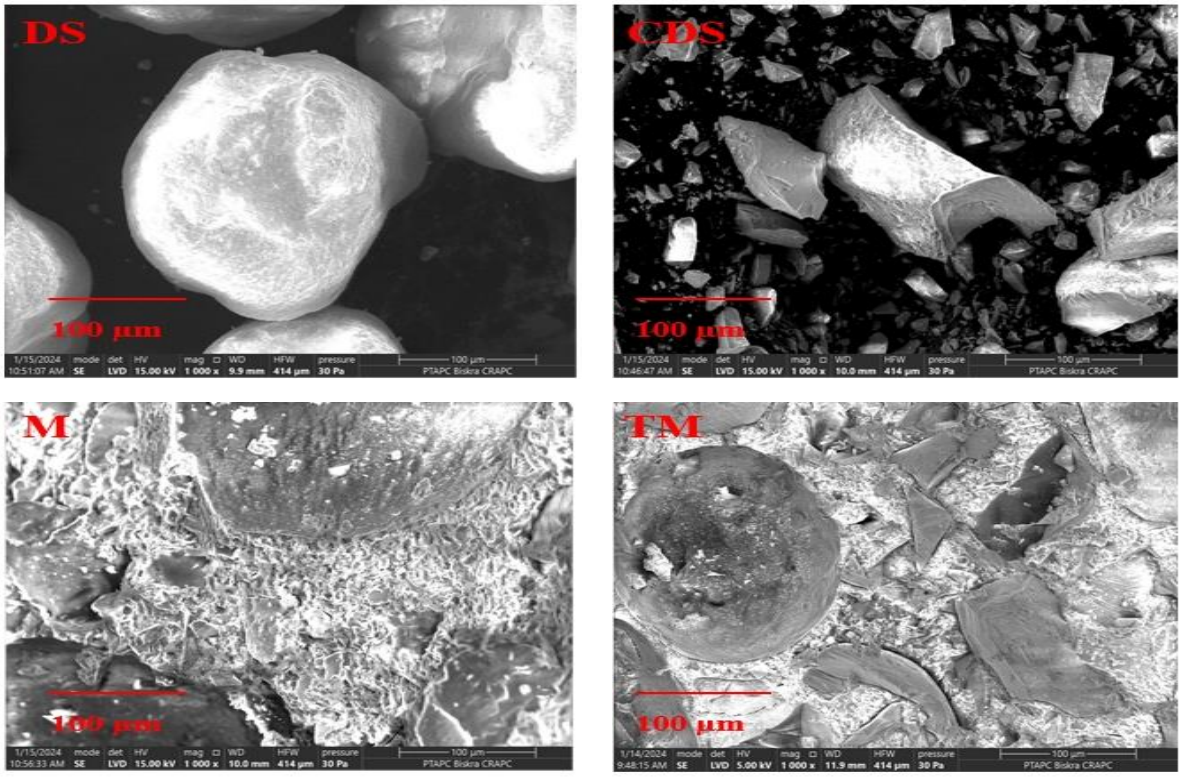

Fig. 4. SEM micrographs of dune sand (DS), Crushed Dune Sand (CDS), leveling mortar (M), treated leveling mortar (TM)

The Energy Dispersive X-ray Spectroscopy (EDS) analysis presented in Fig. 5 offers a detailed comparison between dune sand (DS) and mechanically processed crushed dune sand (CDS), providing insight into how morphological and chemical changes impact material behavior especially when cross-referenced with Scanning Electron Microscopy (SEM) observations from Fig. 4 and the associated analysis in section 3.1.For dune sand (DS) (Fig. 5a), the EDS spectrum and the corresponding quantitative results indicate that the dominant elements are oxygen (50.85 wt%), silicon (30.51 wt%), and aluminum (13.02 wt%), with smaller contributions from calcium (1.28 wt%), magnesium (1.04 wt%), and iron (2.96 wt%). This composition is typical of silicate-rich sands, particularly those dominated by quartz (SiO_2) and aluminosilicates, such as feldspar and clay minerals. The relatively low carbon content (0.34 wt%) suggests a minimal presence of organic or carbonate material in the natural dune sand.

In contrast, crushed dune sand (CDS) (Fig. 5b) displays a dramatically different elemental profile. The most striking feature is the sharp increase in carbon content (45.18 wt%), accompanied by a notable decrease in oxygen (37.68 wt%), silicon (15.16 wt%), and aluminum (0.97 wt%). These changes imply a significant transformation in surface chemistry following mechanical crushing. The elevated carbon may originate from surface contamination, adsorption of airborne organic materials, or testing environments. The decreased silicon and aluminum contents suggest partial masking of silicate phases or loss due to dust or fragmentation during crushing. Iron and calcium are present in trace amounts in both sand types but appear reduced in CDS.

In the leveling mortar (Fig. 6a), the EDS spectrum indicates a dominant presence of carbon (60.36 wt %) and oxygen (31.56 wt %), which together constitute over 90% of the sample by weight. This is consistent with the presence of organic polymeric resins or binders used in the leveling mortar matrix. The relatively low silicon content (7.39 wt %) reflects the limited exposure of sand particles

on the surface, suggesting that they are mostly embedded within the binder. Minor traces of calcium (0.56 wt %) and iron (0.13 wt %) are also observed.

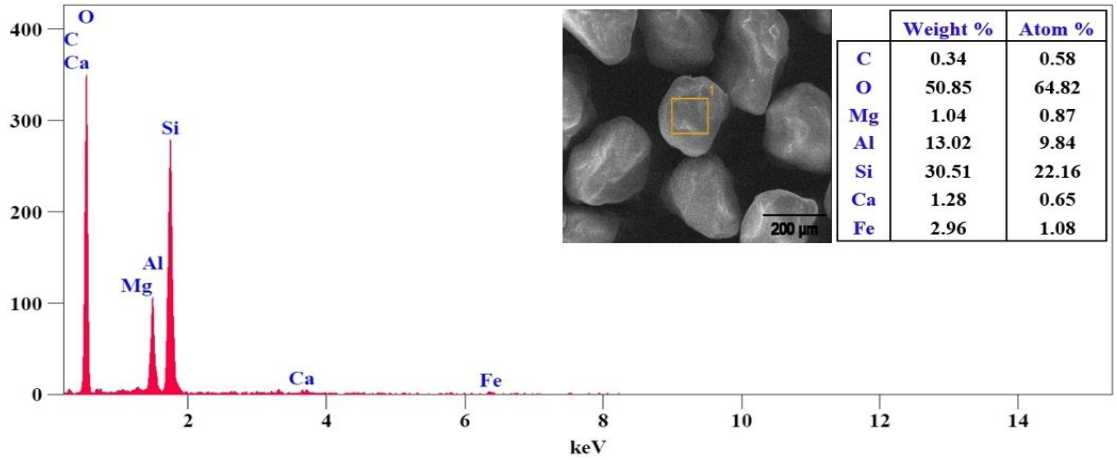

(a)

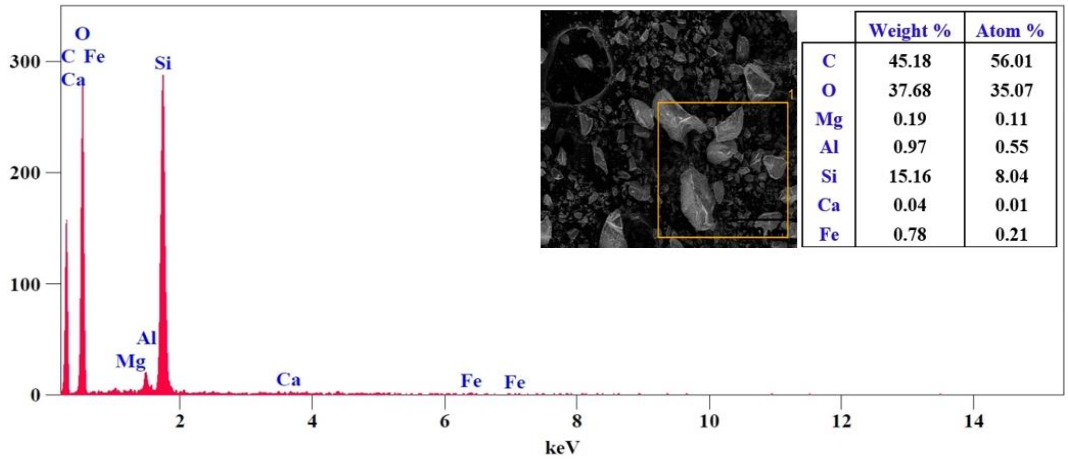

(b)

Fig. 5. SEM-EDS test results of (a) Dune sand and (b)Crushed Dune Sand

Following thermal treatment, the composition of the treated leveling mortar (TM) (Fig. 6b) shifts markedly. Carbon is no longer the dominant element; instead, oxygen content rises significantly to 48.76 wt %, followed by iron (28.68 wt %), silicon (20.19 wt %), and aluminum (2.04 wt %), while carbon is no longer listed, due to degradation, volatilization, or coverage loss of organic components during heating. This shift in elemental profile reflects the decomposition or redistribution of the polymeric resin and increased surface exposure of the mineral aggregates (primarily silicates and oxides). These EDS findings are in strong agreement with the SEM observations discussed in Fig. 4 and section 3.1. Initially, the leveling mortar (M) features a smooth and continuous matrix, with discrete sand-resin interfaces. This structure, rich in organic carbon, appears homogeneous but contains potential weak points due to poor interfacial bonding.

Upon thermal treatment, SEM images reveal that the resin undergoes post-curing and densification, transforming the matrix into a more complex, interlocking morphology. The sand grains become more exposed, and the interface becomes mechanically and chemically more integrated. This is visually supported by the emergence of rough, textured surfaces in the SEM micrographs of TM, indicating better particle–matrix adhesion. Additionally, the higher presence of Fe, Al, and Si detected by EDS in TM suggests that inorganic fillers and natural sand components are more prominently involved in the structural skeleton of the treated leveling mortar. The dramatic drop in carbon percentage and rise in metallic and silicate components in TM highlights the thermally induced transformation of the leveling mortar from an organic-dominant to a mineral-dominant

composite. This transition implies enhanced mechanical performance, thermal resistance, and structural integrity.

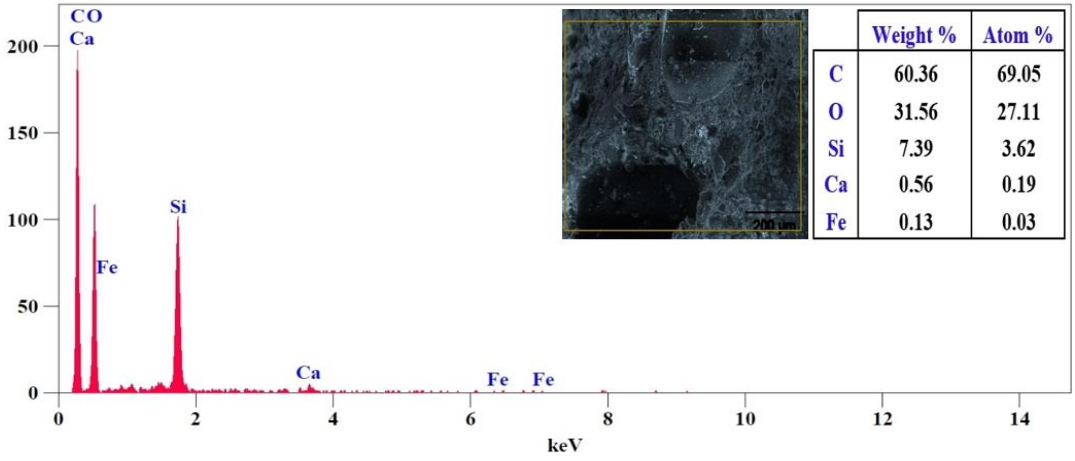

(a)

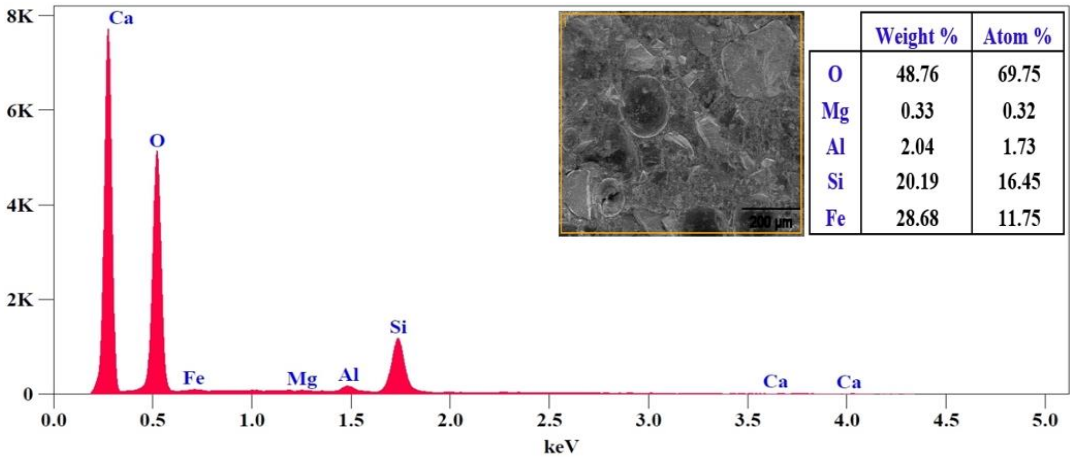

(b)

Fig. 6. SEM-EDS test results of (a) Leveling mortar (M) and (b) Treated Leveling mortar (TM)

Table 3. Elemental composition found in EDX analysis of dune sand (DS), Crushed Dune Sand (CDS), mortar (M), treated mortar (TM).

	DS	CDS	M	TM
Element	C	C	C	O
	O	O	O	Mg
	Mg	Mg	Si	Al
	Al	Al	Ca	Si
	Si	Si	Fe	Fe
	Ca	Ca	-	-
	Fe	Fe	-	-
Weight %	0.34	45.18	60.36	48.76
	50.85	37.68	31.56	0.33
	1.04	0.19	7.39	2.04
	13.02	0.97	0.56	20.19
	30.51	15.16	0.13	28.68
	1.28	0.04	-	-
	2.96	0.78	-	-
Total	100	100	100	100

Atom %	0.58	56.01	69.05	69.75
	64.82	35.07	27.11	0.32
	0.87	0.11	3.62	1.73
	9.84	0.55	0.19	16.45
	22.16	8.04	0.03	11.75
	0.65	0.01	-	-
	1.08	0.21	-	-
Total	100	100	100	100

3.2. Strength of Leveling Mortars

In Figure 7, the leveling mortar mixtures without heat treatment show moderate flexural and high compressive strength values. Leveling mortar made with dune sand (DS) exhibits a compressive strength of 104.2 MPa and a flexural strength of 20.5 MPa. In contrast, leveling mortar made with crushed dune sand (CDS) demonstrates slightly better performance, with a compressive strength of 109.85 MPa and a flexural strength of 22.8 MPa. This marginal improvement in strength for the CDS-based leveling mortar is attributable to the angular and rough texture of crushed sand particles, as highlighted in the SEM analysis (Figure 4).

The improved particle interlocking in CDS enhances the mechanical engagement between the sand and binder matrix, especially under compressive loads. However, due to the presence of significant organic matrix (as shown in the EDS of Leveling mortar M, Figure 6a), the bonding remains limited, and flexural resistance is relatively low in both types. Following thermal treatment, Figure 8 reveals a substantial increase in both flexural and compressive strength for both leveling mortar types. Leveling mortar (DS) after heat treatment reaches a compressive strength of 116.45 MPa and a flexural strength of 38.75 MPa—almost doubling its flexural strength compared to the untreated version. The CDS-based leveling mortar shows even more significant gains, with compressive strength climbing to 119.9 MPa and flexural strength to 45.25 MPa. These improvements are well-supported by the EDS results in Figure 6b, where a clear increase in elemental components associated with sand (Si, Fe, Al) is evident, and carbon content diminishes. This indicates partial decomposition of the organic binder and better exposure of mineral particles, leading to a denser, more cohesive structure. SEM observations (Figure 4) also confirm matrix densification, interfacial interlocking, and resin reconfiguration after thermal treatment, which directly contribute to the improved mechanical behavior. When comparing both figures, the impact of thermal treatment is profound, particularly on flexural strength, which nearly doubles for both DS and CDS leveling mortar s. While compressive strength improves by approximately 10–12%, the increase in flexural resistance is much more significant—from 20.5 MPa to 38.75 MPa in DS leveling mortar s and 22.8 MPa to 45.25 MPa in CDS leveling mortar s. This highlights the role of thermal curing in enhancing the toughness and ductility of the leveling mortar, not just its strength under static load.

The increase in flexural strength following heat treatment was statistically significant for both DS ($p = 0.01$) and CDS mortars ($p = 0.008$). Similarly, compressive strength improvements were statistically significant ($p < 0.05$). The strength differences between mortars made with crushed and uncrushed dune sand were also statistically significant for both flexural and compressive tests ($p < 0.05$) This leveling mortar characterized by several noteworthy chemical properties, primarily derived from its constituents—crushed dune sand and thixotropic polyester resin. The crushed dune sand, mainly composed of quartz (SiO_2), also includes traces of feldspar and mica, and exhibits a fine granulometry that enhances surface reactivity. Upon incorporation with the polyester resin, a polymer derived from unsaturated acids like maleic acid and glycols such as propylene glycol, a strong chemical bond forms through cross-linking when a hardener is added. This polymerization process results in a thermoset matrix with improved chemical resistance, reduced water permeability, and increased structural integrity.

Table 4. Strength of the leveling mortar without heat treatment

Tests	DS (mean ± SD)	CDS (mean ± SD)
Flexion (MPa)	20.5 ± 1.1	20.5 ± 1.1
Compression (MPa)	104.2 ± 2.2	104.2 ± 2.2
Modulus of Elasticity (E) (MPa)	10.2 ± 0.3	10.2 ± 0.3
Poisson's Ratio (ν)	0.21 ± 0.02	0.21 ± 0.02

Table 5. Strength of the leveling mortar after heat treatment

Tests	DS (mean ± SD)	CDS (mean ± SD)
Flexion (MPa)	38.75± 1.1	45.25± 1.1
Compression (MPa)	116.45± 2.2	119.9± 2.2
Modulus of Elasticity (E) (MPa)	10.8± 0.3	10.94± 0.3
Poisson's Ratio (ν)	0.19± 0.02	0.18± 0.02

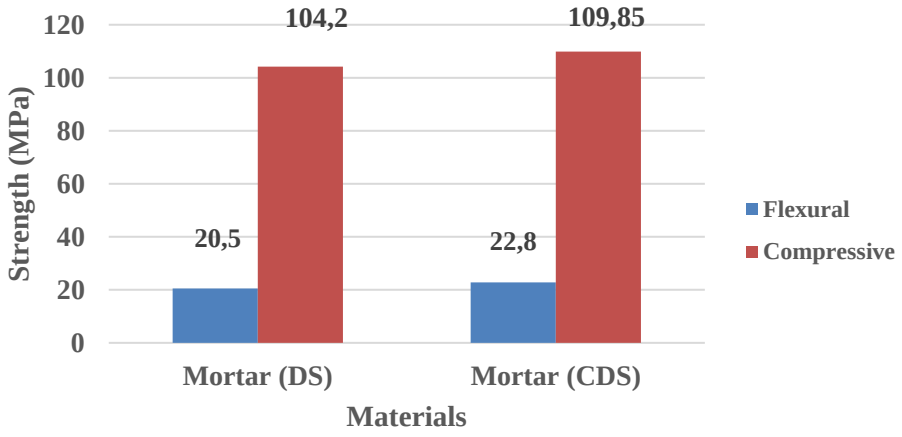

Fig. 7. Strength of leveling mortar without heat treatment

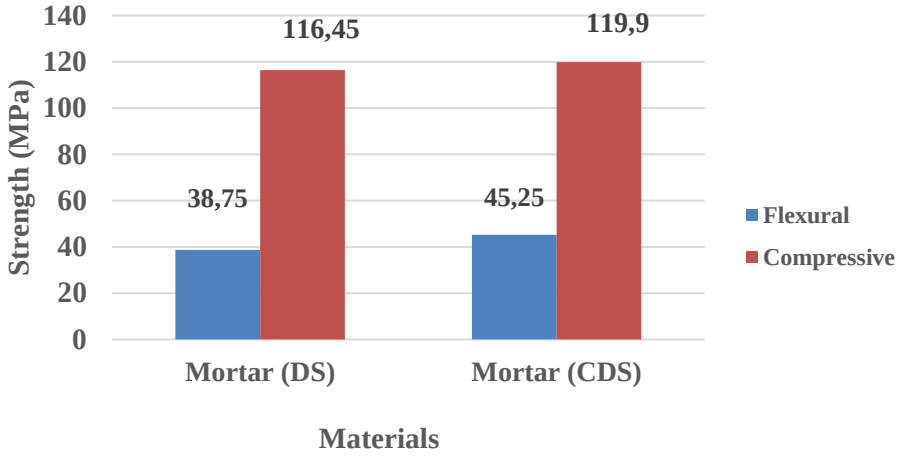

Fig. 8. Strength of treated leveling mortar

3.3. Thermal Analysis

3.3.1 Differential Scanning Calorimetry (DSC)

In the Fig. 9, The Differential Scanning Calorimetry (DSC) curve analysis for the leveling mortar and treated leveling mortar under varying temperatures. Which consists of crushed dune sand and

thixotropic polyester resin, along with the dune sand and crushed dune sand, provides valuable insights into the thermal properties and behavior of these materials.

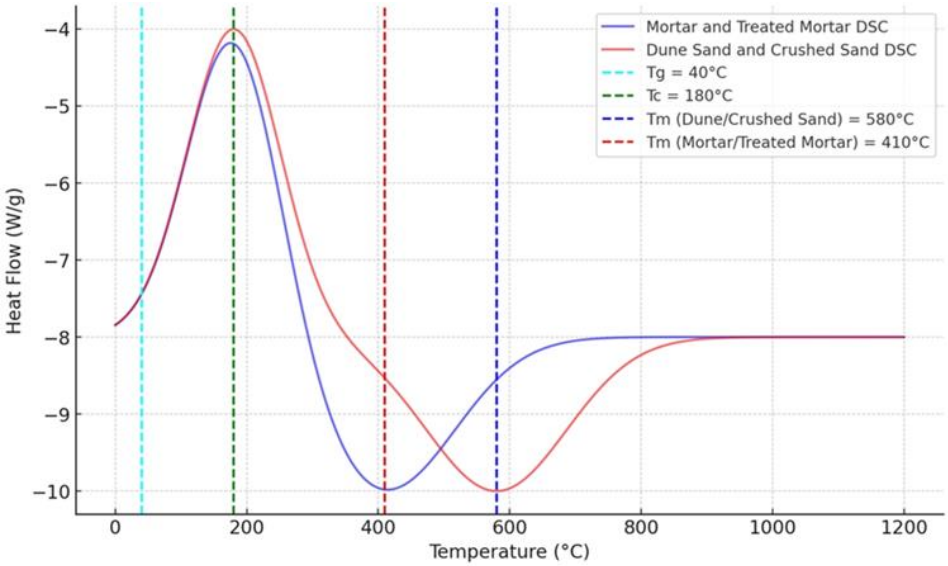

Fig. 9. Differential scanning calorimetry (DSC) curve of dune sand, crushed dune sand, leveling mortar and treated leveling mortar

The first transition, at 40°C, represents the glass transition temperature (Tg) of the polyester resin. This transition is indicative of the shift from a rigid, glassy state to a rubberier state, suggesting that the material experiences increased segmental mobility beyond this temperature. The relatively low Tg is characteristic of polyester resins used in leveling mortar s, confirming their flexibility and adhesion properties at lower temperatures.

A crystallization peak (Tc ≈ 180°C) suggests an exothermic process, it is associated with the rearrangement of the polyester resin polymer chains. Given that the heat-treated leveling mortar was subjected to temperatures up to 170°C, this indicates that partial crystallization may have already occurred before testing. This prior heat exposure could have influenced the polymer structure, making it more stable compared to untreated leveling mortar. The thermal event observed at ~410°C corresponds to the onset of thermal decomposition temperature of the polyester resin matrix. While this is often exothermic in oxidative environments, under the inert nitrogen atmosphere used in DSC, the process may appear as a weakly endothermic transition due to bond cleavage within the polymer chains.

$$(C_2H_4O)n(C_8H_6O_4)m \rightarrow CO_2 + CO + H_2O + C_6H_4(CO)_2O + C_xH_y + \text{residual carbon} \quad (1)$$

In the DSC curves, the endothermic peak observed around 573°C corresponds to the well-documented α-quartz to β-quartz phase transition of silica (SiO_2), which is a reversible solid-state transformation and not a melting event. This transition involves a structural rearrangement in the quartz lattice without material liquefaction. It is important to note that quartz melts at a significantly higher temperature, approximately 1650°C. Therefore, the thermal effect observed at ~573°C reflects the polymorphic transformation of the quartz phase present in the sand aggregates, which can influence the composite's thermal response but does not indicate the melting of mineral components.

3.3.2 Differential Thermal Analysis (DTA)

The Differential Thermal Analysis (DTA) curve of dune sand and crushed dune sand in the Fig. 10 reveals key thermal events related to the decomposition and transformation of its mineral components. The first noticeable feature is an endothermic reaction occurring between 400°C and 600°C, which is attributed to the dehydration of clay minerals and the α-quartz to β-quartz phase transition. This reaction involves the loss of bound water from minerals such as kaolinite, which decomposes into metakaolin and releases water vapor. Additionally, the quartz polymorphic

transition at around 573°C further contributes to this endothermic behavior, as quartz undergoes structural rearrangement, which absorbs heat. These transformations indicate the progressive thermal decomposition of the sand's mineral phases.

$$Al_2Si_2O_5(OH)_4 \rightarrow Al_2Si_2O_7 + 2H_2O \quad (3)$$

The second major feature in the DTA curve is an exothermic reaction occurring between 800°C and 1000°C, corresponding to the crystallization and phase transformation of silica-based compounds. This reaction is associated with the reorganization of amorphous silica (SiO_2) into stable crystalline phases such as cristobalite or tridymite, releasing energy in the process. If organic impurities are present, their oxidation may also contribute to this exothermic peak. The similarity in thermal events between dune sand and crushed dune sand suggests that crushing does not significantly alter the thermal stability of the material, though it may slightly affect reaction intensities due to increased surface area and reactivity.

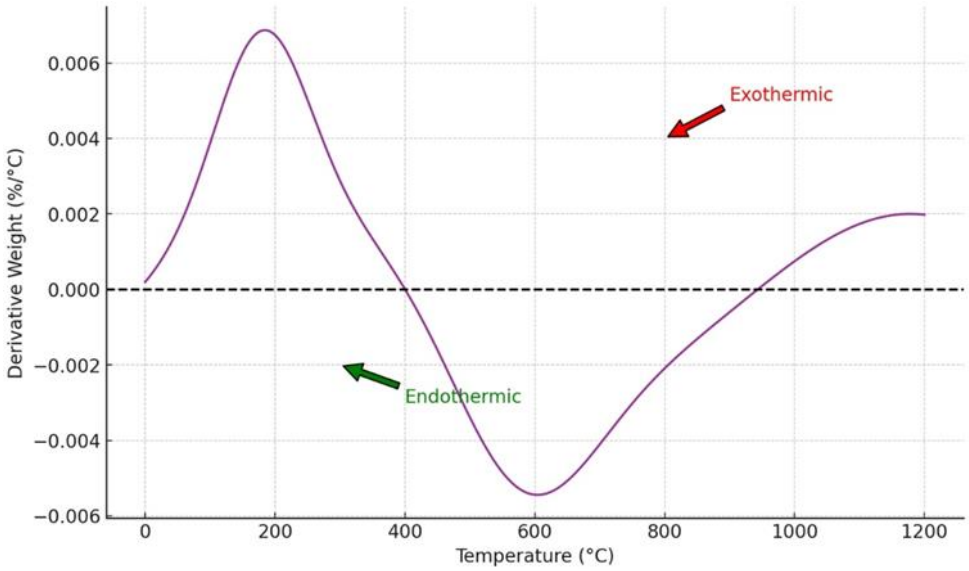

Fig. 10. Differential Thermal Analysis (DTA) curve of dune sand and crushed dune sand

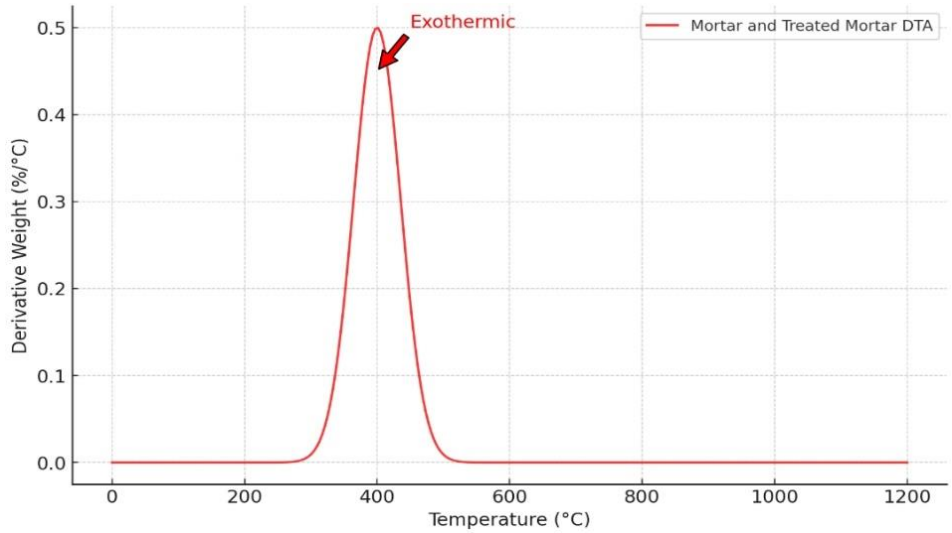

Fig. 11. Differential Thermal Analysis (DTA) curve of leveling mortar and treated leveling mortar

Analyzing the DTA curve of both leveling mortar and treated leveling mortar sheds light on their thermal properties, emphasizing phase changes and decomposition processes (Fig. 11). The pronounced thermal event around 410°C is associated with the degradation of the polyester resin.

While recorded as exothermic in DTA—possibly due to minor oxidative effects or further cross-linking reactions—the same process may appear differently in DSC, which operates under strictly inert conditions. Beyond this exothermic peak, the curve stabilizes, suggesting that no significant thermal events occur at higher temperatures. This indicates that once the polyester resin decomposes, the remaining inorganic components of the leveling mortar, primarily silica (SiO_2) and calcium-based compounds, exhibit thermal stability up to 1200°C. The fact that both leveling mortar and heat-treated leveling mortar exhibit similar exothermic behavior at the same temperature suggests that the heat treatment (up to 170°C) did not significantly alter the decomposition temperature of the resin, but it may have influenced the structural properties of the material.

3.3.3 Gravimetric Thermal Analysis (GTA)

From Fig. 12, The Gravimetric Thermal Analysis (GTA) curve of dune sand and crushed dune sand reveals a gradual weight loss of approximately 0.70% as the temperature increases from 0°C to 1200°C. The initial mass loss below 200°C is primarily due to the evaporation of adsorbed water molecules on the sand particles, following the reaction H_2O (adsorbed) → H_2O (vapor). As the temperature reaches 400-600°C, a slight but continuous weight reduction is observed, corresponding to the dehydroxylation of clay minerals with the release of structural water. Additionally, the phase transition of quartz (SiO_2) from α-quartz to β-quartz occurs around 573°C, though this transformation does not contribute significantly to mass loss. In the 800-1000°C range, a more noticeable decrease in weight is attributed to the thermal decomposition of carbonate impurities, such as calcium carbonate ($CaCO_3$), leading to the release of carbon dioxide gas (CO_2):

$$CaCO_3 \rightarrow CaO + CO_2 \quad 4)$$

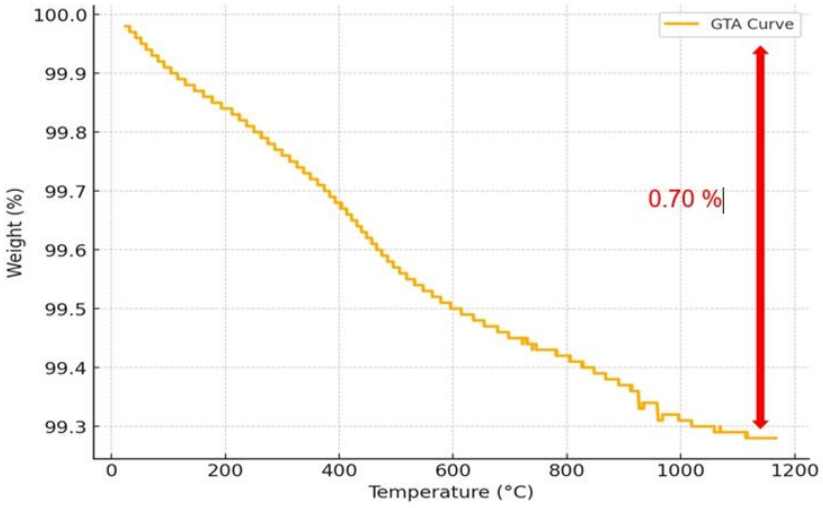

Fig. 12. Gravimetric Thermal Analysis (GTA) curve of dune sand and crushed dune sand

A significant weight loss of approximately 35% is observed in Fig. 13, primarily occurring between 200°C and 500°C, which indicates the decomposition of organic components and polymer degradation. This process is influenced by the polymerization under nitrogen gas (N_2), which creates an inert atmosphere, suppressing oxidation reactions. As a result, thermal decomposition is driven mainly by pyrolysis and volatilization rather than combustion. Beyond 600°C, the GTA curve shows mass stabilization, suggesting that the remaining material is composed mainly of silica (SiO_2) aggregates and calcium oxide (CaO), both of which demonstrate high thermal stability in this temperature range. The first stage of mass loss (below 200°C) corresponds to the evaporation of free and physically adsorbed water within the leveling mortar. As the temperature increases to 250-500°C, a sharp weight loss is observed, corresponding to the pyrolysis of the thixotropic polyester resin used in the leveling mortar. In the nitrogen environment, the polymer undergoes thermal cleavage of ester bonds (-COO-), resulting in the release of hydrocarbon volatiles,

carbonaceous char, and gaseous byproducts such as CO and CO_2. The chemical degradation pathway can be approximated as:

$$(C_2H_4O)n(C_8H_6O_4)m \rightarrow CO_2 + CO + H_2 + C_xH_y + \text{char residue} \quad (5)$$

Beyond 600°C, the remaining mass stabilizes around 65%, indicating that the silica-based aggregates and calcium oxide remain thermally intact under nitrogen conditions. Unlike in an oxygen-rich atmosphere, where complete combustion of organic residues would occur, the inert nitrogen atmosphere promotes the formation of carbonaceous char, which remains in the sample instead of being oxidized into CO_2. If calcium carbonate ($CaCO_3$) is present, it may decompose at higher temperatures (~800-900°C), releasing CO_2 gas.

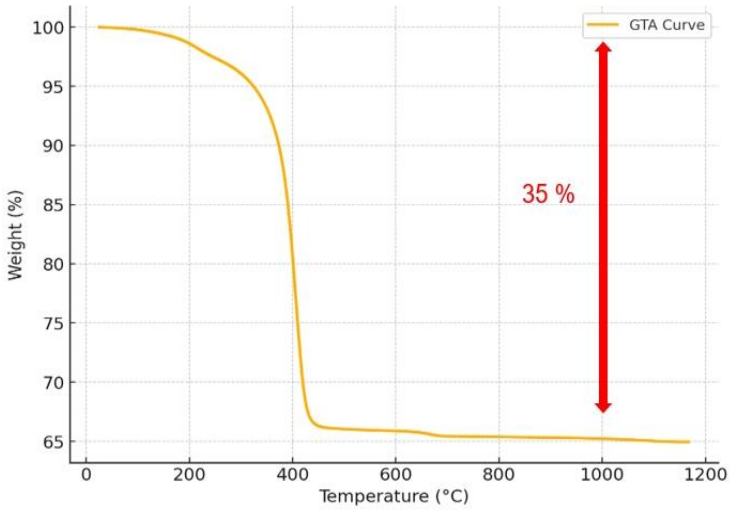

Fig. 13. Gravimetric Thermal Analysis (GTA) curve of leveling mortar and treated leveling mortar

4. Cost and Scalability

Based on the Table 5, the presented system (crushed dune sand + polyester resin + heat treatment) involves higher binder and processing costs due to the use of polyester resin (3–5 USD/kg) and thermal curing (10–15 USD/m^3), compared to the lower cost of OPC (0.1–0.15 USD/kg) and ambient curing in traditional mortars. However, the use of locally sourced dune sand—available at negligible cost—versus commercial silica sand (30–50 USD/ton), along with faster curing and significantly higher mechanical strength, may compensate for the initial investment, particularly in projects requiring high performance, reduced construction time, or limited maintenance.

Table 5. Strength of the leveling mortar after heat treatment

Component / Process	Proposed System (CDS + Polyester + Heat)	Conventional System (OPC + Silica Sand)
Binder cost	High (polyester resin ~10–20× OPC price)	Low (OPC is widely available & cheaper)
Aggregate cost	Very low (local dune sand, negligible transport cost)	Moderate (industrial-grade silica sand, often imported)
Curing time	Fast (minutes to hours post-curing)	Slow (up to 28 days for full strength)
Environmental footprint	Debatable: low transport impact, but polymer & thermal energy involved	High due to clinker production CO_2 emissions

5. Conclusions

This study demonstrated the significant potential of crushed dune sand, when combined with thixotropic polyester resin and subjected to thermal treatment, to serve as a high-performance filler in polymer-based leveling mortars. Through an integrated approach encompassing mechanical, thermal, and microstructural analyses, the research provided compelling evidence that mechanical processing and heat curing substantially enhance the composite's structural integrity and environmental viability.

The transformation of natural dune sand into angular, fractured particles via mechanical crushing not only improved surface roughness but also significantly increased the specific surface area, which in turn promoted better interfacial bonding with the resin matrix. This observation, confirmed by SEM micrographs, aligns with the conclusions drawn in earlier studies on modified desert sands, which also reported similar improvements in mechanical properties through surface alteration techniques. Thermal post-curing at 170°C was shown to further enhance the matrix's densification, as evidenced by EDS analysis indicating a marked decrease in carbon content (i.e., resin pyrolysis) and increased mineral visibility (Si, Al, Fe). This process facilitated additional cross-linking within the polyester resin, thereby reinforcing the sand–resin interface. These findings corroborate earlier thermal studies of unsaturated polyester composites, who emphasized the critical role of post-curing in improving mechanical behavior.

Mechanically, heat-treated mortars exhibited compressive strengths reaching up to 119.9 MPa and flexural strengths nearing 45.25 MPa, marking significant gains of 10–12% and up to 98%, respectively, over untreated samples. These values surpass those of conventional mortars and highlight the efficacy of combining mechanical crushing with thermal treatment for structural applications in arid regions. While prior works achieved moderate improvements through biopolymer stabilization, the current results outperform them in both compressive and flexural domains. The pronounced disparity between the gains in flexural strength (up to 98%) and compressive strength (10–12%) following thermal post-curing can be attributed to the differing failure mechanisms and stress distributions inherent in bending versus compression. Flexural strength is highly sensitive to the quality of the resin-filler interface and the ability of the matrix to transfer tensile stresses without crack initiation or propagation. Thermal treatment promotes extensive cross-linking within the polyester resin, enhances resin crystallinity, and leads to partial volatilization of weak organic phases. These changes improve matrix cohesion and significantly strengthen the interface between resins and crushed sand particles, as confirmed by SEM-EDS analyses. Moreover, the heat-induced densification process leads to better mechanical interlocking between angular filler grains and the polymer matrix, improving stress transfer pathways under tensile or flexural loading. In contrast, compressive strength is less sensitive to interfacial bonding and more dependent on the bulk resistance of the composite to axial loading. Thus, while both modes benefit from thermal treatment, the enhancement in flexural performance is more pronounced due to the microstructural reconfiguration that mitigates crack propagation and stress concentration zones, particularly in tension-dominated zones. This distinction underlines the significance of thermal curing not merely as a means of increasing bulk strength, but as a targeted strategy for improving toughness, ductility, and stress redistribution capabilities in polymer composites, especially under bending conditions.

Thermal analyses (DSC, DTA, and TGA) confirmed the composite's thermal stability up to 410°C, with consistent pyrolytic degradation behavior of the organic matrix and stable mineral structure beyond this threshold. Notably, the treated mortars retained a residual mass of ~65%, indicating high fire resistance and long-term durability. These insights position this composite as a suitable candidate for construction in high-temperature or fire-prone zones, addressing key performance demands unmet by conventional polymer concretes. From a sustainability perspective, the valorization of locally sourced dune sand not only reduces dependency on conventional aggregates but also aligns with circular economy principles by minimizing material transportation and optimizing local resource utilization. This approach directly addresses concerns raised in reviews about the environmental footprint of traditional sand-based construction.

This work contributes a scalable, cost-effective, and environmentally responsible solution for developing thermally stable, mechanically robust, and microstructurally optimized leveling mortars. Future research should explore long-term durability under environmental loading, resin modification techniques to further enhance matrix-filler compatibility, and the applicability of this approach to prefabricated structural elements. The integration of crushed dune sand and thermal treatment into mortar formulation represents not merely a technical enhancement but a strategic pathway toward resilient infrastructure in resource-constrained regions.

Practical durability tests demonstrated excellent resistance to environmental and mechanical stresses. These tests include sensitivity to mass loss, water absorption, heat treatment, and resistance to freeze/thaw cycles. The results indicate that heat treatment gives the mortars increased dimensional stability and impermeability, significantly limiting water penetration and shrinkage-related deformation. Robustness to freeze/thaw cycles confirm the composite's ability to withstand extreme climatic conditions.

The improvements in mechanical performance, particularly in flexural strength (up to 98%), were not only substantial but also statistically significant ($p < 0.05$). These findings were validated through triplicate testing and rigorous statistical analysis, reinforcing the reliability and reproducibility of the results. Despite a higher initial cost related to the use of polyester resin and heat post-treatment, the proposed system is distinguished by its rapid implementation, increased mechanical performance and the exploitation of an abundant and almost free local resource (crushed dune sand). This combination makes it an economically viable and industrializable solution, particularly for projects requiring durability, reduced construction times and minimization of transport costs.

Acknowledgement

The authors acknowledge the financial backing from the Directorate General for Scientific Research and Technological Development (D.G.R.S.D.T., Algeria) for their research. They also extend their thanks to the members, professors, and students affiliated with the Laboratory of Eco-Materials: Innovations & Applications (EMIA).

References

[1] Hanus MJ, Harris AT. Nanotechnology innovations for the construction industry. Prog Mater Sci [Internet]. 2013;58(7):1056–102. http://dx.doi.org/10.1016/j.pmatsci.2013.04.001

[2] Oladele IO, Adelani SO, Agbabiaka OG, Adegun MH. Applications and Disposal of Polymers and Polymer Composites : A Review. Euro J Adv Engg Tech. 2022;9(3):65–89.

[3] Salami BA, Bahraq AA, Haq MM ul, Ojelade OA, Taiwo R, Wahab S, et al. Polymer-enhanced concrete: A comprehensive review of innovations and pathways for resilient and sustainable materials. Next Mater. 2024 Jul 1;4:100225. https://doi.org/10.1016/j.nxmate.2024.100225

[4] Park S, Lee E, Ko J, Yoo J, Kim Y. Rheological properties of concrete using dune sand. Constr Build Mater. 2018 May 30;172:685–95. https://doi.org/10.1016/j.conbuildmat.2018.03.192

[5] Kozhevnikova S V., Elmes MJ, Brameld JM, Jethwa PH. Mortar Based on Dune Sand and Substitute Wood Sawdust: Physico-Mechanical Characterization and Relationship Between Properties in Young Age. Ann Chim - Sci des Matériaux [Internet]. 2021 Jan 1 [cited 2025 Apr 19];2(1).

[6] Hamada HM, Abed F, Al-Sadoon ZA, Elnassar Z, Hassan A. The use of treated desert sand in sustainable concrete: A mechanical and microstructure study. J Build Eng. 2023 Nov 15;79:107843. https://doi.org/10.1016/j.jobe.2023.107843

[7] Laoubi H, Bederina M, Djoudi A, Goullieux A, Dheilly RM. Study of a New Plaster Composite Based on Dune Sand and Expanded Study of a New Plaster Composite Based on Dune Sand and Expanded. 2018;(December). DOI: 10.2174/1874149501812010401

[8] Khaleghi M, Heidarvand M. A novel study on hydro-mechanical characteristics of biopolymer-stabilized dune sand. J Clean Prod. 2023 Apr 20; 398:136518. https://doi.org/10.1016/j.jclepro.2023.136518

[9] Elsawy MBD. Geotechnical Behavior of Stabilized Dunes Sand by Cement. J Civ Eng Constr. 2021;10(2):69–74.

[10] Tafraoui A, Lebaili S. Valorization of the sand of dune of the Western erg (Algeria) in the formulation of the UHPC. Vol. 6, Journal of Applied Sciences. 2006. p. 2833–6.

[11] Zaouai S, Tafraoui A, Makani A, Benmerioul F. Hardened and transfer properties of self-compacting concretes containing pre-coated rubber aggregates with crushed dune sand. J Rubber Res. 2020;23(1):5–12. https://doi.org/10.1007/s42464-019-00030-x
[12] Tsoar H. Types of Aeolian Sand Dunes and Their Formation. 2001 [cited 2025 Apr 19];403–29. https://doi.org/10.1007/3-540-45670-8_17
[13] Refaat AA, Hamdan MA. Mineralogy and grain morphology of the aeolian dune sand of Toshka area , southeastern Western Desert , Egypt. AEOLIAN Res [Internet]. 2015;17:243–54. http://dx.doi.org/10.1016/j.aeolia.2015.04.006
[14] Wu HL, Yu J, Zhang D, Zheng JX, Li VC. Effect of morphological parameters of natural sand on mechanical properties of engineered cementitious composites. Cem Concr Compos. 2019 Jul 1;100:108–19. https://doi.org/10.1016/j.cemconcomp.2019.04.007
[15] Wu Y, Yamamoto H, Cui J, Cheng H. Influence of Load Mode on Particle Crushing Characteristics of Silica Sand at High Stresses. Int J Geomech. 2020;20(3):1–14. https://doi.org/10.1061/(ASCE)GM.1943-5622.0001600
[16] Alahmad F, Al Abdallah H, El Maaddawy T, Abu-Jdayil B. Development of unsaturated polyester mortar made with dune sand as a sustainable alternative in construction. Results Eng. 2025 Mar 1;25:104335. https://doi.org/10.1016/j.rineng.2025.104335
[17] Ioannidou D, Sonnemann G, Suh S. Do we have enough natural sand for low-carbon infrastructure? J Ind Ecol. 2020;24(5):1004–15. https://doi.org/10.1111/jiec.13004
[18] Akhtar MN, Bani-Hani KA, Malkawi DAH, Albatayneh O. Suitability of sustainable sand for concrete manufacturing - A complete review of recycled and desert sand substitution. Results Eng. 2024 Sep 1;23:102478. https://doi.org/10.1016/j.rineng.2024.102478
[19] Oleksy M, Heneczkowski M, Galina H. Thixotropic compositions: Unsaturated polyester resins/modified bentonites. Polimery/Polymers. 2007;52(5):345–50. DOI: 10.14314/polimery.2007.345
[20] Spasojevic PM. Thermal and Rheological Properties of Unsaturated Polyester Resins-Based Composites. Unsaturated Polyest Resins Fundam Des Fabr Appl. 2019 Jan 1;367–406. https://doi.org/10.1016/B978-0-12-816129-6.00015-6
[21] Cakir F, Yildirim P, Gündoğdu M. Effect of catalysts amount on mechanical properties of polymer concrete. Chall J Concr Res Lett. 2020;11(3):46–52. https://doi.org/10.20528/cjcrl.2020.03.001
[22] Wan X, Demir B, An M, Walsh TR, Yang N. Thermal conductivities and mechanical properties of epoxy resin as a function of the degree of cross-linking. Int J Heat Mass Transf. 2021;180:1–20. https://doi.org/10.48550/arXiv.2104.02430
[23] Awaja F, Gilbert M, Kelly G, Fox B, Pigram PJ. Adhesion of polymers. Prog Polym Sci. 2009 Sep 1;34(9):948–68. https://doi.org/10.1016/j.progpolymsci.2009.04.007
[24] Gonçalves FAMM, Santos M, Cernadas T, Alves P, Ferreira P. Influence of fillers on epoxy resins properties: a review. J Mater Sci. 2022; 5732:15183–212. https://doi.org/10.1007/s10853-022-07573-2
[25] Benmerioul F, Makani A, Tafraoui A, Zaouai S. Valorization of the Crushed Dune Sand in the Formulation of Self-compacting-concrete. Procedia Eng. 2017 Jan 1;171:672–8. https://doi.org/10.1016/j.proeng.2017.01.408
[26] Gandolfi MG, Van Landuyt K, Taddei P, Modena E, Van Meerbeek B, Prati C. Environmental Scanning Electron Microscopy Connected with Energy Dispersive X-ray Analysis and Raman Techniques to Study ProRoot Mineral Trioxide Aggregate and Calcium Silicate Cements in Wet Conditions and in Real Time. J Endod. 2010 May 1;36(5):851–7. https://doi.org/10.1016/j.joen.2009.12.007
[27] Corcione CE, Frigione M. Characterization of nanocomposites by thermal analysis. Materials (Basel). 2012;5(12):2960–80. https://doi.org/10.3390/ma5122960
[28] Zhang K, Grimoldi A, Rampazzi L, Sansonetti A, Corti C. Contribution of thermal analysis in the characterization of lime-based mortars with oxblood addition. Thermochim Acta. 2019;678:178303. https://doi.org/10.1016/j.tca.2019.178303
[29] Li H, Xiao H gang, Ou J ping. A study on mechanical and pressure-sensitive properties of cement mortar with nanophase materials. Cem Concr Res. 2004 Mar 1;34(3):435–8. https://doi.org/10.1016/j.cemconres.2003.08.025
[30] Dhakal HN, Ismail SO. Unsaturated Polyester Resins: Blends, Interpenetrating Polymer Networks, Composites, and Nanocomposites. Unsaturated Polyest Resins Fundam Des Fabr Appl. 2019 Jan 1;181–98. https://doi.org/10.1016/B978-0-12-816129-6.00008-9
[31] Chencheni A, Belkhiri S, Tarchoun AF, Abdelaziz A, Bessa W, Boucheffa Y, et al. Unravelling the thermal behavior and kinetics of unsaturated polyester resin supplemented with organo-nanoclay. RSC Adv. 2024;14(1):517–28.

Research on Engineering Structures & Materials
www.jresm.org
Research Group

Research Article

Impact of manufactured sand grading method on durability of self-compacting concrete

Anitha J.[*,1,2,a], Ravi Kumar H.[1,2,b]

[1]*Department of Civil Engineering, Sir M Visvesvaraya Institute of Technology, Bengaluru, India*
[2]*Department of Civil Engineering, Visvesvaraya Technological University, Belagavi, India*

Article Info

Article History:

Received 07 May 2025
Accepted 21 May 2025

Keywords:

Manufactured sand;
Self-compacting concrete;
Grading method;
Compressive strength;
Tensile strength;
Durability

Abstract

This study examines the impact of different grading methods for manufactured sand (M-sand) on the mechanical and durability characteristics of self-compacting concrete (SCC). A detailed experimental program was designed to assess the mechanical and durability properties of SCC containing M-sand processed through two different grading techniques, air-graded M-sand (AGMS) and wet-graded M-sand (WGMS) in comparison with river sand (RS). AGMS & WGMS are used to replace RS in the proportion of 0%, 25%, 50%, 75% & 100%, and the mechanical and durability properties of the concrete have been evaluated. The findings reveal that the grading method has a notable influence on SCC performance. This study also examined the relationship between various durability properties like RCPT, water absorption and porosity using MATLAB. It was observed that AGMS and WGMS increased the compressive strength of M20 SCC by 29% and 14%, respectively. In M40 and M70 mixes, AGMS led to 14% and 13% increase, while WGMS resulted in 9% and 4%. Tensile strength improved by 26%, 25%, and 28% with AGMS, and 22%, 13%, and 26% with WGMS in M20, M40, and M70 mixes, respectively. The M70 grade SCC with AGMS shows the highest resistance to acid attack with 2.54% and 5.50 % weight loss and 3.41% and 6.59 % strength loss for 2% and 5% dilution respectively. The M20 grade SCC with RS shows the least resistance to sulphate attack with 4.43% weight loss and 10.85 % strength loss, while M70 grade SCC with AGMS shows the highest resistance to sulphate attack with 1.06% weight loss and 1.66 % strength loss. Across all SCC grades, AGMS reduced water absorption, porosity, permeability, and charge passed by 40%, 37%, 36%, and 33%, respectively, while WGMS achieved reductions of 20%, 18%, 31%, and 21%, relative to RS. This research concludes that the appropriate selection and grading of M-sand are critical to achieving high-strength, durable SCC.

1. Introduction

Self-compacting concrete (SCC) and manufactured sand (M-sand) have revolutionized modern construction practices, offering sustainable, efficient, and high-performance alternatives to conventional methods and materials [1-2]. As the construction industry grapples with increasing demands for quality, speed, and environmental responsibility, the integration of these advanced technologies has become essential [3]. This paper explores the applications of M-sand in self-compacting concrete, aiming to highlight its contributions to civil engineering.

Manufactured sand is obtained from crushing granite or basalt hard stones to create an artificial variant of river sand [4]. The process of river sand extraction causes ecological problems as well as destroys river beds [5]. Proper selection of river sand becomes crucial for using it in self-compacting concrete because this material contains silt and clay along with organic impurities. M-

[*]Corresponding author: anitha_civil@sirmvit.edu
[a]orcid.org/0000-0002-2057-6205; [b]orcid.org/0000-0003-3172-0839
DOI: http://dx.doi.org/10.17515/resm2025-878me0507rs

sand is produced in controlled facilities to achieve regular grain distribution without organic contaminants. The incorporation of M-sand helps resolve both environmental issues linked to river sand mining and equipment shortages for natural sand resources [6]. M-sand production requires multiple crushing phases followed by screening procedures to guarantee continuous high-quality and correct particle dimension control [7].

Managing the fractions falling below 150 microns represents a major challenge during M-sand production [8]. Extensive amount of fine particle leads to several production issues such as inadequately increased water usage and decreased workability of products which subsequently weakens concrete mixes. Industrial plants use grading methods to handle and separate their fines components for resolving this issue. Wet grading and air grading represent the basic methods which producers currently use for material separation [8]. The production of precise particle size distribution in air-graded M-sand (AGMS) depends on using air separators. The air grading system introduces crushed sand to a chamber where high-speed air streams split the finer components based on density and size and form from the larger particles. The process of grading separates fines as light material at the chamber top from heavier materials at the bottom to gather M-sand into a single group [9]. This technique provides environmental benefits through its closed operating system that reduces water pollutants while also conserving water resources since water is not essential for separation. Continuous check and adjustment of fines content becomes possible through air grading which ensures constant purity levels [9]. The wet-graded M-sand (WGMS) performs particle and contaminant elimination through water-based separation techniques. M-sand manufactured through wet grading produces high-quality material of low silt-clay content, nevertheless, this approach necessitates a dependable water source as well as appropriate wastewater and silt disposal management. The choice between air-graded M-sand and wet-graded M-sand depends on different factors such as water supply conditions and environmental standards along with outcome quality expectations. The technique of wet grading remains widespread in regions with ample water supply. Air grading offers superior options in water-scarce areas and strict environmental restrictions.

The utilization of M-sand in self-compacting concrete provides several performance-based as well as sustainability-oriented advantages. Studies shows that M-sand used along with 0 -15% of silica fume improves the rheological and mechanical properties of SCC [10]. The SCC mixes with recycled coarse aggregate (RCA) showed improved strength when M-sand was used as partial replacement for fine aggregate, also the SEM indicated that cracks and voids in RCA were better filled with M-sand thereby improving the interfacial transition zone (ITZ) [11]. The optimal replacement level for achieving higher strength and durability in SCC was found to be 50% [12]. It was observed that addition of M-sand and fly ash, improved the fresh properties, compressive strength and split tensile strength of SCC while the flexural strength remained constant [13]. The passing ratio of L-box test increased by 21%, the blocking ration in J-ring test increased by 25% and the compressive strength increased by 19% for 100% M-sand in SCC [14]. M-sand was found to result in lower flowability but higher mechanical properties in SCC compared to dune sand [15]. To achieve the desired flowability, a higher paste volume was required compared to SCC with river sand [16]. SCC with quarry dust showed improved performance in fresh state and the mechanical strength of concrete was also observed to increase up to 30% replacement of river sand with quarry dust [17]. SCC with 100% M-sand as replacement for river sand and 30% fly ash showed satisfactory flowability, passing ability and segregation resistance [18]. Shrinkage parameters were the least for conventional concrete made by 20% silica fume as replacement for cement and 60 % replacement of river sand by M-sand [19]. The load-carrying capacity of self-compacting concrete with coconut shell increased by 22% when M-sand was used as replacement for river sand [20]. SCC with manufactured sand possesses higher pumpability and better air content than with river sand, due to better angularity of M-sand particles and presence of stone powder [21].

This research examines how M-sand in SCC contributes to building innovations through comprehensive examination of manufacturing strategies and categorization methods and practical industry applications. This study evaluates the influence of river sand (RS), air graded M-sand (AGMS) and (WGMS) on the mechanical, durability properties and bond behavior of SCC. The building industry currently requires detailed research on M-sand as a replacement of natural river

sand because of escalating environmental problems, increasing construction expenses and declining material availability and supply. This evaluation examines mechanical strength and durability features of river sand in comparison to AGMS and WGMS across concrete grades M20, M40 and M70.

2. Materials and Methods

Self-compacting concrete with grades M20, M40 and M70 has been designed based on Indian standards to perform this experimental investigation. The experimental analysis uses materials listed below with their appropriate properties.

2.1. Cement

The experimental research utilizes 53-grade ordinary portal cement having 3.07 specific gravity that meets IS specifications for binder applications.

Table 1. Physical Properties of Cement

Properties	Observed Value	Permissible Value as per IS: 12269-2013 [22]
Fineness (Blaine's Air Permeability method)	281 m^2/kg	225 m^2/kg (minimum)
Fineness of Cement (retained on 90µ sieve)	2.5%	Less than 10%
Normal Consistency	32%	-
Specific Gravity	3.07	-
Initial Setting Time	120 min	30 min (minimum)
Final Setting Time	475 min	600 min(maximum)
Soundness test	1 mm	10 mm (maximum)
Le-chat expansion (Auto clave %)	0.09%	0.8 % (maximum)
Compressive strength of mortar cubes		
3 days	28.50 N/mm^2	27 N/mm^2 (minimum)
7 days	39.00 N/mm^2	37 N/mm^2 (minimum)
28 days	56.53 N/mm^2	53 N/mm^2 (minimum)

2.2. Fly Ash

The experimental work utilized class 'F' fly ash from Raichur thermal power plant which has a determined specific gravity of 2.4 for this project.

Table 2. Chemical and Physical Properties of fly ash

Chemical Properties		Physical Properties	
Oxide	Content (%)	Property	Value
SiO_2	58.76	Fineness (Blaine's permeability) (m2/kg)	330
Al_2O_3	31.48	Particles retained ON 45 micron IS sieve (%)	30
Fe_2O_3	2.85	28 days compressive strength (N/mm2)	44
CaO	0.75	Soundness (mm)	1.2
MgO	0.85	Specific Gravity	2.4
SO_3	0.01	Color	Light grey
Loss on Ignition (%)	0.81		

2.3. Fine Aggregates

2.3.1 Natural River Sand

The natural river sand that was locally procured adhering to the specifications for fine concrete aggregates in IS: 383:2016 [23] having calculated specific gravity of 2.56 was used after sieving to ensure uniform grading and size distribution.

2.3.2 Manufactured Sand

This research assessed two distinct methods of grading of M-sand as alternative fine aggregate - air grading or wet grading.

- Air-graded M-sand (AGMS) is separated using a dry air grading process, which selectively removes excess fines and ensures a well-graded particle size distribution. This process results in angular, rough-textured particles with improved packing density and inter-particle friction, traits that are particularly beneficial in enhancing the mechanical and rheological properties of self-compacting concrete. The specific gravity was found to be 2.65.
- Wet-graded M-sand (WGMS) was produced by washing and hydro-cycloning to remove fines and impurities. While this process also yields a clean product, it tends to retain slightly higher moisture content and a greater proportion of ultra-fine particles compared to air-graded M-sand. These characteristics can influence the water demand and workability of the resulting concrete mix. The specific gravity was found to be 2.39.

Both types of M-sand were used at varying replacement levels (0%, 25%, 50%, 75% & 100%) to evaluate their impact on the fresh, mechanical, and durability performance of SCC across M20, M40, and M70 grades. The consistent particle gradation and controlled production of manufactured sand provided a reliable basis for comparative assessment against natural river sand.

Table 3. Physical Properties of RS, AGMS & WGMS

Property	RS	AGMS	WGMS	Permissible limit (IS383:2016) [23]
Specific Gravity	2.56	2.65	2.39	2.1 – 3.2
Water Absorption (%)	1.78	0	3.54	<2% - RS <5% - M-sand
Fineness Modulus	2.92	2.71	2.66	2.2 – 3.2

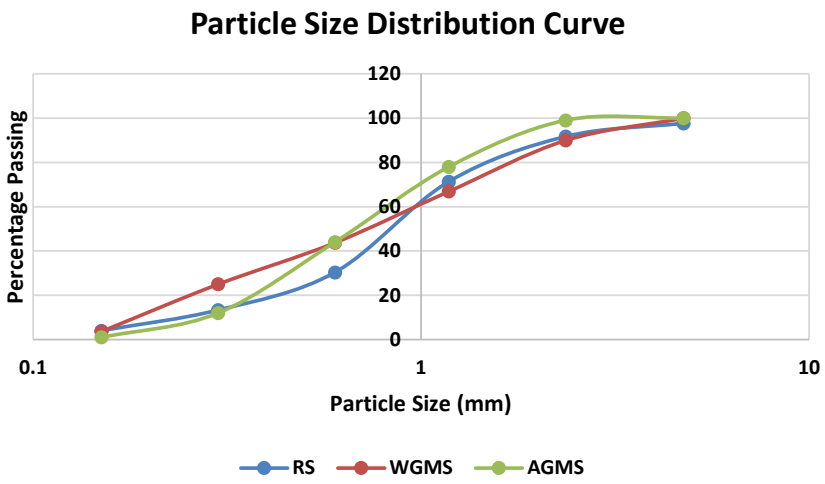

Fig. 1. PSD curve for fine aggregates

Fig 1. Illustrates the particle size distribution curve for all the three types of fine aggregates used in this study, from the PSD curve, it can be inferred that the gradation for river sand shows a more gradual increase in particle passing percentage, indicating a mix of fine and coarse particles. Air-graded M-Sand has the most uniform gradation, with a higher percentage passing in the mid-range

sieves, indicating better grading control. While the Wet-graded M-Sand has a steeper curve in the middle range, meaning finer particles dominate compared to River Sand.

2.4. Coarse Aggregate

The aggregate was sourced from a local quarry and selected based on compliance with the specifications outlined in IS: 383–2016 [23]. The material exhibited a specific gravity of 2.63 thereby satisfying the expectations for high-quality coarse aggregates that can be used in structural concrete applications. Laboratory analysis showed that the aggregate had proper grading where each fraction measured between 10 mm and 20 mm in dimension.

Table 4. Physical properties of Coarse Aggregate

Properties	Results	Permissible limit (IS383:2016) [23]
Specific gravity	2.63	2.5-2.8
Bulk density (kg/m^3)	1590	1650
Aggregate impact value	12.52%	30
Aggregate crushing value	26.67%	30
Fineness modulus	6.37	6 – 7
Water absorption (%)	0.3	< 0.5%
Flakiness index	24.2	25%

2.5. Superplasticizer

Glenium Master Sky 8233 serves as the superplasticizer because its developers conceptualized it using advanced polycarboxylate ether (PCE) technology. The water reduction capability and sustained slump behavior of this material exists within 1.08 ± 0.02 specific gravity and pH range of 6-8.

2.6. Viscosity Modifying Agent

The rheological characteristics of self-compacting concrete experience a boost when using Glenium Stream 2 as a viscosity modifying agent (VMA) because it enhances mix cohesion while minimizing mix segregation and bleeding occurrences. The VMA maintains specific gravity at 1.01 ±0.01 together with pH value at 8 ± 1.

2.7. Methodology

The SCC mixes were developed following the compressive strength-based mix proportioning approach as per IS 10262:2019 [24] and IS 456:2000 [25], with adjustments made to meet the fresh property requirements outlined in the EFNARC guidelines [26] for SCC. The mix design targeted an M40 grade with a characteristic compressive strength (f_{ck}) of 40 MPa. A target mean strength of 48 MPa was adopted considering a suitable margin for variability. A total binder content of 450 kg/m^3 was selected within the recommended SCC range (430–520 kg/m^3), with 20% fly ash used as a mineral admixture (i.e., 360 kg cement + 90 kg fly ash). A water-to-binder ratio of 0.35 was maintained to achieve the desired strength and workability.

Superplasticizer and Viscosity Modifying Agent (VMA) were incorporated at 1% and 0.2% of the total binder weight, respectively, based on product specifications and preliminary trials. Their specific gravities were considered to be 1.08 and 1.01 for volumetric calculations. The coarse aggregate volume fraction was limited to 0.45 of the total aggregate volume to enhance flowability, as recommended by EFNARC [26]. Based on volumetric calculations, the remaining volume was distributed between coarse and fine aggregates (45% and 55%, respectively). This yielded 807.94 kg/m^3 of coarse aggregate and 960.98 kg/m^3 of river sand (for the 0% M-sand control mix). The design process included validation through trial mixes, assessing key SCC properties such as slump flow, V-funnel time, L-box ratio, and segregation resistance, to ensure compliance with EFNARC's performance criteria.

Table 5. Mix proportion for M20, M40 and M70 grade SCC with RS, AGMS and WGMS

Conc. Grade	Mix	Cement (kg/m³)	Fly Ash (kg/m³)	Water (kg/m³)	CA (kg/m³)	River Sand (kg/m³)	Admixture (kg/m³)	M-Sand (kg/m³)
M20 – Ordinary Strength Self-Compacting Concrete	RS100/20	320	80	180	802	955	4.0	0
	AGMS25/20	320	80	180	802	716	4.0	248
	AGMS50/20	320	80	180	802	477	4.0	496
	AGMS75/20	320	80	180	802	239	4.0	744
	AGMS100/20	320	80	180	802	0	4.0	993
	WGMS25/20	320	80	180	802	716	4.0	223
	WGMS50/20	320	80	180	802	477	4.0	446
	WGMS75/20	320	80	180	802	239	4.0	669
	WGMS100/20	320	80	180	802	0	4.0	892
M40 – Medium Strength Self-Compacting Concrete	RS100/40	360	90	158	808	961	4.5	0
	AGMS25/40	360	90	158	808	720	4.5	248
	AGMS50/40	360	90	158	808	480	4.5	497
	AGMS75/40	360	90	158	808	240	4.5	746
	AGMS100/40	360	90	158	808	0	4.5	995
	WGMS25/40	360	90	158	808	720	4.5	224
	WGMS50/40	360	90	158	808	480	4.5	449
	WGMS75/40	360	90	158	808	240	4.5	673
	WGMS100/40	360	90	158	808	0	4.5	897
M70 – High Strength Self-Compacting Concrete	RS100/70	400	100	145	710	1036	7.5	0
	AGMS25/70	400	100	145	710	777	7.5	268
	AGMS50/70	400	100	145	710	518	7.5	536
	AGMS75/70	400	100	145	710	259	7.5	805
	AGMS100/70	400	100	145	710	0	7.5	1073
	WGMS25/70	400	100	145	710	777	7.5	242
	WGMS50/70	400	100	145	710	518	7.5	484
	WGMS75/70	400	100	145	710	259	7.5	726
	WGMS100/70	400	100	145	710	0	7.5	967

(a) (b)

Fig. 2. (a) Casting of specimen (b) mixing of concrete

A total of 9 mixes were prepared for each grade as shown in Table 5, the mix RS100/20 can be read as M20 grade mix with 100% river sand (control mix), the mix AGMS25/20 refers to M20 grade concrete with 25% AGMS, the mix WGMS25/20 refers to M20 grade concrete with 25% WGMS and so on. The mixing was done using a PAN mixer, for the first 30 seconds, fine aggregate and coarse aggregates were mixed after which half the quantity of water was added. The mixing continued for

another 60 seconds till the aggregates absorbed the water, after this the powder content including cement and fly ash were added to the mixer and mixed for 60 seconds, at this stage the superplasticizer and VMA mixed with remaining water were added to the mixer and the entire mix was mixed for 180 seconds.

2.7.1 Fresh Properties

- Slump Flow Test

The slump flow test is one of the most widely used methods for evaluating the fluidity and filling capacity of concrete. Its simplicity and ease of application make it suitable for both laboratory and field conditions. In this test, an Abrams cone is placed on a non-absorptive surface and filled with fresh concrete without compaction. Upon lifting the cone, the concrete spreads under its own weight. The maximum diameter of the spread is measured in two perpendicular directions, and the average value is recorded. Additionally, the *T50 flow time*, which represents the time taken for the concrete to spread to a 50 cm diameter, is documented. IS 10262:2019 [24] provides guidelines on the typical range of slump flow values and their applications in concrete mix design.

- V-Funnel Test

The viscosity of self-compacting concrete (SCC) is evaluated using the V-funnel test, as specified in IS 1199 (Part 6) [27]. This test measures the time required for fresh concrete to flow through a V-shaped funnel, known as the *V-funnel flow time*. Concrete with lower viscosity exhibits a rapid initial flow before stopping, while higher-viscosity concrete may continue flowing gradually over time.
Based on flow time, viscosity is categorized into two classes: V1 and V2. V1-class concrete has superior filling ability, making it suitable for applications with congested reinforcement. It also exhibits self-levelling properties and provides an excellent surface finish. V2-class concrete, while beneficial in reducing formwork pressure and improving segregation resistance, may be prone to thixotropic effects, affecting surface finish and workability during placement.
The flow time for V1-class concrete should not exceed 8 seconds, whereas for V2-class concrete, it ranges between 8 and 25 seconds. A longer flow time indicates higher internal friction and lower flowability, while a very short flow time may suggest poor mix stability due to excessively low viscosity.

- L-box Test

The L-box test is conducted to evaluate the passing ability of self-compacting concrete (SCC). This test measures the concrete's ability to flow through confined spaces, such as reinforcement, without segregation or blocking. The minimum acceptable ratio of concrete depth in the horizontal section to that in the vertical section is 0.8, while a ratio of 1.0 indicates unrestricted flow, similar to that of water.

(a)

(b)

Fig. 3. (a) L-Box test (b) V-Funnel test

In this test, fresh concrete is placed in the vertical section of the L-box and allowed to rest for 60 seconds to account for potential segregation. Upon opening the gate, the concrete flows into the horizontal section, where rebar obstructions may be included to simulate reinforcement congestion. The parameters recorded include the descent of the sample head (*Ha*), which reflects the blocking tendency, the final depth at the far end (*Hi*), representing filling ability, and the time taken for the concrete to reach a specified flow distance, indicating its deformability.

According to EFNARC guidelines [26], the blocking ratio (*Ha/Hi*) is used to assess the mix's passing ability, with an acceptable range between 0.80 and 1.0.

2.7.2 Mechanical Properties

- Compressive Strength

The compressive strength test is a key indicator of concrete quality, providing insight into its overall performance. The test included casting of around 270 cubical specimen of 150 mm size in accordance with IS 516:1959 [28], for each mix proportion at a total of 10 specimen were cast and tested and their average values were recorded. The cubes were removed from the mold after 48 hours and cured for a period of 28 days, before testing them under compression testing machine.

- Tensile Strength

The split tensile strength test is a reliable means of assessing concrete tensile failure resistance in structural members being subjected to tensile failure. It is an indirect method for determining concrete tensile capacity by the split tensile strength test conducted in adherence to IS 516:1959 [28]. In this test, a cylindrical specimen with 300 mm x 150 mm dimensions is loaded axially in compression where tensile stresses are generated perpendicular to the impact force. For this test a total of 270 cylindrical specimen, were cast and tested. For each mix proportion 10 specimen were tested and their average values were recorded. It is one of the important tests which are used to assess concrete durability, predict cracking behavior and enhance structural resilience.

(a) (b)

Fig. 4. (a) Compressive strength test (b) Split Tensile Strength

2.7.3 Durability Properties

- Water Absorption

A total of 270 cubical specimen (10 for each mix proportion) of 150 mm size were cast to determine saturated water absorption test at 56 days in accordance to ASTM C642 standards [29]. First of all, specimens were weighed in their initial state and then dried at 105°C for 24 hours in a hot air oven followed by drying until mass difference between two successive measurement made 24 hours apart was constant. After maintaining a constant dry weight, specimens were then cooled to room temperature and placed in potable water. At regular intervals, specimens were removed, surface

dried over a clean cloth, and weighed. The specimen remained in this manner till it was saturated fully. All the specimen were then oven dried and the saturated weight was measured, calculation of the percentage water absorption from Eq. 1 was then conducted.

$$\% \, Water \, absorption = \frac{(Ws - Wd)}{Wd} \; x \, 100 \tag{1}$$

Where, W_s = weight of specimen at fully saturated condition, and W_d = weight of oven dried specimen.

- Porosity

Saturated water absorption is closely linked to the effective porosity, which quantifies the interconnected voids within the concrete matrix. Effective porosity (%) can be calculated using Eq. (2), after measuring the submerged weight of the specimen, in accordance to ASTM C642 standards [29].

$$Effective \, porosity, \, n = \frac{(w_s - w_d)}{(w_s - w_{sub})} \, x \, 100 \tag{2}$$

Where, W_{sub} = submerged weight of the specimen

- Rapid Chloride Penetration Test

The entry of chloride ions stands as a main factor that triggers reinforcing steel corrosion which results in damage to concrete structures such as bridges and parking lots as well as marine structures and industrial infrastructure. Millions of dollars annually represent the total repair expenses from corrosion damage. Uncracked concrete allows chlorides to enter through capillary absorption and hydrostatic pressure and diffusion and evaporative transport but diffusion shows the strongest effect. The migration of ions occurs from concrete interior to reinforcement when chloride concentration in the exterior surpasses the interior. These environmental conditions consisting of moisture and oxygen and cyclic wetting followed by drying processes speed up steel corrosion. The penetration speed of chloride depends on concrete pore structure that results from mix design and curing conditions and hydration and construction methods. Measuring chloride permeability requires 60V DC to flow through concrete samples with dimensions of 100 mm diameter and 50 mm thickness for a period of six hours with one end submerged in 0.3M NaOH and the other end in 3.0% NaCl solution as per ASTM C1202 [30]. The amount of electrical charge passed during testing enables reliable assessment of concrete permeability along with durability indicators. In this study a total of 45 specimen were tested and the results have been recorded and discussed.

- Water Permeability

The water permeability test is a critical assessment of concrete's durability, particularly its resistance to water ingress under pressure. This test provides insight into the pore structure and overall quality of the concrete matrix, which directly influences long-term performance in aggressive environmental conditions. For this study, a total of 108 concrete cubes of 150 mm size were used in accordance with DIN 1048 Part 5 [31], which outlines the procedure for determining the depth of water penetration under pressure. The test involves subjecting one face of the cube to water pressure (typically 5 bar) for a specified duration, after which the specimen is split to measure the maximum depth of water penetration. This method is widely accepted for evaluating the permeability and densification of concrete, especially in high-performance and self-compacting concretes.

- Acid Attack

Concrete is highly susceptible to acid attack due to its alkaline nature. When exposed to acidic environments, the cementitious matrix undergoes chemical disintegration, primarily through the dissolution of calcium hydroxide ($Ca(OH)_2$). The extent of degradation depends on concrete porosity, acid concentration, solubility of calcium salt, and the transport of acidic solutions through interconnected voids and cracks. Sulfuric acid (H_2SO_4) is particularly aggressive, as it induces both acidic and sulphate attacks, significantly compromising concrete integrity. Acidic solutions with pH<7 contain a high concentration of hydrogen ions (H^+), accelerating chemical degradation.

Groundwater contamination from industrial effluents containing sulfuric, hydrochloric, and nitric acids can severely impact concrete substructures, such as foundations, basements, and trenches. Additionally, marine environments and chemical storage structures are frequently exposed to aggressive acidic conditions, leading to progressive deterioration, loss of strength, and structural failure. The impact of acid attack was evaluated by immersing 162 concrete cubes of 150 mm size in 2% and 5% sulfuric acid (H_2SO_4) solution as per ASTM C1898 – 2000 [32]. Following acid exposure for 56 days, changes in weight and compressive strength were assessed to determine deterioration levels. This study provides insights into the resistance of concrete to acidic environments, which is crucial for ensuring the durability and service life of concrete structures in chemically aggressive conditions.

- Sulphate attack

Sulphate attack represents a major threat to concrete structures which exist in areas with sulphate presence from groundwater and soil or seawater. Sulphate materials originating from agricultural draining water and ocean water cause external sulphate attack on the structure. In sulphate-rich regions, such as coastal and semi-arid areas, effective mix design is essential for durability. To evaluate sulphate resistance, 81 number of concrete cubes of 150 m size, were first cured in water for 28 days, followed by 56 days of immersion in 5% magnesium sulphate ($MgSO_4$) solution as per ASTM C1898 – 2000 [32]. Changes in mass and compressive strength were analyzed to assess deterioration in comparison to water-cured specimens, providing insights into sulphate resistance in aggressive environments.

- Bond strength

The bond strength between concrete and reinforcement bars is a critical parameter influencing the structural performance and serviceability of reinforced concrete elements. The bond between concrete and reinforcement, ensures a composite action facilitating effective stress transfer and crack control under loading.

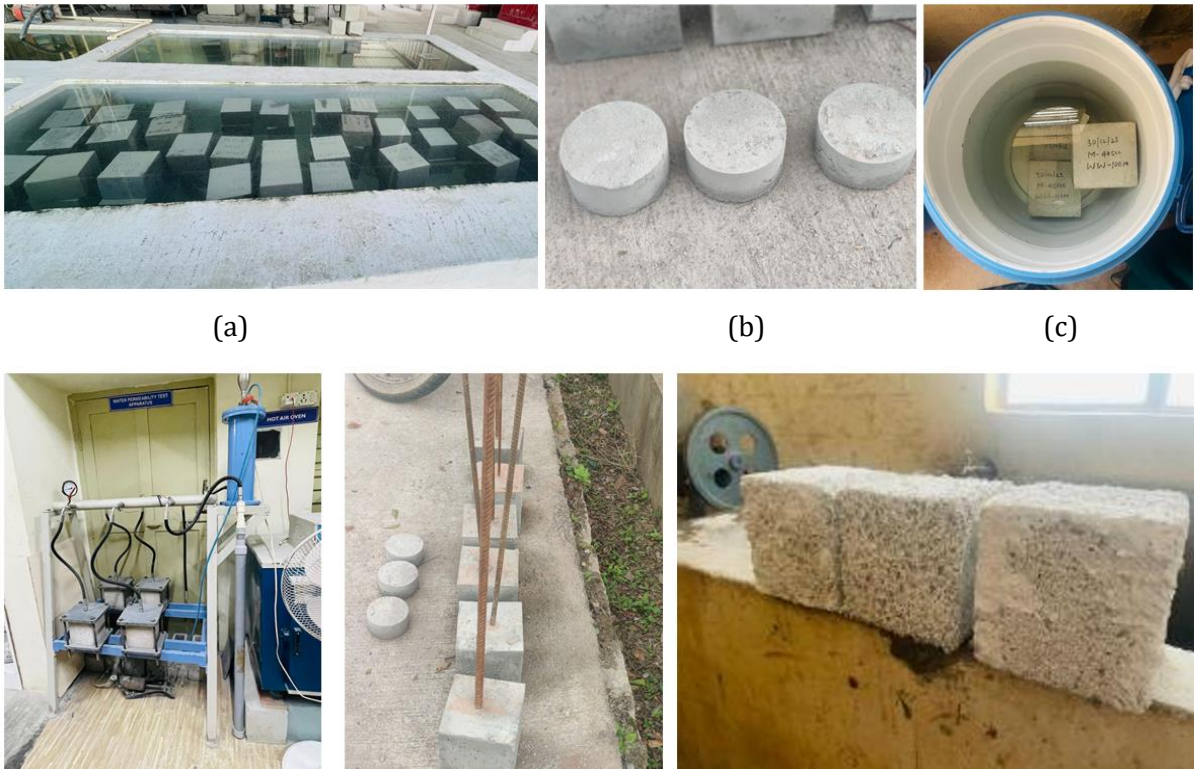

(a) (b) (c)

(d) (e) (f)

Fig. 5. (a) Curing of specimen (b) specimen for RCPT (c) specimen immersed in magnesium sulphate solution (d) specimen subjected to water permeability test (e) bond strength specimen (f) specimen after exposure to acid attack

The present study investigates the bond behavior of reinforcement bars of diameters 10 mm, 12 mm, 16 mm, 20 mm, and 25 mm embedded in 150 mm cubical specimen of SCC made with RS, AGMS and WGMS. A total of 45 specimen were cast and tested in accordance with IS:2770 (Part-I) [33]. The pull-out test method, a widely accepted technique for evaluating bond strength, is used to assess the interaction between the concrete matrix and the embedded steel bars. The test measures the maximum load resisted before slippage, offering insights into the adhesion, friction, and mechanical interlock characteristics governing bond performance. By varying the diameter of the reinforcement bars and the type of fine aggregate used in SCC, the study aims to identify trends and potential improvements in bond strength, with implications for the durability and efficiency of reinforced concrete structures.

3. Results and discussions

3.1. Slump Flow Test

The slump flow values for all mixes, ranging across M20, M40, and M70 grades incorporating various fine aggregate types, are shown in Fig. 6. As per EFNARC guidelines [26], self-compacting concrete should exhibit a slump flow in the range of 650–800 mm to ensure adequate filling ability without segregation. All the mixes tested fall within this permissible range, confirming their suitability as SCC.

Across all grades, AGMS consistently produced the highest slump flows, supporting its role in enhancing SCC workability. WGMS, while suitable, resulted in comparatively lower slump values, likely due to its higher angularity and less favorable gradation. River sand performed well but did not match AGMS in terms of flow enhancement, especially at higher grades.

All recorded values satisfy EFNARC criteria [26], validating the mix designs. The findings confirm that air-graded manufactured sand (AGMS) offers an optimal balance of grading, shape, and packing, making it a highly viable replacement for natural sand in SCC, especially when consistent workability is essential.

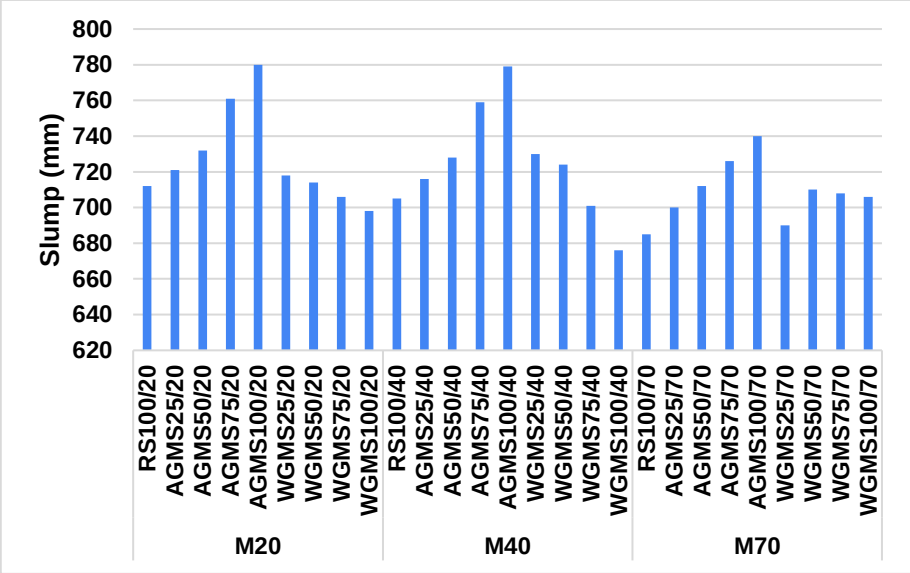

Fig. 6. Slump value for M20, M40 and M70 grade SCC using RS, AGMS ad WGMS

3.2. T50 Slump Flow Test

The T50 slump flow test provides insight into the viscosity and flow rate of self-compacting concrete (SCC). It measures the time (in seconds) taken for the concrete to spread to a 500 mm diameter during the slump flow test. As per EFNARC guidelines [26], acceptable T50 values for SCC typically range from 2 to 5 seconds, where lower times reflect faster flow (lower viscosity) and higher times indicate increased viscosity and resistance to flow. All mixes complied with EFNARC's

T50 limits (2–5 sec), indicating acceptable viscosity and suitability for SCC applications. AGMS at lower replacement levels consistently reduced T50 times, promoting faster flow and better placement ability. WGMS increased viscosity at higher replacement ratios, likely due to angularity and higher water demand. RS-based mixes demonstrated moderate and stable T50 times, serving as a benchmark for comparison. These results confirm that the type and proportion of fine aggregates significantly influence the flow rate and viscosity of SCC. AGMS, emerged as the most favorable for achieving a desirable balance between workability and flow resistance.

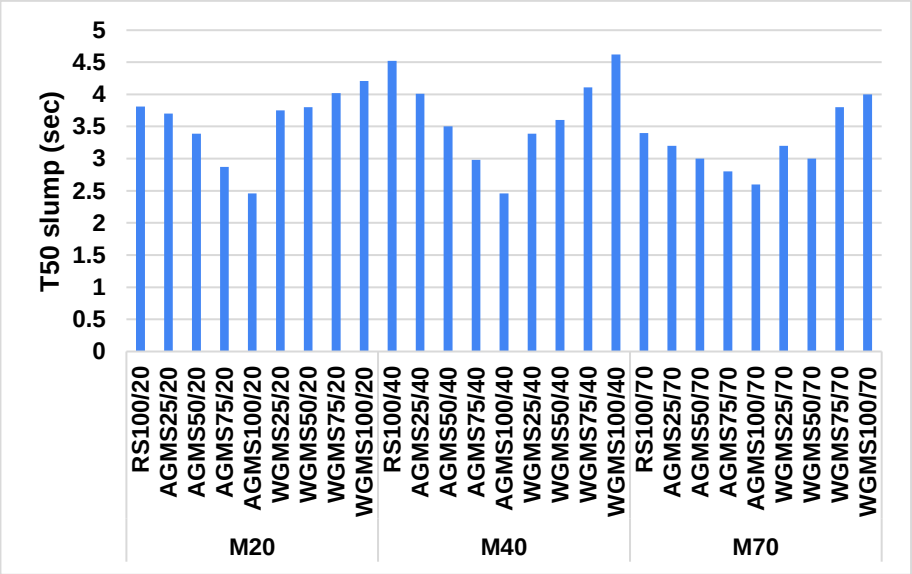

Fig. 7. T50 Slump for M20, M40 and M70 grade SCC using RS, AGMS ad WGMS

3.3. V-Funnel Test

The V-funnel test measures the viscosity and filling ability of SCC, with flow times between 6 to 12 seconds considered satisfactory as per EFNARC guidelines [26]. Higher values indicate greater viscosity and potential risk of blockage, while lower values suggest better flowability. Across all grades, SCC with AGMS recorded the lowest flow time, indicating enhanced flow due to improved particle packing. In contrast, SCC with 75% WGMS showed longer flow times, reflecting increased viscosity at higher replacement levels indicating slightly higher resistance to flow. These findings highlight the influence of sand type and replacement level on the viscosity of SCC, with AGMS mixes offering an optimal balance between flowability and stability.

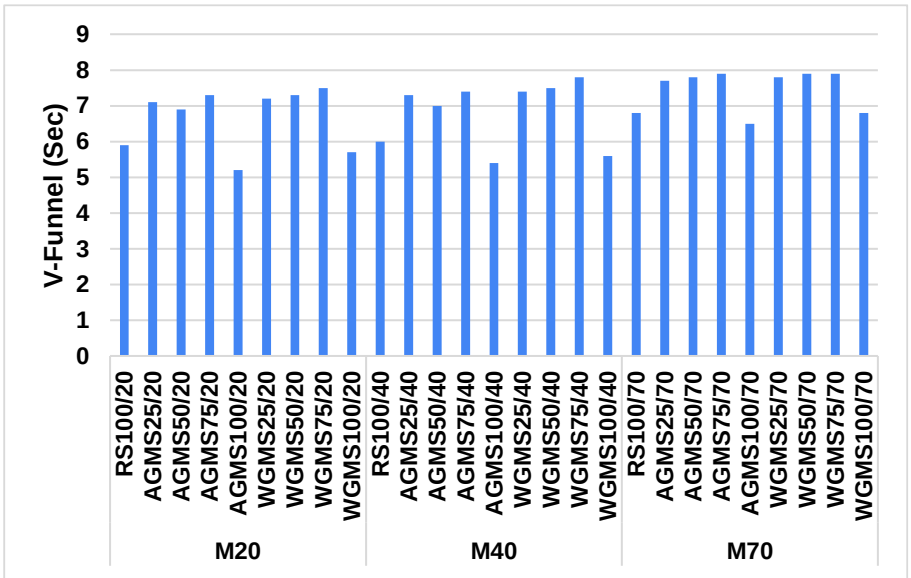

Fig. 8. V-Funnel test for M20, M40 and M70 grade SCC using RS, AGMS ad WGMS

3.4. L-Box Ratio

The L-box test evaluates the passing ability of self-compacting concrete, crucial in determining its suitability for heavily reinforced sections. According to EFNARC [26] and IS: 10262-2019 [24] recommendations, an L-box ratio (H2/H1) between 0.8 and 1.0 is considered acceptable for SCC, indicating good passing ability without segregation or blockage. Across all the grades of SCC, all variants, including those with RS, AGMS, and WGMS, showed L-box ratios between 0.80 and 0.95, fulfilling standard limits. Mixes with AGMS exhibited slightly higher ratios, indicating superior passing ability, likely due to better grading and particle shape compared to RS and WGMS. Overall, the results affirm that replacement of RS with AGMS offers enhanced passing ability while maintaining compliance with SCC workability criteria. WGMS, although viable, may require finer tuning of mix proportions or the use of viscosity modifying admixtures (VMAs) at higher replacement levels to match the performance of AGMS.

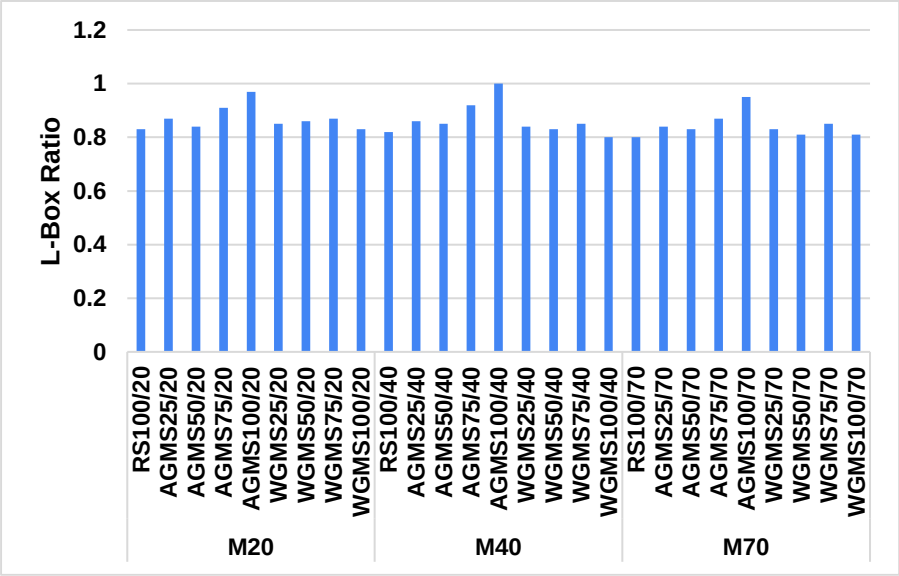

Fig. 9. L-Box Ratio for M20, M40 and M70 grade SCC using RS, AGMS ad WGMS

3.5. Compressive Strength

The compressive strength of M20 grade concrete containing air-graded M-sand increases according to replacement percentage with the strongest results achieved from 100% replacement. An escalation of compressive strength appears across M40 grade concrete as the replacement percentages rise beyond 75% and reach 100%. According to M70 grade concrete results the compressive strength exhibits stable values and reaches its peak level at 100% replacement since air-graded sand functions effectively in high-strength SCC mixes. The strength measures for M20 grade concrete achieve higher values through M-sand replacement taking place by wet grading even though the collected data remains lower than the testing results from air grading.

The M40 grade concrete shows a steady strength growth but the growth rate remains lower when compared to air-graded sand. In M70 grade concrete, strength remains high across all replacement levels, with 100% replacement producing nearly equal strength as natural river sand, indicating the suitability of wet-graded sand for high-strength SCC. Air-graded sand shows a more pronounced increase in compressive strength across all replacement levels, particularly in medium- and high-strength SCC mixes. Wet-graded sand demonstrates a steady but slightly lower strength gain compared to air-graded sand, though it remains suitable for high-performance SCC applications. At higher replacement percentages (75% and 100%), both sands yield comparable results in high-strength mixes (M70), confirming the viability of manufactured sand as a sustainable alternative to river sand. The compressive strength of SCC improves with increasing replacement of river sand with manufactured sand, with air-graded sand demonstrating a greater strength enhancement compared to wet-graded sand. In high-strength SCC (M70), both types of

manufactured sand perform effectively, making them suitable replacements for river sand. Proper mix design adjustments are necessary to optimize the use of manufactured sand in different strength grades of SCC.

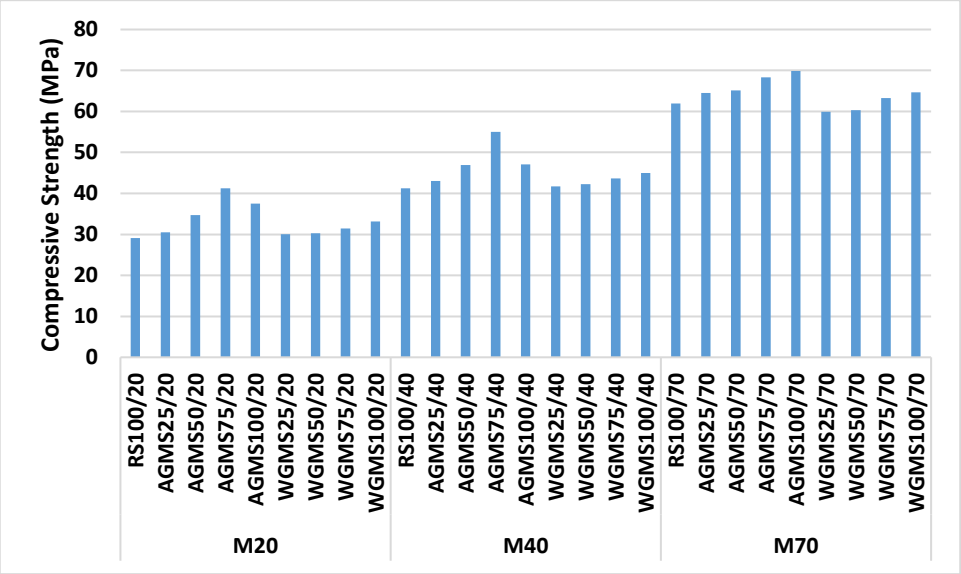

Fig. 10. Compressive Strength of M20, M40 and M70 grade SCC with RS, AGMS and WGMS

3.6. Split Tensile Strength

The Tensile Strength Test was conducted on Self-Compacting Concrete (SCC) incorporating air-graded and wet-graded manufactured sand as a partial and full replacement for river sand. The analysis covers different mix grades: M20, M40, and M70, with replacement percentages of 0%, 25%, 50%, 75%, and 100%. Tests indicate that tension strength progressively rises as replacement levels increase in M20 grade concrete with air-graded M-sand reaching its maximum at full substitution. M40 grade concrete tests revealed that tensile properties increase when more replacement occurs until maximum values occur at total replacement of standard sand by air-graded sand. The effectiveness of air-graded sand for high-strength SCC remains high in M70 grade concrete because tensile strength remains consistent between 75% and 100% replacement levels.

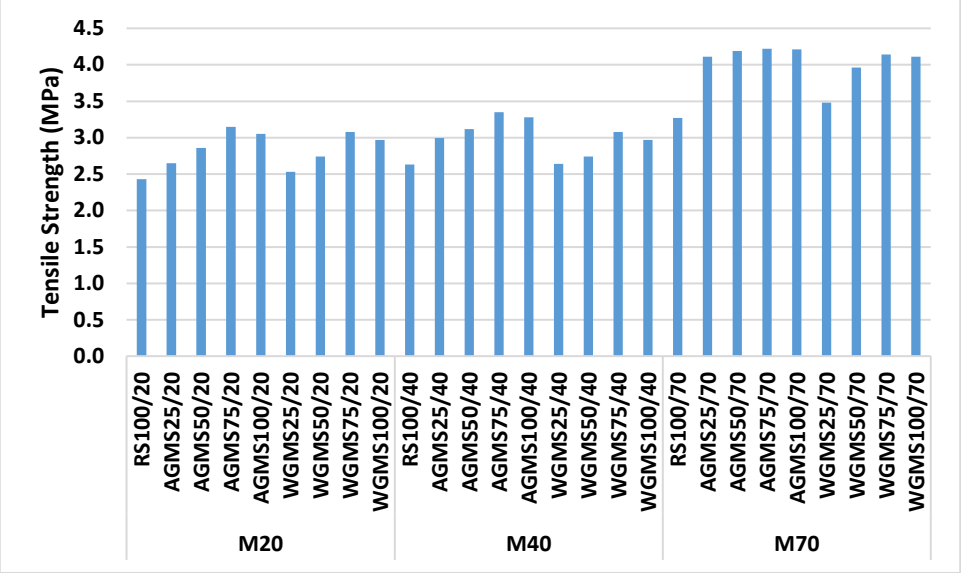

Fig. 11. Tensile Strength of M20, M40 and M70 grade SCC with RS, AGMS and WGMS

Wet-graded M-sand used to make M20 grade concrete leads to rising strength values at each replacement fraction yet produces weaker outcomes than air-graded sand. The strength values in M40 grade concrete show a growing trend until they reach substantial heights starting at a 50% replacement threshold. When used as a substitute in M70 grade concrete the measurements of tensile strength match those from air-graded sand particularly at 75% and 100% replacement levels which establishes its use for high-strength SCC applications.

Air-graded sand exhibits a more pronounced increase in tensile strength across all replacement levels, particularly in medium- and high-strength SCC mixes. Wet-graded sand shows a steady but slightly lower strength gain, though at higher grades (M70), both sands yield nearly identical performance. At 100% replacement, both types of sand achieve optimal tensile strength, demonstrating their potential as sustainable alternatives to river sand. The tensile strength of SCC increases with the replacement of river sand by manufactured sand, with air-graded sand demonstrating slightly superior strength properties compared to wet-graded sand. However, both sands perform effectively at higher grades (M70), making them viable options for SCC production. The results indicate that manufactured sand can be a sustainable substitute for river sand, provided proper mix proportioning and quality control measures are implemented.

3.7. Water Absorption

The water absorption in SCC with air-graded M-sand remains the lowest when compared to the other three sand options. The concrete grade shows a direct correlation with decreasing values of water absorption. Better packing of particles along with decreased porosity characterizes the SCC material according to the lower water absorption readings. The water absorption levels in SCC that uses wet-graded M-sand exceed the values from air-graded M-sand while remaining under river sand absorption. Water absorption shows a declining behavior when concrete grades become higher. Water adsorption levels of air-graded sand are less than those of air-graded sand because of the distinct surface characteristics along with shape.

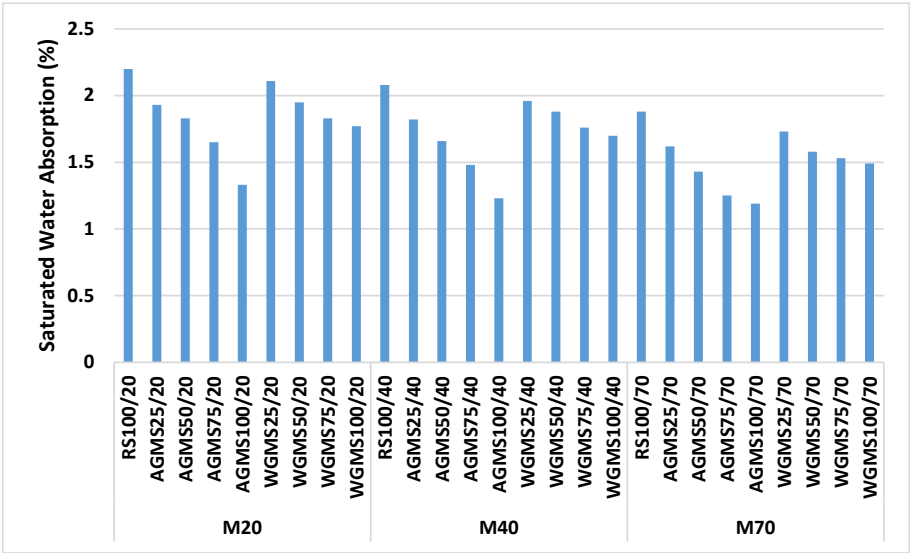

Fig. 12. Water Absorption of M20, M40 and M70 grade SCC with RS, AGMS and WGMS

The highest amount of water absorption exists in SCC manufactured with river sand throughout all concrete grades. Higher absorption values demonstrate both increased material porosity and higher water requirement and could possibly degrade mix workability. The water absorption capability of manufactured sand (whether air-graded or wet-graded) proves to be lower than river sand because manufactured sand shows denser particle packing structures that result in lower porosity in SCC. Air-graded M-sand demonstrates the most efficient water absorption capability because its surface appears smooth and features optimal gradation thus improving the durability of SCC. Wet-graded M-sand has acceptable water absorption levels that open doors to becoming an adequate river sand replacement if mix ratios are adjusted correctly. The water-absorption

capabilities decrease as concrete grade levels increase from M20 to M70 because higher-strength mixes maintain better compaction and possess fewer voids. Air-graded manufactured sand demonstrates maximum efficiency in replacing river sand as an SCC component while wet-graded sand remains a viable alternative for river sand substitution.

3.8. Porosity

Air-graded M-sand concrete exhibits the most compact porosity than any other sand type. Concrete grade has a direct relation to lower porosity values in the material structure. Better durability results from the denser microstructure which achieves optimal particle packing. The porosity of concrete made with wet-graded M-sand demonstrates slightly higher results than air-graded M-sand but remains lower than river sand. The concrete grade increase leads to decreasing values in the examinations. Drastic reduction in porosity exists at higher concrete strengths because it indicates improved aggregate compaction and better contact between aggregates. Steel-fiber-reinforced concrete with river sand possesses the largest interconnected void spaces when comparing all strength levels. Additional voids in SCC affect the durability and strength potential negatively. The low porosity results achieved by air-graded M-sand demonstrates the effectiveness of its better gradation and shape characteristics along with packing efficiency for enhancing SCC mechanical properties. The porosity results of wet-graded M-sand suggest it can replace river sand in concrete as long as the concrete mixture requires small changes during design. The highest porosity observed in river sand leads to inferior SCC durability because of increased permeability. Higher concrete grades lead to lower porosity values that result in better compacted denser concrete because of strong aggregate bonding. The most potent approach to reduce porosity involves air-graded M-sand followed by wet-graded M-sand which makes them suitable alternative options to river sand in SCC applications.

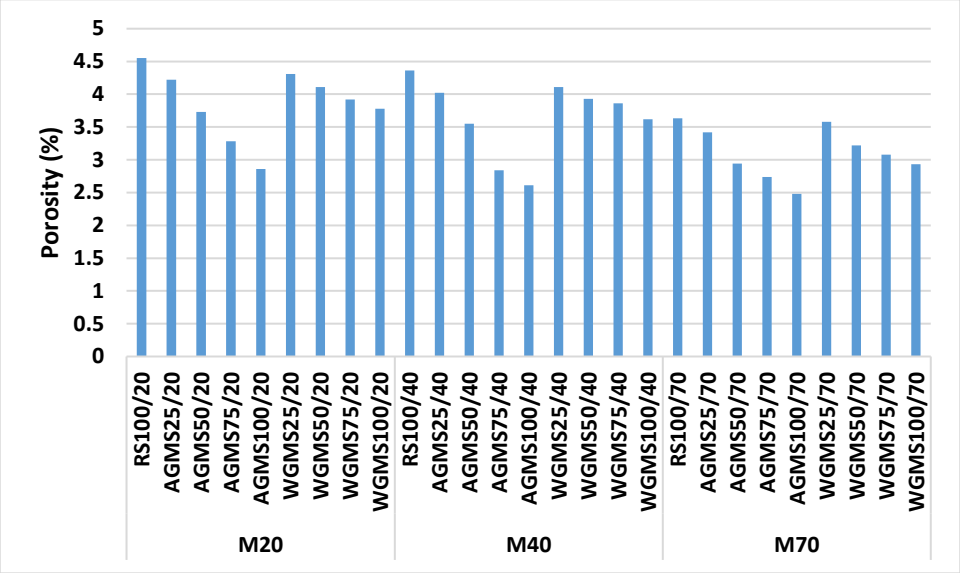

Fig. 13. Porosity of M20, M40 and M70 grade SCC with RS, AGMS and WGMS

3.9. Rapid Chloride Penetration Test

A consistent trend is observed across all grades: as the percentage replacement of river sand with either AGMS or WGMS increases, the charge passed tends to decrease, indicating reduced chloride ion permeability and, consequently, improved durability. This trend is more pronounced in higher-grade mixes, where the total charge passed significantly reduces with increased substitution of natural sand, especially with AGMS.

In the M20 grade mixes, the SCC with 100% river sand exhibits the highest charge passed, exceeding 2400 Coulombs, indicative of high permeability. However, with a complete replacement using AGMS, the charge passed reduces to below 1500 Coulombs, marking a transition from high

to moderate permeability. The effect of WGMS replacement is also beneficial, though slightly less effective than AGMS, with the charge passed nearing 1600-1700 Coulombs at 100% replacement.

In M40 SCC, the mix AGMS100/40 brings the charge passed well below 1200 Coulombs, falling within the low permeability category. WGMS also shows consistent improvement over river sand, although its performance remains marginally inferior to AGMS at each replacement level.

The M70 mixes demonstrate superior performance overall. Even at 100% river sand, the charge passed remains within a relatively low range, suggesting that the dense matrix of high-grade SCC inherently contributes to reduced permeability. However, with increasing proportions of WGMS and AGMS, particularly at 100%, the charge passed dips below 1000 Coulombs, indicating very low permeability. AGMS again shows marginally better performance than WGMS, reinforcing its suitability as a sustainable and durable replacement for river sand.

Overall, the study illustrates that both air-graded and wet-graded manufactured sands significantly enhance the resistance of SCC to chloride ion penetration across all strength grades. AGMS demonstrates superior performance, likely due to better particle grading and reduced fines content, which contribute to a denser microstructure. This finding supports the potential of AGMS and WGMS as effective alternatives to river sand, aligning with sustainability and durability requirements in modern concrete design.

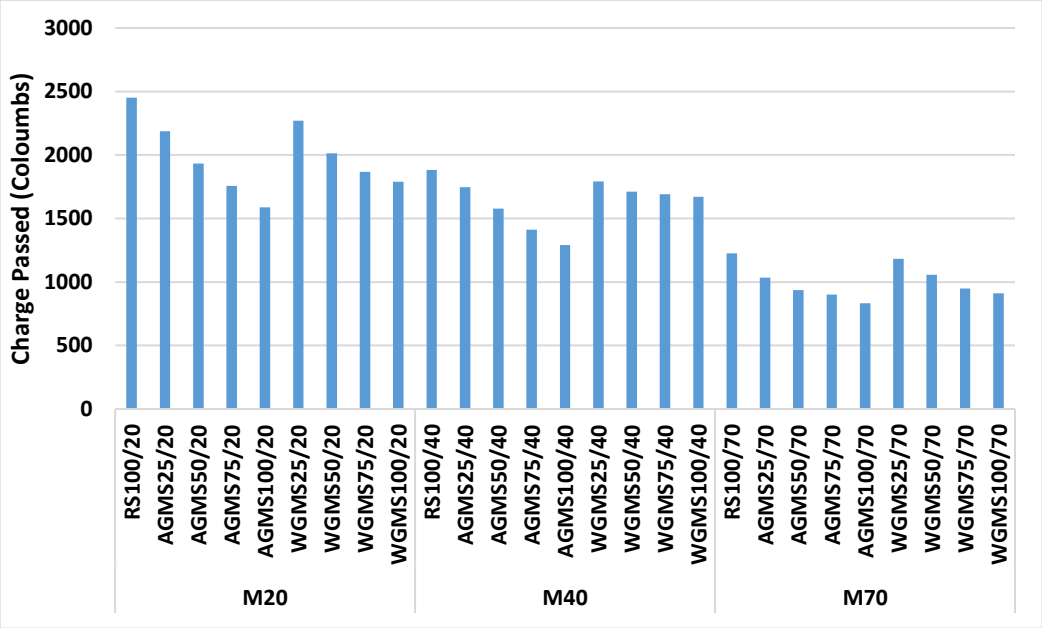

Fig. 14. RCPT values of M20, M40 and M70 grade SCC with RS, AGMS and WGMS

3.10. Water Permeability

The graph presents the water permeability depth (mm) of self-compacting concrete (SCC) of varying grades (M20, M40, M70) incorporating RS, AGMS, and WGMS. The results indicate a clear trend of decreasing water permeability with the incorporation of AGMS and WGMS, in comparison to RS, across all concrete grades.

For M20 grade SCC, the highest permeability depth (~22 mm) is observed in the mix with RS100/20, indicating greater porosity and lower resistance to water penetration. Mixes incorporating AGMS and WGMS, particularly at higher replacement levels (AGMS100/20 and WGMS100/20), show a marked reduction in permeability, suggesting improved pore structure and densification. WGMS mixes, especially, exhibit the lowest permeability values in M20, implying enhanced microstructural refinement due to the finer and possibly more reactive ceramic particles.

In the case of M40 grade SCC, a general improvement in permeability resistance is observed compared to M20. RS100/40 again shows the highest water permeability (~21 mm), whereas mixes with AGMS and WGMS demonstrate significantly reduced permeability values.

WGMS100/40 shows a permeability depth below 15 mm, indicating superior durability characteristics. The results affirm that higher grade concretes benefit more from the inclusion of alternative sands, likely due to better matrix packing and pozzolanic activity.

For M70 grade SCC, the trend continues, with the lowest permeability values recorded overall. The RS100/70 mix still shows the highest permeability within the M70 series, but all AGMS and WGMS mixes display further reduction, with WGMS100/70 achieving the lowest value (~12 mm). This suggests that the ultra-high strength matrix of M70 enhances the benefits offered by ceramic sand incorporation, leading to denser, less permeable concrete.

Overall, the data clearly supports the assertion that substituting RS with AGMS and WGMS significantly improves water impermeability in SCC, particularly at higher grades and higher replacement levels. WGMS consistently outperforms AGMS and RS, indicating its potential as a sustainable and performance-enhancing fine aggregate in durable SCC production.

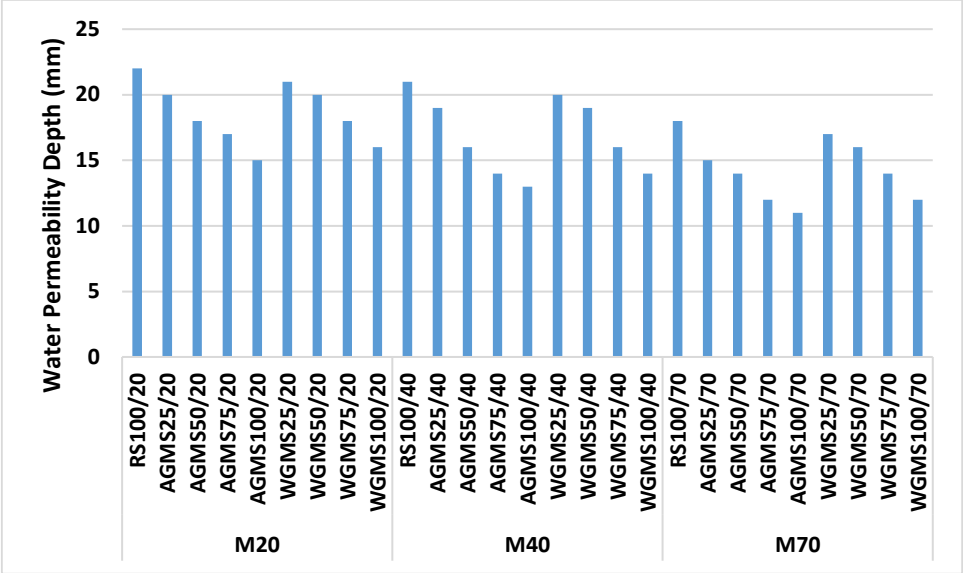

Fig. 15. Water Permeability Depth of M20, M40 and M70 grade SCC with RS, AGMS and WGMS

3.11. Acid Attack

The bar graphs depict the percentage loss in strength and weight of self-compacting concrete (SCC) subjected to sulfuric acid (H_2SO_4) attack at 2% and 5% dilution levels. The strength loss measurement revealed its highest value in RS-based concrete surpassed WGMS-based and AGMS-based SCC. Higher concrete grades went from M20 to M70 which improved the resistance to acid attack by causing reduced strength degradation. All mixes experienced higher strength deterioration when subjected to 5% acid dilution as opposed to 2% acid dilution. Among the different mixtures AGMS based SCC demonstrated maximum resistance to acid deterioration because of its reduced strength loss properties.

Weight loss data tracked strength loss patterns where RS had the highest amount of deterioration but AGMS demonstrated the least impact. The strength level of M70 SCC achieved higher acid resistance as validated by its minimal weight reduction. The 5% diluted acid solution caused stronger material degradation than the 2% diluted acid solution thus leading to increased weight loss. AGMS based SCC exhibits a lower weight loss ratio thus proving its capacity to withstand acid deterioration effectively. The strength reduction together with weight loss appear lower within concrete mixes containing AGMS thus demonstrating this material's proper application within harsh environments. Concrete of higher grade (M70) demonstrates improved durability through which it becomes the optimal solution for situations that tend to become acidic.

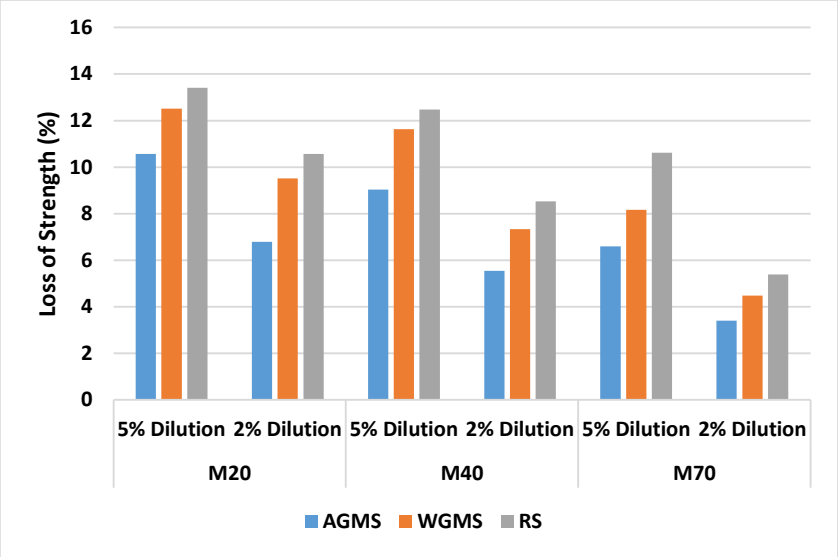

Fig. 16. Loss of strength due to acid attack of M20, M40 and M70 grade SCC with RS, AGMS and WGMS

Table 6. Values of Initial and final weight and strength of acid attack

	Mix Proportions	Weight Initial weight	Weight Final Weight	Percentage Loss	Compressive Strength Initial Strength	Compressive Strength Final Strength	Compressive Strength % Loss in Strength
5% Dilution of H_2SO_4	AGMS100/20	8.12	7.55	7.02	38.09	34.06	10.56
	WGMS100/20	7.53	6.85	9.07	33.32	29.15	12.51
	RS100/20	7.23	6.48	10.42	22.51	19.49	13.40
	AGMS100/40	8.19	7.67	6.35	46.97	42.73	9.04
	WGMS100/40	7.64	7.06	7.55	44.24	39.10	11.63
	RS100/40	7.41	6.79	8.37	32.23	28.20	12.48
	AGMS100/70	8.54	8.07	5.50	69.39	64.82	6.59
	WGMS100/70	8.23	7.65	6.97	64.14	58.90	8.17
	RS100/70	8.12	7.52	7.35	62.45	55.81	10.62
2% Dilution of H_2SO_4	AGMS100/20	8.12	7.78	4.27	38.09	35.50	6.79
	WGMS100/20	7.53	7.13	5.31	33.32	30.15	9.51
	RS100/20	7.23	6.78	6.22	22.51	20.13	10.57
	AGMS100/40	8.19	7.89	3.70	46.97	44.37	5.55
	WGMS100/40	7.64	7.27	4.84	44.24	41.00	7.33
	RS100/40	7.41	7.02	5.22	32.23	29.48	8.54
	AGMS100/70	8.54	8.32	2.54	69.39	67.03	3.41
	WGMS100/70	8.23	7.96	3.24	64.14	61.27	4.48
	RS100/70	8.12	7.73	4.80	62.45	59.08	5.39

The higher resistance to acid attack by SCC with AGMS may be due to its well-graded, angular, and rough-textured particles which enhances particle interlocking and paste-aggregate bonding, reducing capillary porosity. A denser microstructure minimizes acid ingress, which is key to resisting chemical attack. The specimens exhibited surface erosion, discoloration, and in some cases, softening of edges. Progressive exfoliation and minor surface pitting were evident. No deep or structural cracking was observed; however, micro-cracking was noticed in a few specimens upon close inspection.

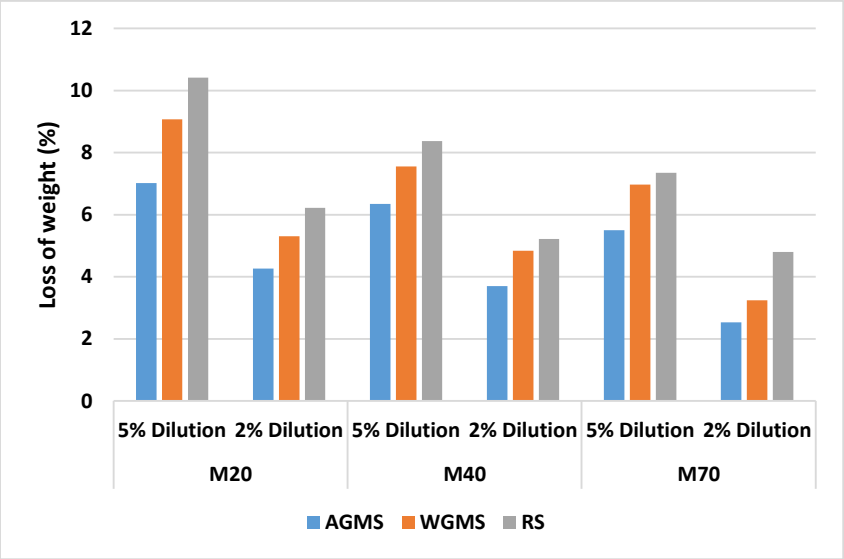

Fig. 17. Loss of weight due to acid attack of M20, M40 and M70 grade SCC with RS, AGMS and WGMS

3.12. Sulphate Attack

The bar graph presents the percentage loss in strength and weight of self-compacting concrete (SCC) subjected to a 5% magnesium sulphate ($MgSO_4$) solution. The SCC containing river sand exhibited maximum weight loss which demonstrated its highest sensitivity to sulphate deterioration. AGMS-based SCC exhibited the minimum weight loss indicating strong sulphate resistance properties. Higher concrete strength levels resulted in better resistance towards sulphate attack which caused weight loss to decrease until the M70 grade exhibited the lowest level of degradation. SCC based on RS showed the maximum strength reduction among all three concrete types tested which was higher than both WGMS and AGMS based samples. Concrete containing AGMS developed minimum strength reduction which confirms AGMS as the most effective material for resisting sulphate attacks.

Table 7. Values of Initial and final weight and strength of sulphate attack

	Weight			Compressive Strength		
	Initial weight	Final Weight	Percentage Loss	Initial Strength	Final Strength	% Loss in Strength
AGMS100/20	8.13	7.93	2.42	37.37	36.08	3.45
WGMS100/20	7.52	7.21	4.17	33.92	32.23	4.98
RS100/20	7.23	6.91	4.43	23.28	20.76	10.85
AGMS100/40	8.19	8.07	1.51	46.97	45.58	2.97
WGMS100/40	7.76	7.52	3.09	44.07	42.38	3.82
RS100/40	7.23	6.96	3.78	31.90	29.16	8.58
AGMS100/70	8.52	8.43	1.06	69.01	67.87	1.66
WGMS100/70	8.22	8.06	1.87	64.71	62.85	2.87
RS100/70	8.13	7.93	2.54	62.12	58.30	6.14

The specimens subjected to sulphate exposure showed signs of surface scaling, minor cracking, and white crystalline deposits (efflorescence) due to sulphate salts. Slight swelling were observed, especially in mixes with higher water-cement ratios, though precise measurements were not taken in this study. Research outcomes demonstrate that specimens utilizing AGMS as a mix ingredient maintain superior magnesium sulphate resistance when compared to concrete made with WGMS and RS. This may be due to better particle packing resulting in a denser microstructure in AGMS as compared to WGMS and RS. The combination of higher concrete strength grades M70 leads to better resistance against sulphate attack since it exhibits minimal weight and strength

deterioration. The utilization of AGMS as a component in SCC makes this concrete mixture a suitable choice for sulphate-rich areas because it produces outstanding deterioration reduction.

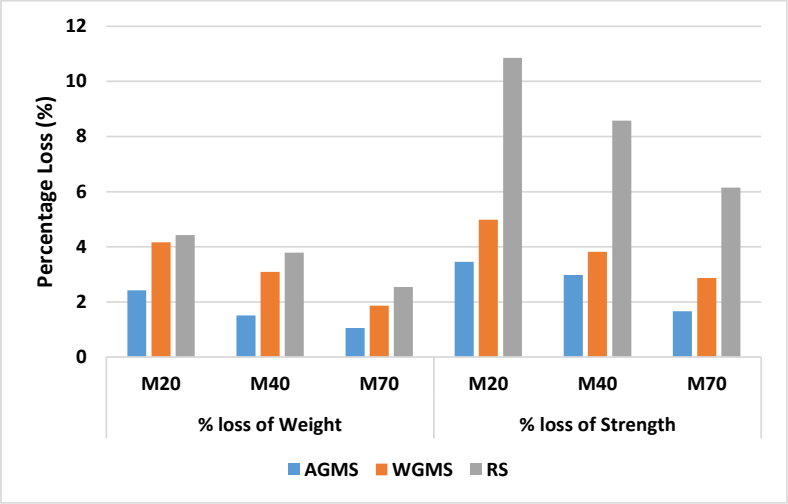

Fig. 18. Loss of weight and strength due to sulphate attack of M20, M40 and M70 grade SCC with RS, AGMS and WGMS

3.13. Correlation Between RCPT, Water Absorption and Porosity

Fig 19. and Fig. 20. represent, MATLAB generated plots correlating Porosity vs RCPT and Water Absorption vs RCPT for M20, M40, and M70 SCC using 2nd-degree polynomial fits. For all grades, both porosity and water absorption exhibit a positive polynomial relationship with RCPT values. The use of a second-degree polynomial provides a superior fit over linear models, effectively capturing the curvature in the data at lower porosity or absorption levels where RCPT reduction becomes more gradual. In M20 SCC, A stronger curvature is observed in both WA–RCPT and PO–RCPT plots, higher water absorption and porosity correspond to significantly increased RCPT, indicating higher ion permeability, which implies that lower-grade SCC is more sensitive to microstructural changes. In M40 SCC, the correlation remains strong, with a clear parabolic relationship, both AGMS and WGMS series show similar trends, though WGMS tends to exhibit slightly higher RCPT for the same water absorption and porosity value. In M70 SCC, the plots show a flattening of the RCPT curve with decreasing water absorption and porosity, this grade demonstrates superior durability, as even marginal reductions in porosity lead to significant reductions in RCPT, the R^2 values are consistently high (exceeding 0.95), confirming the reliability of the polynomial fit. Both water absorption and porosity are indirect indicators of pore connectivity and permeability.

The strong correlation with RCPT demonstrates that reduced capillary porosity significantly impedes chloride ingress. The trend is more pronounced in AGMS, suggesting that the addition of active mineral constituents enhances durability more effectively than conventional methods. The method used for grading manufactured sand creates significant effects on the transportation behavior of SCC before it reaches its medium strength peak. Water absorption together with porosity measure RCPT performance well but processing methods applied to manufactured sand matter most for low-strength SCC concrete designs. The choice of sand for concrete construction requires thorough attention when durability is a key requirement in concrete mixtures with medium to low strength.

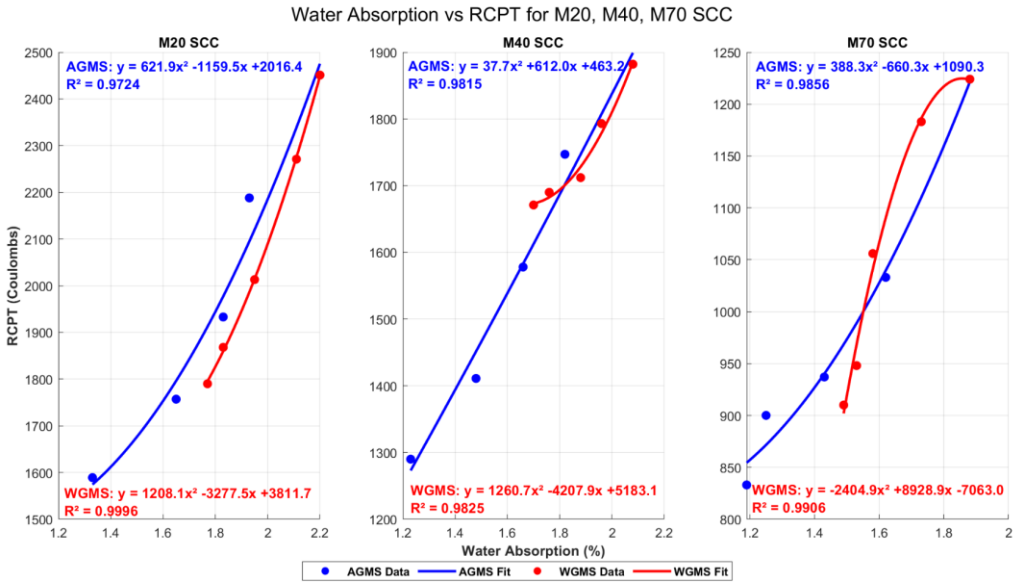

Fig. 19. Correlation between Water absorption- RCPT

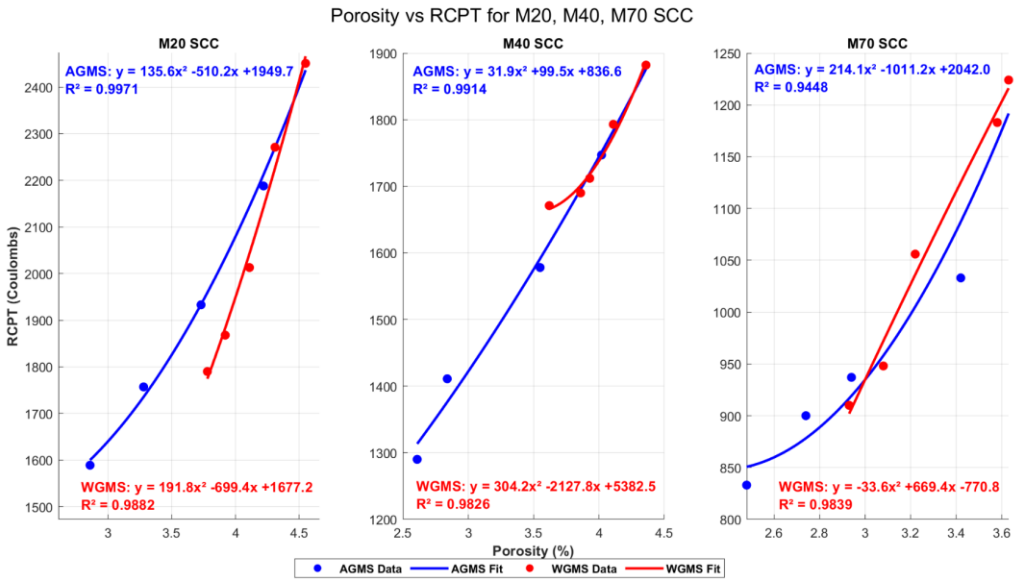

Fig. 20. Correlation between Porosity- RCPT

3.14. Bond Strength

The graph illustrates the variation in bond strength (MPa) of reinforcement bars with different diameters (10 mm, 12 mm, 16 mm, 20 mm, and 25 mm) embedded in SCC of grades M20, M40, and M70, using RS, AGMS, and WGMS. Across all concrete grades, AGMS consistently exhibits the highest bond strength for all bar diameters, indicating superior interfacial bonding between the reinforcement and the SCC matrix. This can be attributed to the angular and rough texture of AGMS, which enhances mechanical interlocking. Bond strength decreases with increasing bar diameter regardless of the concrete mix or sand type. This trend aligns with the principle that larger bars offer a lower surface area-to-volume ratio, reducing the effectiveness of the bond per unit area. With increasing concrete strength from M20 to M70, there is a noticeable improvement in bond strength for all sand types and bar sizes. This suggests that higher grade SCC provides a denser matrix, improving adhesion and confinement around the reinforcement. Among the sands, RS exhibits the lowest bond strength across all mixes and diameters, while WGMS shows intermediate performance, suggesting that although WGMS improves over RS, it does not outperform AGMS. The

findings highlight that SCC mix design should consider the type of manufactured sand to optimize reinforcement bonding characteristics.

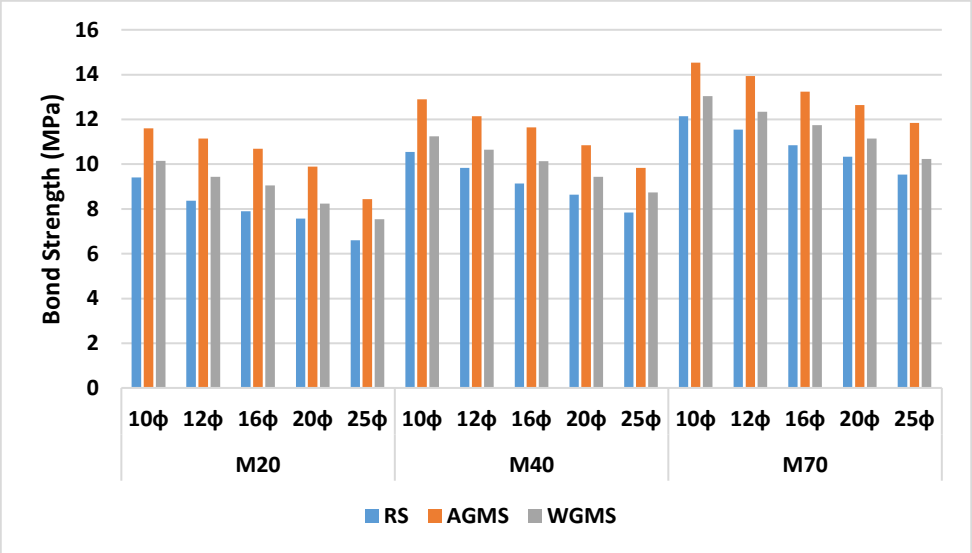

Fig. 21. Bond strength of M20, M40 and M70 grade SCC with RS, AGMS and WGMS

4. Cost Comparison Discussion: AGMS vs WGMS vs RS in Bangalore

In the context of Bangalore's construction material market, the cost of fine aggregates such as River Sand (RS), Air-Graded M-Sand (AGMS), and Wet-Graded M-Sand (WGMS) varies significantly due to availability, processing methods, environmental regulations, and logistics. River Sand (RS) is scarce and highly regulated due to environmental restrictions on river sand mining. It has a high cost due to limited legal supply and increasing transport distance. It often involves additional silt cleaning and quality uncertainty. River sand is not sustainable in the long run due to ecological impacts and mining bans.

Air-Graded M-Sand (AGMS) is produced using air separators to remove fines and control grading. It is relatively cost-effective compared to RS, offers better gradation control and uniformity. It has lower water content due to air grading making it more suitable for batching. Capital and operational cost of air classification is higher than wet processing, but material savings and performance benefits (as seen in durability tests) often justify the cost.

Wet-Graded M-Sand (WGMS) is produced and graded via wet classifiers or hydrocyclones. WGMS is typically the most economical option in terms of cost. It is easily available and has a simpler production process. WGMS may contain higher surface moisture, which can affect mix water demand.

Table 8. Cost Comparison of RS, AGMS and WGMS in Bangalore Region

Material Type	Cost (₹/ft^3)	Cost (₹/ton)	Availability	Quality Control	Sustainability	Durability (Based on Study)
RS	90–120	3200–4200	Low (regulated)	Inconsistent	Low	Moderate
AGMS	60–80	2100–2800	Moderate	High	High	High
WGMS	55–75	1900–2600	High	Moderate	Medium	Moderate

5. Conclusions

- The inclusion of AGMS in SCC shows considerable improvement in the flow properties across all grades of concrete compared to WGMS and RS.
- The evaluation of mechanical properties across M20, M40, and M70 grade self-compacting concrete (SCC) incorporating various proportions of AGMS, and WGMS in replacement of

river sand clearly established that the type and proportion of fine aggregate have a direct impact on the compressive and tensile strength of SCC.

- For compressive strength, the incorporation of air-graded M-sand led to a marked improvement, particularly at 75–100% replacement levels, across all concrete grades. This is likely attributed to the angular particle shape and optimized gradation of air-graded M-sand, which enhances the particle packing density and interlocking. Peak compressive strengths were observed in M40 and M70 grades at full replacement, outperforming river sand mixtures significantly. In contrast, wet-graded M-sand demonstrated a moderate strength gain up to 75% replacement, but showed marginal or plateaued improvements beyond that level, possibly due to its higher water absorption and finer particles that affect effective water–cement ratio and paste quality.
- In terms of tensile strength, both manufactured sand types contributed to strength enhancement, with AGMS again providing superior results, especially at intermediate replacement levels. The enhanced bond between the paste and the rough, angular M-sand particles is believed to contribute to this improvement. WGMS also improved tensile strength but showed slightly lesser performance compared to its air-graded counterpart.
- Taken altogether, the data show that AGMS is an extremely effectual substitution for river sand in SCC to improve the mechanical performance, while the best results are obtained at about 75 to 100 percent replacement. Although WGMS may prove viable, it may require adjustments to mix design in order to compensate for its influence on water demand and workability in full. The mechanical tests show a consistent performance improvement, which as a whole consolidates the ability that fabricated sands have to promote sustainable, durable concrete systems.
- Performance of Self-Compacting Concrete of across all grades with River Sand, AGMS and WGMS varies significantly in terms of different parameters and hence the durability assessment. The durability characteristics of concrete mixes with manufactured sand, in particular AGMS, are found to systematically be much superior to concrete mixes with river sand.
- Results indicate that for AGMS mixes, water absorption and porosity values are lowest of all mixes across all grades, indicating a denser and less permeable microstructure. Second, regardless of sand type, M20 mixed showed the highest water absorption and porosity, M70 showed improved resistance of pore refinement due to higher grade of concrete.
- The experimental results show that inclusion of AGMS and WGMS as fine aggregate replacements in SCC significantly reduces water permeability across all concrete grades, with AGMS showing the most pronounced improvement, particularly at higher replacement levels, thereby enhancing the durability and sustainability of the concrete mix.
- In terms of acid resistance, AGMS mixes experienced the least loss in both strength and weight under sulfuric acid exposure at 2% and 5% dilution levels. RS mixes displayed the greatest deterioration, particularly in M20 grade, indicating that river sand-based SCC is more vulnerable to aggressive environments. The performance of WGMS mixes was intermediate but consistently closer to AGMS than RS.
- The cumulative percentage loss in both weight and strength further confirmed the enhanced resistance of AGMS-based SCC to chemical attack. As concrete grade increased, all mixes showed improved durability; however, the benefit was most pronounced in AGMS, highlighting its potential in high-performance applications.
- Overall, Air Graded M-Sand proved to be the most effective fine aggregate for improving the durability of SCC. Its use can be strongly recommended as a sustainable alternative to natural river sand, especially in environments prone to chemical exposure or requiring long-term structural integrity.
- Water absorption together with porosity in SCC shows a strong correlation with RCPT values. The permeability levels of WGMS exceed those of AGMS particularly in cement-based materials at lower than grade 40. Durability of low- to medium-strength concrete depends on selecting appropriate sand types during production.
- The study confirms that porosity and water absorption can serve as reliable predictors for chloride ion permeability (RCPT) in SCC across all strength grades. The quadratic fit not only

offers accurate correlation but also reflects the nonlinear nature of transport mechanisms in cementitious systems. This relationship becomes increasingly important for high-performance concretes, where marginal improvements in microstructure yield substantial gains in durability.

- In the bond strength study, AGMS proves to be the most effective fine aggregate for enhancing bond strength in SCC, followed by WGMS and RS. The results emphasize the influence of sand type, concrete grade, and bar diameter on bond performance, guiding the selection of materials for optimized structural behavior.
- While river sand is the most expensive and least sustainable option, AGMS, despite a slightly higher production cost than WGMS, offers superior durability and quality control, making it ideal for high-performance concrete applications. WGMS, being more economical, remains a cost-effective alternative for general construction. Therefore, selection should balance performance requirements, cost constraints, and sustainability goals.

6. Implications for Practice

This study suggests that M-Sand, particularly AGMS, is an excellent alternative to natural river sand in the production of SCC, offering improved mechanical properties and durability. The findings also suggest the optimal replacement levels for mix design across various concrete grades, promoting more sustainable construction practices. Additionally, the reduced dependency on RS carries significant ecological benefits, including preservation of river ecosystems and mitigation of illegal sand mining.

The use of different types of sand in practical application should also consider economic feasibility. Due to the limited availability of RS in most parts of the country, the prices are almost two times higher than that of M-sand in the market. While AGMS demonstrated superior performance, its processing cost is typically higher than that of WGMS. Therefore, project-specific cost-benefit analyses are essential to determine the most suitable option, balancing performance gains against financial constraints.

References

[1] Martins MA, Barros RM, da Silva LRR, dos Santos VC, Lintz RC, Gachet LA, et al. Durability indicators of high-strength self-compacting concrete with marble and granite wastes and waste foundry exhaust sand using electrochemical tests. Constr Build Mater. 2021;317:125907. https://doi.org/10.1016/j.conbuildmat.2021.125907

[2] Irico S, Qvaeschning D, Mutke S, Deuse T, Gastaldi D, Canonico F. Durability of high performance self-compacting concrete with granulometrically optimized slag cement. Constr Build Mater. 2021;298:123836. https://doi.org/10.1016/j.conbuildmat.2021.123836

[3] Tufail RF, Naeem MH, Ahmad J, Waheed H, Majdi A, Farooq D, et al. Evaluation of the fresh and mechanical properties of nano-engineered self compacting concrete containing graphite nano/micro platelets. Case Stud Constr Mater. 2022;17:e01165. https://doi.org/10.1016/j.cscm.2022.e01165

[4] Suriya D, Chandar S, Ravichandran PT. Impact of M-Sand on Rheological, Mechanical, and Microstructural Properties of Self-Compacting Concrete. Buildings. 2023;13:1126. https://doi.org/10.3390/buildings13051126

[5] Tripathi D, Kumar R, Mehta P. Development of an environmental-friendly durable self-compacting concrete. Environ Sci Pollut Res. 2022;29:1-14. https://doi.org/10.1007/s11356-022-19638-5

[6] Tripathi D, Kumar R, Mehta P, Rawat V. An experimental study on the properties of SCC with manufactured sand. J Indian Chem Soc. 2020;97(10a):1673-7.

[7] Gonçalves JP, Tavares LM, Toledo Filho RD, Fairbairn EMR, Cunha ER. Comparison of natural and manufactured fine aggregates in cement mortars. Cem Concr Res. 2007;37:924-32. https://doi.org/10.1016/j.cemconres.2007.03.009

[8] Aasly KA, Danielsen SW, Wigum BJ, Norman SH, Cepuritis R, Onnela T. Review report on dry and wet grading of filler materials for concrete (COIN Project Report 52). SINTEF Building and Infrastructure; 2014. ISBN: 978-82-536-1412-0.

[9] Peng S, Wu Y, Tao J, Chen J. Airflow velocity designing for air classifier of manufactured sand based on CPFD method. Minerals. 2022;12:90. https://doi.org/10.3390/min12010090

[10] Mahalakshmi SHV, Khed VCK. Experimental study on M-sand in self-compacting concrete with and without silica fume. Mater Today Proc. 2020;27(2):1061-5. https://doi.org/10.1016/j.matpr.2020.01.432
[11] Mahakavi P, Chithra R. Effect of recycled coarse aggregate and manufactured sand in self-compacting concrete. Aust J Struct Eng. 2019;21(1):33-43. https://doi.org/10.1080/13287982.2019.1636519
[12] Janagan SS, Namachivayam N, Kabilan R, Prasath RN, Naveenkumar M. An experimental study on self compacting concrete by replacing the fine aggregate with M Sand. Int J Curr Eng Sci Res. 2019;6(3).
[13] Kumar KP, Radhakrishna. Characteristics of SCC with fly ash and manufactured sand. IOP Conf Ser Mater Sci Eng. 2016;149:012111. https://doi.org/10.1088/1757-899X/149/1/012111
[14] Baskar S, Nelson D. Experimental investigation of self-compacting concrete using M-Sand. J Chem Pharm Sci. 2015;8:947-51.
[15] Zeghichi L, Benghazi Z, Baali L. Comparative study of self-compacting concrete with manufactured and dune sand. J Civ Eng Archit. 2012;6:1429-34. https://doi.org/10.17265/1934-7359/2012.10.022
[16] Nanthagopalan P, Santhanam M. Fresh and hardened properties of self-compacting concrete produced with manufactured sand. Cem Concr Compos. 2011;33(3):353-8. https://doi.org/10.1016/j.cemconcomp.2010.11.005
[17] Dehwah HAF. Corrosion resistance of self-compacting concrete incorporating quarry dust powder, silica fume and fly ash. Constr Build Mater. 2012;37:277-82. https://doi.org/10.1016/j.conbuildmat.2012.07.078
[18] Kalirajan S, Vishnuram BG. Development of self compacting concrete using manufactured sand. Int J Earth Sci Eng. 2014;7:987-92.
[19] Mane K, Joshi A, Kulkarni D, Prakash K. Study of shrinkage characteristics of concrete made with pozzolanic materials and partly replacing river sand by MS. J Build Pathol Rehabil. 2021;6. https://doi.org/10.1007/s41024-021-00113-6
[20] Prasanth S, Chandar SP, Gunasekaran K. Flexural behaviour of self-compacting coconut shell reinforced concrete beam using manufactured sand. Innov Infrastruct Solut. 2024;9:459. https://doi.org/10.1007/s41062-024-01775-0
[21] Li H, Huang F, Tu H, et al. Pumpability of manufactured sand self-compacting concrete. J Wuhan Univ Technol Mater Sci Ed. 2023;38:1382-90. https://doi.org/10.1007/s11595-023-2832-z
[22] Bureau of Indian Standards. IS 12269:2013 - Ordinary Portland cement, 53 grade - Specification. New Delhi: BIS; 2013.
[23] Bureau of Indian Standards. IS 383:2016 - Coarse and fine aggregate for concrete - Specification (Third Revision). New Delhi: BIS; 2016.
[24] Bureau of Indian Standards. IS 10262:2019 - Concrete mix proportioning - Guidelines (Second Revision). New Delhi: BIS; 2019.
[25] Bureau of Indian Standards. IS 456:2000 - Plain and reinforced concrete - Code of practice (Fourth Revision). New Delhi: BIS; 2000.
[26] EFNARC. Specification and guidelines for self-compacting concrete. European Federation for Specialist Construction Chemicals and Concrete Systems; 2006.
[27] Bureau of Indian Standards. IS 1199 (Part 6):2018 - Fresh concrete - Methods of sampling, testing and analysis. Part 6: Tests on fresh self-compacting concrete (First Revision). New Delhi: BIS; 2018.
[28] Bureau of Indian Standards. IS 516 (Part 1/Sec 1):2021 - Compressive, flexural and split tensile strength. New Delhi: BIS; 2021.
[29] ASTM International. ASTM C642 - Standard test method for unit weight, porosity, and density of compressed building stone. West Conshohocken (PA): ASTM; 2021.
[30] ASTM International. ASTM C1202 - Standard test method for electrical indication of concrete's ability to resist chloride ion penetration. West Conshohocken (PA): ASTM; 2019.
[31] Deutsches Institut für Normung. DIN 1048-5:1991 - Testing of concrete - Part 5: Testing of hardened concrete (specimens prepared on site). Berlin: DIN; 1991.
[32] ASTM International. ASTM C1898 - Chemical resistance of concrete products to acid attack. West Conshohocken (PA): ASTM; 2000.
[33] Bureau of Indian Standards. IS 2770 (Part 1):1967 - Methods of testing bond in reinforced concrete: Part 1 - Pull-out test. New Delhi: BIS; 1967.

Research on Engineering Structures & Materials
www.jresm.org
Research Group

Research Article

Optimizing Inconel 825 machinability: A comprehensive approaches using Taguchi design, Grey-Fuzzy, and principal component analysis

V Jayaseelan [1,a], S Sambath [2,b], Vijay Ananth Suyamburajan [*,3,c]

[1]*Department of Mechanical Engineering, Saveetha Engineering College, Chennai, 602105, India*
[2]*Department of Mechanical Engineering, SRM Madurai College for Engineering and Technology, Pottapalayam, Sivagangai District, Tamil Nadu 63061, India*
[3]*Department of Mechanical Engineering, VELS Institute of science, Technology & Advanced Studies, Chennai, 600117, Tamil Nadu, India*

Article Info

Article History:

Received 13 Feb 2025

Accepted 28 April 2025

Keywords:

Inconel 825;
Optimization;
Grey-Fuzzy;
Surface roughness;
Tool wear;
Cutting force

Abstract

Nickel super alloys have remarkable thermo mechanical capabilities, making them important in industries such as nuclear, chemical, petrochemical, and aerospace. Conversely its difficult machining and cause the poor surface finish and tool wear and so on. This study proposes optimizing machining parameters of Inconel 825 such as cutting speed, feed, and depth of cut towards the responses such as surface roughness, tool flank wear, and cutting force. Optimization of process parameter for this study; the Taguchi Design of Experiments, Grey Relational Analysis, Fuzzy Logic, and Principal Component Analysis (PCA) were used. Experimental were conducted using an L9 orthogonal array and outcomes were evaluated using ANOVA towards the most influencing process parameter. Form the results indicated that the cutting is the most influencing compare with the other parameters. The optimal parameters for turning Inconel 825 were found to be 50 m/min cutting speed, 0.2 mm/rev feed rate, and 0.6 mm depth of cut towards the machining responses. This results conduits towards the machining efficiency of Inconel 825 for industrial applications.

1. Introduction

Nickel based super alloy were most essential materials in contemporary industrial owing to their superior mechanical properties and corrosion resistance at higher temperature [1]. Due to this properties and it is most suitable for many application such as aerospace, petrochemical, nuclear power and chemical industries[2]. Amongst these Inconel 825 has exceptional properties such as corrosion resistance and thermal stability [3]. It contains nickel, chromium, iron, molybdenum, copper and titanium enhancing the resistance to oxidation. However, while machining of Inconel 825 is difficult in challenges in industrial environments [4]. Due to deprived machinability and often outcomes in higher cutting force, irregular surface and tool wear happen. While Inconel 825 is extoled for its routine in difficult operating environments; which remain a challenging such as higher work hardening rate, lower thermal conductivity, poor chip control and wear [5]. Hence optimization is required for better surface roughness, minimum tool degradation and reduction in operational cost [6]. These problems combine reduce the production rate but increase the manufacturing cost. Consequently, an optimization of machining parameters is most significant towards improve the machinability, reduction in surface defects and better tool life [7] . Thakur et al. examined tool wear in Inconel 825 turning and discovered that flank wear increases with greater

*Corresponding author: ssvijayananth@gmail.com
[a]orcid.org/0000-0002-5754-8216; [b]orcid.org/0009-0005-5972-0525; [c]orcid.org/0000-0003-3883-5938
DOI: http://dx.doi.org/10.17515/resm2025-677st0213rs

cutting speeds and also studied on Inconel 718 and found that coated tools performs with respect to the cutting and fee force [8] .

Senthilkumaar et al investigated surface roughness in relation to feed rate and discovered that larger feed rates, as well as lower speeds and deeper cuts, resulted in a higher material removal rate and surface polish [9]. Rajyalakshmi and Ramaiah studied the combination of Grey Relational Analysis (GRA) and Taguchi for WEDM optimization of Inconel 825, which shows that the improvement has been observed in machining [10]. Even though, the fuzzy logic results were autonomously and latest studies improvements of GRA in ambiguous machining conditions [11] . To overcome this principal compound analysis is the better choice towards the variable influencing machining responses [12] . Asiltürk and Akkus reported that the better outcome such as surface roughness and material removal rate in turning. In Inconel 738 and Inconel 718, PCA optimization were used for better performance in machining but these not scientifically used to Inconel 825 [13]. Lila Imani et al. examined both the Artificial Neural Networks (ANN) and Genetic Algorithms (GA) in Inconel 738; the outcome inveterate the ANN but the impediment in ANN and also deficiency in physical interpretability [14]. The traditional methods such as response surface methodology, GA and ANN were used in optimization towards turning. But these techniques require maximum experimentation and also need huge data. Taguchi combined with multi objective optimization had accepted owing to the accuracy and woks in limited experimental data's and produce better results [15].

Novelty of this research work was cohesive use of Taguchi Design of Experiments, Grey Fussy and PCA for optimization of machining parameters of Inconel 825 with limited earlier study in this background. Whereas the previous studies reported that single approaches, in this work distinctively combines these three approaches for multi response optimization. This cohesive approach enhances the prediction correctness for machining performances in respect with the machining parameters such as cutting speed, feed rate and depth of cut. These novel and effective findings improve the machinability of Inconel 825 while also facilitating the way for further materials.

2. Materials and Methods

Inconel 825, a nickel-based super alloy and widely employed in a range of industries such as aerospace and automobile, etc., This study focuses on turning of Inconel 825 and optimization techniques were employed. Machined components will has 3mm layer of the outer surface been pre-machined to ensure excellent machining quality. The raw material consisted of bars 30 mm in diameter and 80 mm in length. It has largely composed of nickel, iron, and chromium. Fig. 1, shows the machined Inconel 825.

Fig. 1. Inconel 825

Based on previous research, three cutting parameters such as cutting speed, feed rate, and depth of cut were selected for this experimental work [4, 16, 17]. The CNC Super Jobber 500 LM machine, which has a 10 KW motor drive and an operating range of 30 to 300 rpm, was chosen due to its low. The trials were planned using Taguchi's relational analysis. An L9 orthogonal array with 3 variables at three levels was used for optimization results. MINITAB 16 software was used for the Design of

Experiments, which generated the L9 orthogonal array and provided a wide range of potential cutting settings [18]. Table 1 presents the cutting parameter and their range.

Table 1. Input process parameters and level

Parameter	Unit	Level		
		1	2	3
Cutting Speed	m/min	50	70	90
Depth of cut	mm	0.2	0.4	0.6
Feed rate	mm/rev	0.1	0.2	0.3

3. Results and Discussions

3.1 Taguchi Analysis

Table 2 denotes the Taguchi L9 orthogonal array; the three-input parameter used in this study as cutting speed, feed rate and depth of cut and their three different level. The identifications of individual and interaction of the input parameter; which succeeding analysis of surface roughness, cutting force and flank wear in machining i.e., turning of Inconel 825.

Table 2. Design of experiments (DoE) – L9 results

Run Order	Cutting Speed	Depth of Cut	Feed Rate	Surface Roughness (µm)	Cutting Force (N)	Flank wear (µm)	S-N Ratio	Std. Dev.	Mean
1	50	0.2	0.1	2.54	428.36	152.63	-3.21	215.98	194.51
2	50	0.4	0.2	4.15	449.54	172.65	-2.77	224.88	208.78
3	50	0.6	0.3	3.75	444.25	176.28	-2.63	221.97	208.09
4	70	0.2	0.2	4.23	461.62	189.69	-2.45	230.05	218.51
5	70	0.4	0.3	4.05	463.52	191.25	-2.44	231.04	219.61
6	70	0.6	0.1	3.15	470.67	196.25	-2.44	234.94	223.36
7	90	0.2	0.3	4.94	490.57	220.39	-2.02	243.33	238.63
8	90	0.4	0.1	3.59	486.54	215.36	-2.14	242.08	235.16
9	90	0.6	0.2	4.48	475.67	203.57	-2.25	236.54	227.91

Table 3. Analysis of variance (ANOVA)

Source	DF	Contribution	Seq SS	Adj SS	Adj MS	F	P
S-N Ratio							
Cutting Speed	2	79.41%	0.80834	0.80834	0.40417	7.91	0.011
Depth of Cut	2	2.49%	0.02534	0.02534	0.01267	0.25	0.080
Feed Rate	2	8.06%	0.08204	0.08204	0.04102	0.80	0.055
Residual Error	2	10.04%	0.10223	0.10223	0.05111		
Total	8	100.00%	1.01795				
Means							
Cutting Speed	2	87.09%	1365.03	1365.03	682.51	9.47	0.009
Depth of Cut	2	1.55%	24.26	24.26	12.13	0.17	0.085
Feed Rate	2	2.17%	33.96	33.96	16.98	0.24	0.080
Residual Error	2	9.20%	144.14	144.14	72.07		
Total	8	100.00%	1567.39				
Std. Dev.							
Cutting Speed	2	87.89%	585.513	585.513	292.757	9.14	0.009
Depth of Cut	2	1.87%	12.486	12.486	6.243	0.19	0.083
Feed Rate	2	0.62%	4.132	4.132	2.066	0.06	0.093
Residual Error	2	9.62%	64.086	64.086	32.043		
Total	8	100.00%	666.217				

It designates the signal to noise ratio, standard deviation and mean values of nine readings; which supporting a complete estimation of process inconsistency and stability [19]. The results deliver the statistical analysis which including ANOVA and identify the furthermost influencing input parameter for machinability of Inconel 825.Table 3 reported that the ANOVA outcomes for the responses established on the signal to noise ratio (S-N ratio), standard deviation and mean. The results inferred that the cutting speed is the most influencing input process parameter among the other two; the contribution of the S-N ratio, standard deviation and mean are 79.41%, 87.09% and 87.89% respectively. The influences of depth of cut and feed rate are suggestively minimum and indicated the lower impact on the responses. It is calculated through the delta values; which is the difference in the lowest and highest performance for all the input parameter. Form the table clearly indicates that the cutting speed is most influencing parameter for these three measures and followed by feed rate and depth of cut. Table 4 and Fig. 2, confirm that the rankings for the S-N ratio, standard deviation, and mean are A1B3C2, A1B3C2, and A1B2C3, respectively. This ranking emphasizes the ANOVA outcomes; additional confirmation for cutting speed is the most influences on machining responses during the turning of Inconel 825.

Table 4. Ranking for response

Level	S-N Ratio			Means			Standard deviation		
	Cutting Speed	Depth of Cut	Feed Rate	Cutting Speed	Depth of Cut	Feed Rate	Cutting Speed	Depth of Cut	Feed Rate
1	-2.869	-2.558	-2.597	203.8	217.2	217.7	220.9	229.8	231.0
2	-2.443	-2.451	-2.491	220.5	221.2	218.4	232.0	232.7	230.5
3	-2.139	-2.441	-2.363	233.9	219.8	222.1	240.6	231.1	232.1
Delta	0.731	0.117	0.233	30.1	4.0	4.4	19.7	2.9	1.6
Rank	1	3	2	1	3	2	1	2	3

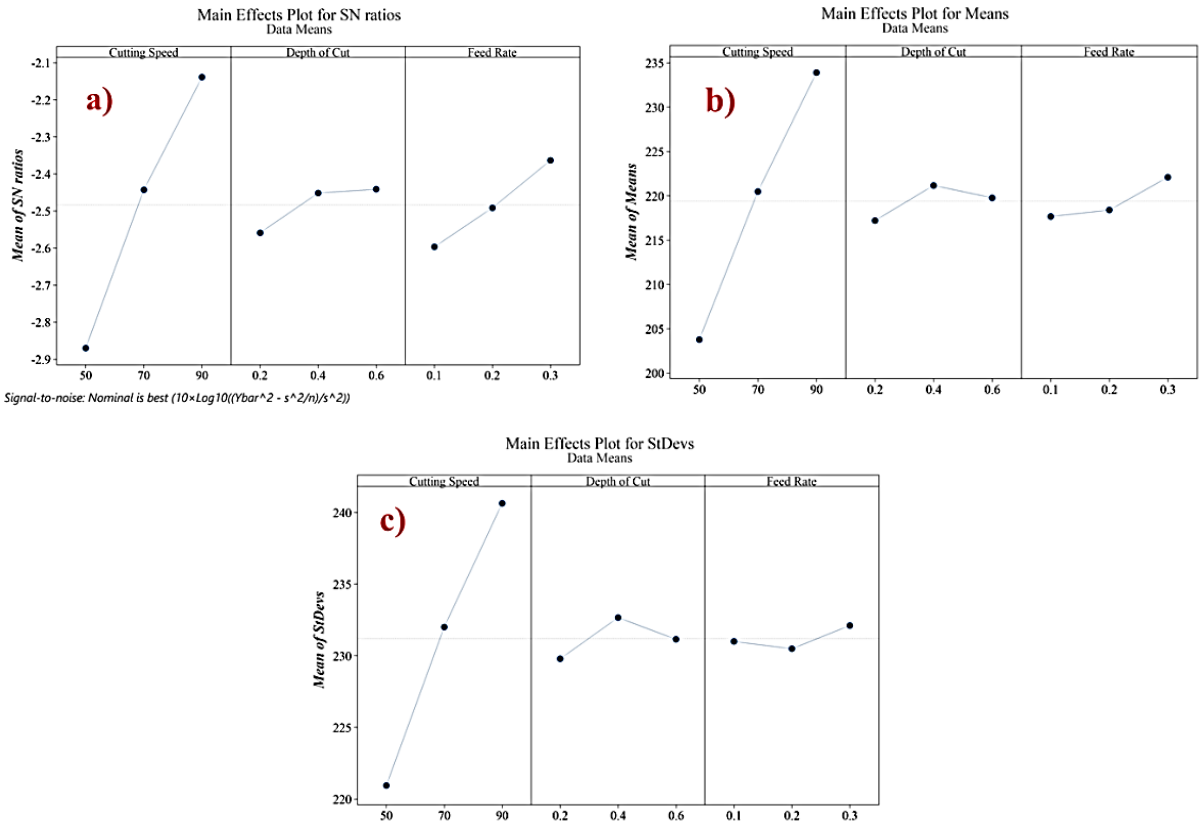

Fig. 2. Residual Analysis (a) S-N Ratio, (b) Means, and (c) standard deviation

These graphs are employed to authenticate the appropriateness of the Taguchi through the residual distribution. The outlines in the graph recommend that the residuals are follows the normal trend but randomly distributed; which indicates that the experimental findings are fits with

the model and the designated parameter are statistically momentous [20]. It confirms the consistency of the experimental data and inference obtained from the Taguchi and ANOVA studies towards the turning of Inconel 825.

3.2 Results of Grey Relational Analysis

Grey relational analysis is often utilized in multi-response optimization situations. This method is based on the relationship between sequences, specifically their difference or similarity. This transforms multiple performances into a single grey relation grade for comparison and optimization. For larger the better as presented in Eq. (1).

$$x_i^*(k) = \frac{x_i(k) - min\, xi\,(k)}{max\, xi\,(k) - \ min\, xi\,(k)} \tag{1}$$

Where, $x_i(k)$: Original value of the k^{th} response for the i^{th} experiment, $x_i*(k)$: Normalized value, min $x_i(k)$: Minimum value of the k^{th} response, max $x_i(k)$: Maximum value of the k^{th} response. When a lower value is better as shown in Eq. (2).

$$x_i^*(k) = \frac{max\, xi\,(k) - \ x_i(k)}{max\, xi\,(k) - \ min\, xi\,(k)} \tag{2}$$

The original sequence can be normalized by dividing all values by the series' first value if there is a target value to be reached. The following is an expression for the grey relational coefficient and can be written and given in Eq. (3).

$$\zeta_i(k) = \frac{\Delta_{min} + \zeta\Delta_{max}}{\Delta_i(k) + \zeta\Delta_{max}} \tag{3}$$

Where, $\xi_i(k)$: Grey Relational Coefficient (GRC) for the i^{th} experiment and k^{th} response, $\Delta_i(k)$ - $|x0*(k)-x_i*(k)|$: Absolute difference between the ideal normalized value and the actual normalized value, Δ_{min}: Minimum of all $\Delta_i(k)$ values, Δmax: Maximum of all $\Delta_i(k)$ values, ζ: Distinguishing coefficient. The GRC indicates how close a particular experimental result is to the ideal normalized result. The grey relational grade is can be written as and given in Eq. (4).

$$\gamma_i = \frac{1}{n}\sum_{k=1}^{n} \zeta_i(k) \tag{4}$$

where, γ_i: Grey Relational Grade (GRG) for the i^{th} experiment, n: Total number of performance characteristics, $\xi_i(k)$: Grey Relational Coefficient for the k^{th} response.

The GRG can also define as the weighted or unweighted mean of the GRCs for all the outcomes. It also supplies a single value on behalf of whole performance for multi objective optimization. The degree of influence that the comparison sequence can have on the reference sequence is shown by the grey relationship grade. The grey relational grade for the reference and comparison sequences would be higher than the other grey relational grades if the comparison sequence is considered to be more significant than the others [21, 22]. Table 5 shows the Sequence of grey relational analysis.

It inferred that the responses variation with respect to the cutting speed, feed rate, and depth of cut. Particularly, the higher cutting speed results in higher cutting forces and tool wear and also poor machinability of Inconel 825. The S-N ratio and standard deviation are providing the process stability and response consistency which supports and succeeding ANOVA and multi response optimization studies. Based on the observation, out of the 27 trials, the sixth trial ran is the ideal one. The maximum value of GRG is found to be 0.8721 for the input conditions. The optimal conditions for cutting at 50 m/min, 0.2 mm/rev feed rate, and 0.6 mm depth of cut which produced 3.52 µm surface roughness, 430.26 N cutting force, and 150.84 µm flank wear. A comparison sequence's grey relational grade associated with a reference would be greater than the further grey relational grade if that reference is deemed to be more essential than the others [23]. Fig. 3, shows the residual analysis for the outcomes such as flank wear, surface roughness and cutting force. These graphs are important in confirming the assumptions of randomness and normality in the experimental readings. It is follow the normal pattern and consistently distributed and also

confirming noise in the random system [20]. This also support the statistical reliability of the model used in this work and confirms that the input process parameters with respect to the responses. Form figure confirm that the Taguchi are valid and the outcomes are reliable for decision making.

Table 5. Sequence of grey relational analysis

Sl. No	Cutting Speed (m/min)	Depth of Cut (mm)	Feed Rate (mm/rev)	SR (µm)	Cutting Force (N)	Flank wear (µm)	Grey Relational Coefficient (GRC)			Grey Relational Grade (GRG)	Rank
							Surface roughness	Cutting force	Flank wear		
1	50	0.2	0.1	2.54	428.36	152.63	0.5104	0.6666	0.904	0.6936	4
2	50	0.4	0.1	2.62	456.25	168.34	0.4881	0.582	0.8011	0.6238	10
3	50	0.6	0.1	2.86	480.61	175.06	0.7975	0.4182	1	0.7386	3
4	50	0.2	0.2	3.84	440.34	162.58	0.4343	0.7821	0.8206	0.679	5
5	50	0.4	0.2	4.15	449.54	172.65	0.5481	0.6524	0.8025	0.6677	7
6	50	0.6	0.2	3.52	430.26	150.84	0.7206	1	0.8957	0.8721	1
7	50	0.2	0.3	4.28	445.35	170.67	0.4038	0.7057	0.7642	0.6246	9
8	50	0.4	0.3	3.95	435.58	164.52	0.4589	0.8718	0.7028	0.6779	6
9	50	0.6	0.3	3.75	444.25	176.28	1	0.7212	0.829	0.8501	2
10	70	0.2	0.1	2.85	454.64	185.36	0.4248	0.5975	0.5385	0.5203	13
11	70	0.4	0.1	2.96	462.38	190.54	0.4739	0.5298	0.5289	0.5108	15
12	70	0.6	0.1	3.15	470.67	196.25	0.8811	0.4725	0.5623	0.6386	8
13	70	0.2	0.2	4.23	461.62	189.69	0.4001	0.5358	0.5052	0.4803	17
14	70	0.4	0.2	4.64	472.64	198.57	0.4495	0.4606	0.5018	0.4706	16
15	70	0.6	0.2	4.45	458.38	180.69	0.6514	0.5627	0.5732	0.5958	11
16	70	0.2	0.3	4.56	475.26	201.35	0.356	0.4457	0.5073	0.4363	21
17	70	0.4	0.3	4.05	463.52	191.25	0.4025	0.5211	0.4704	0.4647	19
18	70	0.6	0.3	3.92	471.36	199.65	0.7095	0.4682	0.4997	0.5592	14
19	90	0.2	0.1	3.46	495.25	218.62	0.3711	0.3577	0.3711	0.3666	25
20	90	0.4	0.1	3.59	486.54	215.36	0.4322	0.3914	0.3671	0.3969	23
21	90	0.6	0.1	3.74	502.64	230.54	0.6548	0.3333	0.4067	0.465	18
22	90	0.2	0.2	4.31	494.61	219.35	0.3333	0.36	0.3582	0.3505	26
23	90	0.4	0.2	4.51	501.83	222.36	0.3752	0.3358	0.3524	0.3545	24
24	90	0.6	0.2	4.48	475.67	203.57	0.5077	0.4435	0.388	0.4464	22
25	90	0.2	0.3	4.94	490.57	220.39	0.3465	0.375	0.3547	0.3588	27
26	90	0.4	0.3	4.51	479.31	206.68	0.624	0.4246	0.3333	0.4606	20
27	90	0.6	0.3	4.54	495.45	205.4	0.9952	0.4782	0.5165	0.5658	12

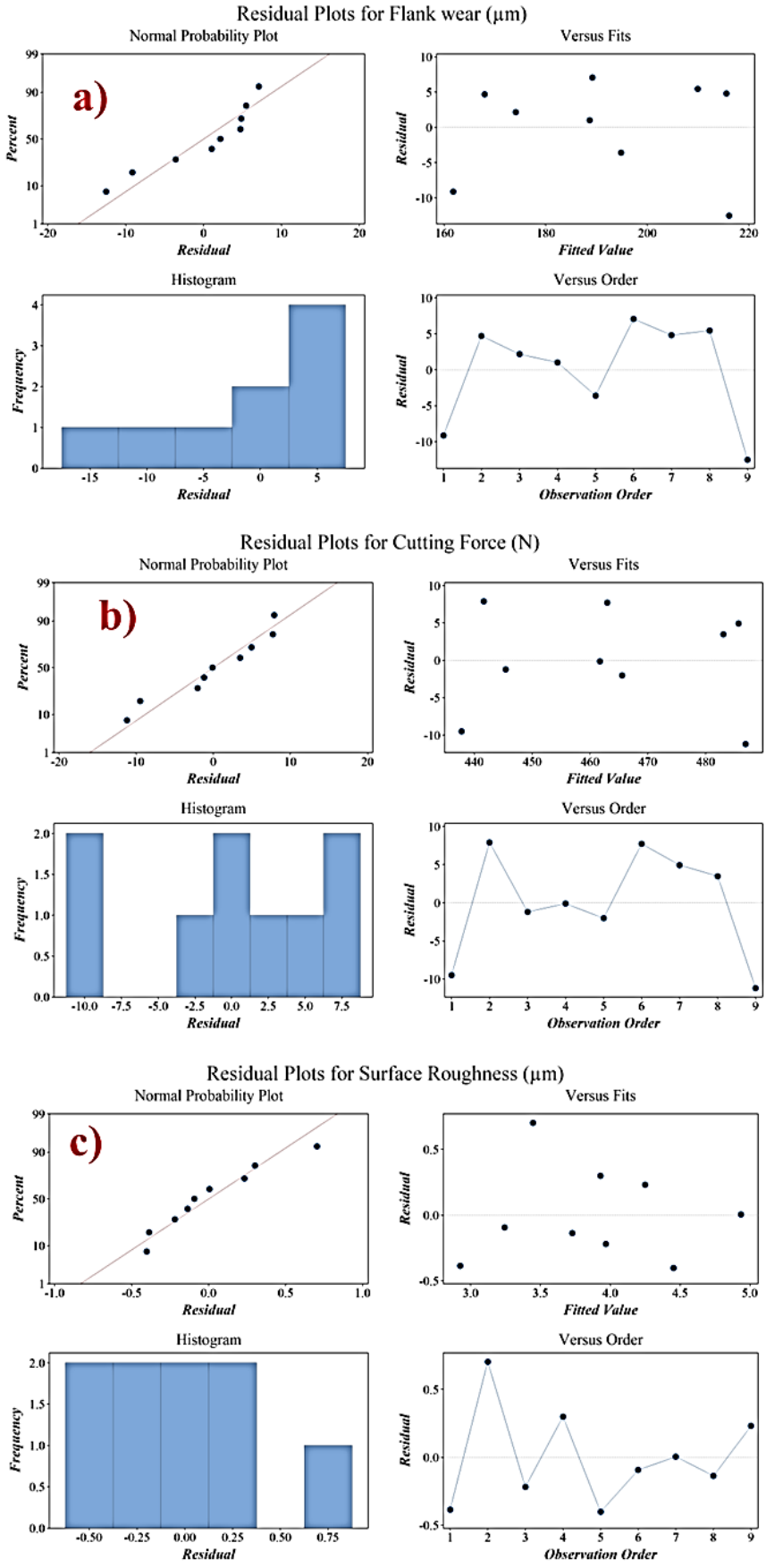

Fig. 3. Residual analysis (a) flank wear, (b) cutting force, and (c) surface roughness

3.3 Fuzzy Inference System

One important artificial intelligence technique that is well-known for its efficiency in managing intricate nonlinear systems is fuzzy logic. A more sophisticated and less ambiguous grey-fuzzy relational grade can be attained by applying fuzzy logic. The basic ideas behind fuzzy modeling are fuzzy set theory and language systems, which are designed to simulate the analysis of a human professional. The system for fuzzy inference is shown in Fig. 4. Eqs. (5) - (7) were obtained from grey relational analysis. Table 6 shows the regression analysis findings for the responses produced by the fuzzy inference system. Flank wear has the highest R^2 (89.54%) and adjusted R^2 (83.27%), confirming the prediction of tool wear based on input machining parameters. The cutting force has R^2 (88.40%) and an adjusted R^2 (81.44%), while surface roughness has lower R^2 (75.27%) and adjusted R^2 (60.44%). It confirms that the fuzzy model produces nonlinear interactions between the input parameter and responses [24]. Table 7 indicated that the minimum responses obtained from the input parameter such as cutting speed as 50, depth of cut as 0.2 and feed rate as 0.1.

$$\text{Flank wear } (\mu m) = 98.2 + 1.148 \text{ Cutting Speed} + 11.2 \text{ Depth of Cut} + 39.5 \text{ Feed Rat} \quad (5)$$

$$\text{Surface Roughness } (\mu m) = 1.333 + 0.02142 \text{ Cutting Speed} - 0.275 \text{ Depth of Cut} + 5.77 \text{ Feed Rate} \quad (6)$$

$$\text{Cutting Force } (N) = 379.6 + 1.089 \text{ Cutting Speed} + 8.4 \text{ Depth of Cut} + 21.3 \text{ Feed Rate} \quad (7)$$

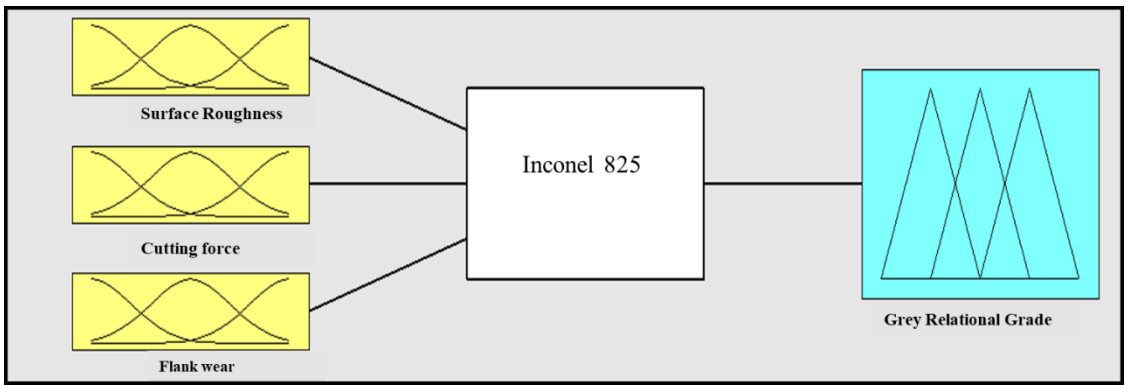

Fig. 4. Fuzzy inference system

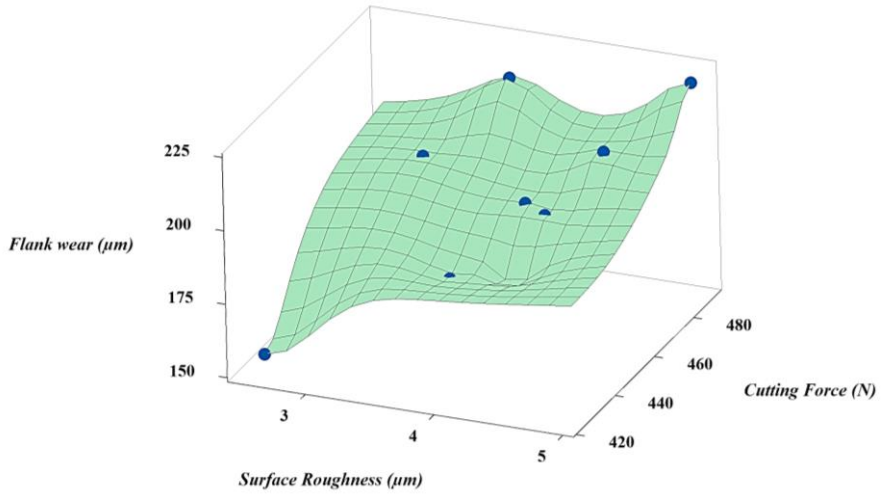

Fig. 5. Optimal Response Analysis

From Grey-Fuzzy logic optimal responses were arrived and the input parameter such as cutting speed as 50 m/min, feed rate as 0.1 mm/rev and depth of cut as 0.2 mm as revealed in Fig. 5. For these conditions the anticipated responses of surface roughness, cutting force, flank wear is 2.925

µm, 437.84 N, 161.76 µm, respectively. The composite desirability has a high level of optimization effectiveness (0.85067). The composite desirability has a high optimization effectiveness of 0.85067. This result demonstrates that the indicated input parameter drastically improved the Inconel 825 machining effectiveness.

Table 6. Response

Responses	R^2	R^2(adj)
Flank wear	89.54%	83.27%
Surface Roughness	75.27%	60.44%
Cutting Force	88.40%	81.44%

Table 7. Solution

Cutting Speed	50
Depth of Cut	0.2
Feed Rate	0.1
Flank Wear (µm)	161.758
Cutting Force (N)	437.842
Surface Roughness (µm)	2.92556
Composite Desirability	0.85067

3.4 PCA Analysis

PCA entails applying a statistical technique to simplify and gain a better understanding of big datasets. This method allows the evaluation of important components by converting associated machining features into a collection of independent components [12, 25]. Through this method, the multi-objective response matrix is subsequently built. Three principal components PC1, PC2, and PC3 have been determined using PCA. The variation is seen by the Eigen analysis of the correlation matrix in Table 8. Interestingly, it has been found that 63% of the variability may be explained by the first principal component alone. The Multi-Response Performance Index (MRPI) calculates each key component's unique weight based on its proportion of accountability.

Table 8. Eigen analysis of the Correlation Matrix

Principal Component	Eigenvalue	Variations (%)
First	1.8909	63
Second	0.8121	27.1
Third	0.2970	9.9

Table 9. Eigenvectors for principal components

Performance Characteristics	Eigenvectors			Contribution
	First Principal component	Second Principal component	Third Principal component	
Surface Roughness (µm)	0.433	-0.885	-0.168	0.1874
Cutting Force (N)	0.618	0.428	-0.660	0.3819
Flank Wear (µm)	0.656	0.182	0.733	0.4303

The eigenvectors of the principal components were obtained via PCA for the responses such as surface roughness, flank wear and cutting force as shown in Table 9. From these PCA has 63% of the total variance; which indicated the substantial role with the other responses. Flank wear has the maximum contribution of 0.656, followed by cutting force as 0.618 and surface roughness as 0.433. It recommends that the wear is the furthermost influential factor towards the machinability.

The contributions of the responses such as flank wear, cutting force and surface roughness are 43.03%, 38.19% and 18.74% respectively.

Table 10. Grey coefficient with principal component analysis

	Individual Principal components			
Trials	PC1	PC2	PC3	MRPI
1	0.096	0.255	0.389	0.739
2	0.092	0.222	0.345	0.659
3	0.150	0.160	0.430	0.740
4	0.081	0.299	0.353	0.733
5	0.103	0.249	0.345	0.697
6	0.135	0.382	0.385	0.902
7	0.076	0.270	0.329	0.674
8	0.086	0.333	0.302	0.721
9	0.187	0.275	0.357	0.820
10	0.080	0.228	0.232	0.540
11	0.089	0.202	0.228	0.519
12	0.165	0.180	0.242	0.588
13	0.075	0.205	0.217	0.497
14	0.084	0.176	0.216	0.476
15	0.122	0.215	0.247	0.584
16	0.067	0.170	0.218	0.455
17	0.075	0.199	0.202	0.477
18	0.133	0.179	0.215	0.527
19	0.070	0.137	0.160	0.366
20	0.081	0.149	0.158	0.388
21	0.123	0.127	0.175	0.425
22	0.062	0.137	0.154	0.354
23	0.070	0.128	0.152	0.350
24	0.095	0.169	0.167	0.432
25	0.065	0.143	0.153	0.361
26	0.117	0.162	0.143	0.423
27	0.133	0.241	0.159	0.533

The proportions of accountability were used to establish each primary component's weights [26]. The MRPI, which measures performance, was computed using this data. Higher MRPI values correspond to better results. The experiment with the lowest cutting force, flank wear, and surface roughness also produced the highest MRPI. The highest MRPI value observed in Table 10 is 0.902. The MRPI, designated as A1B2C3, provides the ideal parameter settings, which are 50 m/min for cutting speed, 0.2 mm/rev for feed rate, and 0.6 mm for cut depth. This yields 3.52 µm surface roughness, 430.26 N cutting force, and 150.84 µm flank wear.

3.5 Validation of Result

It has been machined and the best turning parameters have been determined, a verification test is needed to evaluate how accurate the analysis. The precision was predicted using confirmation studies, which showed a decrease in cutting force from 445.35 N to 430.26 N, a decrease in flank wear from 170.67 µm to 150.84 µm, and a decrease in surface roughness from 4.28 µm to 3.52 µm. Fig. 6, shows the Inconel 825 microstructure for the turning with optimal machining conditions. It is inferred that from the image the grain distribution are uniform and the nonexistence of significant surface defects [27]. This uniformity is imperative for the application in the aerospace and chemical industries which requires corrosion resistance and mechanical strength.

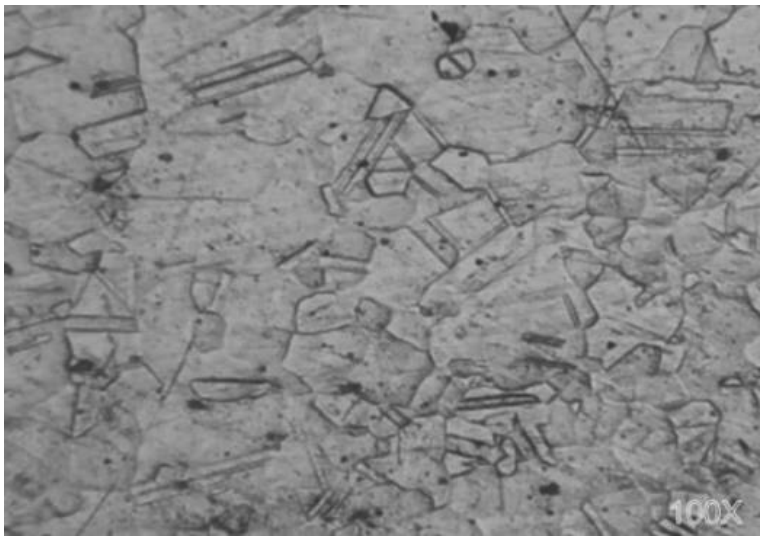

Fig. 6. Inconel' 825 microstructure

Table 11. Confirmation Test of GFRG and GPCA on the optimal level

Method	Surface roughness (μm)		Cutting force (N)		Flank wear (μm)	
	Predicted	Experimental	Predicted	Experimental	Predicted	Experimental
Grey A1B3C2	3.52	3.52	430.26	430.26	150.84	150.84
Fuzzy A1B1C1	2.92	2.54	437.842	428.36	161.758	152.63
PCA A1B3C2	3.52	3.52	430.26	430.26	150.84	150.84

Table 11 shows a comparison of the grey, fuzzy, and PCA models that predict Inconel 825 machining responses such as surface roughness, cutting force, and flank wear. The Grey and PCA methods match closely with the predicted and experimental findings and have higher accuracy with the optimum selection as A1B3C2. The ideal selection from the Fuzzy technique is A1B1C1, and the percentage deviation is substantial. The analysis using the Grey and PC approaches produces consistent predictions for the experimental settings. The limitation of the works is three input parameters were used in this study and tool coating not considered in this study.

5. Conclusions

This research work presented a cohesive optimization of Taguchi design, Grey-Fuzzy and PCA towards the machinability improvements. The followings findings were made from the experiment:

- Cutting speed is the most influencing parameter for all the three responses such as surface roughness, flank wear and cutting force.
- Grey-Fuzzy provides the distinguished estimation of multi responses and has superior GFRG of 0.882, which is compared to other technique. These values produced a surface roughness of 2.925 μm, a cutting force of 437.84 N, and flank wear of 161.76 μm.
- PCA assisted dimensionally enabled that the First PCA for 63% of the response inconsistency and the better multi response performance index as 0.902; which optimum process parameter as cutting speed 50 m/min, fees rate 0.2 mm/rev, and depth of cut 0.6 mm.
- A Grey and PCA method are closely agreements with the Predicted and experimental results and has higher accuracy with the optimum selection as A1B3C2. The optimum selection from Fuzzy approach as A1B1C1and has the percentage deviation is high. From the analysis Grey and PC methods yields the consistent predictions for the experimental conditions.

- This cohesive approach presented in this research work more reliable and better tactic for optimization the machining parameter and may use for other alloys in manufacturing industries.

Acknowledgement

The authors acknowledge that this study is supported by Saveetha Engineering College, Chennai, 602105, India

References

[1] Darolia R. Development of strong, oxidation and corrosion resistant nickel-based superalloys: critical review of challenges, progress and prospects. International Materials Reviews 2019; 64:355-380. https://doi.org/10.1080/09506608.2018.1516713

[2] Shahwaz M, Nath P, Sen I. A critical review on the microstructure and mechanical properties correlation of additively manufactured nickel-based superalloys. Journal of Alloys and Compounds 2022; 907:164530. https://doi.org/10.1016/j.jallcom.2022.164530

[3] Thakur A, Mohanty A, Gangopadhyay S, Maity KP. Tool Wear and Chip Characteristics during Dry Turning of Inconel 825. Procedia Materials Science 2014; 5:2169-2177. https://doi.org/10.1016/j.mspro.2014.07.422

[4] Al-Tamimi AA, Sanjay C. Intelligent Systems to Optimize and Predict Machining Performance of Inconel 825 Alloy. In: Metals. 2023. https://doi.org/10.3390/met13020375

[5] Thakur A, S. G, and Mohanty A. Investigation on Some Machinability Aspects of Inconel 825 During Dry Turning. Materials and Manufacturing Processes 2015; 30:1026-1034. https://doi.org/10.1080/10426914.2014.984216

[6] Krishna M, Kumar SD, Ezilarasan C et al. Application of MOORA & COPRAS integrated with entropy method for multi-criteria decision making in dry turning process of Nimonic C263. Manufacturing Rev. 2022; 9. https://doi.org/10.1051/mfreview/2022014

[7] Yadav RK, Abhishek K, Mahapatra SS, Nandi G. A study on machinability aspects and parametric optimization of Inconel 825 using Rao1, Rao2, Rao3 approach. Materials Today: Proceedings 2021; 47:2784-2789. https://doi.org/10.1016/j.matpr.2021.03.386

[8] Thakur DG, Ramamoorthy B, Vijayaraghavan L. Study on the machinability characteristics of superalloy Inconel 718 during high-speed turning. Materials & Design 2009; 30:1718-1725. https://doi.org/10.1016/j.matdes.2008.07.011

[9] Senthilkumaar JS, Selvarani P, Arunachalam RM. Intelligent optimization and selection of machining parameters in finish turning and facing of Inconel 718. The International Journal of Advanced Manufacturing Technology 2012; 58:885-894. https://doi.org/10.1007/s00170-011-3455-7

[10] Rajyalakshmi G, Ramaiah PV. Application of Taguchi, Fuzzy-Grey Relational Analysis for Process Parameters Optimization of WEDM on Inconel-825. Indian Journal of Science and Technology 2015; 8:1-12. https://doi.org/10.17485/ijst/2015/v8i35/50946

[11] Chakraborty S, Das PP, Kumar V. Application of grey-fuzzy logic technique for parametric optimization of non-traditional machining processes. Grey Systems: Theory and Application 2018; 8:46-68. https://doi.org/10.1108/GS-08-2017-0028

[12] Greenacre M, Groenen PJF, Hastie T et al. Principal component analysis. Nature Reviews Methods Primers 2022; 2:100. https://doi.org/10.1038/s43586-022-00184-w

[13] Sahu NK, Singh MK, Getrude Mutono-Mwanza B, Sahu AK. Investigation of Machinability Characteristics of EDMed Inconel 825 Alloy under Multidimensional Parametric Modeling by Using Holistic Grey-PCA Statistical Models. Advances in Materials Science and Engineering 2022. https://doi.org/10.1155/2022/3147586

[14] Imani L, Rahmani Henzaki A, Hamzeloo R, Davoodi B. Modeling and optimizing of cutting force and surface roughness in milling process of Inconel 738 using hybrid ANN and GA. Proceedings of the Institution of Mechanical Engineers, Part B 2019; 234:920-932. https://doi.org/10.1177/0954405419889204

[15] Sharma P, Kishore K, Singh V, Sinha MK. Optimization of Process Parameters for Better Surface Morphology of Electrical Discharge Machining-Processed Inconel 825 Using Hybrid Response Surface Methodology-Desirability Function and Multi-objective Genetic Algorithm Approaches. Journal of Materials Engineering and Performance 2024; 33:11321-11337. https://doi.org/10.1007/s11665-023-08751-2

[16] Abbas AT, Al-Abduljabbar AA, El Rayes MM et al. Multi-Objective Optimization of Performance Indicators in Turning of AISI 1045 under Dry Cutting Conditions. In: Metals. 2023. https://doi.org/10.3390/met13010096

[17] Özdemir M, Abidin Ş, Mohammad R, and Yilmaz V. Analysis and optimisation of the cutting parameters based on machinability factors in turning AISI 4140 steel. Canadian Metallurgical Quarterly 2022; 61:407-417. https://doi.org/10.1080/00084433.2022.2058154
[18] Manikandan P, Elayaperumal A, Franklin Issac R. Influence of mechanical alloying process on structural, mechanical and tribological behaviours of CNT reinforced aluminium composites - a statistical analysis. Bulletin of the Polish Academy of Sciences Technical Sciences 2021; 69:e136745-e136745. https://doi.org/10.24425/bpasts.2021.136745
[19] S MA, A E, R FI et al. Tribology Characterization of Plasma Sprayed Zirconia-Alumina and Fused Zirconia-Alumina Composite Coated Al-Si Alloy at Different Sliding Velocity and Load Conditions. Silicon 2022; 14:4707-4722. https://doi.org/10.1007/s12633-021-01234-w
[20] R FI, A D. Effect of Laser Treatment on Surface and Interface of Silicon Nitride Coated Ti6Al7Nb Alloy - A Statistical Analysis. Silicon 2023; 15:1545-1561. https://doi.org/10.1007/s12633-023-02319-4
[21] Kazeem RA, Aregbesola DS, Jen TC et al. Multi-response optimization of process parameters for sustainable machining of AISI 1018 steel with palm kernel oil-assisted minimum quantity lubrication technique. International Journal on Interactive Design and Manufacturing (IJIDeM) 2024; 18:771-787. https://doi.org/10.1007/s12008-023-01696-9
[22] Gandhi A, Kumari S, Sunil Kumar M et al. Enhancing machining performance of Inconel 825 alloy using grey relation analysis and JAYA-TLBO optimization techniques. International Journal on Interactive Design and Manufacturing (IJIDeM) 2025; 19:1357-1369. https://doi.org/10.1007/s12008-024-01810-5
[23] Prasad G, S. VG, and Kamath C R. Evaluation of tool wear and surface roughness in high-speed dry turning of Incoloy 800. Cogent Engineering 2024; 11:2376913. https://doi.org/10.1080/23311916.2024.2376913
[24] Manikandan P, Elaya Perumal A, Franklin Issac R. Mapping of Wear Mechanism for Mechanical Alloyed Aluminum Carbon Nanotube Composites-An In Situ Analysis. Journal of Tribology 2020; 143. https://doi.org/10.1115/1.4047854
[25] Li N, Chen Y-J, Kong D-D. Multi-response optimization of Ti-6Al-4V turning operations using Taguchi-based grey relational analysis coupled with kernel principal component analysis. Advances in Manufacturing 2019; 7:142-154. https://doi.org/10.1007/s40436-019-00251-8
[26] Payal H, Sachin M, and Bharti PS. Parametric optimization of EDM process for Inconel 825 using GRA and PCA approach. Journal of Information and Optimization Sciences 2019; 40:291-307. https://doi.org/10.1080/02522667.2019.1578090
[27] Senthil TS, Babu SR, Puviyarasan M. Mechanical, microstructural and fracture studies on inconel 825-SS316L functionally graded wall fabricated by wire arc additive manufacturing. Scientific Reports 2023; 13:5321. https://doi.org/10.1038/s41598-023-32124-3

Research on Engineering Structures & Materials
www.jresm.org
Research Group

Research Article

Flexural performance of composite beam with high-strength steel girder and ECC slab: A comprehensive parametric study

Anh-Duc Mai [1,a], Chi-King Lee [2,b], Cong-Luyen Nguyen [*,3,c]

[1]*Construction Management Division, The University of Danang – University of Science and Technology, Danang 550000, Vietnam*
[2]*School of Engineering and Technology, The University of New South Wales, Canberra, ACT 2600, Australia*
[3]*Construction Informatics Division, The University of Danang – University of Science and Technology, Danang 550000, Vietnam*

Article Info

Article History:

Received 02 May 2025

Accepted 28 May 2025

Keywords:

HSS-ECC composite beams;
Flexural performance;
Numerical parametric investigation;
Rotation capacity;
Initial bending stiffness

Abstract

The combination of high-strength steel (HSS) girder and engineered cementitious composites (ECC) slab in composite beam exhibits excellent structural performance with enhanced strength and superior ductility. However, the effects of different parameters on the structural performance of this type of composite beam have yet to be thoroughly investigated. This study presents a numerical parametric study on the flexural performance of composite beams made of HSS girder and ECC slab. A validated numerical model developed by the authors using finite element ABAQUS software was adopted for the parametric investigation. The material nonlinearities and real contact between components were incorporated into the model. The effects of crucial parameters on the flexural performance of this composite beam type were examined based on the modelling results of total 136 HSS-ECC composite beam models. These key parameters consist of the mechanical properties of HSS and ECC materials, cross-section parameters, construction details, shear connection degree, and slab type. The bending performance of the composite beams was represented by initial bending stiffness, rotation, and normalized bending moment capacity. The results of parametric investigations revealed that the initial bending stiffness, rotation capacity, and normalized bending moment capacity of the modelled composite beams were sensitive to the mechanical properties of constitutive materials, cross-section dimensions, and construction details. It was also found that the slab type had a marginal effect on the flexural performance of HSS-ECC beams, while shear stud spacing significantly affected all the investigated indicators.

1. Introduction

Steel grades with a yield strength greater than 550 MPa are categorized as high-strength steel (HSS), which has become increasingly popular in structural engineering applications thanks to its advantage of high strength/weight ratio. Smaller in dimension, lighter in weight and greater in strength of HSS could reduce the construction cost owing to a significant reduction in welding, fabrication, and erection. As a result, HSS can be applied in various types of structures, including bare steel and composite columns [1-10], connections [11-15], encased beams [16-19]. It is evident from these studies that HSS has been utilized with its favorable strength, which led to the enhancement of structural performance. For a composite beam made of HSS girder connected with normal concrete slab through means of shear studs, when it is subjected to a sagging moment, a

*Corresponding author: ncluyen@dut.udn.vn
[a]orcid.org/0000-0002-1243-0230; [b]orcid.org/0000-0001-8342-6442; [c]orcid.org/0009-0009-6572-3932
DOI: http://dx.doi.org/10.17515/resm2025-860ma0502rs

HSS I-section is used at the bottom and plays a role in carrying tension, while in contrast, the concrete slab is placed on top of the steel I-section and resists compressive internal load. Thus, each material is employed in an efficient way as its favorable attributes are being fully utilized. If HSS is used to replace normal strength steel (NSS) I-section, the composite beam can theoretically take advantage of the superior strength of HSS. However, experimental [20,21], numerical [22,23], and analytical [24,25] studies on HSS-concrete composite beams reported that sudden crushing of concrete slab in bending region could occur, and the HSS-concrete composite beam could not reach its plastic strength capacity due to strain incompatibility between HSS and concrete. To be more specific, higher strain capacity of HSS at the bottom (0.35% for HSS grade 690 MPa) versus lower strain of concrete (0.23% - 0.3%) could result in a premature crushing of concrete, and thus, the superior strength of HSS could not be employed [20-25]. Furthermore, longitudinal shear failure may occur in a concrete composite beam utilizing an HSS I-section due to an imbalance longitudinal shear load between the HSS I-section and the normal concrete slab if the slab is transversely reinforced inadequately [26,27]. As a result, the bending capacity of the beam constructed with HSS girder and concrete slab is even lower than the case having a failure mode of concrete crushing in the bending area as longitudinal shear failure occurred at the very early stage of the loading process [27].

To address aforementioned drawback of composite beam made of HSS girder and concrete slab, Nguyen and Lee [28] recently proposed a novel composite beam based on two constitutive materials of HSS and ECC, in which ECC slab was employed to replace concrete slab on top connected with HSS I-section at the bottom by shear studs. Indeed, ECC possesses high compressive strain capacity (over 0.5%, which is higher than any HSS grades available to date), allowing it to resist the compressive load in the slab until HSS reaches its full strength. Besides, high shear resistance and better bond strength of ECC help prevent longitudinal shear failure [29-30]. On top of that, employing HSS-ECC composite beams could substantially reduce embodied carbon content and carbon footprint since bi-products of steel and ferrosilicon alloy producing processes (i.e., fly ash, silica fume) are utilized to partially replace cement in the ECC mix which normally includes cement, fly ash, silica fume, sand, fiber, water, superplasticizer [31-34]. To examine the bending behavior of composite beam made of HSS girder and ECC slab (hereafter referred as HSS-ECC beam for brevity), Nguyen and Lee [28] conducted a four-point bending test of four beams, including three HSS-ECC beams manufactured with different slab thicknesses and compressive strengths of ECC, and one NSC-HSS beam used as a control beam. The results found that HSS-ECC beams demonstrated a great enhancement in flexural strength and ductility compared to HSS-concrete counterparts, which showed a failure mode of brutal crushing of concrete in the bending region. In addition, to complement the experimental result, a numerical finite element (FE) model as well as an analytical model have been constructed and validated against experimental findings [35]. It has been revealed that although the bending behavior of HSS-ECC beams has received attention from researchers recently [28,35], available studies on the bending behavior of HSS-ECC beams are very limited. In order to promote this type of composite beam to be widely applied in practical (e.g., structures under extreme conditions such as long span structures or structures subjected to high loading), an insight into the influence of different crucial parameters on the bending behavior of HSS-ECC beam is required. Thus, a parametric investigation on the flexural performance of HSS-ECC beams is essentially needed.

In this study, the finite element (FE) model using ABAQUS developed and validated by Nguyen and Lee [28], which has been proven as a reliable and accurate model for simulating the bending behavior of HSS-ECC beams, was used to conduct the parametric investigation. A total of 136 HSS-ECC beam models were generated and investigated to elucidate the effect of different parameters (i.e., mechanical properties of HSS and ECC materials, cross-section parameters, construction details, shear connection degree, and slab type) on their flexural performance represented by initial bending stiffness, rotation, and flexural capacities. The influences of these parameters were then discussed based on the numerical results.

2. The Validated Finite Element Model Adopted

This parametric investigation employs a verified nonlinear finite element (FE) model reported in the author's previous study [28]. The mentioned FE model was built using ABAQUS software with details of modelling and validation processes. Thus, the following sections will only summarize the key features of the model.

2.1. Element Types

The full model of HSS-ECC beam is used to realistically reflect the actual condition of the beams. Figure 1(a) indicates typical cross-section dimensions of the HSS-ECC beam. Solid elements C3D8R is employed to simulate the HSS, ECC, shear stud, and strengthened bolts [Figure 1(b)] as it is expected to minimize convergence issue and use less computational cost in comparison to other types of elements, such as tetrahedra C3D4. Four-node shell element S4R is utilized for simulating profiled steel sheeting (PSS) while truss element T3D2 is deployed for the steel meshes.

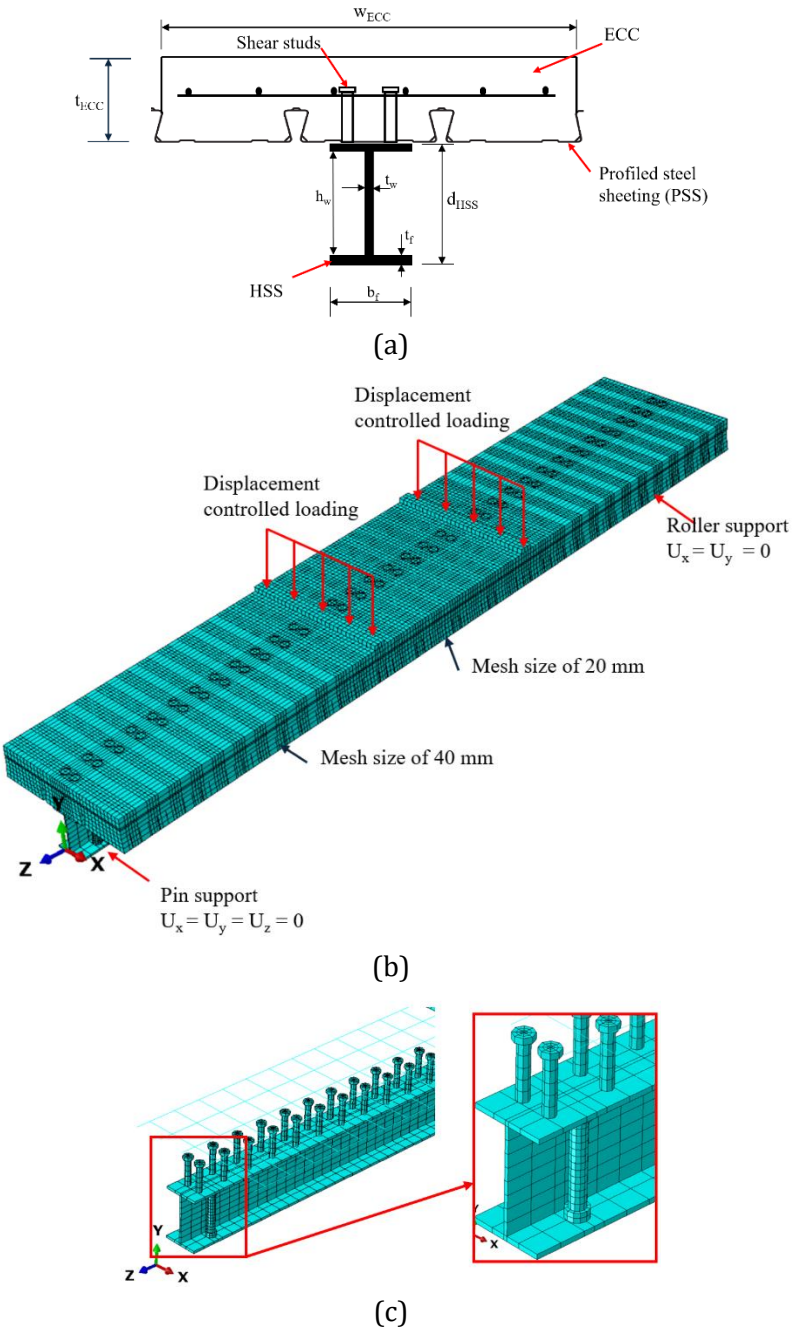

Fig. 1. HSS-ECC beam and FE model: (a) Typical cross-section configuration; (b) Typical FE model, (c) Partition method for components

2.2. Mesh Sizes

The mesh sizes used for HSS I-section is 40 mm and this guarantees that it is divided into more than 8 elements along the web of the HSS I-section [Figure 1(c)]. For its flange, it should be discretised in such a way that at least one common node between flange and centre point of shear stud's base [Figure 1(c)]. The nominal element size of shear stud, PSS and bar mesh, strengthened bolts are respectively 10 mm, 40 mm, 100 mm and 5 mm. After a mesh sensitivity analysis [28], mesh sizes for ECC slab in two shear spans and in the bending region are respectively 40 mm and 20 mm, as seen in Figure 1(b).

2.3. Interaction Properties Between Components

The interactions between HSS I-beam and PSS, between ECC slab and shear studs, between ECC slab and PSS were simulated using surface-to-surface contact available in ABAQUS [36]. The interaction between the HSS section top flange and the shear studs bottom was simulated using Tie constraint as shear stud is welded to HSS's top flange through resistance welding. This interaction type is also used for the contact between loading plates and the ECC slab. Embedded region available in ABAQUS [30] is utilised for the connection properties between the reinforcement mesh and ECC slab.

2.4. Constitutive models

Tensile and compression stress-strain models of ECC, which were suggested by Meng et al. [37], are adopted in the numerical modelling [Figure 2(a)-(c)]. For HSS section, its constitutive model indicated in Figure 2(d) is represented by a bilinear curve. The PSS is modelled using elastic-perfectly plastic curve that has been widely adopted in other studies [38], and shown in Figure 2(e). Regarding shear stud, as it is experimentally proven to have an excellent ductility, a constitutive model [Figure 2(f)] developed by Hassan et al. [39] is used. Mechanical properties of key materials employed in the constitutive models corresponding to the tests reported in [28] are listed Tables 1–2. These values were employed in the model validation and are the baseline values for the parametric investigation.

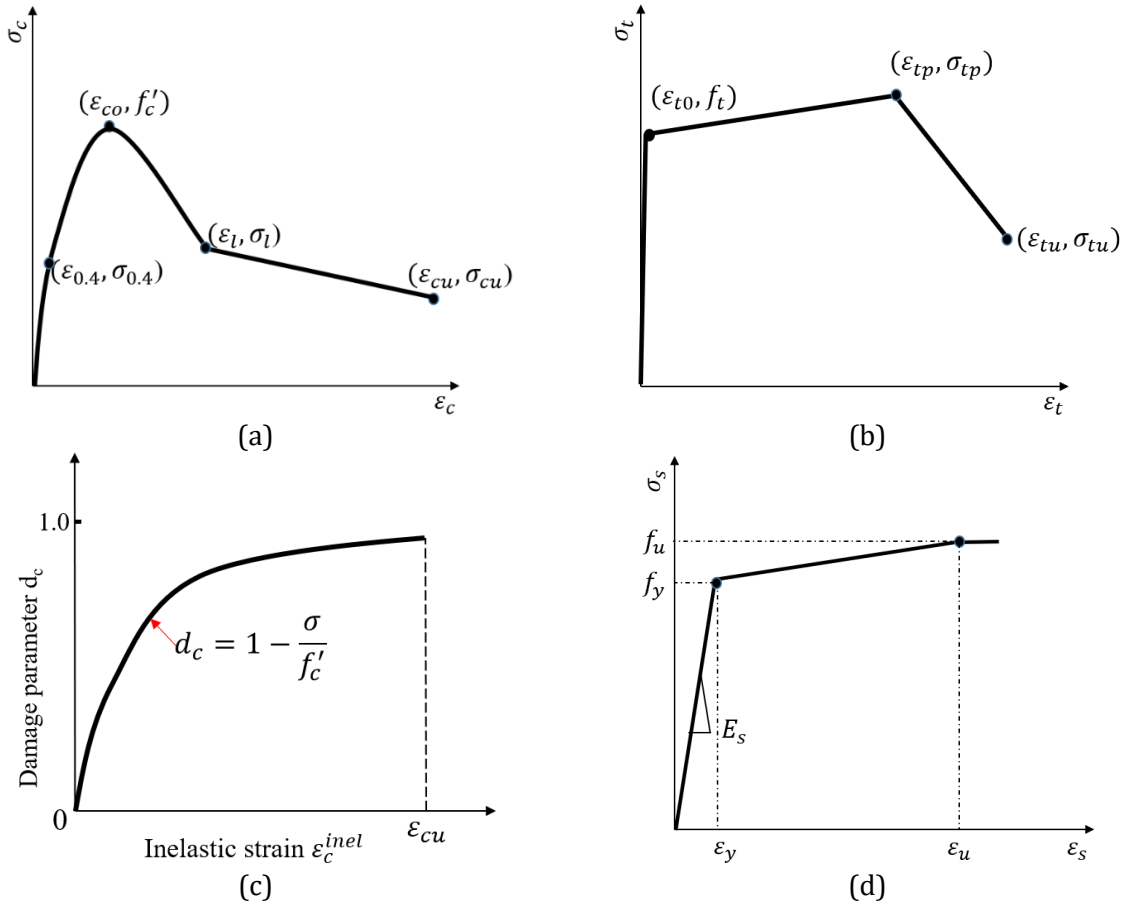

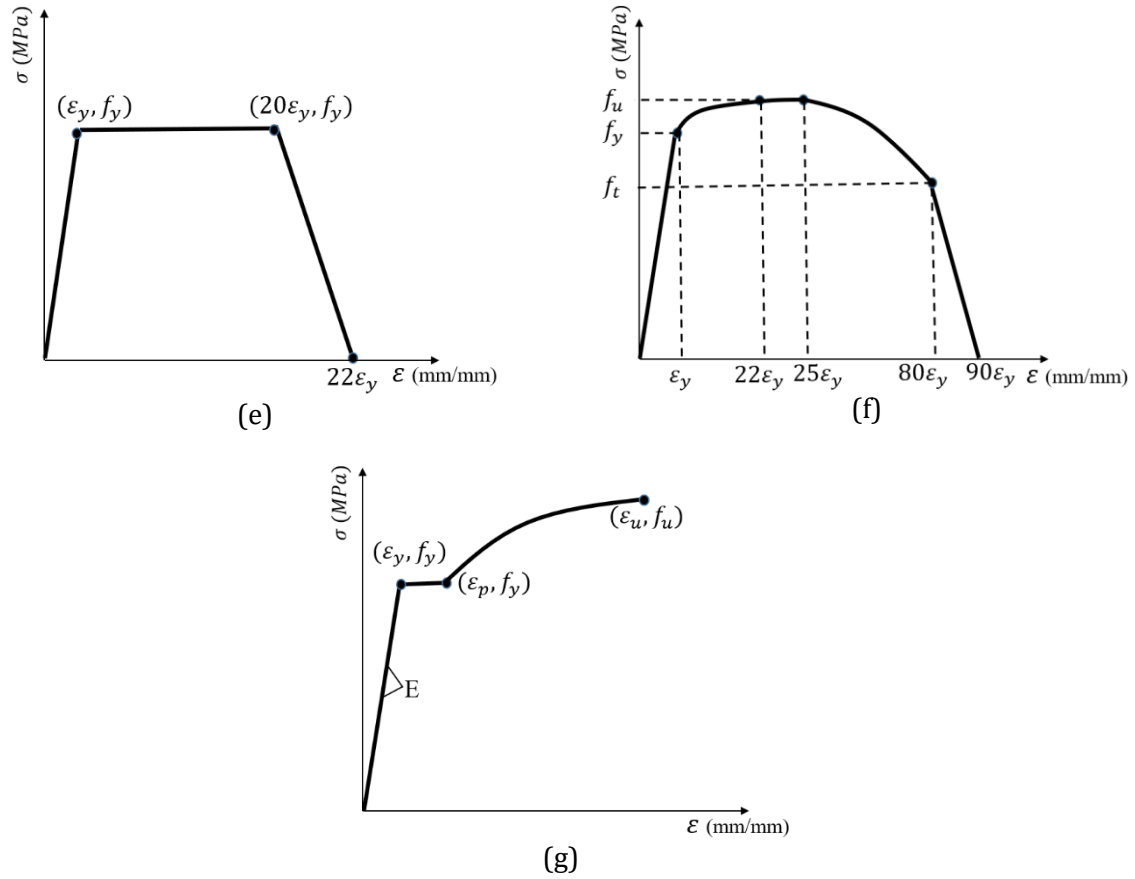

Fig. 2. Stress–strain models of materials for parametric investigation. (a) ECC stress-strain model under compression; (b) ECC stress-strain model under tensile; (c) ECC damage model under compression; (d) HSS; (e) PSS; (f) Headed shear stud; (g) Steel reinforcement

Table 1. Properties of materials for FE model

Material	E (GPa)	f_y (MPa)	f_u (MPa)	f_t (MPa)	ε_y(%)	ε_p(%)	ε_u(%)
Shear stud	200	344	410	331	0.17	-	-
PSS	248	691	-	-	0.28	-	-
Steel mesh	200	543	632	-	0.27	2.4	20.8
HSS Grade 690	200	690	770	-	0.35	-	8.0
HSS Grade 960	200	960	980	-	0.48	-	5.5

Table 2. ECC properties for FE model

Material	E_c (GPa)	$\sigma_{0.4}$ (MPa)	σ_{co} (MPa)	σ_l (MPa)	σ_{cu} (MPa)	$\varepsilon_{0.4}$ (%)	ε_{co} (%)	ε_l (%)	ε_{cu} (%)
CF40	15.5	16.0	40.0	20.0	10.0	0.10	0.50	0.85	1.20
CF70	20.5	28.0	70.0	30.0	13.5	0.14	0.53	0.95	1.40

Table 2. ECC properties for FE model (continued)

Material	σ_{to} (MPa)	σ_{tp} (MPa)	σ_{tu} (MPa)	ε_{to} (%)	ε_{tp} (%)	ε_{tu} (%)
CF40	2.43	3.2	1.7	0.016	1.2	2.2
CF70	4.40	5.3	3.0	0.021	1.0	1.7

2.5. Loading and Boundary Conditions

As simple supported beams with two loading points were employed in the experimental program [28], pin and roller supports are modelled in the simulation by restraining either two or three translational directions. Load is applied to those nodes located on the surface of the two loading points by applying downward displacement with the rate similar the rate that were used in the test [Figure 1(b)]. The self-weight is also applied in the simulation by inclusion of self-weight in the first step and propagated to the remaining steps of the simulation process.

By comparing with the test results, it was shown that the developed FE model has successfully captured the test results. The failure mode of HSS-ECC beams was that the large proportion of HSS at middle region was yielded before ECC top surface crushing (Figure 3), which is well-agreed with the test results reported in [28]. In addition, load (P)-mid-span deformation (δ) curves (hereafter referred as $P-\delta$ curves for brevity) obtained from all of the tested beams were confirmed by the verified FE model, not only in terms of bending capacity but also the bending stiffness. Thus, in this study, this verified nonlinear FE model is employed for the parametric analysis.

3. Parametric Investigation Design

The parametric analysis explored a broad spectrum of crucial parameters that influence the bending performance of HSS-ECC beams. A total of nine parameters were classified into three groups consisting of mechanical properties of materials [i.e., (1) ECC compressive strength, f'_{ECC} and (2) HSS tensile strength, $f_{y,HSS}$], cross-sectional dimension [i.e., (3) HSS section depth, d_{HSS}; (4-5) ECC slab thickness and width, t_{ECC}, w_{ECC}, respectively] (see Figure 1(a)) and construction details [e.g., (6) ratio of HSS section flange width and thickness, b_f/t_f; (7) ratio of HSS section web height and thickness, h_w/t_w; (8) shear stud spacing, s_{stud} and (9) ECC slab type].

For the mechanical properties of materials, two values of f'_{ECC} (i.e., 40 MPa and 70 MPa) and two values of $f_{y,HSS}$ (i.e., 690 MPa and 960 MPa) were considered. For cross-section dimensions, the w_{ECC} was varied from 600 to 1400 mm with an interval of 400 mm, the t_{ECC} was changed from 140 to 200 mm with an interval of 30 mm and the d_{HSS} was varied from 180 to 280 mm with an interval of 50 mm. For the construction details, three values of b_f/t_f of 10, 12 and 15; three values of the h_w/t_w of 16, 20 and 27, three values of the s_{stud} of 75, 100 and 200 mm and two types of ECC slab including profiled steel sheeting (PSS) and solid slab were utilized.

If all possible combinations of the nine parameters listed above were modelled, it would require creating a total of 5,832 models (calculated as 2×2×3×3×3×3×3×3×2). Clearly, generating such a plenty of models would surpass the available computational resources and produce an overwhelming amount of data that is likely unable to understand. Therefore, the parametric investigation was categorized into two groups in which the first group examined the effects of the mechanical properties of materials and cross-section dimensions by varying parameters (1)-(5), resulting in the creation of 108 models. The second group evaluated the effects of construction details with the variation of remaining parameters (6)-(9), which generated 28 models. Accordingly, a total of 136 models was generated for parametric analysis.

The 108 models in the first group of this study all shared the same construction details with s_{stud} of 100 mm, b_f of 120 mm, t_f of 8 mm (b_f/t_f = 15), t_w of 6 mm, h_w of 6 mm (h_w/t_w = 27), and an identical PSS slab. Given the expected strong influence of $f_{y,HSS}$ on the beams' flexural performance, the 108 models were subdivided into two portions with each value of $f_{y,HSS}$ for each group. Table 3 lists 54 models with an identical S690 HSS I-section, while Table 4 describes 54 models with an identical S960 HSS I-section. Although s_{stud} was consistently kept at 100 mm, variations in cross-section dimensions and mechanical properties of materials resulted a non-constant degree of shear connection (η) among these models. Accordingly, all HSS-ECC beams of the first group were partially shear connected in which η varied from 0.42 to 0.82.

To evaluate the effects of construction details in the second group, a standard cross-section of the beam with the w_{ECC} of 600 mm, t_{ECC} of 140 mm, d_{HSS} of 180 mm was adopted. The effects of s_{stud} on the bending behaviour of the HSS-ECC beam were evaluated by considering three values of s_{stud} of 75, 100 and 200 mm in combination with four pairs of material, which were defined based on a

combination of f'_{ECC} and $f_{y,HSS}$ (i.e., f'_{ECC} = 40 Mpa, $f_{y,HSS}$= 690 Mpa; f'_{ECC} = 40 Mpa, $f_{y,HSS}$= 960 Mpa; f'_{ECC} = 70 Mpa, $f_{y,HSS}$= 690 Mpa; and f'_{ECC} = 70 Mpa, $f_{y,HSS}$= 960 Mpa). The remaining construction details were kept constant with b_f/t_f of 15, h_w/t_w of 27 and PSS slab. Accordingly, eight models were created with the variation of η from 0.41 to 1.23. For examining the effect of the b_f/t_f and h_w/t_w on the bending behaviour of the HSS-ECC beam, two values of b_f/t_f (10 and 12) and two value of h_w/t_w (16 and 20) were chosen while four pairs of ECC and HSS were employed (i.e., f'_{ECC} = 40 Mpa, $f_{y,HSS}$= 690 Mpa; f'_{ECC} = 40 Mpa, $f_{y,HSS}$= 960 Mpa; f'_{ECC} = 70 Mpa, $f_{y,HSS}$= 690 Mpa; and f'_{ECC} = 70 Mpa, $f_{y,HSS}$= 960 Mpa). For evaluating the effect of b_f/t_f and h_w/t_w, the s_{stud} of 100 mm and PSS slab were adopted. Accordingly, sixteen models were generated for evaluating the effect of the b_f/t_f and h_w/t_w. The effects of ECC slab type were determined by using solid slab instead of PPS in combination of with four material properties. The other construction details with s_{stud} of 100 mm, b_f/t_f of 15 and h_w/t_w of 27 were adopted in modelling the performance of HSS-ECC beam. As a result, four models were created with s_{stud} of 100 mm, b_f/t_f of 15 and h_w/t_w of 27. Table 5 presents 28 models of HSS-ECC beam used in the second group.

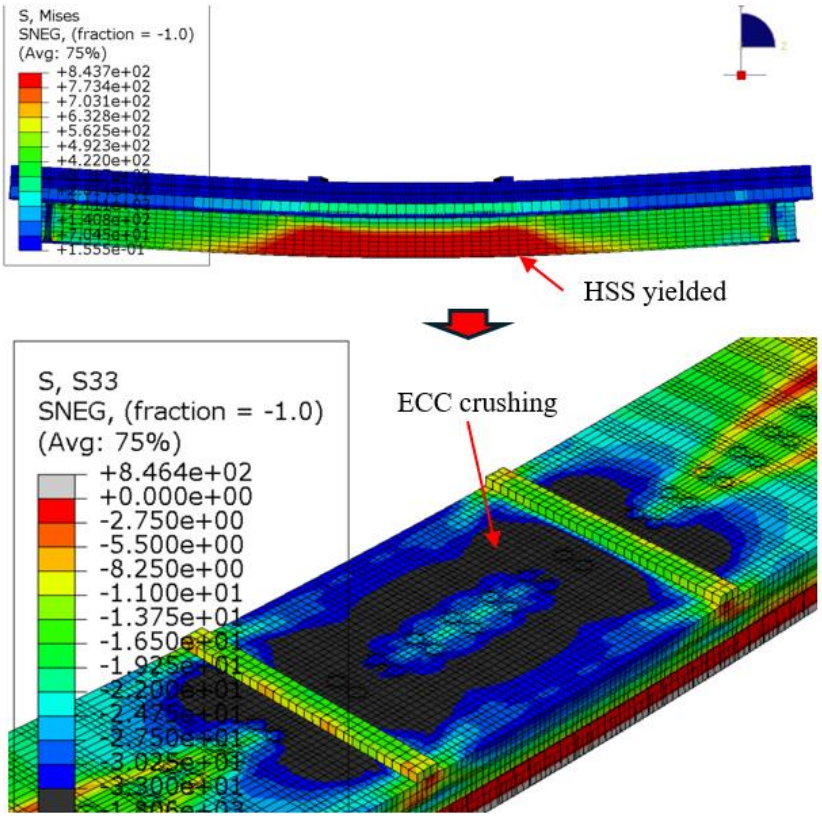

Fig. 3. Typical failure mode of HSS-ECC beam

As illustrated in Tables 3-5, the notations of HSS-ECC beams modelled in the parametric analysis consisted of five parts separated by a hyphen. Each part of notation includes two capital letters (e.g., CF) and a number (e.g., 40). The first capital letter represents the material, which is either letter C or S (C stands for ECC and S stands for high strength steel). The following capital letter represents either the cross-section dimension or strength of material in which F denotes the compressive strength/yield strength of ECC/HSS, W and T present the ECC slab width and ECC slab thickness, respectively, and D denotes the depth of HSS I-section. The number indicates the value of the cross-section dimension is in mm while MPa for material strength. For example, the CF40-CW600-CT140-SF690-SD180 beam refers to the HSS-ECC beam with the f'_{ECC} of 40 MPa, w_{ECC} of 600 mm, t_{ECC} of 140 mm, $f_{y,HSS}$ of 690 MPa and d_{HSS} of 180 mm.

4. Parametric Study Results

Parametric investigation was undertaken to evaluate the effect of key parameters [i.e., ECC compressive strength (f'_{ECC}), HSS yield strength ($f_{y,HSS}$), ECC slab width (w_{ECC}), ECC slab thickness (t_{ECC}), HSS section depth (d_{HSS}), ratio of HSS section flange width and thickness (b_f/t_f), ratio of HSS section web height and thickness (h_w/t_w), shear stud spacing (s_{stud}), and ECC slab type] on the bending behaviour of beams that is represented by three main indicators consisting of rotation capacity (R), initial bending stiffness (EI_0), and normalised bending capacity (M_{FE}/M_{ps}) . M_{FE}/M_{ps} presents ratio of moment capacity of composite beam (M_{FE}) to moment capacity of HSS section alone (M_{ps}) . The R of a composite beam is crucial for determining moment redistribution in plastic design. The R is computed by dividing the rotation at the ultimate moment (θ_u) by that at the yielding moment (θ_y) [24]. The R of simply supported beams adopted in this study is computed by dividing the mid-span deflection at the maximum load by the mid-span deflection at the yield load. Tables 3 and 4, respectively, present the effect of cross-section dimensions and mechanical properties of materials on the flexural strength of HSS-ECC beam while Table 5 indicates the effect of construction details on the flexural strength of HSS-ECC beam. Given that the parametric analysis encompasses 136 models; to present the findings concisely, the following sections will present the overall tendency and then focus on the effects of different parameters by presenting the results from selected beams.

Table 3. Influence of the mechanical properties of materials and cross-section dimensions on flexural strength of HSS-ECC beam with S690 HSS I-section

Beam (HSS S690 MPa)*		η	EI_0 (kN/mm)	R	M_{FE}/M_{ps}
CW600-CT140-SD180	CF40-SF690	0.82	23.11	2.32	2.36
	CF70-SF690	0.82	26.30	2.90	2.73
CW600-CT140-SD230	CF40-SF690	0.82	32.22	2.56	2.15
	CF70-SF690	0.74	35.85	3.10	2.44
CW600-CT140-SD280	CF40-SF690	0.82	43.46	2.71	2.05
	CF70-SF690	0.68	48.61	3.38	2.29
CW600-CT170-SD180	CF40-SF690	0.71	28.39	2.09	2.64
	CF70-SF690	0.82	32.34	2.60	3.18
CW600-CT170-SD230	CF40-SF690	0.64	37.60	2.10	2.37
	CF70-SF690	0.74	43.52	2.92	2.79
CW600-CT170-SD280	CF40-SF690	0.61	48.61	2.22	2.22
	CF70-SF690	0.68	55.42	3.03	2.56
CW600-CT200-SD180	CF40-SF690	0.71	33.91	1.84	3.00
	CF70-SF690	0.82	39.94	2.38	3.63
CW600-CT200-SD230	CF40-SF690	0.64	45.97	2.07	2.68
	CF70-SF690	0.74	52.45	2.57	3.20
CW600-CT200-SD280	CF40-SF690	0.59	56.08	1.91	2.41
	CF70-SF690	0.68	64.51	2.57	2.83
CW1000-CT140-SD180	CF40-SF690	0.71	26.35	2.23	2.62
	CF70-SF690	0.82	30.10	2.91	3.10
CW1000-CT140-SD230	CF40-SF690	0.64	37.01	2.72	2.40
	CF70-SF690	0.74	41.45	3.55	2.82
CW1000-CT140-SD280	CF40-SF690	0.59	48.93	3.11	2.25
	CF70-SF690	0.68	54.44	3.78	2.55
CW1000-CT170-SD180	CF40-SF690	0.71	33.23	2.04	3.05
	CF70-SF690	0.82	38.32	2.52	3.70
CW1000-CT170-SD230	CF40-SF690	0.65	44.65	2.35	2.70
	CF70-SF690	0.74	50.38	2.81	3.20

CW1000-CT170-SD280	CF40-SF690	0.59	57.13	2.89	2.51
	CF70-SF690	0.68	64.44	3.24	2.91
CW1000-CT200-SD180	CF40-SF690	0.71	39.84	1.82	3.54
	CF70-SF690	0.82	47.78	2.28	4.40
CW1000-CT200-SD230	CF40-SF690	0.65	52.77	2.00	3.15
	CF70-SF690	0.74	60.63	2.31	3.75
CW1000-CT200-SD280	CF40-SF690	0.59	66.76	2.12	2.81
	CF70-SF690	0.68	75.85	2.46	3.35
CW1400-CT140-SD180	CF40-SF690	0.71	25.51	2.65	2.97
	CF70-SF690	0.82	33.11	4.25	3.54
CW1400-CT140-SD230	CF40-SF690	0.65	38.91	2.91	2.69
	CF70-SF690	0.74	44.04	4.05	3.05
CW1400-CT140-SD280	CF40-SF690	0.59	50.64	3.01	2.50
	CF70-SF690	0.68	57.11	4.18	2.76
CW1400-CT170-SD180	CF40-SF690	0.71	36.39	2.45	3.68
	CF70-SF690	0.82	42.02	3.16	4.23
CW1400-CT170-SD230	CF40-SF690	0.65	49.05	4.18	3.08
	CF70-SF690	0.74	50.40	4.28	3.66
CW1400-CT170-SD280	CF40-SF690	0.59	59.81	4.58	2.80
	CF70-SF690	0.68	69.79	4.07	3.27
CW1400-CT200-SD180	CF40-SF690	0.71	46.06	2.59	4.50
	CF70-SF690	0.82	54.36	3.58	5.34
CW1400-CT200-SD230	CF40-SF690	0.65	57.91	2.65	3.55
	CF70-SF690	0.74	65.32	3.50	4.36
CW1400-CT200-SD280	CF40-SF690	0.59	71.90	2.77	3.33
	CF70-SF690	0.68	78.93	3.58	3.83
Mean					3.06
SD					0.67

*b_f/t_f=15 (b_f=120 mm, t_f=8 mm), t_w=6 mm, s_{stud} =100 mm, and PSS slab.

Table 4. Influence of the mechanical properties of materials and cross-section dimensions on flexural strength of HSS-ECC beam with S960 HSS I-section

Beam (HSS S960 MPa)*		η	EI_0 (kN/mm)	R	M_{FE}/M_{ps}
CW600-CT140-SD180	CF40-SF960	0.82	20.93	1.44	2.00
	CF70-SF960	0.59	25.99	2.59	2.33
CW600-CT140-SD230	CF40-SF960	0.82	28.29	1.62	1.84
	CF70-SF960	0.54	34.39	2.00	2.10
CW600-CT140-SD280	CF40-SF960	0.82	47.63	1.34	1.69
	CF70-SF960	0.54	47.04	2.16	2.02
CW600-CT170-SD180	CF40-SF960	0.61	25.99	1.34	2.15
	CF70-SF960	0.59	29.93	1.53	2.58
CW600-CT170-SD230	CF40-SF960	0.61	33.00	1.36	1.97
	CF70-SF960	0.53	40.90	1.72	2.31
CW600-CT170-SD280	CF40-SF960	0.61	45.14	1.50	1.86
	CF70-SF960	0.49	52.39	1.78	2.15
CW600-CT200-SD180	CF40-SF960	0.51	30.78	1.25	2.39
	CF70-SF960	0.59	36.37	1.44	2.89

CW600-CT200-SD230	CF40-SF960	0.48	40.54	1.26	2.18
	CF70-SF960	0.53	49.40	1.60	2.61
CW600-CT200-SD280	CF40-SF960	0.48	49.82	1.21	1.97
	CF70-SF960	0.49	59.37	1.54	2.31
CW1000-CT140-SD180	CF40-SF960	0.51	23.80	1.37	2.20
	CF70-SF960	0.59	28.41	1.76	2.55
CW1000-CT140-SD230	CF40-SF960	0.49	34.43	1.65	2.03
	CF70-SF960	0.53	39.48	2.03	2.34
CW1000-CT140-ID280	CF40-SF960	0.49	45.48	1.92	1.94
	CF70-SF960	0.49	51.85	2.20	2.19
CW1000-CT170-SD180	CF40-SF960	0.51	30.57	1.36	2.50
	CF70-SF960	0.59	35.78	2.46	2.94
CW1000-CT170-SD230	CF40-SF960	0.46	38.67	1.32	2.29
	CF70-SF960	0.53	48.13	1.71	2.61
CW1000-CT170-SD280	CF40-SF960	0.42	53.07	2.58	2.14
	CF70-SF960	0.49	61.17	1.80	2.42
CW1000-CT200-SD180	CF40-SF960	0.51	35.83	1.17	2.84
	CF70-SF960	0.59	44.69	1.47	3.48
CW1000-CT200-SD230	CF40-SF960	0.46	48.65	1.23	2.62
	CF70-SF960	0.53	55.95	1.43	3.03
CW1000-CT200-SD280	CF40-SF960	0.42	63.74	1.51	2.40
	CF70-SF960	0.49	71.96	1.67	2.76
CW1400-CT140-SD180	CF40-SF960	0.51	25.37	1.57	2.43
	CF70-SF960	0.59	30.81	2.38	2.88
CW1400-CT140-SD230	CF40-SF960	0.46	34.17	1.73	2.29
	CF70-SF960	0.53	41.88	2.59	2.54
CW1400-CT140-SD280	CF40-SF960	0.42	48.44	1.85	2.14
	CF70-SF960	0.49	54.41	2.73	2.33
CW1400-CT170-SD180	CF40-SF960	0.51	33.95	1.46	2.79
	CF70-SF960	0.59	38.44	2.11	3.40
CW1400-CT170-SD230	CF40-SF960	0.46	43.60	3.02	2.56
	CF70-SF960	0.53	52.57	3.18	2.96
CW1400-CT170-SD280	CF40-SF960	0.42	56.51	3.06	2.35
	CF70-SF960	0.49	67.13	3.24	2.68
CW1400-CT200-SD180	CF40-SF960	0.51	43.02	1.55	3.61
	CF70-SF960	0.59	49.18	2.10	4.25
CW1400-CT200-SD230	CF40-SF960	0.46	53.57	1.32	2.77
	CF70-SF960	0.53	62.98	2.35	3.57
CW1400-CT200-SD280	CF40-SF960	0.42	69.21	1.74	2.76
	CF70-SF960	0.49	77.50	2.42	3.15
Mean					2.52
SD					0.50

*b_f/t_f=15 (b_f=120 mm, t_f=8 mm), t_w=6 mm, s_{stud} =100 mm, and *PSS slab.*

Table 5. Effect of different construction details on the flexural strength of HSS-ECC beam

Beam construction details *		η	EI_0 (kN/mm)	R	M_{FE}/M_{ps}
CW600-CT140-SD180	CF40-SF690	0.41	21.29	2.51	2.27
(stud spacing = 200 mm)	CF40-SF960	0.41	23.44	3.07	2.61
PSS, b_f/t_f = 15	CF70-SF690	0.41	19.24	1.68	1.91
h_w/t_w = 27	CF70-SF960	0.29	20.26	2.13	2.21
CW600-CT140-SD180	CF40-SF690	1.23	23.40	2.32	2.36
(stud spacing = 75 mm)	CF40-SF960	1.23	25.84	2.63	2.73
PSS, b_f/t_f= 15	CF70-SF690	1.22	22.23	1.65	2.01
h_w/t_w = 27	CF70-SF960	0.88	25.38	1.89	2.33
CW600-CT140-SD180	CF40-SF690	0.82	24.95	2.16	2.12
stud spacing = 100 mm	CF40-SF960	0.82	27.60	2.56	2.46
PSS, (b_f/t_f= 12)	CF70-SF690	0.71	22.46	1.32	2.49
h_w/t_w = 27	CF70-SF960	0.54	26.50	1.75	2.90
CW600-CT140-SD180	CF40-SF690	0.82	26.05	1.94	1.95
stud spacing = 100 mm	CF40-SF960	0.82	30.05	1.96	2.25
PSS, (b_f/t_f= 10)	CF70-SF690	0.62	23.36	1.65	2.29
h_w/t_w = 27	CF70-SF960	0.54	27.85	1.54	2.65
CW600-CT140-SD180	CF40-SF690	0.82	25.73	1.97	2.16
stud spacing = 100 mm	CF40-SF960	0.82	29.71	2.54	2.51
PSS, b_f/t_f= 15	CF70-SF690	0.64	23.55	1.33	2.52
(h_w/t_w= 20)	CF70-SF960	0.54	27.74	1.59	2.94
CW600-CT140-SD180	CF40-SF690	0.82	26.80	1.86	2.20
stud spacing = 100 mm	CF40-SF960	0.82	30.60	2.34	2.56
PSS, b_f/t_f= 15	CF70-SF690	0.59	23.77	1.22	2.52
(h_w/t_w= 16)	CF70-SF960	0.54	28.49	1.47	2.95
CW600-CT140-SD180	CF40-SF690	0.71	23.11	2.32	2.36
stud spacing = 100 mm	CF40-SF960	0.81	26.30	2.90	2.73
(solid slab), b_f/t_f = 15	CF70-SF690	0.51	20.93	1.44	2.00
h_w/t_w = 27	CF70-SF960	0.59	25.99	2.59	2.33
Mean					2.40
SD					0.29

* The bold words/symbols inside brackets show the variation of construction details.

4.1. Overall Tendency

To better understand the overall tendency of initial stiffness and bending capacity (M_{FE}/M_{ps}), their values for all composite beam models of different material properties and beam configurations are plotted in Figures 4 and 5. It is exhibited in Figure 4 that initial stiffness is significantly increased with the increase in beam cross-section dimensions including HSS section depth, ECC slab width and thickness. It is also worth noting that group with higher ECC compressive strength (group 70-690 and 70-960) show much higher intial stiffness. For M_{FE}/M_{ps} shown in Figure 5, it is indicated that in the same group of material properties, M_{FE}/M_{ps} decreases with the rise in HSS section depth but increases with the increase of ECC slab thickness and width. In all four groups of material properties, beams with ECC of 70 Mpa compressive strength and 690 Mpa HSS tensile strength (group 70-690) show highest normalized bending capacity while the least accounting for the 40-960 group.

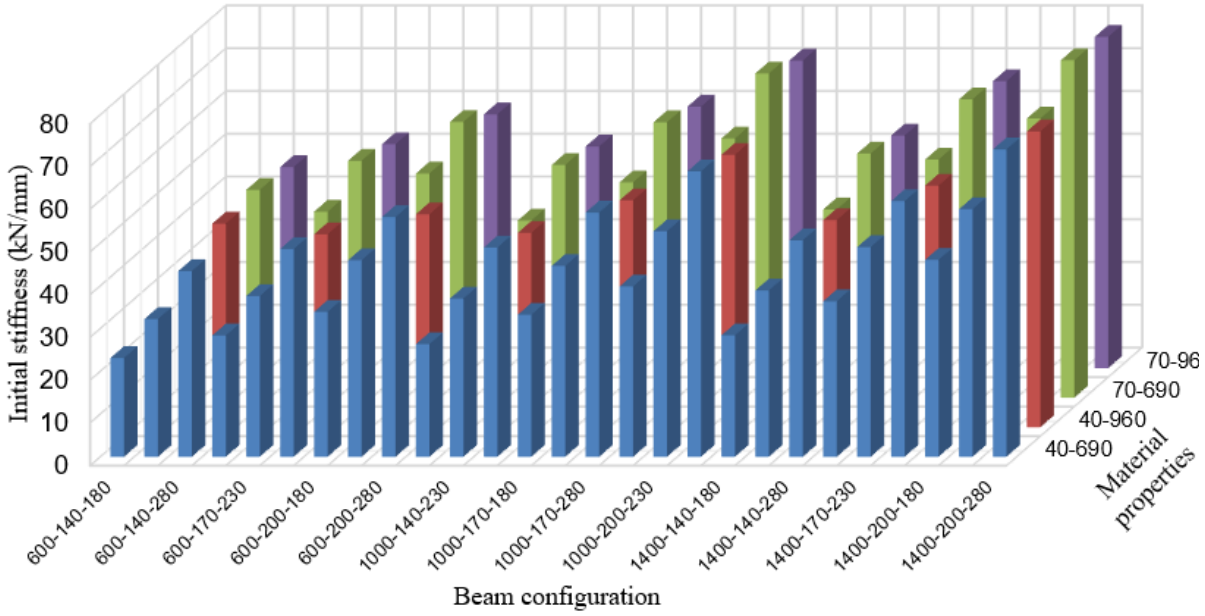

Fig. 4. Variation of initial stiffness for different material properties and beam configurations

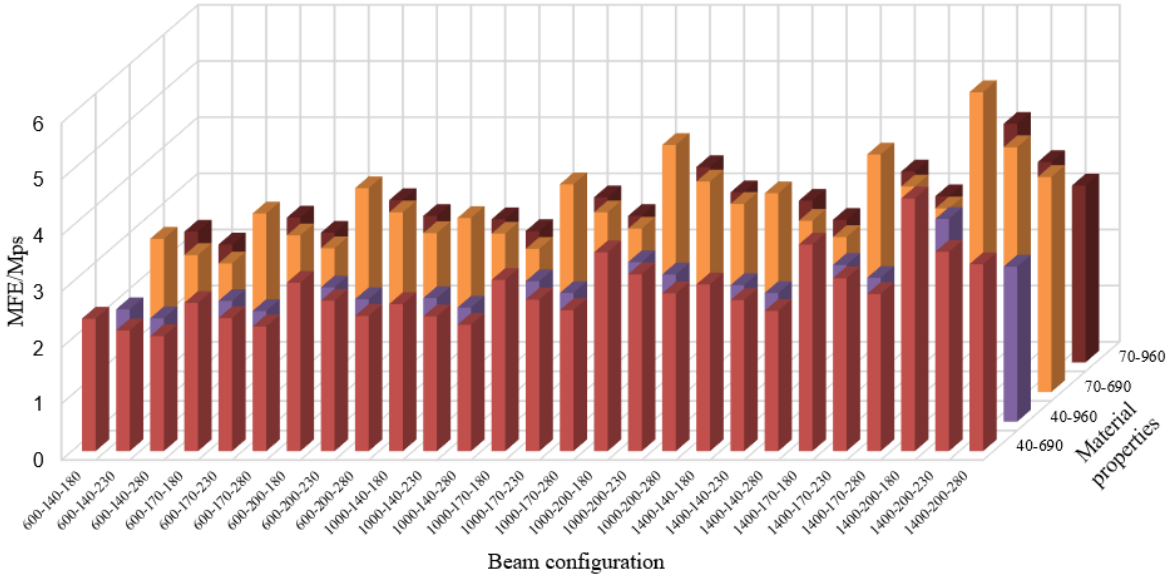

Fig. 5. Variation of M_{FE}/M_{ps} for different material properties and beam configurations

4.2. Effect of ECC compressive strength (f'_{ECC}) and HSS yield strength ($f_{y,HSS}$)

4.2.1 Initial Bending Stiffness (EI_0)

Figure 6 illustrates the $P-\delta$ relationship for two typical HSS-ECC beams (e.g., CW600-CT140-SD180 and CW600-CT200-SD230) having the variation of f'_{ECC} and $f_{y,HSS}$. Figure 7(a) compares the effects of mechanical properties of materials on the EI_0. The data reveals that EI_0 is highly sensitive to f'_{ECC}. For instance, in the CW600-CT140-SD180 Beam, increasing f'_{ECC} from 40 MPa to 70 MPa resulted in a 12% increase in EI_0, from 23.62 kN/mm to 26.52 kN/mm, as shown in Figures 6(a) and 7(a). Similarly, the CW600-CT200-SD230 Beam experienced the same 12% increase in EI_0 [Figures 7(b) and 7(a)]. Also, Figures 6 and 7(a) indicate that EI_0 is not significantly affected by $f_{y,HSS}$, as beams with identical f'_{ECC} but different $f_{y,HSS}$ exhibited the same EI_0. This can be attributed to the fact that EI_0 is influenced by the elastic modulus of beam's material properties. It is clear that ECC with higher f'_{ECC} has a higher elastic modulus (Table 2), while the Young's modulus of HSS remains consistent across different grades.

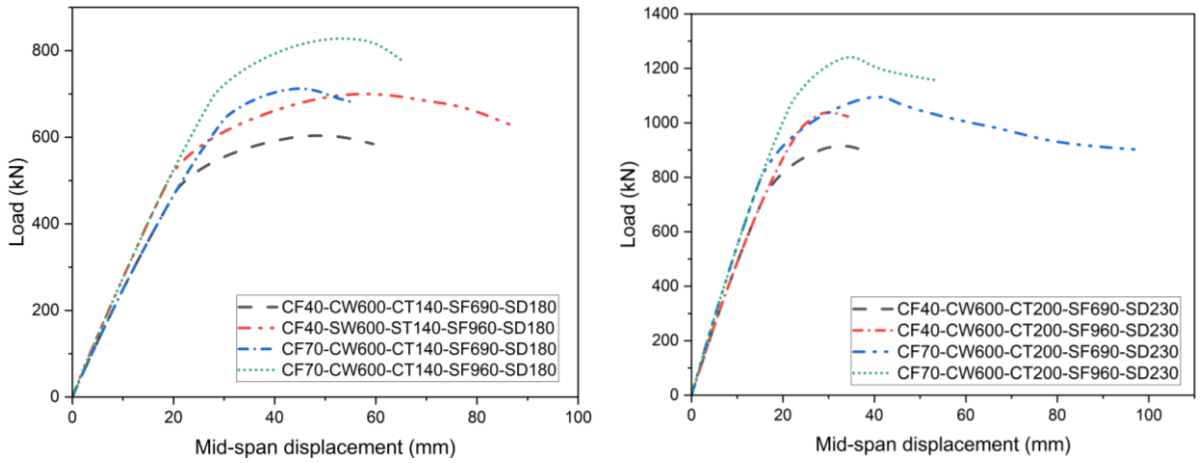

(a) (b)

Fig. 6. $P-\delta$ relationship of HSS-ECC beam with various f'_{ECC} and $f_{y,HSS}$. (a) CW600-CT140-SD180 Beam; (b) CW600-CT200-SD230 Beam

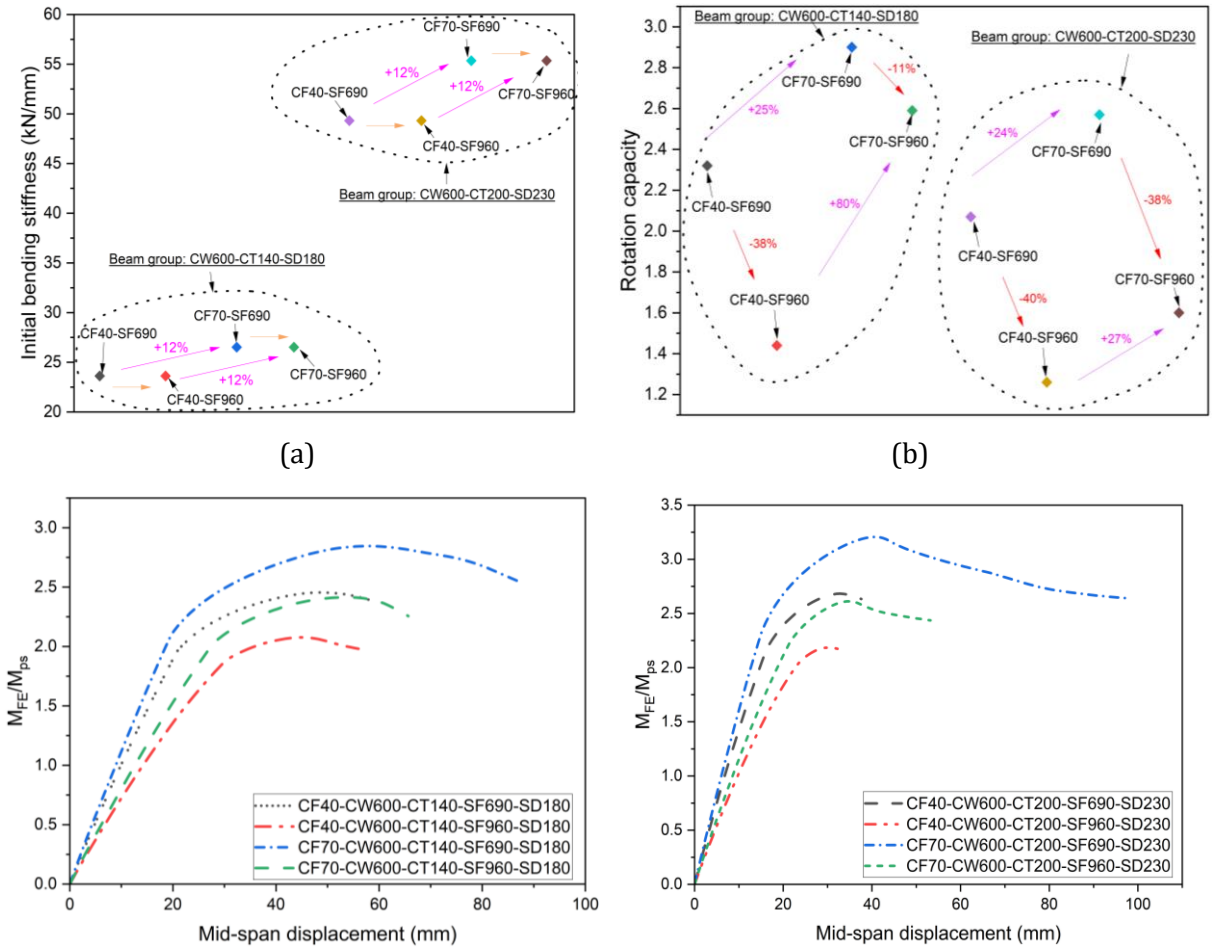

(a) (b)

(c) (d)

Fig. 7. Effect of f'_{ECC} and $f_{y,HSS}$ on flexural strength of HSS-ECC beam: (a) Initial bending stiffness; (b) Rotation capacity; (c) and (d) Normalized bending capacity

4.2.2 Rotation Capacity (R)

The effect of mechanical properties of constitutive materials on R for two typical HSS-ECC beams (e.g., CW600-CT140-SD180 and CW600-CT200-SD230) is depicted in Figure 7(b). When f'_{ECC} changed from 40 MPa to 70 MPa, R for the CW600-CT140-SD180 Beam with S690 HSS I-section obtained an increase by 25%, from 2.32 to 2.90. For S960 HSS I-section, this increase was even more pronounced, with an 80% rise from 1.44 to 2.59. A similar pattern was observed for the CW600-CT200-SD230 Beam in which R obtained an increase by 24% for S690 HSS I-sections and 27% for S960 HSS I-sections. Regarding the effects of $f_{y,HSS}$, an increase in $f_{y,HSS}$ resulted in a decrease in R. It can be seen in Figure 7(b) that, for the CW600-CT140-SD180 Beam with 40 MPa ECC, increasing $f_{y,HSS}$ from 690 MPa to 960 MPa led to a 38% reduction in R, from 2.32 to 1.44, and an 11% reduction, from 2.9 to 2.59 for a similar beam with 70 MPa ECC. A similar trend was noted for the CW600-CT200-SD230 Beam with 40 MPa ECC, R decreased by 40% when $f_{y,HSS}$ changed from 690 MPa to 960 MPa, and by 38% when the ECC had the f'_{ECC} of 70 MPa.

4.2.3 Bending Capacity (M_{FE}/M_{ps})

The effect of mechanical properties of constitutive materials on the HSS-ECC beam bending capacity can be represented by the normalized moment capacity M_{FE}/M_{ps}, where M_{FE} is the HSS-ECC beam's moment capacity (determined through FE modelling) and M_{ps} is the HSS I-section's full plastic moment capacity. Figures 7(c) and 7(d) display typical plots of M_{FE}/M_{ps} versus δ for the CW600-CT140-SD180 and CW600-CT200-SD230 Beams. As shown in Figure 5(c), increasing f'_{ECC} from 40 MPa to 70 MPa resulted in a 15.6% increase in M_{FE}/M_{ps} (from 2.43 to 2.81) for the S690 HSS section and a 13.8% increase (from 2.10 to 2.39) for S960 HSS beams. For the CW600-CT200-SD230 Beam, a 20% increase in M_{FE}/M_{ps} was observed for both steel grades. This increase is attributed to the upward shift of the plastic neutral axis (PNA) towards the ECC slab top surface when f'_{ECC} is increased, which lengthens the moment lever arm between the HSS section and the ECC slab, thus enhancing the bending capacity. Regarding the effect of $f_{y,HSS}$, Figures 7(c), (d) indicate that M_{FE}/M_{ps} reduced as $f_{y,HSS}$ changed from 690 MPa to 960 MPa. This is because as $f_{y,HSS}$ increases, the term M_{ps} rises proportionally. However, in the HSS-ECC beam, the PNA shifts closer to the bottom of the beam and reduces the lever arm length. Consequently, although M_{FE} increased, the rate of increase was lower than that of M_{ps}, resulting in a decreased M_{FE}/M_{ps} ratio.

4.3. ECC slab width (w_{ECC}) effect

4.3.1 Initial Bending Stiffness (EI_0)

Figure 8 presents the $P-\delta$ curves for two typical HSS-ECC beams (e.g., CF40-CT140-SF690-SD180 and CF40-CT140-SF690-SD230) with variation of w_{ECC},. Figure 9(a) compares their EI_0, showing that EI_0 increases with the increase of w_{ECC}.

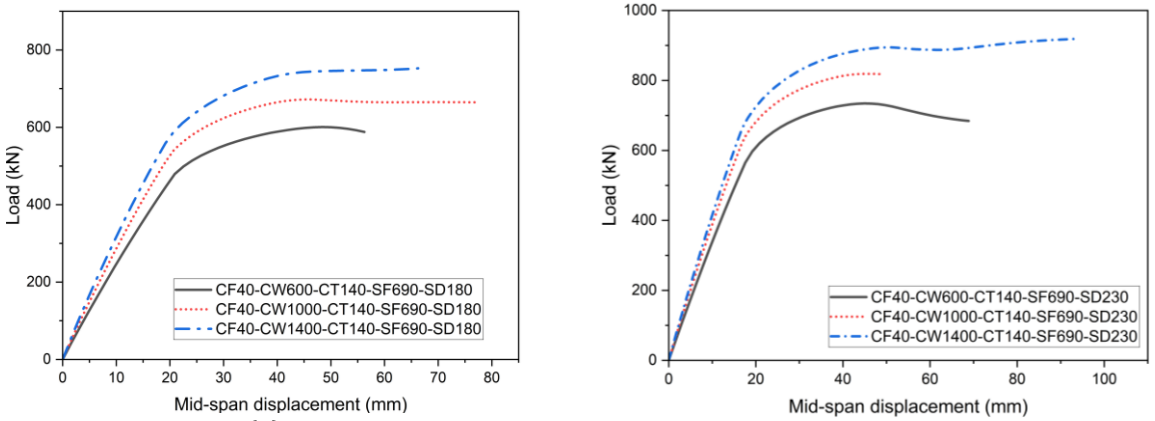

Fig. 8. Effect of w_{ECC} on $P-\delta$ relationship: (a) CF40-CT140-SF690-SD180 Beam; (b) CF40-CT140-SF690-SD230 Beam

Specifically, for the CF40-CT140-SF690-SD180 Beam, increasing the w_{ECC} from 600 mm to 1000 mm and 1400 mm resulted in EI_0 increase of 17% and 34%, respectively. A similar trend is observed for the CF40-CT140-SF690-SD230 Beam.

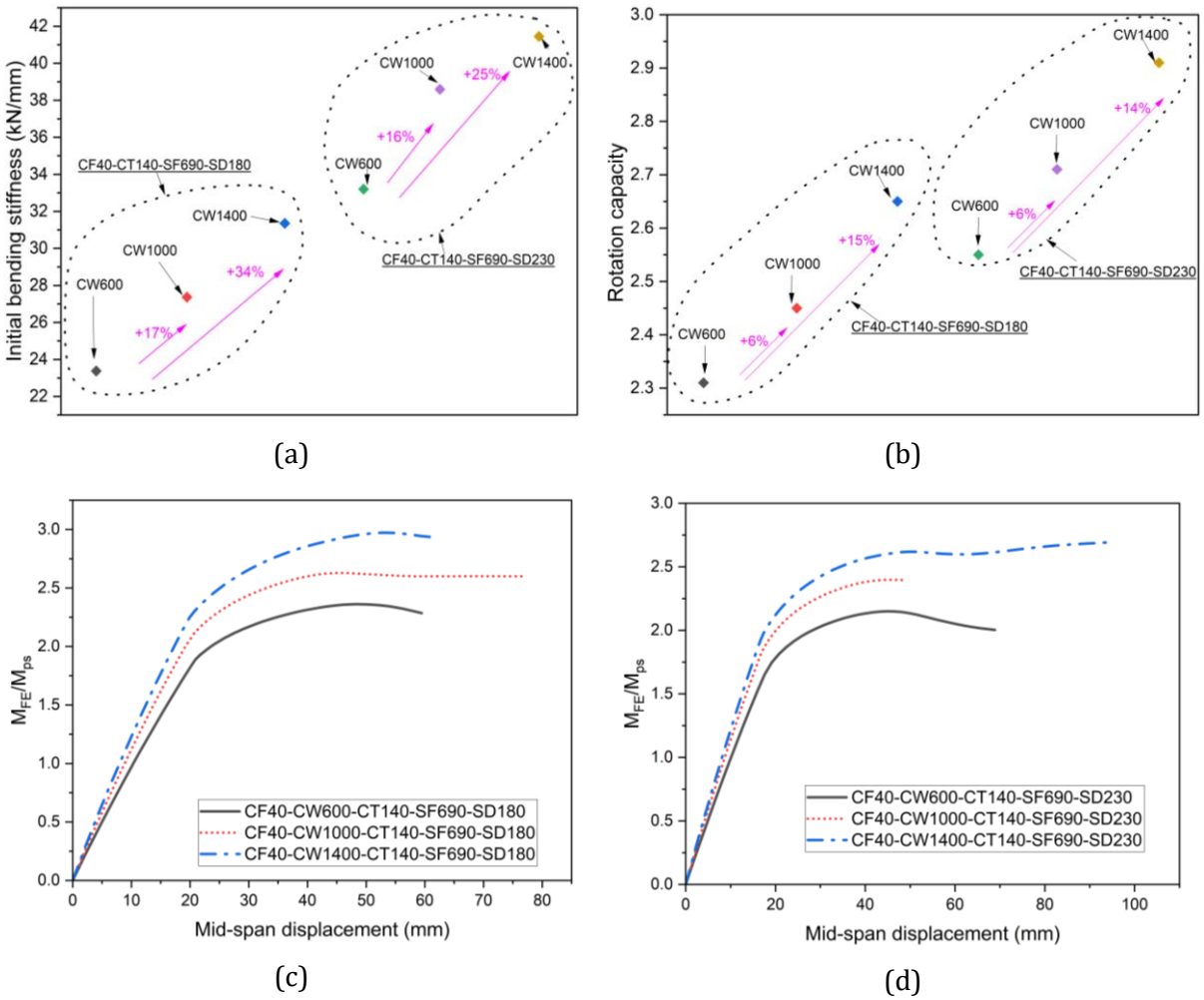

Fig. 9. Effect of w_{ECC} on flexural strength of HSS-ECC beam: (a) Initial bending stiffness; (b) Rotation capacity; (c) and (d) Normalized bending capacity

4.3.2 Rotation Capacity (R)

Figure 9(b) illustrates the impact of w_{ECC} on R for the same beams. Increasing w_{ECC} from 600 mm to 1000 mm and 1400 mm led to a 6% and 15% rise in R, respectively. This is because a wider slab shifts the plastic neutral axis (PNA) upwards, leading to a smaller strain value at the slab's top surface and delaying its crushing, allowing for greater rotation capacity.

4.3.3 Bending Capacity (M_{FE}/M_{ps})

Regarding bending strength capacity, Figures 9(c) and 9(d) show that increasing w_{ECC} from 600 mm to 1000 mm and 1400 mm led to approximately a 15% and 30% increase in M_{FE}/M_{ps}, respectively. This tendency is also due to the upward shift of the PNA, which lengthens the moment lever arm.

4.4. ECC Slab Thickness (t_{ECC}) Effect

4.4.1 Initial Bending Stiffness (EI_0)

Figures 10(a) and 10(b) depict the $P-\delta$ curves for two typical HSS-ECC beams (e.g., CF40-CW600-SF690-SD180 and CF70-CW1000-SF690-SD230) with a variation of t_{ECC}, showing that EI_0 increases with the rise of t_{ECC}. According to Figure 9(a), increasing t_{ECC} from 140 mm to 170 mm

and 200 mm resulted in a 28% and 57% increase in EI_0, respectively. This increase is clearly because of the greater resistance offered by a larger slab section.

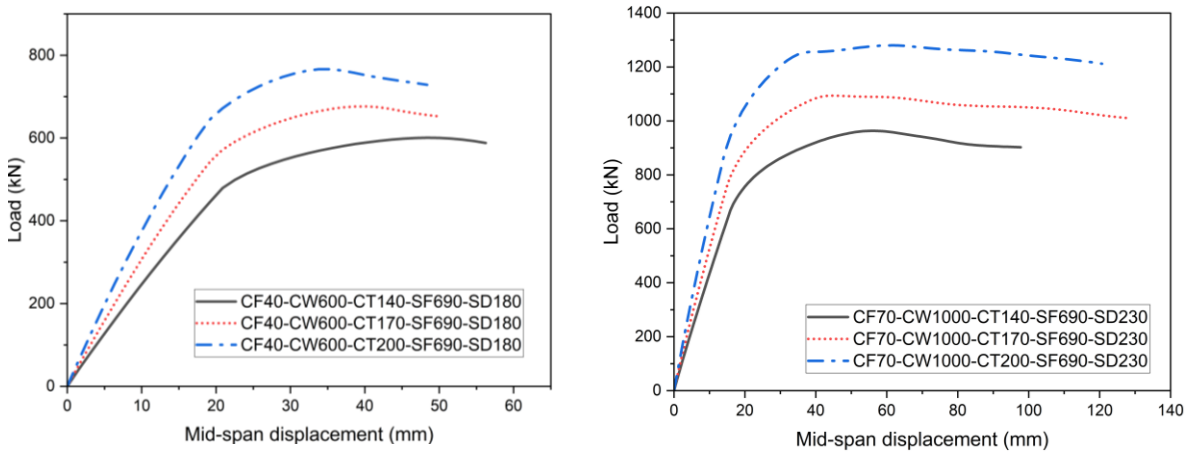

(a) (b)

Fig. 10. Effect of t_{ECC} on $P-\delta$ relationship: (a) CF40-CW600-SF690-SD180 Beam; (b) CF70-CW1000-SF690-SD230 Beam

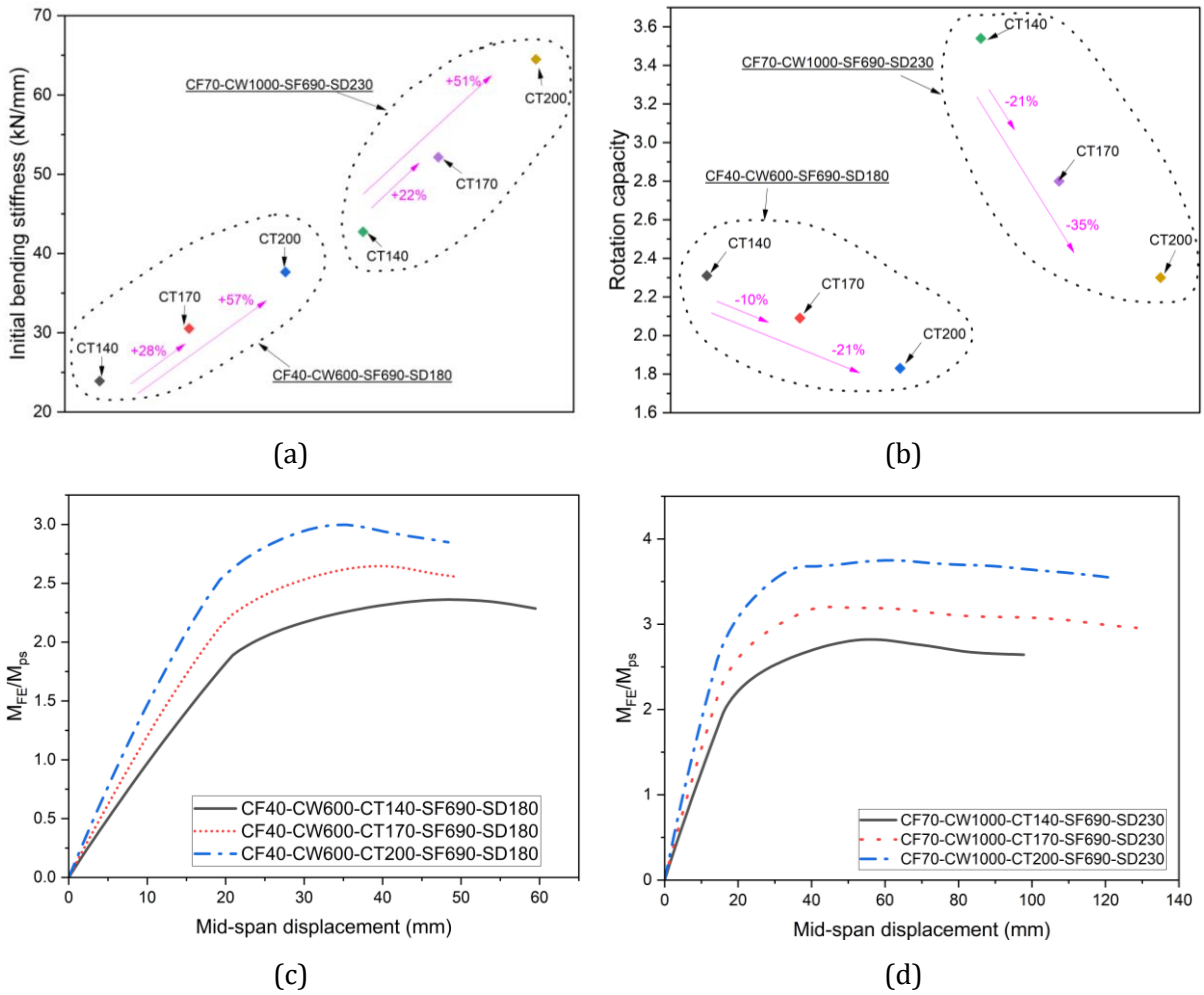

(a) (b)

(c) (d)

Fig. 11. Effect of t_{ECC} on flexural strength of HSS-ECC beam: (a) Initial bending stiffness; (b) Rotation capacity; (c) and (d) Normalized bending capacity

4.4.2 Rotation Capacity (R)

Figure 11(b) shows that increasing t_{ECC} decreases R. Specifically, for the CF40-CW600-SF690-SD180 Beam, increasing t_{ECC} from 140 mm to 170 mm and 200 mm resulted in R reductions of 10% and 21%, respectively. For the CF70-CW1000-SF690-SD230 Beam, the reductions were even greater, at 21% and 35%. This is because a thicker slab increases the distance between the PNA and the top surface of the slab, leading to higher compressive strain at the top surface and causing the ECC to crush at a lower rotation capacity.

4.4.3 Bending Capacity (M_{FE}/M_{ps})

Figures 11(c) and 11(d) illustrate the effects of t_{ECC} on M_{FE}/M_{ps} for two typical beams. As expected, with the HSS section and M_{ps} unchanged, M_{FE}/M_{ps} increased with t_{ECC}. This is because a thicker slab results in a longer lever arm and greater bending resistance.

4.5. Effect of HSS section depth (d_{HSS})

4.5.1 Initial Bending Stiffness (EI_0)

Figures 12(a) and (b) display the $P-\delta$ curves for beams with different d_{HSS}, indicating that EI_0 increases with d_{HSS}. Figure 13(a) further demonstrates that increasing the d_{HSS} from 180 mm to 280 mm nearly doubled the EI_0 value. This outcome is expected as a deeper HSS I-section increases the moment of inertia, resulting in higher EI_0.

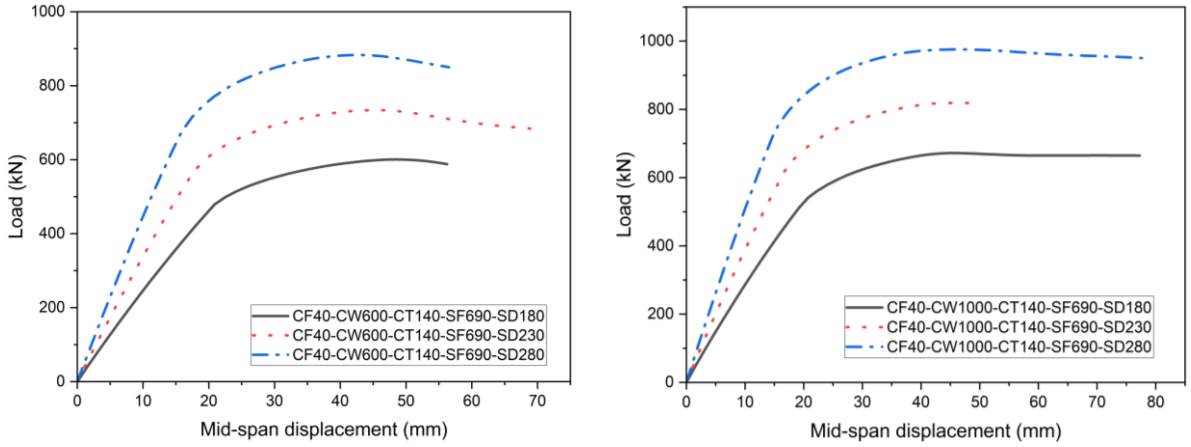

(a) (b)

Fig. 12. Effect of d_{HSS} on $P-\delta$ relationship: (a) CF40-CW600-CT140-SF690 Beam; (b) CF40-CW1000-ST140-SF690 Beam

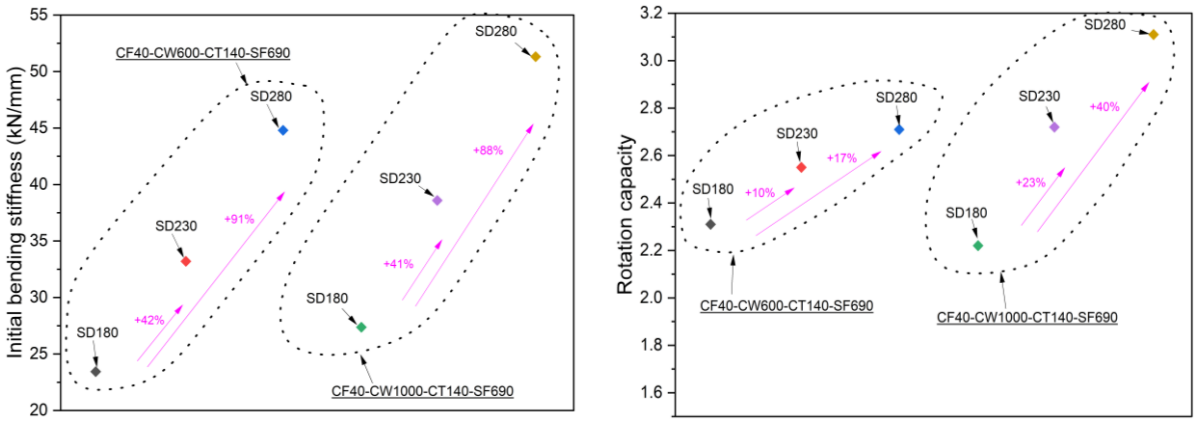

(a) (b)

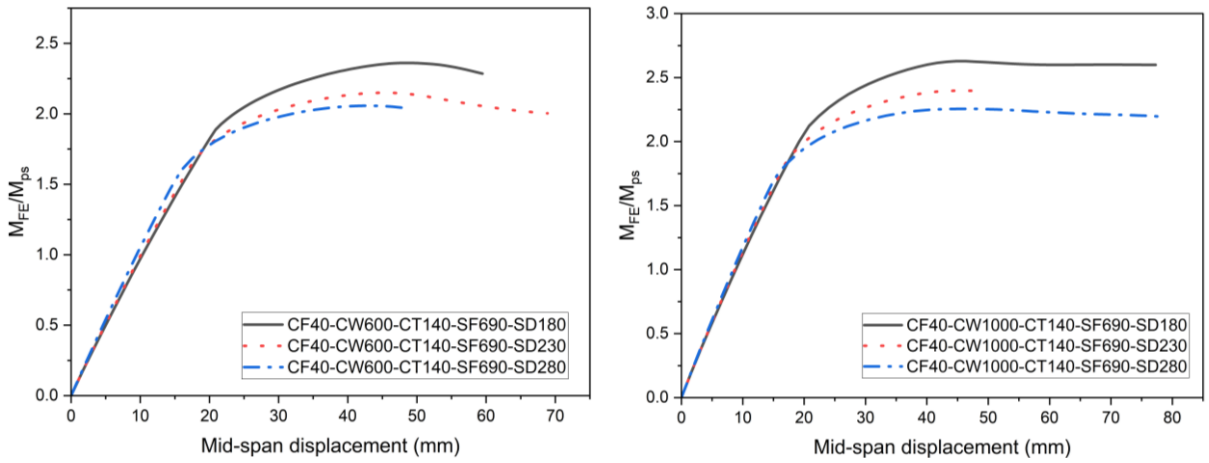

(c) (d)

Fig. 13. Effect of d_{HSS} on flexural strength of HSS-ECC beam: (a) Initial bending stiffness; (b) Rotation capacity; (c) and (d) Normalized bending capacity

4.5.2 Rotation Capacity (R)

Figure 13(b) shows that for the CF40-CW600-CT140-SF690 Beam, R experienced an increase by 10% and 17%, respectively, when d_{HSS} varied from 180 mm to 230 mm and 280 mm. Similar trends were observed for the CF40-CW1000-CT140-SF690 Beam in which R obtained an increase by approximately 23% and 40%.

4.5.3 Bending Capacity (M_{FE}/M_{ps})

Figures 13(c) and 13(d) present the M_{FE}/M_{ps} versus δ for beams with different values of d_{HSS}. These figures indicate that increasing d_{HSS} from 180 mm to 280 mm resulted in a 12% decrease in M_{FE}/M_{ps}. This is similar to the effect of increasing $f_{y,HSS}$, where M_{FE} increased but at a lower rate than M_{ps}. A deeper HSS section moves the PNA towards the HSS section, which reduces the tensile stress within it and thereby lowers the increased rate of M_{FE}.

4.6. HSS Section Web Height to Web Thickness Ratio (h_w/t_w) Effect

To study the effect of h_w/t_w, t_w was changed from 6 mm to 8 mm and 10 mm while h_w remained constant at 164 mm (Table 5). Figures 14(a) and 14(b) indicate the curves of M_{FE}/M_{ps} and bending capacity versus deflection δ. As h_w/t_w decreased, both M_{FE}/M_{ps} and bending capacity increased because a thicker t_w, mainly under tension, enhanced bending capacity. For EI_0, Figure 14(c) shows a small increase of 11% as t_w varied from 6 mm to 10 mm. However, Figure 14(d) reveals that R decreased by 14%. This is because a thicker web moved the PNA closer to the bottom of the beam, increasing ECC compressive strain at the top surface, leading to earlier ECC slab crushing and thus reducing R.

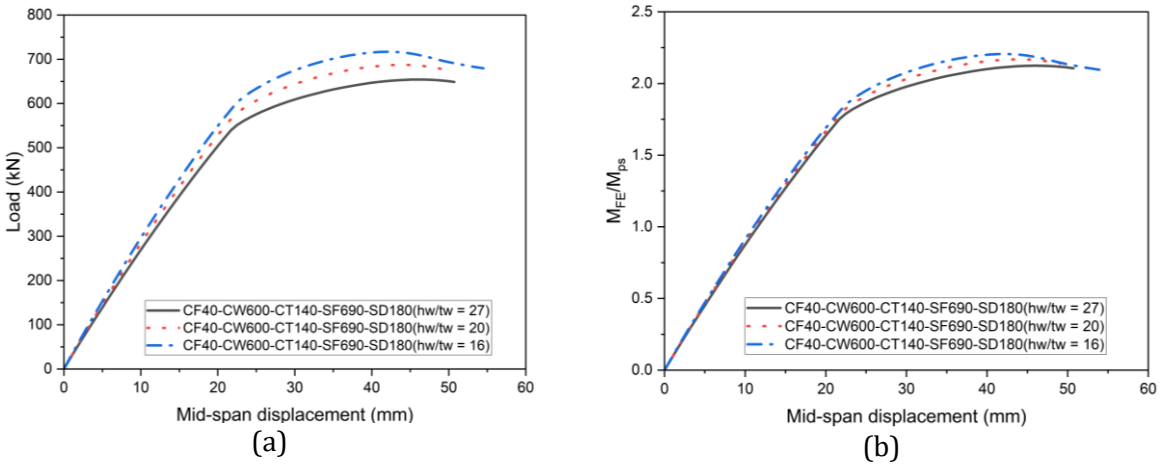

(a) (b)

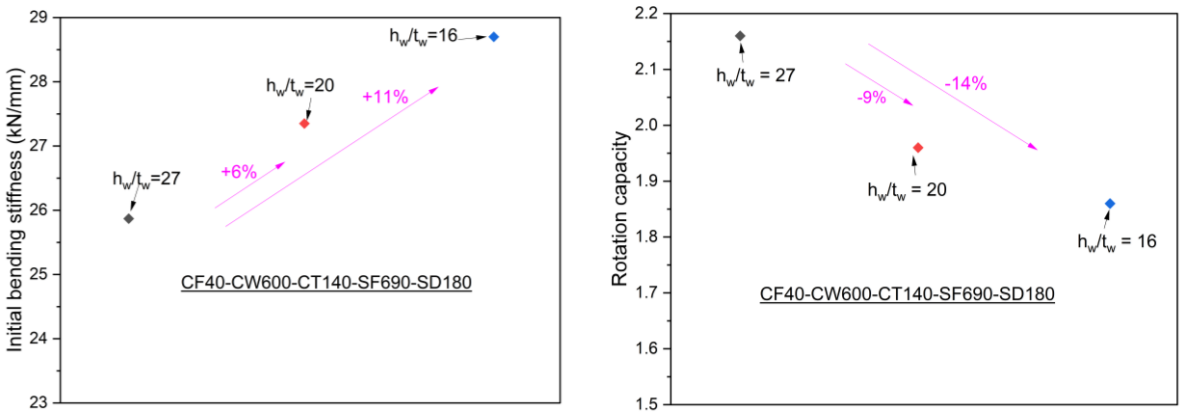

(c) (d)

Fig. 14. Effect of h_w/t_w on flexural strength of HSS-ECC beam: (a) Load carrying capacity; (b) Normalised bending moment capacity; (c) Initial bending stiffness; (d) Rotation capacity

4.7. HSS Section Flange Width and Flange Thickness (b_f/t_f) Effect

The effects of the b_f/t_f were examined by changing t_f (8, 10, and 12 mm) while keeping b_f constant at 120 mm. By increasing t_f from 8 mm to 10 mm and 12 mm, respectively, the EI_0 experienced an increase by 9% and 18%, as shown in Figure 15(a). Similar to the case of h_w/t_w effect, increasing t_f resulted in a decrease in R (Figure 15(b)). Additionally, although the load-carrying capacity increased [Figure 15(c)], M_{FE}/M_{ps} decreased as t_f increased [Figure 15(d)]. This is because increasing t_f quickly raises M_{ps}, while the PNA shifts closer to the HSS section top flange, leading to the reduction of HSS section contribution to the composite beam's overall flexural resistance. Consequently, M_{FE} increased at a lower rate than M_{ps}. This suggests that a more effective way to increase M_{FE}/M_{ps} is to increase only the HSS flange thickness at the bottom.

4.8. Slab Type Effect

Solid slab is often considered as an alternative to profiled steel sheeting (PSS). A study was conducted to assess its influence on composite beams' flexural behavior. Two sets of beams having identical cross-section dimensions and mechanical properties of materials were modelled, one using a solid slab (refer to Table 5) and the other employing PSS. Figure 16 illustrates that HSS-ECC beams having solid slab and those having PSS exhibited nearly identical behaviors. Therefore, it is observed that the type of slab has marginal impact on the bending behavior of HSS-ECC beams.

4.9. Shear Stud Spacing/Shear Connection Degree Effect

Three values of s_{stud} including 75 mm, 100 mm, and 200 mm were utilized for the CW600-CT140-SD180 Beam to examine the influence of shear connection degree (η) and shear stud spacing (s_{stud}) on the beams' bending behaviour. The results depicted in Figure 17 demonstrate that beams with smaller s_{stud} (resulting in higher η) generally exhibited greater EI_0 and M_{FE}/M_{ps}, but a smaller R.

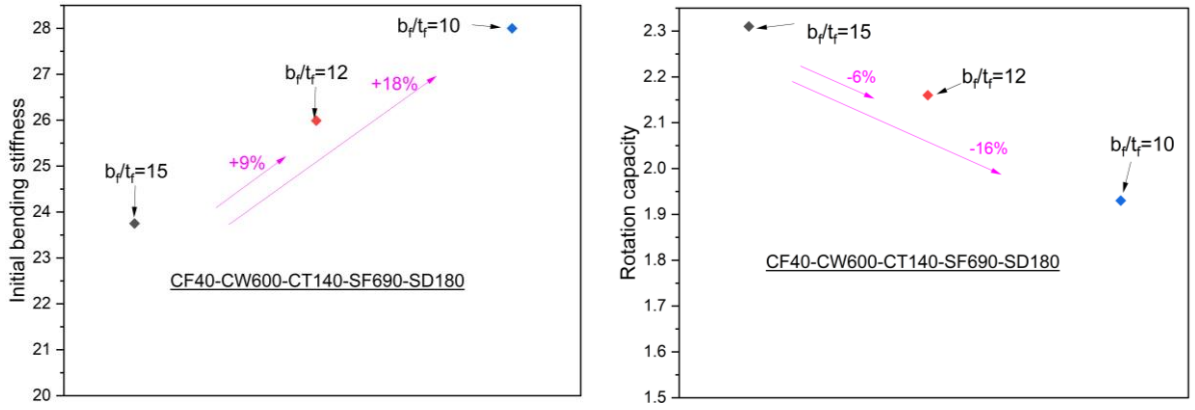

(a) (b)

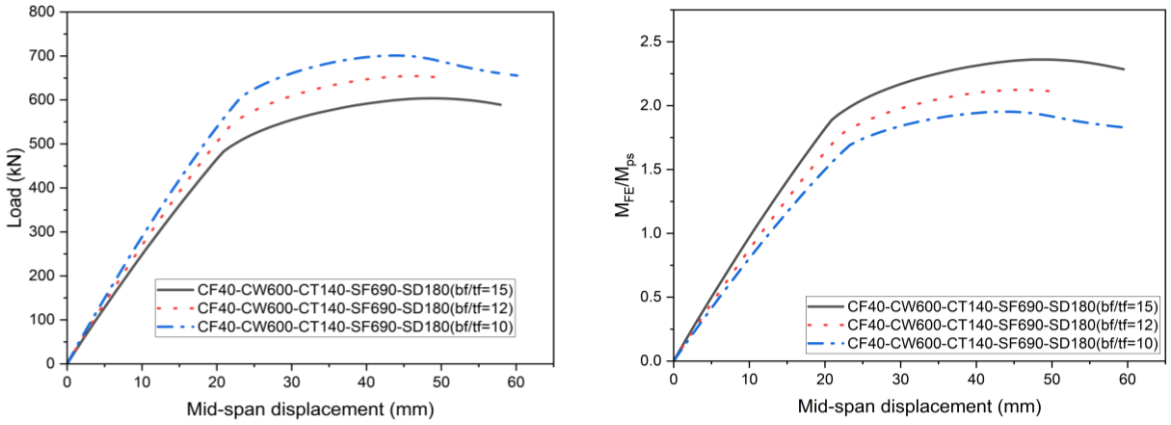

(c) (d)

Fig. 15. Effect of b_f/t_f on flexural strength of HSS-ECC beam: (a) Initial bending stiffness; (b) Rotation capacity; (c) Load carrying capacity; (d) Normalised bending moment capacity

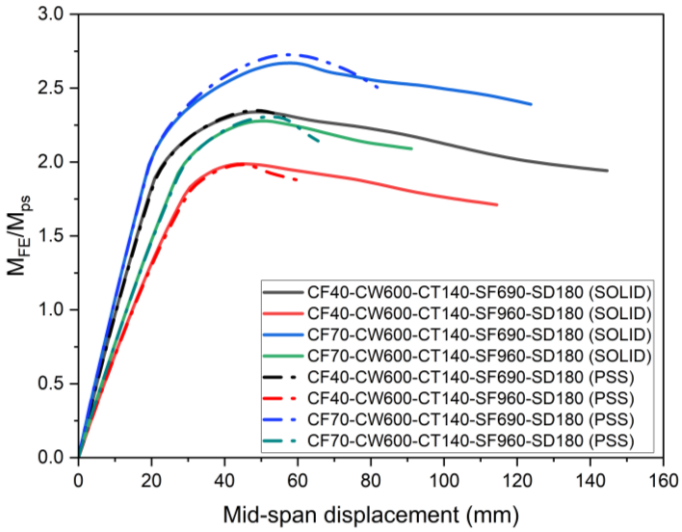

Fig. 16. Effect of slab types on M_{FE}/M_{ps} of HSS-ECC beams

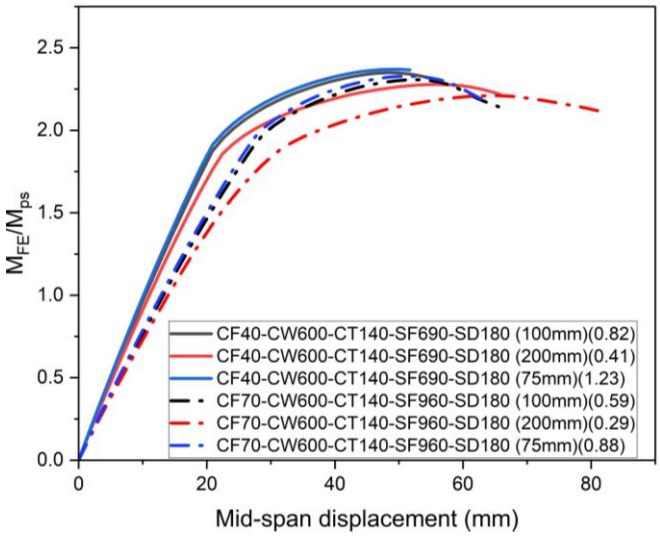

Fig. 17. Effect of shear stud spacing/degree of shear connection (η) on M_{FE}/M_{ps} of HSS-ECC beam. The number in the legend in the first bracket followed by mm is the value of s_{stud} and the number in the second bracket is the value of η

Figure 17 also illustrates that beams with s_{stud} of 75 mm and 100 mm exhibited similar bending behaviors because they shared a comparable degree of η. For instance, for CF40-SF690 Beam, s_{stud} of 100 mm resulted in η = 0.82, which is close to unity, indicating near-full shear connection. Thus, reducing s_{stud} to 75 mm and achieving full shear connection, beams' behaviour is almost similar. As anticipated, beams with s_{stud} of 200 mm showed significant differences compared to those with s_{stud} of 75 mm due to a substantially lower shear connection degree.

5. Conclusions

This paper thoroughly examined the effect of various parameters, categorized into three groups: mechanical properties of materials, cross-section dimensions, and construction details, on the bending behavior composite beams made of high strength steel (HSS) girder and engineered cementitious composites (ECC) slab through a parametric investigation. The bending behavior of 136 HSS-ECC composite beams was simulated using a validated nonlinear finite element (FE) model. The bending performance was assessed based on three indicators, including initial bending stiffness, rotation capacity, and flexural strength. The following concluding remarks can be given according to the parametric analysis results:

- The initial bending stiffness of HSS-ECC beam can be substantially improved to more than 50% by increasing the compressive strength of ECC, ECC slab width and ECC slab thickness as well as HSS section depth. However, the increase in HSS section web height to web thickness ratio, HSS section flange width to flange thickness ratio and shear stud spacing led to a considerable decrease in the initial bending stiffness of HSS-ECC beam. The influences of the HSS tensile strength and ECC slab type were found to be negligible.
- For rotation capacity, it was found that the increase in the compressive strength of ECC material, ECC slab width, HSS section depth, HSS section flange width to flange thickness ratio, HSS section web height to web thickness ratio and shear stud spacing resulted in a substantial enhancement in the rotation capacity of HSS-ECC beam. In contrast, the increase in the HSS yield strength, ECC slab thickness led to a significant decrease in the rotation capacity of the HSS-ECC beam. It was found that ECC slab type had almost no effect on the HSS-ECC beam's rotation capacity.
- For normalized bending moment capacity, it can be substantially enhanced by increasing the material property and dimensions of ECC slab (i.e., compressive strength, slab width and slab thickness). In contrast, the increase in the material property and dimensions of HSS section (i.e., tensile strength, section depth, section web height to web thickness ratio) led to a significant decrease in the normalized bending moment capacity of HSS-ECC beams. On the other hand, the increase of section flange width to flange thickness ratio and shear stud spacing resulted in the rise of the normalized bending moment capacity. In all four groups of material properties, beams with ECC of 70 MPa compressive strength and 690 MPa HSS tensile strength (group 70-690) show highest normalized bending capacity while the least accounting for the 40-960 group.

References

[1] Uy B. Stability and ductility of high-performance steel sections with concrete infill. Journal of Constructional Steel Research, 2008, 64(7-8): 748-754. https://doi.org/10.1016/j.jcsr.2008.01.036

[2] Kim C. S., Park H. G., Chung K. S., and Choi I. R. Eccentric axial load capacity of high-strength steel-concrete composite columns of various sectional shapes. Journal of Structural Engineering, 2014, 140(4): 04013091.3. https://doi.org/10.1061/(ASCE)ST.1943-541X.0000879

[3] Khan M. K. I., Rana M. M., Zhang Y., and Lee C. K. Behaviour of engineered cementitious composite-encased stub concrete columns under axial compression. Magazine of Concrete Research, 2020, 72(19): 984-1005. https://doi.org/10.1680/jmacr.19.00111

[4] Sheta A., Ma X., Zhuge Y., ElGawady M., Mills J. E., & Abd-Elaal E. Axial compressive behaviour of thin-walled composite columns comprise high-strength cold-formed steel and PE-ECC. Thin-Walled Structures, 2023, 184: 110471. https://doi.org/10.1016/j.tws.2022.110471

[5] Shi G., Zhou W., Bai Y., and Lin C. Local buckling of 460 MPa high strength steel welded section stub columns under axial compression. Journal of Constructional Steel Research, 2014, 100: 60-70. https://doi.org/10.1016/j.jcsr.2014.04.027

[6] Shi G., Ban H., and Bijlaard F.S.K. Tests and numerical study of ultra-high strength steel columns with end restraints. Journal of Constructional Steel Research, 2012, 70: 236-247. https://doi.org/10.1016/j.jcsr.2011.10.027
[7] Shi G., Zhou W., and Lin C. Experimental investigation on the local buckling behavior of 960 MPa high strength steel welded section stub columns. Advances in Structural Engineering, 2015, 18. https://doi.org/10.1260/1369-4332.18.3.423
[8] Shi G., Xu K., Ban H., and Lin C. Local buckling behavior of welded stub columns with normal and high strength steels. Journal of Constructional Steel Research, 2016, 119: 144-153.9. https://doi.org/10.1016/j.jcsr.2015.12.020
[9] Ban H., Shi G., Shi Y., and Bradford M. A. Experimental investigation of the overall buckling behaviour of 960 MPa high strength steel columns. Journal of Constructional Steel Research, 2013, 88: 256-266. https://doi.org/10.1016/j.jcsr.2013.05.015
[10] Rasmussen K. and Hancock G. Tests of high strength steel columns. Journal of Constructional Steel Research, 1995, 34: 27-52. https://doi.org/10.1016/0143-974X(95)97296-A
[11] Jixiang X. and Zhang Y. Seismic performance of the extended end-plate high-strength steel beam-to-column connections after fire. Structures. 2024, 70. https://doi.org/10.1016/j.istruc.2024.107786
[12] Fangxin H. and Wang Z. Cyclic behavior of high-strength steel beam-to-column welded flange-bolted web connections. Thin-Walled Structures, 2024, 201: 111999. https://doi.org/10.1016/j.tws.2024.111999
[13] Coelho A.M.G. and Bijlaard F.S. Experimental behaviour of high strength steel end-plate connections. Journal of Constructional Steel Research, 2007, 63(9): 1228-1240. https://doi.org/10.1016/j.jcsr.2006.11.010
[14] Jiang S., Shi G., Zhang N., Hou L., and Zhao H. Experimental study on seismic behavior of high strength steel flange-plate connections with box columns. Thin-Walled Structures, 2024, 194: 111285. https://doi.org/10.1016/j.tws.2023.111285
[15] Jiang S., Shi G., Zhang N., Zhao H., and Sun T. Experimental study on seismic behavior of cover-plate connections between steel beams and high strength steel box columns. Thin-Walled Structures, 2023, 193: 111208. https://doi.org/10.1016/j.tws.2023.111208
[16] Kabir, M.I., et al., Flexural behaviour of ECC-LWC encased slender high strength steel composite beams. Journal of Constructional Steel Research, 2020. 173: p. 106253. https://doi.org/10.1016/j.jcsr.2020.106253
17. Kabir, M.I., et al., Strength enhancement of high strength steel beams by engineered cementitous composite encasement. Engineering Strength, 2020. 207 p. 110288. https://doi.org/10.1016/j.engstruct.2020.110288
[18] Liu Z., Zhang,Y., Wang X., Chen Z., Xue J., and Ren B. Experimental study on the flexural response of UHPC beams encased high-strength section steel. Engineering Structures, 2025, 336: 120466. https://doi.org/10.1016/j.engstruct.2025.120466
[19] Hao N., Yang Y., Xue Y., Xu L., Feng S., Yu Y., and Huang B. Shear performance of partially encased composite beams with high-strength steel and UHPC. Journal of Constructional Steel Research, 2023, 211: 108217. https://doi.org/10.1016/j.jcsr.2023.108217
[20] Uy, B. and R. Sloane, Behavior of composite tee beams constructed with high strength steel. Journal of Constructional Steel Research, 1998, 1: 203-204. https://doi.org/10.1016/S0143-974X(98)00126-6
[21] Zhao H. and Yuan Y. Experimental studies on composite beams with high-strength steel and concrete. Steel and Composite Structures, 2010, 10(5): 373-383. https://doi.org/10.12989/scs.2010.10.5.373
[22] Ban H. and Bradford M.A. Flexural behaviour of composite beams with high strength steel. Engineering Structures, 2013, 56: 1130-1141. https://doi.org/10.1016/j.engstruct.2013.06.040
[23] Shamass R. and Cashell K.A. Behaviour of Composite Beams Made Using High Strength Steel. Structures, 2017, 12: 88-101. https://doi.org/10.1016/j.istruc.2017.08.005
[24] Ban H., Bradford M. A., Uy B., and Liu X. Available rotation capacity of composite beams with high-strength materials under sagging moment. Journal of Constructional Steel Research, 2016, 118: 156-168. https://doi.org/10.1016/j.jcsr.2015.11.008
[25] Ban H. and Bradford M.A. Elastoplastic cross-sectional behavior of composite beams with high-strength steel: analytical modeling. Journal of Structural Engineering, 2015, 141(10): 04014236. https://doi.org/10.1061/(ASCE)ST.1943-541X.0001208
[26] Jun S.-C., Lee C.-H., Han K.-H., and Kim J.-W. Flexural behavior of high-strength steel hybrid composite beams. Journal of Constructional Steel Research, 2018, 149: 269-281. https://doi.org/10.1016/j.jcsr.2018.07.020
[27] Nguyen C.-L. and Lee C.-K. Experimental study of flexural behaviour of high strength steel (HSS) - Engineered Cementitious Composites (ECC) composite beam with profiled steel sheeting. ce/papers, 2021, 4: 781-786. https://doi.org/10.1002/cepa.1361

[28] Nguyen C. L. and Lee C.K. Flexural behaviours of Engineered Cementitious Composites - High strength steel composite beams. Engineering Structures, 2021, 249. https://doi.org/10.1016/j.engstruct.2021.113324
[29] Lee S. W., Kang S.-B., Tan K. H., and Yang E.-H. Experimental and analytical investigation on bond-slip behaviour of deformed bars embedded in engineered cementitious composites. Construction and Building Materials, 2016, 127: 494-503. https://doi.org/10.1016/j.conbuildmat.2016.10.036
[30] Rana M. M., Lee C. K., and, Al-Deen S. A study on the bond stress-slip behavior between engineered cementitious composites and structural steel sections. Ce/papers, 2017, 1(2-3): 2247-2256. https://doi.org/10.1002/cepa.271
[31] Li V. C. On engineered cementitious composites (ECC) a review of the material and its applications. Journal of advanced concrete technology, 2003, 1(3): 215-230. https://doi.org/10.3151/jact.1.215
[32] Li V.C. Engineered Cementitious Composites (ECC): Bendable Concrete for Sustainable and Resilient Infrastructure, Springer, 2019. https://doi.org/10.1007/978-3-662-58438-5
[33] Emamjomeh H., Behfarnia K., Raji A., Almohammad-albakkar M. Influence of PVA and PP fibers addition on the durability and mechanical properties of engineered cementitious composites blended with silica fume and zeolite. Research on Engineering Structures and Materials, 2023; 9(2): 457-473. http://dx.doi.org/10.17515/resm2022.491me0804
[34] Yeşilmen S. Strength prediction of engineered cementitious composites with artificial neural networks. Research on Engineering Structures and Materials, 2021; 7(2): 173-182. https://doi.org/10.17515/resm2020.222ma1013
[35] Nguyen C.-L., and Lee C.-K. Development of analytical models for predicting the flexural behaviour of engineered cementitious composites-high strength steel composite beams. Advanced Steel Construction, 2023, 19(3): 197-208.
[36] Abaqus V. 6.14-1. Abaqus/standard user's manual and Abaqus CAE manual. Providence, RI, USA: Dassault Systemes Simulia Corp, 2014.
[37] Meng D., Huang T., Zhang Y. X., and Lee C. K. Mechanical behaviour of a polyvinyl alcohol fibre reinforced engineered cementitious composite (PVA-ECC) using local ingredients. Construction and Building Materials, 2017, 141: 259-270. https://doi.org/10.1016/j.conbuildmat.2017.02.158
[38] Katwal U., Tao Z., and Hassan M. K. Finite element modelling of steel-concrete composite beams with profiled steel sheeting. Journal of Constructional Steel Research, 2018, 146: 1-15. https://doi.org/10.1016/j.jcsr.2018.03.011
[39] Hassan M. K. Behaviour of hybrid stainless-carbon steel composite beam-column joints. Ph.D. Dissertation, Western Sydney University (Australia). 2016.

www.jresm.org

Research on Engineering Structures and Materials

Compendex on Engineering Village

Scopus

DRJI

TÜBİTAK ULAKBİM

ProQuest

crossref

Google Scholar

Universal Impact Factor
Scientifically derived Journal Impact Factor

SIS Scientific Indexing Services

Journal Seeker Research Bible

CiteFactor
Academic Scientific Journals

EZB Elektronische Zeitschriftenbibliothek

Open Academic Journals Index

GIF GLOBAL IMPACT FACTOR

ASOS indeks

Cosmos

Publication Forum

İNFOBASE INDEX

ROOTINDEXING
JOURNAL ABSTRACTING AND INDEXING SERVICE

Scope Database
Journal Indexing & Citation Analysis

Research Group
https://mimrg.net/